A QUANTITATIVE AND PREDICTIVE MODEL FOR MECHANOCHEMICAL KINETICS AND ITS EXPERIMENTAL VALIDATION

BY

TIMOTHY JOHN KUCHARSKI

DISSERTATION

Submitted in partial fulfillment of the requirements
for the degree of Doctor of Philosophy in Chemistry
in the Graduate College of the
University of Illinois at Urbana–Champaign, 2011

Urbana, Illinois

Doctoral Committee:

Assistant Professor Roman Boulatov, Chair
Professor Gregory S. Girolami
Professor Jeffrey S. Moore
Professor Kenneth S. Suslick

Abstract

The fact that the application of mechanical force to materials can change the reactivity of their constituent molecules (or ions) has been known for millennia, but the complexity of these multi-scale phenomena limited their partial explanation to the theoretical until the advances in micromanipulation techniques in recent decades allowed for the application of force to single molecules. Traditional theories of chemical reactivity have failed to explain the phenomenal rate enhancements observed (up to 10^{15}-fold), and though a body of empirical relationships between force and reactivity exists, a physically sound and quantitative model for mechanochemical kinetics did not. Truly taking advantage of all that mechanochemistry offers for the design of novel mechanoresponsive and actuating materials requires a clear conceptual framework describing *how* and *why* mechanical force affects chemical reactivity. This work describes the development of such a model for mechanochemical kinetics and its experimental validation using a series of paradigmatic electrocyclic and S_N2 reactions.

Pioneering a new technique for mechanochemical analysis complementary to single-molecule force experiments, we synthesized several series of macrocycles containing the reactive moieties of interest and a photoisomerizable molecular actuator, stiff stilbene (1,1′-Δ-biindan). In small enough macrocycles, irradiation with UV light generates a highly strained *E* isomer in which the reactive moiety experiences nearly uniaxial strain. The difference in reactivity between the strained and unstrained isomers is quantified experimentally, and the difference in strain between the two photoisomers is quantified as force (i.e., the gradient of energy with respect to position). Through theory and experiment, the local molecular degree of freedom which dictates a molecule's response to force is identified, and the relationship between its elongation and stretching compliance is demonstrated.

As expected by historical and contemporary thought, acceleration by tensile force is observed when the reactive moiety elongates to reach the transition state, as is observed in the electrocyclic ring opening of *trans*-3,4-dimethylcyclobutene and the hydrolysis of primary sulfonates. However, two other possibilities exist which arise from the cancellation or complete negation of scissile bond elongation: force insensitivity and inhibition by tensile force; our model predicts and explains both of these situations and also explains why the same reaction can be both accelerated by force in one direction and inhibited by force in another. In more complex

reaction sequences, such as pre-equilibrium kinetics, the application of force can even change the overall kinetic profile of a sequence of reactions. As the relative energies of transition states and minima change as increasing amounts of force are applied, the identity of the rate-determining step can change at critical amounts of force, leading to kinetic crossover, a phenomenon whose richness and complexity is underappreciated. By clarifying the fundamental relationship between force and reactivity, our model provides a deeper understanding of the operational principles of phenomena at the interfaces of chemistry, biology, soft matter physics and materials science.

Along with the description of the experimental work to validate our model for mechanochemical kinetics, this work also provides speculation for the future directions of the field of mechanochemistry, both identifying old questions that may now be assailable and new questions that have not yet been asked. Because mechanochemistry bridges the disciplines of chemistry, materials science, soft-matter physics and molecular biology, the opportunities for a clearer understanding of mechanochemical kinetics to have a broad impact on science and technology are great.

Acknowledgments

This work would not have been possible without the efforts of many past and present members of the Boulatov research group. As the second student in the group to earn a Ph.D., I am grateful to Dr. Zhen Huang, who paved the way as the group's first Ph.D. graduate and was a great colleague to interact with. I am very grateful to Dr. Qing-Zheng Yang, who provided me with many high-purity compounds, and I also thank Drs. Sergey Akbulatov and Binglin Wang for their synthetic successes. I thank Drs. Yancong Tian and Daria Khvostichenko along with Matthew Hermes and Nicholas Rubin for their computational modeling and Nicholas Rubin, Ho Yee "Ivan" Hui, Xinxin Feng, and Sizhu You for their efforts in kinetics measurements. In addition, I thank Zhen, Nick, and Matt for stimulating discussions.

I am deeply grateful to my advisor, Roman Boulatov, for being readily available, pushing me to meet high expectations, treating me like a colleague, and giving me the freedom to learn some lessons the hard way. He readily applied his keen intellect to point out the conceptual connections that I either did not see or did not verbalize, and he taught me how to formulate and answer meaningful scientific questions; his contributions to my development have been invaluable.

I thank my committee members for their suggestions and guidance. In particular, I thank Greg Girolami for his continual support, particularly regarding my involvement in the Inorganic Chemistry Gordon Research Seminars and Gordon Research Conferences as well as the Inorganic and Materials Chemistry Student-Selected Seminar Series at Illinois.

I am grateful to the many friends I have made at Illinois who helped me unwind and laugh; our paths will cross again. Special thanks to Dr. Scott Daly and Luke Davis, who not only are good friends but also were valuable colleagues to have in our conference and seminar organizing. I thank my family for their love and support, especially my wife Kate Vigour, my parents Beth and Joseph Kucharski, and Theresa "T" and Tom Vigour; you are all the best I could ever ask for. Special thanks also go to our family's resident author, T, for proofing my writing through the years. Thanks also to my grandfather Dr. J. Gerald Byrne for being a continuous inspiration and role model.

Table of Contents

List of Tables

List of Figures

Preface

This dissertation comprises eight papers and one book chapter, three of which have been (Chapter 1, Chapter 2 and Chapter 4) featured on the covers of the *Journal of Materials Chemistry*, *Nature Nanotechnology* and *Angewandte Chemie*. Four of the papers have been published,[1-4] and the remaining five are at various stages of progress (Chapter 5, Chapter 6 and Chapter 7) or publication (ref. 5 and Chapter 9). I am the lead author on three of the published works[2-4] as well as the two in the publication process (ref. 5 and Chapter 9) and am an equally-contributing author on the other published work.[1] The other two papers from the Boulatov group of which I am an author[6,7] are not described here. For the material in this dissertation, only work in which I played a major role is reported; work that was carried out mostly by others is not included in this dissertation and the published works where that content has been reported are indicated. For those works still in progress or in preparation (Chapter 5, Chapter 6, Chapter 7 and Chapter 9), the titles and author lists of the papers remain tentative.

The first chapter of this dissertation reviews the model for chemomechanical kinetics which the Boulatov lab has developed over the course of the time encompassing the other projects described in this dissertation. The following six chapters describe the results that allowed for these and further developments in a progression of increasing conceptual complexity. The penultimate chapter is a book chapter that highlights fundamental issues in the design of molecular photoactuators which involve the generation of macroscopic stresses and strains from molecular-level phenomena. The final chapter is based on a review highlighting fundamental aspects of the design of closed-system solar fuels, which involves the modulation of chemical reactivity with molecular strain. As such, both areas can benefit greatly from the insights described therein which are enabled by our understanding of chemomechanical phenomena.

During my time in the Boulatov group, I have transitioned between theoretical, synthetic and mechanistic and kinetics studies, both intellectually leading the specific area of a given project and contributing to the other areas. All of the projects in the Boulatov group are inherently collaborative efforts, and the work described here would not have been possible without the efforts of those listed as authors on the published works. The contributions of those co-authors are described in the Acknowledgments above, and the contributions of individuals to unpublished work are detailed in the Acknowledgments sections of the individual chapters. As I have done in the chapters which have been published, in those which have not yet been published (Chapter 5, Chapter 6, Chapter 7) I describe only the material for which I contributed a majority of the work. In these cases I led the kinetics efforts for the projects: I designed the kinetics experiments and carried out the majority of them, wrote all of the Matlab scripts used to fit rate constants to all of the experimental data, and conceived and carried out the NMR and/or HPLC experiments for mechanistic determination and/or stereochemical assignments (e.g., those in Chapter 6). Other details for these projects (e.g., the synthesis of siloxane- and pyrophosphate-containing macrocycles, all computational modeling) will be reported upon subsequent publication.

References

1. Yang, Q.-Z.; Huang, Z.; Kucharski, T. J.; Khvostichenko, D.; Chen, J.; Boulatov, R., A Molecular Force Probe. *Nat. Nanotechnol.* **2009**, *4*, 302–306.
2. Kucharski, T. J.; Huang, Z.; Yang, Q.-Z.; Tian, Y.; Rubin, N. C.; Concepcion, C. D.; Boulatov, R., Kinetics of Thiol/Disulfide Exchange Correlate Weakly with the Restoring Force in the Disulfide Moiety. *Angew. Chem. Int. Ed.* **2009**, *48*, 7040–7043.
3. Kucharski, T. J.; Yang, Q.-Z.; Tian, Y.; Boulatov, R., Strain-Dependent Acceleration of a Paradigmatic S_N2 Reaction Accurately Predicted by the Force Formalism. *J. Phys. Chem. Lett.* **2010**, *1*, 2820–2825.
4. Kucharski, T. J.; Boulatov, R., The Physical Chemistry of Mechanoresponsive Polymers. *J. Mater. Chem.* **2011**, *21*, 8237–8255.
5. Kucharski, T. J.; Boulatov, R., Fundamentals of Molecular Photoactuation. In *Optical Nano and Micro Actuator Technology*, Knopf, G. K.; Otani, Y., Eds. CRC Press: 2011.
6. Huang, Z.; Yang, Q.-Z.; Kucharski, T. J.; Khvostichenko, D.; Wakeman, S. M.; Boulatov, R., Macrocyclic Disulfides for Studies of Sensitized Photolysis of the S–S Bond. *Chem. Eur. J.* **2009**, *15*, 5212–5214.
7. Huang, Z.; Yang, Q.-Z.; Khvostichenko, D.; Kucharski, T. J.; Chen, J.; Boulatov, R., Method to Derive Restoring Forces of Strained Molecules from Kinetic Measurements. *J. Am. Chem. Soc.* **2009**, *131*, 1407–1409.

Chapter 1. A Physically Sound and Predictive Model for Mechanochemical Kinetics

Adapted from Kucharski, T. J.; Boulatov, R., The Physical Chemistry of Mechanoresponsive Polymers. *J. Mater. Chem.* **2011**, *21*, 8237–8255. (*invited review*). © Royal Society of Chemistry. Reproduced by permission of The Royal Society of Chemistry.

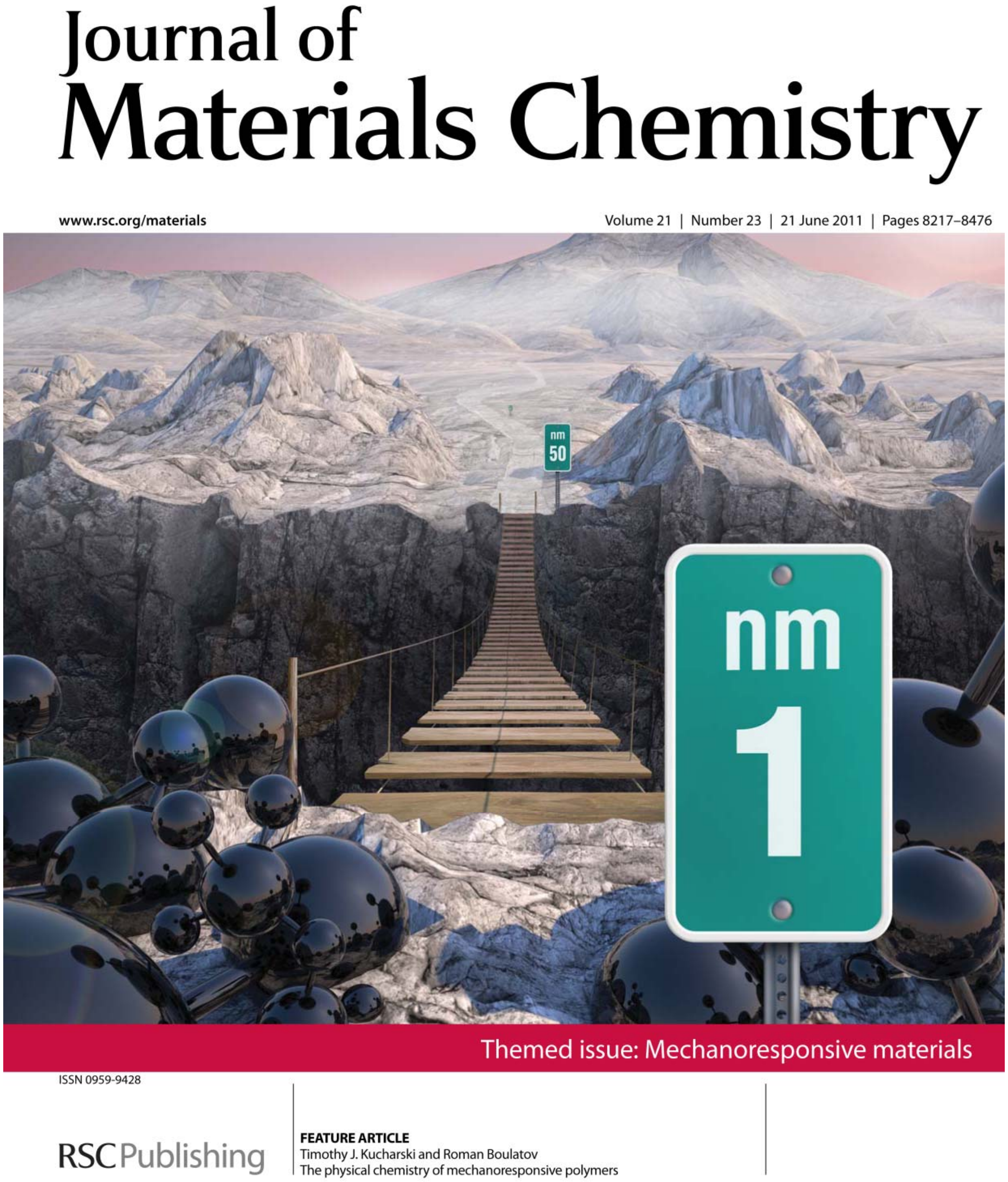

Journal of
Materials Chemistry

www.rsc.org/materials
Volume 21 | Number 23 | 21 June 2011 | Pages 8217–8476

Themed issue: Mechanoresponsive materials

ISSN 0959-9428

RSC Publishing

FEATURE ARTICLE
Timothy J. Kucharski and Roman Boulatov
The physical chemistry of mechanoresponsive polymers

The figure above reproduces the inside front cover of the June 21, 2011 issue of the *Journal of Materials Chemistry*. © Royal Society of Chemistry. Reproduced by permission of The Royal Society of Chemistry.

1.1 Abstract

Stretching a polymer can accelerate chemical reactions of its monomers by many orders of magnitude. Exploiting such effects may enable materials scientists to engineer a material's response to mesoscopic loads at the single-monomer level. Such mechanochemical coupling underlies diverse phenomena including the operation of actuating polymers, the catastrophic failure of strained materials, the behaviour of polymer flows and chemical mechanosensing. Yet, our conceptual understanding of this coupling, which cannot be described either by continuum mechanics or chemical kinetics alone, is very limited. A general, physically sound and quantitative model to relate structural distortion at any length scale to reaction rates is needed to facilitate the design of new mechanoresponsive polymers. This article reviews the state of the art of the recent effort to understand the physical chemistry of such polymers, particularly the effect of mechanical loads on the reactivity of its building blocks.

1.2 Introduction

Directional motion at meso- and macroscales (>50 nm) can dramatically affect the rates of chemical reactions (i.e., the motion of atoms at <1 nm scales). Greater than 10^{15}-fold accelerations of localized reactions in polymers subjected to micro- or macroscopic loads,[1-3] in shear flows[4-7] or at evolving interfaces[8,9] have been reported. Such dynamic coupling forms the basis of biological motility (e.g., motor proteins[10]), the operation of photoactuating polymers[11-13] and early prototypes of stress-responsive polymers.[1,2,14] It operates in both directions: large-scale loads on materials can drastically change the reactivity of their building blocks (e.g., monomers), and localized reactions can induce large-scale stresses in materials. Though these phenomena are based on the same principles, distinct terms have been suggested:[15] *mechanochemistry* for reactions that relieve macroscopic strain and *chemomechanics* for the reversible generation of macroscopic strain by chemical reactions. In this review, we will use mechanochemistry and chemomechanics interchangeably. Mechanochemical processes, such as those during the milling of materials have long been studied,[15-17] and the relevant phenomenology of mechanochemistry has been reviewed extensively.[3,12,13,18-23] Designers of stress-responsive polymers are becoming increasingly aware of the complexity of the relationships between localized reactivity and large-scale distributed stresses and the need for atomistic models of these phenomena in order for mechanochemistry to become an enabling concept in chemistry and materials science.[24] Our review describes the recent progress in developing such models.

Despite the biological[25-29] and technological[3,20,21,30,31] significance of mechanochemical phenomena, a general interpretational framework for their quantitative understanding is lacking. Mechanochemistry is fundamentally multiscale, i.e., it arises when dynamic processes at multiple length scales, from molecular to macroscopic, are correlated. In contrast, the existing dynamic models are limited to scales above ~50 nm (continuum mechanics, i.e., balance of forces in three-dimensional, or Cartesian, space) or below ~1 nm (chemical kinetics, i.e., activated escape from multidimensional energy wells). Mechanochemistry spans the "formidable gap"[31] between ~50 and ~1 nm, where molecular meets bulk and neither formalism alone is adequate (Fig. 1.1).

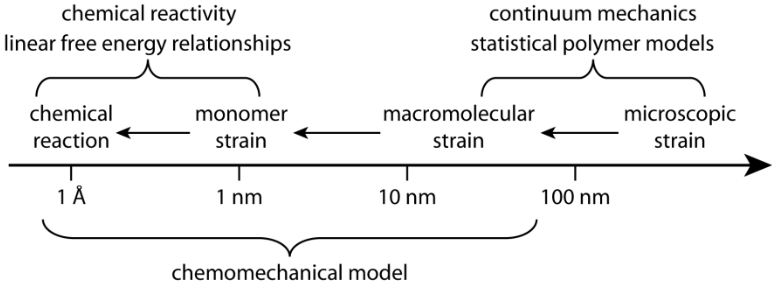

Fig. 1.1. The hierarchy of length scales involved in multiscale phenomena and the regimes of the established models that describe phenomena at various length scales (top). Because the length scales of continuum mechanics and chemical kinetics do not overlap, a new model integrating the two formalisms is required to arrive at quantitative descriptions of mechanochemical phenomena.

A quantitatively accurate model for multiscale dynamics requires a self-consistent and fundamentally sound integration of the two conventional dynamic formalisms, effectively bridging the "formidable gap".[32] From a chemist's perspective, such an integrated model is crucial for gaining a truly molecular understanding of the relationships between chemical composition, structure and mechanical properties of macromolecular systems at the single-chain and bulk levels. This understanding is, in turn, essential for the efficient design of functional materials whose molecular-level response to bulk strains is predicable and useful.

1.3 Models of Multiscale Reaction Dynamics

Chemical reactions are concerted motions of atoms that convert a reactant into the product(s). The correlation lengths (i.e., the internuclear distance over which the motion of one atom affects the motion of the other) of the vast majority of reactions studied and used by chemists rarely exceed 1 nm. The atomic motion beyond this limit remains random.[33,34] The dynamics of such reactions can be modelled by defining a few unique configurations of a small (<100) number of atoms[35] in internal mechanical equilibrium. The randomly fluctuating environment surrounding these small nuclear assemblies can be approximated by a continuum, whose average (bulk) properties, such as temperature, pressure, viscosity or dielectric constant, determine how much (or little) the structures and relative energies of the reacting molecule(s) differ from those in vacuum. The simplicity of this model—a small molecule in an isotropic continuum whose few relevant degrees of freedom represent readily measurable bulk properties of the environment—tremendously facilitates the conceptual and technical[35,36] understanding of chemical reactivity.

This strategy, however, breaks down for remarkably diverse phenomena, including ATP-powered biological motility,[25,37] active intracellular transport,[38-40] cell division,[41] and possibly mechanosensing,[42] chemical actuating materials[11,43-45] and the chemistry of material failure.[15] Their underlying chemical reactions are quite simple—hydrolysis of the pyrophosphate bond, cis/trans isomerization of an N=N bond or homolysis of a C–C bond—but the correlation lengths that control the overall molecular dynamics may span lengths from nm to microns. In other words, the concerted motion of atoms that characterizes these reaction is not limited to a few atoms whose chemical bonding changes, but involves directional translation at lengthscales of up to 1 μm.

The straightforward application of transition state theory (TST) to the kinetics of such reactions is untenable. TST relates the reaction rate (or probability) to the free-energy difference between the ground and transition states, i.e., the minimal nuclear configurations in internal mechanical equilibrium. In multiscale processes, the ground and transition states may consist of quadrillions of atoms.[29] Treating such a large number of atoms with any meaningful level of accuracy is impossible with existing computational capabilities. Even if it were possible, making sense of the results (i.e., incorporating them into chemical intuition) would require reducing the impossibly large number of variables into some collective degree of freedom and expressing it as a function of the experimental control parameters. A general strategy for such coarse-graining would obviate the need for the full atomistic description of the reacting system as it does in conventional chemical kinetics in isotropic environments.

A central question in chemistry is how to predict, from the molecular structure of the reactant, its kinetic and thermodynamic stability under a variety of conditions. A useful model of multiscale reaction dymanics must at least offer a usefully accurate answer to the question "How does the kinetic (or thermodynamic) stability of a macromolecule changes as it is stretched?" without relying on any empirical data. If the stability of the stretched macromolecule is controlled by the reactivity of one of its monomers, which is often the case for synthetic polymers and is the topic of this review, then the readily available data about the minimal reactive site should suffice to make the prediction. Below we introduce a model of such localized reactions in stretched polymers. First, we derive the model using simple intuitive arguments, which can be followed without much physicochemical background. A rigorous statistical-mechanical derivation of the model follows, which may be of interest to chemical and polymer physicists who would like to understand the assumptions and the limitations of the model.

1.4 An Intuitive Model Based on Mechanical and Chemical Coordinates

The traditional approach to describing multiscale reaction dynamics is to treat local changes in chemical bonding and structural rearrangements at the macromolecular level and beyond separately.[28,29] Such a separation of variables is justified by the vastly different time scales of the local changes in bonding, which are rare but very rapid (ps), and global structural rearrangements at scales of tens or hundreds of nm, which are far slower (μs–ms). Consequently, a model of macromolecular reaction is quite different from that of an analogous small-molecule transformation. A small reactant can be viewed as following the minimum energy reaction path (black line, Fig. 1.2A), starting from the lowest-energy nuclear configuration (ground state), progressing through the saddle point (highest-energy nuclear configuration of the path, i.e., the transition state) and relaxing directly to the minimum-energy nuclear configuration of the product. All internal degrees of freedom (bond distances, angles and dihedra) change synchronously from their values in the reactant to their values in the product.

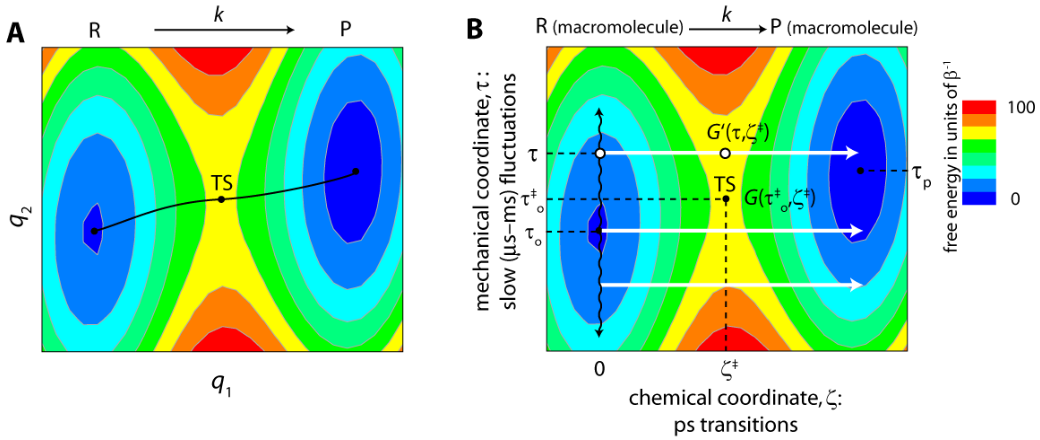

Fig. 1.2. A comparison of generic reduced-dimensionality reaction energy surfaces of a small-molecule (**A**) and a macromolecule (**B**). **A**: The small-molecule surface is a function of two internal molecular degrees of freedom q_1 and q_2, and the reacting molecule follows the minimum-energy path (black line) from the minimum-energy configuration, R, through saddle point, TS, to the minimum-energy configuration of product, P. The kinetics are described by the energy difference between the lowest-energy (on the reactant side) and highest-energy stationary points along the minimum energy path (transition state theory). **B**: The macromolecular reactant and product differ both in the pattern of local chemical bonding, described by a generalized degree of freedom, ζ (chemical coordinate), and the global structure, captured by a macroscopic degree of freedom, τ (mechanical coordinate). Because of the vastly different time scales at which local chemical bonding and global structure evolve, the conversion of the reactant to the product is modelled as two independent processes: (1) slow thermal fluctuations of the global structure (black wavy lines) that have negligible effect on the chemical bonding within the much stiffer reactive moiety ($\zeta = 0$) and (2) rare but rapid changes in local bonding in a "frozen" global environment (white arrows). The probability of the localized reaction depends on the global configuration, τ, and the overall dynamics is driven by both processes.

The equivalent reduced-dimensionality surface for a thermally activated localized reaction in a macromolecule is a function of two generalized degrees of freedom: a mechanical coordinate, τ, and a chemical coordinate, ζ, (Fig. 1.2B). These two coordinates are numbers that quantify the global geometry of the macromolecule and the pattern of chemical bonding within the reactive moiety, respectively. In contrast to a single minimum-energy reaction path, which suffices to describe the dynamics of a small reactant, a reacting macromolecule is modelled to undergo two distinct dynamic processes: slow (μs–ms) fluctuations of its global geometry (vertical black line, Fig. 1.2B) and rare but rapid (ps) changes in chemical bonding within the reactive moiety (white horizontal lines).

The two processes are assumed to occur largely independently of each other: fluctuations of the global geometry, which is considerably more compliant than the localized reactive moiety, do not affect bonding within the reactive moiety. And highly localized chemical (covalent) bonding rearranges too fast for the global geometry to adapt synchronously. In other words, the concerted motion of atoms required to change the pattern of covalent bonding from that in the macromolecular reactant to that in macromolecular product occurs within an essentially frozen macromolecular environment, which subsequently adapts (relaxes) to the new local geometry.

In this model, each global geometry acts as a unique reactant, with its own characteristic probability of undergoing change in chemical bonding. The overall reaction rate constant, k, is the product of the probabilities that (1) a global geometry, τ, is populated, $\rho(\tau)$, and (2) the reactive site will change its local bonding pattern, $k(\tau)$.

As any model, the two described above are simplified descriptions of the phenomena. The minimum-energy reaction path is an average of many paths followed by an ensemble of small reactants.[34] Likewise, there is no strict separation of global and local degrees of freedom of macromolecular reactants. Nonetheless, the two models allow quantitatively-accurate predictions of reaction dynamics in many systems of practical interest.

The popular Brownian ratchet and power stroke models[25,28,29] are the limiting cases of the chemomechanical formalism described above in which the local reaction is assumed to occur in a single global configuration: either that of the product, τ_p, (Brownian ratchet, Fig. 1.3) or reactant (power stroke). In a "Brownian-ratchet" reaction the thermally-populated high-energy conformer of the reactant, τ_p, is "trapped" by the "instantaneous" local change in chemical bonding. Mathematically, the Brownian ratchet model corresponds to $k(\tau) \equiv 0$ for all macromolecular conformations except that of the strain-free product ($\tau = \tau_p$). At the other extreme, in the power stroke model a local change in covalent bonding generates a strained macromolecule with the global geometry of the reactant ($\tau = 0$), which then relaxes to τ_p. Mathematically, the power stroke model corresponds to $k(\tau) \equiv 0$ for all conformations τ except $\tau = 0$. These models are popular in biophysics because they require minimal chemical information, and the values of $k(\tau_p)$ or $k(0)$ are usually selected to reproduce the observed or postulated macromolecular conformational dynamics, rather than the underlying chemistry.

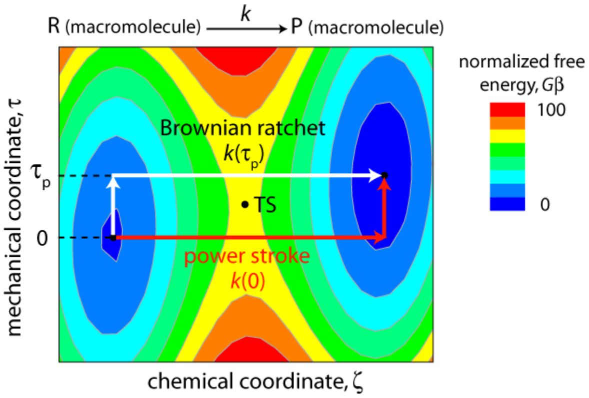

Fig. 1.3. Two limiting cases of the chemomechanical model: the Brownian ratchet in which the localized reaction occurs only in the macromolecular conformation corresponding to the strain-free product (τ_p) and the power stroke model in which the localized reaction proceeds only in the macromolecular conformation of the strain-free reactant. In the Brownian ratchet model, the localized reaction "traps" the unstable macromolecular conformation, in chemical analogy to the Feynman ratchet.[29] In the power stroke model, the overall transformation resembles that of a macroscopic motor, in which the free energy of a chemical reaction is used to create a strained state, followed by its relaxation to the (new) equilibrium geometry, τ_p. This relaxation can, in theory, be used to perform work on an external object.

Both models are essentially continuum (macroscopic) constructs: the Brownian ratchet derives from the gedanken Feynman ratchet with the local reaction replacing the microscopic pawl and the power stroke model is analogous to the deterministic description of macroscopic motors. Indeed, both models have been criticized for misrepresenting the fundamental aspects of coupling between mechanical (global) and chemical (local) dynamics.[46]

As appealing as these two models are in their simplicity, they offer few, if any, insights that could help a synthetic chemist design new molecules or reactions to exploit the directionality of coupling between local changes in chemical bonding and large-scale changes in strain that characterizes chemomechanical phenomena.

1.5 Molecular and Materials Strains Are Qualitatively Different Concepts

Mechanochemical processes occur when localized reactions result in the dissipation or build-up of large-scale, persistent and anisotropic strains in the environment. The importance of strains in mechanochemistry may lead to a false conclusion that the existing formalism relating molecular strain and reaction kinetics, based on linear free energy relationships (LFERs[33,47]), may suffice in understanding chemical reactivity in multiscale phenomena. Chemists have long studied reactions of strained molecules. However, whereas strain in materials science is defined rigorously and quantitatively,[48] molecular strain is qualitative, and consequently, there is no numerical relationship between the two concepts. A molecule is said to be strained if (some of) its internal coordinates (internuclear distances, angles and dihedra) deviate from their "standard" values. However, because such internal coordinates are not independent, no overall standard geometry can be defined against which to compare the strained molecule to calculate its total strain (normal modes are independent, but it is impossible to define the standard value of a normal mode since no two molecules, one strained and one strain-free, exist that have identical normal modes).

Consequently, chemists quantify molecular strain not geometrically, but energetically, using ground-state strain energy, ΔH_{strain}. It is usually defined as the difference of standard enthalpies (or free energies) of a reaction of the strained molecule and its strain-free analog. For example, the standard enthalpy of hydrogenation of cyclooctyne, cyclononyne and cyclodecyne are -69 kcal/mol, -62 kcal/mol and -56 kcal/mol, respectively.[49] Relative to c-$C_{10}H_{14}$, c-C_8H_{10} and c-C_9H_{12} are strained by 13 and 6 kcal/mol, respectively. This data allows a rough estimate of the acceleration of cyclooctyne reactions relative to cyclodecyne (or any unstrained alkyne). In the simplest estimate, we can assume that a fraction of the ground-state strain energy of c-C_8H_{10} is relieved in the transition state; if this fraction is 50%, $\sim 10^4$-fold acceleration is expected at room temperature.

The linear free energy relationships that originate from the Hammond-Leffler postulate[33] and underlie Marcus theory allow a more sophisticated estimate, but require additionally the standard enthalpy of the strain-free reaction, ΔH_{o} (eq. (1.1), where $\Delta H_{\text{o}}^{\ddagger}$ is the activation enthalpy of the strain-free reaction). Such estimates, however crude, have been remarkably useful in guiding attempts to control reaction rates through molecular structure.[50-54] For example, alkyl azides add to cyclooctyne $\sim 10^4$-fold faster than to strain-free alkynes, allowing the use of click chemistry in living organisms.[55]

$$\Delta H^{\ddagger}_{\text{strain}} = \Delta H^{\ddagger}_{\text{o}} - \frac{\Delta H_{\text{strain}}}{2} - \frac{\Delta H_{\text{strain}}(\Delta H_{\text{strain}} + \Delta H_{\text{o}})}{8\left(\sqrt{\Delta H^{\ddagger\,2}_{\text{o}} - \Delta H_{\text{o}}\Delta H^{\ddagger}_{\text{o}}} - 0.5\Delta H_{\text{o}} + \Delta H^{\ddagger}_{\text{o}}\right)} \tag{1.1}$$

This formalism, however, cannot be used to estimate changes in reaction kinetics in multiscale processes. Consider a long flexible inert polymer chain containing a single reactive moiety. We would like to estimate how stretching this polymer changes the kinetic (or thermodynamic) stability of this moiety. The simplest way of controllably stretching a single macromolecule is to attach its termini to a tip of an atomic force microscope (AFM) cantilever and a piezoelectric stage or to a pair of micron-size polymer spheres (so-called microscopic force probes).[56] The polymer is stretched by retracting the piezoelectric stage or separating the polymer spheres in a laser or hydrodynamic trap.[57] This non-equilibrium separation of the microscopic probes is maintained by exerting force on them. In the first approximation, the applied time-average force (so-called "mechanical" force) can be equated with the macromolecular force, f_τ, the gradient of macromolecular strain energy along the molecular axis defined by its termini.

The macromolecular strain energy depends on the total size, composition and strain of the macromolecule. On the other hand, the properties of the reactive moiety should be independent of the composition of the polymer beyond that in its immediate vicinity because of the local nature of wavefunctions. Consequently, the relationship between activation energy of a localized reaction and macromolecular strain energy is not unique to each reaction, but depends on non-reactive parts of the polymer, negating any potential utility of LFERs.

1.6 Molecular Restoring Force Rather Than Strain Energy Relates Strain and Reactivity

Unlike LFERs, the chemomechanical formalism allows the question posed in the preceding section—how the rate of a localized reaction changes as a polymer containing the reactive moiety is stretched—to be answered generally. A stretched macromolecule can be modelled as a macromolecule coupled to a constraining potential across its internal coordinate τ (usually an internuclear distance). We will assume that τ is the end-to-end separation of the polymer (i.e., the polymer is stretched at its termini). In the simplest case, the constraining potential is harmonic and characterized by a single non-fluctuating compliance, λ_c, and equilibrium distance, q_c (Table 1.1 defines all relevant variables used in this section).

Table 1.1. Variables of the intuitive model of force-dependent kinetics

τ	"mechanical" coordinate: the constrained macromolecular degree of freedom
τ_0	Strain-free contour length of the polymer in the ground state

Table 1.1 (cont.)

$\tau_o^{\ddagger}$	Strain-free contour length of the polymer in the transition state
$\Delta\tau^{\ddagger}$	Contour length difference between the ground and transition states of localized reaction
q_l	Internal coordinate of the reactive site satisfying the conditions of local approximation
ζ	Chemical coordinate: a descriptor of the pattern of chemical bonding in the reactive site
$k(\tau)$	Rate constant of a localized reaction in a macromolecule with an end-to-end distance of τ
$k(f_\tau)$	The rate constant for a Helmholtz ensemble of constrained macromolecular reactants defined by "mechanical" force f_τ
$\rho(\tau)$	Probability density function of macromolecular end-to-end distance
f_τ	"mechanical" force; restoring force of the constrained macromolecular degree of freedom
λ_c, q_c	Harmonic compliance and equilibrium distance of the constraining potential
λ_τ	Harmonic compliance of the contour length of the polymer (superscripts R and ‡ refer to the ground and transition states, respectively)
β	Inverse thermal energy
$G(\tau,\zeta)$	Free energy of the macromolecule with end-to-end distance τ and chemical coordinate ζ
$\Delta G_o^{\ddagger}$	Approximate free energy of activation of a localized reaction in a free macromolecule

Flexible macromolecules have very many conformers, i.e., their energy surface is very corrugated. For simplicity, we will ignore this corrugation and model the surface around the reactant (or transition state) as a single harmonic well centred at τ_o and characterized by harmonic compliance λ_τ. The subsequent section discusses the case of multiple conformers.

Macromolecular force-extension curves are generally anharmonic until the end-to-end distance approaches the contour length (Fig. 1.4). We will therefore assume that the conformational basin is centred at the ground vibrational state of the strain-free macromolecular conformer with the longest end-to-end distance, i.e., that τ_o is the contour length of the polymer. For example, this conformer would be all-anti for simply polyalkanes, polyethers, etc. The subsequent section discusses a general case. The focus on reactions in macromolecules stretched close to or more than their contour length (overstretched polymers) is justified because localized rearrangements of covalent bonds (which is the focus of this review) are characterized by high activation barriers (>>β^{-1}) and modest sensitivities to molecular strain. Consequently, significant accelerations of localized reactions are typically observed at forces >500 pN.

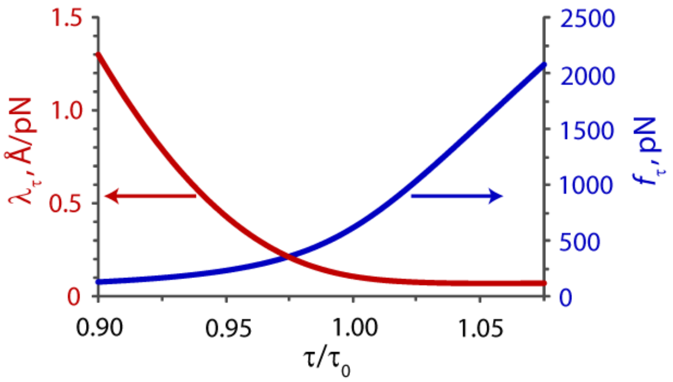

Fig. 1.4. The compliance (λ_τ, red) and restoring force (f_τ, blue) of a single molecule of polyethylene as a function of its strain τ/τ_o.[58,59] Calculated for τ_o = 150 nm from parameters in ref. 60.

Our objective is to derive the ensemble-average rate constant, $k(f_\tau)$ for a polymer whose restoring force at equilibrium is f_τ. This rate constant is given by eq. (1.2), where $\rho(\tau, f_\tau)$ is the probability density function of τ and $k(\tau)$ is the reaction rate constant in a macromolecule with end-to-end distance τ (Fig. 1.2B).

$$k(f_\tau) \propto \int_{-\infty}^{\infty} \rho(\tau, f_\tau) k(\tau) d\tau \tag{1.2}$$

In the classical harmonic oscillator limit, thermal fluctuations of the unconstrained macromolecular geometry increase its energy (relative to the vibrational ground state of the minimum-energy conformer) by $(\tau - \tau_o)^2/2\lambda_\tau$. The end-to-end distance of the vibrational ground state of the same macromolecule coupled to a harmonic constraining potential with compliance λ_c and equilibrium distance q_c is determined by the condition of internal mechanical equilibrium, i.e., $\tau_c = (\tau_o\lambda_c + q_c\lambda_\tau)/(\lambda_c + \lambda_\tau)$. The energy of this ground vibrational state, relative to that of the separated free macromolecule and the constraining potential is $(\tau_c - \tau_o)^2/2\lambda_\tau + (\tau_c - q_c)^2/2\lambda_c$ = $(\tau_o + q_c)^2/2(\lambda_c + \lambda_\tau)$ = $(\lambda_c + \lambda_\tau)f_\tau^2/2$. Thermal fluctuations of the end-to-end distance of the coupled system away from τ_c increase its energy by $(\lambda_c^{-1} + \lambda_\tau^{-1})(\tau - \tau_c)^2/2$ = $(\lambda_c^{-1} + \lambda_\tau^{-1})(\tau - \tau_o - \lambda_\tau f_\tau)^2/2$. Assuming a Boltzmann distribution[46] of macromolecular conformations gives eq. (1.3) for the classical probability density function $\rho(\tau, f_\tau)$, where β is inverse thermal energy.

$$\rho(\tau, f_\tau) = \sqrt{\frac{\beta(\lambda_\tau^{-1} + \lambda_c^{-1})}{2\pi}} e^{-(\lambda_\tau^{-1} + \lambda_c^{-1})(\tau - f_\tau\lambda_\tau - \tau_o)^2 \beta/2} \tag{1.3}$$

The canonical transition state theory expression[34] for $k(\tau)$ is given by eq. (1.4), where $G(\tau, 0)$ and $G(\tau,\zeta^{\ddagger})$ are the free energies of the ground and transition states, respectively, with end-to-end distance τ.

$$k(\tau) \propto e^{-\left(G(\tau,\zeta^{\ddagger})-G(\tau,0)\right)\beta} \tag{1.4}$$

Consequently, the evaluation of eq. (1.2) requires the function $G(\tau,\zeta)$at least at $\zeta = 0$ and $\zeta = \zeta^{\ddagger}$. Empirical steered molecular dynamics simulations can now yield estimates of $G(\tau,\zeta)$ for the unfolding of biopolymers during which only weak non-covalent chemical interactions rearrange.[61] This approach, however, is not yet possible for covalent reactions, whose transition states require quantum-chemical descriptions. Quantum-mechanical steered molecular dynamics simulations have been limited to only very simple reactions in small molecules under very high straining rates.[62-65] Because of the prohibitive scaling of quantum-chemical methods with the size of the reactant, such dynamic calculations are likely to remain non-routine for years. Consequently, the design of monomers and reactions for mechanoresponsive polymers cannot rely on dynamic calculations to identify candidates with desired strain-rate profiles. Instead, as is the case in conventional chemistry, a model is required to estimate reactivity from static properties of the reactants (e.g., their energies) and the macroscopic control parameters.

In the harmonic regime assuming that the reactive site is much stiffer than τ allows $G(\tau,\zeta)$ to be expanded around the strain-free ground and transition states up to quadratic terms (eqs. (1.5)–(1.6), where $\tau_{\mathrm{o}}^{\ddagger}$ is macromolecular contour length of the strain-free transition state (Fig. 1.2B), $\lambda_{\tau}^{\mathrm{R}}$ and $\lambda_{\tau}^{\ddagger}$ are the apparent harmonic stretching compliances of τ in the ground and transition states, and $\Delta G_{\mathrm{o}}^{\ddagger}$ is approximately the free energy of activation of the reaction in the unconstrained polymer).

$$G(\tau,0) = G(\tau_{\mathrm{o}},0) + \frac{\partial G(\tau_{\mathrm{o}},0)}{\partial \tau}(\tau-\tau_{\mathrm{o}}) + \frac{\partial^2 G(\tau_{\mathrm{o}},0)}{\partial \tau^2}\frac{(\tau-\tau_{\mathrm{o}})^2}{2} + \cdots \approx \frac{(\tau-\tau_{\mathrm{o}})^2}{2\lambda_{\tau}^{\mathrm{R}}} \tag{1.5}$$

$$\begin{aligned} G(\tau,\zeta^{\ddagger}) &= \Delta G_{\mathrm{o}}^{\ddagger} + \frac{\partial G\left(\tau_{\mathrm{o}}^{\ddagger},\zeta^{\ddagger}\right)}{\partial \tau}\left(\tau-\tau_{\mathrm{o}}^{\ddagger}\right) + \frac{\partial^2 G\left(\tau_{\mathrm{o}}^{\ddagger},\zeta^{\ddagger}\right)}{\partial \tau^2}\frac{\left(\tau-\tau_{\mathrm{o}}^{\ddagger}\right)^2}{2} + \cdots \\ &\approx \Delta G_{\mathrm{o}}^{\ddagger} + \frac{\left(\tau-\tau_{\mathrm{o}}^{\ddagger}\right)^2}{2\lambda_{\tau}^{\ddagger}} \end{aligned} \tag{1.6}$$

Combining eqs. (1.2)–(1.6) yields eq. (1.7) for the ratio of the net rate constants in a strain-free macromolecule, k_o, and in the macromolecule stretched to restoring force f_τ, $k(f_\tau)$. Eq. (1.7) reduces to eq. (1.8) if $\lambda_\mathrm{c} + \lambda_\tau^\ddagger > 0$.

$$\frac{k(f_\tau)}{k_\mathrm{o}} = \frac{e^{-\Delta G_\mathrm{o}^\ddagger \beta} \int_{-\infty}^{\infty} e^{-\left(\left({\lambda_\tau^\mathrm{R}}^{-1} + {\lambda_\mathrm{c}}^{-1}\right)(\tau - f_\tau \lambda_\tau - \tau_\mathrm{o})^2 + \left(\tau - \tau_\mathrm{o}^\ddagger\right)^2 / \lambda_\tau^\ddagger - (\tau - \tau_\mathrm{o})^2 / \lambda_\tau^\mathrm{R}\right)\beta/2} d\tau}{e^{-\Delta G_\mathrm{o}^\ddagger \beta} \int_{-\infty}^{\infty} e^{-\left((\tau - \tau_\mathrm{o})^2/\lambda_\tau^\mathrm{R} + \left(\tau - \tau_\mathrm{o}^\ddagger\right)^2 / \lambda_\tau^\ddagger - (\tau - \tau_\mathrm{o})^2/\lambda_\tau^\mathrm{R}\right)\beta/2} d\tau} \tag{1.7}$$

$$\beta^{-1} \ln \frac{k(f_\tau)}{k_\mathrm{o}} \approx \frac{\lambda_\tau^\mathrm{R} + \lambda_\mathrm{c}}{\lambda_\tau^\ddagger + \lambda_\mathrm{c}} \left(f_\tau \Delta\tau^\ddagger + \frac{f_\tau^2}{2} \Delta\lambda_\tau^\ddagger \right) - \frac{{\Delta\tau^\ddagger}^2}{\lambda_\tau^\ddagger + \lambda_\mathrm{c}} \tag{1.8}$$

The f^2 term quantifies Hammond effects,[66] the differential destabilization of the ground and transition states because their harmonic compliances are different. The empirical Eyring–Bell–Evans[67-70] (EBE) ansatz (eq. (1.9)) is a limiting case of eq. (1.8) for an "infinitely" compliant constraining potential ($\lambda_\mathrm{c} \rightarrow \infty$) and neglected Hammond effects. The EBE equation can also be derived from Kramers theory,[71] but in that approach inclusion of the 2nd-order (Hammond) effects becomes problematic and the molecular interpretation of τ is uncertain.[72]

$$\beta^{-1} \ln \frac{k(f_\tau)}{k_\mathrm{o}} \xrightarrow[\substack{\lambda_\mathrm{c} \rightarrow \infty \\ \Delta\lambda_\tau^\ddagger \rightarrow 0}]{} f_\tau \Delta\tau^\ddagger \tag{1.9}$$

Although the chemomechanical formalism clearly defines the molecular meaning of the "mechanical" force and the corresponding mechanical coordinate, eq. (1.8) is not practical, because the values of $\Delta\tau^\ddagger$ and $\Delta\lambda_\tau^\ddagger$ are not available. After introducing a statistical mechanical model, we show that eq. (1.8) can be written in terms of a local internal coordinate of the reactive moiety instead of the macromolecular degree of freedom that is being controlled macroscopically.[73-78] Such an equation allows predictions of changes in the kinetic stability of polymers upon stretching.

1.7 Free Energy of a Canonical Ensemble of Stretched Macromolecules

Coarse-grained statistical mechanics of an ensemble of individual macromolecules stretched by micromanipulation techniques is well developed.[79,80] Two limiting cases are generally considered: stretching by an "infinitely" soft or by an "infinitely" stiff constraining potential. These are sometimes called Helmholtz and Gibbs ensembles, because an infinitely soft constraining potential yields constant (non-fluctuating) restoring force of the constrained degree of freedom, whereas an infinitely stiff constraining potential corresponds to stretching under non-fluctuating extension of the constrained degree of freedom. In other words, Helmholtz and Gibbs ensembles are created by imposing additional conditions on the standard canonical ensemble (constant temperature, T; volume, V and composition, n) of macromolecules by holding constant either the constraining force, f_c, or the extension, respectively. The two limits are popular because they yield force-extension curves that depend only on the averaged properties of the macromolecule, without any contribution of the constraining potential. They also simplify the task of connecting computations (e.g., steered molecular dynamics simulations of individual macromolecules under tensile constraints) with single-molecule force experiments.

Here we will introduce a general statistical mechanical model of the activation barrier of a localized reaction for a canonical ensemble of stretched macromolecules without any additional constraints. All variables used in this section are defined in Table 1.2.

Table 1.2. Variables of statistical mechanical model of activation energies in stretched polymers

$\boldsymbol{Q}$	$3N$–6×1 column vector of non-redundant independent internal coordinates of a molecule
$\boldsymbol{Q}^{\mathrm{o}}$	$3N$–6×1 column vector of non-redundant independent internal coordinates defining the ground vibrational state of a free molecule
$\boldsymbol{Q}_{\mathrm{c}}{}^{\mathrm{o}}$	$3N$–6×1 column vector of non-redundant independent internal coordinates defining the ground vibrational state of a molecule coupled to a constraining potential
$U(\boldsymbol{Q})$	Molecular potential energy surface
$U_{\mathrm{c}}(\boldsymbol{Q})$	The PES of a molecule coupled to a constraining potential
$\boldsymbol{H}_i$	Hessian in non-redundant internal coordinates of conformer i of a free molecule
$\boldsymbol{H}_i^{\mathrm{c}}$	Hessian in non-redundant internal coordinates of conformer i coupled to a constraining potential
$\boldsymbol{H}^{-1}$	Inverse Hessian (compliance matrix)
$\boldsymbol{Q}(1)$	The constrained degree of freedom of a molecule (equivalent to the “mechanical” coordinate of the chemomechanical model)
λ_{c}, q_{c}	The harmonic compliance and equilibrium distance of the constraining potential
ΔG_i^{o}	Free energy of conformer i of a free molecule relative to that of the global conformational minimum
$G_{\mathrm{min}}{}^{\mathrm{o}}$	Free energy of the global conformational minimum of a canonical ensemble of free molecules
$G_{\mathrm{c}}(\lambda_{\mathrm{c}},q_{\mathrm{c}})$	Free energy of a conformer of a molecule coupled to the constraining potential with a compliance of λ_{c} and an equilibrium distance of q_{c}
$G_{\{\mathrm{c}\}}(\lambda_{\mathrm{c}},q_{\mathrm{c}})$	Free energy of a canonical conformational ensemble of molecules coupled to the constraining potential with compliance λ_{c} and equilibrium distance of q_{c}

Table 1.2 (cont.)

k_j	Harmonic force constant of normal mode ξ_j of a free molecule
k_j^{c}	Harmonic force constant of normal mode ξ_j of a molecule coupled to a constraining potential
Z_i^{o}	Vibrational partition function of conformer i of a free molecule
Z_i^{c}	Vibrational partition function of conformer i coupled to the constraining potential
$\Delta q_i^{\ddagger}$	The difference of internal coordinate $\boldsymbol{Q}(i)$ between the strain-free transition state and reactant
$\Delta\lambda_i^{\ddagger}$	The difference of harmonic compliances of internal coordinate $\boldsymbol{Q}(i)$ between the strain-free transition state and reactant
$\Delta G_{\mathrm{o}}^{\ddagger}$	The standard free energy of activation for a free reactant
$\Delta G_{\mathrm{c}}^{\ddagger}(\lambda_{\mathrm{c}},q_{\mathrm{c}})$	The free energy of activation of a reactant coupled to a constraining potential with parameters λ_{c} and q_{c}
Z_{pot}	Classical vibrational partition function of the constraining potential
N_{A}	Avogadro's number
$2\pi\hbar$	Plank's constant
β	Inverse thermal energy either per molecule or per mole, depending on context
$\langle\rangle$	Average over a conformational ensemble

Consider a macromolecule whose potential energy surface, $U(\boldsymbol{Q})$, is described by eq. (1.10), where $\boldsymbol{Q}$ is a $3N$–6×1 column vector of non-redundant independent internal coordinates, $\boldsymbol{Q}^{\mathrm{o}}$ is the equilibrium (strain-free) values of these coordinates corresponding to the ground vibrational state and $\boldsymbol{H}$ is a $3N$–6×$3N$–6 symmetrical matrix of second derivatives of energy $U(\boldsymbol{Q}^{\mathrm{o}})$ with respect to internal coordinates (internal Hessian), i.e., $\boldsymbol{H}(i,j) = \boldsymbol{H}(j,i) = \partial^2U/\partial\boldsymbol{Q}(i)\partial\boldsymbol{Q}(j)$.

$$U(\boldsymbol{Q}) = U(\boldsymbol{Q}^{\mathrm{o}}) + \frac{1}{2}\sum_{j=1}^{3N-6}\sum_{i=1}^{3N-6}\frac{\partial^2 U(\boldsymbol{Q}^{\mathrm{o}})}{\partial\boldsymbol{Q}(i)\,\partial\boldsymbol{Q}(j)} = U(\boldsymbol{Q}^{\mathrm{o}}) + \frac{1}{2}[\boldsymbol{Q}-\boldsymbol{Q}^{\mathrm{o}}]^{\mathrm{T}}\times\boldsymbol{H}_q\times[\boldsymbol{Q}-\boldsymbol{Q}^{\mathrm{o}}] \qquad (1.10)$$

We will again assume that the constraining potential that stretches the macromolecule is harmonic and characterized by a single non-fluctuating compliance, λ_{c}, and equilibrium distance, q_{c}. Let $\boldsymbol{Q}(1)$ be the constrained internuclear distance of the macromolecule (it is equivalent to the "mechanical" coordinate τ of the chemomechanical model described above). Setting the ground-state energy of the isolated constraining potential to 0 gives eq. (1.11) for the potential energy surface of the coupled system. If $q_{\mathrm{c}} \neq \boldsymbol{Q}^{\mathrm{o}}(1)$, the geometry of the ground vibrational state of the coupled system will deviate from that of the free macromolecule. The new vibrational ground state, $\boldsymbol{Q}_\mathrm{c}^\mathrm{o}$ is defined by the condition of the internal mechanical equilibrium (eq. (1.12)), where $\boldsymbol{H}^\mathrm{c}$ is the Hessian of the coupled system (eq. (1.13), δ_{i1} is the Kronicker delta).

$$U_\mathrm{c}(\boldsymbol{Q}) = U(\boldsymbol{Q}^\mathrm{o}) + \frac{[\boldsymbol{Q}-\boldsymbol{Q}^\mathrm{o}]^\mathrm{T} \times \boldsymbol{H} \times [\boldsymbol{Q}-\boldsymbol{Q}^\mathrm{o}] + \lambda_\mathrm{c}^{-1}(\boldsymbol{Q}(1)-q_\mathrm{c})^2}{2} \tag{1.11}$$

$$\boldsymbol{H}^\mathrm{c} \times [\boldsymbol{Q}_\mathrm{c}^\mathrm{o} - \boldsymbol{Q}^\mathrm{o}] = \begin{bmatrix} \lambda_\mathrm{c}^{-1}(\boldsymbol{Q}^\mathrm{o}(1)-q_\mathrm{c}) \\ 0 \\ 0 \\ \vdots \\ 0 \end{bmatrix} \tag{1.12}$$

$$\boldsymbol{H}^\mathrm{c}(i,j) = \boldsymbol{H}(i,j) + \lambda_\mathrm{c}^{-1}\delta_{i1}\delta_{j1} \tag{1.13}$$

The solution of eq. (1.12) is eq. (1.14), where $(\boldsymbol{H}^\mathrm{c})^{-1}(:,1)$ is the $3N$–6×1 column vector from the inverse Hessian of the coupled system (eq. (1.13)), which is related to the inverse Hessian of the macromolecule (molecular compliance matrix by eq. (1.15)).

$$\boldsymbol{Q}_\mathrm{c}^\mathrm{o} = \boldsymbol{Q}^\mathrm{o} - \lambda_\mathrm{c}^{-1}(\boldsymbol{Q}^\mathrm{o}(1)-q_\mathrm{c}) \times (\boldsymbol{H}^c)^{-1}(:,1) \tag{1.14}$$

$$(\boldsymbol{H}^\mathrm{c})^{-1}(i,1) = \frac{\boldsymbol{H}^{-1}(i,1)}{1+\boldsymbol{H}^{-1}(1,1)/\lambda_\mathrm{c}} \tag{1.15}$$

By definition of the matrix inverse, $\boldsymbol{H}^\mathrm{c}(:,i)\times(\boldsymbol{H}^\mathrm{c})^{-1}(j,:)=\delta_{ij}$, where δ_{ij} is the Kronicker delta and consequently, $\boldsymbol{H}(:,i)\times(\boldsymbol{H}^\mathrm{c})^{-1}(1,:) = \delta_{i1} - \lambda_\mathrm{c}^{-1}(\boldsymbol{H}^\mathrm{c})^{-1}(1,1)$. Applying this equality to eqs. (1.11)–(1.12) yields the potential energy of the vibrational ground state of the coupled system, $U_\mathrm{c}(\boldsymbol{Q}_\mathrm{c}^\mathrm{o})$, relative to that of the free macromolecule, $U(\boldsymbol{Q}^\mathrm{o})$ (eq. (1.16)).

$$\begin{aligned} 2\big(U_\mathrm{c}(\boldsymbol{Q}_\mathrm{c}^\mathrm{o}) - U(\boldsymbol{Q}^\mathrm{o})\big) &= [\boldsymbol{Q}_\mathrm{c}^\mathrm{o}-\boldsymbol{Q}^\mathrm{o}]^\mathrm{T} \times \boldsymbol{H} \times [\boldsymbol{Q}_\mathrm{c}^\mathrm{o}-\boldsymbol{Q}^\mathrm{o}] + \lambda_\mathrm{c}^{-1}(\boldsymbol{Q}_\mathrm{c}^\mathrm{o}(1)-q_\mathrm{c})^2 \\ &= [\boldsymbol{Q}_\mathrm{c}^\mathrm{o}-\boldsymbol{Q}^\mathrm{o}]^\mathrm{T} \times \begin{bmatrix} 1-\lambda_\mathrm{c}^{-1}(\boldsymbol{H}^c)^{-1}(1,1) \\ 0 \\ 0 \\ \vdots \\ 0 \end{bmatrix} + \lambda_\mathrm{c}^{-1}(\boldsymbol{Q}_\mathrm{c}^\mathrm{o}(1)-q_\mathrm{c})^2 \\ &= \frac{(\boldsymbol{Q}^\mathrm{o}(1)-q_\mathrm{c})^2}{\lambda_\mathrm{c}+\boldsymbol{H}^{-1}(1,1)} \end{aligned} \tag{1.16}$$

The free energy of the coupled system subject only to harmonic vibrational excitation is given by eq. (1.17), where G^o is the free energy of the free macromolecule, $\Delta ZPE(\lambda_\mathrm{c})$ is the excess of zero-point energy of the coupled system relative to the free molecule (eq. (1.18)); Z^o

and $Z^{\mathrm{c}}(\lambda_{\mathrm{c}})$ are the vibrational partition functions of the free and constrained macromolecule, respectively (eqs. (1.19)–(1.20)); $Z_{\mathrm{pot}}(\lambda_{\mathrm{c}}) \propto \lambda_{\mathrm{c}}^{1/2}$ is the classical vibrational partition function of the constraining potential; and β is inverse thermal energy. Note that ΔZPE, Z^{c} and Z_{pot} depend on the compliance of the constraining potential, but not on its equilibrium distance, whereas G^{o}, $\boldsymbol{H}$ and $\boldsymbol{Q}^{\mathrm{o}}$ are independent of both λ_{c} and q_{c}. In eqs. (1.18)–(1.20), μ_j is the reduced mass of normal mode ξ_j and $2\pi\hbar$ is Plank's constant.

$$G_{\mathrm{c}}(\lambda_{\mathrm{c}}, q_{\mathrm{c}}) = G^{\mathrm{o}} + \frac{N_{\mathrm{A}}}{2}\left(\frac{(\boldsymbol{Q}^{\mathrm{o}}(1) - q_{\mathrm{c}})^2}{\lambda_{\mathrm{c}} + \boldsymbol{H}^{-1}(1,1)} + \Delta ZPE(\lambda_{\mathrm{c}})\right) + \beta^{-1}\ln\frac{Z^{\mathrm{o}}Z_{\mathrm{pot}}}{Z^{\mathrm{c}}} \tag{1.17}$$

$$\Delta ZPE(\lambda_{\mathrm{c}}) = \frac{\hbar}{2}\sum_{j=1}^{3N-6}\left(\sqrt{\frac{k_j^{\mathrm{c}}}{\mu_j^{\mathrm{c}}}} - \sqrt{\frac{k_j}{\mu_j}}\right) \tag{1.18}$$

$$Z^{\mathrm{o}} = \prod_{j=1}^{3N-6}\left(1 - e^{-\hbar\beta\sqrt{\frac{k_j}{\mu_j}}}\right)^{-1} \tag{1.19}$$

$$Z^{\mathrm{c}}(\lambda_{\mathrm{c}}) = \prod_{j=1}^{3N-6}\left(1 - e^{-\hbar\beta\sqrt{\frac{k_j^{\mathrm{c}}}{\mu_j}}}\right)^{-1} \tag{1.20}$$

If the constraining potential is massless, the normal force constants of the coupled system, k_j^{c} can be approximated as eigenvalues of its Hessian, $\boldsymbol{H}^{\mathrm{c}}$. The individual normal modes or their force constants of the coupled system cannot be expressed in general as closed analytical functions of the normal modes and force constants of the free molecule. For minima, eqs. (1.21)–(1.23) are available from the relationship between the eigenvalues, trace and determinant of a positive-definite Hessian and the following equalities: $\det\boldsymbol{H}^{\mathrm{c}} = (1 + \lambda_{\mathrm{c}}^{-1}\boldsymbol{H}(1,1))\det\boldsymbol{H}$, where det is determinant and $[\boldsymbol{H}\times(\boldsymbol{H}^{\mathrm{c}})^{-1}](i,j) = \delta_{ij} + \delta_{i1}\lambda_{\mathrm{c}}^{-1}\boldsymbol{H}^{-1}(1,j)$, which derive from eq. (1.15) (δ is the Kronicker delta).

$$\prod_{j=1}^{3N-6} k_j^{\mathrm{c}} = \left(1 + \frac{\boldsymbol{H}^{-1}(1,1)}{\lambda_{\mathrm{c}}}\right)\prod_{j=1}^{3N-6} k_j \tag{1.21}$$

$$\sum_{j=1}^{3N-6} k_j^{\mathrm{c}} = \lambda_{\mathrm{c}}^{-1} + \sum_{j=1}^{3N-6} k_j \tag{1.22}$$

$$\sum_{j=1}^{3N-6} \frac{1}{k_j^{\mathrm{c}}} = \sum_{j=1}^{3N-6} \frac{1}{k_j} - \frac{\boldsymbol{H}^{-1}(1,:) \times \boldsymbol{H}^{-1}(:,1)}{\lambda_{\mathrm{c}} + \boldsymbol{H}^{-1}(1,1)} \tag{1.23}$$

In single-molecule force experiments q_{c} of eqs. (1.11)–(1.17) corresponds to the strain-free separation of the force probes and is the experimentally controlled parameter (even in so-called “constant” force experiments, the force is controlled by a feedback loop that adjusts the position of the force probe). The deviation of the probe from its equilibrium position, $\boldsymbol{Q}(1) - q_{\mathrm{c}}$, is measured and converted to the “mechanical” force, $f_{\mathrm{c}} = (\boldsymbol{Q}(1) - q_{\mathrm{c}})/\lambda_{\mathrm{c}}$, which in our model is the restoring force of the constraining potential. Assuming mechanical equilibrium, $-f_{\mathrm{c}}$ is equated to $f_1 = (\boldsymbol{Q}(1) - \boldsymbol{Q}^{\mathrm{o}}(1))/\boldsymbol{H}^{-1}(1,1)$, the restoring force of the constrained molecular degree of freedom. The results are typically recorded as force-extension curves, f_{c} vs. $\boldsymbol{Q}(1)$ and the objective of the experiments is to obtain the potential of mean force, i.e., the molecular free energy as a function of the constrained internal coordinate, in this case, $G^{\mathrm{o}}(\boldsymbol{Q}(1))$.

If the stretched macromolecule exists as a single conformer, its harmonic restoring force $f_1 \propto \partial G_{\mathrm{c}}/\partial q_{\mathrm{c}}$ is purely enthalpic, i.e., it is temperature-independent, because the vibrational component of the free energy of the coupled system, G_{c} (eq. (1.17)), is independent of q_{c}. The variance of f_1 increases with temperature, but its distribution remains centred at $(\boldsymbol{Q}^{\mathrm{o}}(1) - q_{\mathrm{c}})/(\lambda_{\mathrm{c}} + \boldsymbol{H}^{-1}(1,1))$.

Long flexible macromolecules have very corrugated energy landscapes with multiple accessible conformers. The free energy of an ensemble of non-interacting maromolecules coupled to the potential described by λ_{c} and q_{c}, $G_{\{\mathrm{c}\}}(\lambda_{\mathrm{c}}, q_{\mathrm{c}})$, is given by eq. (1.24), neglecting the dependence of the molar volume, V, on λ_{c} and q_{c} (i.e., $\partial \ln Z_i^{\mathrm{c}}/\partial V \sim \partial \ln Z_i^{\mathrm{o}}/\partial V$). Here $G_{\mathrm{min}}{}^{\mathrm{o}} \propto \min\{U_i(\boldsymbol{Q}_i{}^{\mathrm{o}}) - \beta^{-1}\ln Z_i{}^{\mathrm{o}}\}_{i=1:m}$ is the free energy of the global conformational minimum of m conformations of the free macromolecule; $G_{\mathrm{min}}{}^{\mathrm{o}} + \Delta G_i{}^{\mathrm{o}}$, $\boldsymbol{Q}^{\mathrm{o}}{}_i(1)$, $\boldsymbol{H}_i{}^{-1}(1,1)$ and $Z_i{}^{\mathrm{o}}$ are the free energy, end-to-end distance, harmonic compliance, and vibrational partition function of free conformer i, respectively; $Z_i{}^{\mathrm{c}}$ and $\Delta ZPE_i(\lambda_{\mathrm{c}})$ are the vibrational partition function and excess ZPE of conformer i coupled to the constraining potential λ_{c}, and $\Delta G_i{}^{\mathrm{c}}$ is defined by eq. (1.27).

$$G_{\{\mathrm{c}\}}(\lambda_{\mathrm{c}}, q_{\mathrm{c}}) = G^{\mathrm{o}}_{\mathrm{min}} + \beta^{-1}\ln\left(Z_{\mathrm{pot}}\sum_{i=1}^{m}\frac{Z_i^{\mathrm{o}}}{Z_i^{\mathrm{c}}}e^{-\Delta G_i^{\mathrm{c}}\beta}\right) \tag{1.24}$$

$$\langle f_1\rangle = \left(\frac{\partial G_{\{\mathrm{c}\}}(\lambda_{\mathrm{c}}, q_{\mathrm{c}})}{\partial q_{\mathrm{c}}}\right)_{T,V,n,\lambda_{\mathrm{c}}} = \frac{\sum_{i=1}^{m} f_1^{(i)}\frac{Z_i^{\mathrm{o}}}{Z_i^{\mathrm{c}}}e^{-\Delta G_i^{\mathrm{c}}\beta}}{\sum_{i=1}^{m}\frac{Z_i^{\mathrm{o}}}{Z_i^{\mathrm{c}}}e^{-\Delta G_i^{\mathrm{c}}\beta}} \xrightarrow[\substack{\lambda_{\mathrm{c}}\to\infty \\ q_{\mathrm{c}}\to\infty}]{} \frac{q_{\mathrm{c}}}{\lambda_{\mathrm{c}}} \tag{1.25}$$

$$\langle \boldsymbol{Q}_{\{\mathrm{c}\}}(1)\rangle = \langle \boldsymbol{Q}^{\mathrm{o}}(1)\rangle + \langle f_1\rangle\frac{\sum_{i=1}^{m}\boldsymbol{H}_i^{-1}(1,1) f_1^{(i)}\frac{Z_i^{\mathrm{o}}}{Z_i^{\mathrm{c}}}e^{-\Delta G_i^{\mathrm{c}}\beta}}{\sum_{i=1}^{m} f_1^{(i)}\frac{Z_i^{\mathrm{o}}}{Z_i^{\mathrm{c}}}e^{-\Delta G_i^{\mathrm{c}}\beta}} \tag{1.26}$$

$$\Delta G_i^{\mathrm{c}}(\lambda_{\mathrm{c}}, q_{\mathrm{c}}) = \Delta G_i^{\mathrm{o}} + \frac{N_{\mathrm{A}}}{2}\left(\frac{(\boldsymbol{Q}_i^{\mathrm{o}}(1) - q_{\mathrm{c}})^2}{\lambda_{\mathrm{c}} + \boldsymbol{H}_i^{-1}(1,1)} + \Delta ZPE_i(\lambda_{\mathrm{c}})\right) \xrightarrow[\substack{\lambda_{\mathrm{c}}\to\infty \\ q_{\mathrm{c}}\to\infty}]{} \Delta G_i^{\mathrm{o}} + \frac{N_{\mathrm{A}}}{2} f(Q_i^{\mathrm{o}}(1) - q_{\mathrm{c}}) \tag{1.27}$$

The corresponding ensemble-average restoring force, $\langle f_1\rangle$, is given by eq. (1.25), where $f_1^{(i)} = (\boldsymbol{Q}_i^{\mathrm{o}}(1) - q_{\mathrm{c}})/(\lambda_{\mathrm{c}} + \boldsymbol{H}_i^{-1}(1,1))$ is the average restoring force of coordinate $\boldsymbol{Q}_i(1)$ in conformer i. Since for each conformer product $f_1^{(i)}\times\boldsymbol{H}_i^{-1}(1,1)$ equals the difference of coordinate $\boldsymbol{Q}_i(1)$ in the vibrational ground states of the free and coupled macromolecules, $\boldsymbol{Q}^{\mathrm{o}}_{\mathrm{c},i}(1) - \boldsymbol{Q}_i^{\mathrm{o}}(1)$, the ensemble-average length of the constrained molecular degree of freedom, $\langle \boldsymbol{Q}_{\{\mathrm{c}\}}(1)\rangle$ as a function of the average "mechanical" force, $\langle f_1\rangle$, is given by eq. (1.26).

Unlike the restoring force of individual conformers, the ensemble-average restoring force, $\langle f_1\rangle$, is temperature-dependent and can have a substantial entropic component, particularly if the constraining potential is stiff. The measured force-extension profiles, which ideally approach eq. (1.26), depend on the properties of both the macromolecule and the constraining potential. The potential of mean force, $\Delta G^{\mathrm{o}}(\boldsymbol{Q}^{\mathrm{o}}(1))$ cannot be extracted from eq. (1.26) without further approximations because the required Hessians are not available with useful accuracy.

Eq. (1.26) simplifies in the limit of an "infinitely" flexible ($\lambda_{\mathrm{c}}\to\infty$, $q_{\mathrm{c}}\to\infty$) constraining potential when all conformers experience the same average restoring force $f = q_{\mathrm{c}}/\lambda_{\mathrm{c}}$ (eq. (1.25)) and the vibrational states of the coupled system are identical to that of the free macromolecule (neglecting inertia of the constraining potential). Combining the $\lambda_{\mathrm{c}}\to\infty$, $q_{\mathrm{c}}\to\infty$ limit of ΔG_i^{c} (eq. (1.27)) with eq. (1.26), yields eq. (1.28), where $\langle \boldsymbol{H}^{-1}(1,1)\rangle_f$ is force-dependent ensemble-average compliance of $\boldsymbol{Q}(1)$, Fig. 1.4. At low forces $\langle \boldsymbol{H}^{-1}(1,1)\rangle_f$ is approximately proportional to f, but it approaches the harmonic compliance of the strain-free conformer with longest $\boldsymbol{Q}^{\mathrm{o}}(1)$, which is similar to the compliance of the contour length. An empirical equivalent of eq. (1.28) is a generalized Langevin equation (eq. (1.29), where q_{contour} and $\lambda_{\mathrm{contour}}$ is the contour length of the macromolecule and its compliance and b is an empirical fitting parameter, called the Kuhn length).[81]

$$\langle \boldsymbol{Q}_{\{c\}}(1)\rangle \xrightarrow[\substack{\lambda_{\mathrm{c}}\to\infty\\ q_{\mathrm{c}}\to\infty}]{} \langle \boldsymbol{Q}^{o}(1)\rangle + f\,\frac{\sum_{i=1}^{m}\boldsymbol{H}_i^{-1}(1,1)e^{-\Delta G_i^{\mathrm{c}}\beta}}{\sum_{i=1}^{m}e^{-\Delta G_i^{\mathrm{c}}\beta}} = \langle \boldsymbol{Q}^{\mathrm{o}}(1)\rangle + f\langle \boldsymbol{H}^{-1}(1,1)\rangle_f \tag{1.28}$$

$$\langle \boldsymbol{Q}_{\{c\}}(1)\rangle \xrightarrow[\substack{\lambda_{\mathrm{c}}\to\infty\\ q_{\mathrm{c}}\to\infty}]{} \langle \boldsymbol{Q}^{\mathrm{o}}(1)\rangle + \left(q_{\mathrm{contour}} + f\lambda_{\mathrm{contour}} - \langle \boldsymbol{Q}^{\mathrm{o}}(1)\rangle\right)\left(\coth(fb\beta) - \frac{1}{fb\beta}\right) \tag{1.29}$$

The limit of an infinitely stiff constraining potential ($\lambda_{\mathrm{c}}\to 0$) is not amenable to general analysis, because relative free energies of individual conformers, ΔG_i^{c}, (and hence their contributions to the ensemble) are dominated by $\Delta ZPE(\lambda_{\mathrm{c}})$, eq. (1.18), which cannot be evaluated generally. Moreover, $\Delta ZPE(\lambda_{\mathrm{c}})\to\infty$ as $\lambda_{\mathrm{c}}\to 0$ because according to eq. (1.22) $\sum_{j=1}^{3N-6} k_j^{\mathrm{c}} \to \infty$ as $\lambda_{\mathrm{c}} \to 0$ and so must the sum of the square-roots of the normal force constants of eq. (1.18). The result is expected, because an infinitely rigid constraint precisely defines the positions and momenta of at least the two atoms across which it acts. Note, that Z^{c}, however, is finite regardless of λ_{c}, because all harmonic force constants of the coupled system, k_j^{c}, must satisfy eq. (1.30) (which derives from eq. (1.23)).

$$k_j^{\mathrm{c}} > \left(\sum_{j=1}^{3N-6}\frac{1}{k_j}\right)^{-1} \tag{1.30}$$

Because the difference of zero-point destabilizations of any two conformers, ΔZEP_i-ΔZEP_j, appears to be finite for any λ_{c}, in theory the $\lambda_{\mathrm{c}} \to 0$ limit of eq. (1.26) (i.e., restoring force of an ensemble of macromolecules coupled to an infinitely stiff constraining potential) can be estimated by calculating free energies of individual conformers (eq. (1.27)) relative to a single constrained conformer. In practice, such calculations require Hessians of multiple conformers, which are usually not available.

1.8 Statistical Mechanical Model of Reaction Barriers in Stretched Polymers

Eqs. (1.11)–(1.20) and (1.24)–(1.27) are valid for any stationary point of the coupled system, including the transition states. According to transition state theory (TST),[34] the rate of a chemical reaction is proportional to the exponential of the difference between the free energies of the lowest- and highest-energy stationary points along the reaction path. The timescale of localized reactions (picoseconds) is too short for any changes in the equilibrium distance of the constraining potential, so that both λ_{c} and q_{c} can be assumed to be identical in the reactant and the transition state.

If both states are ensembles of conformers, the standard free energy of activation, $\Delta G_{\mathrm{o}}{}^{\ddagger}$, is given by eq. (1.31), where $G_{\{\mathrm{R}\}}{}^{\mathrm{o}}$ and $G_{\{\ddagger\}}{}^{\mathrm{o}}$ are the free energies of the ground and transition states, respectively and $\Delta G_{\mathrm{min}}{}^{\ddagger}$ is the free-energy difference of *the lowest-energy conformers* of the ground and transition states (see eq. (1.24) relating the free energies of individual conformers with the free energy of their ensemble). Eq. (1.32) is the activation free energy in the coupled system, where $(\Delta G_i{}^{\mathrm{c}})_{\ddagger}$ and $(\Delta G_i{}^{\mathrm{c}})_{\mathrm{R}}$ are the free energies of the i^{th} conformer of the coupled transition and ground states, respectively, relative to the global conformational minima of each state in the *free* macromolecule (eq. (1.27)).

$$\Delta G_{\mathrm{o}}^{\ddagger} = G_{\{\ddagger\}}^{\mathrm{o}} - G_{\{\mathrm{R}\}}^{\mathrm{o}} = \Delta G_{\mathrm{min}}^{\ddagger} - \beta^{-1}\ln\frac{\sum_{i=1}^{m} e^{-(\Delta G_i^{\mathrm{o}})_{\ddagger}\beta}}{\sum_{i=1}^{l} e^{-(\Delta G_i^{\mathrm{o}})_{\mathrm{R}}\beta}} \tag{1.31}$$

$$\begin{aligned}\Delta G_{\mathrm{c}}^{\ddagger}(\lambda_{\mathrm{c}}, q_{\mathrm{c}}) &= G_{\{\ddagger\}}^{\mathrm{c}}(\lambda_{\mathrm{c}}, q_{\mathrm{c}}) - G_{\{\mathrm{R}\}}^{\mathrm{c}}(\lambda_{\mathrm{c}}, q_{\mathrm{c}}) \\ &= \Delta G_{\mathrm{o}}^{\ddagger} + \beta^{-1}\ln\frac{\sum_{i=1}^{m}\left(\frac{Z_i^{\mathrm{o}}}{Z_i^{\mathrm{c}}}\right)_{\ddagger} e^{-(\Delta G_i^{\mathrm{c}})_{\ddagger}\beta}}{\sum_{i=1}^{m} e^{-(\Delta G_i^{\mathrm{o}})_{\ddagger}\beta}} - \beta^{-1}\ln\frac{\sum_{i=1}^{l}\left(\frac{Z_i^{\mathrm{o}}}{Z_i^{\mathrm{c}}}\right)_{\mathrm{R}} e^{-(\Delta G_i^{\mathrm{c}})_{\mathrm{R}}\beta}}{\sum_{i=1}^{l} e^{-(\Delta G_i^{\mathrm{o}})_{\mathrm{R}}\beta}}\end{aligned} \tag{1.32}$$

As is the free energy of a conformational ensemble of a coupled reactant, eq. (1.32) is intractable and cannot be used to estimate the kinetics of localized reactions in stretched polymers. Eq. (1.33) is the limit of eq. (1.32) for an infinitely compliant constraining potential ($\lambda_{\mathrm{c}}\rightarrow\infty$, $q_{\mathrm{c}}\rightarrow\infty$), where $\langle\rangle$ refers to averaging over the conformational ensemble of the *free* ground or transition state. For many simple synthetic polymers with random tertiary structure, the distribution of $\boldsymbol{Q}_i^{\mathrm{o}}(1)$ is approximately truncated skew-normal,[81] precluding any further general simplification of eq. (1.33). Again, eq. (1.33) is intractable.

$$\Delta G_{\mathrm{c}}^{\ddagger}(f) \xrightarrow[\substack{\lambda_{\mathrm{c}}\to\infty \\ q_{\mathrm{c}}\to\infty}]{} -\beta^{-1} \ln \frac{\sum_{i=1}^{m} e^{-\left(\Delta G_i^{\mathrm{o}} - N_{\mathrm{A}} f\left(q_i^{\mathrm{o}} + f\lambda_i^{\mathrm{o}}/2\right)\right)_{\ddagger}\beta}}{\sum_{j=1}^{m} e^{-\left(\Delta G_j^{\mathrm{o}} - N_{\mathrm{A}} f\left(q_j^{\mathrm{o}} + f\lambda_j^{\mathrm{o}}/2\right)\right)_{\ddagger}\beta}} \tag{1.33}$$

Because localized rearrangements of covalent bonds are typically characterized by high activation barriers and modest sensitivities to molecular strain, significant changes in their rates are observed only in overstretched macromolecules (i.e., molecules whose constrained distance exceeds the corresponding contour length). Overstretching a macromolecule drastically reduces the number of thermally accessible conformers.[81] Consequently, the limit of a *single* dominant conformer for both the ground and transition states (eq. (1.34)) may be of greater practical relevance than the general solution (eq. (1.32)).

$$\begin{aligned}\Delta\Delta G^{\ddagger}(\lambda_{\mathrm{c}}, f_1^{\mathrm{R}}) &= \left(f_1^{\mathrm{R}}\Delta q_1^{\ddagger} + (f_1^{\mathrm{R}})^2\frac{\Delta\lambda_1^{\ddagger}}{2}\right)\frac{\lambda_{\mathrm{c}} + \boldsymbol{H}_{\mathrm{R}}^{-1}(1,1)}{\lambda_{\mathrm{c}} + \boldsymbol{H}_{\ddagger}^{-1}(1,1)} - \frac{\left(\Delta q_1^{\ddagger}\right)^2}{\lambda_{\mathrm{c}} + \boldsymbol{H}_{\ddagger}^{-1}(1,1)} \\ &\quad - \beta^{-1}\ln\left(\frac{Z^{\mathrm{o}}}{Z^{\mathrm{c}}}\right)^{\ddagger}\left(\frac{Z^{\mathrm{c}}}{Z^{\mathrm{o}}}\right)^{\mathrm{R}} \xrightarrow[\substack{\lambda_{\mathrm{c}}\to\infty \\ q_{\mathrm{c}}\to\infty}]{} f_1^{\mathrm{R}}\Delta q_1^{\ddagger} + (f_1^{\mathrm{R}})^2\frac{\Delta\lambda_1^{\ddagger}}{2}\end{aligned} \tag{1.34}$$

Eq. (1.34) is valid for an arbitrary compliance of the harmonic constraining potential and expresses the activation barrier as a function of the restoring force in the dominant conformer of the ground state $f_1^{\mathrm{R}} = (\boldsymbol{Q}_{\mathrm{R}}^{\mathrm{o}}(1) - q_{\mathrm{c}})/(\lambda_{\mathrm{c}} + \boldsymbol{H}_{\mathrm{R}}^{-1}(1,1))$. The $\Delta q_1^{\ddagger} = \boldsymbol{Q}_{\ddagger}^{\mathrm{o}}(1) - \boldsymbol{Q}_{\mathrm{R}}^{\mathrm{o}}(1)$ and $\Delta\lambda_1^{\ddagger} = \boldsymbol{H}_{\ddagger}^{-1}(1,1) - \boldsymbol{H}_{\mathrm{R}}^{-1}(1,1)$ variables are extension (contraction) and softening (stiffening) of internal degree of freedom $\boldsymbol{Q}(1)$ in a single unconstrained conformer of the ground and the transition states. These conformers dominate the respective ensembles at force f_1^{R} but may be rare in free macromolecules. In the overstretched regime $\Delta q_1^{\ddagger}$ and $\Delta\lambda_1^{\ddagger}$ could be equated to the elongation (contraction) and stiffening (softening) of the *contour* length of the strain-free macromolecule between the ground and transition states.

All but the final terms of eq. (1.34) are enthalpic. The elongation (contraction) of the contour length of the reacting molecule ($\Delta q^{\ddagger}_1$) requires that the strain energy and the restoring force of the constraining potential be different in the two states as well (remember that transition state theory state refers to nuclear configurations in internal mechanical equilibrium). This change in the strain energy of the constraining potential contributes to, and may even dominate, the $f_1^R \Delta q_1^{\ddagger}$ term. The quadratic force term, $(f_1^R)^2 \Delta \lambda_1^{\ddagger}$, accounts for differential destabilization of the ground and transition states, because of the different compliances of their contour lengths. It is equivalent to the Hammond effect in linear-free energy relationships of small strained reactants.[33,66] The energetic consequence of softening (stiffening) of the contour length during the reaction is captured by the ratio of the compliances, $(\lambda_c + \boldsymbol{H}_R^{-1}(1,1))/(\lambda_c + \boldsymbol{H}_{\ddagger}^{-1}(1,1))$.

Note that accounting for changes in the constraining potential between the ground and transition states does not imply that the constraining potential "adjusts" in real time to changes in the local chemical bonding. Most of the nuclear configurations comprising a molecular ensemble are not in internal mechanical equilibrium. For example, a non-negligible fraction of the ensemble may have chemical bonding within the reactive site corresponding to the ground state, while the geometry of the constraining potential and most of the macromolecule outside of the reactive site corresponding to the transition state. Eq. (1.34) simply means that a localized reaction preferentially occurs in such nuclear configurations, even though they are present in a smaller fraction than those described by the "optimal" parameters of the ground state, i.e., $\boldsymbol{Q}_R^{o}(1)$, $\boldsymbol{H}_R^{-1}(1,1)$ and $-f_c = f_1^R$.

1.9 A Practical Model of Force-Dependent Kinetics

Because the geometries of macromolecular transition states (and hence the values of $\Delta q_1^{\ddagger}$, $\Delta\lambda_1^{\ddagger}$ and $H_{\ddagger}^{-1}(1,1)$) cannot yet be estimated reliably, practical applications of eq. (1.34) for predicting the kinetics of localized reactions in stretched polymers require reformulation in terms of internal coordinates of the localized reaction site. The chemomechanical formalism is an approach of simplifying the description of an intractably complex dynamic system by partitioning it into a pair of mechanically coupled subsystems:[79] the macromolecule, which is treated molecularly and the constraining potential, which is a continuum description of very many molecular degrees of freedom behaving collectively. For localized reactions, which involve chemical changes of only a tiny fraction of the atoms of the macromolecular reactant, the bulk of the macromolecular degrees of freedom may also be assumed to behave collectively and thus need not be considered explicitly but rather can be subsumed into the continuum model of the constraining potential.

Let the new molecular subsystem contain only the reactive moiety (defined more precisely below), coupled to a harmonic continuum (mechanical) subsystem at internal coordinate $\boldsymbol{Q}(l)$. The latter is a part of the $3N$–6 internal degrees of freedom used to describe the full macromolecule. In the vibrational ground state of any stretched macromolecular conformer, the restoring force of $\boldsymbol{Q}(l)$, $f_l = (\boldsymbol{Q}_c^{o}(l) - \boldsymbol{Q}^{o}(l))/\boldsymbol{H}^{-1}(l,l)$, is exactly determined by the restoring force of the constrained degree of freedom, f_1 (eq. (1.35)). In the limit of a single dominant macromolecular conformer, or an infinitely compliant constraining potential, f_1 is uniquely related to the experimental control parameter, q_c, and thus eq. (1.35) establishes a unique relationship between the macroscopic variable, q_c, and the molecular parameter, f_l.

$$f_l = f_1 \frac{\boldsymbol{H}^{-1}(1,l)}{\boldsymbol{H}^{-1}(l,l)} \tag{1.35}$$

For constraining potentials of finite compliance, λ_c, the equilibrium distance, q_c', and harmonic compliance, λ_c', of the new mechanical subsystem are defined by eqs. (1.36)–(1.37), which result from the condition of (1) the potential energy of a system being invariant to how the system is partitioned into the molecular and continuum parts (eq. (1.38)) and (2) internal mechanical equilibrium between the molecular and continuum parts (eq. (1.39)).

$$q_c' = (\boldsymbol{H}^{-1}(1,1) + \lambda_c) f_1 \frac{\boldsymbol{H}^{-1}(l,l)}{\boldsymbol{H}^{-1}(1,l)} + q_l^0 \tag{1.36}$$

$$\lambda_c' = (\boldsymbol{H}^{-1}(1,1) + \lambda_c)\left(\frac{\boldsymbol{H}^{-1}(l,l)}{\boldsymbol{H}^{-1}(1,l)}\right)^2 - \boldsymbol{H}^{-1}(l,l) \tag{1.37}$$

$$\left(\lambda_c + \boldsymbol{H}^{-1}(1,1)\right) f_1^2 = \left(\lambda_c' + \boldsymbol{H}^{-1}(l,l)\right) f_l^2 \tag{1.38}$$

$$f_l = -\frac{\boldsymbol{Q}_c^o(l) - q_c'}{\lambda_c'} = \frac{\boldsymbol{Q}_c^o(l) - \boldsymbol{Q}^o(l)}{\boldsymbol{H}^{-1}(l,l)} \tag{1.39}$$

The parameters of the mechanical subsystem (eqs. (1.36)–(1.37)) must be independent of the chemical state of the reactive moiety for such chemomechanical partitioning to simplify the calculation of the activation barriers. The requirement of a state-independent q_c' (eq. (1.36)) is expressed by eq. (1.40), whose left-hand side depends on macromolecular strain (quantified as f_1^R), but whose right-hand side does not. This equation is valid for an arbitrary strain only if the ratio of the compliances involving the local coordinate, $\boldsymbol{H}^{-1}(1,l)/\boldsymbol{H}^{-1}(l,l)$ are identical for the two states. This ratio is sometimes called the chemomechanical coupling coefficient, α, as it describes the coupling between the degrees of freedom that control reaction kinetics, $\boldsymbol{Q}(l)$, and the one controlled macroscopically, $\boldsymbol{Q}(1)$.

$$f_1^{\mathrm{R}}\left(\frac{\boldsymbol{H}_{\mathrm{R}}^{-1}(l,l)}{\boldsymbol{H}_{\mathrm{R}}^{-1}(1,l)}-\frac{\boldsymbol{H}_{\ddagger}^{-1}(l,l)}{\boldsymbol{H}_{\ddagger}^{-1}(1,l)}\right)=\Delta q_l^{\ddagger}-\frac{\boldsymbol{H}_{\ddagger}^{-1}(l,l)}{\boldsymbol{H}_{\ddagger}^{-1}(1,l)}\Delta q_1^{\ddagger} \tag{1.40}$$

The parameters of a local coordinate $\boldsymbol{Q}(l)$ that satisfies eq. (1.40) can replace the (yet-unobtainable) macromolecular parameters of eq. (1.34) yielding eqs. (1.41)–(1.42) (the ratios of the vibrational partition functions may be estimated with useful accuracy using as normal force constants the eigenvalues of a truncated Hessian based only on the internal coordinates of the reactive moiety, but this speculation remains to be validated). As discussed below, quantum-chemical calculations show that the chemomechanical coupling coefficient, α, is not only independent of the length of the macromolecule, but also of its chemical composition. In other words, for long flexible polymers, α appears to be determined exclusively by the geometry of the reactive site. Because the stretching compliances of long flexible polymers, $\boldsymbol{H}_{\mathrm{R}}^{-1}(1,1)$, are available experimentally and $\Delta q_l^{\ddagger}$ and $\Delta\lambda_l^{\ddagger}$ can be calculated with useful accuracy quantum-chemically, eq. (1.43) may allow useful predictions of changes in kinetic stability of overstretched polymers dominated by a single conformer.

$$\Delta q_1^{\ddagger}=\frac{\boldsymbol{H}_{\mathrm{R}}^{-1}(1,l)}{\boldsymbol{H}_{\mathrm{R}}^{-1}(l,l)}\Delta q_l^{\ddagger}=\alpha\Delta q_l^{\ddagger} \tag{1.41}$$

$$\Delta\lambda_1^{\ddagger}=\left(\frac{\boldsymbol{H}_{\mathrm{R}}^{-1}(1,l)}{\boldsymbol{H}_{\mathrm{R}}^{-1}(l,l)}\right)^2\Delta\lambda_l^{\ddagger}=\alpha^2\Delta\lambda_l^{\ddagger} \tag{1.42}$$

$$\begin{aligned}\Delta\Delta G_{\mathrm{c}}^{\ddagger}&=\left(f_l^{\mathrm{R}}\Delta q_l^{\ddagger}+\frac{\left(f_l^{\mathrm{R}}\right)^2}{2}\Delta\lambda_l^{\ddagger}\right)\frac{\lambda_{\mathrm{c}}'+\boldsymbol{H}_{\mathrm{R}}^{-1}(l,l)}{\lambda_{\mathrm{c}}'+\boldsymbol{H}_{\ddagger}^{-1}(l,l)}-\frac{\left(\Delta q_l^{\ddagger}\right)^2}{\lambda_{\mathrm{c}}'+\boldsymbol{H}_{\ddagger}^{-1}(l,l)}-\beta^{-1}\ln\left(\frac{Z^{\mathrm{o}}}{Z^{\mathrm{c}}}\right)^{\ddagger}\left(\frac{Z^{\mathrm{c}}}{Z^{\mathrm{o}}}\right)^{\mathrm{R}}\\&\xrightarrow[\substack{\lambda_{\mathrm{c}}\to\infty\\ q_{\mathrm{c}}\to\infty}]{}f_l^{\mathrm{R}}\Delta q_l^{\ddagger}+\frac{\left(f_l^{\mathrm{R}}\right)^2}{2}\Delta\lambda_l^{\ddagger}\end{aligned} \tag{1.43}$$

Note that the only difference between eqs. (1.34) and (1.43) is the molecular coordinate at which the two subsystems are coupled. In other words, a change in the activation barrier due to constraining a macromolecular degree of freedom can be estimated using any convenient molecular degree of freedom that is coupled to the macroscopically controlled distance.

In addition to providing a means of estimating the activation barrier of a localized reaction in a stretched polymer using readily available parameters, eq. (1.43) allows experimental validation of the whole chemomechanical formalism. The current methods of measuring kinetics of localized reactions in stretched polymers lack the accuracy to yield molecular interpretation of the results. In contrast, eq. (1.43) suggests that the relationship between the restoring force of a strained molecular degree of freedom and the activation free energy underlying the chemomechanical formalism is not limited to stretched polymers but is common to any strained reactant, even small and highly tractable ones.

The conceptual analogy between rate perturbations in stretched polymers and in conventional non-macromolecular strained reactants was recognized long ago.[33] Yet, until recently we lacked both the theoretical support for such a relationship and molecular architectures to vary the restoring force of a local coordinate in sufficiently small increments and over a significant range of forces to validate the theory. Consequently, the idea that restoring force provides a general, size-independent quantifier of kinetically significant molecular strain remains foreign to most classical chemists, despite its potential to revolutionize our understanding of the chemistry of complex, multiscale dynamic phenomena.

1.10 Quantum-Chemical Identification of the Local Coordinate and Validation of Eq. (1.43)

At present, measurements of reaction rates in stretched macromolecules lack the accuracy, scope and throughput needed for broad experimental validation of the chemomechanical hypothesis or for the acquisition of sufficient empirical data to allow intuitive approaches to designing new molecules and reactions to exploit multiscale reaction dynamics. We have advocated a complementary, two-step approach. First, for a specific reaction, a convenient local coordinate q_l is identified and its chemomechanical coupling coefficient is obtained from quantum-chemical calculations of the activation energies on a series of reactive moieties bearing increasingly long, inert chains whose ends are constrained by a harmonic potential. Calculating the force-dependent activation energies for such a series of homologous reactants allows extrapolation to the limit of reaction in a long stretched polymer. Second, the computational results are validated experimentally by measuring activation energies of the reaction as a function of the restoring force of this coordinate using a series of increasingly strained macrocycles instead of stretched polymers. This strategy is illustrated in the subsequent sections.

Force-dependent kinetics of most mechanistically similar reactions even at structurally distinct reactive sites appear amenable to analysis using the same single type of local coordinate q_l. For example, in nucleophilic substitution the nonbonding separation of the atoms that connect the electrophilic atom to the rest of the polymer backbone serves as a convenient and general local coordinate (Fig. 1.5) that allows intuitive estimates of how stretching a polymer would affect the susceptibilities of its electrophilic sites in the backbone to ligand displacement, as illustrated below.

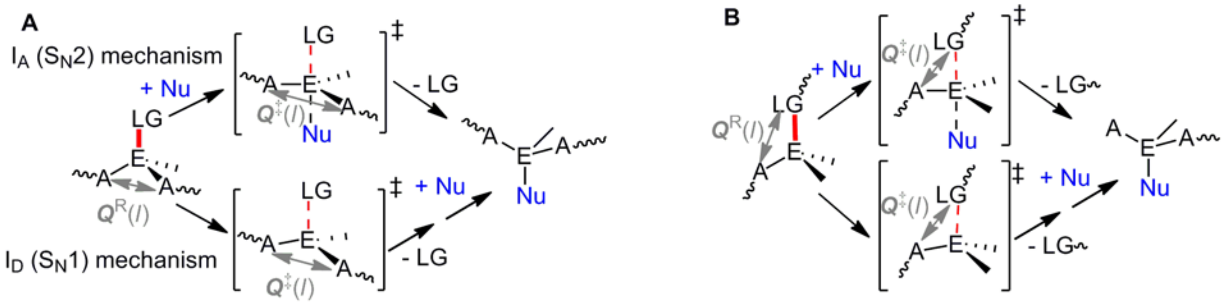

Fig. 1.5. An intuitive local coordinate ***Q***(l) for analysis of force–dependent kinetics of single-barrier nucleophilic displacement of a side chain (**A**) or the backbone (**B**) leaving group (LG) at an electrophilic atom (E). The scissile bond is highlighted in red; A are the spectator atoms bound to E, Nu is the nucleophile, and wavy lines represent the rest of the stretched polymer.

Consider first nucleophilic displacement of a side-chain, i.e., heterolytic dissociation of a bond *orthogonal* to the backbone and hence to the stretching axis (Fig. 1.5A). Conventional wisdom, based on macroscopic experience and the existing small strained molecules, would suggest that the reaction rate will be unaffected. A chemomechanical analysis suggests an acceleration regardless of the nature of the electrophilic atom, E, or the side-chain, LG. The reaction can proceed either by an associative (I_A or S_N2) mechanism through a (pseudo)trigonal-bipyramidal transition state,[82,83] or a dissociative (I_D or S_N1) mechanism with a rate-determining trigonal-pyramidal transition state. In either case, the contour length of the polymer in the transition state exceeds that in the ground state because the atoms A that connect E to the rest of the polymer must move apart to form the (equatorial) plane of the pyramid. Because the elongation occurs along the restoring force vector, stretching the polymer stabilizes the transition state relative to the ground state (excluding second-order effects). When atoms A can be approximated as omni-directional joints, the contour-length change would result solely from the change in the separation of atoms A, (i.e., $\alpha \approx 1$) because only the bonding at a single backbone atom, E, changes between the ground and transition state. It remains to be established experimentally how accurately various atoms can be modelled as omni-directional joints.

The conventional wisdom suggests that fragmentation along the stretching axis should be accelerated, but quantitative analysis reveals a much richer behaviour. Now, the formation of the transition state requires contraction of the angle between the two backbone bonds at the electrophilic atom (i.e., contraction of the A–E–LG angle, Fig. 1.5B). Such contraction will decrease the contour length in the transition state, relative to the ground state but may be (partially) compensated for by the obligatory elongation of the scissile E–LG bond. The relative effect of the two structural changes on the contour length is again captured by q_l, because no backbone atoms other than E change bonding. If $\Delta q_l^{\ddagger} > 0$ (net increase of the contour length because the scissile bond elongation dominates), nucleophilic backbone fragmentation will be accelerated as the polymer is (over)stretched. If $\Delta q_l^{\ddagger} \approx 0$ (the two effects are of similar magnitude) (over)stretching the polymer will not affect the kinetics of its nucleophile-assisted fragmentation (but may affect other fragmentation mechanisms). Finally, if $\Delta q_l^{\ddagger} < 0$ (angle contraction is more important than bond elongation), the fragmentation will be *decelerated* by stretching, a response that may be hard to accept based on macroscopic experience.

Macromolecular fragmentation by single-bond dissociation is the most commonly studied localized reaction in single-molecule force experiments. The molecular interpretation of such experiments too often is based on the scissile bond as the degree of freedom through which the molecular and mechanical subsystems are coupled. The equations above make it clear why such partitioning lacks a physical basis. The parameters of the mechanical subsystem, by definition, are independent of the state of the reactive site, which is only possible if the ratios of compliances of the molecular coordinate mediating coupling are identical in the ground and transition states. The compliance of a covalent bond in the transition state of its dissociation is often negative, whereas it is necessarily positive in the ground state. In other words, although the scissile bond elongates in the transition state, the obligatory contributions of other local degrees of freedom to the overall reaction coordinate may negate or even invert the correlation between the scissile bond and the contour length of the polymer.[75,76] Consequently, a chemomechanical model of molecular fragmentation by single bond dissociation cannot be based on the molecular subsystem comprised of just the scissile bond. Admittedly, such partitioning is appealing in its simplicity, but its lack of physical validity prevents the recognition and exploitation of the full complexity of the chemical response to large-scale strains.[72]

The value of a local coordinate of a reactive site in allowing usefully accurate predictions of reaction rates in stretched polymers is predicated on the chemomechanical coupling coefficient being independent of the length or chemical composition of the macromolecule beyond the reaction site. Such independence must be established computationally. Below we illustrate results of such computations for a simple electrocyclic isomerization of cyclobutene to butadiene (Fig. 1.6) during which a single C–C bond undergoes homolysis. We optimized the ground and transition states of substituted *trans*-3,4-dimethylcyclobutene with alkyl, ethylene glycol or polyester chains of varying length (Fig. 1.6). In all such calculations, the separation of the terminal CH_3 groups was constrained with a very compliant harmonic potential ($\lambda_c > 10$ nm/nN),represented by red spring in Fig. 1.6A), whose equilibrium distance, q_c, was incremented to yield restoring forces from <100 pN to >600 pN.

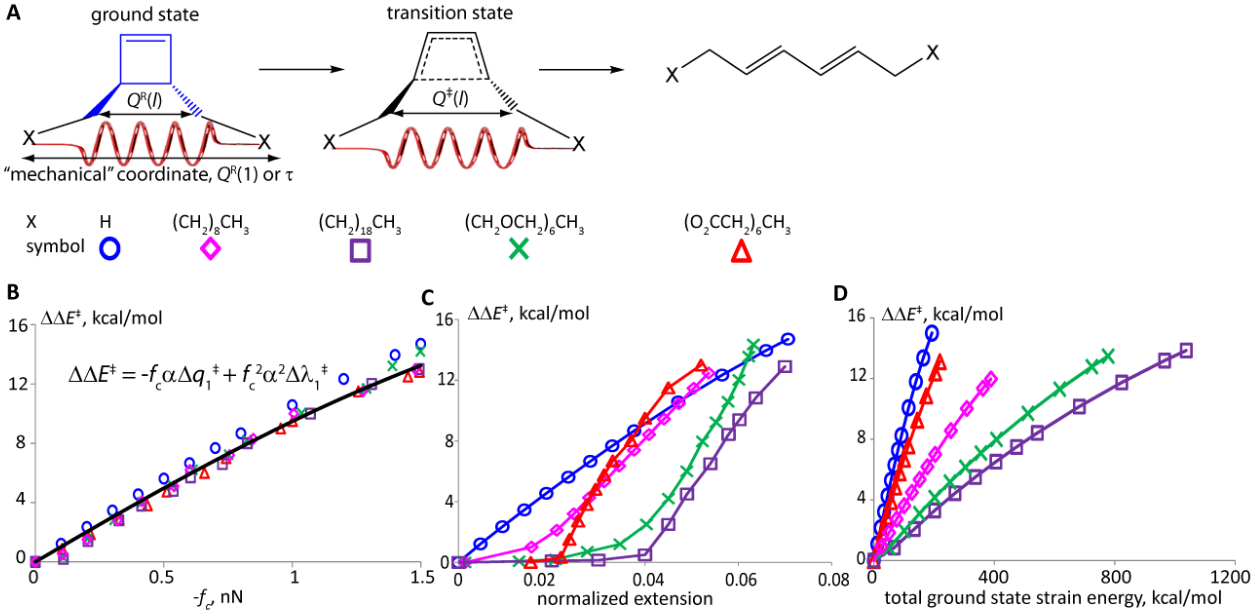

Fig. 1.6. The effect of stretching a polymer fragment containing cyclobutene (**A**) on the activation energy of its isomerisation. Calculated (B3LYP/6-31G*, gas phase) change in the electronic activation energy, $\Delta\Delta E^‡$, vs. **B**: the applied force; **C**: normalized extension (the $CH_3 \cdots CH_3$ distance divided by the contour length minus 1); and **D**: the total ground state strain energy. The solid line in **B** is the change in the barrier calculated by eq. (1.43) in the limit of infinitely compliant constraining potential using $\Delta q_l^‡$ and $\Delta\lambda_l^‡$ values of *trans*-3,4-dimethylcyclobutene (calculated at the B3LYP/6-311++G(3df,2pd) in the gas phase) and $\alpha = 1$. In **C** and **D** solid lines are for guiding eyes only. From ref. 73.

The relationship between the restoring force of the potential (mechanical force), $f_c = -f_l$, and the change in activation barrier is clear (Fig. 1.6B). These explicitly calculated barriers are predicted with excellent accuracy by eq. (1.43) using the coordinate q_l shown in Fig. 1.6A. Whereas explicit calculation of the barrier in the longest *trans*-3,4-cyclobutene derivative required ~500 cpu-hours at a modest B3LYP/6-31G* level of density functional theory, obtaining the same values from eq. (1.43) required <5 cpu-hours to calculate $\Delta q_l^‡$ and $\Delta \lambda_l^‡$ for *trans*-3,4-dimethylcyclobutene at the much higher B3LYP/6-311++G(3df,2pd) level.

Whereas the correlation between strain-induced barrier lowering and the restoring force of the local coordinate is independent of the length or the chemical composition of the "polymer," this is not the case for either strain itself or ground-state strain energy (Fig. 1.6C–D). Consequently, restoring force is the only measure of structural distortion of a long flexible polymer that is related to changes in its reactivity.

1.11 Experimental Validation of the Mechanochemical Formalism

To validate these conclusions experimentally, we have developed[73-78,81] an alternative to conventional force spectroscopy. In the latter, a reactive moiety is incorporated in a long flexible polymer, which is controllably stretched using micromanipulation techniques[56] or with far less control by sonicating its dilute solution.[3] Our approach relies on a series of increasingly strained macrocycles of the *E* isomer of stiff stilbene (red, Fig. 1.7) whose C6,C6′ axis is constrained by a molecular strap (X, Y) containing the reactive moiety (blue sphere). The strained *E* macrocycle is readily available by photoisomerization of the strain-free *Z* analog at ~400 nm. This *Z* macrocycle serves both as a convenient precursor to and an electronically equivalent strain-free reference for the strained *E* analog. Varying the length and conformational flexibility of the inert parts of the strap (X, Y) is a simple way to increment the restoring force of a specific local coordinate of the reactive moiety over a range of >600 pN.

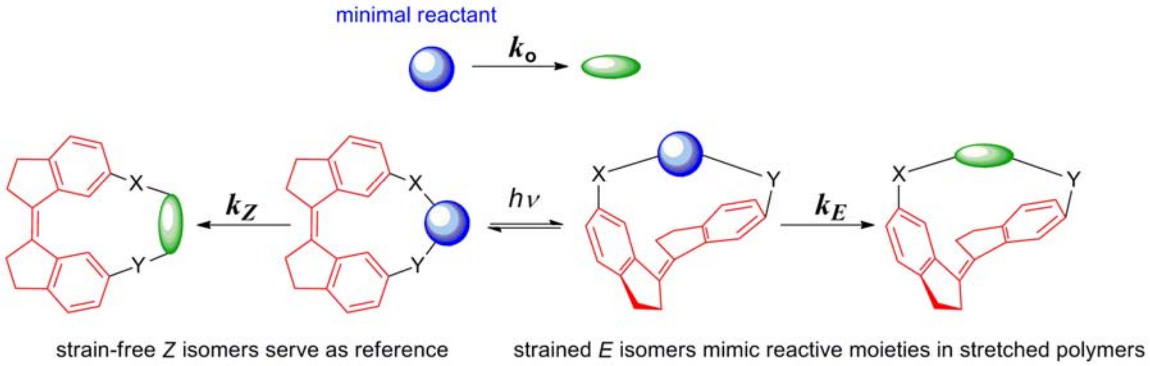

Fig. 1.7. A general scheme of a strategy to measure force-dependent kinetics of a localized reaction (blue sphere converting to green oval) using strained macrocycles of (*E*)-stiff stilbene (red) without the complications of manipulating polymers. Adapted from ref. 75.

The chemical inertness of stiff stilbene makes it compatible with diverse chemical reactions, allowing the relationship between the restoring force of a local coordinate and reaction rates to be studied broadly within the same general molecular architecture. The high aspect ratio of stiff stilbene (its strain-free *E* isomer is planar and the *Z* isomer is nearly planar) limits the steric interaction between the reactive moiety and stiff stilbene, mimicking the highly anisotropic tensile strains in stretched polymers. The large free energy of activation of thermal $E \leftrightarrows Z$ isomerization of free stiff stilbene (~43 kcal/mol) inhibits thermal relaxation of even highly strained *E* macrocycles. Hence, stiff stilbene is the molecular-scale functional analog of microscopic force probes used in single-molecule force spectroscopy (Fig. 1.8), and we call it a molecular force probe.

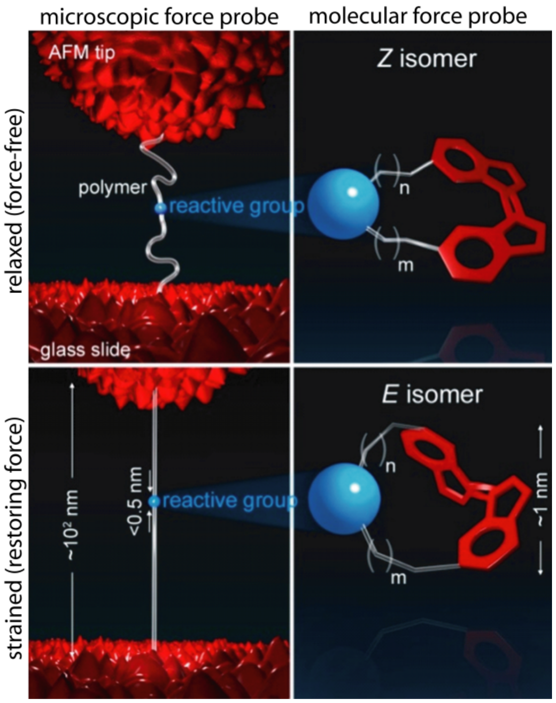

Fig. 1.8. Left: Measurements of force-dependent kinetics of localized reactions by conventional single-molecule force spectroscopy require the incorporation of the reactive moiety (blue sphere) into a long flexible polymer, attaching the polymer to a pair of microscopic force probes (here, the tip of the atomic force microscope cantilever and a glass slide on a piezoelectric stage) and stretching it by separating the probes. The size of the reactive moiety is typically less than the surface roughness of the probes or the magnitude of their thermal fluctuations, which significantly limits the accuracy of the measurements and the scope of reactions amenable to such studies. Right: a reactive moiety incorporated in a 5–10 atom-long inert strap constraining the *E* isomer of stiff stilbene (red) experiences approximately the same pattern of strain as in stretched polymer. The modest size of the reactant facilitates the design, implementation and molecular interpretation of the measured rates. The strain of the reactive moiety is controlled by the length and conformational flexibility of the strap so that a series of ~10–12 macrocycles of 15–20 endocyclic atoms can reproduce the range of the restoring forces accessible in a typical single-molecule force experiment. The strained *E* isomers are obtained by photoisomerization of strain-free *Z* analogs, which are synthesized using conventional chemistry. From ref. 74.

Stiff stilbene allows the kinetics of diverse chemical reactions to be measured as a function of the restoring force of any molecular degree of freedom of the reactive moiety in four steps:[73]

A series of strain-free *Z* macrocycles containing between 15 and 22 endocyclic atoms is synthesized using standard methods, such as stereoselective intramolecular McMurry coupling[84] of a pair of indanones linked by a strap containing the reactive moiety.

Irradiation of dilute solutions of *Z* macrocycles at ~400 nm generates photostationary mixtures containing 3–70% of the strained *E* isomer. The smaller (and hence the more strained) the *E* macrocycle is, the lower its fraction in the photostationary state due to the lower quantum yield of *Z*→*E* photoisomerization. This strain-dependent quantum yield is the primary factor limiting the maximum strain (and restoring force) accessible with this method.

Although individual isomers are readily available by chromatographic separation of the photostationary mixture, such separation is rarely necessary or even desired. Instead, the kinetics of the substrate reaction is measured in both isomers simultaneously in competition experiments using the photostationary mixture. When the difference in the relative reactivities of the two isomers is so large that only one isomer reacts under given experimental conditions, the more inert analog serves as a convenient internal standard. The modest size of the reactants greatly simplifies, and increases the accuracy of, measurements of the activation parameters using the whole range of experimental techniques of chemical kinetics. We typically monitor reaction progress by UV-vis spectrophotometry or HPLC, because of the ease of automation and the small amount of material required.

The interpretation of the experimental results within the force formalism relies on quantum chemical calculations of the structures of the ground and transition states and the corresponding restoring forces, which cannot be measured directly. Good agreement between the calculated and measured activation parameters (i.e., free energies and enthalpies of activation, $\Delta G^{\ddagger}$ and $\Delta H^{\ddagger}$, respectively) supports the validity of such calculations.

Several strategies exist to estimate the restoring forces of molecular degrees of freedom using optimized structures of the macrocycles and of isolated minimal reactants. The simplest method is given by eq. (1.44), where $\boldsymbol{Q}_X(l)$ (X is Z or E) is local coordinate l in the X isomer of a macrocycle, and q_l^{o} and λ_l are the corresponding coordinate and its compliance in an isolated reactive moiety (the minimal reactant). This method is reliable for modestly stiff coordinates (e.g., compliances on the order of 1 Å/nN for internuclear distances).

$$f_l^X = \frac{\boldsymbol{Q}_X(l) - q_l^{\mathrm{o}}}{\lambda_l} \tag{1.44}$$

The strain of much stiffer degrees of freedom, such as covalent bonds, in *E* macrocycles is too small to estimate their restoring forces reliably by eq. (1.44). Likewise, if the reactive moiety has multiple conformers, a small energy penalty may be required for it to adopt a conformation in a macrocycle that deviates from the lowest-energy conformation of the minimal reactant, making the strain-free value of the local coordinate derived from the minimal reactant ambiguous. The restoring forces of such coordinates are best estimated by eq. (1.45), where $\boldsymbol{Q}_X(1)$ is the value of the central dihedral of stiff stilbene in the *X* isomer of a macrocycle and q_1^{o} is the value of the same dihedral in the *X* isomer of *free* stiff stilbene, $\boldsymbol{H}_X^{-1}(1,1)$ and $\boldsymbol{H}_X^{-1}(1,l)$ are the compliances of the stiff stilbene dihedral and the off-diagonal element of the compliance matrix of the *X* isomer of a macrocycle.[85,86]

$$f_l^X = \frac{\boldsymbol{H}_X^{-1}(1,l)}{\lambda_l \boldsymbol{H}_X^{-1}(1,1)}\left(\boldsymbol{Q}_X(1) - q_1^{\mathrm{o}}\right) \qquad (1.45)$$

Because even small macrocycles have multiple thermally accessible conformers, the restoring forces are calculated for each conformer individually and then Boltzmann-averaged. The measured difference in the free energy of activation between the *Z* and *E* isomers of each macrocycle, $\Delta\Delta G^{\ddagger}$, is compared with those predicted by the chemomechanical formalism, using a suitably modified version of eq. (1.43) (eq. (1.46): note that the last two terms are <0.1 kcal/mol and we typically neglect them).

$$\begin{aligned}\Delta G_{\mathrm{Z}}^{\ddagger} - \Delta G_{\mathrm{E}}^{\ddagger} = {} & \left(\left(\langle f_l^{\mathrm{R}}\rangle \frac{\boldsymbol{H}_{\mathrm{R}}^{-1}(l,l)}{\boldsymbol{H}_{\ddagger}^{-1}(l,l)}\right)_{\mathrm{E}} - \left(\langle f_l^{\mathrm{R}}\rangle \frac{\boldsymbol{H}_{\mathrm{R}}^{-1}(l,l)}{\boldsymbol{H}_{\ddagger}^{-1}(l,l)}\right)_{\mathrm{Z}}\right)\Delta q_l^{\ddagger} \\ & + \left(\left(\langle f_l^{\mathrm{R}}\rangle^2 \frac{\boldsymbol{H}_{\mathrm{R}}^{-1}(l,l)}{\boldsymbol{H}_{\ddagger}^{-1}(l,l)}\right)_{\mathrm{E}} - \left(\langle f_l^{\mathrm{R}}\rangle^2 \frac{\boldsymbol{H}_{\mathrm{R}}^{-1}(l,l)}{\boldsymbol{H}_{\ddagger}^{-1}(l,l)}\right)_{\mathrm{Z}}\right)\frac{\Delta\lambda_l^{\ddagger}}{2} \\ & - \left(\frac{1}{\boldsymbol{H}_{\mathrm{E}^{\ddagger}}^{-1}(l,l)} - \frac{1}{\boldsymbol{H}_{\mathrm{Z}^{\ddagger}}^{-1}(l,l)}\right)\left(\Delta q_l^{\ddagger}\right)^2 - \beta^{-1}\ln\left(\frac{Z^{\mathrm{Z}}}{Z^{\mathrm{E}}}\right)^{\ddagger}\left(\frac{Z^{\mathrm{E}}}{Z^{\mathrm{Z}}}\right)^{\mathrm{R}}\end{aligned} \qquad (1.46)$$

Fig. 1.9 shows representative examples of the measured (points) and calculated (lines) correlations between rate constants of three simple reactions and the restoring forces of the local coordinate shown by black arrows. The two nucleophilic-displacement reactions (sulfonate hydrolysis, red, and thiol/disulfide exchange, green) manifest force–rate correlations consistent with the intuitive model in Fig. 1.5. In both cases, the angle between the scissile and the other endocyclic bonds to the electrophilic atom (C in sulfate and S in disulfide) contracts. In sulfonate hydrolysis, this contraction is more than compensated by the elongation of the scissile C–O bond. In contrast, the combination of longer C–S spectator bond that serves as a lever and the smaller elongation of the scissile S–S bond in the disulfide/thiol exchange results in very small $\Delta q_l^\ddagger$ (0.08 Å) and consequently, force-independent kinetics. The changes in the bond angles are also important in electrocyclic C–C bond dissociation (blue), which nearly double $\Delta q_l^\ddagger$ relative to the scissile bond elongation, resulting in ~5 × 10^6-fold acceleration of this reaction at room temperature in response to a force of 600 pN. Interestingly, a very large number of substituted cyclobutenes have been prepared and studied over the years by physical organic chemists, who eventually concluded that the reaction is insensitive to strain. This erroneous conclusion simply reflects the limited type of molecular architectures that physical organic chemists rely on to control molecular strain rather than the intrinsic properties of electrocyclic reactions.

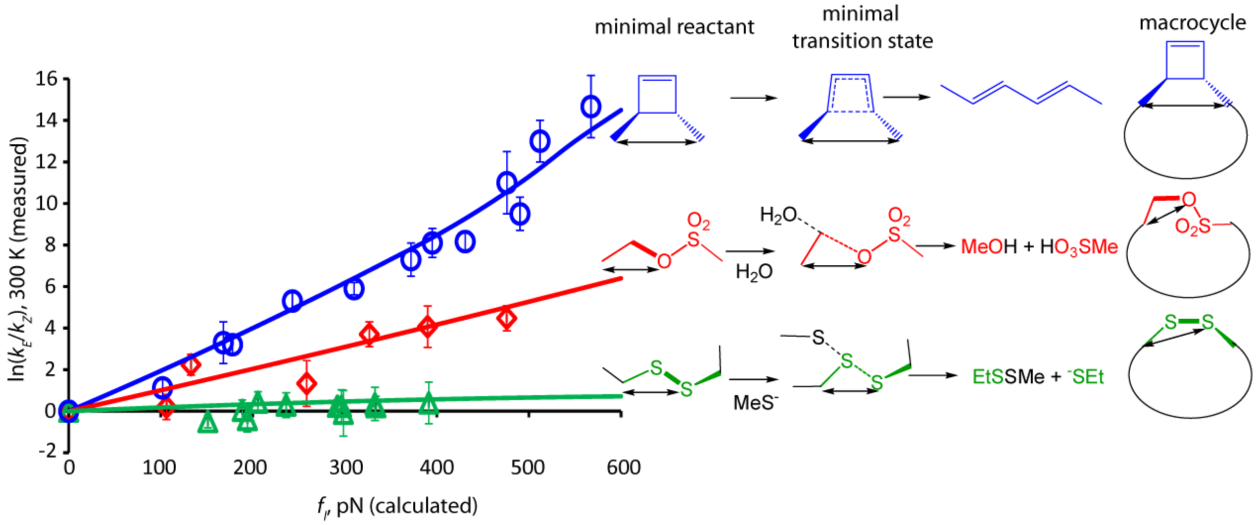

Fig. 1.9. Measured (points) and calculated (lines, eq. (1.46)) rate–force correlations of three reactions (right).[74-76,78] The rate constants are plotted against the restoring force of the local coordinate, q_l, which is shown on structures by arrows.

The validity of eq. (1.46) for reactions as mechanistically diverse as electrocyclic isomerization and nucleophilic displacements suggest that factors known to control the reactivity of small strained molecules such as differential solvation, steric hindrance or substituent effects[33,51,87] contribute negligibly to measured $\Delta\Delta G^\ddagger$ values either within a single macrocyclic pair or across the series. In other words, stiff stilbene mimics the overstretched polymer in its effect on reaction kinetics.

1.12 The Chemomechanical Coupling Coefficient

The reactive moieties discussed above all contained local coordinates with the chemomechanical coefficient $\alpha \sim 1$, which makes them intuitive. However, such local coordinates are unlikely to always exist. For example, a motor protein, such as kinesin, undergoes a conformational change on the order of 1 nm per 1 ATP molecule hydrolyzed.[10] No local coordinate of ATP changes as much. A fundamental question relevant to the design of mechanoresponsive polymers is the maximum magnitude of the chemomechanical coefficient α attainable for different types of reactions and how to increase it by molecular design of the reactive site. Simple calculations indicate that incorporating flexurally rigid molecular moieties (e.g., acetylene) between the atom(s) whose bonding changes during the reaction and the rest of the polymer backbone may be a simple way to magnify α. In motor proteins α is probably $\sim 10^3$, but this amplification comes at the expense of large 2nd-order effects that result in complete inhibition of the ATPase activity at restoring forces of <10 pN.[29]

1.13 Future Directions

Many potential applications of mechanochemistry in the operation of various functional materials have been discussed elsewhere recently.[3,24] The design of chemically driven actuating materials and their relaxation kinetics while loaded are inherently mechanochemical questions of anisotropic coupling between micro- or macroscopic and molecular dynamics. The conception of molecular-level probes to enable studies and efficient exploitation of such multiscale coupling is generally agreed to be a goal for contemporary polymer science,[88] and their development offers the potential for both conceptual and practical advances in the physics of polymers, soft matter, and biomolecules.[89] Much of the discussion of self-healing and self-assessing materials focuses on the identification and design of monomers whose reaction kinetics are sensitive to large-scale stress (occasionally called mechanophores). Though many moieties have been shown qualitatively to respond to large-scale stresses, their force-dependent kinetics remain little understood. Until such data is available, these molecules cannot be used as practical functional or diagnostic components of bulk materials or molecular systems. Below we discuss a few of the conceptual problems which may now be assailable with the tools of mechanochemical kinetics in hand.

1.13.1 Mechanochemical Activation Is Not a Binary On/Off Response

Too often a chemical response of a molecular moiety to bulk stresses is discussed in terms of a binary event in which a certain threshold force “switches” a reaction on, i.e. once enough force is applied reactivity changes dramatically and suddenly. Yet, mechanochemical phenomena are thermally activated processes whose kinetic barriers are lowered (or raised) as the reactants are strained. The kinetics of the response may be limited by a variety of dynamic processes, from actual chemistry to large-scale rearrangement of stressed materials. Which process will dominate the observed response depends not only on the underlying chemistry but also on the mechanical properties of the matrix and the temporal resolution of the measurements. Because the spatial distribution of stresses in bulk materials may be highly non-uniform, knowing the extent of a reaction over a finite period of time does not allow one to differentiate between a uniform conversion across the sample at lower force or accumulation of rapid but highly localized reactions at much higher local forces.

If one knows the relationship between the restoring force of a local internal coordinate of the reactive site and its rate, at least the upper and lower bounds can be placed on volume-averaged and highly localized stresses. In addition, stressing a sample of uniformly distributed reactive sites with different force–rate profiles allows the duration and magnitude of force to be inferred. Such a self-assessing material does not require constant monitoring to infer maximum and average forces over a desired time period.

The sensitivity and resolution of such self-assessing materials is ultimately limited by strain-free and force-dependent kinetics of its mechanochromic monomers. For example, if the two isomers of a mechanochromic monomer are in a rapid equilibrium at room temperature (as is the case for spiropyranes), the temporal characterization of the mechanochromic response of a material containing them would reveal information about non-chemical dynamics, such as the redistribution of stresses at scales >10 nm. An inert strain-free mechanochrome with a large linear ($\Delta q_l^{\ddagger}$) term of its $\Delta\Delta G^{\ddagger}(f_l)$ dependence (eq. (1.43)) would be particularly useful in measuring fairly small forces, but will saturate at larger forces. To reliably monitor high (and possibly transient) forces, a mechanochrome with a large positive quadratic ($\Delta\lambda_l^{\ddagger}$) term is required. While our ability to design new latent chromophores with a desired $\Delta\Delta G^{\ddagger}(f_l)$ profile remains limited, the theoretical and experimental platforms reviewed here make such an endeavour much more plausible then ever before.

1.13.2 Temporaspatial Distributions of Stress in Complex Dynamic Systems

The realization of the potential of mechanochemistry to yield quantitative stress–strain maps of materials at the molecular level has also been suggested as an important goal for chemists and materials scientists.[24] We suggest that mechanochromes as molecular-level force detectors can help solve at least four important questions in modern materials science:

1.13.2.1 Affine/Nonaffine Response in Strained Materials

Perhaps the most fundamental question of elasticity in polymeric materials is how macroscopic strains are transmitted to the molecular level and how molecular-level properties and arrangements dictate the macroscopic properties. While elastic (affine) descriptions relating stress and strain are accurate at the macroscopic level, they break down at smaller length scales where the anharmonic (nonaffine) force–elongation behaviour of individual polymer chains dominates. The importance of affine/nonaffine transition has been noted in crosslinked or entangled polymer networks,[90] networks of semi-flexible protein filaments[91,92] and other fibrous or foamy materials,[93] and nonaffine displacements underlie the macroscopic strain-hardening properties of glassy polymers.[94] Such materials can exhibit complex mechanical responses which are not readily described by macroscopic theories of elasticity that apply to rubbery materials.

The challenge of explaining how macroscopic stress–strain behaviour relates to molecular force–elongation and of experimentally validating the existing models remains at the forefront for materials science and biophysics. Such experimental validation remains a particular challenge because of the need of sub-nm spatial resolution over large areas. Nonaffine strain fields can be visualized with micron-level resolution by tracking embedded tracer particles with confocal microscopy,[95] but the smaller scales remain invisible. Indeed, in rigid polymer networks (e.g., those with high cross linking density), the affine/nonaffine transition is likely at length scales of ~10 nm, far below the spatial resolution of optical methods. Monomers with well-defined force-dependent chemistry allow one to bypass optical methods. For example, sulfolene undergoes electrocyclic expulsion of gaseous SO_2 to generate sulfur-free butadiene, which is accelerated by tensile strain. If SO_2 escapes from the material on the timescale of interest, the relative concentration of sulfolene and its sulfur-free produce can be mapped using various X-ray surface (and subsurface) characterization methods.

The challenge of explaining how macroscopic stress–strain behaviour relates to molecular force–elongation and of experimentally validating the existing models remains at the forefront for materials science and biophysics. Such experimental validation remains a particular challenge because of the need of sub-nm spatial resolution over large areas. Nonaffine strain fields can be visualized with micron-level resolution by tracking embedded tracer particles with confocal microscopy,[95] but the smaller scales remain invisible. Indeed, in rigid polymer networks (e.g., those with high cross linking density), the affine/nonaffine transition is likely at length scales of ~10 nm, far below the spatial resolution of optical methods. Monomers with well-defined force-dependent chemistry allow one to bypass optical methods. For example, sulfolene undergoes electrocyclic expulsion of gaseous SO_2 to general sulfur-free butadiene, which is accelerated by tensile strain. If SO_2 escapes from the material on the timescale of interest, the relative concentration of sulfolene and its sulfur-free produce can be mapped using various X-ray surface (and subsurface) characterization methods.

1.13.2.2 Viscoelastic Deformation

Viscoelasticity involves a balance between the mechanical properties of solids and liquids over different time scales. Entangled polymer melts deform (approximately) elastically on short time scales but exhibit flow over longer time scales as polymer chains move past one another.[59] This behaviour results from dissipation of local stresses in polymeric materials requiring macromolecular mobility, which can be a slow, thermally activated process in restricted environments. How much force is required for a polymer chain to flow? How does the entangled network around the macromolecule deform in response to these forces? Are these forces high enough to significantly accelerate covalent reactions? Mechanochemistry of viscoelastic flows provides a unique opportunity to probe the molecular events responsible for dissipation of stresses by translation.

1.13.2.3 Fluid Dynamics

The questions of molecular-level forces involved in fluids are related. The now-enormous and hugely interdisciplinary field of microfluidics has a rich physics that describes it, and it has played host to a number of studies that have further elucidated concepts in polymer dynamics.[96] Single macromolecules can be held with exquisite control at stagnation points in crossed flow cells,[97] and at high enough strain rates induced by the flows, macromolecular rupture occurs.[3]

Just as employing advances in manipulating elongational and shear flows has allowed for advancements in polymer physics, mechanochemistry may further enlighten the understanding of non-Newtonian fluids. The existing models used to describe the forces of flowing polymer solutions may be complemented with the information about internal molecular forces available from mechanochemical kinetics.

1.13.2.4 Forces Experienced During Sonication

Despite the fact that chain scission in ultrasonicated polymer solutions has been studied for decades, the chemistry and the reaction mechanism of fragmentation remains uncertain.[3,81] Similarities between polymer degradation in acoustic fields and in transient elongational flows have been noted, but there are also distinct differences, such as the timescale and geometry of the flows, which complicates generalizations.[98,99] While complex models accounting for the transduction of acoustic energy into heat can yield numerical simulations that reproduce bubble dynamics,[100] a model relating the acoustic energy absorbed during cavitation to the shock waves formed upon bubble collapse was reported only recently.[101]

The dynamics of individual macromolecules, including the tensile forces they may experience, their distribution and duration, remains unknown. Monomers with well-defined force-dependent kinetics properly distributed throughout the polymer chain could reveal the distribution of forces during sonication. Such experiments can also address a major controversy of such experiments: the relative contribution of purely thermal and strain-accelerated kinetics.

1.13.3 Photomechanochemistry

We are also intrigued by the possibility of developing a similar understanding of the effect of molecular restoring force on photochemical processes. Evidence exists that the quantum yields for photochemical reactions decrease as the amount of molecular strain in the product increases.[78] The key to understanding this phenomenon may be in discerning the effect of molecular restoring force on electronically excited energy surfaces and their conical intersections with ground state energy surfaces, the set of molecular configurations through which molecules evolve as they relax during photochemical isomerization. Though there is a growing body of work regarding the properties of conical intersections,[102,103] to our knowledge only a few recent theoretical studies have begun to examine the effect of varying mechanical constraints on photochemical processes.[104,105] Again, properly designed and calibrated monomers would be useful for such studies and would also facilitate the design of chromophores for photomechanical energy conversion in photoactuating polymers.

1.14 Conclusions

The efficient design of mechanoresponsive polymers at the monomer level requires a detailed understanding of how the kinetics of localized reactions in materials are affected by the dynamic build-up and relaxation of large-scale (>50 nm) strains. Chemists have studied the reactivity of small strained molecules for over a century now, and the empirical model of linear free energy relationships has proven quite useful in guiding chemical thinking about strain-induced reactions in conventional chemistry. However, the analogy between strain as understood by chemists and strain that perturbs chemical reactions in loaded materials is tenuous enough to be even qualitatively misleading. The ground-state strain energy that serves as the quantitative proxy of kinetically-significant molecular strain in small reactants cannot be defined in mechanochemical processes because of the intractably large size of the corresponding ground states.

More importantly, the effect of an anisotropically strained environment on the kinetics of even localized reactions cannot be described by the standard variables of conventional kinetic models: temperature, pressure, dielectric constant and viscosity. What new macroscopic parameter is required is not entirely clear. In the simplest mechanochemical processes, such as reactions in individual macromolecules stretched by micromanipulation techniques or pressure gradients that drive polymer flows in dilute solutions or interfaces, the experimental control parameter (e.g., strain rate or surface tension gradient) can be related to the restoring force of an effective constrained degree of freedom of the polymer (or its fragment) reasonably accurately. The availability of an internally consistent and physically sound formalism to relate the macromolecular restoring force and reaction rate establishes the general and predictive relationship between the macroscopic and molecular variables. In other words, chemomechanics is a valid kinetic theory for this subset of multiscale dynamic phenomena.

The primary challenges in expanding the practical utility of the chemomechanical formalism to broader phenomena, such as reactions in viscoelastic polymer flows, may have to be addressed using new coarse-graining strategies. To estimate steady-state reaction kinetics in these processes using the chemomechanical model requires a probability density function of the time-average extension of polymer fragments containing the reactive moieties. It may be possible to use simple chemical reactions whose dependence on the restoring force of local coordinates is known to infer the distribution of macromolecular strains in such complex systems. This approach will be greatly facilitated by the ability to measure such dependences on single reactive moieties using molecular force probes, as described above.

1.15 Acknowledgments

We are grateful to Drs. Z. Huang, Q.-Z. Yang, D. Khvostichenko, and Y. Tian; and X. Feng, M. R. Hermes, and N. C. Rubin for their contribution to the ideas and data presented in this review. The work was supported by the National Science Foundation (NSF) CAREER Award (CHE-0748281), the US Air Force Office of the Scientific Research Young Investigator Award (FA9550-08-1-0072), the American Chemical Society Petroleum Research Fund (48454-AC3 and 43354-G3), and the University of Illinois. T.K. thanks the Office of Naval Research and the NSF for predoctoral fellowships. The HPCMP of the DoD and NSF-supported NCSA provided grants of computational time.

1.16 References

1. Lee, C. K.; Davis, D. A.; White, S. R.; Moore, J. S.; Sottos, N. R.; Braun, P. V., Force-Induced Redistribution of a Chemical Equilibrium. *J. Am. Chem. Soc.* **2010**, *132*, 16107–16111.
2. Davis, D. A.; Hamilton, A.; Yang, J.; Cremar, L. D.; Van Gough, D.; Potisek, S. L.; Ong, M. T.; Braun, P. V.; Martinez, T. J.; White, S. R.; Moore, J. S.; Sottos, N. R., Force-Induced Activation of Covalent Bonds in Mechanoresponsive Polymeric Materials. *Nature* **2009**, *459*, 68–72.
3. Caruso, M. M.; Davis, D. A.; Shen, Q.; Odom, S. A.; Sottos, N. R.; White, S. R.; Moore, J. S., Mechanically-Induced Chemical Changes in Polymeric Materials. *Chem. Rev.* **2009**, *109*, 5755–5798.
4. Lenhardt, J. M.; Ong, M. T.; Choe, R.; Evenhuis, C. R.; Martinez, T. J.; Craig, S. L., Trapping a Diradical Transition State by Mechanochemical Polymer Extension. *Science* **2010**, *329*, 1057–1060.

5. Lenhardt, J. M.; Black, A. L.; Craig, S. L., gem-Dichlorocyclopropanes as Abundant and Efficient Mechanophores in Polybutadiene Copolymers under Mechanical Stress. *J. Am. Chem. Soc.* **2009**, *131*, 10818–10819.
6. Wiggins, K. M.; Hudnall, T. W.; Shen, Q.; Kryger, M. J.; Moore, J. S.; Bielawski, C. W., Mechanical Reconfiguration of Stereoisomers. *J. Am. Chem. Soc.* **2010**, *132*, 3256–3257.
7. Kryger, M. J.; Ong, M. T.; Odom, S. A.; Sottos, N. R.; White, S. R.; Martinez, T. J.; Moore, J. S., Masked Cyanoacrylates Unveiled by Mechanical Force. *J. Am. Chem. Soc.* **2010**, *132*, 4558–4559.
8. Sheiko, S. S.; Sun, F. C.; Randall, A.; Shirvanyants, D.; Rubinstein, M.; Lee, H.-i.; Matyjaszewski, K., Adsorption-Induced Scission of Carbon-Carbon Bonds. *Nature* **2006**, *440*, 191–194.
9. Park, I.; Shirvanyants, D.; Nese, A.; Matyjaszewski, K.; Rubinstein, M.; Sheiko, S. S., Spontaneous and Specific Activation of Chemical Bonds in Macromolecular Fluids. *J. Am. Chem. Soc.* **2010**, *132*, 12487–12491.
10. Schliwa, M., *Molecular Motors*. Wiley-VCH: New York, 2003.
11. Hugel, T.; Holland, N. B.; Cattani, A.; Moroder, L.; Seitz, M.; Gaub, H. E., Single-Molecule Optomechanical Cycle. *Science* **2002**, *296*, 1103–1106.
12. Corbett, D.; Warner, M., Changing Liquid Crystal Elastomer Ordering with Light - A Route to Opto-Mechanically Responsive Materials. *Liq. Cryst.* **2009**, *36*, 1263–1280.
13. Ikeda, T.; Mamiya, J. i.; Yu, Y., Photomechanics of Liquid-Crystalline Elastomers and Other Polymers. *Angew. Chem. Int. Ed.* **2007**, *46*, 506–528.
14. O'Bryan, G.; Wong, B. M.; McElhanon, J. R., Stress Sensing in Polycaprolactone Films via an Embedded Photochromic Compound. *ACS Appl. Mater. Interfaces* **2010**, *2*, 1594–1600.
15. Casale, A.; Porter, R. S., *Polymer Stress Reactions: Introduction*. Academic Press: New York, 1978; Vol. 1.
16. Beyer, M. K.; Clausen-Schaumann, H., Mechanochemistry: The Mechanical Activation of Covalent Bonds. *Chem. Rev.* **2005**, *105*, 2921–2948.
17. Basedow, A. M.; Ebert, K. H., Ultrasonic Degradation of Polymers in Solution. *Advances in Polymer Science* **1977**, *22*, 83–148.

18. Anquetil, P. A.; Madden, J. D.; Yu, H.-h.; Swager, T. M.; Hunter, I. W., Biologically Inspired Large Contraction Conducting Polymer Actuators. In *Handbook of Organic Electronics and Photonics*, Nalwa, H. S., Ed. American Scientific Publishers: 2008.

19. Barrett, C. J.; Mamiya, J.-i.; Yager, K. G.; Ikeda, T., Photo-Mechanical Effects in Azobenzene-Containing Soft Materials. *Soft Matter* **2007**, *3*, 1249–1261.

20. Yu, Y.; Ikeda, T., Photodeformable Materials and Photomechanical Effects Based on Azobenzene-Containing Polymers and Liquid Crystals. In *Smart Light-Responsive Materials*, Zhao, Y.; Ikeda, T., Eds. John Wiley & Sons, Inc.: Hoboken, NJ, 2008; pp 95–144.

21. Koerner, H.; White, T. J.; Tabiryan, N. V.; Bunning, T. J.; Vaia, R. A., Photogenerating Work from Polymers. *Mater. Today* **2008**, *11*, 34–42.

22. Browne, W. R.; Feringa, B. L., Making Molecular Machines Work. *Nat. Nanotechnol.* **2006**, *1*, 25–35.

23. Euan , R. K.; David , A. L.; Francesco, Z., Synthetic Molecular Motors and Mechanical Machines. *Angew. Chem. Int. Ed.* **2007**, *46*, 72–191.

24. Black, A. L.; Lenhardt, J. M.; Craig, S. L., From Molecular Mechanochemistry to Stress-Responsive Materials. *J. Mater. Chem.* **2011**, *21*, 1655–1663.

25. Kolomeisky, A. B.; Fisher, M. E., Molecular Motors: A Theorist's Perspective. *Annu. Rev. Phys. Chem.* **2007**, *58*, 675–695.

26. Astumian, R. D., Thermodynamics and Kinetics of Molecular Motors. *Biophys. J.* **2010**, *98*, 2401–2409.

27. Schliwa, M.; Woehlke, G., Molecular Motors. *Nature* **2003**, *422*, 759–765.

28. Bustamante, C.; Keller, D.; Oster, G., The Physics of Molecular Motors. *Acc. Chem. Res.* **2001**, *34*, 412–420.

29. Reimann, P., Brownian Motors: Noisy Transport Far from Equilibrium. *Phys. Rep.* **2002**, *361*, 57–265.

30. White, S. R.; Caruso, M. M.; Moore, J. S., Autonomic Healing of Polymers. *MRS Bull.* **2008**, *33*, 766–769.

31. *Directing Matter and Energy: Five Challenges for Science and the Imagination*; Basic Energy Sciences Advisory Committee, U.S. Department of Energy: 2007.

32. French, R. H.; Parsegian, V. A.; Podgornik, R.; Rajter, R. F.; Jagota, A.; Luo, J.; Asthagiri, D.; Chaudhury, M. K.; Chiang, Y.-m.; Granick, S.; Kalinin, S.; Kardar, M.; Kjellander, R.; Langreth, D. C.; Lewis, J.; Lustig, S.; Wesolowski, D.; Wettlaufer, J. S.; Ching, W.-Y.; Finnis, M.; Houlihan, F.; von Lilienfeld, O. A.; van Oss, C. J.; Zemb, T., Long Range Interactions in Nanoscale Science. *Rev. Mod. Phys.* **2010**, *82*, 1887–1944.

33. Leffler, J. E.; Grunwald, E., *Rates and Equilibria of Organic Reactions*. Dover: New York, 1989.

34. Berry, R. S.; Rice, S. A.; Ross, J., *Physical and Chemical Kinetics*. 2nd ed.; Oxford University Press: New York, 2001.

35. Truhlar, D. G.; Garrett, B. C.; Klippenstein, S. J., Current Status of Transition-State Theory. *J. Phys. Chem.* **1996**, *100*, 12771–12800.

36. Fukui, K., The Path of Chemical Reactions - The IRC Approach. *Acc. Chem. Res.* **1981**, *14*, 363–368.

37. Allen, M. J.; Rudd, R. E.; McElfresh, M. W.; Balhorn, R., Time-Dependent Measure of a Nanoscale Force-Pulse Driven By the Axonemal Dynein Motors in Individual Live Sperm Cells. *Nanomed.-Nanotechnol.* **2010**, *6*, 510–515.

38. Hua, W.; Chung, J.; Gelles, J., Distinguishing Inchworm and Hand-Over-Hand Processive Kinesin Movement by Neck Rotation Measurements. *Science* **2002**, *295*, 844–848.

39. Miller, K. E.; Heidemann, S. R., What Is Slow Axonal Transport? *Exp. Cell Res.* **2008**, *314*, 1981–1990.

40. Kodera, N.; Yamamoto, D.; Ishikawa, R.; Ando, T., Video Imaging of Walking Myosin V by High-Speed Atomic Force Microscopy. *Nature* **2010**, *468*, 72–76.

41. Yardimci, H.; van Duffelen, M.; Mao, Y.; Rosenfeld, S. S.; Selvin, P. R., The Mitotic Kinesin CENP-E is a Processive Transport Motor. *Proc. Natl. Acad. Sci.* **2008**, *105*, 6016–6021.

42. Vogel, V., Mechanotransduction Involving Multimodular Proteins: Converting Force into Biochemical Signals. *Annu. Rev. Biophys. Biomol. Struct.* **2006**, *35*, 459–488.

43. Serak, S.; Tabiryan, N.; Vergara, R.; White, T. J.; Vaia, R. A.; Bunning, T. J., Liquid Crystalline Polymer Cantilever Oscillators Fueled by Light. *Soft Matter* **2010**, *6*, 779–783.

44. Harris, K. D.; Cuypers, R.; Scheibe, P.; Oosten, C. L. v.; Bastiaansen, C. W. M.; Lub, J.; Broer, D. J., Large Amplitude Light-Induced Motion in High Elastic Modulus Polymer Actuators. *J. Mater. Chem.* **2005**, *15*, 5043–5048.

45. Camacho-Lopez, M.; Finkelmann, H.; Palffy-Muhoray, P.; Shelley, M., Fast Liquid-Crystal Elastomer Swims into the Dark. *Nat. Mater.* **2004**, *3*, 307–310.

46. Astumian, R. D., The Unreasonable Effectiveness of Equilibrium Theory for Interpreting Nonequilibrium Experiments. *Am. J. Phys.* **2006**, *74*, 683–688.

47. Brauman, J. I.; Dodd, J. A.; Han, C.-C., Intrinsic Nucleophilicity. In *Nucleophilicity*, Harris, J., Ed. American Chemical Society: Washington, DC, 1987.

48. Tauchert, T. R., *Energy Principles in Structural Mechanics*. McGraw-Hill: New York, 1974.

49. Krebs, A.; Wilke, J., Angle Strained Cycloalkynes *Top. Curr. Chem.* **1983**, *109*, 189–233.

50. Greenberg, A.; Liebman, J. F., *Strained Organic Molecules*. Academic Press: New York, 1978.

51. Stirling, C. J. M., Evaluation of the Effect of Strain upon Reactivity. *Tetrahedron* **1985**, *41*, 1613–1666.

52. Wiberg, K. B., The Concept of Strain in Organic Chemistry. *Angew. Chem., Int. Ed. Engl.* **1986**, *25*, 312–322.

53. Cremer, D.; Kraka, E., The Concept of Molecular Strain: Basic Principles, Utility, and Limitations. In *Structure and Reactivity*, Liebman, J. F.; AGreenberg, A., Eds. VCH Publishers: New York, 1988.

54. Halton, B., Strain in Organic Chemistry: A Perspective. In *Advances in Strain in Organic Chemistry*, Halton, B., Ed. JAI Press Ltd.: London, 1991; Vol. 1, pp 1–17.

55. Codelli, J. A.; Baskin, J. M.; Agard, N. J.; Bertozzi, C. R., Second-Generation Difluorinated Cyclooctynes for Copper-Free Click Chemistry. . *J. Am. Chem. Soc.* **2008**, *2008*, 11486–11493.

56. Neuman, K. C.; Nagy, A., Single-Molecule Force Spectroscopy: Optical Tweezers, Magnetic Tweezers and Atomic Force Microscopy. *Nat. Methods* **2008**, *5*, 491–505.

57. Tanyeri, M.; Johnson-Chavarria, E. M.; Schroeder, C. M., Hydrodynamic Trap for Single Particles and Cells. *Appl. Phys. Lett.* **2010**, *96*, 224101/1–3.

58. Flory, P. J., *Statistical Mechanics of Chain Molecues*. Interscience Publishers: New York, 1969.
59. Rubinstein, M.; Colby, R. H., *Polymer Physics*. Oxford University Press: New York, 2003.
60. Hugel, T.; Rief, M.; Seitz, M.; Gaub, H. E.; Netz, R. R., Highly Stretched Single Polymers: Atomic-Force-Microscope Experiments Versus *Ab-Initio* Theory. *Phys. Rev. Lett.* **2005**, *94*, 048301/1–4.
61. Sotomayor, M.; Schulten, K., Single-Molecule Experiments in Vitro and in Silico. *Science* **2007**, *316*, 1144–1148.
62. Kochhar, G. S.; Bailey, A.; Mosey, N. J., Competition Between Orbitals and Stress in Mechanochemistry. *Angew. Chem. Int. Ed.* **2010**, *49*, 7452–7455.
63. Ong, M. T.; Leiding, J.; Tao, H.; Virshup, A. M.; Martinez, T. J., First Principles Dynamics and Minimum Energy Pathways for Mechanochemical Ring Opening of Cyclobutene. *J. Am. Chem. Soc.* **2009**, *131*, 6377–6379.
64. Ribas-Arino, J.; Shiga, M.; Marx, D., Mechanochemical Transduction of Externally Applied Forces to Mechanophores. *J. Am. Chem. Soc.* **2010**, *132*, 10609–10614.
65. Iozzi, M. F.; Helgaker, T.; Uggerud, E., Assessment of Theoretical Methods for the Determination of the Mechanochemical Strength of Covalent Bonds. *Mol. Phys.* **2009**, *107*, 2537–2546.
66. Jencks, W. P., A Primer for the Bema Hapothle. An Empirical Approach to the Characterization of Changing Transition-State Structures. *Chem. Rev.* **1985**, *85*, 511–527.
67. Kauzmann, W.; Eyring, H., The Viscous Flow of Large Molecules. *J. Am. Chem. Soc.* **1940**, *62*, 3113–3125.
68. Bell, G. I., Models for the Specific Adhesion of Cells to Cells. *Science* **1978**, *200*, 618–627.
69. Evans, E.; Ritchie, K., Dynamic Strength of Molecular Adhesion Bonds. *Biophys. J.* **1997**, *72*, 1541–1555.
70. Evans, E., Probing the Relation Between Force—Lifetime—and Chemistry in Single Molecular Bonds. *Annu. Rev. Biophys. Biomol. Struct.* **2001**, *30*, 105–128.
71. Hyeon, C.; Thirumalai, D., Measuring the Energy Landscape Roughness and the Transition State Location of Biomolecules Using Single Molecule Mechanical Unfolding Experiments. *J. Phys.: Condens. Matter* **2007**, *19*, 113101/1–27.

72. Wu, D.; Lenhardt, J. M.; Black, A. L.; Akhremitchev, B. B.; Craig, S. L., Molecular Stress Relief through a Force-Induced Irreversible Extension in Polymer Contour Length. *J. Am. Chem. Soc.* **2010**, *132*, 15936–15938.

73. Boulatov, R., Reaction Dynamics in the Formidable Gap. *Pure Appl. Chem.* **2011**, *83*, 25–41.

74. Yang, Q.-Z.; Huang, Z.; Kucharski, T. J.; Khvostichenko, D.; Chen, J.; Boulatov, R., A Molecular Force Probe. *Nat. Nanotechnol.* **2009**, *4*, 302–306.

75. Kucharski, T. J.; Yang, Q.-Z.; Tian, Y.; Boulatov, R., Strain-Dependent Acceleration of a Paradigmatic S_N2 Reaction Accurately Predicted by the Force Formalism. *J. Phys. Chem. Lett.* **2010**, *1*, 2820–2825.

76. Kucharski, T. J.; Huang, Z.; Yang, Q.-Z.; Tian, Y.; Rubin, N. C.; Concepcion, C. D.; Boulatov, R., Kinetics of Thiol/Disulfide Exchange Correlate Weakly with the Restoring Force in the Disulfide Moiety. *Angew. Chem. Int. Ed.* **2009**, *48*, 7040–7043.

77. Huang, Z.; Boulatov, R., Chemomechanics with Molecular Force Probes. *Pure Appl. Chem.* **2010**, *82*, 931–951.

78. Huang, Z.; Yang, Q.-Z.; Khvostichenko, D.; Kucharski, T. J.; Chen, J.; Boulatov, R., Method to Derive Restoring Forces of Strained Molecules from Kinetic Measurements. *J. Am. Chem. Soc.* **2009**, *131*, 1407–1409.

79. Kreuzer, H. J.; Payne, S. H., Stretching a Macromolecule in an Atomic Force Microscope: Statistical Mechanical Analysis. *Phys. Rev. E* **2001**, *63*, 021906/1–4.

80. Franco, I.; Schatz, G. C.; Ratner, M. A., Single-Molecule Pulling and the Folding of Donor-Acceptor Oligorotaxanes: Phenomenology and Interpretation *J. Chem. Phys.* **2009**, *131*, 124902/1–13.

81. Huang, Z.; Boulatov, R., Chemomechanics: Reaction Kinetics in Multiscale Phenomena. *Chem. Soc. Rev.* **2011**, *40*, 2359–2384.

82. Brauman, J. I., Not So Simple. *Science* **2008**, *319*, 168.

83. Chabinyc, M. L.; Craig, S. L.; Regan, C. K.; Brauman, J. I., Gas-Phase Ionic Reactions: Dynamics and Mechanism of Nucleophilic Displacements. *Science* **1998**, *279*, 1882–1886.

84. McMurry, J. E., Carbonyl-Coupling Reactions Using Low-Valent Titanium. *Chem. Rev.* **1989**, *89*, 1513–1524.

85. Baker, J., A Critical Assessment of the Use of Compliance Constants as Bond Strength Descriptors for Weak Interatomic Interactions. *J. Chem. Phys.* **2006**, *125*, 014103/1–6.

86. Brandhorst, K.; Grunenberg, J., Efficient Computation of Compliance Matrices in Redundant Internal Coordinates from Cartesian Hessians for Nonstationary Points. *J. Chem. Phys.* **2010**, *132*, 184101/1–7.

87. Lopez, X.; Dejaegere, A.; Karplus, M., Mechanism of Alkaline Hydrolysis of Cyclic and Acyclic Sulfates: An ab Initio Study with Solvation Correction. *J. Am. Chem. Soc.* **1999**, *121*, 5548–5558.

88. Ober, C. K.; Cheng, S. Z. D.; Hammond, P.; Muthukumar, M.; Reichmanis, E.; Wooley, K. *Interdisciplinary, Globally-Leading Polymer Science and Engineering*; National Science Foundation sponsored workshop: Arlington, VA, 2007.

89. Rubinstein, M., Polymer Physics—The Ugly Duckling Story: Will Polymer Physics Ever Become a Part of "Proper" Physics? *J. Polym. Sci. Pol. Phys.* **2010**, *48*, 2548–2551.

90. Rubinstein, M.; Panyukov, S., Nonaffine Deformation and Elasticity of Polymer Networks. *Macromolecules* **1997**, *30*, 8036–8044.

91. Missel, A. R.; Bai, M.; Klug, W. S.; Levine, A. J., Affine-Nonaffine Transition in Networks of Nematically Ordered Semiflexible Polymers. *Phys. Rev. E* **2010**, *82*, 041907/1–5.

92. Kang, H.; Wen, Q.; Janmey, P. A.; Tang, J. X.; Conti, E.; MacKintosh, F. C., Nonlinear Elasticity of Stiff Filament Networks: Strain Stiffening, Negative Normal Stress, and Filament Alignment in Fibrin Gels. *J. Phys. Chem. B* **2009**, *113*, 3799–3805.

93. Heussinger, C.; Frey, E., Stiff Polymers, Foams, and Fiber Networks. *Phys. Rev. Lett.* **2006**, *96*, 017802/1–4.

94. Vorselaars, B.; Lyulin, A. V.; Michels, M. A. J., Microscopic Mechanisms of Strain Hardening in Glassy Polymers. *Macromolecules* **2009**, *42*, 5829–5842.

95. Liu, J.; Koenderink, G. H.; Kasza, K. E.; MacKintosh, F. C.; Weitz, D. A., Visualizing the Strain Field in Semiflexible Polymer Networks: Strain Fluctuations and Nonlinear Rheology of F-Actin Gels. *Phys. Rev. Lett.* **2007**, *98*, 198304/1–4.

96. Squires, T. M.; Quake, S. R., Microfluidics: Fluid Physics at the Nanoliter Scale. *Rev. Mod. Phys.* **2005**, *77*, 977–1026.

97. Schroeder, C. M.; Babcock, H. P.; Shaqfeh, E. S. G.; Chu, S., Observation of Polymer Conformation Hysteresis in Extensional Flow. *Science* **2003**, *301*, 1515–1519.
98. Kuijpers, M. W. A.; Iedema, P. D.; Kemmere, M. F.; Keurentjes, J. T. F., The Mechanism of Cavitation-Induced Polymer Scission; Experimental and Computational Verification. *Polymer* **2004**, *45*, 6461–6467.
99. Nguyen, T.; Kausch, H.-H., Mechanochemical Degradation in Transient Elongational Flow. In *Macromolecules: Synthesis, Order and Advanced Properties*, Springer Berlin / Heidelberg: 1992; Vol. 100, pp 73–182.
100. Yasui, K., Effects of Thermal Conduction on Bubble Dynamics Near the Sonoluminescence Threshold. *J. Acoust. Soc. Am.* **1995**, *98*, 2772–2782.
101. Peshkovsky, S. L.; Peshkovsky, A. S., Shock-Wave Model of Acoustic Cavitation. *Ultrason. Sonochem.* **2008**, *15*, 618–628.
102. Domcke, W.; Yarkony, D. R.; Köppel, H., *Conical Intersections: Electronic Structure, Dynamics and Spectroscopy*. World Scientific: New Jersey, 2004; Vol. 15.
103. Levine, B. G.; Martínez, T. J., Isomerization through Conical Intersections. *Annu. Rev. Phys. Chem.* **2007**, *58*, 613–634.
104. Turanský, R.; Konôpka, M.; Doltsinis, N. L.; Štich, I.; Marx, D., Switching of Functionalized Azobenzene Suspended between Gold Tips by Mechanochemical, Photochemical, and Opto-Mechanical Means. *Phys. Chem. Chem. Phys.* **2010**, *12*, 13922–13932.
105. Creatini, L.; Cusati, T.; Granucci, G.; Persico, M., Photodynamics of Azobenzene in a Hindering Environment. *Chem. Phys.* **2008**, *347*, 492–502.

Chapter 2. Mechanochemical Acceleration of a Single-Barrier, Unimolecular Electrocyclic Reaction: Dimethylcyclobutene Ring Opening

Adapted from Yang, Q.-Z.*; Huang, Z.*; Kucharski, T. J.*; Khvostichenko, D.*; Chen, J.; Boulatov, R., A Molecular Force Probe. *Nat. Nanotechnol.* **2009**, *4*, 302–306. (*equal contribution) Copyright held by authors.

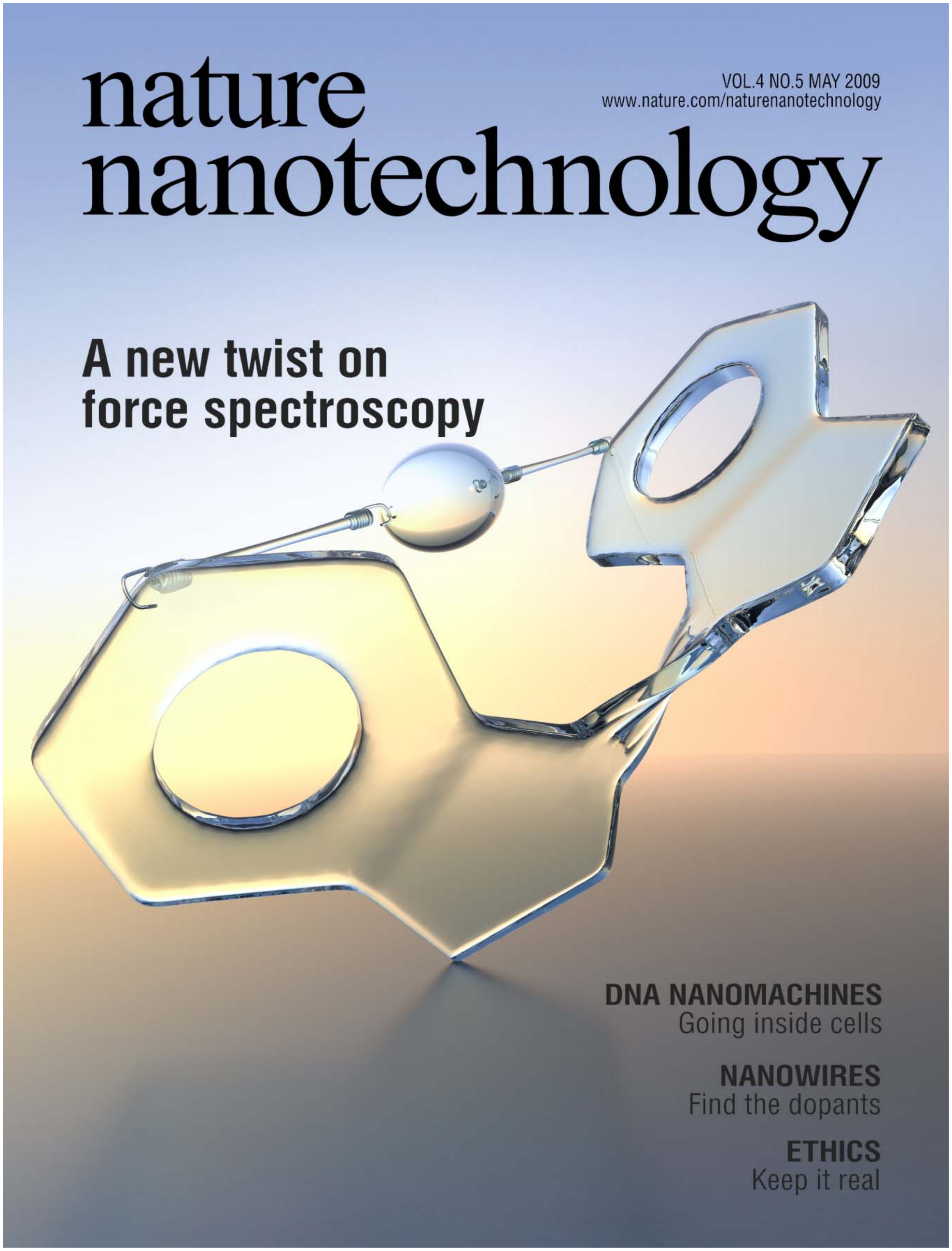

The figure above reproduces the May 2009 cover of *Nature Nanotechnology*. Reproduced with permission. © Nature Publishing Group, 2009.

2.1 Abstract

Force probes[1] allow reaction rates to be measured as a function of the restoring force in a molecule that has been stretched or compressed. Unlike strain energy,[2] approaches based on restoring force enable a quantitative molecular understanding[3] of phenomena as diverse as translation of microscopic objects by reacting molecules,[4-6] crack propagation[7,8] and mechanosensing.[9] Conceptually, localized reactions offer the best opportunity to gain fundamental insights into how rates vary with restoring forces but such reactions are particularly difficult to study systematically using microscopic force probes.[10-14] Here we show how a molecular force probe, stiff stilbene, simplifies force spectroscopy of localized reactions. We illustrate the capabilities of our approach by validating the central postulate of chemomechanical kinetics[15]—force lowers the activation barrier proportionally to the difference in a single internuclear distance between the ground and transition states projected on the force vector—on a paradigmatic unimolecular reaction: concerted dissociation of a C–C bond.

2.2 Introduction

In addition to comprising the most tractable systems for testing and improving kinetic models that incorporate force as a variable (so called chemomechanical models), covalent reactions of functional groups underlie many processes at the interface between molecular and microscopic scales, from the operation of motor proteins[4] and their synthetic analogs[5,16] to the fragmentation of macromolecules in shear flows[17,18] and upon surface absorption.[19] The potential of the force formalism to support quantitative molecular description of these processes is rooted in the size-invariant nature of molecular restoring force,[3] i.e. the relationship between the restoring force and rate is the same whether the reacting moiety is a part of a stretched polymer or a properly-designed small molecule.

Consequently, chemomechanical kinetics of localized reactions may be studied more productively by replacing the microscopic force probe with a *molecular* one (Fig. 2.1): an inert molecule whose restoring force can be varied systematically in <50 pN increments over at least a 500 pN range by constraining a single internuclear distance. By incorporating a functional group of interest (substrate) in the linker that constrains this distance and varying the length and/or conformational flexibility of this linker, a homologous series of macrocycles with increasing restoring force is synthesized. Standard methods of chemical kinetics are suitable for measuring the activation enthalpies and entropies of the substrate reaction. The restoring forces are available from high-level quantum-chemical calculations, whose accuracy is benchmarked against the experimental activation parameters. Studies of functional groups' reactivities by microscopic force probes are complicated not only by the inherent challenges of resolving localized reactions in macromolecules but also by the difficulties of measuring activation parameters, the lack of product characterization and the need for empirical models to estimate the molecular restoring force from distortions of the force probe, with concomitant uncertainties in the relative orientations of the force vector and the reacting moiety.[10-12,20] By eliminating these limitations, a molecular force probe would significantly simplify both the acquisition and interpretation of ensemble-average force–rate data.

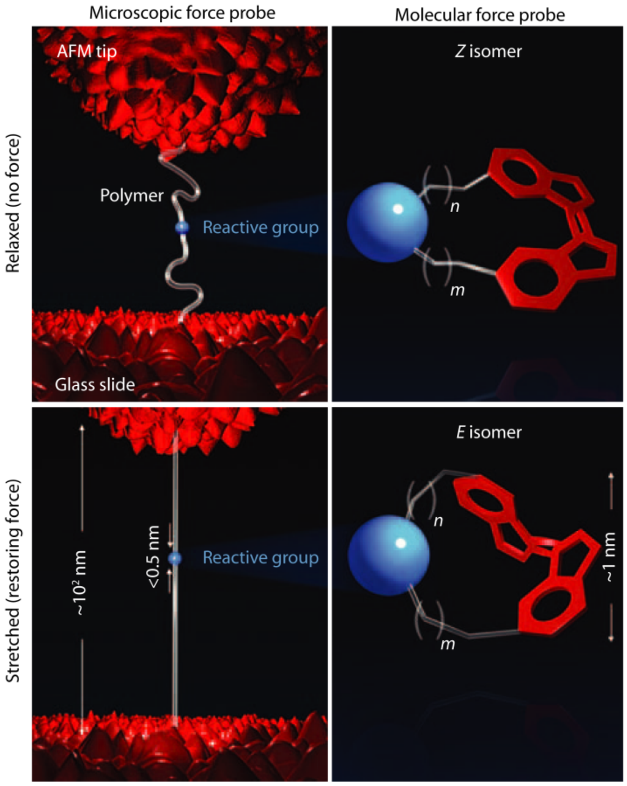

Fig. 2.1. Microscopic versus molecular force probes. Force spectroscopy studies reaction kinetics as a function of the restoring force of a stretched or compressed reactant. Microscopic force probes (left) are suited for reactions involving nm-scale structural changes such as protein unfolding. However, their energy surface roughness and thermal fluctuations obscure most localized chemical reactions. The latter are amenable to studies with a molecular force probe, such as stiff stilbene (red moiety in the right panels)—an inert molecular fragment whose restoring force is easily incrementable over hundreds of pico-Newtons (pN) by constraining a single internuclear distance. Series of strained macrocycles containing (*E*)-stiff stilbene are distinct from all previously reported strained molecules in enabling the application of the restoring force formalism, which has hitherto been limited to reactions

of polymers, to much smaller and more tractable molecules. The linkers are connected to the C6,C6′ atoms of stiff stilbene.

We are unaware of any reported series of strained molecules across which rate variations could be interpreted within the force formalism, which we attribute to the design of such molecules that traditionally focused on maximizing distortions of the reacting moiety within disparate molecular scaffolds.[2,21,22] We propose that studies of strained molecules can yield fundamental insights into the relationships between rates and restoring forces if they utilize a molecular moiety (force probe) that satisfies three criteria. First, a probe that is larger and more structurally anisotropic that the functional group bound to it would localize the kinetically-significant strain primarily in the non-reactive part of the macrocycle, minimizing changes in intrinsic barrier due to distortions of the reacting moiety, which cannot generally be accommodated within the modern chemomechanical models.[15] Second, a probe compatible with diverse functional groups and chemical reactions would facilitate establishing broad trends by minimizing the importance of the exact procedure for quantifying the restoring force. Third, the probe design should allow large restoring forces to be accessed without the traditionally daunting syntheses of highly strained molecules.[21,22]

Stiff stilbene (1,1-biindane, Fig. 2.1), which has two stable, structurally distinct isomers, appears unique in satisfying these criteria. Bridging the C6,C6′ atoms of (*E*)-stiff stilbene with a linker of ~14 atoms or fewer generates a strained macrocycle. Because many functional groups in chemistry contain <10 non-H atoms,[23,24] a series of macrocycles of varying strain should be accessible for most such groups, making diverse types of thermal reactions, including nucleophilic substitutions, eliminations and electrocyclic reactions, amenable to force-spectroscopic studies. The large difference in the C6···C6′ distance between the *Z* and *E* isomers, the high thermal barrier that separates the isomers and their clean photoisomerization by ~400 nm light makes macrocycles with up to 30 kcal/mol of strain energy readily available upon irradiation of strain-free *Z* analogs. Macrocyclic series of many functional groups are accessible from the same set of stiff stilbene derivatives in one-step reactions at little additional synthetic cost. The availability of strain-free *Z* isomers offers an additional advantage in that the differences in the activation parameters between the two isomers can be measured and calculated with higher accuracy than individual values and are free from kinetic perturbations such as polar effects that are not accommodated within the force formalism.

Here we illustrate the use of stiff stilbene as a molecular force probe by demonstrating (1) up to 5 × 10^6-fold acceleration of a paradigmatic unimolecular reaction[25]—electrocyclic dissociation of the C–C bond in *trans*-3,4-dimethylcyclobutene—across a series of 9 macrocycles (Fig. 2.2) and (2) the exponential dependence of the measured rate on the calculated restoring force of the non-reactive part of the macrocycle (Fig. 2.3). Except for the smallest macrocycles **1**–**3**, the standard chemomechanical model[15] based on the separation of the methyl carbons of *trans*-3,4-dimethylcyclobutene as a one-dimensional reaction coordinate predicts well the observed rate enhancements (Fig. 2.4). Because the geometry of the transition state of the C–C bond dissociation in cyclobutenes is well established,[26] the results calibrate the method of quantifying the restoring force of strained stiff stilbene and define a reference dataset for comparisons with other reactions whose transition states remain controversial.

2.3 Results and Discussion

We synthesized the *Z* isomers of macrocycles **1**–**9** in 3–11 steps and 2–34% overall yields from commercial indanones using McMurry coupling[27] to effect macrocyclization. The *E* isomers were prepared by irradiating dilute solutions of the *Z* analogs in hexanes at 365–375 nm until the photostationary state was reached. The kinetics of the substrate reaction in all *Z* isomers and in *E* isomers of **4**–**9** were measured by heating each macrocycle as an alkane solution in the dark at 343–413 K (*Z* isomers) or 313–383 K (*E* isomers), which resulted in clean C–C bond dissociation. The enthalpies and entropies of activation were derived from linear Eyring plots. The *E* isomers of **1**–**3** were too thermally labile to be isolable. We continuously irradiated a solution of each *Z* isomer at temperatures (313–363 K) that were too low for it to react thermally. Under these conditions we observed an accumulation of the diene products (Fig. 2.2B) at rates that depended both on temperature and photon flux. The measured dependence was consistent with a photochemically generated, thermally-labile intermediate, the *E* isomer, and yielded the activation enthalpy of the substrate. Our tests indicated that upon photoisomerization, stiff stilbene dissipated excess energy before the substrate reaction could occur, i.e. “hot ground states” were kinetically insignificant.

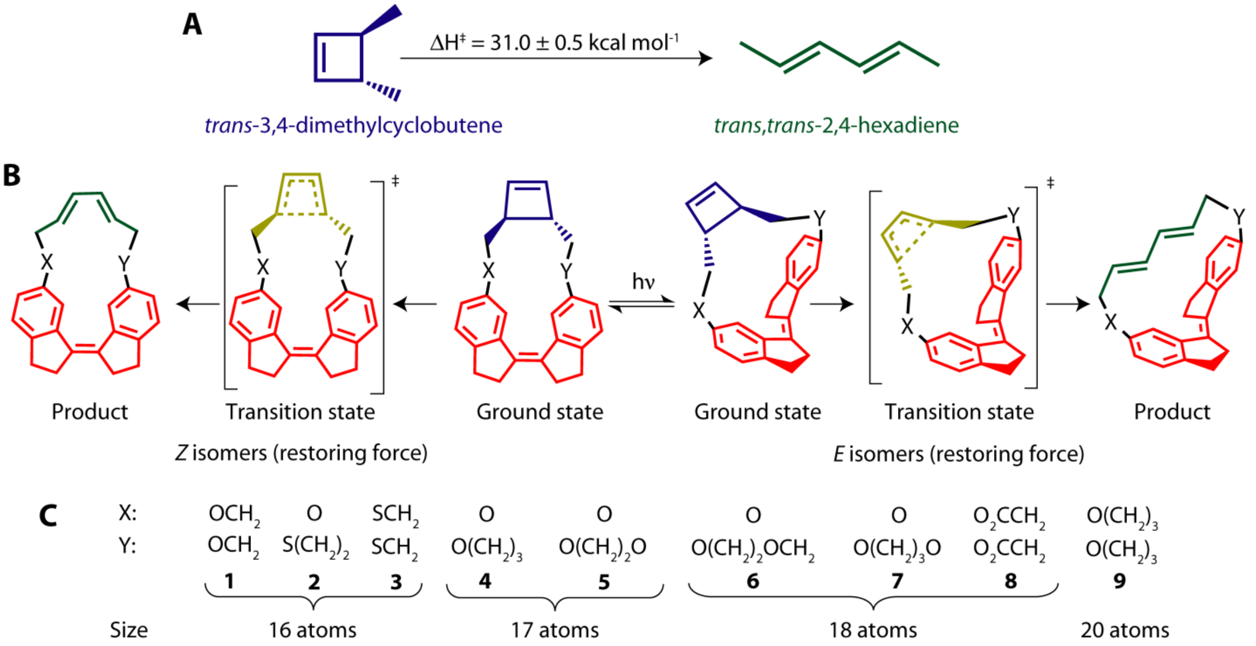

Fig. 2.2. The experimental system used to illustrate the use of a molecular force probe—stiff stilbene (red)—for studies of chemomechanical kinetics of localized reactions. **A**: The substrate reaction. **B**: The general structure of the macrocycles. **C**: The chemical composition of the linkers. The macrocycles are numbered in the order of decreasing $\Delta\Delta H_{\mathrm{exp}}{}^{\ddagger}$—the difference in the activation enthalpy of the substrate reaction in the *Z* and *E* isomers of the same macrocycle.

The acceleration of the C–C bond dissociation across the series of **1**–**9** was primarily due to a decrease in its activation enthalpy: $\Delta\Delta H_{\mathrm{exp}}{}^{\ddagger} = \Delta H_Z{}^{\ddagger} - \Delta H_E{}^{\ddagger}$ increased from 1.7 ± 0.5 kcal/mol in the largest 20-atom macrocycle, **9**, to 9.1 ± 0.7 kcal/mol in the smallest 16-atom congener, **1** (Fig. 2.3A).

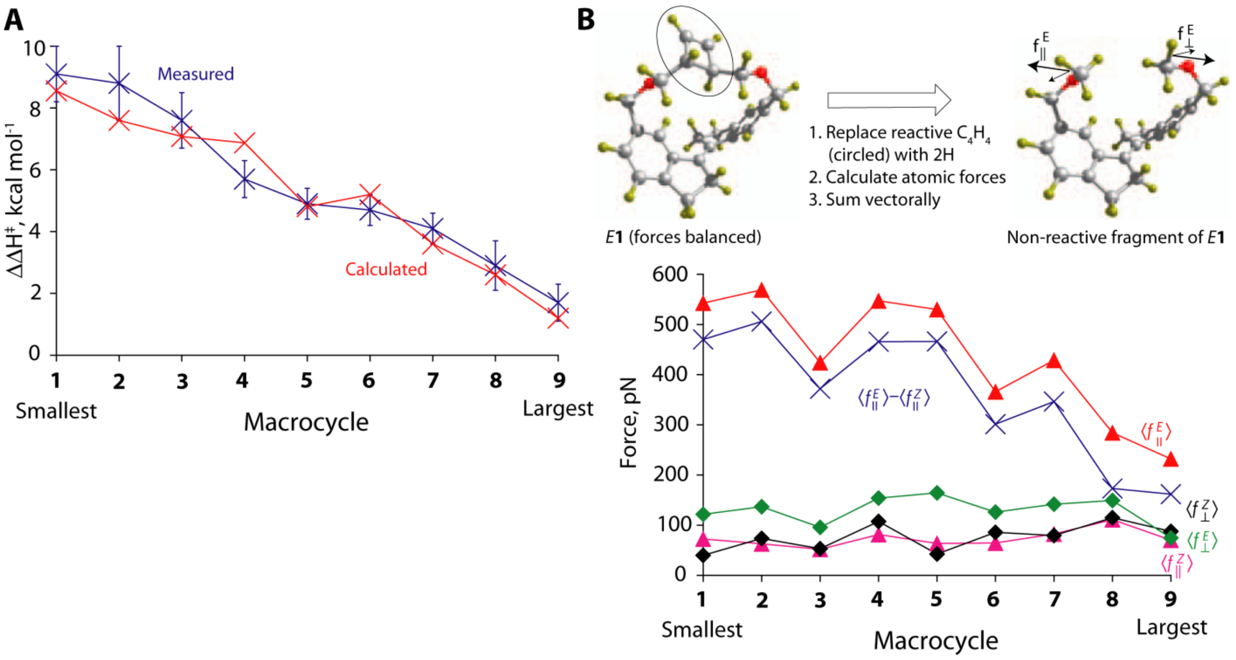

Fig. 2.3. Kinetic and force data for macrocycles **1**–**9**. **A**: Measured (blue) and calculated (red) difference in the activation enthalpies of the substrate reaction in the *Z* and *E* isomers of the same macrocycle, $\Delta\Delta H^{\ddagger}$; the error bars define the 95% confidence interval. The activation entropies were small and varied little across the series (tabulated elsewhere[28]). **B**: Restoring forces of the non-reactive part of the macrocycle were calculated quantum-chemically using fragments obtained by replacing C_4H_4 with a pair of H atoms (example of *E***1** is shown, C, O and H atoms are grey, red and yellow, respectively). The forces are presented as components along ($f_{\|}$) and orthogonal ($f_{\perp}$) to the $CH_3\cdots CH_3$ axis; ⟨ ⟩ signifies forces averaged over multiple structures along the reaction path. For all fragments, the total restoring force of one indanyl group and its attached linker was equal in magnitude and opposite in sign to that of the other indanyl group and its linker regardless of the fragment symmetry.

To obtain the restoring forces we first optimized all conformers of the ground and transition states (Fig. 2.2A) of each macrocycle at the O3LYP/6-311G(2d,p) level of the density functional theory. These calculations accurately reproduced the measured activation enthalpies and entropies (Fig. 2.3A, further details described elsewhere[28]), suggesting comparable accuracy of the calculated restoring forces.[29]

In macrocycles the restoring force of strained stiff stilbene is exactly balanced by that of the substrate. Excising C_4H_4 and adding H atoms to the newly terminal CH_2 groups (Fig. 2.3B) reveals the uncompensated atomic forces, which we quantified by two independent quantum-chemical methods. In one, we calculated the analytical derivatives of the electronic energy with respect to the position of each atom, which gave the force experienced by each nuclei due to its unfavorable bonding geometry (strain). In the other we added external force only to the terminal

C atoms and the O (or S in **2** and **3**) atoms connected to them and varied these external forces until the original structure became a local energy minimum, i.e. until the external forces exactly compensated the total internal force of the strained fragment. For each fragment, the vectoral sums of forces on the atoms of each indanyl moiety and its linker (Fig. 2.3B) were equal, yielding the total restoring force. Because the relaxation of stiff stilbene during the substrate reaction decreases its restoring force we averaged forces calculated for a series of structures along the dissociation path.

The forces obtained by the two methods were similar (Fig. 2.3B), indicating that a single force vector is appropriate for quantifying the total molecular strain. The forces in the (*E*)-stiff stilbene-containing fragments were primarily along the $CH_3 \cdots CH_3$ axis and correlated inversely with the macrocyclic size. Forces in the fragments of largely strain-free *Z* isomers were small and similar in all fragments, probably reflecting the steric and electronic perturbations resulting from macrocycle fragmentation, such as repulsion between the added H atoms. Consequently, we used differences $<f_{\parallel}^{E}> - <f_{\parallel}^{Z}>$ (Fig. 2.3B) and $<f_{\perp}^{E}> - <f_{\perp}^{Z}>$ as the restoring force of the non-reactive part of *E* macrocycles. In all macrocycles the orthogonal term was small.

The data above offer the first opportunity to test the key postulate of the standard chemomechanical kinetic model,[15] that restoring force lowers the activation barrier proportionally to an ensemble-average difference of a single internuclear distance between the ground and transition states projected onto the restoring force vector. The observed accelerations in macrocycles **4**–**9** are predicted accurately using the difference in the separation of the methyl groups in the ground and transition states of free *trans*-3,4-dimethylcyclobutene (Fig. 2.4A, red line). Contrary to conventional thinking,[11,15] predictions based on the elongation of the scissile bond (green line) were poor, reflecting the importance of the changes in the angles involving the scissile bond in determining the reaction barrier. We suggest that scissile bonds are rarely if ever adequate single coordinates for the standard chemomechanical model. The standard model based on any internuclear distance other than the $CH_3 \cdots CH_3$ separation described above underestimated the observed accelerations in the smallest macrocycles **1**–**3** by more than two orders of magnitude.

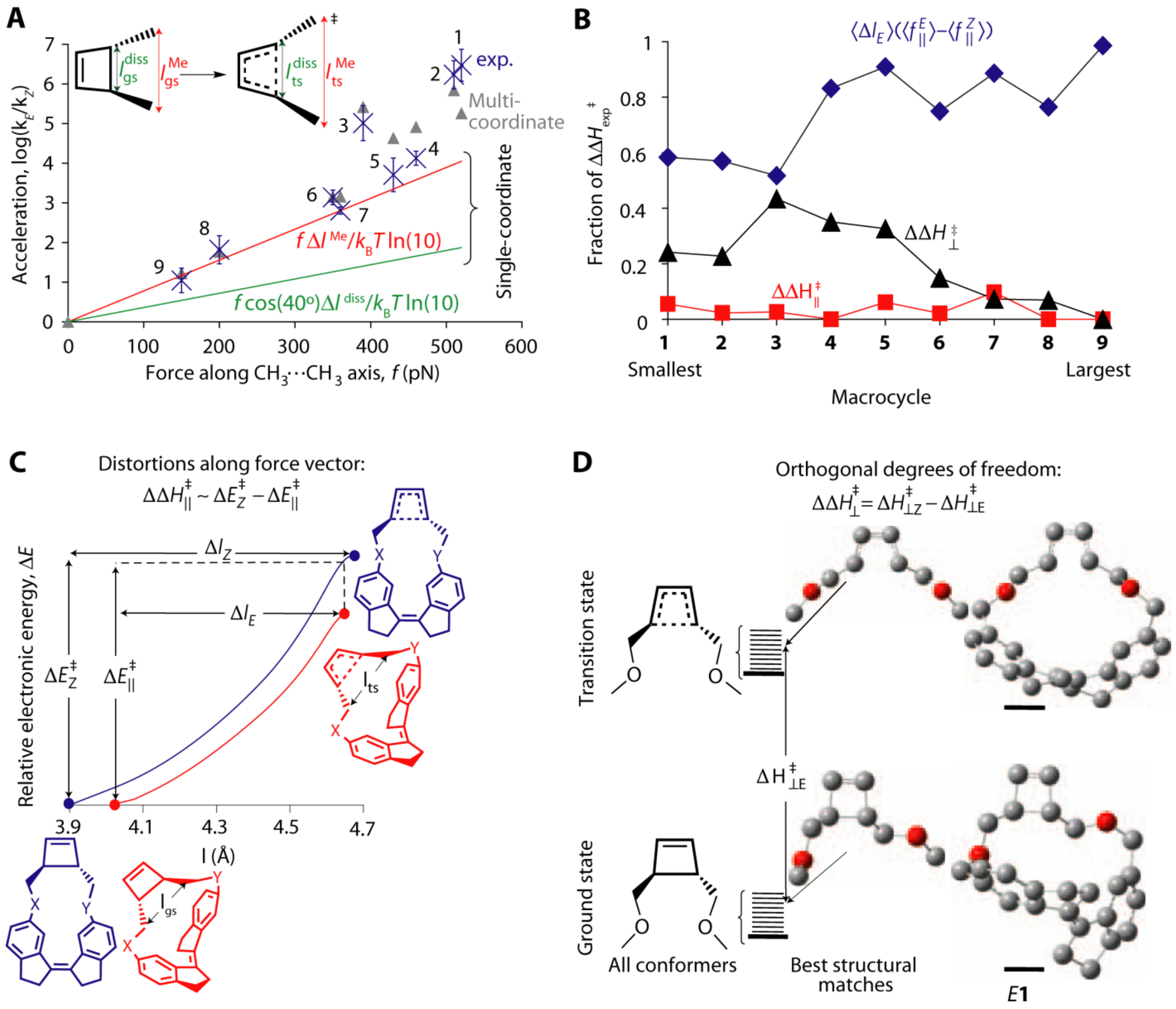

Fig. 2.4. Validation of the single-coordinate model of chemomechanical kinetics. **A**: The measured accelerations of C–C bond dissociation in **1**–**9** versus the predictions based on the elongations of the $CH_3\cdots CH_3$ distance (red line) and dissociating bond (green line) in *trans*-3,4-dimethylcyclobutene and after accounting for the contributions of the orthogonal degrees of freedom as $\Delta\Delta H_{\perp}^{\ddagger}$ (black triangles). The $f\cos(40^{o})$ term in the formula for the single-coordinate model based on the dissociating bond gives the projection of the restoring force on the dissociating bond, which forms ~40° angle with the $CH_3\cdots CH_3$ axis; k_B is the Boltzmann constant and T is absolute temperature. **B**: Relative differential activation enthalpies due to the relaxation of the non-reactive part of the macrocycle in the transition state of the substrate reaction (blue), and due to the distortion of the substrate along (red) and orthogonal to (black) the restoring force vector; $<\Delta l_E>$ is the Boltzmann-weighted average difference in the separation of the CH_2 groups closest to the dissociating bond between the ground and transition states of each macrocycle. The sums of the three fractions deviate slightly from 1 because of the approximations inherent to estimates of $\Delta\Delta H_{||}^{\ddagger}$ and $\Delta\Delta H_{\perp}^{\ddagger}$ and the contributions of neglect degrees of freedom to $\Delta\Delta H_{\text{exp}}^{\ddagger}$. **C**: Cartoon representation of the method of estimating the decrease in the intrinsic activation enthalpy due to the distortion of the substrate along the restoring force vector; blue and red curves are relative *electronic* energies along the reaction path in a Z and E macrocycle,

ΔE_Z and ΔE_E, respectively as a function of the $CH_2 \cdots CH_2$ separation, *l*. Because the zero-point-energy and thermal corrections to the activation energy are close for the two isomers of the same macrocycles, $\Delta\Delta H_{\|}^{\ddagger}$ can be approximated as the difference of electronic energies, $\Delta E_Z^{\ddagger}$-$\Delta E_{\|}^{\ddagger}$. Shown are calculated reaction paths in **1**. **D**: Cartoon representation of the method of estimating the lowering of the activation enthalpy of the substrate reaction due to degrees of freedom orthogonal to the $CH_2 \cdots CH_2$ single coordinate of the standard chemomechanical model, $\Delta\Delta H_{\perp}^{\ddagger}$; *E***1** shown as example, H atoms are omitted for clarity.

Deviations from the standard model are typically ascribed to changes in the intrinsic reaction barrier due to distortions of the reacting moiety (as opposed to conformational relaxation of the non-reactive part).[15] According to the Hammond postulate,[30] any barrier-lowering perturbation distorts the ground and transition state toward a common geometry. In macrocycles **1**–**9**, the difference between the *E* and *Z* isomers of the Boltzmann-weighted average elongation of the $CH_2 \cdots CH_2$ distance closest to the scissile bond (Fig. 2.4C, $\Delta l_Z - \Delta l_E$) between the ground and transition states decreased from ~0 Å at ≤200 pN (**1**–**2**) to -0.11 Å at ≥500 pN (**9**). As a result, the fraction of the barrier lowering due to relaxation in the transition state of the non-reactive part of the macrocycles decreased steadily as the force increased (blue diamonds, Fig. 2.4B). This barrier lowering was partially compensated by a decrease in the intrinsic barrier of the C–C bond dissociation ($\Delta\Delta H_{\|}^{\ddagger}$, red points in Fig. 2.4B and Fig. 2.4C). Overall, however, accounting for distortions of the reacting moiety along the force vector further decreased the predicted rate accelerations.

An alternative explanation for the failure of the standard model is its neglect of internal degrees of freedom orthogonal to the $CH_2 \cdots CH_2$ axis. To estimate their enthalpic contributions, we optimized all conformers of the ground and ring-opening transition states of *trans*-(*cyclo*-C_4H_4)$(CH_2OCH_3)_2$ (and the corresponding thio derivatives, Fig. 2.4D), identified the conformers that best reproduced the geometries of the corresponding moieties in each isomer of macrocycles **1**–**9** and calculated the differences of the activation enthalpies of C–C bond dissociations between these conformers, $\Delta\Delta H_{\perp}^{\ddagger} = \Delta H_{\perp Z}^{\ddagger} - \Delta H_{\perp E}^{\ddagger}$. The inclusion of $\Delta\Delta H_{\perp}^{\ddagger}$, which reached ~50% of the measured differential enthalpy of activation (black triangles, Fig. 2.4B), improved the predicted rate accelerations (black triangles, Fig. 2.4A).

In summary, the standard model based on the scissile bond elongation underestimates observed accelerations at any force, indicating that the scissile bond is a poor approximation of the full reaction coordinate. The change in the separation of the terminal methyl groups of *trans*-

3,4-dimethylcyclobutene captures the reaction-coordinate contributions of the angles involving the scissile bond and permits accurate predictions of rate enhancements up to ~450 pN. At even higher forces, the contributions of the degrees of freedom orthogonal to the $CH_3\cdots CH_3$ axis become important, which, however, cannot be accommodated within the standard model, accounting for the >100-fold underestimation of the observed accelerations at forces >450 pN. Distortions of the reacting moiety along the force vector decrease the enthalpy gain due to relaxation of the non-reactive part of macrocycles, partially offsetting the barrier-lowering contributions of the neglected orthogonal degrees of freedom.

2.4 Conclusions

The data we described illustrate the use of a molecular force probe to study relationships between restoring forces and kinetics of localized reactions. Restoring forces up to ~600 pN are readily obtained by photoisomerization of stiff stilbene and are limited by the quantum yield of *Z*→*E* and activation barrier of thermal *E*→*Z* isomerizations. Larger forces should become accessible if stiff stilbene derivatives whose isomerization kinetics is less sensitive to restoring force can be invented. The modest size of the macrocycles permits accurate quantum-chemical calculations, which are essential for a molecular interpretation of the observed force–rate correlations and for testing the key postulates of chemomechanical kinetics.[3,15] The surprisingly good performance of the standard model for this C–C bond dissociation is partially attributable to the mutual cancellation of neglected effects. Such cancellation is unlikely to be unique for cyclobutene, suggesting that the standard model may be quite robust. Our method is well suited to test this supposition broadly. If correct, it would also permit a series of increasingly strained stiff stilbenes to be used as a molecular *ruler*: the dimensions of transition states that cannot yet be calculated reliably could be obtained by comparing the slopes of the measured force–rate relationships for such reactions with that of the cyclobutene reference reported here.

2.5 Acknowledgments

We thank J. I. Brauman, M. Gruebele, J. F. Hartwig, J. S. Moore, T. J. Martinez, K. S. Suslick and G. M. Whitesides for helpful discussions. The work was supported by the NSF CAREER Award (CHE-0748281), the US Air Force Office of the Scientific Research Young Investigator Award (FA9550-08-1-0072), the American Chemical Society Petroleum Research

Fund (48454-AC3 and 43354-G3) and the University of Illinois. T.K. thanks the Office of the Naval Research and the NSF for pre-doctoral fellowships. We gratefully acknowledge grants of computational time by the Air Force Research Lab Major Shared Resource Center and the National Center for Supercomputing Applications.

2.6 Supporting Experimental Information

Details for the generation of photostationary states, the HPLC chromatographic data, and all details for the kinetic measurements are reported elsewhere.[28] The details and results of DFT calculations are also reported elsewhere.[28]

2.6.1 Materials and General Methods

Commercial reagents of the highest available purity were purchased from Aldrich, Fisher and/or VWR and were used without further purification unless stated otherwise. Analytical and preparative thin layer chromatography (TLC) was performed on silica gel 60 (Fisher and Aldrich, respectively). High-resolution mass spectrometry (HRMS) was performed on a Q-ToF Ultima mass spectrometer at the University of Illinois Mass Spectrometer Center. ^{1}H NMR spectra were recorded on 400 or 500 MHz Unity-INOVA Varian spectrometers at 21 ± 1 °C and are reported as chemical shifts in ppm relative to TMS. Spin multiplicities are reported as a singlet (s), doublet (d), triplet (t), quartet (q) and quintet (quint) with coupling constants (J) given in Hz, or multiplet (m); broad peaks are denoted br. The peaks were assigned by comparison with analogous reported compounds and with the aid of additional 2D NMR spectra, though these experiments are not reported here.

Abbreviations: DCC: *N*,*N*'-dicyclohexylcarbodiimide; DMAP: 4-dimethylaminopyridine; DMF: dimethylformamide; THF: tetrahydrofuran; THP: tetrahydropyranyl; Ts: *p*-tolylsulfonyl.

2.6.2 Synthesis

trans-1,2-Bis(hydroxymethyl)-*cyclo*-but-3-ene (**S1**), 2-(6-indan-1-one)acetic acid (**S2**) and 3-(6-indan-1-one)propionic acid (**S3**) (Fig. 2.5) were prepared according to the reported procedures in refs. 31-33, respectively. Syntheses of the remaining compounds are shown schematically in Fig. 2.6–Fig. 2.8 (the target macrocycles are highlighted in green). *trans*-3,4-Dimethylcyclobutene has two stereogenic centers and stiff stilbene is axially chiral by virtue of its two atropisomers. Thus, our syntheses probably produced mixtures of 4 stereoisomers, i.e.

two diastereomeric pairs of two enantiomers: (*R*, *R*, *P*; *S*, *S*, *M*) and (*S*, *S*, *P*; *R*, *R*, *M*). The exception being **4**, for which crystallographic, HPLC and preliminary ^{1}H NMR data suggest that only the (*R*, *R*, *P*; *S*, *S*, *M*) enantiomeric pair was obtained. Diastereomeric *Z* isomers of all macrocycles were indistinguishable by ^{1}H NMR and non-separable by HPLC; the two diastereomers of the *E* isomers of **5**–**9** were separated by HPLC and characterized independently.

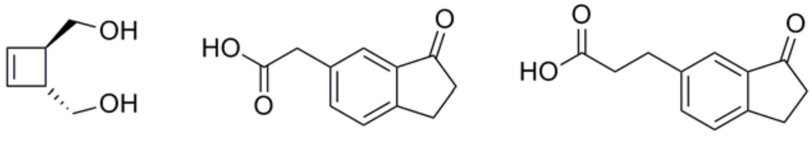

S1 **S2** **S3**

Fig. 2.5. Chemical structures of starting materials for the synthesis of **1**–**9**.

The synthesis of all *Z* macrocycles relied on the same three general procedures, which are described below: alkylation of *trans*-1,2-bis(tosyloxymethyl)-*cyclo*-but-3-ene or a monoalkylated analog using weakly basic nucleophiles (phenoxide or thiolate anions, procedure 1), alkylation of tosylated alkoxy indanones (e.g., **S10** and **S13**, Fig. 2.6 and Fig. 2.7, respectively) with an *in situ* generated monoanion of *trans*-1,2-bis(hydroxymethyl)-*cyclo*-but-3-ene (procedure 2) and intramolecular McMurry coupling of a pair of linked indanones (e.g., **S4**, **S6**, **S9**, **S12**, **S15**, **S16**, **S19**, **S20**, **S21**, procedure 3). No effort was made to optimize any of the described procedures. The conversion of alkyl tosylates to alkylthiols (**S7** and **S8**, Fig. 2.6) followed a protocol described in the literature.[34]

Procedure 1. To a DMF solution of *trans*-1,2-bis(tosyloxymethyl)-*cyclo*-but-3-ene or a monoalkylated analog **S5**, **S11**, **S14**, **S17** or **S18** excess K_2CO_3, 6-hydroxyindan-1-one (1.1 equiv.) or the thiol derivatives **S7** (2.2 equiv.) or **S8** (1.1 equiv.) and Bu_4NBr (0.05 equiv.) were added. The resulting mixture was stirred at 60 °C for 24 h under N_2. The reaction mixture was cooled to room temperature and poured into water. The product was extracted with CH_2Cl_2. The combined organic layers were washed with H_2O, dried with $MgSO_4$, filtered and the solvent was removed under vacuum. The crude product was purified with preparative centrifugally-accelerated radial thin layer chromatography. Eluents, approximate R_f values and the yields are in Table 2.1.

Table 2.1. Summary of conditions for chromatographic purification of intermediates and the final targets, yields of Procedures 1–3 and the total yields of macrocycles **1**–**9**.

Procedure 1				**Procedure 3**				**total yield, %**
product	eluent	Rf	yield, %	product	eluent	Rf	yield, %	
S5	Hexane/CH_2Cl_2 (1:4)	0.33	46	**1**	Hexane/CH_2Cl_2 (1:1)	0.36	55	15
S6	CH_2Cl_2/ether (6:1)	0.32	66	**2**	Hexane/CH_2Cl_2 (1:1)	0.39	46	9.8
S9	CH_2Cl_2/ether (6:1)	0.32	60	**3**	Hexane/CH_2Cl_2 (1:1)	0.39	40	8.4
S12	CH_2Cl_2/ether (6:1)	0.31	65	**4**	Hexane/CH_2Cl_2 (1:1)	0.37	80	4.5
S16	CH_2Cl_2/ether (6:1)	0.31	70	**5**	Hexane/CH_2Cl_2 (1:1)	0.35	68	12
S19	CH_2Cl_2/ether (6:1)	0.31	62	**6**	Hexane/CH_2Cl_2 (1:1)	0.35	65	13
S20	CH_2Cl_2/ether (6:1)	0.31	68	**7**	Hexane/CH_2Cl_2 (1:1)	0.35	70	2.3
Procedure 2				**8**	CH_2Cl_2	0.39	56	34
S11	Hexane/CH_2Cl_2 (1:4)	0.33	25	**9**	Hexane/CH_2Cl_2 (1:1)	0.37	66	8.2
S14	Hexane/CH_2Cl_2 (1:4)	0.33	20					
S15	CH_2Cl_2/ether (6:1)	0.31	31					

Procedure 2. To a solution of *trans*-1,2-bis(hydroxymethyl)-*cyclo*-but-3-ene, **S1**, in dry DMF was added NaH (2.2 equiv.), followed by 1,3-dioxolane-protected indanyl tosylate **S10** (1 equiv.) or **S13** (1 equiv. for synthesis of **S14**, 2 equiv. for synthesis of **S15**). The resulting mixture was stirred at room temperature for 1 h. Water was added slowly to quench the reaction and the product was extracted into CH_2Cl_2, the combined organic fractions were dried over $MgSO_4$, filtered, and the solvent evaporated under reduced pressure. The crude product was dissolved in THF/water (3:1) and excess *p*-tolylsulfonic acid was added. The resulting solution was stirred at room temperature overnight. The product was extracted with CH_2Cl_2, which was dried over Mg_2SO_4, followed by filtration and evaporation of the solvent. The product was isolated with preparative centrifugally-accelerated radial thin layer chromatography. Eluents, approximate R_f values and the yields are tabulated in Table 2.1.

Procedure 3. To a stirred suspension of zinc powder (12 equiv.) in dry THF $TiCl_4$ (6 equiv.) was added over 10 minutes at 0 °C. The resulting slurry was heated at reflux for 1.5 h. A THF solution of **S4**, **S6**, **S9**, **S12**, **S14**, **S16**, **S19**, **S20** or **S21** was added over a 3–6 h period by syringe pump to the refluxing reaction mixture. The reflux was continued for 20–40 minutes after the addition was complete. After cooling to room temperature, the reaction mixture was poured into a saturated aqueous solution of NH_4Cl and product was extracted with CH_2Cl_2. The combined organic solutions were dried with Mg_2SO_4, the solvent was evaporated, and the crude product was purified with preparative centrifugally-accelerated radial thin layer chromatography. Eluents, approximate R_f values and the yields are tabulated in Table 2.1.

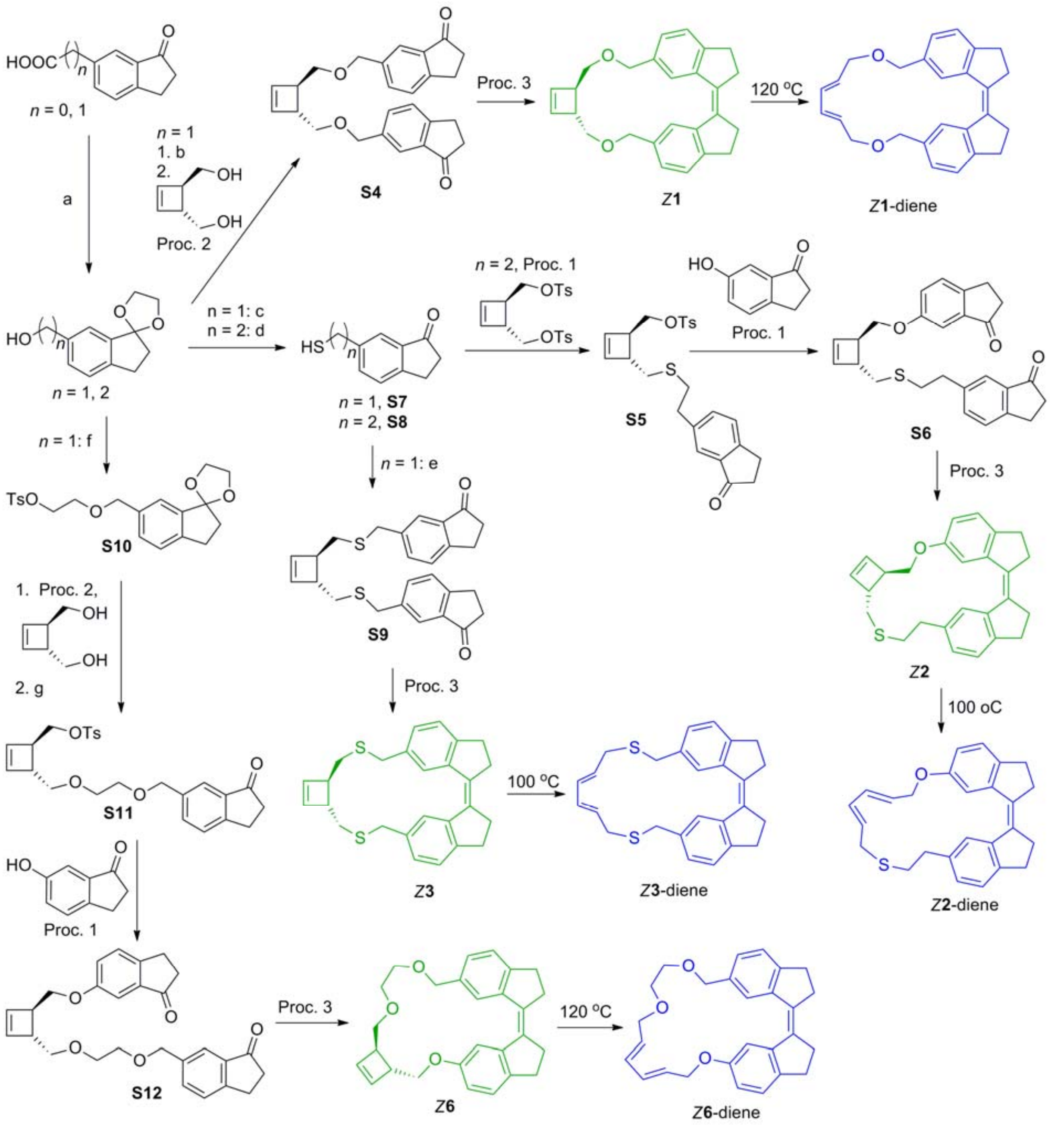

Fig. 2.6. Syntheses of *Z*1, *Z*2, *Z*3 and *Z*6 and the corresponding diene-containing analogs. Reagents used: a: 1. EtBr, K_2CO_3, Bu_4NBr, acetone, 2. ethylene glycol, TsOH, benzene, 3. $LiAlH_4$, THF; b: TsCl, KOH, THF; c: 1. TsCl, KOH, THF, 2. thiourea, DMF, 3. aqueous NaOH, 4. aqueous HCl; d: 1. TsOH, H_2O/THF, 2. TsCl, Et_3N,

CH_2Cl_2, 3. thiourea, DMF, 4. aqueous NaOH, 5. aqueous HCl; e: 1. **S4**, Proc. 1, 2. TsOH, THF/H_2O; f: 1. TsCl, KOH, THF, 2. ethylene glycol, Na, DMF, 3. TsCl, Et_3N, CH_2Cl_2; g: TsCl, Et_3N, CH_2Cl_2

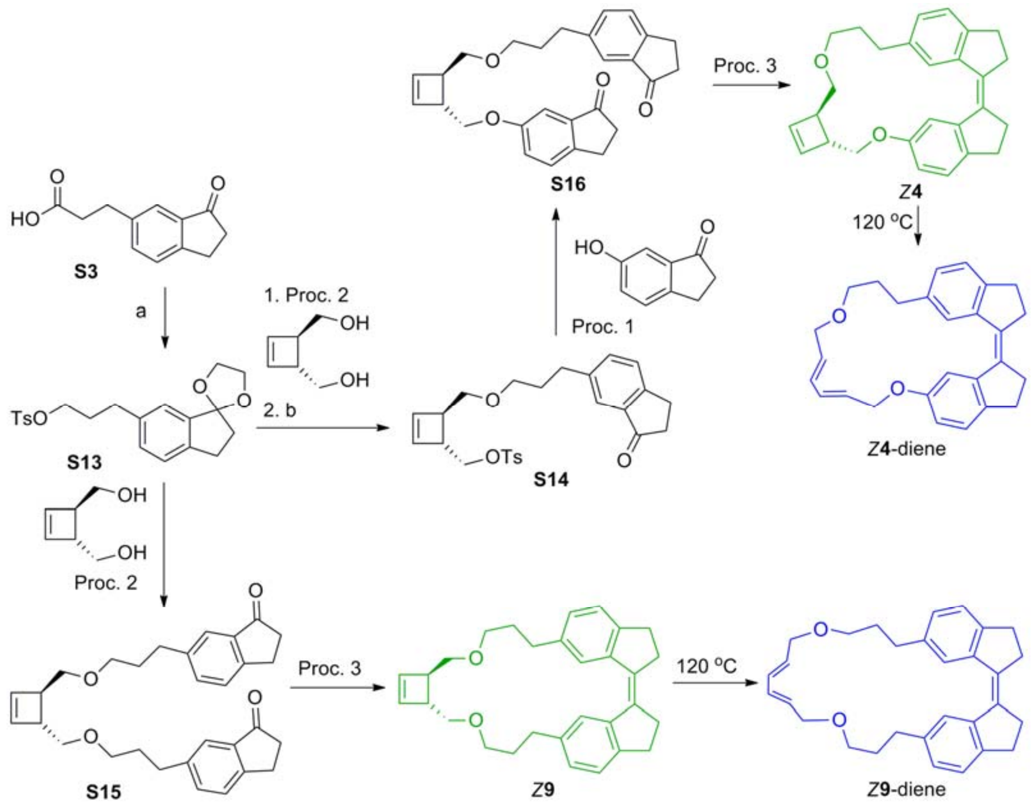

Fig. 2.7. Syntheses of *Z***4** and *Z***9** and the corresponding diene-containing analogs. Reagents used: a: 1. EtBr, K_2CO_3, Bu_4NBr, acetone, 2. ethylene glycol, TsOH, benzene, 3. $LiAlH_4$, THF, 4. TsCl, Et_3N, CH_2Cl_2; b: TsOH, THF/H_2O

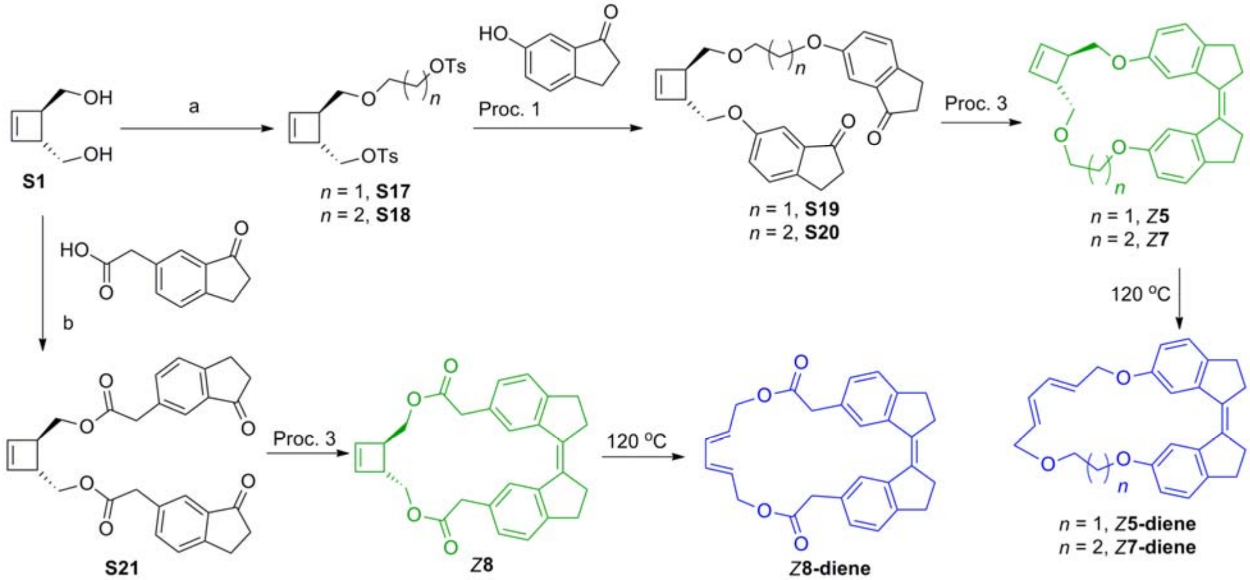

Fig. 2.8. Syntheses of *Z***5**, *Z***7** and *Z***8** and the corresponding diene-containing analogs. Reagents used: a: 1. $Br(CH_2)_{n+1}OTHP$, NaH, dry DMF, 2. TsOH, THF/H_2O, 3. TsCl, Et_3N, CH_2Cl_2; b: DCC, DMAP, CH_2Cl_2.

The *E* isomers were prepared by photoisomerization of the *Z* analogs (detailed elsewhere[28]). The *Z* isomers of macrocycles containing the diene product of cyclobutene ring opening (blue structures, Fig. 2.6–Fig. 2.8) were prepared by heating *Z***1**–*Z***9** in toluene at reflux. *E***1**-diene–*E***9**-diene were prepared by photoisomerization of the respective *Z* isomers.

2.6.3 Spectroscopic Characterization of Synthetic Targets

Table 2.2–Table 2.4 list the ^{1}H NMR spectra of *Z*-**1** through *Z*-**9**, *Z*-**1**-diene through *Z*-**9**-diene and *E*-**1**-diene through *E*-**9**-diene, respectively. The UV-vis spectra of all isomers of each macrocycle are tabulated and shown elsewhere;[28] the high-resolution mass spectrometric data are presented in Table 2.5. The HPLC retention times for all relevant species are tabulated elsewhere, and the corresponding chromatograms showing chemical homogeneity and high (>95%) purity of samples of the primary synthetic targets (*Z***1**–*Z***9**) are shown elsewhere.[28]

The ^{1}H NMR spectra are characterized by the presence of a large number of diastereotopic protons. In *Z***1**–*Z***9**, the methine hydrogens of the cyclobutene moiety are distinguished by unusually large coupling (9–11 Hz) to the diastereotopic methylene protons and the absence of coupling to each other in asymmetric macrocycles. As a result, the methine hydrogens always appeared as highly characteristic triplet(s). The methylene protons of the cyclobutene moiety appeared as two (symmetric macrocycles **1**, **3**, **8** and **9**) or 4 sets of doublets of slightly second order. The chemical shifts of these methine and methylene protons vary significantly among macrocycles, probably reflecting shielding/deshielding by the phenyl groups of stiff stilbene, which can change dramatically as a result of only minor changes in the relative positions of the two groups. The unusually downfield position of the *ortho*-H (Fig. 2.9) is characteristic of the *Z* isomers.

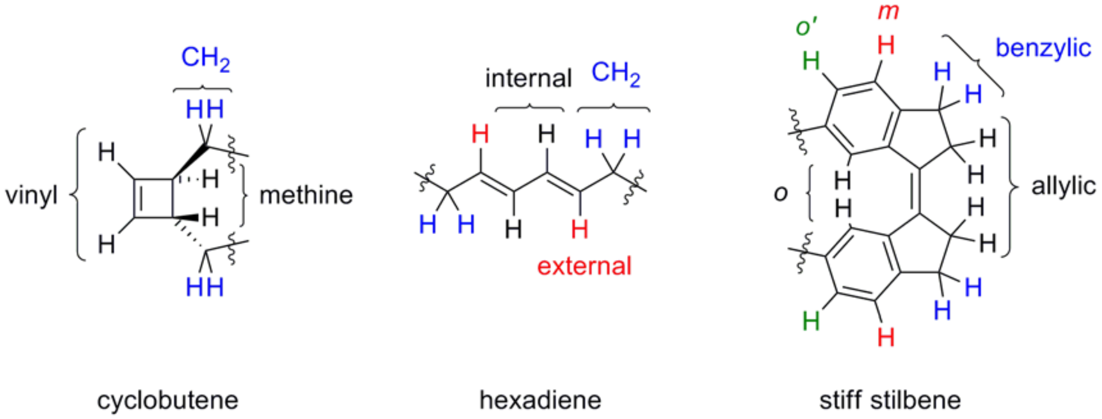

Fig. 2.9. Notations of protons used in tabulation of ^{1}H NMR spectra assignments of macrocycles **1**–**9** (see Table 2.2–Table 2.4).

Table 2.2. Assignments of the ^{1}H NMR resonances of the *Z* isomers of macrocycles **1**–**9** containing cyclobutene. See Fig. 2.9 for the illustration of notations. All spectra are in $CDCl_3$ at 21 ± 1 °C unless noted otherwise.

	1	**2** ($C_6D_5CD_3$)	**3**	**4**	**5**
vinyl	5.97 (s, 2H)	6.25 (d, ^3J(H,H) = 3 Hz, 1H); 6.22 (d, ^3J(H,H) = 3 Hz, 1H)	6.04 (s, 2H)	6.17 (dd, ^3J(H,H) = 3.0 Hz, ^3J(H,H) = 1.0 Hz, 1H), 6.18 (dd, ^3J(H,H) = 3.0 Hz, ^3J(H,H) = 1.0 Hz, 1H)	6.10 (d, ^3J(H,H) = 2.9 Hz, 1H), 5.86 (dd, ^3J(H,H) = 2.8 Hz, ^3J(H,H) = 1 Hz, 1H)
meth-ine	3.42 (t, ^3J(H,H) = 10.1 Hz, 4H)	2.96 (m, 4H)	2.65 (m, 4H)	3.88 (t, ^3J(H,H) = 9.5 Hz, 1H), 3.60 (m, 4H)	3.85 (t, ^3J(H,H) = 10.5 Hz, 1H), 3.5 – 3.35 (m, 4H)
CH_2	3.54 (dd, ^3J(H,H) = 10 Hz, ^2J(H,H) = 4.8, 2H), 2.89 (dd, ^3J(H,H) = 10 Hz, ^2J(H,H) = 4.8, 2H)	4.20 (dd, 10.5 Hz, 8 Hz); 4.11 (dd, ^3J(H,H) = 10 Hz, ^2J(H,H) = 7.5 Hz); 2.96 (m)	2.6 – 2.5 (m, 6H), 2.45 (dd, ^3J(H,H) = 14 Hz, ^2J(H,H) = 8.4, 2H)	4.24 (dd, ^3J(H,H) = 9.5 Hz, ^2J(H,H) = 5.5 Hz), 3.0-2.9 (m, 6H)	4.07 (dd, ^3J(H,H) = 10.2 Hz, ^2J(H,H) = 7.6 Hz, 1H), 3.86 (dd, ^3J(H,H) = 10.2 Hz, ^2J(H,H) = 7.5 Hz, 1H), 3.5 – 3.35 (m, 4H)
allyl-ic	2.74 (m, 2H), 2.66 (m, 2H)	2.9 – 2.75 (m)	2.5 – 2.6 (m, 6H)	2.8 (m, 4H)	2.6 (m, 4H)
benz-ylic	2.53 (m, 4H)	2.9 – 2.75 (m)	2.8 – 2.7 (m, 2H), 2.65 (m, 4H)	2.9 (m, 4H)	2.7 (m, 4H)
o	8.58 (s, 2H)	8.03 (br. s) 7.81 (d, ^4J(H,H) = 2.5 Hz)	8.19(s, 2H)	8.04 (s, 1H), 7.75 (d, ^3J(H,H) = 2.5 Hz, 1H)	8.09 (d, ^4J (H,H) = 2 Hz, 1H), 8.08 (d, ^4J(H,H) = 2 Hz, 1H)

Table 2.2 (cont.)

o'	7.00 (d, ^3J(H,H) = 7.4 Hz, 2H)	7.00 (dd, ^3J(H,H) = 7.5 Hz, ^4J (H,H) = 1 Hz, 1H); 6.78 (dd, ^3J(H,H) = 7.5 Hz, ^4J (H,H) = 2.5 Hz, 1H)	7.07 (d, ^3J(H,H) = 7.5 Hz, 2H)	6.72 (dd, ^3J(H,H) = 8.3 Hz, ^4J (H,H) = 2.5 Hz, 1H), 7.00 (dd, ^3J(H,H) = 7.5 Hz, ^4J (H,H) = 1.5 Hz, 1H)	6.80 (dd, ^3J(H,H) = 8.1 Hz, ^4J (H,H) = 2 Hz, 1H), 6.65 (dd, ^3J(H,H) = 8.3 Hz, ^4J (H,H) = 2.2 Hz, 1H)
m	7.10 (d, ^3J(H,H) = 7.4 Hz, 2H)	7.22 (d, 7.5 Hz, 1H); 7.20 (d, 8 Hz, 1H)	7.15 (d, ^3J(H,H) = 8 Hz, 2H)	7.19 (t*, ^3J(H,H) = 8.5 Hz, 2H)	7.03 (m, 1H), 7.01 (m, 1H)
linkers	4.34 (s, 4H)	2.96 (m); 2.9 – 2.75 (m)	3.61 (d, 2J(H,H) = 12.3 Hz, 2H); 3.49 (t, ^2J(H,H) = 12 Hz, 2H)	3.6 (m, 4H, alkoxy); 2.64 (t, ^3J(H,H) = 7.5 Hz, 2H; benzylic); 1.97 (m, 2H)	3.8 – 3.75 (m, 1H), 2.97 (t, ^3J(H,H) = 7.4 Hz, 1H), 2.63 (t, ^3J(H,H) = 7.2 Hz, 1H)

Table 2.2 (cont.)

	6	**7**	**8**	**9**
vinyl	6.17 (dd, ^3J(H,H) = 2.7 Hz, ^3J(H,H) = 1 Hz, 1H); 6.07 (dd, ^3J(H,H) = 2.8 Hz, ^3J(H,H) = 1 Hz, 1H);	5.75 (d, 1H, ^3J(H,H) = 2.8 Hz, 1H), 6.06 (d, 1H, ^3J(H,H) = 2.8 Hz)	5.54 (s, 2H)	6.07 (s, 2H)
meth-ine	3.93 (t, ^3J(H,H) = 9 Hz, 1H), 3.48 (t, ^3J(H,H) = 11.2 Hz, 1H)	3.31 (t, ^3J(H,H) = 10.9 Hz, 2H)	2.5(m, 6H)	3.40 (t, ^3J(H,H) = 10 Hz, 2H)
CH_2	4.09 (dd, ^3J(H,H) = 9 Hz, ^2J(H,H) = 4.9 Hz, 1H), 3.98 (dd, ^3J(H,H) = 7 Hz, ^2J(H,H) = 4.6 Hz, 1H), 3.85 (dd, ^3J(H,H) = 11.2 Hz, ^2J(H,H) = 3.3 Hz, 1H), 3.7 – 3.6 (m, 4H)	3.98 (dd, ^3J(H,H) = 9.3 Hz, ^2J(H,H) = 7.3 Hz, 1H), 3.75 (dd, ^3J(H,H) = 9.2 Hz, ^2J(H,H) = 6.3 Hz, 1H), 3.44 (dd, ^3J(H,H) = 11 Hz, ^2J(H,H) = 3.3 Hz, 1H), 2.8-2.7 (m, 5H)	4.11 (dd, ^2J(H,H) = 11.3 Hz, ^3J(H,H)= 4.7 Hz, 2H); 3.90 (dd, ^2J(H,H) = 11.2 Hz, ^3J(H,H) = 9 Hz, 2H)	3.70 (dd, ^3J(H,H) = 10.2 Hz, ^2J(H,H) = 4.1, 2H); 2.84 (dd, ^3J(H,H) = 10.3 Hz, ^2J(H,H) = 4.0 Hz, 2H)
allyl-ic	2.85 – 2.75 (m, 4H)	2.7 – 2.6 (m, 5H)	2.5 (m, 6H)	2.7 – 2.6 (m, 4H)
benz-ylic	3.0 – 2.9 (m, 5H)	2.8 – 2.7 (m, 5H)	2.66 (m, 4H)	2.81 (m, 4H)
o	8.22 (s, 1H); 7.70 (d, ^4J (H,H) = 2.3 Hz)	8.09(d, ^3J(H,H) = 2.4 Hz, 1H), 8.14(d, ^3J(H,H) = 2.4 Hz, 1H)	8.472 (br. s, 2H)	7.99 (d, ^4J (H,H) = 1 Hz, 2H)
o'	7.04 (dd, ^3J(H,H) = 7.3 Hz, ^4J (H,H) = 1 Hz, 1H); 6.71 (dd, ^3J(H,H) = 8.2 Hz, ^4J (H,H) = 2.5 Hz, 1H)	6.80 (dd, ^3J(H,H) = 8.4 Hz, ^4J (H,H) = 2.4 Hz, 1H), 6.92 (dd, ^3J(H,H) = 8.2 Hz, ^4J (H,H) = 2.4 Hz, 1H)	6.97 (dd, ^3J(H,H)=9.5 Hz; ^4J (H,H)=1.5 Hz, 2H	7.00 (dd, ^3J(H,H) = 7.8 Hz, ^4J(H,H) = 1 Hz, 2H)
m	7.22 (d, ^3J(H,H) = 7.5 Hz, 1H), 7.2 (d, ^3J(H,H) = 8.2 Hz, 1H)	7.08 (t*, ^3J(H,H) = 8.6 Hz, 2H)	7.04 (d, ^3J(H,H) = 9.5 Hz, 2H)	7.20 (d, ^3J(H,H) = 7.8 Hz, 2H)
linkers	4.56 (d, ^2J(H,H) = 11.5 Hz, 1H, benzylic); 4.44 (d, ^2J(H,H) = 11.6 Hz, 1H, benzylic); 3.7 – 3.6 (m, 4H); 3.03 (dd, ^3J(H,H) = 9.4 Hz, ^3J(H,H) = 4.7 Hz, 1H), 3.0 – 2.9 (m, 5H)	3.99 (t, ^3J(H,H) = 6.5 Hz); 3.4 – 3.3 (m, 1H); 2.95(t, ^3J(H,H) = 6.7 Hz, 1H); 2.7 – 2.6 (m, 5H); 1.90 (quint. d, J(H,H) = 6.8 Hz, J(H,H) = 3.9 Hz, 2H)	3.51 (s, 4H)	3.62 (dt, ^2J(H,H) = 9 Hz, ^3J(H,H) = 6.5 Hz, 2H); 3.51(dt, ^2J(H,H) = 9 Hz, ^3J(H,H) = 6.8 Hz, 2H); 2.95 (m, 4H); 1.94 (quint., ^3J(H,H) = 7.5 Hz, 4H)

Table 2.3. Assignments of the ^{1}H-NMR resonances of the Z isomers of macrocycles **1**–**9** containing hexadiene. See Fig. 2.9 for the illustration of notations. All spectra are in toluene-d_8 at 21 ± 1 °C unless noted otherwise.

	1	**2**	**3**	**4**	**5**
internal	5.96 (m, 2H)	6.18 (dd, ^{3}J(H,H) = 15.3 Hz, ^{3}J(H,H) = 9.7 Hz, 1H); 5.60 (d, ^{3}J(H,H) = 15.3 Hz, ^{3}J(H,H) = 9.7 Hz, 1H)	5.69 (m, 2H)	6.46 (dd, ^{3}J(H,H) = 15.4 Hz, ^{3}J(H,H) = 10.4 Hz, 1H), 6.22 (ddt, ^{3}J(H,H) = 15.3 Hz, ^{3}J(H,H) = 10.7 Hz, ^{4}J(H,H) = 1.3 Hz, 1H)	6.91 (ddt, ^{3}J(H,H) = 13.9 Hz, ^{3}J(H,H) = 10.8 Hz, ^{4}J(H,H) = 1.9 Hz,1H), 6.32 (dd, ^{3}J(H,H) = 15.4 Hz, ^{3}J(H,H) = 10.5 Hz, 1H)
external	5.40 (m, 2H)	5.46 (m, 1H), 5.41 (td, ^{3}J(H,H) = 15.4 Hz, ^{3}J(H,H) = 5.4 Hz, 1H)	5.22 (m, 2H)	5.55 (td, ^{3}J(H,H) = 15.4 Hz, ^{3}J(H,H) = 4.5 Hz, 1H), 5.35 (td, ^{3}J(H,H) = 15.4 Hz, ^{3}J(H,H) = 5.0 Hz, 1H)	3.85 (dt, ^{3}J(H,H) = 15.4 Hz, ^{3}J(H,H) = 5.4 Hz, 1H), 5.35 (dt, ^{3}J(H,H) = 15.4 Hz, ^{3}J(H,H) = 4.0 Hz, 1H)
CH_2	3.94 (d, ^{3}J(H,H) = 6.9 Hz, 4H)	4.27 (dd, ^{3}J(H,H) = 5.7 Hz, ^{4}J(H,H) = 1.0 Hz, 2H); 2.91 (d, ^{3}J(H,H) = 7.5, 2H);	2.84 (d, ^{3}J(H,H) = 7.2 Hz, 4H)	4.28 (d, ^{3}J(H,H) = 4.6 Hz, 2H), 3.70 (d, ^{2}J(H,H) = 4.9 Hz, 2H)	4.27 (d, ^{3}J(H,H) = 5.3 Hz, 2H), 3.83 (d, ^{3}J(H,H) = 3.2 Hz, 2H)
allylic	2.56 (m, 4H)	2.65 – 2.55 (m, 4H)	2.53 (m, 4H)	2.6 (m, 4H)	2.6 (m, 4H)
benzylic	2.73 (m, 4H)	2.8 – 2.7 (m, 6H)	2.71 (m, 4H)	2.8 – 2.65 (m, 6H)	2.76 (m, 2H), 2.70 (m, 2H)
o	7.89 (s, 2H)	7.75 (br. s, 1H) 7.59 (d, ^{4}J(H,H) = 2.3 Hz, 1H)	7.95 (s, 2H)	7.86 (s, 1H), 7.59 (d, ^{4}J(H,H) = 2.3 Hz, 1H)	7.75 (d, ^{4}J (H,H) = 2.3 Hz, 1H), 7.64 (d, ^{4}J(H,H) = 2.3 Hz, 1H)
o'	7.35 (dd, ^{3}J(H,H) = 7.6 Hz, ^{4}J(H,H) = 1.0 Hz, 2H)	6.92 (dd, ^{3}J(H,H) = 8.2 Hz, ^{4}J (H,H) = 2.2 Hz); 6.76 (dd, ^{3}J(H,H) = 7.7 Hz, ^{4}J (H,H) = 1.3 Hz)	7.36 (dd, ^{3}J(H,H) = 7.7 Hz, ^{4}J(H,H) = 1.0 Hz, 2H)	6.93 (dd, ^{3}J(H,H) = 8.3 Hz, ^{4}J (H,H) = 2.4 Hz, 1H), 6.91 (dd, ^{3}J(H,H) = 6.3 Hz, ^{4}J (H,H) = 1.3 Hz, 1H)	6.93 (dd, ^{3}J(H,H) = 8.1 Hz, ^{4}J (H,H) = 2.3 Hz, 1H), 6.52 (dd, ^{3}J(H,H) = 8.3 Hz, ^{4}J (H,H) = 2.2 Hz, 1H)
m	7.15 (d, ^{3}J(H,H) = 7.5 Hz, 1H)	7.07 (d, ^{3}J(H,H) = 7.9 Hz, 1H); 7.04 (d, ^{3}J(H,H) = 7.9 Hz, 1H)	7.12 (d, ^{3}J(H,H) = 8 Hz, 1H)	7.12 – 7.05 (overlap with solvent)	7.05 (d, ^{3}J(H,H) = 5.6 Hz, 1H), 7.03 (d, ^{3}J(H,H) = 5.6 Hz, 1H)
linkers	4.31 (s, 4H)	2.8 – 2.7 (m, 6H); 2.44 (m, 2H)	3.51 (s, 4H)	3.43 (t, ^{3}J(H,H) = 4.9 Hz, 2H, alkoxy); 2.80 – 2.65 (m, 6H; benzylic); 1.60 (m, 2H)	3.68 (m, 2H), 3.47 (m, 2H)

Table 2.3 (cont.)

	6	**7**	**8**	**9**
internal	6.57 (ddt, ^{3}J(H,H) = 15.8 Hz, ^{3}J(H,H) = 10.7 Hz, ^{4}J(H,H) = 1.8 Hz, 1H), 6.13 (dd, ^{3}J(H,H) = 15.3 Hz, ^{3}J(H,H) = 10.7 Hz, 1H)	6.76 (ddt, ^{3}J(H,H) = 15.8 Hz, ^{3}J(H,H) = 10.7 Hz, ^{4}J(H,H) = 1.8 Hz, 1H), 6.27 (dd, ^{3}J(H,H) = 15.1 Hz, ^{3}J(H,H) = 10.7 Hz, 1H)	6.14 (m, 2H)	6.18 (m, 2H)
external	5.80 (dt, ^{3}J(H,H) = 15.1 Hz, ^{3}J(H,H) = 6.4 Hz, 1H), 5.36 (t, ^{3}J(H,H) = 15.2 Hz, ^{3}J(H,H) = 3.7 Hz, 1H)	6.05 (dt, ^{3}J(H,H) = 15.2 Hz, ^{3}J(H,H) = 5.4 Hz, 1H), 5.13 (dt, ^{3}J(H,H) = 15.8 Hz, ^{3}J(H,H) = 3.5 Hz, 1H)	5.62 (m, 2H)	6.5 – 5.5 (m, 2H)
CH_2	4.27 (d, ^{3}J(H,H) = 6.5 Hz, 2H), 3.83 (dd, ^{3}J(H,H) = 4.1 Hz, ^{4}J(H,H) = 1.1 Hz, 2H)	4.32 (d, ^{3}J(H,H) = 5.4 Hz, 2H), 3.80 (br. s, 2H),	4.30 (d, ^{3}J(H,H) = 6.1 Hz, 4H);	3.83 (d, ^{3}J(H,H)= 5.7 Hz, 4H)
allylic	2.65 – 2.55 (m, 4H)	2.6 (m, 4H)	2.75 – 2.65 (m, 4H)	2.60 (m, 4H)
benzylic	2.8 – 2.7 (m, 4H)	2.76 (dd, ^{3}J(H,H) = 7.9, ^{3}J(H,H) = 5.8, 2H), 2.66 (m, 2H)	2.50 (m, 4H)	2.78 (m, 4H)

Table 2.3 (cont.)

o	7.97 (s, 1H); 7.72 (d, ^{4}J (H,H) = 2.4 Hz, 1H)	7.78 (d, ^{4}J(H,H) = 2.3 Hz, 1H), 7.68 (d, ^{4}J(H,H) = 2.4 Hz, 1H)	7.83 (br. s, 2H)	8.13 (br. s, 2H)
o'	7.42 (d, ^{3}J(H,H) = 7.3 Hz, 1H); 6.90 (dd, ^{3}J(H,H) = 8.1 Hz, ^{4}J (H,H) = 2.4 Hz, 1H)	6.93 (dd, ^{3}J(H,H) = 8.1 Hz, ^{4}J (H,H) = 2.4 Hz, 1H), 6.56 (dd, ^{3}J(H,H) = 8.3 Hz, ^{4}J (H,H) = 2.4 Hz, 1H)	6.89 (dd, ^{3}J(H,H) = 7.8 Hz, ^{4}J(H,H) = 1.5 Hz, 2H)	6.97 (dd, ^{3}J(H,H)=9.5 Hz; ^{4}J (H,H)=1.2 Hz, 2H
m	7.16 (d, ^{3}J(H,H) = 7.8 Hz, 1H), 7.05 (d, ^{3}J(H,H) = 8.3 Hz, 1H)	7.05 (d, ^{3}J(H,H) = 8.7 Hz, 1H), 7.03 (d, ^{3}J(H,H) = 8.7 Hz, 1H)	7.07 (d, ^{3}J(H,H) = 7.8 Hz, 2H)	7.12 (overlap with solvent)
linkers	4.24 (s, 2H, benzylic); 4.44 (d, ^{2}J(H,H) = 11.6 Hz, 1H, benzylic); 3.45 – 3.35 (m, 4H)	4.10 (t, ^{3}J(H,H) = 5.1 Hz, 2H); 3.28 (t, ^{3}J(H,H) = 5.6 Hz, 2H); 1.62 (quint, ^{3}J(H,H) = 5.6 Hz, 2H)	3.26(s, 4H)	3.15 (t, ^{3}J(H,H) = 6.0 Hz, 4H), 2.69 (m, 4H); 1.85 – 1.75 (m, 4H)

Table 2.4. Assignments of the ^{1}H-NMR resonances of the *E* isomers of macrocycles **1–9** containing hexadiene. See Fig. 2.9 for the illustration of notations. All spectra are in toluene-d_8 at 25 ± 1 °C unless noted otherwise.

	1	**2**	**3**	**4** (C_6D_6)	**5**
internal	4.91 (s, 2H)	5.35 (dm, ^{3}J(H,H) = 14.9 Hz, 1H); 5.22 (ddd, ^{3}J(H,H) = 15.6 Hz, ^{3}J(H,H) = 9.0 Hz, ^{3}J(H,H) = 6.3 Hz, 1H)	5.02 (s, 2H)	5.56 (dd, ^{3}J(H,H) = 15.4 Hz, ^{3}J(H,H) = 10.7 Hz, 1H), 5.39 (dd, ^{3}J(H,H) = 15.3 Hz, ^{3}J(H,H) = 10.6 Hz, 1H)	5.47 (m, 1H), 5.20-5.10 (m, 3H)
external	5.16 (m, 2H)	4.92 (m, 4H)	4.65 (m, 2H)	5.10 (ddd, ^{3}J(H,H) = 15.3 Hz, ^{3}J(H,H) = 7.5 Hz, ^{3}J(H,H) = 4.8 Hz, 1H), 5.01 (ddd, ^{3}J(H,H) = 15.6 Hz, ^{3}J(H,H) = 9.2 Hz, ^{3}J(H,H) = 5.4 Hz, 1H)	3.85 (t, ^{3}J(H,H) = 10.5 Hz, 1H), 3.5 – 3.35 (m, 4H)
CH_2	4.04 (dd, ^{3}J(H,H) = 13.6 Hz, ^{4}J(H,H) = 3.6 Hz, 2H), 3.13 (dd, ^{3}J(H,H) = 13.6 Hz, ^{4}J(H,H) = 8.6 Hz, 2H)	4.57 (dd, ^{2}J(H,H) = 11.7 Hz, ^{3}J(H,H) = 6.3 Hz); 3.75 (dd, ^{2}J(H,H) = 11.7 Hz, ^{3}J(H,H) = 9.0 Hz); 1.86 (ddd, ^{2}J(H,H) = 13.9 Hz, ^{3}J(H,H) = 10.7 Hz, ^{4}J(H,H) = 2.5 Hz, 1H); 1.43 (dd, ^{3}J(H,H) = 13.5 Hz, ^{2}J(H,H) = 5.8 Hz);	2.84 (dd, ^{3}J(H,H) = 6.7 Hz, ^{4}J(H,H) = 1.5 Hz, 2H), 2.75 – 2.6 (m, 6H)	4.55 (dd, ^{2}J(H,H) = 12.4 Hz, ^{3}J(H,H) = 9.1 Hz, 1H), 4.38 (dd, ^{2}J(H,H) = 12.4 Hz, ^{3}J(H,H) = 5.3 Hz, 1H), 3.50 (dd, ^{2}J(H,H) = 13.2 Hz, ^{3}J(H,H) = 7.5 Hz, 1H), 3.36 (dd, ^{2}J(H,H) = 13.2 Hz, ^{3}J(H,H) = 4.9 Hz, 1H)	4.55 (m, 1H), 4.42 (ddd, ^{2}J(H,H) = 14.4 Hz, ^{3}J(H,H) = 6.4 Hz, ^{4}J(H,H) = 1.7 Hz, 1H), 3.83 (ddd, ^{2}J(H,H) = 13.9 Hz, ^{3}J(H,H) = 5.4 Hz, ^{4}J(H,H) = 1.5 Hz, 1H), 3.26 (ddd, ^{2}J(H,H) = 11.0 Hz, ^{3}J(H,H) = 5.4 Hz, ^{4}J(H,H) = 1.0 Hz, 1H)
allylic	2.73 (m, 4H)	2.5-2.8 (m, 11H)	2.75 – 2.6 (m, 6H)	2.5 (m, 11H);	2.65- 2.5 (m, 4H)
benzylic	2.56 (m, 4H)	2.5-2.8 (m, 11H)	3.0 – 2.9 (m, 4H)	2.5 (m, 11H);	2.9 (m, 4H)
o	7.76 (s, 2H)	7.94 (br. s, 1H) other peak overlaps with solvent	7.60 (s, 2H)	7.48 (s, 1H), 6.86 (s, 1H)	7.63 (d, ^{4}J (H,H) = 2.2 Hz, 1H), 6.97 (d, ^{4}J(H,H) = 2.4 Hz, 1H)
o'	6.75 (dd, ^{3}J(H,H) = 7.5 Hz, ^{4}J(H,H) = 1.2 Hz, 2H)	6.82 (dd, ^{3}J(H,H) = 7.9 Hz, ^{4}J (H,H) = 2.1 Hz, 1H); 6.70 (dd, ^{3}J(H,H) = 7.7 Hz, ^{4}J (H,H) = 1.4 Hz, 1H)	6.78 (d, ^{3}J(H,H) = 7.3 Hz, 2H)	6.87 (dd, ^{3}J(H,H) = 6.1 Hz, ^{4}J (H,H) = 2.3 Hz, 1H), 6.85 (dd, ^{3}J(H,H) = 4.6 Hz, ^{4}J (H,H) = 1.2 Hz, 1H)	6.96 (dd, ^{3}J(H,H) = 8.1 Hz, ^{4}J (H,H) = 2 Hz, 1H), 6.84 (dd, ^{3}J(H,H) = 8.0 Hz, ^{4}J (H,H) = 2.2 Hz, 1H)
m	7.05 (d, ^{3}J(H,H) = 7.5 Hz, 2H)	7.07 (d, 6.7 Hz, 2H)	7.04 (d, ^{3}J(H,H) = 8 Hz, 1H)	7.14 (t, ^{3}J(H,H) = 7.6 Hz, 2H)	7.03 (^{3}J (H,H) = 8.3 Hz, 2H)

Table 2.4 (cont.)

linkers	4.94 (d, ^{3}J(H,H) = 12 Hz, 2H), 4.13 (^{3}J(H,H) = 12 Hz, 2H)	2.5-2.8 (m, 11H); 2.50 (dd, ^{2}J(H,H) = 12.3 Hz, J (H,H) = 2.5 Hz, 1H)	3.67 (d, ^{2}J(H,H) = 13.8 Hz, 2H), 3.50 (d, ^{2}J(H,H) = 13.9 Hz, 2H)	3.06 (ddd, ^{2}J(H,H) = 10.9 Hz, ^{3}J(H,H) = 6.3 Hz, ^{3}J(H,H) = 4.6 Hz, 1H) 3.0 – 2.5 (m, 11H); 1.65-1.55 (m, 1H); 2.0 – 1.9 (m, 1H)	4.0 (m, 1H), 3.11 (ddd, ^{2}J(H,H) = 8.9 Hz, ^{3}J(H,H) = 4.8 Hz, ^{4}J(H,H) = 1.7 Hz, 1H), 2.98 (m, 2H)

Table 2.4 (cont.)

	6	**7**	**8**	**9**
internal	5.57 (ddm, ^{3}J(H,H) = 15.8 Hz, ^{3}J(H,H) = 10.2 Hz, 1H), 5.00 (dd, ^{3}J(H,H) = 15.7 Hz, ^{3}J(H,H) = 10.3 Hz, 1H)	5.51 (dd, ^{3}J(H,H) = 15.5 Hz, ^{3}J(H,H) = 10.2 Hz, 1H); 5.37 (dd, ^{3}J(H,H) = 15.3 Hz, ^{3}J(H,H) = 9.6 Hz, 1H);	5.41 (m, 2H)	5.78 (m, 2H)
external	5.32 (m, 2H)	5.30 – 5.15 (m, 2H)	4.98 (m, 2H)	5.54 (m, 2H)
CH_2	3.78 (dd, ^{2}J(H,H) = 11.3 Hz, ^{3}J(H,H) = 9.4 Hz, 1H), 3.47 (dd, ^{2}J(H,H) = 13.5 Hz, ^{3}J(H,H) = 5.0 Hz, 1H), 3.0 – 2.8 (m, 8H)	4.57 (dd, ^{2}J(H,H) = 12.3 Hz, ^{3}J(H,H) = 7.8 Hz, 1H), 4.19 (dd, ^{2}J(H,H) = 12.0 Hz, ^{3}J(H,H) = 6.8 Hz, 1H), 3.21 (m, 1H), 2.57 (dd, ^{2}J(H,H) = 14.7 Hz, ^{3}J(H,H) = 8.3 Hz, 1H)	4.33 (m, 4H)	3.91 (dd, ^{2}J(H,H) = 14.1 Hz, ^{3}J(H,H) = 4.6, 2H); 3.45 (dd, ^{2}J(H,H) = 13.8 Hz, ^{3}J(H,H) = 6.1 Hz, 2H)
allylic	2.66 (m, 4H)	3.0 – 2.75 (m, 8H)	2.85 (m, 2H), 2.64 (dt, ^{2}J(H,H)=14.8 Hz; ^{3}J (H,H)=4.9 Hz, 2H)	2.78 (td, ^{2}J(H,H) = 15.8 Hz, ^{3}J(H,H) = 5.5 Hz, 2H), 2.70 (td, ^{2}J(H,H) = 14.1 Hz, ^{3}J(H,H) = 5.5 Hz, 2H)
benzylic	3.0 – 2.8 (m, 8H)	3.0 – 2.75 (m, 8H)	3.00 (m, 4H)	3.00-2.85 (m, 8H);
o	7.40 (d, ^{3}J(H,H) = 2.3 Hz, 1H), 6.92 (d, ^{3}J(H,H) = 2.0 Hz, 1H)	7.88 (s, 1H); 6.97 (d, ^{4}J (H,H) = 2.3 Hz)	7.61 (br. s, 2H)	7.73 (br. s, 2H)
o'	6.90 (dd, ^{3}J(H,H) = 7.7 Hz, ^{4}J (H,H) = 2.5 Hz, 1H), 6.83 (dd, ^{3}J(H,H) = 8.2 Hz, ^{4}J (H,H) = 2.0 Hz, 1H)	6.86 (dd, ^{3}J(H,H) = 7.7 Hz, ^{4}J (H,H) = 2.0 Hz, 1H), 6.80 (dd, ^{3}J(H,H) = 7.4 Hz, ^{4}J (H,H) = 1.3 Hz, 1H)t	6.78 (dd, ^{3}J(H,H)=7.9 Hz; ^{4}J (H,H)=1.5 Hz, 2H)	6.87 (dd, ^{3}J(H,H) = 7.7 Hz, ^{4}J(H,H) = 1.5 Hz, 2H)
m	7.08 (d, ^{3}J(H,H) = 7.8 Hz, 1H), 7.03 (d, ^{3}J(H,H) = 7.8 Hz, 1H)	7.07 (d, ^{3}J(H,H) = 6.1 Hz, 1H); the other peak overlaps with solvent	6.99 (overlap with solvent)	7.12 (overlap with solvent)
linkers	4.59 (td, ^{2}J(H,H) = 13.2 Hz, ^{3}J(H,H) = 3.7 Hz, 1H); 3.88 (dt, ^{2}J(H,H) = 12.6 Hz, ^{3}J(H,H) = 4.6 Hz, 1H); 3.0 – 2.8 (m, 8H); 1.75 – 1.65 (m, 2H)	4.86 (d, ^{2}J(H,H) = 12.6 Hz, 1H, benzylic); 4.00 (d, ^{2}J(H,H) = 12.8 Hz, 1H, benzylic); 3.4 – 3.3 (m, 4H);	3.60 (d, ^{2}J (H,H)=14.5 Hz, 2H); 3.29 (d, ^{2}J (H,H)=14.5 Hz, 2H)	3.16 (m, 4H); 3.15 (td, ^{2}J(H,H) = 9.5 Hz, ^{3}J(H,H) = 3.3 Hz, 2H); 3.05(quint, J(H,H) = 5 Hz, 2H); 3.00-2.85 (m, 8H); 1.95 – 2.05 (m, 2H) 1.60-1.50 (m, 2H)

Table 2.5. High-resolution mass spectrometry data on all synthetic target macrocycles, *Z***1** through *Z***9** and the corresponding diene products.

macrocycle	formula	cyclobutene,^{a} m/z		diene,^{b} m/z	
		calc'd M+H^{+}	found M+H^{+}	calc'd M^{+}	found M^{+}
1	$C_{26}H_{26}O_2$	371.2011	371.2019	370.19328	370.19330
2	$C_{26}H_{26}OS$	387.1783	387.1781	386.1704	386.1703
3	$C_{26}H_{26}S_2$	403.1554	403.1557	402.14760	402.14759^{c}

Table 2.5 (cont.)

4	$C_{26}H_{26}O_3$	387.1960	387.1961	386.1882	386.18966
5	$C_{27}H_{28}O_2$	385.2168	385.2162	384.2089	384.2101
6	$C_{27}H_{28}O_3$	401.2117	401.2112	400.2039	400.2038
7	$C_{27}H_{28}O_3$	401.2117	401.2105	400.2039	400.2040
8	$C_{28}H_{26}O_4$	427.1909	427.1909	426.1831	426.1831
9	$C_{30}H_{34}O_2$	427.2637	427.2638	426.25588	426.25590

[a] ESI-MS [b] FAB-MS (EI-MS for **3**)

2.7 References

1. Neuman, K. C.; Nagy, A., Single-Molecule Force Spectroscopy: Optical Tweezers, Magnetic Tweezers and Atomic Force Microscopy. *Nat. Methods* **2008**, *5*, 491–505.
2. Cremer, D.; Kraka, E., The Concept of Molecular Strain: Basic Principles, Utility, and Limitations. In *Molecular Structure and Energetics*, Liebman, J. F.; Greenberg, A., Eds. VCH Publishers: New York, 1988; Vol. 7: Structure and Reactivity, pp 65–138.
3. Reimann, P., Brownian Motors: Noisy Transport Far from Equilibrium. *Phys. Rep.* **2002**, *361*, 57–265.
4. Schliwa, M., *Molecular Motors*. Wiley-VCH: New York, 2003.
5. Browne, W. R.; Feringa, B. L., Making Molecular Machines Work. *Nat. Nanotechnol.* **2006**, *1*, 25–35.
6. Hugel, T.; Holland, N. B.; Cattani, A.; Moroder, L.; Seitz, M.; Gaub, H. E., Single-Molecule Optomechanical Cycle. *Science* **2002**, *296*, 1103–1106.
7. Casale, A.; Porter, R. S., *Polymer Stress Reactions*. Academic Press: New York, 1979; Vol. 2.
8. Granick, S.; Bae, S. C., Stressed Molecules Break Down. *Nature* **2006**, *440*, 160.
9. Vogel, V., Mechanotransduction Involving Multimodular Proteins: Converting Force into Biochemical Signals. *Annu. Rev. Biophys. Biomol. Struct.* **2006**, *35*, 459-488.
10. Schmidt, S. W.; Beyer, M. K.; Clausen-Schaumann, H., Dynamic Strength of the Silicon–Carbon Bond Observed over Three Decades of Force-Loading Rates. *J. Am. Chem. Soc.* **2008**, *130*, 3664–3668.

11. Ainavarapu, S. R. K.; Wiita, A. P.; Dougan, L.; Uggerud, E.; Fernandez, J. M., Single-Molecule Force Spectroscopy Measurements of Bond Elongation During a Bimolecular Reaction. *J. Am. Chem. Soc.* **2008**, *130*, 6479–6487.

12. Wiita, A. P.; Perez-Jimenez, R.; Walther, K. A.; Grater, F.; Berne, B. J.; Holmgren, A.; Sanchez-Ruiz, J. M.; Fernandez, J. M., Probing the Chemistry of Thioredoxin Catalysis with Force. *Nature* **2007**, *450*, 124–127.

13. Kersey, F. R.; Yount, W. C.; Craig, S. L., Single-Molecule Force Spectroscopy of Bimolecular Reactions: System Homology in the Mechanical Activation of Ligand Substitution Reactions. *J. Am. Chem. Soc.* **2006**, *128*, 3886–3887.

14. Grandbois, M.; Beyer, M.; Rief, M.; Clausen-Schaumann, H.; Gaub, H. E., How Strong Is a Covalent Bond? *Science* **1999**, *283*, 1727–1730.

15. Hyeon, C.; Thirumalai, D., Measuring the Energy Landscape Roughness and the Transition State Location of Biomolecules Using Single Molecule Mechanical Unfolding Experiments. *J. Phys.: Condens. Matter* **2007**, 113101/1–27.

16. Eelkema, R.; Pollard, M. M.; Vicario, J.; Katsonis, N.; Ramon, B. S.; Bastiaansen, C. W. M.; Broer, D. J.; Feringa, B. L., Molecular Machines: Nanomotor Rotates Microscale Objects. *Nature* **2006**, *440*, 163.

17. Nguyen, T. Q.; Kausch, H. H., *Flexible Polymer Chains in Elongational Flow. Theory and Experiment*. Springer-Verlag: Berlin, Germany, 1999; p 398.

18. Hickenboth, C. R.; Moore, J. S.; White, S. R.; Sottos, N. R.; Baudry, J.; Wilson, S. R., Biasing Reaction Pathways with Mechanical Force. *Nature* **2007**, *446*, 423–427.

19. Sheiko, S. S.; Sun, F. C.; Randall, A.; Shirvanyants, D.; Rubinstein, M.; Lee, H.-i.; Matyjaszewski, K., Adsorption-Induced Scission of Carbon–Carbon Bonds. *Nature* **2006**, *440*, 191–194.

20. Sotomayor, M.; Schulten, K., Single-Molecule Experiments in Vitro and in Silico. *Science* **2007**, *316*, 1144–1148.

21. Stirling, C. J. M., Evaluation of the Effect of Strain Upon Reactivity. *Tetrahedron* **1985**, *41*, 1613–1666.

22. Tani, K.; Stoltz, B. M., Synthesis and Structural Analysis of 2-Quinuclidonium Tetrafluoroborate. *Nature* **2006**, *441*, 731–734.

23. Carey, F. A.; Sundberg, R. J., *Advanced Organic Chemistry*. Springer: New York, 2007.

24. Tobe, M. L.; Burgess, J., *Inorganic Reaction Mechanisms*. Longman: New York, 1999.
25. Gajewski, J. J., *Hydrocarbon Thermal Isomerizations*. Elsevier: Amsterdam, 2004.
26. Guner, V.; Khuong, K. S.; Leach, A. G.; Lee, P. S.; Bartberger, M. D.; Houk, K. N., A Standard Set of Pericyclic Reactions of Hydrocarbons For the Benchmarking of Computational Methods: The Performance of ab initio, Density Functional, CASSCF, CASPT2, and CBS-QB3 Methods For the Prediction of Activation Barriers, Reaction Energetics, and Transition State Geometries. *J. Phys. Chem. A* **2003**, *107*, 11445–11459.
27. McMurry, J. E., Carbonyl-Coupling Reactions Using Low-Valent Titanium. *Chem. Rev.* **1989**, *89*, 1513–1524.
28. Yang, Q.-Z.; Huang, Z.; Kucharski, T. J.; Khvostichenko, D.; Chen, J.; Boulatov, R., A Molecular Force Probe. *Nat. Nanotechnol.* **2009**, *4*, 302–306.
29. Cramer, C. J., *Essentials of Computational Chemistry: Theories and Models*. J. Wiley: West Sussex, England; New York, 2002; p 542.
30. Jencks, W. P., A Primer For the Bema Hapothle. An Empirical Approach to the Characterization of Changing Transition-State Structures. *Chem. Rev.* **1985**, *85*, 511–527.
31. Jung, M. E.; Sledeski, A. W., Efficient Total Synthesis of Racemic and Optically Active Cyclobutanes and Simple Analogs. *J. Chem. Soc., Chem. Commun.* **1993**, 589–591.
32. Smith, C. E.; Williamson, W. R. N.; Cashin, C. H.; Kitchen, E. A., Potential Antiinflammatory Compounds. 3. Compounds Derived from Acenaphthene and Indan. *J. Med. Chem.* **1979**, *22*, 1464–1469.
33. Neudeck, H. K., Aromatic Spirane. XIV. Syntheses of 2,2'-Spirobi(σ-hydrindacene) and Its Precursors. *Monatsh. Chem.* **1987**, *118*, 627–657.
34. Snow, A. W.; Foos, E. E., Conversion of Alcohols to Thiols via Tosylate Intermediates. *Synthesis* **2003**, *4*, 509–512.

Chapter 3. Mechanochemical Acceleration of a Single-Barrier Bimolecular Nucleophilic Substitution: Primary Sulfonate Hydrolysis

Adapted with permission from Kucharski, T. J.; Yang, Q.-Z.; Tian, Y.; Boulatov, R., Strain-Dependent Acceleration of a Paradigmatic S_N2 Reaction Accurately Predicted by the Force Formalism. *J. Phys. Chem. Lett.* **2010**, *1*, 2820–2825. © 2010 American Chemical Society.

3.1 Abstract

Experiment and theory suggest that the effect of strain on the kinetics of S_N2 reactions is predicted accurately within the force formalism using a single structural parameter: the difference of the non-bonding separation of two atoms bound to the electrophilic atom in the ground and transition states of the corresponding strain-free reaction. We show that the difference of $H_3C\cdots O_{Ms}$ distance in EtOMs (Ms: SO_2Me) and in the corresponding transition state of its hydrolysis, $H_2O\cdots(Me)CH_2\cdots OMs$, calculated at the B3LYP/6-311++G(3df,2pd) level with the SMD solvent model accurately predicts the measured lowering of the free energy of activation across a series of increasingly strained macrocyclic sulfonates. The equivalent distance $H_2C\cdots S$ in EtSSEt also accurately predicts the previously reported kinetics of thiol/disulfide exchange in stained disulfides. The elongation of the scissile C–O or S–S bond yields qualitatively incorrect predictions. The results are consistent with the established structural origin of the S_N2 activation barrier and enable predictions of the kinetics of S_N2 reactions in stretched polymers. Such ability is critical to the development of a conceptual framework for controlling chemically-driven multiscale dynamics through molecular design and of polymers with stress-responsive properties engineered at the monomer level.

3.2 Introduction

Stretching a macromolecule can dramatically change its reactivity. Examples include up to 10^{15}-fold acceleration of localized reactions in polymeric materials under microscopic loads,[1] in macromolecules in shear flows[2,3] or at evolving interfaces[4] and the operation of motor proteins[5] and actuating polymers.[6] Understanding and exploiting these phenomena requires a model that relates changes in macromolecular strain to changes in the kinetics of its reactions. The classical approaches based on strain energy, however, become unreliable as the total size of the reactant relative to that of the reactive moiety increases, and they fail to explain strain-induced perturbations of reaction rates in stretched polymers.

Models based on restoring force (the gradient of strain energy) have yielded quantitative insights into the microscopic response of materials to microscopic and macroscopic strains.[7] Extending them to the atomic scale where chemical reactions occur has proven more challenging. Eyring's original proposal[2] that activation barriers are proportional to the restoring force of the reactants has been validated experimentally,[8] and the Eyring–Bell–Evans equation[2,9-

[11] ($\Delta\Delta G^{\ddagger} = F\Delta x$) is used to describe chemomechanical kinetics. However, the experimentally derived proportionality constants Δx are empirical, and they cannot be ascribed to changes in molecular structure of isolated strain-free reactive moieties. Without such a molecular interpretation, the restoring force formalism lacks the predictive capabilities needed to guide the design of new molecules and reactions for stress-responsive and actuating polymers.

In the absence of mass transport limitations, a localized reaction in a stretched polymer is accelerated if the reactive moiety elongates along the strain axis in order to form the transition state as this allows (partial) strain relaxation elsewhere in the molecule. The barrier lowering is approximately the product of the restoring force and the change in the internal coordinate of the reactive moiety (i.e., internuclear distance, angle, torsion or a combination thereof) that describes the structural difference between its ground and transition states along the strain axis. The primary structural difference between the ground and transition state of an S_N2 reaction (Fig. 3.1) is (1) elongation of the scissile bond and (2) contraction of the bond angles to it. In axially strained reactive moieties (which is typical in stretched flexible polymers), the strain axis coincides with the contour length. Consequently, the non-bonding distance between the pair of atoms that connects the electrophilic atom to the rest of the polymer describes the structural difference between the ground and transition states of the reactive moiety.

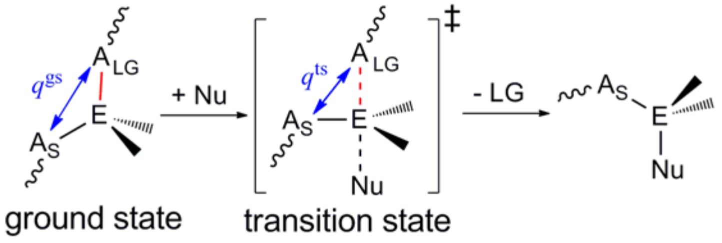

Fig. 3.1. We propose that the strain-dependent change in the activation free energy of an S_N2 reaction is proportional to the product of restoring force that quantifies strain and $\Delta q = q_{ts} - q_{gs}$, the elongation (or contraction) of the separation of a pair of atoms connecting the electrophilic atom E to the rest of the strained molecule. This difference, Δq, accounts for changes in bond lengths E–A_S and E–A_{LG} and bond angle A_S–E–A_{LG} between the ground and transition states, capturing the salient structural basis of the activation barrier. A stands for an atom, S and LG are spectator and leaving group; Nu is nucleophile; the wavy lines denote the rest of the molecule.

The activation energies of localized reactions are typically more sensitive to strain than the geometries of their stationary points.[12] Consequently, useful predictions of strain-dependent kinetics of such S_N2 reactions would require only the restoring force of the reactive moiety, F, and a single geometric parameter, $\Delta q = q_{ts} - q_{gs}$, in the suitable strain-free analog. Since restoring force is intensive (scale independent) and ground and transition states are in internal mechanical equilibrium,[13] each moiety of a strained (macro)molecule experiences the same force. The difficult, or even impossible, task of optimizing the transition state of a large strained molecule is replaced by estimating its total restoring force, which for a stretched macromolecule is available from the knowledge of its fractional strain or the dynamics of the process that stretches it.[14]

Here we compare the measured kinetics of two paradigmatic S_N2 reactions,[15-17] hydrolysis of primary alkyl sulfonates (1) and thiol/disulfide exchange (2, Fig. 3.2), as a function of the restoring force of the reactive moiety with that predicted by the Eyring–Bell–Evans equation using the value of Δq (Fig. 3.1) calculated quantum-chemically for the simplest (Alk = CH_3, Fig. 3.2) examples of the two reactions: hydrolysis of strain-free ethyl mesylate (EtOMs) and reduction of strain-free ethyl disulfide (Et_2S_2). We show the quantitative agreement between the experiment and the model, demonstrating for the first time the predictive capabilities of the restoring force formalism.

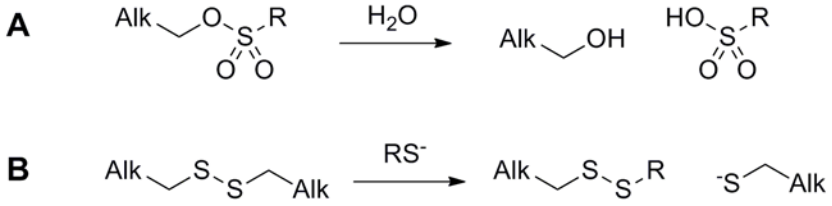

Fig. 3.2. Paradigmatic S_N2 reactions: hydrolysis of primary sulfonates (**A**) and thiol/disulfide exchange (**B**); Alk = alkyl.

The rest of the manuscript is organized in three sections: (1) we describe our method of measuring force-dependent kinetics of localized reactions and of computing the restoring forces of the reactive moiety; (2) we present the measured force-dependent kinetics and (3) we compare the results with the predictions.

3.3 Methods

The conventional method of studying force-dependent kinetics requires incorporating the reactive moiety into a long inert polymer, which is then stretched with a laser trap or atomic force microscope.[8,18] This approach has been particularly successful for studying the kinetics of unfolding and refolding of biopolymers but is far less informative for highly localized reactions.

The intensive (scale-invariant) nature of the restoring force was long recognized[12] to result in rate-force relationships being largely independent of the size of the molecule within which the reaction occurs. In other words, a reactive moiety strained to a given restoring force would manifest approximately similar reactivity regardless of how this strain is generated: by stretching a macromolecule or by incorporating the reactive moiety into a properly designed strained macrocycle. The much more tractable macrocycles allow experimental tests of various models of reaction kinetics in stretched macromolecules.

Until recently, realization of this small-molecule approach was precluded by the lack of (1) molecular architectures to strain diverse reactive groups uniaxially over a sufficiently wide range and in sufficiently small increments to reveal broad trends; and (2) computational methods to estimate the restoring force of these groups. We previously showed that stiff stilbene (red, Fig. 3.3) provides a convenient method to control the axial strain of diverse reactive moieties by incorporating them in an inert linker that constraints the C6,C6′ distance of *E*-stiff stilbene (red, Fig. 3.3).[19,20] A series of such macrocycles of varying size allows the restoring force of diverse reactive moieties to be varied over a ~0.5 nN range in ~50 pN increments. The reaction rates in both isomers of each macrocycle are measured with the standard methods of chemical kinetics at different temperatures to yield differential free energies of activation, $\Delta\Delta G^{\ddagger} = RT\ln(k_E/k_Z)$, resulting from the different strain of the reactive moiety in the two isomers.

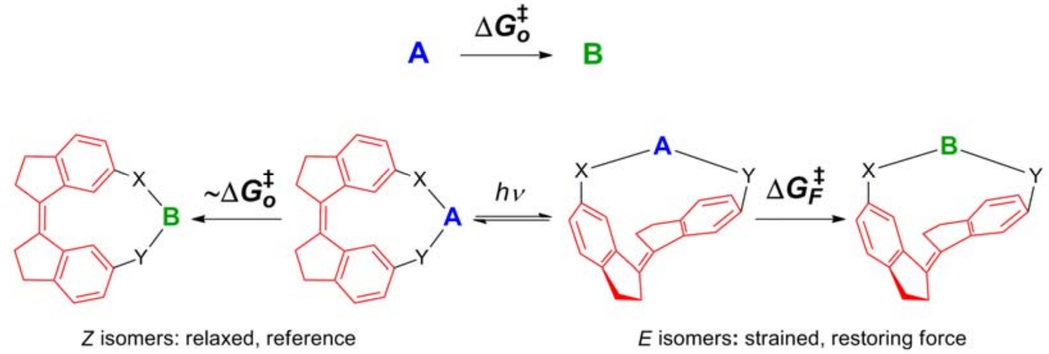

Fig. 3.3. General scheme for studying force-dependent kinetics of a reaction A→B using stiff stilbene (red) to control the axial strain (and hence the restoring force) of the reactive moiety A. Macrocycles of (*Z*)-stiff stilbene are mostly strain-free. The strained *E* isomers are generated upon photoisomerization of (*Z*)-stiff stilbene; the direction and magnitude of strain generated in A is controlled by the length and conformational flexibility of the inert linkers X and Y.

A significant challenge in studying force-dependent kinetics is to quantify the restoring force. In single-molecule force experiments, the net average restoring force along the macromolecular contour length is estimated from the strain of a reference object (typically a force probe) using empirical calibration curves. Such estimates, despite important recent advances, remain subject to systematic errors particularly at large strains and considerable uncertainty of the absolute values of force remains.[18]

The modest size of our macrocycles allows the restoring force of any internal coordinate to be obtained directly by electronic structure methods, typically as the force required to distort the corresponding non-macrocyclic reference fragment (e.g., parent macrocycle sans A, blue, in Fig. 3.3) to its geometry in the full macrocycle.[19] The reference fragment is optimized with harmonic potentials imposed between 1 or more pairs of its non-H atoms within the ONIOM[21] scheme as implemented in Gaussian09. The force constants and the equilibrium distances of the potentials are varied iteratively to minimize the root-mean-square deviation of the non-H atoms of the reference fragment in the converged ONIOM geometry and in the corresponding macrocycle. To obtain ensemble average values the procedure is conducted for all conformers within 1.5 kcal/mol of the global minima of each isomer of each macrocycle and the forces are Boltzmann-averaged. Since restoring forces cannot be measured, experimental validation of these quantum-chemical calculations relies on the agreement between the measured and calculated free energies and enthalpies of activation. A difference of <1 kcal/mol suggests a faithful representation of transition state structures,[22] and hence the restoring forces, which describe strain and thus are descriptors of the deviation between "ideal" and actual molecular geometries.[12]

3.4 Force-Dependent Kinetics

Here we applied this methodology to evaluate the predictive capabilities of the Eyring–Bell–Evans model for S_N2 reactions, using a series of six macrocyclic sulfonates (Fig. 3.4A). The force-dependent kinetics of thiol/disulfide exchange was previously reported,[23] but it was not used to test the predictive capabilities of the Eyring–Bell–Evans equation.

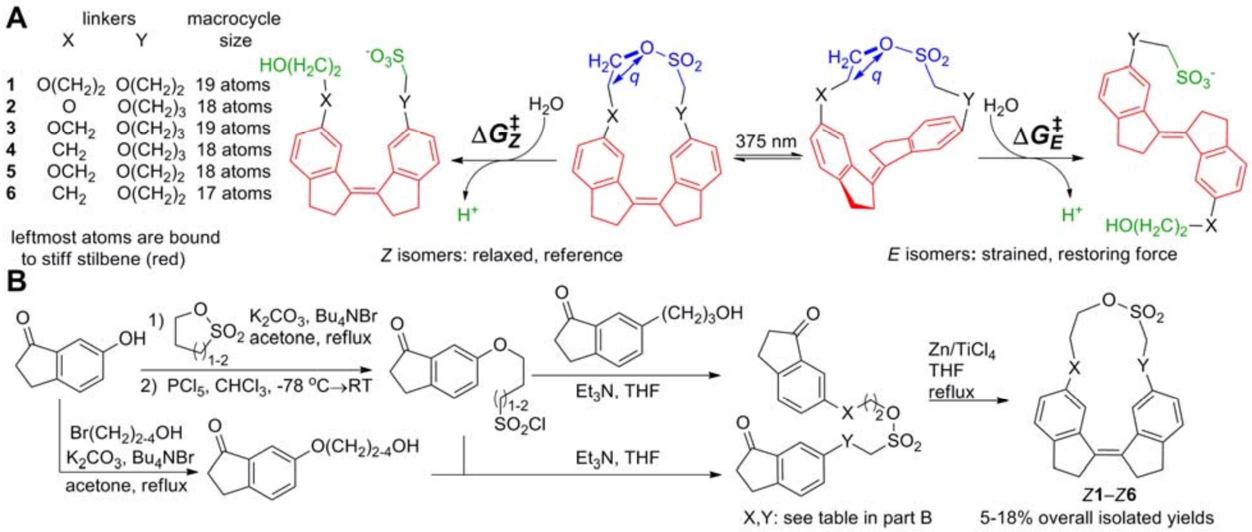

Fig. 3.4. **A**: The macrocyclic series for measuring force-dependent kinetics of hydrolysis of primary alkyl sulfonates; the reactive moiety is blue with the electrophilic C shown explicitly; stiff stilbene is red. **B**: Synthesis of strain-free Z isomers, *Z***1**–*Z***6**.

We synthesized strain-free macrocycles *Z***1**–*Z***6** in three steps and 5–18% overall yields (Fig. 3.4B). Irradiating dilute solutions of *Z***1**–*Z***6** in CH_2Cl_2 at 375 ± 7 nm yielded strained *E* isomers as components of photostationary mixtures. The identities of **1**–**6** were established by ^{1}H and ^{13}C NMR spectroscopy and HR-MS; the chemical homogeneity of the samples was also verified by HPLC (Fig. 3.15–Fig. 3.26).

We measured the kinetics of hydrolysis of both isomers of **1**–**6** in H_2O solutions containing 18% (mol) THF at 25–60 °C by monitoring generation of H^+ (Fig. 3.4A) spectrophotometrically with bromophenol blue. This is a standard method for kinetic measurements of reactions that create or consume H^+.[24,25] Spectrophotometric titration of the indicator with TfOH in the H_2O–THF mixtures of the same composition over 25–60 °C yielded its pK_a. The $\Delta H^‡$ and $\Delta S^‡$ values for hydrolysis of EtOMs measured by our method were within 5% of the literature values.[15] In addition, we found good agreement between the rate constants for hydrolysis of *Z***1** measured spectrophotometrically and by ^{1}H NMR, further validating the use of spectrophotometry for kinetic measurements of C–O bond hydrolysis. To eliminate the contribution of OH^-, hydrolysis was carried out at pH ~ 5, with rates corrected for indicator buffering by eq. (3.12). Analysis of the reaction mixtures by ^{1}H NMR spectroscopy, HR-MS and HPLC confirmed the corresponding sulfonic acid to be the only product of the reaction.

Hydrolysis of the *Z* isomers was characterized by the values of $\Delta H^{\ddagger}$ and $\Delta G^{\ddagger}$ (Table 3.9) that were comparable to the literature values for related sulfonates.[15,16] *E* isomers hydrolyzed faster than their *Z* analogs, with the measured difference in the free energy of activation among the two isomers of the same macrocycle, $\Delta\Delta G^{\ddagger} = RT\ln(k_E/k_Z)$, increased from ~0 kcal/mol in the largest macrocycle, **1**, to 2.7 ± 0.1 kcal/mol in the smallest one, **6** (Table 3.1) at 298 K.

Table 3.1. The measured free energies of activation for sulfonate hydrolysis in **1**–**6**, $\Delta\Delta G^{\ddagger}_{Z\text{–}E} = RT\ln(k_E/k_Z)$.

	1	**2**	**3**	**4**	**5**	**6**
$\Delta\Delta G^{\ddagger}_{Z\text{–}E}$ (298 K), kcal/mol	0.0(0.6)	0.8(0.4)	1.3(0.7)	2.2(0.2)	2.4(0.9)	2.7(0.1)

To estimate the restoring force of the strained sulfonate moiety in macrocycles **1**–**6** we first optimized all conformers of each isomer within 1.5 kcal/mol of its conformational minimum at the B3LYP/6-311+G** level with SMD[26] as the solvent model. Mean absolute deviations of calculated and experimental absolute ($\Delta G_E^{\ddagger}$ and $\Delta G_Z^{\ddagger}$) and differential ($\Delta\Delta G^{\ddagger}$) activation energies were 0.4 and 0.6 kcal/mol, respectively (Table 3.11), lending credence to the calculated structures and forces. All converged wavefunctions were stable. The transition state geometries in **1**–**6** were typical for the S_N2 mechanism, with the structural parameters in strain-free *Z* isomers similar to those calculated for EtOMs (see below). The ensemble-average *difference* of the scissile bond or the non-bonding $H_2C\cdots O$ distance, Δq (Fig. 3.4A), between the ground and transition states of the *E* isomers were comparable in weakly strained (large) and highly strained (small) macrocycles (Fig. 3.38), suggesting negligible Hammond effects[27] at the range of strains accessible across the series of **1**–**6**. This allows the application[28] of the Eyring–Bell–Evans equation.[2,9-11]

The calculated total restoring forces of the reactive moiety in both isomers of macrocycles **1**–**6**, F_t, are listed in Table 3.2. Similarly to other macrocycles of stiff stilbene,[19,20,23] restoring forces of the reactive moiety in the strain free *Z* isomers were at or below ~100 pN and their orientations varied randomly across the series. In contrast, the total restoring force in *E* isomers increased monotonously from the largest macrocycle, **1**, to the smallest one, **6**. Over 85% of the force was along the non-bonding $H_2C\cdots O$ vector of the reactive moiety, q (Fig. 3.4A, F_q, Table 3.2), confirming that in *E***1**–*E***6** the moiety is strained uniaxially. The ensemble-averaged restoring force in the transition states of *E* macrocyclic sulfonates were up to 15% less than in the ground state (tabulated elsewhere[29]), which is consistent with partial conformational relaxation of *E* stiff stilbene resulting from structural differences of the ground and transition-state geometries of the sulfonate moiety (Fig. 3.4A).

Table 3.2. Ensemble-average total restoring forces, $\langle F_t \rangle$, and their projections on q, $\langle F_q \rangle$ at the B3LYP/6-311+G** level in SMD.

	$\langle F_t \rangle_Z$, pN	$\langle F_t \rangle_E$, pN	$\langle F_q \rangle_Z$, pN	$\langle F_q \rangle_E$, pN	net force, $\langle F_t \rangle_E - \langle F_t \rangle_Z$, pN
1	130	220	80	190	110
2	70	290	40	260	220
3	110	320	70	230	210
4	60	370	50	380	310
5	–70	380	0	340	450
6	–70	500	–20	490	570

3.5 Comparison of Experiment and Theory

According to our hypothesis (Fig. 3.1), force dependent kinetics of an S_N2 reaction can be predicted by the Eyring–Bell–Evans equation[2,9-11] ($\Delta\Delta G^{\ddagger} = F\Delta q$) using the difference in the separation of a pair of atoms bound to the electrophilic center between the ground and transition states of the simplest strain-free reactant. To evaluate this hypothesis for the two S_N2 reactions with the measured force-dependent kinetics (sulfonate presented above and thiol/disulfide previously reported) we optimized the ground and transition states for hydrolysis of EtOMs and for EtS^- displacement in EtSSEt (Fig. 3.5) at the B3LYP/6-311++G(3df,2pd) level in H_2O-parameterized SMD[26] as the solvent model. These calculations reproduced accurately the experimental activation free energies[15] (e.g., for EtOMs 25.8 kcal/mol vs. calculated 24.9 kcal/mol both at 298 K) and frequencies[30] (e.g., mean absolute deviation for EtOMs: 38 cm^{-1}, tabulated elsewhere[29]). The calculations yielded classical S_N2 transition states (Fig. 3.5) with the scissile bonds elongations of 0.65 Å and 0.42 Å in the transition states of EtOMs hydrolysis and of thiol/disulfide exchange in EtSSEt, respectively. In macrocycles **1**–**6** (and the corresponding disulfide analogs) the electrophilic C and S atoms, respectively, are coupled to the rest of the molecule through the equivalents of the H_3C/O_{Ms} pair in EtOMs and H_2C/S_{Et} pair in Et_2S_2. According to calculations, these two non-bonding distances elongate by 0.333 Å and 0.070 Å, respectively.[31]

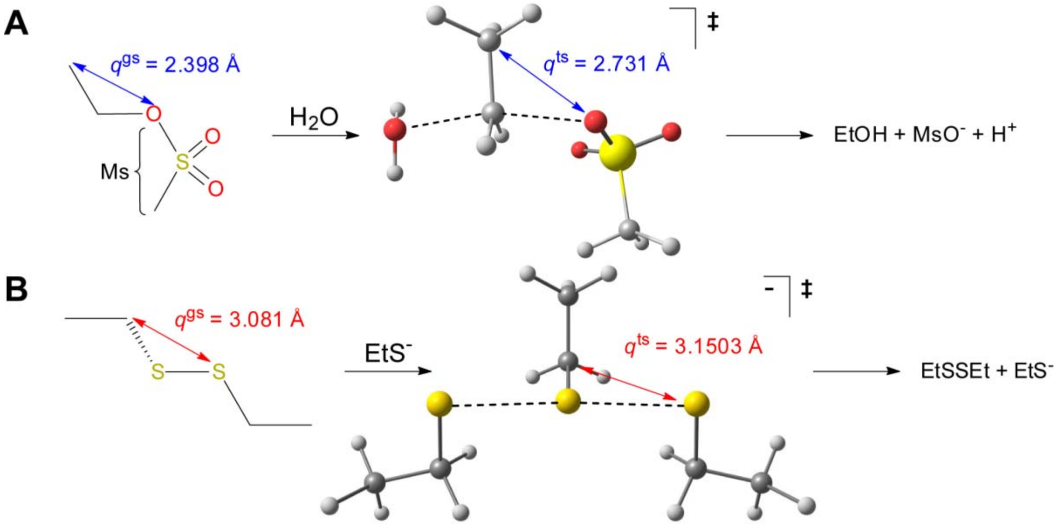

Fig. 3.5. The paradigmatic S_N2 reactions used to verify the predictive capabilities of the force formalism, showing the calculated transition state geometries and the internuclear vector used to estimate strain-dependent barrier lowering. **A**: Hydrolysis of EtOMs: in the transition state the scissile C–O_{Ms} bond and the O_{Nu}–C–O_{LG} angle are 2.125 Å and 170°, respectively. The two O atoms and both C atoms of the ethyl moiety are coplanar. **B**: Thiol/disulfide exchange: in the transition state the scissile S–S bond and the S_{Nu}–S–S_{LG} angle are 2.473 Å and 175°, respectively.

Fig. 3.6 compares the measured calculated difference in the activation free energy (at 298 K) as a function of the restoring force of the reactive moiety with those predicted by the Eyring–Bell–Evans equation using the elongation of the scissile bond and of the non-bonding distance, *q* (Fig. 3.1) as the proportionality coefficient between the restoring force and $\Delta\Delta G^{\ddagger}$. The elongation of the scissile bond vastly overestimates the strain-induced acceleration. In contrast, the calculated elongations of the non-bonding distance $H_3C\cdots O_{Ms}$ and $H_2C\cdots S_{Et}$ results in accurate predictions. In other words, these distances allow >80% of the molecular degrees of freedom of macrocycles *E***1**-*E***6** (and their disulfide analogs), including the most strained ones of the stiff stilbene moiety, to be coarse-grained to a single parameter, force.

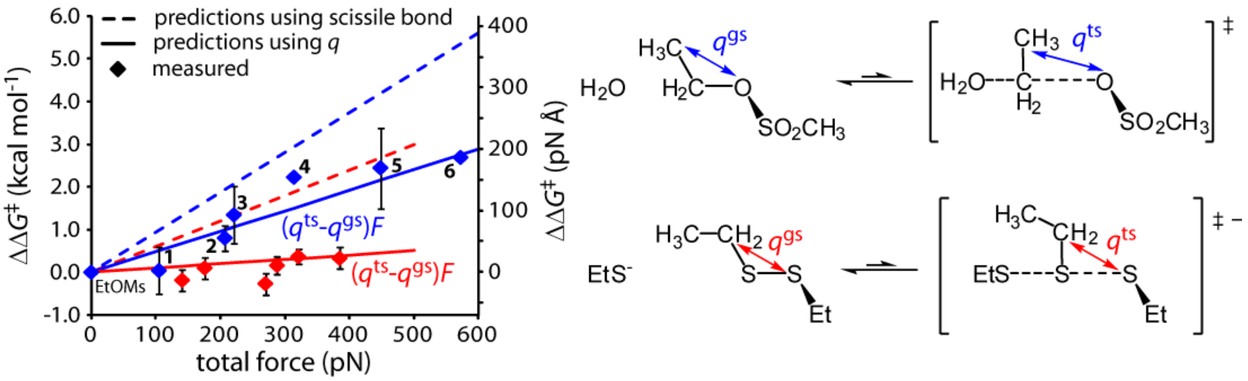

Fig. 3.6. A comparison between the measured strain-induced differences in the activation free energy ($\Delta G^{\ddagger}{}_{Z} - \Delta G^{\ddagger}{}_{E}$ at 298 K, ♦) for two S_N2 reactions, hydrolysis of EtOMs (**1**–**6**, blue) and thiol/disulfide exchange (red), and the predictions by the Eyring–Bell–Evans equation[2,9-11] using the non-bonding $H_2C\cdots O_{Ms}$ (sulfonates, blue) or $H_2C\cdots S_{Et}$ (disulfides, red) distances (solid lines) or the scissile bonds (broken lines) as the internal coordinate, q at 298 K. The uncertainty limits on the $\Delta\Delta G^{\ddagger}$ values (derived as $RT\ln(k_E/k_Z)$, Table 3.1) of macrocycles **4** and **6** are smaller than the size of the symbols.

3.6 Conclusions

These results illustrate the value of the force formalism for estimating the contribution to the activation barrier from changes in strain of most molecular degrees of freedom without describing them explicitly. The intensive property of force[12,28] ensures that such estimates are largely invariant to the number of coarse-grained degrees of freedom (e.g., ~10^2 in **1**–**6** and millions in polymers) but depend critically on the choice of the molecular coordinate, q, which integrates the quantum-mechanical and classical-mechanical (force) descriptions of a reacting molecule.

By studying reactants whose size and structure allow both exact (fully quantum-mechanical) and approximate (hybrid QM/classical-mechanical) descriptions, we can test how sensitive the force formalism is to the choice of q and to define rules to select q effectively for broad reaction classes. Here we applied this strategy to S_N2 reactions, where the endergonic contributions to activation barriers are (a) the elongation of the scissile bond and (b) the contraction of angles between the scissile bond and all other bonds to the electrophilic center needed to form the trigonal-bipyramidal transition state (Fig. 3.5).[32] The non-bonding separation between any pair of atoms bound to the electrophilic center reports on both changes, i.e., it approximates the reaction coordinate. When such a pair is aligned with the strain axis (i.e., restoring force vector) it can be used to estimate the barrier lowering due to partial relaxation of strain outside of the reactive moiety as it rearranges to the transition state. Since restoring force is the gradient of the strain energy, the barrier lowering is simply the restoring force and change in the dimension along the gradient, which is given by changes in q.

In contrast to a pair of atoms bound to the electrophilic site, scissile or forming bonds are *not* appropriate internal coordinates to predict force-dependent kinetics, because changes in their distances do not fully account for structural differences between the ground and transition states of the reactive moiety. Such differences are also due to contraction of bond angles at the electrophilic site (Fig. 3.1). This contraction is not a result of strain relief, as it occurs even in the absence of strain, and its energetic contribution is not captured by restoring force. Consequently, using the elongation/contraction of the scissile/forming bond at the transition state yields incorrect predictions (broken lines, Fig. 3.6). For example, Fig. 3.1 suggests that S_N2 reactions could be (1) accelerated by strain *orthogonal* to the scissile bond (because the spectator ligands also move away from each other to form the transition state, in some reactions by a larger amount than the scissile bond elongates) and (2) inhibited by strain *along* the scissile bond when the contraction of the bond angles in the transition state exceeds scissile bond elongation. These intriguing patterns of rate/strain coupling cannot be identified if q is chosen incorrectly. Here we have described the approach that should facilitate the realization of such S_N2 reactions, which we suggest offer great promise for the design of novel stress-responsive polymers.

3.7 Acknowledgments

The work was supported in part by the NSF (CHE-0748281) and the US AFOSR (FA9550-08-1-0072). T.K. thanks the ONR and NSF for predoctoral fellowships. The HPCMP program of the DoD and NSF NCSA granted computational time.

3.8 Supporting Experimental Information

3.8.1 Materials and General Methods

Commercial reagents of the highest available purity from Aldrich or Fisher were used without further purification unless stated otherwise. Water was obtained from a Milli-Q water purification system. Water used in the preparation of stock indicator solutions and reaction mixtures was also thoroughly sparged with He and stored under N_2. Dry, inhibitor-free THF was obtained from an MBraun solvent purification system and was kept under N_2. All liquids were transferred with a syringe or cannula under N_2. Analytical and preparative thin layer chromatography (TLC) was performed on silica gel 60 (Fisher and Aldrich, respectively).

Irradiation was performed in vessels sealed under N_2 using high-intensity diode light sources from Opto Technology with light output at 375 ± 7 nm. Light intensity was controlled with a custom-made constant-current controller. UV-vis spectra were recorded on a Cary 50 UV-vis spectrophotometer. Multiple UV-vis kinetics experiments were simultaneously recorded using a Turret 400™ four-position cuvette holder equipped with a TC 425 temperature controller. UV-vis kinetic data was processed and models were fitted to the resulting data with custom-written scripts in Matlab (7.9.0 R2009b).

Analytical-scale HPLC was performed on a Shimadzu Prominence LC system with LC-20AT solvent delivery unit, DGU-20A5 degasser, SPD-M20A photodiode array detector, CBM-20A system controller, and Rheodyne 7725i manual injector, with either a J. T. Baker C_{18} column (25 cm × 4.6 mm, 5 μm particles) or a Macherey–Nagel Nucleodur C_{18}-ec column (25 cm × 4.6 mm, 5 μm particles). Preparative-scale HPLC was performed on a Waters LC system with a 600E multisolvent delivery system with He gas solvent sparging, 996 photodiode array detector, and Rheodyne 7725i manual injector, with a Vydac C_{18} column (25 cm × 2 cm, 10 μm particles).

High-resolution mass spectrometry (HRMS) was performed on a Micromass 70-VSE mass spectrometer (EI) or a Waters Q-Tof Ultima mass spectrometer (ESI) at the University of Illinois Mass Spectrometry Center. NMR spectra of macrocycles **1**–**6** and synthetic intermediates were recorded on 400 or 500 MHz Unity-INOVA Varian spectrometers at room temperature (~20 °C). Chemical shifts are reported in ppm downfield from that of tetramethylsilane and are referenced to either the residual ^1H resonances or the ^{13}C resonances of the deuterated solvents. $^{31}P\{^1H\}$ resonances are reported in ppm downfield from 85% H_3PO_4, but were not externally referenced. Spin multiplicities are reported as singlet (s), doublet (d), triplet (t), quartet (q) and quintet (quint) with coupling constants (*J*) given in Hz or multiplet (m); br = broad; app = apparent.

The synthesis and characterization of **1**–**6** is described elsewhere.[29]

3.8.2 Kinetics measurements

Strategy

The hydrolysis of alkyl sulfonates under neutral or acidic conditions produces the corresponding alkyl alcohol and sulfonic acid. In general, the hydrolysis of alkyl esters of inorganic acids is more likely to proceed by C–O cleavage the stronger the corresponding acid.[33] Alkyl sulfonic acids are strong, with the ${}^{\mathrm{w}}_{\mathrm{w}}\mathrm{p}K_{\mathrm{a}}$ for ethane sulfonic acid of -1.68 ± 0.02.[34] Thus, the hydrolysis of alkyl sulfonic acids primarily proceeds via C–O cleavage.[15,33] Only basic hydrolysis of 4- and 5-membered ring sultones and 2-hydroxyethyl sulfonyl chlorides are known to manifest S–O cleavage; even in these substrates, C–O cleavage dominates under neutral or acidic conditions.[35]

Two general methods for measuring the kinetics involving the generation of H^+ are conductimetry and spectrophotometry.[24,25] Conductimetry has typically been used for measurements in pure aqueous solutions and requires the use of a supporting electrolyte. Reactions need be followed to at least 1–2 half-lives for accurate measurements,[16] which is inconvenient for very slow reactions. Spectrophotometry does not constrain the choice of non-aqueous co-solvents and requires no added electrolyte but does require an acid-base indicator. In both approaches an additive may perturb the "intrinsic" reactivity of the substrate. Measurements of differences of rates, especially by competition experiments, are generally thought to be less sensitive to such perturbations, since both reactants of very similar stereoelectronic properties would probably be affected to an approximately similar degree. Nonetheless, we demonstrated that the indicator has no effect on the measured kinetics as described in the main text. Furthermore, even kinetic measurements in complex systems, spectrophotometry with pH indicators has been shown to perform as well as conductimetry and are in some cases preferred over conductimetry, due to their simpler calibration and fast response.[24,25]

Thus, for this study the reaction kinetics were conveniently monitored by spectrophotometrically observing the generation of H^+ with an appropriate pH indicator (e.g., Fig. 3.7). Acid-base equilibration in aqueous media is very fast so that the ratio of the protonated to deprotonated indicator reflects the instantaneous fraction of hydrolyzed sulfonate.

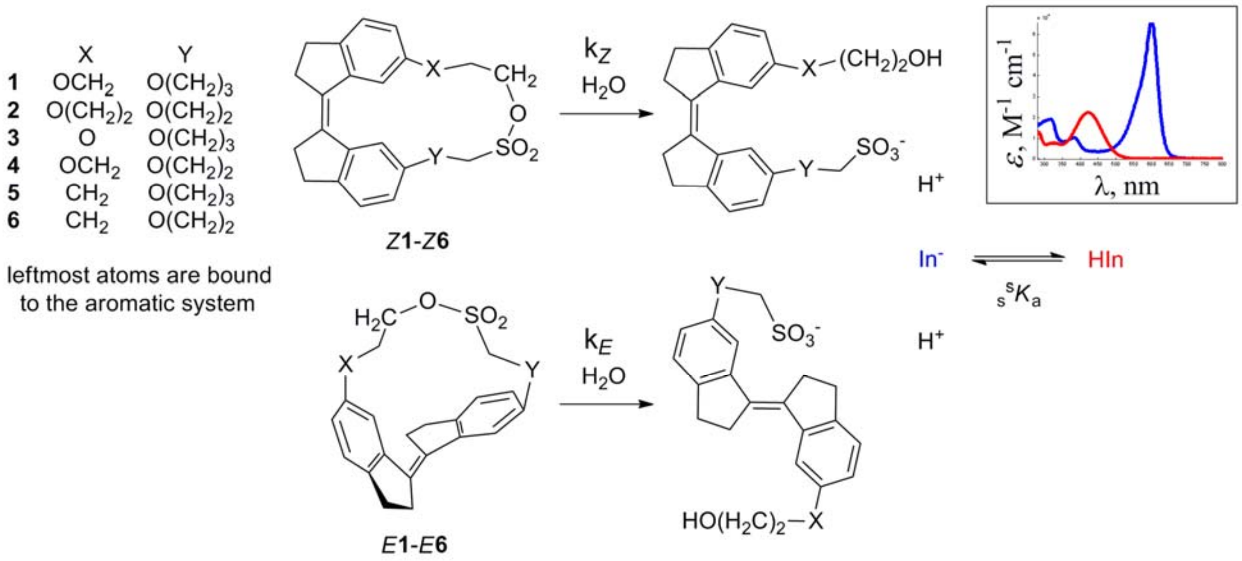

Fig. 3.7. Reaction scheme for monitoring hydrolysis kinetics of sulfonates **1**–**6**; inset: spectra of the protonated (HIn) and anionic (In^-) forms of bromophenol blue in H_2O–THF (18% mol).

To increase the solubility of sulfonates **1**–**6** in the reaction medium, hydrolysis reactions were carried out in H_2O containing 18% mol THF. The choice of solvent subsequently determines the appropriate pH scale to be used.[36] The macroscopic autoprotolysis constant measured (superscript) and referenced (subscript) in solvent s is noted as ${}^{\mathrm{s}}_{\mathrm{s}}\mathrm{p}K_{\mathrm{ap}}$. In H_2O containing 18% (mol) THF ${}^{\mathrm{s}}_{\mathrm{s}}\mathrm{p}K_{\mathrm{ap}}$ is 15.13.[36] Since acidity constants depend strongly on the composition of the solvent, accurate kinetic measurements in H_2O–THF mixtures require ${}^{\mathrm{s}}_{\mathrm{s}}\mathrm{p}K_{\mathrm{ap}}$ values measured in such mixtures.

To eliminate the contribution of OH^-, hydrolysis was carried out at pH ~ 5, with rates corrected for indicator buffering by eq. (3.12). Under these conditions, hydrolysis of the *Z* isomers is slow ($\tau_{½}$ ranging from 9 to 2×10^3 h). However, the rate constants can be determined conveniently by applying the initial rate approximation for a (pseudo-)first order reaction (i.e., $\nu = k[\mathrm{R}] \approx k[\mathrm{R}]_0$ for conversion ≤ 10%, which only introduces < 5.1% error in k_Z. We have no a priori knowledge of the values of k_E, though they are presumably larger than k_Z since we observe faster H^+ generation from mixtures of *E* and *Z* isomers than from *Z* isomers alone. *E* isomers thus proceed to >10% conversion, and the initial rate approximation cannot be applied. Instead, the rate constants for hydrolysis in *E* isomers were determined by numerically solving the full system of differential equations describing the generation of H^+ from the hydrolysis of a mixture of *E* and *Z* isomers (eq. (3.16)–(3.18)), Analysis of kinetic data, below) using the measured values of k_Z. Concentrations of all species in solution were determined by deconvolution of the absorbance spectra (eq. (3.5)–(3.8), Deconvolution of Optical Absorbance Spectra, below) using independently measured extinction coefficients.

Titration and Stability of Bromophenol Blue

All liquids were transferred by a syringe or cannula. A solution of known concentration of bromophenol blue (3′,3″,5′,5″-tetrabromophenolsulfonephthalein; ${}^{\mathrm{w}}_{\mathrm{w}}\mathrm{p}K_\mathrm{a} = 4.0$)[37] was prepared in N_2-flushed volumetric glassware by dissolving the commercially available sodium salt in water. Titrant solutions of the indicator (15.3 µM, 4 mL) in H_2O–THF (0.82/0.18 mol) were prepared by combining aqueous bromophenol blue stock solution (610 µM), water, and THF in a clean, dry cuvette under N_2. A 10-mM solution of triflic acid in water (prepared by dilution from a stock aqueous solution titrated against commercial sodium hydroxide standards) was used as the titrant, which was added in 5-µL increments by syringe.

Given the equilibrium

$$\mathrm{HIn} \xrightleftharpoons{{}^{\mathrm{s}}_{\mathrm{s}}K_\mathrm{a}} \mathrm{In}^- + \mathrm{H}^+$$

Then,

$$[\mathrm{HIn}] = T_\mathrm{in} - c_{\mathrm{In}^-,0}$$
$$[\mathrm{In}^-] = c_{\mathrm{In}^-,0}$$
$$[\mathrm{H}^+] = c_{\mathrm{In}^-,0}$$

defining $T_\mathrm{in} = [\mathrm{In}^-] + [\mathrm{HIn}]$ and assuming that $c_{\mathrm{In}^-,0} \ll 2.72 \times 10^{-8}$ so $c_{\mathrm{In}^-,0} + [H^+]_\mathrm{neutral} \approx c_{\mathrm{In}^-,0}$. After the addition of the titrand, the equilibrium shifts such that

$$[\mathrm{HIn}] = T_\mathrm{in} - c_\mathrm{in,0} + \Delta c_\mathrm{in}$$
$$[\mathrm{In}^-] = c_\mathrm{in,0} - \Delta c_\mathrm{in}$$
$$[\mathrm{H}^+] = c_\mathrm{in,0} - \Delta c_\mathrm{in} + c_\mathrm{H}$$

where c_H is the amount of strong acid *added to the system* per unit volume, ignoring the negligible increase in volume of 5 µL. (Note that c_H is different from $[\mathrm{H}^+]$, the *concentration of free* H^+ *in solution*.) With the knowledge of the molar extinction coefficient of In^-, $\varepsilon_{\mathrm{In}^-}$, $\Delta c_{\mathrm{In}^-} = \Delta Abs/\varepsilon_{\mathrm{In}^-}$, and rearranging the equilibrium expression yields eq. (1.3) for sample *i*. Plotting $\frac{\varepsilon_{\mathrm{In}^-} c_{\mathrm{H},i}}{Abs_0 - Abs_i}$ vs. $\frac{T_\mathrm{in}\varepsilon_{\mathrm{In}^-}{}^2}{Abs_i Abs_0}$ gives a linear plot with slope ${}^{\mathrm{s}}_{\mathrm{s}}K_\mathrm{ap}$. Linear least squares regressions for three replicates yielded the values listed in Table 3.3, which yield an average ${}^{\mathrm{s}}_{\mathrm{s}}K_{\mathrm{a}}$value of (4.8 ± 0.2) × 10^{-6} M (${}^{\mathrm{s}}_{\mathrm{s}}\mathrm{p}K_{\mathrm{a}} = 5.3$).

$$\frac{\varepsilon_{\mathrm{In}^-} c_{\mathrm{H},i}}{Abs_0 - Abs_i} = 1 + {}^{\mathrm{s}}_{\mathrm{s}}K_{\mathrm{ap}} \frac{T_{\mathrm{in}} \varepsilon_{\mathrm{In}^-}{}^2}{Abs_i Abs_0} \tag{3.1}$$

Table 3.3. Measured acidity constants of bromophenol blue in H_2O–THF (0.82/0.18 mol); deviations are standard regression errors.

${}^{\mathrm{s}}_{\mathrm{s}}K_{\mathrm{a}} \times 10^6$	R^2
4.4 ± 0.1	0.997
5.1 ± 0.1	0.994
4.82 ± 0.04	0.999

Acidic solutions of bromophenol blue were stable under the conditions of the kinetics experiments, with the absorption intensities changing at rate constants of ~10^{-10} s^{-1} (Table 3.4), which were 10^5-fold slower than the rates of hydrolysis of **1–6** and were therefore neglected in the analysis.

Table 3.4. Stability of bromophenol blue in H_2O–THF (0.82/0.18 mol)

T, °C	${}^{\mathrm{s}}_{\mathrm{s}}\mathrm{pH}(t = 0)$	average k_{drift}, s^{-1}
25	5.04 - 5.06	$(1.38 \pm 0.06) \times 10^{-10}$
60	4.75 - 4.9	$(3.0 \pm 0.1) \times 10^{-10}$

Molar Extinction Coefficients for Bromophenol Blue and Sulfonates 1–6

Conversion of temporal absorbance changes into changes in concentration required accurate molar extinction coefficients for the anionic (In^-) and protonated (HIn) forms of bromophenol blue, which we measured in H_2O–THF (0.82/0.18 mol). A solution of NaOH was added to samples of known indicator concentration until the UV-vis absorption spectrum no longer changed, indicating that all of the indicator was in the anionic form which subsequently allowed for the calculation of molar extinction coefficients for the anionic form. The extinction coefficients of the protonated form were calculated from absorption of neutral solutions of the indicator using formula $Abs = \left(\varepsilon_{\mathrm{In}^-} c_{\mathrm{In}^-} + \varepsilon_{\mathrm{HIn}} c_{\mathrm{HIn}}\right) l$.

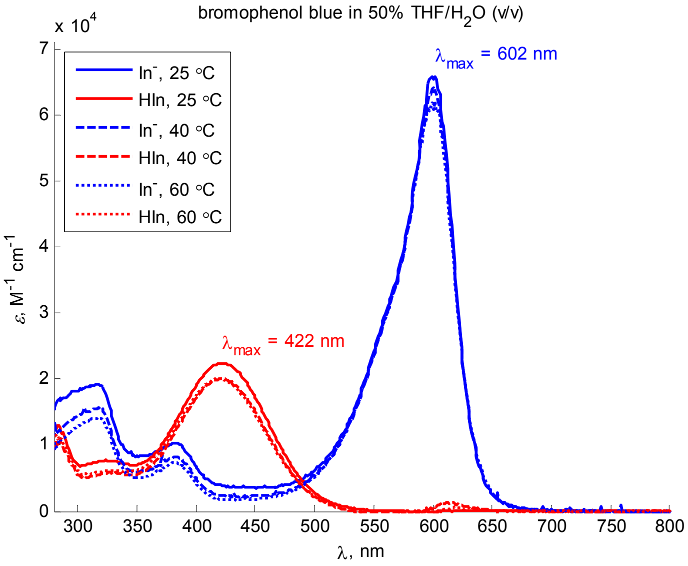

Fig. 3.8. Molar extinction coefficients for bromophenol blue in H_2O–THF (0.82/0.18 mol) at 25–60 °C.

The molar extinction coefficients for *Z***1**–*Z***6** were determined from the UV-vis absorption spectra of THF solutions of known concentration. The extinction coefficients for *E***1**– *E* **6** were calculated from the spectra of the photostationary mixtures in hexanes following irradiation according to Eq. 2, where χ_E is the molar fraction of the E isomer in the photostationary mixture, as quantified by HPLC at the isosbestic point of irradiation, and c_{total} is the total concentration of the two isomers, determined from the absorbance prior to irradiation. In general, the absorbance spectra for *E* isomers were blue-shifted with $\varepsilon_{E,\text{max}} > \varepsilon_{Z,\text{max}}$.

$$Abs = (\varepsilon_Z(1-\chi_E) + \varepsilon_E\chi_E)c_{\text{total}}l \tag{3.2}$$

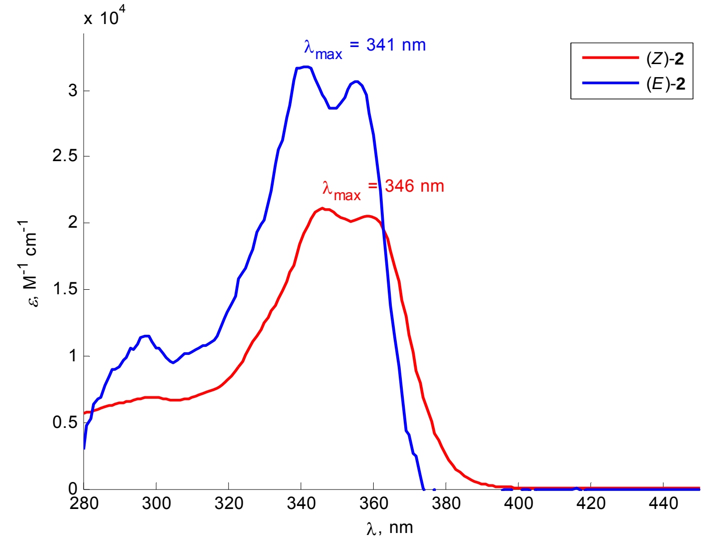

Fig. 3.9. Molar extinction coefficients for *Z***1** (in THF) and *E***1** (in hexanes)

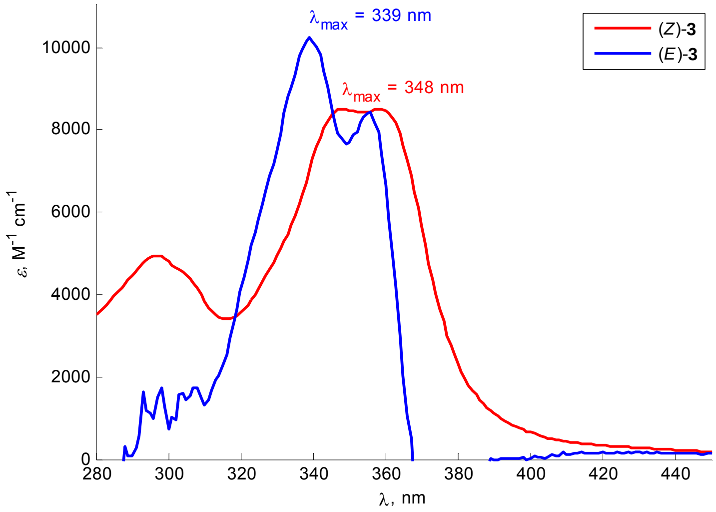

Fig. 3.10. Molar extinction coefficients for *Z***2** (in THF) and *E***2** (in hexanes)

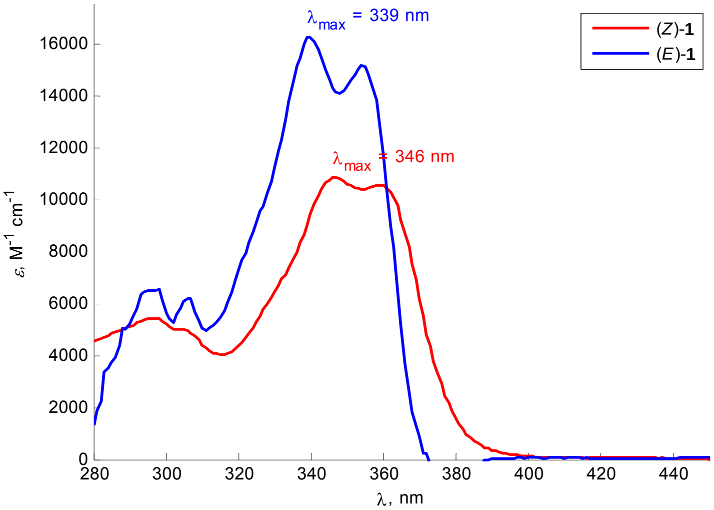

Fig. 3.11. Molar extinction coefficients for *Z*3 (in THF) and *E*3 (in hexanes)

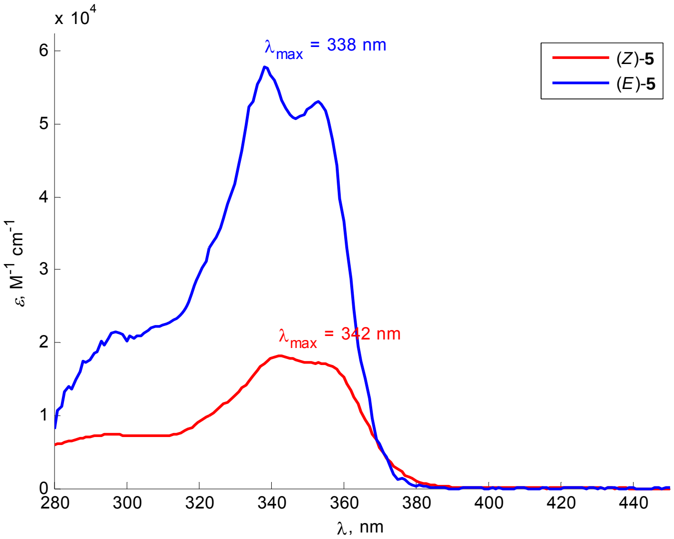

Fig. 3.12. Molar extinction coefficients for *Z*4 (in THF) and *E*4 (in hexanes)

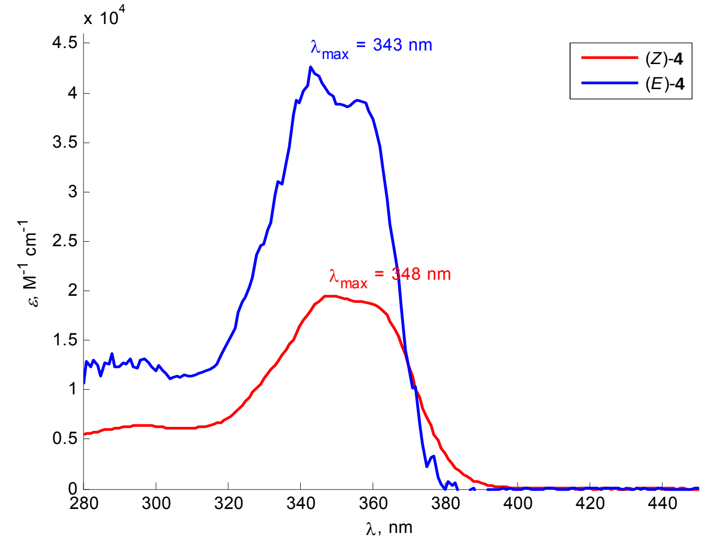

Fig. 3.13. Molar extinction coefficients for *Z***5** (in THF) and *E***5** (in hexanes)

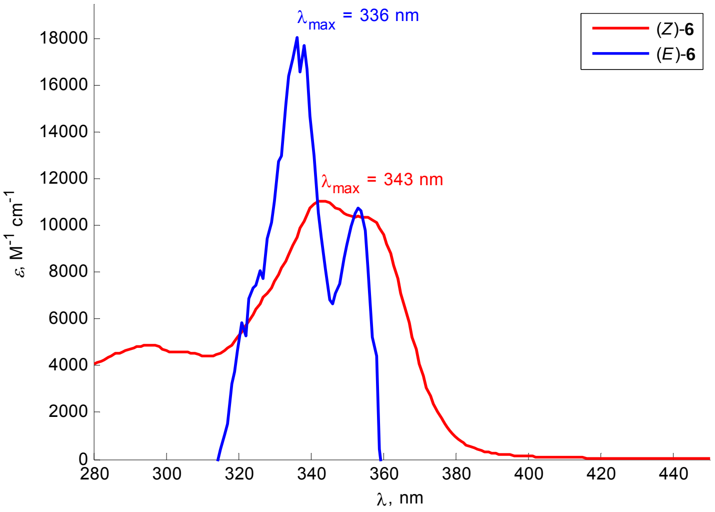

Fig. 3.14. Molar extinction coefficients for *Z***6** (in THF) and *E***6** (in hexanes)

General Procedure for Kinetic Measurements

Acidic samples of *Z***1**–*Z***6** were prepared by first diluting 610 μM aqueous bromophenol blue (0.4 mL) with water (1.1 mL) and THF (1.5 mL) and adding 1 mM aqueous TfOH (<10 μL) until the absorbance of the solution at 601 nm decreased to <1.7 (to ensure the pH of the mixture was within the response range of the indicator), and then adding a solution of *Z***1**–*Z***6** in THF (20–40 μL depending on the macrocycle's molar extinction coefficient and the stock solution concentration so that the absorbance due to stiff stilbene was ~1).

*E***1**–*E***6** were prepared as photostationary mixtures with their *Z* analogues by irradiating solutions of the *Z* isomers in hexanes (3 mL, absorbance due to stiff stilbene was ~1) at 375 nm until the absorbance spectrum ceased changing. Following irradiation, the samples were transferred to a vial and concentrated to dryness under a stream of N_2 at RT. THF was added (1.7 mL), and a 1.5-mL aliquot of the solution was used immediately for kinetic measurements. The remainder of the solution was concentrated to dryness in a stream of N_2 at RT, taken up in HPLC-grade methanol, and immediately analyzed by HPLC (see below). Samples for the hydrolysis of photostationary mixtures of **1**–**6** under acidic conditions were prepared in the same manner as those for measuring the *Z* isomers alone, substituting pure THF and stock solution of Z isomers for the 1.5-mL aliquot of photostationary mixture in THF.

Photostationary states were analyzed by reverse-phase HPLC. The fraction of *E* isomer present is related to the integrated areas of the peaks in the chromatogram by eq. (3.3). When the chromatogram is observed at the isosbestic point for a given macrocycle (where $\varepsilon_Z = \varepsilon_E$) $\chi_{E,\mathrm{HPLC}}$ yields the actual value for χ_E. The fraction of *E* isomer of **2** and **6** whose absorbance spectra did not exhibit clear isosbestic points during irradiation, was determined by eq. (3.4), where Abs_{initial} and Abs_{mixture} are the absorbance before and after irradiation, respectively. The isosbestic points and average χ_E in the photostationary states of **1**–**6** is shown in Table 3.5.

$$\chi_{E,\mathrm{HPLC}} = \frac{IA_E}{IA_Z + IA_E} = \frac{c_E\varepsilon_E}{c_Z\varepsilon_Z + c_E\varepsilon_E} \tag{3.3}$$

$$\chi_E = 1 - \left(1 - \chi_{E,\mathrm{HPLC}}\right)\frac{Abs_{\mathrm{mixture}}}{Abs_{\mathrm{initial}}} \tag{3.4}$$

Table 3.5. Characteristic photochemical data for **1**–**6**

sulfonate	$\lambda_{\max}$, nm	$\varepsilon_{\max}$, M^{-1} cm^{-1}	isosbestic point, nm	average χ_E in photostationary state
*Z***1**	346	21100	363	32%
*Z***2**	348	8510	-	20%
*Z***3**	346	10800	361	35%
*Z***4**	342	18200	369	22%
*Z***5**	348	19500	370	16%
*Z***6**	343	11100	-	6%

The chromatograms of *Z***1**–*Z***6** and photostationary mixtures are shown below.

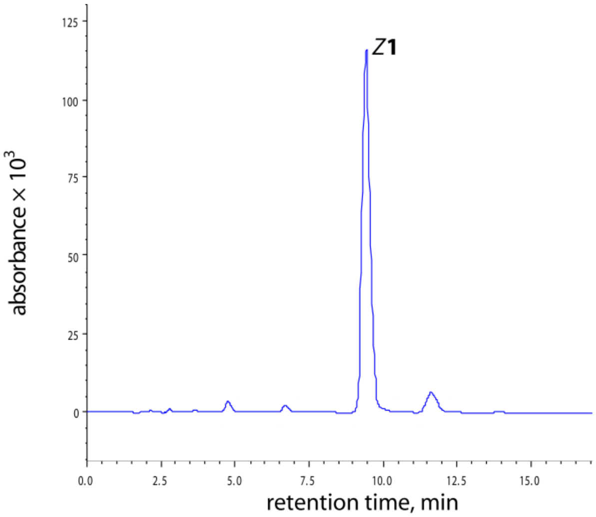

Fig. 3.15. Chromatogram at 367 nm of *Z***1**, J. T. Baker C18 column, 10% H_2O in MeOH, 1 mL/min

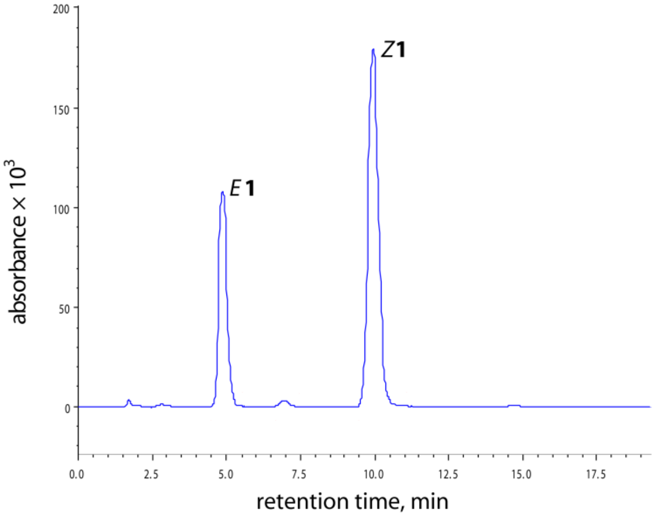

Fig. 3.16. Chromatogram at 363 nm of photostationary mixture of **1**, J. T. Baker C18 column, 10% H_2O in MeOH, 1 mL/min

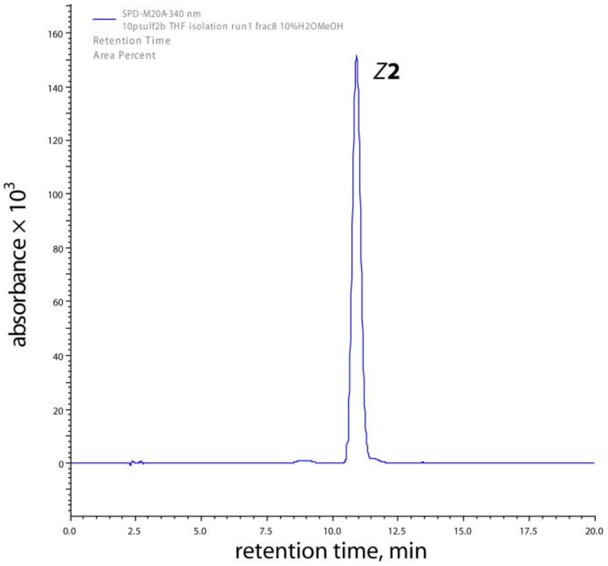

Fig. 3.17. Chromatogram at 340 nm of *Z*2, Macherey-Nagel C18 column, 100% MeOH, 1 mL/min

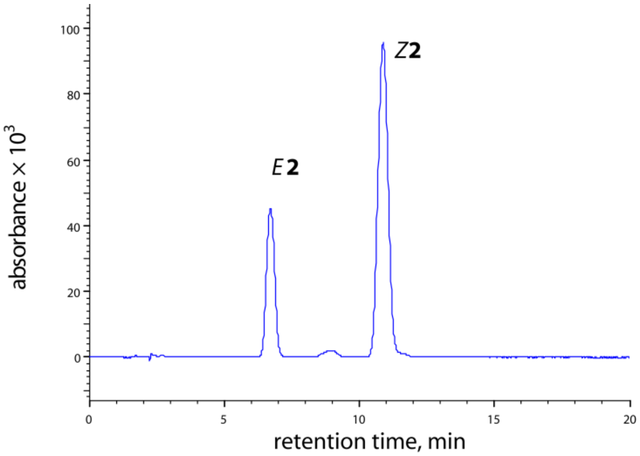

Fig. 3.18. Chromatogram at 340 nm of photostationary mixture of **2**, Macherey-Nagel C18 column, 10% H_2O in MeOH, 1 mL/min

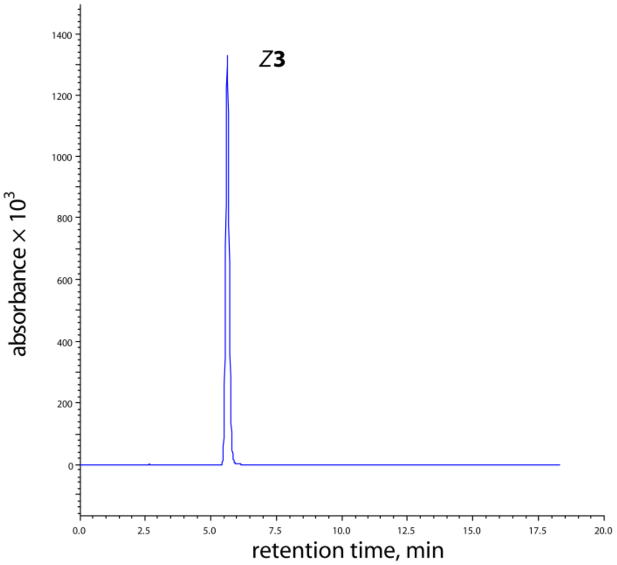

Fig. 3.19. Chromatogram at 340 nm of *Z***3**, Macherey-Nagel C18 column, 100% MeOH, 1 mL/min

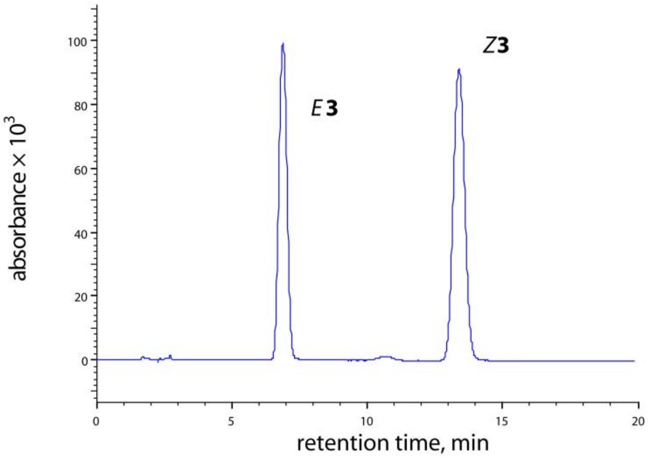

Fig. 3.20. Chromatogram at 340 nm of photostationary mixture of **3**, Macherey-Nagel C18 column, 10% H_2O in MeOH, 1 mL/min

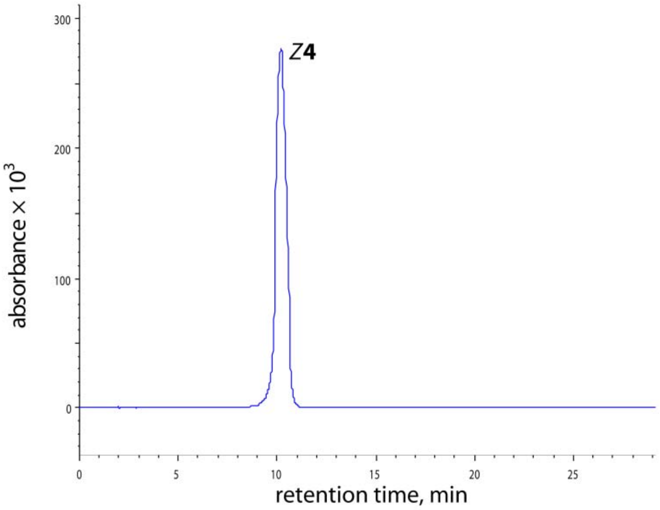

Fig. 3.21. Chromatogram at 340 nm of *Z***4**, J. T. Baker column, 10% H_2O in MeOH, 1 mL/min

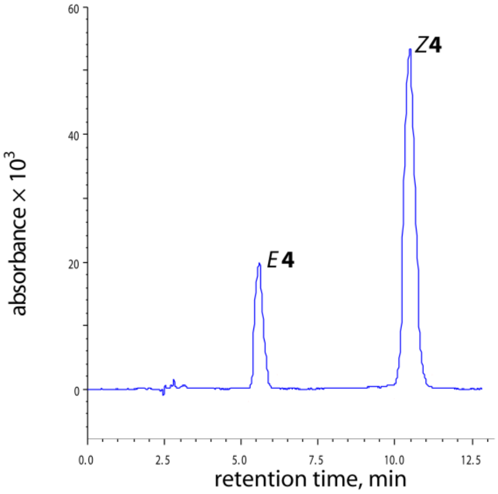

Fig. 3.22. Chromatogram at 369 nm of photostationary mixture of **4**, J. T. Baker column, 10% H_2O in MeOH, 1 mL/min

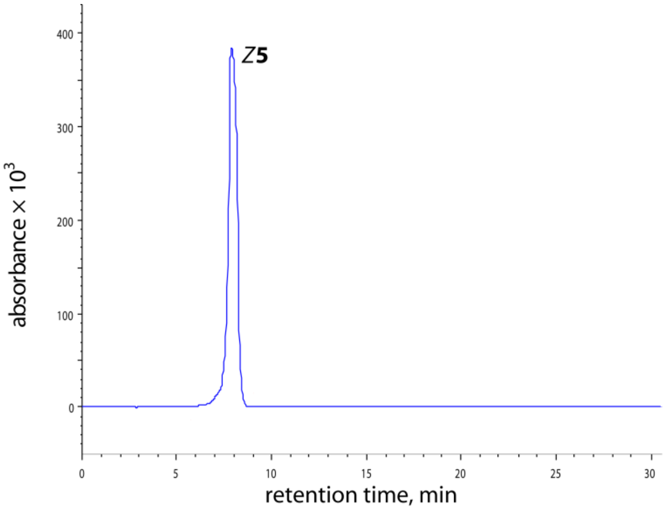

Fig. 3.23. Chromatogram at 340 nm of *Z***5**, J. T. Baker column, 10% H_2O in MeOH, 1 mL/min

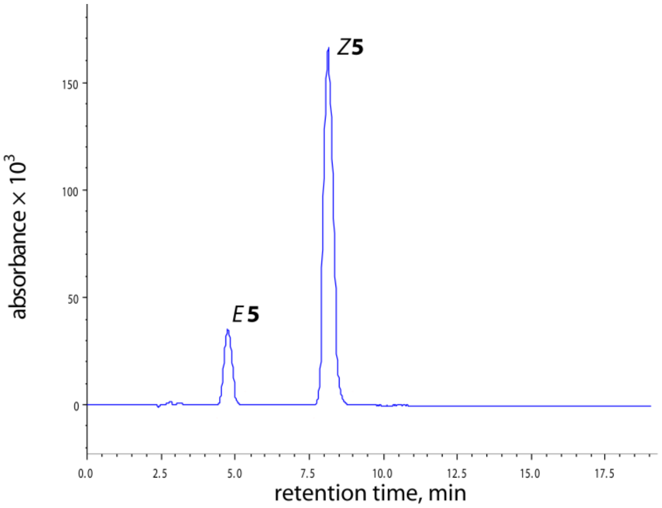

Fig. 3.24. Chromatogram at 370 nm of photostationary mixture of **5**, J. T. Baker column, 10% H_2O in MeOH, 1 mL/min

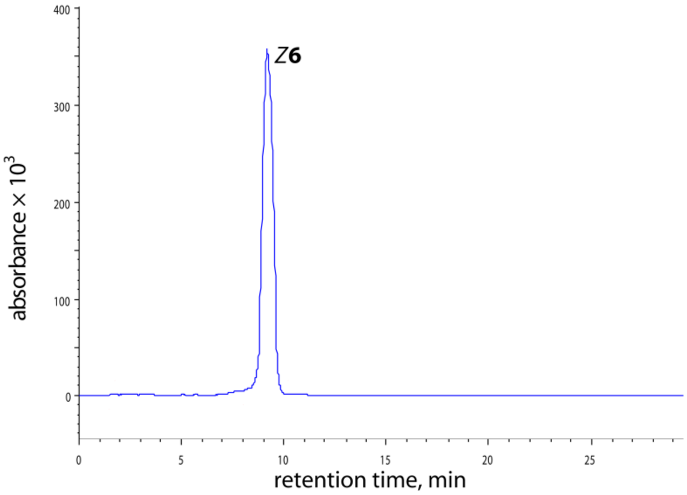

Fig. 3.25. chromatogram at 340 nm of *Z*6, J. T. Baker column, 10% H_2O in MeOH, 1 mL/min

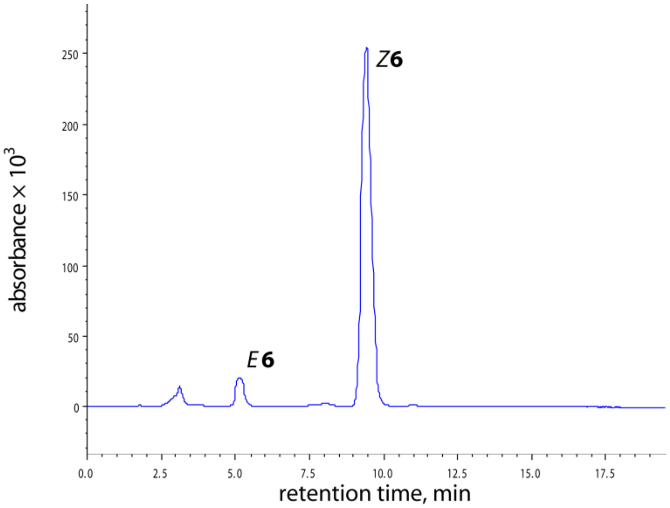

Fig. 3.26. Chromatogram at 340 nm of photostationary mixture of **6**, J. T. Baker column, 10% H_2O in MeOH, 1 mL/min

Analysis of Hydrolysis Products

Kinetic measurements by ^{1}H-NMR. The hydrolysis of *Z***1** was followed by ^{1}H NMR spectroscopy. A sample of *Z***1** was prepared in D_2O–d_8THF (0.85/0.15 mol) in a J. Young tube, degassed (freeze-pump-thaw × 2), and heated to 60 °C, recording the ^{1}H NMR spectra (after cooling to RT) over time (Fig. 3.27–Fig. 3.29; and Table 3.6). The pseudo-first order rate constant calculated from integration in the aromatic region of the three spectra was $(6.6 \pm 0.4) \times 10^{-6}$ s^{-1}, which was within a factor of 3.5 of the value determined spectrophotometrically. The NMR spectrum of the hydrolyzed product is consistent with an alkyl sulfonic acid.

Table 3.6. ^{1}H NMR chemical shifts for species in the hydrolysis of *Z***1** in D_2O–d_8THF/D_2O (0.85/0.15 mol)

compound	^{1}H NMR chemical shifts
*Z***1**	1.82 (m, 2H), 1.90 (quint, J = 6.5 Hz, 2H), 2.15 (m, 2H), 2.69 (m, 4H), 2.79 (m 4H), 3.33 (m, 2H), 3.93 (t, J = 5.4 Hz, 2H), 3.99 (t, J = 5.4 Hz, 2H), 4.23 (t, J = 6.2 Hz, 2H), 6.69 (dd, J = 8.4 Hz, J = 2.2 Hz, 1H), 6.73 (dd, J = 8.4 Hz, J = 2.2 Hz, 1H), 7.11 (d, J= 8.4 Hz, 1H), 7.13 (d, J = 8.4 Hz, 1H), 7.51 (d, J = 1.7 Hz, 1H), 7.56 (d, J = 1.7 Hz, 1H)
hydrolysis product of *Z***1**	1.58 (m, 2H), ~1.7 (obscured, m, 2H), 2.10 (m, 2H), 2.68 (m, 4H), 2.78 (m, 4H), 2.83 (m, 2H), 3.51 (t, J = 6.3 Hz, 2H), 3.85 (t, J = 6.3 Hz, 2H), 3.99 (t, J = 6.3 Hz, 2H), 6.67 (d, J = 8.4 Hz, 1H), 6.74 (d, J = 8.4 Hz, 1H), 7.09 (d, J = 7.9 Hz, 1H), 7.11 (d, J = 8.3 Hz, 1H), 7.48 (bs, 2H)

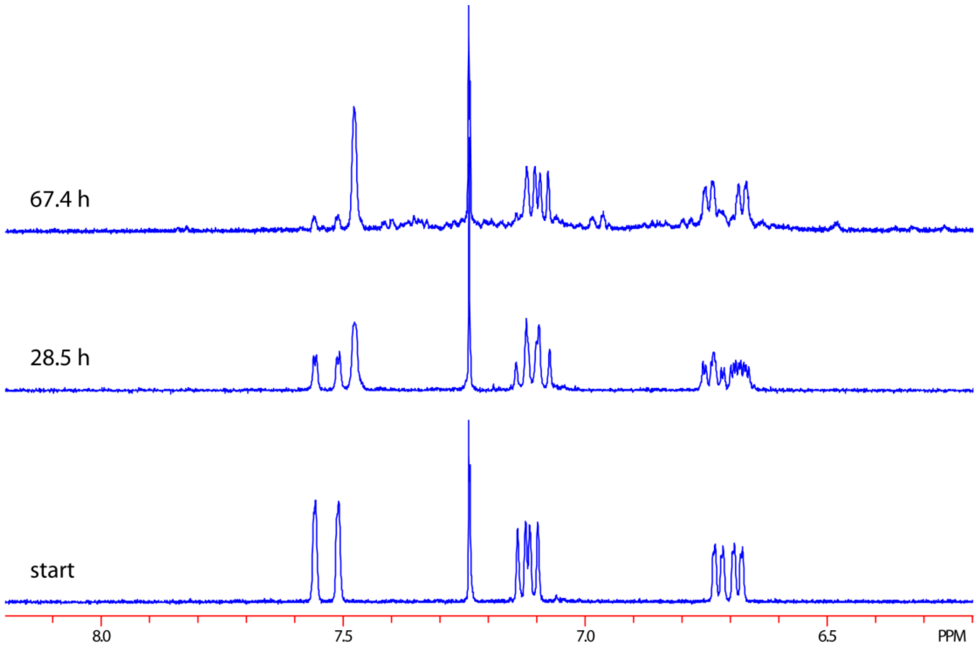

Fig. 3.27. ^{1}H NMR spectra of *Z***1** in D_2O–d_8THF (0.85/0.15 mol)

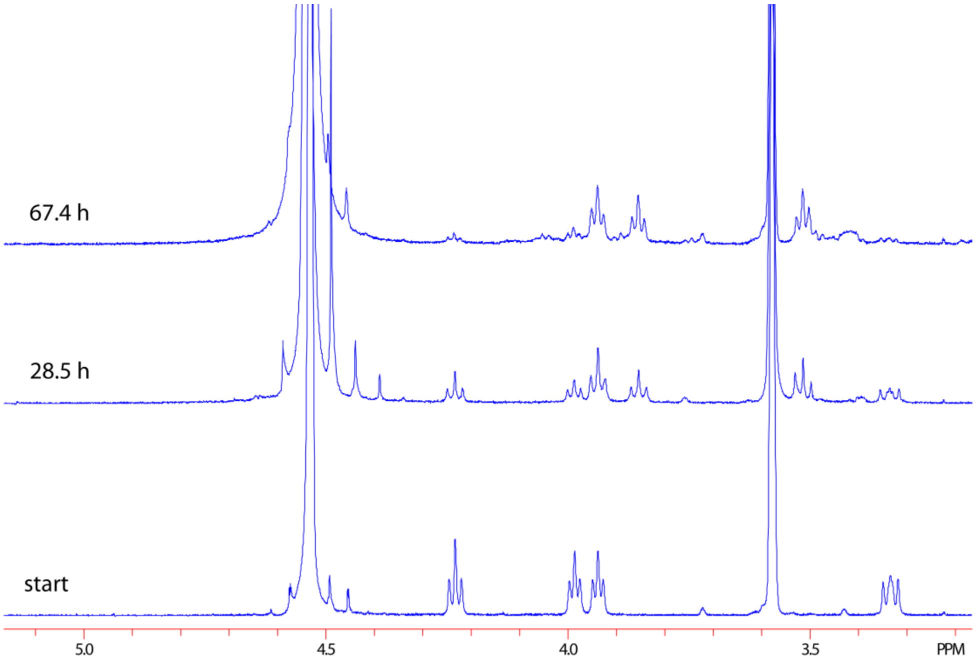

Fig. 3.28. ^{1}H NMR spectra of *Z*1 in D_2O–d_8THF (0.85/0.15 mol)

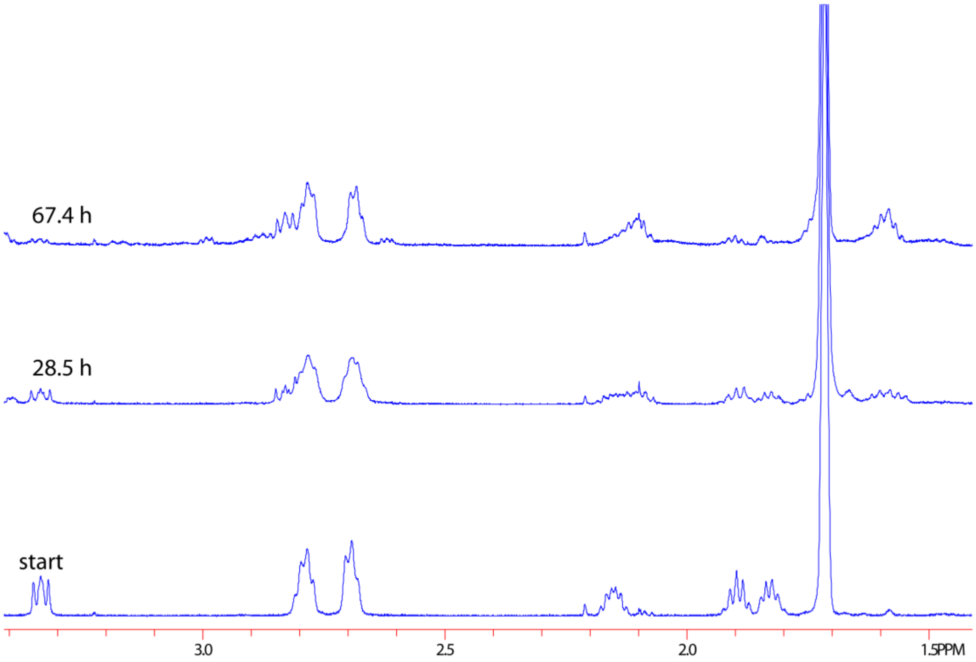

Fig. 3.29. ^{1}H NMR spectra of *Z*1 in D_2O–d_8THF (0.85/0.15 mol)

Spectrophotometric measurements. Reaction mixtures for the hydrolysis of *Z***1**–*Z***6** were analyzed by reverse phase HPLC. The chromatograms contained a peak for bromophenol blue, peaks for *Z***1**–**6**, and a product peak at short retention times. The high-resolution mass spectra of the product peaks were again consistent with the formation of alkyl sulfonic acids (Table 3.7).

Table 3.7. HPLC retention times of the reaction mixtures and high-resolution mass spectra (ESI+) of the product of hydrolysis of *Z***1**–*Z***6** after chromatographic separation on a Macherey-Nagel C18 column with 10% H_2O in MeOH, 1 mL/min

macrocycle	retention times (assignment), min	product formula (M)	expected molecular ion (MH^+)	m/z calc'd	m/z found	error, mmu
1	1.50 (BpB), 1.90 (product), 14.44 (*Z***2**)	$C_{25}H_{30}O_6S$	$C_{25}H_{31}O_6S^+$	459.18359	459.1837	0.1
2	1.60 (BpB), 3.04 (product), 11.01 (*Z***3**)	$C_{24}H_{28}O_6S$	$C_{24}H_{29}O_6S^+$	445.16794	445[a]	-
3	1.68 (BpB), 2.04 (product), 13.69 (*Z***1**)	$C_{25}H_{30}O_6S$	$C_{25}H_{31}O_6S^+$	459.18359	459.1810	-2.6
4	1.60 (BpB), 2.21 (product), 14.72 (*Z***5**)	$C_{25}H_{30}O_5S$	$C_{25}H_{31}O_5S^+$	443.1887	443.1898	1.1
5	1.73 (BpB), 2.05 (product), 12.27 (*Z***4**)	$C_{24}H_{28}O_6S$	$C_{24}H_{29}O_6S^+$	445.1679	445.1667	-1.2
6	1.58 (BpB), 2.18 (product), 13.49 (*Z***6**)	$C_{24}H_{28}O_5S$	$C_{24}H_{29}O_5S^+$	429.173	429.1746	1.6

[a] The molecular ion for the hydrolysis product of **2** in the low-res spectra did not yield high-quality high-res data in positive mode ESI, possibly due to the presence of background pump oil (peaks with m/z ~446). However, pump oil did not obscure peaks in samples of hydrolyzed **5**, presumably because of higher concentrations and/or better back ground subtraction.

Deconvolution of Optical Absorbance Spectra

The initial concentration of the macrocycle, $c_{\text{macro},0}$, was obtained from its absorbance in the initial spectrum of the reaction mixture, by removing the absorbance due to the indicator ($Abs_{\text{In}^-,\lambda}$ and $Abs_{\text{HIn},\lambda}$) using eq. (3.5)–(3.7). At λ ≈ 602 nm, $\varepsilon_{\text{macro}} = \varepsilon_{\text{HIn}} = 0$, so $Abs_{\text{obs},602} = \varepsilon_{\text{In}^-,602}c_{\text{In}^-}l$, and c_{In^-}can be calculated with the measured value of $\varepsilon_{\text{In}^-,600}$. Using the calculated value for c_{In^-}, $Abs_{\text{In}^-,\lambda}$ at all wavelengths can be calculated. Subtracting $Abs_{\text{In}^-,\lambda}$ from eq. (3.5) yields eq. (3.6).

$$Abs_{\text{obs},\lambda} = Abs_{\text{In}^-,\lambda} + Abs_{\text{HIn},\lambda} + Abs_{\text{macro},\lambda} = \left(\varepsilon_{\text{In}^-,\lambda}c_{\text{In}^-} + \varepsilon_{\text{HIn},\lambda}c_{\text{HIn}} + \varepsilon_{\text{macro},\lambda}c_{\text{macro}}\right)l \tag{3.5}$$

$$Abs_{\text{obs},\lambda} - Abs_{\text{In}^-,\lambda} = Abs_{\text{HIn},\lambda} + Abs_{\text{macro},\lambda} = \left(\varepsilon_{\text{HIn},\lambda}c_{\text{HIn}} + \varepsilon_{\text{macro},\lambda}c_{\text{macro}}\right)l \tag{3.6}$$

At λ ≈ 422 nm, $\varepsilon_Z = 0$, so $Abs_{\mathrm{obs},422} - Abs_{\mathrm{In^-},\,422} = Abs_{\mathrm{HIn},\,422} = \varepsilon_{\mathrm{HIn},\,422}c_{\mathrm{HIn}}l$, and c_{HIn} can be calculated with the measured value of $\varepsilon_{\mathrm{HIn},\,422}$. Using the calculated value for c_{HIn}, $Abs_{\mathrm{HIn},\lambda}$ at all wavelengths can be calculated. Subtracting $Abs_{\mathrm{HIn},\lambda}$ from eq. (3.6) yields eq. (3.7). For reactions of Z isomers, $Abs_{\mathrm{macro},\lambda}$ is $Abs_{Z,\lambda}$. Then c_Z (and thus $Abs_{Z,\lambda}$ at all wavelengths) can be calculated from $Abs_{Z,\lambda}$ with the measured values of $\varepsilon_{Z,\lambda}$, where $\lambda_{\mathrm{scaling}} = \lambda_{\mathrm{max}}$ for the given macrocycle. A representative deconvoluted spectrum is shown in Fig. 3.30, and the corresponding calculated spectrum for the determination of $c_{Z,0}$ is shown in Fig. 3.31.

$$Abs_{\mathrm{obs},\lambda} - Abs_{\mathrm{In^-},\lambda} - Abs_{\mathrm{HIn},\lambda} = Abs_{\mathrm{macro},\lambda} = \varepsilon_{\mathrm{macro},\lambda}c_{\mathrm{macro}}l \tag{3.7}$$

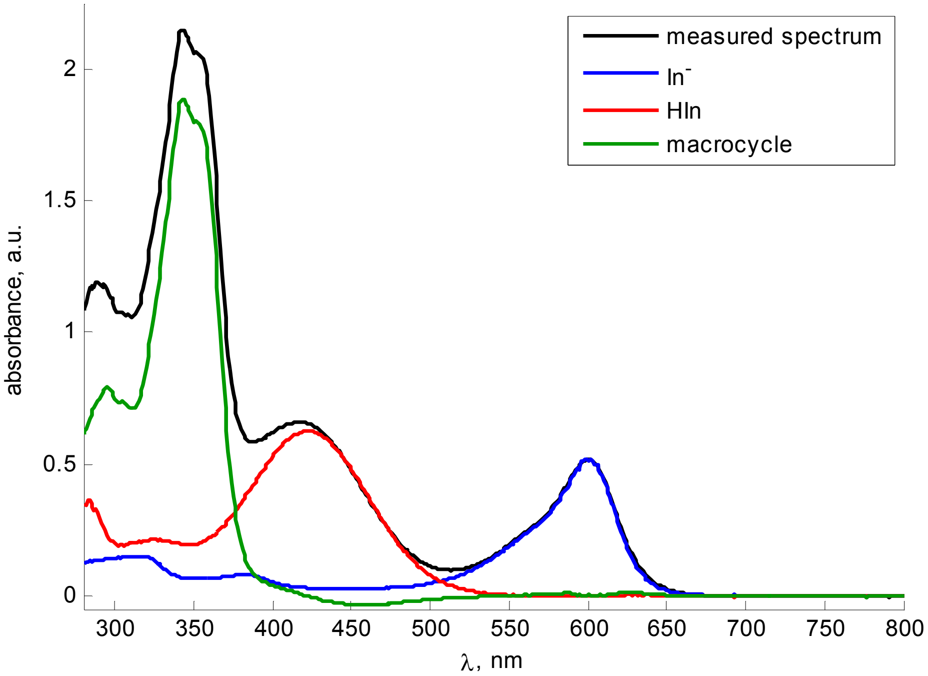

Fig. 3.30. Spectrum deconvolution for the hydrolysis of *Z***6** at 25 °C

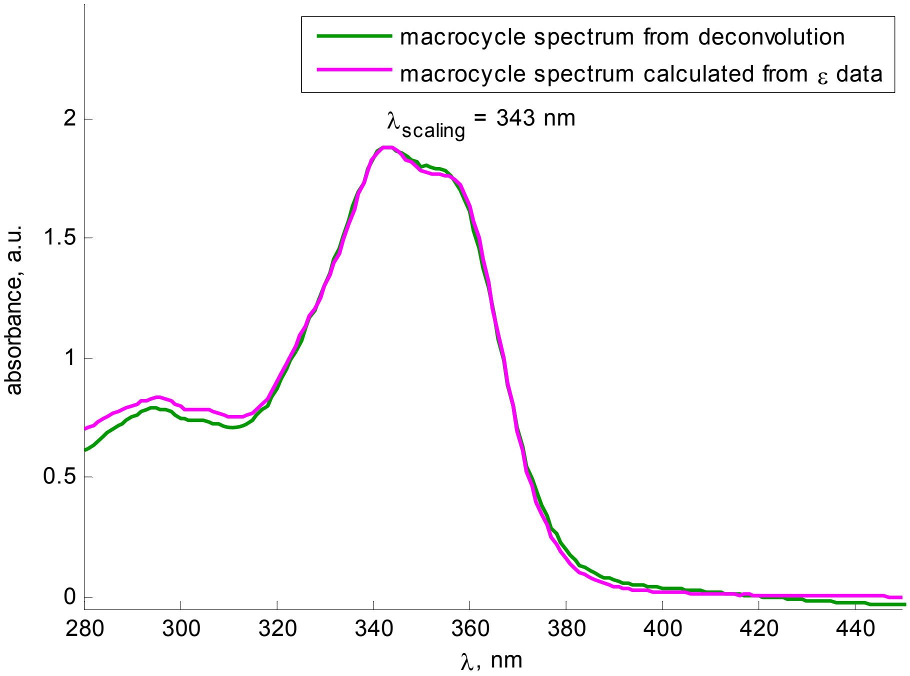

Fig. 3.31. Spectrum of *Z***6** from deconvolution shown in Fig. 3.30 and the corresponding calculated spectrum based on its extinction coefficient

To determine the concentrations of the *E* and *Z* isomers for samples of photostationary mixtures, the initial absorbance spectrum of the reaction mixture was deconvoluted identically, using eq. (3.5)–(3.8). Eq. (3.8) was solved for c_{macro} (and thus $Abs_{\mathrm{macro},\lambda}$ at all wavelengths) using the measured values of $\varepsilon_{Z,\lambda}$, $\varepsilon_{E,\lambda}$, and χ_E with $\lambda_{\mathrm{scaling}} = \lambda_{\mathrm{max},Z}$, which then yields the initial concentrations of both the *Z* and *E* isomers, $c_{Z,0}$ and $c_{E,0}$. A representative deconvoluted spectrum is shown in Fig. 3.32, and the corresponding calculated spectrum for the determination of $c_{Z,0}$ and $c_{E,0}$ is shown in Fig. 3.33.

$$Abs_{\mathrm{macro},\lambda} = \left(\varepsilon_{Z,\lambda} c_Z + \varepsilon_{E,\lambda} c_E\right) l = c_{\mathrm{macro}}\left(\varepsilon_{Z,\lambda}(1-\chi_E) + \varepsilon_{E,\lambda}\chi_E\right) l \qquad (3.8)$$

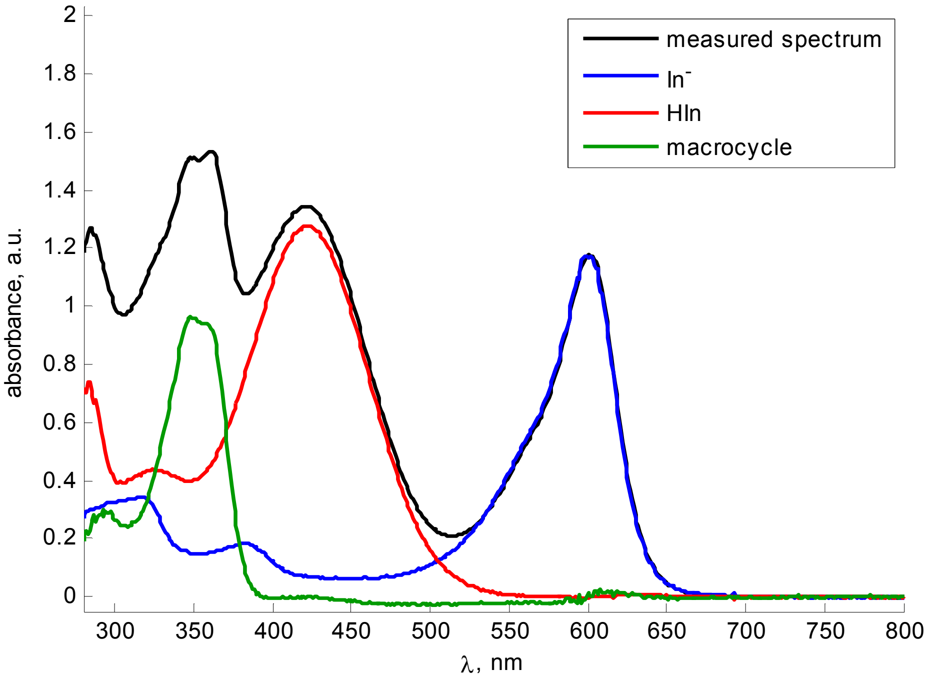

Fig. 3.32. Spectrum deconvolution for the hydrolysis of photostationary mixture of **5** at 25 °C

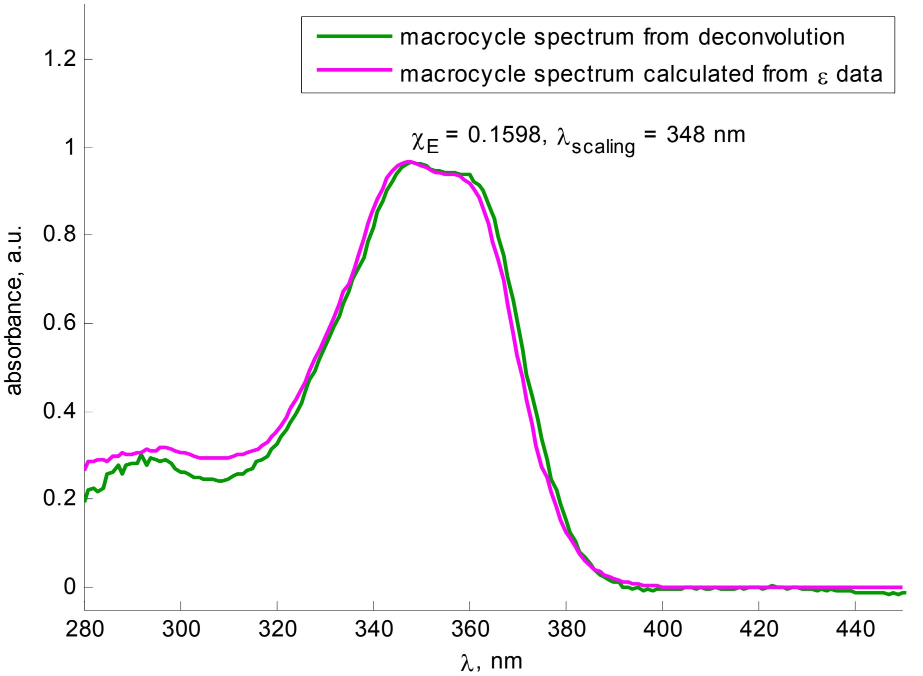

Fig. 3.33. Spectrum of photostationary mixture of **5** from deconvolution shown in Fig. 3.32 and the corresponding calculated spectrum based on ε_{Z4}, ε_{E4}, and χ_{E4}

Analysis of Kinetic Data

Hydrolysis kinetics were determined from the change in absorbance of the anionic form of the pH indicator. The generation of sulfonic acid during hydrolysis changes the fraction of the protonated indicator, increases the concentration of free H^+ and decreases the concentration of free OH^- (eq. (3.9)), where c_{H} is the amount of strong acid formed in solution per unit volume.

$$c_{\mathrm{H}} = \Delta[\mathrm{HIn}] + \Delta[\mathrm{H}^+] - \Delta[\mathrm{OH}^-] \tag{3.9}$$

Let c_{OH} be the concentration of OH^- without hydrolysis of the indicator ($c_{\mathrm{OH}} = \sqrt{{}^{\mathrm{s}}_{\mathrm{s}}K_{\mathrm{ap}}}$ for solutions prepared under neutral conditions.) The equilibrium expression for ${}^{\mathrm{s}}_{\mathrm{s}}K_{\mathrm{b}}$ yields the following expressions:

$$\mathrm{H_2O} \quad + \quad \mathrm{In^-} \quad \xrightleftharpoons{{}_{\mathrm{s}}^{\mathrm{s}}K_{\mathrm{b}}} \quad \mathrm{HIn} \quad + \quad \mathrm{OH^-}$$

$$[\mathrm{HIn}]_0 = \frac{1}{2}\left(-c_{\mathrm{OH}} - {}^{\mathrm{s}}_{\mathrm{s}}K_{\mathrm{b}} + \sqrt{(c_{\mathrm{OH}} + {}^{\mathrm{s}}_{\mathrm{s}}K_{\mathrm{b}})^2 + 4\,{}^{\mathrm{s}}_{\mathrm{s}}K_{\mathrm{b}}T_{\mathrm{in}}}\right) \tag{3.10}$$

$$[\mathrm{OH}^-]_0 = c_{\mathrm{OH}} + [\mathrm{HIn}]_0 = \frac{1}{2}\left(c_{\mathrm{OH}} - {}^{\mathrm{s}}_{\mathrm{s}}K_{\mathrm{b}} + \sqrt{(c_{\mathrm{OH}} + {}^{\mathrm{s}}_{\mathrm{s}}K_{\mathrm{b}})^2 + 4\,{}^{\mathrm{s}}_{\mathrm{s}}K_{\mathrm{b}}T_{\mathrm{in}}}\right) \tag{3.11}$$

Then, expanding eq. (3.9) yields eq. (3.12), where ${}^{\mathrm{s}}_{\mathrm{s}}K_{\mathrm{a}} = (4.8 \pm 0.2) \times 10^{-6}$ M, ${}^{\mathrm{s}}_{\mathrm{s}}\mathrm{p}K_{\mathrm{ap}} = 15.13$,[36] and $c_{\mathrm{OH}} = 2.72 \times 10^{-8}$ M. Thus, with knowledge of T_{in}, $\varepsilon_{\mathrm{in}}$, ${}^{\mathrm{s}}_{\mathrm{s}}K_{\mathrm{a}}$, and ${}^{\mathrm{s}}_{\mathrm{s}}\mathrm{p}K_{\mathrm{a}}$, eq. (3.12) can be used to transform the experimentally observed Abs_t vs. t into c_{H} vs. t.

$$\begin{aligned}
c_{\mathrm{H}} &= [\mathrm{HIn}]_t - [\mathrm{HIn}]_0 + [\mathrm{H}^+]_t - [\mathrm{H}^+]_0 - ([\mathrm{OH}^-]_t - [\mathrm{OH}^-]_0) \\
&= T_{\mathrm{in}} - \frac{Abs_t}{\varepsilon_{\mathrm{in}}} + c_{\mathrm{OH}} + \frac{{}^{\mathrm{s}}_{\mathrm{s}}K_{\mathrm{a}}\varepsilon_{\mathrm{in}}\left(T_{\mathrm{in}} - \frac{Abs_t}{\varepsilon_{\mathrm{in}}}\right)}{Abs_t} - \frac{{}^{\mathrm{s}}_{\mathrm{s}}K_{\mathrm{ap}}Abs_t}{{}^{\mathrm{s}}_{\mathrm{s}}K_{\mathrm{a}}\varepsilon_{\mathrm{in}}\left(T_{\mathrm{in}} - \frac{Abs_t}{\varepsilon_{\mathrm{in}}}\right)} \\
&\quad + \frac{2\,{}^{\mathrm{s}}_{\mathrm{s}}K_{\mathrm{ap}}}{c_{\mathrm{OH}} - \frac{{}^{\mathrm{s}}_{\mathrm{s}}K_{\mathrm{ap}}}{{}^{\mathrm{s}}_{\mathrm{s}}K_{\mathrm{a}}} + \sqrt{\left(c_{\mathrm{OH}} + \frac{{}^{\mathrm{s}}_{\mathrm{s}}K_{\mathrm{ap}}}{{}^{\mathrm{s}}_{\mathrm{s}}K_{\mathrm{a}}}\right)^2 + 4\frac{{}^{\mathrm{s}}_{\mathrm{s}}K_{\mathrm{ap}}}{{}^{\mathrm{s}}_{\mathrm{s}}K_{\mathrm{a}}}T_{\mathrm{in}}}}
\end{aligned} \tag{3.12}$$

For reactions of Z isomers alone, application of the initial rate approximation yields eq. (3.13)–(3.15) where dc_{H}/dt is the slope of the linear plot of c_{H} vs. t and $c_{Z,0}$ is determined as described above, yielding pseudo-first order rate constants k_{Z}.

$$\frac{d[\mathrm{P}_Z]}{dt} = \frac{dc_{\mathrm{H}}}{dt} = kc_{\mathrm{total}} \approx k_{\mathrm{obs}}c_{\mathrm{total,0}} = k_Z c_{Z,0} \tag{3.13}$$

$$\frac{dc_{\mathrm{H}}}{dt}\left(c_{\mathrm{total,0}}\right)^{-1} \approx k_{\mathrm{obs}} \tag{3.14}$$

$$\frac{dc_{\mathrm{H}}}{dt}\left(c_{Z,0}\right)^{-1} \approx k_{Z} \tag{3.15}$$

For simultaneous hydrolysis of *E* and *Z* isomers, the generation of strong acid in solution (c_{H}) under pseudo-first order conditions is described by the system of differential equations (3.16)–(3.18). Using the values of k_Z measured for *Z* isomers along, the series of the differential equation was solved self-consistently using solver ode45 in Matlab (the initial concentrations, $c_{Z,0}$ and $c_{E,0}$ were determined by spectral deconvolution) in combination with lsqnonlin to minimize the residuals of the fit for calculated values of c_{H} vs. t was minimized. The quality of the fit was determined by performing a χ^2 goodness-of-fit test (chi2gof) on the residuals; in all cases the null hypothesis that the residuals are a random sample from a normal distribution could not be rejected at the 5% significance level. The optimized values of k_E are tabulated in Table 3.8. The standard errors, *s*, for k_E were calculated as previously described,[38] using unit weighting for the data points. A representative fit is shown in Fig. 3.34.

$$\frac{dc_Z}{dt} = -k_Z c_Z \tag{3.16}$$

$$\frac{dc_E}{dt} = -k_E c_E \tag{3.17}$$

$$\frac{dc_{\mathrm{H}}}{dt} = k_Z c_Z + k_E c_E \tag{3.18}$$

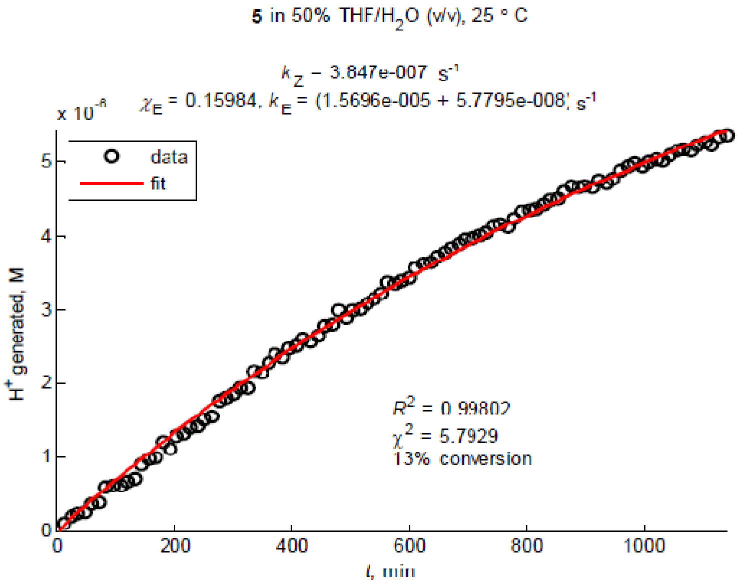

Fig. 3.34. Data fitted for the hydrolysis of a photostationary mixture of **5** in H_2O–THF (0.82/0.18 mol) at 25 °C

Measured Rate Constants and Activation Parameters

The rate constants for hydrolysis of **1**–**6** in H_2O–THF (0.82/0.18 mol) are tabulated in Table 3.8, where σ is the standard deviation of the temperature T, which was recorded every 2 s; s are standard errors on the rate constants from the regressions used to obtain the values; χ_E is the fraction of E isomer present, as determined by HPLC for the reaction mixture; R^2 is the coefficient of correlation for the regression; χ^2 is the χ^2 statistic for the residuals of the regression. The values tabulated below agree with the expectation that the activation parameters for Z**1**–Z**6** should be minimally perturbed. The enthalpies of activation ($\Delta H^\ddagger$ = 18.9–26.5 kcal mol^{-1}) are consistent with the literature values for related primary sulfonates ($\Delta H^\ddagger$ = 19.7–21.2 kcal mol^{-1}),[15,16] and the activation free energies at 25 °C ($\Delta G^\ddagger_{298K}$ = 26.2–27.0 kcal mol^{-1}, derived from the k_Z at 25 °C) also agree well with literature values ($\Delta G^\ddagger_{298K}$ = 24.6–25.6 kcal mol^{-1}).[15,16] The Eyring plots for the hydrolysis of sulfonates **1**–**6** in 50% THF/H_2O (v/v) are shown in Fig. 3.35 and Fig. 3.36. The activation parameters derived from those plots are tabulated in Table 3.9. Differential activation parameters derived from plots of $\ln(k_E/k_Z)$ vs. $1/T$ (Fig. 3.37) are tabulated in Table 3.10. See below for further explanation.

Table 3.8. Measured rate constants, standard errors and correlation coefficients

	pH(t=0)	T, °C	σ	k_{obs}, s^{-1}	s	χ_E	k_E, s^{-1}	s	R^2	χ^2
*Z***1**	4.70	60.0	0.2	2.24E-05	2E-07					
	4.86	40.0	0.1	1.948E-06	4E-09					

Table 3.8 (cont.)

	5.06	25.00	0.02	2.089E-07	5E-10					
	4.56	24.999	0.003	1.50E-07	3E-09					
	4.97	25.000	0.002	2.07E-07	5E-09					
*E*1	4.77	60.00	0.05			0.318	5.0E-05	2.5E-06	0.9751	1.24
	5.01	40.000	0.004			0.323	2.3E-06	1.7E-06	0.9991	7.97
	4.83	25.000	0.001			0.331	1.6E-07	1E-08	0.8385	0.52
*Z*2	4.57	60.000	0.002	7.1E-06	1E-07					
	4.35	40.000	0.001	1.67E-06	5E-08					
	4.80	25.000	0.001	2.181E-07	1.135E-08					
*E*2	4.99	60.00	0.05			0.209	5.2E-05	2E-06	0.9820	0.82
	4.91	40.000	0.004			0.192	7.6E-06	2E-07	0.9999	0.19
	4.88	25.000	0.001			0.196	8.8E-07	4E-08	0.8850	3.52
*Z*3	4.58	60.000	0.002	7.4E-06	1E-07					
	4.25	40.000	0.001	5.9E-07	3E-08					
	4.89	25.000	0.001	1.0E-07	1E-08					
*E*3	4.88	59.997	0.047			0.357	1.24E-04	2E-06	0.9994	0.25
	4.96	40.000	0.003			0.332	1.39E-05	1E-07	0.9979	6.53
	4.91	25.000	0.001			0.358	9.8E-07	2E-08	0.9994	0.00013
*Z*4	4.56	60.000	0.002	1.14E-05	1E-07					
	4.53	40.0	0.2	1.25E-06	2E-08					
	4.50	24.999	0.003	1.41E-07	3E-09					
	5.10	25.000	0.002	1.09E-07	9E-09					
*E*4	4.77	60.00	0.05			0.221	2.4E-04	2E-05	0.9980	0.18
	4.79	40.0	0.2			0.222	2.09E-05	2E-07	0.9743	6.07
	4.86	25.000	0.001			0.227	5.03E-06	3E-08	0.9898	3.73
*Z*5	4.52	60.0	0.0	1.9E-05	3E-06					
	4.26	40.000	0.001	2.18E-06	4E-08					
	4.60	24.998	0.004	3.8E-07	6E-08					
*E*5	4.90	60.00	0.05			0.160	5.2E-04	5E-05	0.9831	0.02
	4.92	40.000	0.003			0.157	1.56E-04	7E-06	0.9989	0.80

Table 3.8 (cont.)

	4.83	25.000	0.001			0.157	2.71E-05	3E-07	0.9971	4.67
	4.89	25.000	0.001			0.156	2.67E-05	2E-07	0.9948	5.63
	4.82	25.000	0.001			0.160	1.570E-05	6E-08	0.9980	5.79
*Z***6**	4.62	60.0	0.2	1.57E-05	2E-07					
	4.71	40.0	0.2	1.66E-06	1E-08					
	4.77	24.998	0.006	3.13E-07	1E-09					
*E***6**	4.92	60.00	0.05			0.060	7E-04	1E-04	0.9979	0.11
	4.94	40.000	0.003			0.060	1.06E-04	7E-06	0.9978	5.26
	4.87	25.000	0.001			0.056	2.75E-05	6E-07	0.9948	0.03

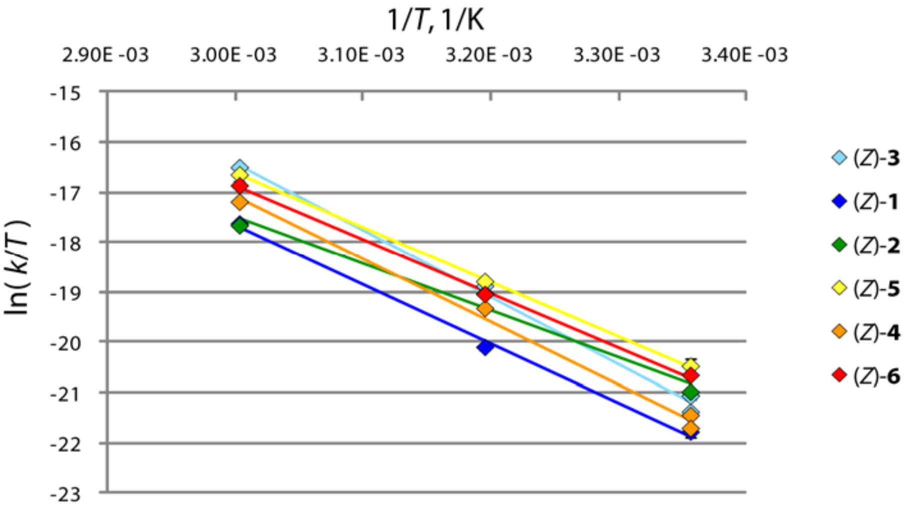

Fig. 3.35. Eyring plots for the hydrolysis of *Z***1**–*Z*6 in H_2O–THF (0.82/0.18 mol); error bars represent the standard error of the regressions used to obtain the values

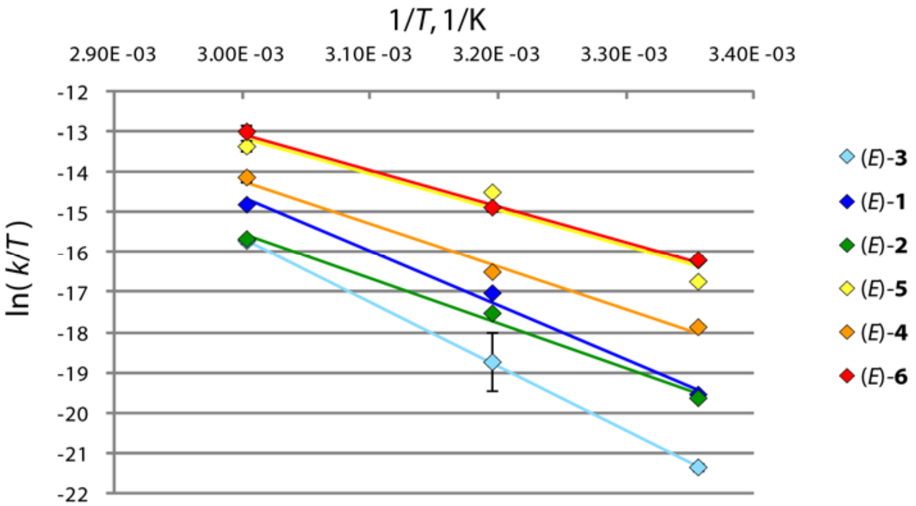

Fig. 3.36. Eyring plots for the hydrolysis of *E*1–*E*6 in H_2O–THF (0.82/0.18 mol); error bars represent the standard error of the regressions used to obtain the values

Table 3.9. Activation parameters for the hydrolysis of **1**–**6** in H_2O–THF (0.82/0.18 mol)obtained from linear plots of ln(*k*/*T*) vs. 1/*T* (Fig. 3.35 and Fig. 3.36)

macrocycle	$\Delta H^{\ddagger}_{Z}$, kcal/mol	$\Delta S^{\ddagger}_{Z}$, e.u.	$\Delta H^{\ddagger}_{E}$, kcal/mol	$\Delta S^{\ddagger}_{E}$, e.u.
1	23.5(1.4)	1.4(-11.9)	26.6(2.3)	2.3(3.3)
2	26.5(1.1)	1.1(-0.2)	31.6(0.3)	0.3(16.6)
3	18.5(2.8)	2.8(-26.6)	22.3(2)	2(-11.2)
4	21.5(0.4)	0.4(-15.8)	17.7(2.3)	2.3(-20.3)
5	25(1.4)	1.4(-6.1)	21.2(2.2)	2.2(-11.8)
6	21.5(0.7)	0.7(-16.3)	17.9(0.9)	0.9(-19.4)

“Compensating” variation between $\Delta H^{\ddagger}$ and $\Delta S^{\ddagger}$ is well known,[39-41] with empirical relationships based on it reported as early as 1925.[39,42] The interpretation and proper demonstration of such extrathermodynamic relationships[12,39] has caused a great deal of confusion and debate in the literature.[39,42-47] Simply plotting $\Delta H^{\ddagger}$ vs. $\Delta S^{\ddagger}$ is insufficient proof for an isokinetic relationship, particularly when both parameters are derived from reaction rate data. In such situations, plots of $\Delta H^{\ddagger}$ vs. $\Delta S^{\ddagger}$ can be misleading in that they may mainly reflect the dependence of $\Delta H^{\ddagger}$ on itself.[43] Isokinetic relationships are demonstrated by a common point (or small area) of intersection of ln(*k*) vs. 1/*T* plots or other mathematically equivalent relationships (e.g., a linear relationship between $\Delta H^{\ddagger}$ vs. $\Delta S^{\ddagger}$) but only when a proper statistical analysis has been performed to demonstrate dependence.[39,40,43] (We have not done so, and thus make no claim of such a relationship; see below.)

Regardless of whether such variation reflects a true isokinetic relationship or variation that remains unexplained, the phenomenological observation of variation of $\Delta H^{\ddagger}$ and $\Delta S^{\ddagger}$ across series of related reactions has been reported throughout the literature. Even when $\Delta H^{\ddagger}$ and $\Delta S^{\ddagger}$ are determined from the measurement of $\Delta G^{\ddagger}$ over a given temperature range, claims that such variation *in itself* is incorrect (i.e., that it is physically impossible) is equivalent to claiming either that the rate constants are incorrect or that the Eyring (or Arrhenius) equations do not hold. The range of values spanned by the activation enthalpies and entropies for *E* and *Z* isomers of **1**–**6** are 14.0 kcal/mol and 43.1 e.u., respectively. Similarly large ranges are present in the literature: For the aminolysis of dimethyl carbonate with a series of amines,[48] $\Delta H^{\ddagger}$ spans 22.3 kcal/mol and $\Delta S^{\ddagger}$ spans 68.5 e.u. while $\Delta G^{\ddagger}$ at 298 K spans only 2.9 kcal/mol. For a series of S_NV reactions resulting in the replacement of halogen with charged nucleophiles (entries 5, 6, 8, 9, 10, 11, and 12 in Table 7 of ref. 41), $\Delta H^{\ddagger}$ spans 15.8 kcal/mol and $\Delta S^{\ddagger}$ spans 54.6 e.u. while $\Delta G^{\ddagger}$ at 298 K spans only 2.7 kcal/mol. For a series of S_NAr reactions at the sp^2-hybridized carbon atom in ArLG with charged nucleophiles (entries 17–21 in Table 3 of ref. 41), $\Delta H^{\ddagger}$ spans 21.0 kcal/mol and $\Delta S^{\ddagger}$ spans 59.0 e.u. while $\Delta G^{\ddagger}$ at 298 K spans only 3.5 kcal/mol.

However, because demonstrating the existence (or absence) of an isokinetic relationship is beyond the scope of this work, we have not performed the requisite measurements and statistical analysis to properly do so. Furthermore, we emphasize that we are interested here only in $\Delta G^{\ddagger}$, which is given by the measured rate constants. We derived $\Delta H^{\ddagger}$ and $\Delta S^{\ddagger}$ to support the validity of our measurements by comparison to expected values (p. 117); for *Z***1**–*Z***6**, the comparisons of $\Delta H^{\ddagger}$ are reasonable. We make no comparisons for *E***1**–*E***6** because we expect $\Delta G^{\ddagger}$ to be perturbed. We do note that the agreements (as MADs, Table 3.11) between calculated and measured energy barriers are much better for $\Delta G^{\ddagger}$, which are the barriers on which we base our conclusions, than for $\Delta H^{\ddagger}$.

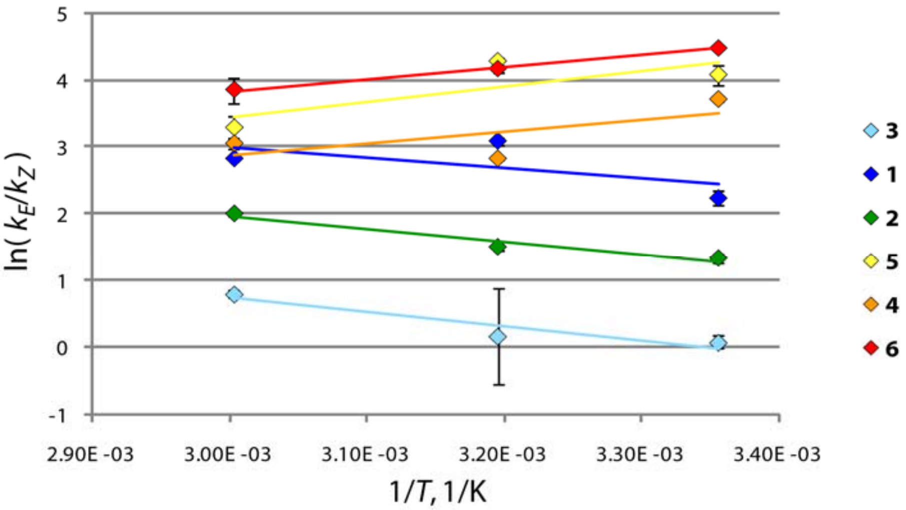

Fig. 3.37. Eyring plots for k_E/k_Z for the hydrolysis of **1**–**6** in H_2O–THF (0.82/0.18 mol) error bars represent the standard errors derived from those of k_E and k_Z

Table 3.10. Differential activation parameters for the hydrolysis of **1**–**6** in H_2O–THF (0.82/0.18 mol) obtained from linear plots of ln(k_E/k_Z) vs. 1/*T* (Fig. 3.37)

macrocycle	$\Delta\Delta H^{‡}_{Z\text{-}E}$, kcal/mol	$\Delta\Delta S^{‡}_{Z\text{-}E}$, e.u.	$\Delta\Delta G^{‡}_{Z\text{-}E,\ 298\ K}$, kcal/mol
1	-4.2(1.5)	-13.9(4.9)	0.0(0.6)
2	-3.8(0.9)	-15.4(2.8)	0.8(0.4)
3	-3.1(3.7)	-15.3(12)	1.3(0.7)
4	3.5(3.8)	4.9(12)	2.2(0.2)
5	4.6(3.6)	6.9(12)	2.4(0.9)
6	3.5(0.2)	3.0(0.5)	2.7(0.1)

Selected Computational Results

The remainder of the computational details and results not specifically referenced in this text are described and tabulated elsewhere.[29]

Table 3.11. Comparison of calculated values to experimental values; deviations are calculated – experimental; values are in kcal/mol

	calculated					deviations from experiment				
	$\Delta H^{‡}_Z$	$\Delta H^{‡}_E$	$\Delta G^{‡}_Z$	$\Delta G^{‡}_E$	$\Delta\Delta G^{‡}$	$\Delta H^{‡}_Z$	$\Delta H^{‡}_E$	$\Delta G^{‡}_Z$	$\Delta G^{‡}_E$	$\Delta\Delta G^{‡}$
1	27.1	26.2	27.8	27.0	0.8	0.6	-5.4	0.0	-0.8	0.7
2	27.5	26.4	27.6	26.4	1.3	9.0	4.1	0.0	-0.5	0.5
3	27.3	26.1	28.1	25.8	2.3	3.8	5.9	-0.1	-1.1	1.0
4	26.9	26.7	28.4	25.8	2.7	1.9	5.5	0.4	-0.2	0.4

Table 3.11 (cont.)

5	28.5	26.4	27.5	25.6	1.9	7.0	8.8	0.1	0.7	-0.5
6	25.6	22.1	25.9	22.4	3.5	4.1	4.2	-1.7	-2.5	0.8
MADs						**4.2**		**0.4**		**0.6**

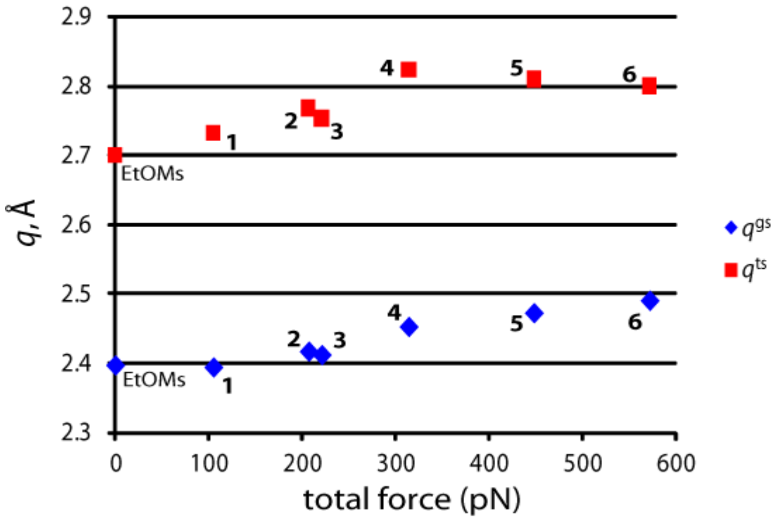

Fig. 3.38. Variation in the non-bonding C···O distance q in E**1**–E**6**

A full tabulation of calculated restoring forces projected along across a variety of pairs of nuclei in the reactive moiety are reported elsewhere.[29]

3.9 References

1. Caruso, M. M.; Davis, D. A.; Shen, Q.; Odom, S. A.; Sottos, N. R.; White, S. R.; Moore, J. S., Mechanically-Induced Chemical Changes in Polymeric Materials. *Chem. Rev.* **2009**, *109*, 5755–5798.
2. Kauzmann, W.; Eyring, H., The Viscous Flow of Large Molecules. *J. Am. Chem. Soc.* **1940**, *62*, 3113–3125.
3. Lenhardt, J. M.; Black, A. L.; Craig, S. L., *gem*-Dichlorocyclopropanes as Abundant and Efficient Mechanophores in Polybutadiene Copolymers under Mechanical Stress. *J. Am. Chem. Soc.* **2009**, *131*, 10818–10819.
4. Sheiko, S. S.; Sun, F. C.; Randall, A.; Shirvanyants, D.; Rubinstein, M.; Lee, H.-i.; Matyjaszewski, K., Adsorption-Induced Scission of Carbon–Carbon Bonds. *Nature* **2006**, *440*, 191–194.
5. Schliwa, M., *Molecular Motors*. Wiley-VCH: New York, 2003.

6. Hugel, T.; Holland, N. B.; Cattani, A.; Moroder, L.; Seitz, M.; Gaub, H. E., Single-Molecule Optomechanical Cycle. *Science* **2002**, *296*, 1103–1106.
7. de Pablo, J. J.; Curtin, W. A., Multiscale Modeling in Advanced Materials Research: Challenges, Novel Methods, and Emerging Applications. *MRS Bull.* **2007**, *32*, 905–911.
8. Hyeon, C.; Thirumalai, D., Measuring the Energy Landscape Roughness and the Transition State Location of Biomolecules Using Single Molecule Mechanical Unfolding Experiments. *J. Phys.: Condens. Matter* **2007**, *19*, 113101.
9. Bell, G. I., Models for the Specific Adhesion of Cells to Cells. *Science* **1978**, *200*, 618–627.
10. Evans, E.; Ritchie, K., Dynamic Strength of Molecular Adhesion Bonds. *Biophys. J.* **1997**, *72*, 1541–1555.
11. Evans, E., Probing the Relation Between Force—Lifetime—and Chemistry in Single Molecular Bonds. *Annu. Rev. Biophys. Biomol. Struct.* **2003**, *30*, 105–128.
12. Leffler, J. E.; Grunwald, E., *Rates and Equilibria of Organic Reactions*. Dover: New York, 1989.
13. Astumian, R. D., The Unreasonable Effectiveness of Equilibrium Theory for Interpreting Nonequilibrium Experiments. *Am. J. Phys.* **2006**, *74*, 683–688.
14. Rubinstein, M.; Colby, R. H., *Polymer Physics*. Oxford University Press: New York, 2003.
15. Barnard, P. W. C.; Robertson, R. E., The Hydrolysis of a Series of Straight-Chain Alkyl Methanesulphonic Esters in Water. *Can. J. Chem.* **1961**, *39*, 881–888.
16. Robertson, R. E., Solvolysis in Water. *Prog. Phys. Org. Chem.* **1967**, *4*, 213–280.
17. Singh, R.; Whitesides, G. M., Thiol-Disulfide Interchange. In *Supplement S: The Chemistry of Sulphur-Containing Functional Groups*, Patai, S.; Rappoport, Z., Eds. John Wiley & Sons: New York, 1993; pp 633–658.
18. Sotomayor, M.; Schulten, K., Single-Molecule Experiments in Vitro and in Silico. *Science* **2007**, *316*, 1144–1148.
19. Yang, Q.-Z.; Huang, Z.; Kucharski, T. J.; Khvostichenko, D.; Chen, J.; Boulatov, R., A Molecular Force Probe. *Nat. Nanotechnol.* **2009**, *4*, 302–306.
20. Huang, Z.; Yang, Q.-Z.; Khvostichenko, D.; Kucharski, T. J.; Chen, J.; Boulatov, R., Method to Derive Restoring Forces of Strained Molecules from Kinetic Measurements. *J. Am. Chem. Soc.* **2009**, *131*, 1407–1409.

21. Vreven, T.; Morokuma, K., On the Application of the IMOMO (Integrated Molecular Orbital + Molecular Orbital) Method. *J. Comput. Chem.* **2000**, *21*, 1419–1432.

22. Cramer, C. J., *Essentials of Computational Chemistry: Theories and Models*. John Wiley & Sons, Inc.: 2004.

23. Kucharski, T. J.; Huang, Z.; Yang, Q.-Z.; Tian, Y.; Rubin, N. C.; Concepcion, C. D.; Boulatov, R., Kinetics of Thiol/Disulfide Exchange Correlate Weakly with the Restoring Force in the Disulfide Moiety. *Angew. Chem. Int. Ed.* **2009**, *48*, 7040–7043.

24. Maróti, P.; Wraight, C. A., Flash-Induced H^+ Binding by Bacterial Photosynthetic Reaction Centers: Comparison of Spectrophotometric and Conductimetric Methods. *Biochim. Biophys. Acta* **1988**, *934*, 314–328.

25. Maróti, P., Flash-Induced Proton Transfer in Photosynthetic Bacteria. *Photosynth. Res.* **1993**, *37*, 1–17.

26. Marenich, A. V.; Cramer, C. J.; Truhlar, D. G., Universal Solvation Model Based on Solute Electron Density and on a Continuum Model of the Solvent Defined by the Bulk Dielectric Constant and Atomic Surface Tensions. *J. Phys. Chem. B* **2009**, *113*, 6378–6396.

27. Jencks, W. P., A Primer for the Bema Hapothle. An Empirical Approach to the Characterization of Changing Transition-State Structures. *Chem. Rev.* **1985**, *85*, 511–527.

28. Huang, Z.; Boulatov, R., Chemomechanics with Molecular Force Probes. *Pure Appl. Chem.* **2010**, *82*, 931–951.

29. Kucharski, T. J.; Yang, Q.-Z.; Tian, Y.; Boulatov, R., Strain-Dependent Acceleration of a Paradigmatic S_N2 Reaction Accurately Predicted by the Force Formalism. *J. Phys. Chem. Lett.* **2010**, *1*, 2820–2825.

30. Tuttolomondo, M. E.; Navarro, A.; Peña, T.; Varetti, E. L.; Altabef, A. B., Theoretical Structure and Vibrational Analysis of Ethyl Methanesulfonate, $CH_3SO_2OCH_2CH_3$. *J. Phys. Chem. A* **2005**, *109*, 7946–7956.

31. The calculations yielded large imaginary frequencies (>500i cm^{-1}), indicating sharp barriers. Hence, the calculated bond distances of the transition states are certainly reliable to <0.01 Å (e.g., ref. 22).

32. Regan, C. K.; Craig, S. L.; Brauman, J. I., Steric Effects and Solvent Effects in Ionic Reactions. *Science* **2002**, *295*, 2245–2247.

33. Smith, M. B.; March, J., *March's Advanced Organic Chemistry*. 5th ed.; John Wiley & Sons, Inc.: New York, 2001.

34. Guthrie, J. P., Hydrolysis of Esters of Oxy Acids; pK_a Values for Strong Acids: Brønsted Relationship for Attack of Water at Methyl; Free Energies of Hydrolysis of Esters of Oxy Acids; and a Linear Relationship Between Free Energy of Hydrolysis and pK_a Holding over a Range of 20 pK Units. *Can. J. Chem.* **1978**, *56*, 2342–2354.

35. King, J. F.; Khemani, K. C.; Skonieczny, S.; Payne, N. C., Sulphur–Oxygen Cleavage in the Reaction of Four- and Five-Membered Sultones with Hydroxide: Evidence for a Stereoelectronic Effect in Sulphonyl Reactions. *J. Chem. Soc., Chem. Commun.* **1988**, 415–417.

36. Rosés, M.; Bosch, E., Influence of Mobile Phase Acid-Base Equilibria on the Chromatographic Behaviour of Protolytic Compounds. *Journal of Chromatography A* **2002**, *982*, 1–30.

37. Green, F. J., *The Sigma-Aldrich Handbook of Stains, Dyes and Indicators*. Aldrich Chemical Company, Inc.: Milwaukee, WI, 1990.

38. Gans, P., *Data Fitting in the Chemical Sciences By the Method of Least Squares*. John Wiley & Sons: New York, 1992.

39. Liu, L.; Guo, Q.-X., Isokinetic Relationship, Isoequilibrium Relationship, and Enthalpy-Entropy Compensation. *Chem. Rev.* **2001**, *101*, 673–696.

40. Linert, W., Mechanistic and Structural Investigations Based on the Isokinetic Relationship. *Chem. Soc. Rev.* **1994**, *23*, 429–438.

41. Vlasov, V. M., Energetics of Bimolecular Nucleophilic Reactions in Solution. *Russ. Chem. Rev.* **2006**, *75*, 765–796.

42. Exner, O., The Enthalpy-Entropy Relationship. *Prog. Phys. Org. Chem.* **1973**, *10*, 411–482.

43. Exner, O., Entropy-Enthalpy Compensation and Anticompensation: Solvation and Ligand Binding. *Chem. Comm.* **2000**, 1655–1656.

44. Alper, J. S.; Gelb, R. I., Determination of the existence, value and uncertainty of the compensation or isokinetic temperature. *J. Phys. Org. Chem.* **1993**, *6*, 273–280.

45. Linert, W.; Sapunov, V. N., The Isokinetic Relationship. IX. Connections to Linear Free Energy Relationships. *Chem. Phys.* **1988**, *119*, 265–274.

46. Exner, O., Determination of the Isokinetic Temperature. *Nature* **1970**, *227*, 366–367.
47. Exner, O., Concerning the Isokinetic Relationship. *Nature* **1964**, *201*, 488–490.
48. Aresta, M.; Dibenedetto, A.; Quaranta, E.; Boscolo, M.; Larsson, R., The Kinetics and Mechanism of the Reaction Between Carbon Dioxide and a Series of Amines: Observation and Interpretation of an Isokinetic Effect. *Journal of Molecular Catalysis A: Chemical* **2001**, *174*, 7–13.

Chapter 4. When Bond Elongation Is Not Enough: Mechanochemical Insensitivity of Thiol/Disulfide Exchange

Adapted from Kucharski, T. J.; Huang, Z.; Yang, Q.-Z.; Tian, Y.; Rubin, N. C.; Concepcion, C. D; Boulatov, R., Kinetics of Thiol/Disulfide Exchange Correlates Weakly with the Restoring Force in the Disulfide Moiety. *Angew. Chem. Int. Ed.* **2009**, *48*, 7040–7043. © Wiley-VCH Verlag GmbH & Co. KGaA. Reproduced with permission.

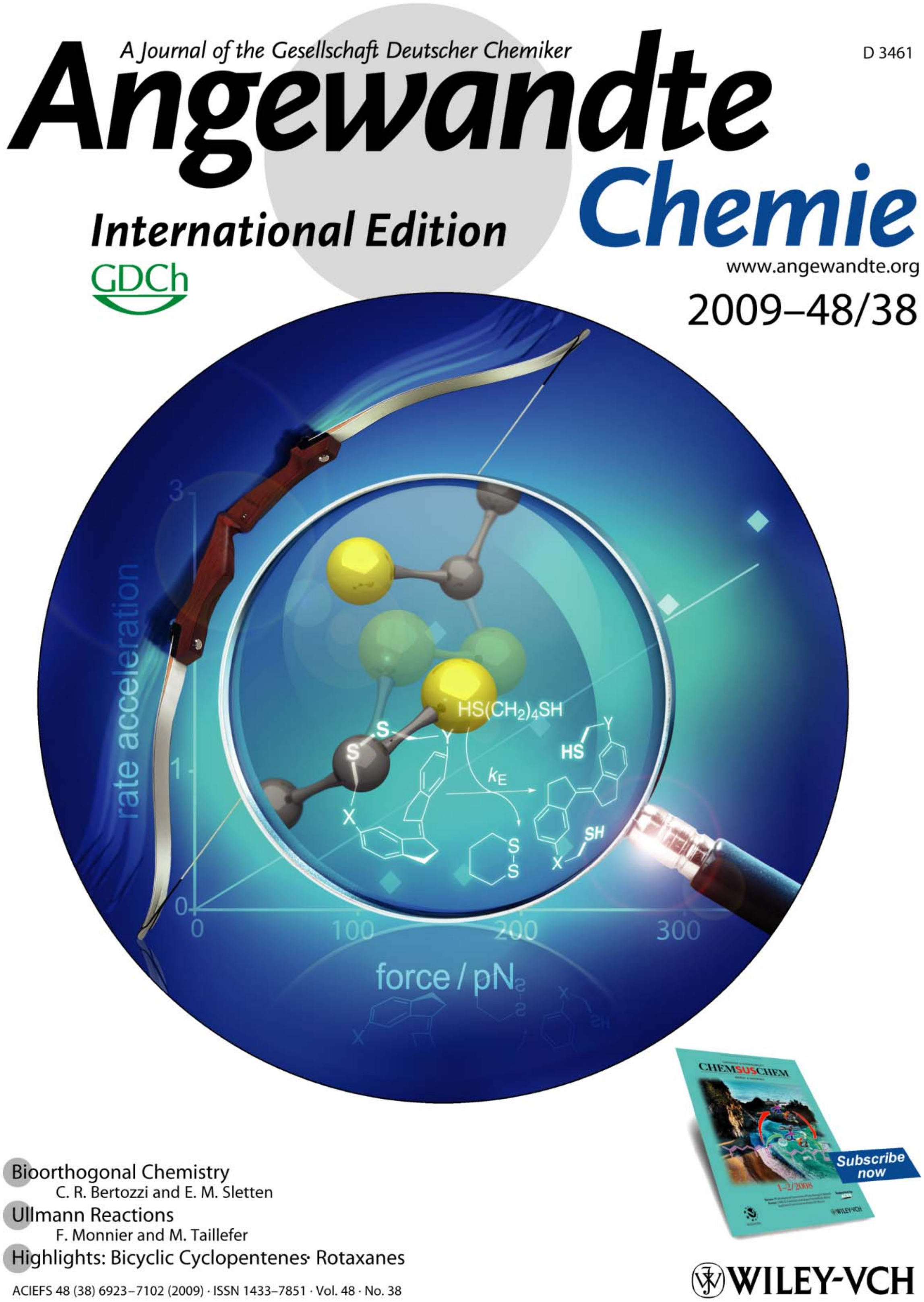

A Journal of the Gesellschaft Deutscher Chemiker

D 3461

Angewandte Chemie

International Edition

GDCh

www.angewandte.org

2009–48/38

Bioorthogonal Chemistry
C. R. Bertozzi and E. M. Sletten
Ullmann Reactions
F. Monnier and M. Taillefer
Highlights: Bicyclic Cyclopentenes· Rotaxanes

ACIEFS 48 (38) 6923–7102 (2009) · ISSN 1433–7851 · Vol. 48 · No. 38

WILEY-VCH

The figure above reproduces the September 7, 2009 issue of *Angewandte Chemie, International Edition*. © Wiley-VCH Verlag GmbH & Co. KGaA. Reproduced with permission.

4.1 Abstract

A series of increasingly strained macrocyclic disulfides investigated experimentally and by high-level DFT calculations reveals that the kinetics of thiol/disulfide exchange are independent of the restoring force in the disulfide moiety. This finding is consistent with the S_N2 mechanism of thiol/disulfide exchange and lends insight into the acceleration of disulfide reduction upon stretching of certain proteins.

4.2 Introduction

A series of macrocycles **1–11** (Fig. 4.1A) revealed that stretching the disulfide moiety up to a restoring force of 350 pN along the S–S bond negligibly accelerates its reduction by thiols. The measured rates of thiol/disulfide exchange in the increasingly strained *E* macrocycles were within a factor of 2 of those in strain-free *Z* analogs with the activation enthalpies differing by <1 kcal/mol. This contrasts with $>10^6$-fold acceleration of a reference reaction, electrocyclic C–C bond dissociation, across a structurally-equivalent series (Fig. 4.1B).[1] Quantifying the strain in the *E* isomers of **1–11** as restoring force offers insights into the mechanism of acceleration of disulfide bond reduction observed when certain proteins are stretched[2-4] and more broadly, factors that determine the changes in the reactivity of molecules that have been stretched or compressed.

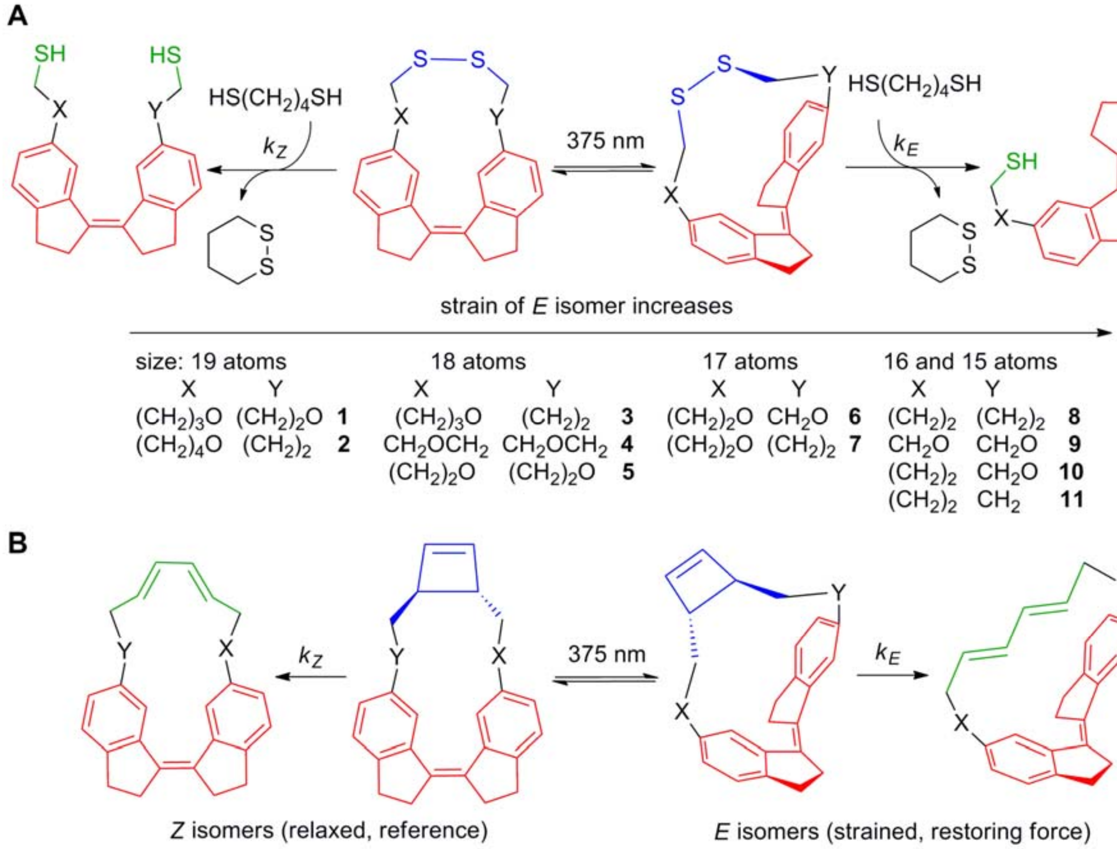

Fig. 4.1. **A**: The series of macrocycles for measuring the kinetics of thiol/disulfide exchange as a function of the restoring force of stretched disulfide moiety. In the definitions of inert linkers X and Y, the rightmost atom is bound to stiff stilbene. **B**: A reference series of cyclobutene-containing analogs of **1**–**11**. The reactive moieties (CH_2SSCH_2 and cyclobutene) are blue, products are green and stiff stilbene is red.

Such accelerations have profound implications for the stability of proteins to mechanical stresses and for biological mechanotransduction.[3] A series of single-molecule force experiments, which measured kinetics of thiol/disulfide exchange as a function of the total restoring force of polyprotein assemblies, are broadly consistent with at least three mechanisms: (1) partial unfolding of the protein which increases the access of water-soluble thiols to the disulfide bond, (2) distortion of the disulfide moiety which increases its reactivity and (3) stabilization of the transition state by partial conformational relaxation of the rest of the molecule if the disulfide moiety is longer in the transition state than the ground state. The relative importance of each mechanism remains controversial.

Mechanism 1 can only occur in proteins. Mechanisms 2–3, however, reflect the intrinsic properties of the disulfide moiety (i.e., its stiffness and difference in dimensions between the ground and transition states) and are testable using more tractable small molecules in which the disulfide moiety is stretched. Although the potential of small molecules to yield quantitative insights into the mechanism(s) of acceleration of localized reactions in stretched polymers has long been recognized,[5,6] its realization was until recently precluded by the lack of molecular architectures that allow the restoring forces of diverse functional groups to be systematically varied. Unlike strain energy, its gradient—molecular restoring force—is a size-invariant measure of molecular strain.[7] As such, it provides a unifying conceptual framework for interpreting the effect of molecular strain on the kinetics of localized reactions regardless of the overall size of the reactant. We recently reported[1,8] that incorporating a reactive moiety of interest (substrate) into an inert linker that constrains the C6,C6′ atoms of (*E*)-stiff stilbene (Fig. 4.1, red moiety) to a below-equilibrium distance and systematically varying the length and conformational flexibility of the linker creates a series of strained macrocycles. Changes in the kinetics of the substrate reaction across such series are amenable to interpretation within the restoring force formalism.

Here we used this strategy to measure the kinetics of thiol/disulfide exchange as a function of the restoring force of the disulfide moiety under tensile strain. Although the effect of compressive strain on the reactivity of the disulfide moiety has been extensively studied in dithiacyclopropane, -butane and -pentane,[9,10] such is not the case for tensile strains. The known larger aliphatic cyclic disulfides are either strain-free or their modest ring strains apparently perturb the kinetics of thiol/disulfide exchange insignificantly.[11,12]

4.3 Results and Discussion

We synthesized strain-free *Z* isomers of **1**–**11** in 4–6 steps and >10% overall yields. The strained *E* isomers of **1**–**7** were obtained by irradiating dilute solutions of the *Z* analogs in CH_3CN at 375 nm until the photostationary state was reached. Irradiation of the *Z* isomers of smallest macrocycles (**8**–**11**) resulted in homolysis of the S–S bond.[13] The activation parameters of the thiol/disulfide exchange in the *E* isomers of **8**–**11** were obtained computationally (see below).

We studied the kinetics of S–S bond reduction with 1,4-butanedithiol (BDT, Fig. 4.1) in 1:1.4 (mol) H_2O–CH_3CN mixtures using HPLC to follow the reaction progress. All rates were first order in both BDT and the macrocycle. We measured the ratios k_E/k_Z (Fig. 4.1A) by competition experiments in which both isomers of each macrocycle reacted with excess BDT in the same solution. Unlike individual rates, the ratios so obtained were independent of the solvent composition or the concentration of BDT. We obtained the differential activation parameters, $\Delta\Delta H^{\ddagger} = \Delta H_Z^{\ddagger} - \Delta H_E^{\ddagger}$ and $\Delta\Delta S^{\ddagger}$ (Table 4.4, below) from the slopes and the intercepts, respectively, of the linear Eyring plots of k_E/k_Z at 295–313 K (Fig. 4.25, below). The rate constants of thiol/disulfide exchange in the *Z* isomers derived from competition experiments were within the experimental uncertainty of those measured directly, ruling out cross-reaction between the two isomers in competition experiments.

The mechanism of disulfide reduction by BDT has been extensively studied:[14,15] the reaction proceeds by a rate-determining nucleophilic attack of the thiolate anion $HS(CH_2)_4S^-$ on a S atom of the disulfide, followed by rapid intramolecular formation of 1,2-dithiacyclohexane and release of reduced dithiol. Both steps are thought to be simple S_N2 reactions, with protonated thiol being inert. In agreement with this mechanism we did not observe the mixed disulfides (Fig. 4.2) in any of our reaction mixtures either by ^{1}H-NMR spectroscopy or HPLC. Consequently, the k_E/k_Z ratios reflect the difference of the free energy of activation of the initial rate-determining step.

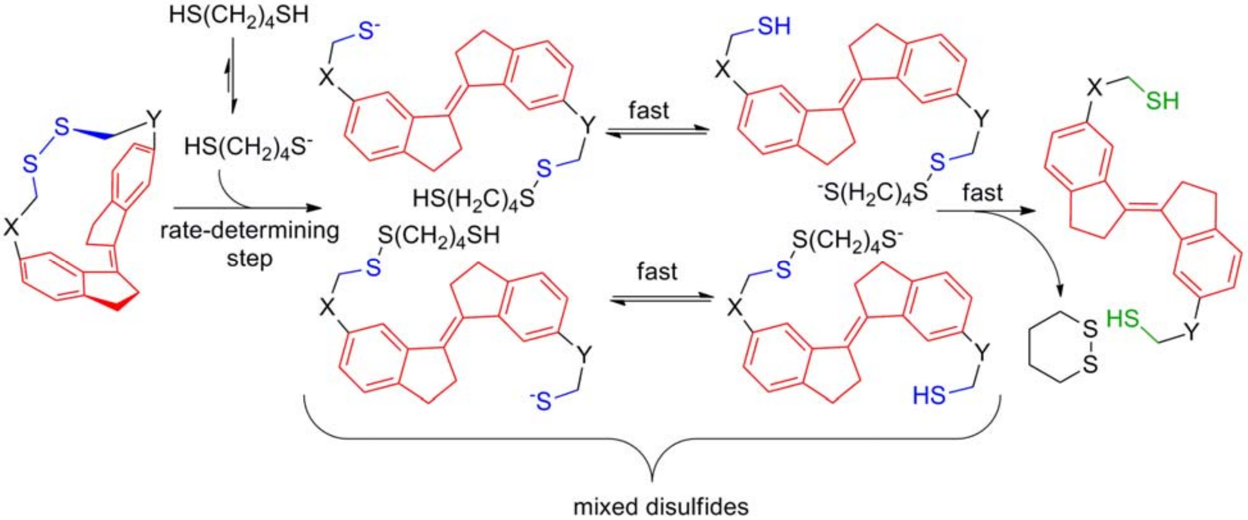

Fig. 4.2. A plausible mechanism of thiol/disulfide exchange in **1**–**11**. The mechanism is assumed to be identical in *E* and *Z* isomers.

To obtain convenient pseudo-first-order kinetics in $HS(CH_2)_4S^-$ without additional buffers the reductions were carried out with ~250-fold excess of BDT. The use of mixed solvents was dictated by the limited aqueous solubility of BDT. The protonation equilibria in this solvent mixture established at least 100-fold faster ($\tau_{½}$ < 10 s) than thiol/disulfide exchange, as inferred from the rate of H/D exchange between BDT and D_2O in D_2O-CD_3CN measured by ^{1}H-NMR spectroscopy.

To interpret the kinetic data within the restoring force formalism, we optimized multiple conformers of each ground and transition state in both isomers of **1–11** at the B3LYP/6-311+G** level of DFT. For computational efficiency we modeled the solvent as a conducting polarized continuum with the united-atom topological model cavities (CPCM-UA)[16] and replaced $HS(CH_2)_4S^-$ with EtS^-. The calculated activation enthalpies (tabulated elsewhere[17]) included the difference in the enthalpies of the solvated solute and the temperature-independent part of the solute/solvent interaction energies at the ground and transition states. The enthalpies calculated with the H_2O-parameterized CPCM and UFF-radii cavities were closest to the experiment (mean absolute deviation (MAD) ~2 kcal/mol). The MAD for the differential enthalpies, $\Delta\Delta H^{\ddagger}$, was ~1 kcal/mol.

The optimized geometries of the *Z* isomers were largely strain free. In the *E* analogs distortions of stiff stilbene were significantly more pronounced than those of the much stiffer disulfide moiety. In the ground-state conformers, the difference of the S–S bond lengths between the *Z* and *E* isomers of the same macrocycle was limited to ±0.006 Å, but the softer C–S–S–C dihedrals increased from ~90° in largest macrocycles **1–3** to a Boltzmann-weighted average of 97° in the smallest congeners, *E***10** and *E***11**. The calculated transition states were typical of an S_N2 reaction,[18] with the forming and dissociating S–S bonds of comparable length (average of **1–11**: 2.51 ± 0.03 Å and 2.53 ± 0.03 Å, respectively, tabulated elsewhere[17]), and a single imaginary frequency of >100*i* cm^{-1} (tabulated elsewhere[17]), corresponding primarily to the oscillation of the central S atom long the S–S–S axis. This data suggests that the chosen model chemistry describes thiol/disulfide exchange in macrocycles **1–11** with useful accuracy, lending credence to the calculated restoring forces.

Restoring forces were obtained as previously described.[1,8] Briefly, in macrocycles, the restoring force of the disulfide moiety is exactly balanced by that of the rest of the macrocycle. Excising the former and adding H atoms to satisfy the valencies of the newly terminal atoms reveals uncompensated forces on each atom of the resulting fragments due to the molecular strain. These forces were calculated as analytical gradients of the electronic energy. A vectoral sum of atomic forces in each indanyl moiety and its linker gave the total restoring force. As was the case for cyclobutene-containing macrocycles,[1] the forces in **1–11** were nearly parallel to the axis defined by the terminal methyl groups of the fragments. The restoring forces projected on the S–S bond were ~0.8 of the total. Ensemble-average forces along the S–S bond were obtained by Boltzmann-weighted averaging over all conformers. This force in each ground state was comparable to that in its corresponding transition state and was averaged.

The restoring force along the S–S bond varied with the macrocycle size from 100 pN in *E***1** to 350 pN in *E***11**. This range is comparable to that in the cyclobutene-containing reference series (Fig. 4.3). The very different rate-force dependences of these two reactions have, however, the same molecular basis. Theoretical considerations suggest[19] that the height of “sharp” activation barriers decreases as the product of the difference between the ground and transition states of the internuclear distance that best approximates the full reaction coordinate and the restoring force along it. In both cases, the slopes of the $\Delta\Delta H^{\ddagger}$ vs. force plots corresponded to the change in the separation of the CH_2 groups closest to the scissile bond (C1/C2, Fig. 4.4) between the corresponding ground and transition states (0.08 and 0.8 Å, for the disulfide and cyclobutene-containing macrocycles, respectively, Fig. 4.5). That the C1···C2 distance better approximates the full reaction coordinates than the scissile bond is fully consistent with the established mechanisms of these reactions. The formation of the pseudo-trigonal bipyramidal S_N2 transition state in thiol/disulfide exchange requires contraction of the angle between the scissile and the spectator bond at the central S.[20] The contribution of this bond angle to the full reaction coordinate[21] is not captured by the elongation of the scissile bond in the transition state but is reflected in the change in the C1···C2 separation. Had the scissile bond dominated the full reaction coordinate, its elongation would have yielded 10-fold acceleration of thiol/disulfide exchange per ~240 pN of restoring force along the S–S axis by Mechanism 3.

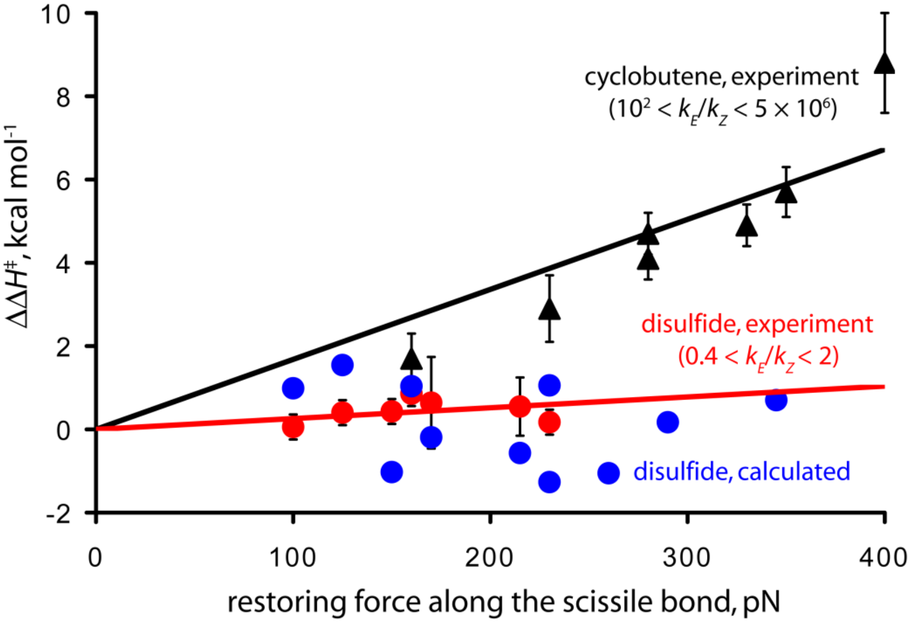

Fig. 4.3. The differences in the activation enthalpies (300 K) of thiol/disulfide exchange (red: measured; blue: B3LYP/6-311G** (CPCM-UA0)) and electrocyclic C–C bond homolysis (black triangles: measured) between the *Z* and *E* isomers of the same macrocycle, $\Delta\Delta H^‡ = \Delta H_Z^‡ - \Delta H_E^‡$, as a function of the calculated restoring force along the scissile S–S or C–C bond. The values of $\Delta\Delta S^‡$ were small in both series (Table 4.4). The error bars define the 95% probability intervals; solid lines are linear least-squares regression fits to the experimental data. The regressions are forced to pass through origin because in the absence of restoring force the rate must by definition be unperturbed. In the cyclobutene series the deviation of several experimental $\Delta\Delta H^‡$ values from direct proportionality reflects deficiencies of the scissile bond as the approximate reaction coordinate.[1] The more appropriate approximation of the reaction coordinate (C1/C2, Fig. 4.4) yields direct proportionality of $\Delta\Delta H^‡$ and force (Fig. 4.5).

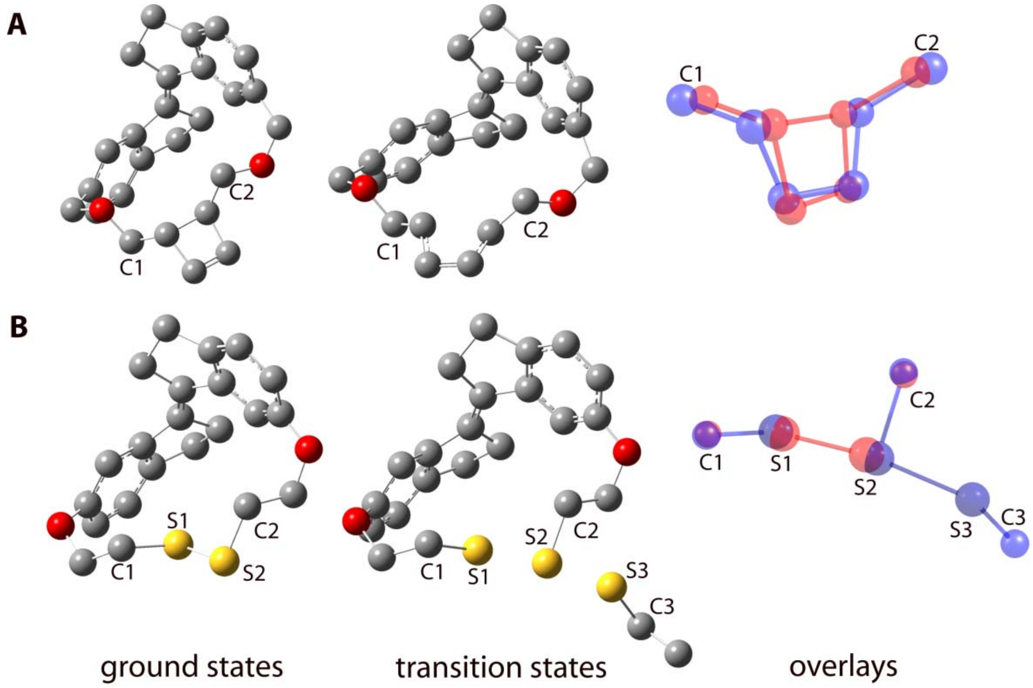

Fig. 4.4. Minimum energy conformers of the *E* isomers of a 16-atom cyclobutene-containing macrocycle (**A**, O3LYP/6-311G(2d,p)) and **9** (**B**) in the ground and transition states. C, O and S atoms are grey, red and yellow, respectively; H atoms are omitted for clarity. The right most structures shown the minimum-RMSD overlays of the reacting moieties in the ground (red) and transition (blue) states. Note the nearly constant relative position of the CH_2 groups in the disulfides.

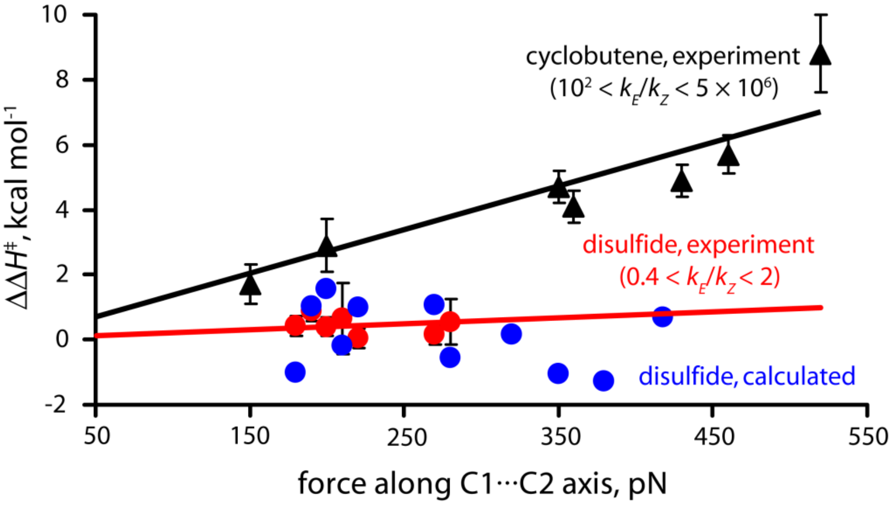

Fig. 4.5. Difference in the activation enthalpy of thiol/disulfide exchange (dots, red: measured; blue: calculated at the B3LYP/6-311+G** (CPCM-UA0) level of theory) and of electrocyclic C–C bond dissociation in cyclobutene between the *Z* and *E* isomers of the same macrocycle, $\Delta\Delta H^{\ddagger}$, as a function of the restoring force along the C1···C2 axis (see Fig. 4.4 for the definition of C1 and C2). The solid lines are least-squares fits to the experimental data;

their slopes correspond to 0.03 Å and 0.85 Å, respectively. Error bars define the 95% confidence level; the enthalpies are at 300 K.

4.4 Conclusions

Our data suggest that pulling on the disulfide moiety with up to ~350 pN of force along the S–S bond does not accelerate its reduction by thiolates. The significance of this finding is two-fold. First, it calls into question large contributions of Mechanisms 2 and 3 to the acceleration of thiol/disulfide exchange in stretched proteins.[4] For example, although the S–S bond elongates by ~0.4 Å in the transition state, the distance between the CH_2 groups attached to the S atoms does not appreciably change. This precludes relaxation of the non-reactive parts of the stretched molecule, which is required for Mechanism 3. Under these circumstances such relaxation may still occur if different stereoelectronic and solvation preferences of the disulfide moiety in its ground and transition states change the minimum-energy tertiary structure of the protein. The importance of such an effect cannot be evaluated using disulfides **1**–**11** but may be probed in single-molecule force experiments using polymers with simpler tertiary structures than proteins studied so far, e.g. S–S-bond containing PEGs. Until such experiments are performed, the acceleration of thiol/disulfide exchange in stretched proteins should probably be assumed to predominantly reflect the increased accessibility of the disulfide moiety to water-soluble reductants.

More broadly, our finding challenges the conventional notion that stretching a molecule necessarily accelerates its fragmentation.[4] This assumption is based on macroscopic experience (e.g., a stretched rubber band breaks faster than an unstretched one), which, however, maps poorly onto the molecular world. Even in simple bond dissociation reactions, the formation of the transition states require structural changes that are not limited to elongation of the scissile bond. Consequently, the length of the scissile bond is not a suitable state variable and the assumption that the dissociation rate of a covalent bond under tensile strain is proportional to the product of the restoring force and the difference in the scissile bond length between the ground and transition state may rarely if ever be true. Our data shows that the kinetically important structural changes in a reacting molecule can be captured using a single (non-bonding) internuclear distance, whose choice can be guided by knowledge of the molecular mechanism of the reaction. This unexpected fact preserves the intuitively appealing “single-coordinate” model of chemomechanical kinetics.[19,22]

4.5 Acknowledgments

This work was supported by the NSF, the US AFOSR, the ACS PRF and the University of Illinois. Predoctoral fellowships from ONR and NSF (T.K.) and the Bailar fund (Z.H.) are gratefully acknowledged. The NSF NCSA and DoD HPCMP provided grants of computational time.

4.6 Supporting Experimental Information

4.6.1 Materials and General Methods

Commercial reagents of the highest available purity from Aldrich, Fisher, and/or VWR were used without further purification unless stated otherwise. Acetonitrile and water used for the kinetics experiments and HPLC analysis were HPLC grade and obtained from a Milli-Q UV Plus water purification system, respectively. Analytical and preparative thin layer chromatography (TLC) was performed on silica gel 60 (Fisher and Aldrich, respectively).

Irradiation was performed in vessels sealed under a N_2 atmosphere using high-intensity diode light sources from Opto Technology with light output at 375 ± 7 nm. Light intensity was controlled with a custom-made constant-current controller. UV-vis spectra were recorded on a Cary 50 UV-vis spectrophotometer.

HPLC was performed on a Shimadzu Prominence system with an LC-20AT solvent delivery unit, DGU-20A5 degasser, SPD-M20A photodiode array detector, CBM-20A system controller and Rheodyne 7725i manual injector or on a Waters system with a 600E multisolvent delivery system with He gas solvent sparging, 996 photodiode array detector, and Rheodyne 7725i manual injector. Three columns were used for the HPLC analysis, as specified in the separation conditions: J.T. Baker C_{18} column (25 cm × 4.6 mm, 5 μm particles), Supleco C_{18} column (15 cm × 4.6 mm, 5 μm particles), or Agilent Hypersil AA-ODS (C_{18}) column (20 cm × 2.1 mm, 5 μm particles).

High-resolution mass spectrometry (HRMS) was performed on Micromass 70-VSE mass spectrometer at the University of Illinois Mass Spectrometry Center.

^{1}H NMR spectra of macrocycles **1**–**11** and synthetic intermediates were recorded on 400 or 500 MHz Unity-INOVA Varian spectrometers at room temperature (~20 °C). Chemical shifts are reported in ppm downfield from that of tetramethylsilane and are referenced to either the residual ^{1}H resonances or the ^{13}C resonances of the deuterated solvents. Spin multiplicities are reported as singlet (s), doublet (d), triplet (t), quartet (q) and quintet (quint) with coupling constants (*J*) given in Hz or multiplet (m), broad (br) or apparent (app).

4.6.2 Synthesis and Characterization of Disulfides 1–11

2-(6-Indan-1-one)acetic acid (**S38**) and 3-(6-indan-1-one)propionic acid (**S39**) were prepared according to methods reported in refs. 23 and 24, respectively. Fig. 4.6 shows the synthesis of disulfides **1–11** (shown in blue). The synthetic procedures for compounds that were not prepared using a general method appear at the ends of the subsections for the general methods for similar compounds.

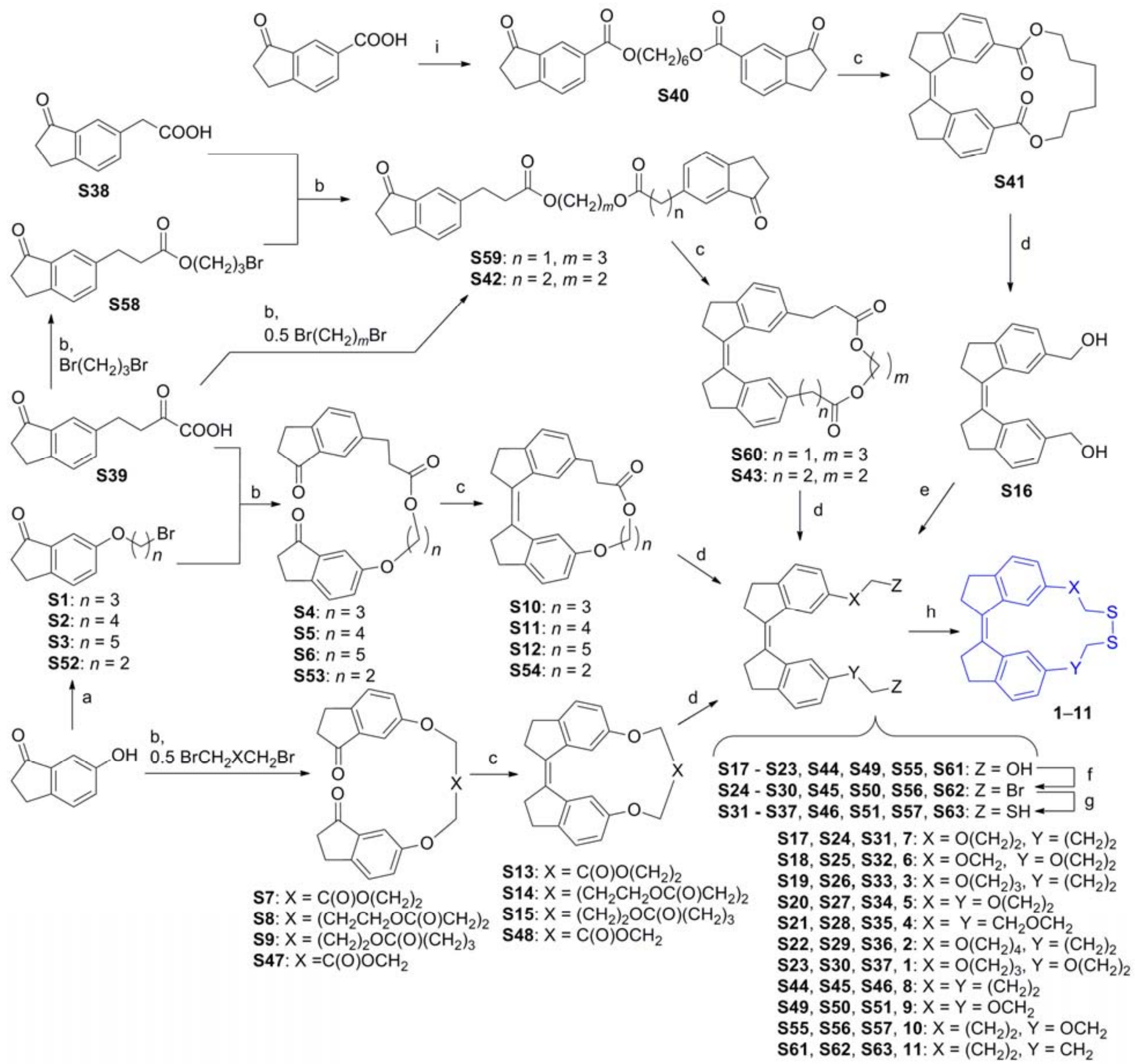

Fig. 4.6. Synthesis of **1**–**11**. Reaction conditions: a: $Br(CH_2)_nBr$, Bu_4NBr, K_2CO_3, acetone, reflux; b: Bu_4NBr, K_2CO_3, DMF, 65–70 °C; c: $TiCl_4$, Zn, THF, reflux; d: $LiAlH_4$, THF, reflux; e: NaH, $BrCH_2CH_2OTHP$, DMF, RT, then THF/1 M HCl, RT; f: CBr_4, PPh_3, acetone, CH_2Cl_2, RT; g: thiourea, DMF, 80 °C, then NaOH, RT, then HCl, RT; h: I_2, NEt_3, $CHCl_3$, RT; i: $Br(CH_2)_6Br$, Bu_4NBr, K_2CO_3, acetone, reflux.

General Procedure for the Synthesis of S1–S3 and S52

6-Hydroxyindanone (300 mg), potassium carbonate (1.5 equiv.), and tetrabutylammonium bromide (0.1 equiv.) were combined in acetone (20 mL). Dibromoalkane (1,3-dibromopropane for **S1**, 1,4-dibromobutane for **S2**, 1,5-dibromopantane for **S3**, 1,2-dibromoethane for **S52**) (6.0 equiv.) was added, and the resulting mixture was heated to reflux in air. After ~16 h, the mixture was cooled to RT. The mixture was poured into water (60 mL) and the product was extracted with Dichloromethane (3 × 40 mL). The combined organic phase was dried over magnesium sulfate, filtered, and concentrated to a small volume under reduced pressure. The crude product was purified by flash column chromatography eluting with hexanes and then Dichloromethane to afford pure product as a pale yellow solid.

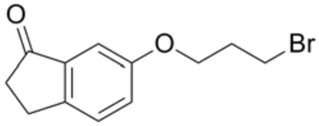

6-(3-bromopropyloxy)indanone, S1: Yield: 75%. ^{1}H NMR (CDCl$_3$, 400 MHz): δ 2.33 (quint, ^3J = 6.0 Hz, 2H), 2.72 (m, 2H), 3.07 (t, ^3J = 5.6 Hz, 2H), 3.60 (t, ^3J = 6.4 Hz, 2H), 4.13 (t, ^3J = 6.0 Hz, 2H), 7.18 (m, 2H), 7.37 (m, 1H).

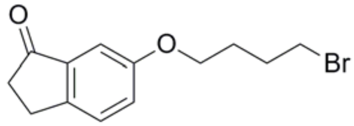

6-(4-bromobutyloxy)indanone, S2: Yield: 74%. ^{1}H NMR (CDCl$_3$, 400 MHz): δ 1.96 (m, 2H), 2.07 (m, 2H), 2.71 (m, 2H), 3.07 (t, ^3J = 5.6 Hz, 2H), 3.49 (t, ^3J = 6.8 Hz, 2H), 4.02 (t, ^3J = 6.4 Hz, 2H), 7.18 (m, 2H), 7.37 (m, 1H).

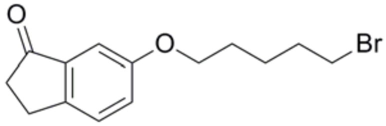

6-(5-bromopentyloxy)indanone, S3: Yield: 81%. ^{1}H NMR (CDCl$_3$, 500 MHz): δ 1.62 (m, 2H), 1.82 (quint, ^3J = 7.0 Hz, 2H), 1.94 (quint, ^3J = 7.0 Hz, 2H), 2.71 (m, 2H), 3.06 (t, ^3J = 5.5 Hz, 2H), 3.44 (t, ^3J = 7.0 Hz, 2H), 3.99 (t, ^3J = 6.5 Hz, 2H), 7.18 (m, 2H), 7.36 (d, ^3J = 8.0 Hz, 1H).

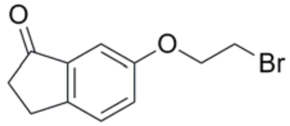

6-(2-bromoethyl)indanone, S52: Yield: 54%. ^{1}H NMR (CDCl$_3$, 400 Mhz): δ 2.72 (m, 2H), 3.08 (br t, ^3J = 5.9 Hz, 2 H), 3.65 (t, ^3J = 6.1 Hz, 2H), 4.32 (t, ^3J = 6.2 Hz, 2H), 7.17 (br d, ^4J = 2.6 Hz, 1H), 7.23 (dd, ^3J = 8.4 Hz, ^4J = 2.6 Hz), 7.39 (dq, ^3J = 8.4 Hz, ^4J = 0.6 Hz).

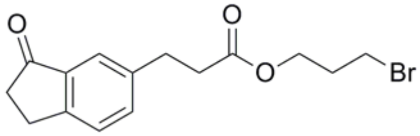

3-bromopropyl indanon-6-propanoate, S58: Indanon-6-propanoic acid (1.0 g), potassium carbonate (2 equiv.), tetrabutylammonium bromide (0.1 equiv.), and 1,3-dibromopropane (6 equiv.) were combined in DMF (30 mL) and stirred at 70 °C overnight. The mixture was cooled to RT, water was added, and the product was extracted with dichloromethane (3 × 40mL). The organic phase was washed with water, dried over magnesium sulfate, filtered, and concentrated to a brown oil under vacuum. The crude product was purified with flash column chromatography eluting with a gradient from hexanes to dichloromethane to afford the product as pale yellow solid. Yield: 86%. ^{1}H NMR ($CDCl_3$, 500MHz): δ 2.14 (quintet, $^3J = 6.5$ Hz, 2H), 2.68 (t, $^3J = 7.5$ Hz, 2H), 2.71 (m, 2H), 3.02 (t, $^3J = 7.5$ Hz, 2H), 3.12 (t, $^3J = 6.5$ Hz, 2H), 3.37 (t, $^3J = 6.5$ Hz, 2H), 4.20 (q, $^3J = 6.0$Hz, 2H), 7.42 (dd, $^3J = 8.0$ Hz, $^5J = 1.0$ Hz, 1H), 7.46 (dd, $^3J = 8.0$ Hz, $^4J = 2.0$ Hz, 1H), 7.60 (s, 1H).

General Procedure for the Synthesis of Compounds S4–S6 and S53

Indanon-6-propanoic acid (~300 mg), potassium carbonate (1.5 equiv.), compound **S1**, **S2**, **S3**, or **S52** (1.0 equiv.), and tetrabutylammonium bromide (0.1 equiv.) were combined in dry DMF (20 mL) and heated at 65–70 °C for ~16–20 h. The mixture was cooled to RT, dichloromethane (100 mL) was added, and the mixture was washed with water (4 × 100 mL), using brine to assist in the separation of emulsions. The organic phase was dried over magnesium sulfate, filtered, and concentrated under vacuum to afford **S4–S6** or **S53** as light brown solids, which were sufficiently pure for subsequent steps.

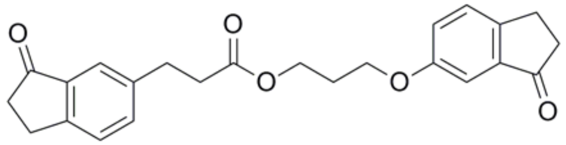

3-(indanon-6-oxy)propyl indanon-6-propanoate, S4: Yield: 85%. ^{1}H NMR ($CDCl_3$, 400 MHz): δ 2.09 (quint, $^3J = 6.0$ Hz, 2H), 2.68 (m, 6H), 3.00 (t, $^3J = 7.6$ Hz, 2H), 3.08 (m, 4H), 3.99 (t, $^3J = 6.4$ Hz, 2H), 4.26 (t, $^3J = 6.4$ Hz, 2H), 7.16 (m, 2H), 7.38 (m, 2H), 7.45 (dd, $^3J = 7.6$ Hz, $^4J = 1.6$ Hz, 1H), 7.58 (d, $^4J = 1.2$ Hz, 1H).

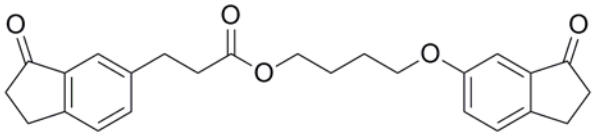

4-(indanon-6-oxy)butyl indanon-6-propanoate, S5: Yield: 86%. ^{1}H NMR ($CDCl_3$, 500 MHz): δ 1.80 (m, 4H), 2.64 (t, $^3J = 8.0$ Hz, 2H), 2.69 (m, 4H), 3.00 (t, $^3J = 8.0$ Hz, 2H), 3.06 (t,

^3J = 6.0 Hz, 2H), 3.09 (t, ^3J = 6.0 Hz, 2H), 3.98 (t, ^3J = 6.0 Hz, 2H), 4.13 (t, ^3J = 6.0 Hz, 2H), 7.16 (m, 2H), 7.36 (dd, ^3J = 8.0 Hz, ^4J = 1.0 Hz, 1H), 7.40 (dd, ^3J = 8.0 Hz, ^4J = 1.0 Hz, 1H), 7.45 (dd, ^3J = 8.0 Hz, ^4J = 2.0 Hz, 1H), 7.57 (s, 1H).

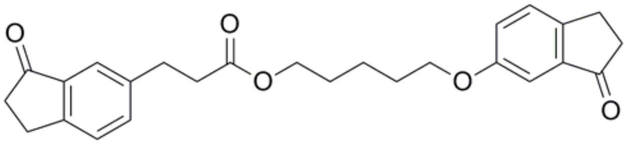

5-(indanon-6-oxy)pentyl indanon-6-propanoate, S6: Yield: 86%. ^{1}H NMR ($CDCl_3$, 500 MHz): δ 1.51 (m, 2H), 1.70 (quint, ^3J = 7.0 Hz, 2H), 1.82 (quint, ^3J = 7.0 Hz, 2H), 2.70 (m, 6H), 3.03 (t, ^3J = 8.0 Hz, 2H), 3.09 (t, ^3J = 5.5 Hz, 2H), 3.12 (t, ^3J = 5.5 Hz, 2H), 3.99 (t, ^3J = 6.5 Hz, 2H), 4.11 (t, ^3J = 6.5 Hz, 2H), 7.19 (m, 2H), 7.38 (dd, ^3J = 7.0 Hz, ^4J = 2.5 Hz, 1H), 7.42 (d, ^3J = 7.5 Hz, 1H), 7.47(dd, ^3J = 8.0 Hz, ^4J = 2.0 Hz, 1H), 7.61 (s, 1H).

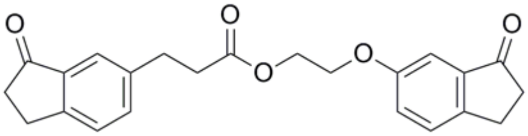

2-(indanon-6-oxy)ethyl indanon-6-propanoate, S53: Yield: 89%. ^{1}H NMR ($CDCl_3$, 400 MHz,): δ 2.09 (quint, ^3J = 6.3 HZ, 2H), 2.66 (t, ^3J = 7.8 Hz, 2H), 2.67 (m, 2H), 2.72 (m, 2H), 3.00 (t, ^3J = 7.7 Hz, 2H), 3.07 (br t, ^3J = 5.3 Hz, 2H), 3.08 (br t, ^3J = 5.5 Hz, 2H), 3.99 (t, ^3J = 6.1 Hz, 2H), 4.26 (t, ^3J = 6.2 Hz, 2H), 7.14 (br d, ^4J= 2.5 Hz, 1H), 7.16 (dd, ^3J = 8.3 Hz, ^4J = 2.5 Hz, 1H), 7.38 (dd, ^3J = 8.3 Hz, ^4J = 0.6 Hz, 1H), 7.39 (dd, ^3J = 8.9 Hz, ^4J = 0.4 Hz, 1H), 7.45 (dd, ^3J = 7.9 Hz, ^4J = 1.7 Hz, 1H), 7.58 (d, ^4J = 1.0 Hz, 1H).

General Procedure for the Synthesis of S7–S9 and S47

To a solution of 6-hydroxyindanone (0.70 g) in 20 mL dry DMF was added dibromoester (3-bromopropyl 2-bromoacetate for **S7**, bis(3-bromopropyl) succinate for **S8**, 3-bromopropyl 4-bromobutanoate for **S9**, 2-bromoethyl 2-bromoacetate for **S47**) (0.5 equiv.), tetrabutylammonium bromide (0.1 equiv.), and excess potassium carbonate (2 equiv.) under N_2. The resulting mixture was stirred at 65 °C overnight. Upon cooling to RT, dry dichloromethane (50 mL) was added, and the solid was removed via filtration. The filtrate was washed with water (3 × 100 mL). The organic phase was dried over magnesium sulfate and filtered. Evaporation of the solvent under reduced pressure afforded **S7–S9** or **S47** as brown solids, which were sufficiently pure for subsequent steps.

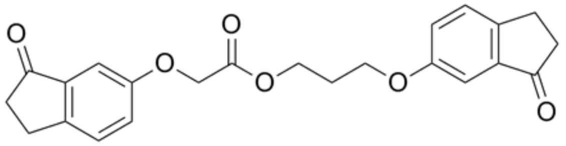

3-(indanon-6-oxy)propyl 2-(indanon-6-oxy)acetate, S7: Yield: 75%. ^{1}H NMR (CDCl$_3$, 500 MHz): δ 2.16 (quint, ^3J = 6.0 Hz, 2H), 2.71 (m, 4H), 3.06 (m, 4H), 4.01 (t, ^3J = 6.0 Hz, 2H), 4.41 (t, ^3J = 6.0 Hz, 2H), 4.68 (s, 2H), 7.11 (d, ^4J = 3.0 Hz, 1H), 7.13 (d, ^4J = 2.5 Hz, 1H), 7.17 (dd, ^3J = 8.5 Hz, ^4J = 2.5 Hz, 1H), 7.27 (dd, ^3J = 8.5 Hz, ^4J = 3.0 Hz, 1H), 7.36 (d, ^3J = 8.5 Hz, 1H), 7.39 (d, ^3J = 8.5 Hz, 1H).

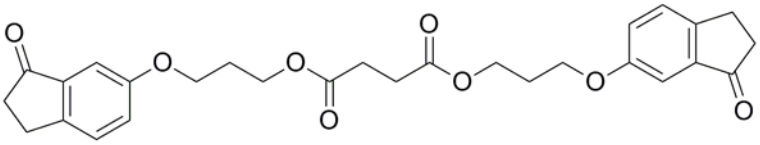

bis(3-(indanon-6-oxy)propyl) succinate, S8: Yield: 95%. ^{1}H NMR (CDCl$_3$, 500 MHz): δ 2.14 (quint, ^3J = 6.0 Hz, 4H), 2.66 (s, 4H), 2.73 (m, 4H), 3.08 (t, ^3J = 6.0 Hz, 4H), 4.08 (t, ^3J = 6.0 Hz, 4H), 4.30 (t, ^3J = 6.0 Hz, 2H), 7.24 (m, 4H), 7.37 (m, 2H).

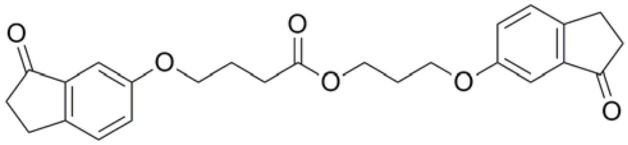

3-(indanon-6-oxy)propyl 4-(indanon-6-oxy)butanoate, S9: Yield: 91%. ^{1}H NMR (CDCl$_3$, 500 MHz): δ 2.14 (m, 4H), 2.54 (t, ^3J = 7.5 Hz, 2H), 2.72 (m, 4H), 3.07 (m, 4H), 4.03 (t, ^3J = 6.0 Hz, 2H), 4.08 (t, ^3J = 6.0 Hz, 2H), 4.30 (t, ^3J = 6.0 Hz, 2H), 7.17 (m, 4H), 7.37 (m, 2H).

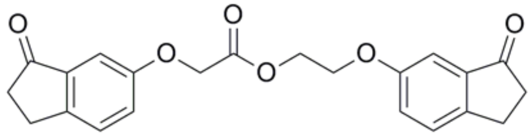

2-(indanon-6-oxy)ethyl 2-(indanon-6-oxy)acetate, S47: Yield: 78%. ^{1}H NMR (CDCl$_3$, 500 MHz): δ 2.72 (m, 4H), 3.08 (m, 4H), 4.23 (t, ^3J = 4.5 Hz, 2H), 4.58 (t, ^3J = 4.5 Hz, 2H), 4.73 (s, 2H), 7.13 (d, ^4J = 3.0 Hz, 1H), 7.17 (d, ^4J = 2.0 Hz, 1H), 7.22 (dd, ^3J = 8.5 Hz, ^4J = 3.0 Hz, 1H), 7.29 (dd, ^3J = 8.5 Hz, ^4J = 3.0 Hz, 1H), 7.40 (m, 2H).

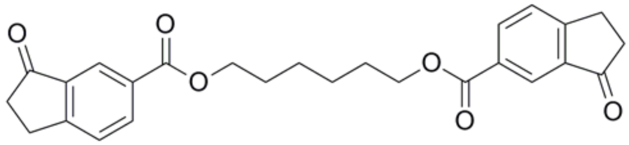

1,6-bis(indanon-6-carboxylate)hexane, S40: To a solution of indanone-6-carboxylic acid (2.5 g) in 120 mL acetone was added 1,6-dibromohexane (0.5 equiv.), tetrabutylammonium bromide (0.1 equiv.), and excess potassium carbonate (3 equiv.). The resulting mixture was refluxed overnight. Upon cooling to RT, water was added and the product was extracted with dichloromethane. The combined organic phase was dried over magnesium sulfate followed by filtration and evaporation of the solvent to afford compound **S40** as a white solid, which was sufficiently pure for subsequent steps. Yield: 96%. ^{1}H NMR (CDCl$_3$, 500 MHz): δ 1.54 (m, 4H), 1.83 (m, 4H), 2.77 (m, 4H), 3.22 (t, ^3J = 6.0 Hz, 4H), 4.36 (t, ^3J = 7.0 Hz, 4H), 7.57 (d, ^3J = 8.0 Hz, 2H), 8.28 (dd, ^4J = 2.0 Hz, ^3J = 8.0 Hz, 2H), 8.41 (s, 2H).

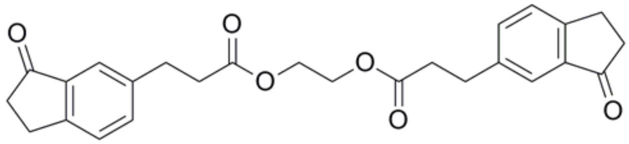

1,2-bis(indanon-6-propanoate)ethane, S42: Indanon-6-propanoic acid (1.01 g), potassium carbonate (1.38 g), tetrabutylammonium bromide (166 mg), and 1,2-dibromoethane (213 µL) were combined in DMF (60 mL) and heated to 70 °C. After 20 h, the mixture was cooled to RT, taken up in dichloromethane (250 mL), and washed with water (7 × 200 mL) and brine (200 mL). The organic phase was dried over magnesium sulfate, filtered, and concentrated to a brown oil under vacuum. Yield: 0.72 g (67%). ^{1}H NMR (400 MHz, CDCl$_3$): δ 7.58 (d, ^3J = 1 Hz, 2H), 7.45 (dd, ^3J = 8.0 Hz, ^4J = 1.8 Hz, 2H), 7.40 (dd, ^3J = 7.9 Hz, ^4J = 0.8 Hz, 2H), 4.24 (s, 4H), 3.10 (m, 4H), 3.00 (t, ^3J = 7.9 Hz, 4H), 2.68 (m, 4H), 2.67 (t, ^3J = 7.5 Hz, 4H).

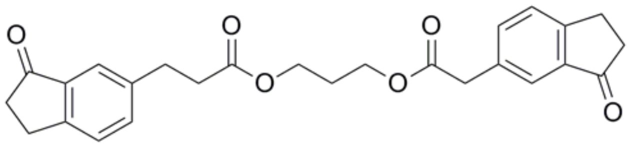

1-(indanon-6-acetate)-3-(indanon-6-propanoate)propane, S59: Indanon-6-acetic acid (0.56 g), potassium carbonate (2 equiv.), tetrabutylammonium bromide (0.1 equiv.), and **S58** (1 equiv.) were combined in DMF (30 mL) and heated to 70 °C overnight. The mixture was cooled to RT, water was added, and the product was extracted with dichloromethane (3 × 40mL). The organic phase was washed with water, dried over magnesium sulfate, filtered, and concentrated to brown solids under vacuum. Yield: 82%. ^{1}H NMR (CDCl$_3$, 400MHz): δ 1.92 (quintet, ^3J = 6.0 Hz, 2H), 2.64 (t, ^3J = 7.6 Hz, 2H), 2.69 (m, 4H), 2.99(t, ^3J = 7.6 Hz, 2H), 3.11 (m, 4H), 3.67 (s, 2H), 4.10 (q, ^3J = 6.0Hz, 4H), 7.42 (m, 3H), 7.51 (dd, ^3J = 8.0 Hz, ^4J = 1.6 Hz, 1H), 7.57 (s, 1H), 7.64 (s, 1H).

General Procedure for the McMurry Coupling Reaction

To a stirred suspension of zinc powder (12 equiv.) in dry THF (~50–100 mL), TiCl$_4$ (6 equiv.) was added over 10 minutes at 0 °C. The resulting slurry was heated at reflux for 1.5 h. A THF solution (~100–150 mL) of **S4**, **S5**, **S6**, **S7**, **S8**, **S9**, **S40**, **S42**, **S47**, **S53**, or **S59** (~600 mg) was added over a 5–7 h period by syringe pump to the refluxing reaction mixture. The reflux was continued for 20–40 minutes after the addition was complete. After cooling to RT, the reaction mixture was poured into a saturated aqueous solution of ammonium chloride, and the product was extracted with dichloromethane. The combined organic solutions were dried over magnesium sulfate, and the solvent was evaporated to afford the product **S10**, **S11**, **S12**, **S13**, **S14**, **S15**, **S41**, **S43**, **S48**, **S54**, or **S60** as a yellow solid.

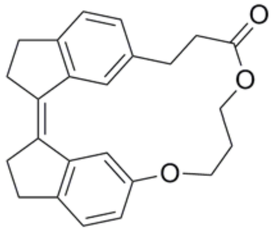

Compound S10: Yield: 82%. ^{1}H NMR (CDCl$_3$, 400 MHz): δ 2.09 (m, 2H), 2.80 (m, 6H), 2.93 (m, 6H), 4.04 (t, ^3J = 7.2 Hz, 2H), 4.33 (^3J = 5.6 Hz, 2H), 6.79 (dd, ^3J = 8.0 Hz, ^4J = 2.4 Hz, 1H), 7.08 (dd, ^3J = 7.6 Hz, ^4J = 1.2 Hz, 1H), 7.17 (d, ^3J = 8.0 Hz, 1H), 7.27 (d, ^3J = 7.6 Hz, 1H), 7.66 (d, ^4J = 2.4 Hz, 1H), 7.92 (s, 1H).

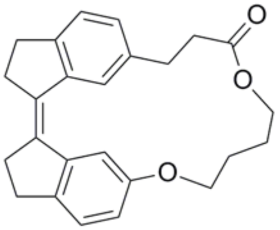

Compound S11: Yield: 78%. ^{1}H NMR (CDCl$_3$, 500 MHz): δ 1.84 (m, 2H), 1.98 (m, 2H), 2.75 (t, ^3J = 7.0 Hz, 2H), 2.82 (m, 4H), 2.94 (m, 6H), 4.05 (t, ^3J = 7.0 Hz, 2H), 4.18 (t, ^3J =

5.5 Hz, 2H), 6.76 (dd, ^3J = 8.5 Hz, ^4J = 2.5 Hz, 1H), 7.04 (dd, ^3J = 8.0 Hz, ^4J = 1.5 Hz, 1H), 7.17 (d, ^3J = 8.5 Hz, 1H), 7.23 (d, ^3J = 8.0 Hz, 1H), 7.60 (d, ^4J = 2.5 Hz, 1H), 8.02 (s, 1H).

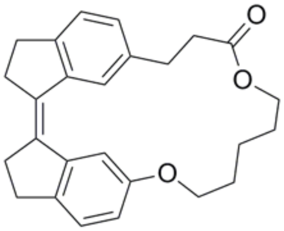

Compound S12: Yield: 70%. ^{1}H NMR (CDCl$_3$, 500 MHz): δ 1.69 (m, 4H), 1.79 (quint, ^3J = 6.0 Hz, 2H), 2.69 (m, 2H), 2.81 (t, ^3J = 7.0 Hz, 4H), 2.94 (m, 6H), 3.99 (t, ^3J = 5.5 Hz, 2H), 4.20 (t, ^3J = 5.5 Hz, 2H), 6.72 (dd, ^3J = 8.0 Hz, ^4J = 2.5 Hz, 1H), 7.00 (dd, ^3J = 7.5 Hz, ^4J = 1.5 Hz, 1H), 7.19 (d, ^3J = 7.5 Hz, 1H), 7.20(d, ^3J = 8.0 Hz, 1H), 7.68 (d, ^4J = 2.5 Hz, 1H), 8.05(s, 1H).

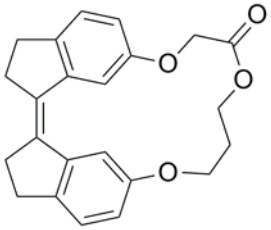

Compound S13: Yield: 61%. ^{1}H NMR (CDCl$_3$, 500 MHz): δ 2.13 (quint, ^3J = 6.0 Hz, 2H), 2.81 (m, 4H), 2.92 (m, 4H), 4.15 (t, ^3J = 6.5 Hz, 2H), 4.44 (t, ^3J = 5.5 Hz, 2H), 4.69 (s, 2H), 6.82 (dd, ^3J = 8.0 Hz, ^4J = 2.5 Hz, 1H), 6.88 (dd, ^3J = 8.5 Hz, ^4J = 2.5 Hz, 1H), 7.18 (d, ^3J = 8.5 Hz, 1H), 7.21 (d, ^3J = 8.0 Hz, 1H), 7.58 (d, ^4J = 2.5 Hz, 1H), 7.59 (d, ^4J = 2.5 Hz, 1H).

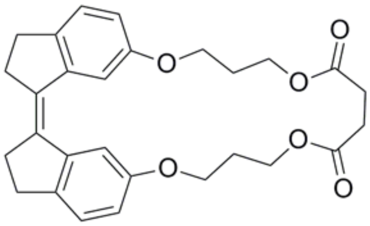

Compound S14: Product containing 24% *E* isomer was used without further isolation. Yield: 70% (*Z* + *E*). ^{1}H NMR of *Z*-**S14** (CDCl$_3$, 500 MHz): δ 2.07 (quint, ^3J = 6.0 Hz, 4H), 2.65 (s, 4H), 2.84 (t, ^3J = 6.5 Hz, 4H), 2.95 (t, ^3J = 6.5 Hz, 4H), 4.09 (t, ^3J = 6.0 Hz, 4H), 4.28 (t, ^3J = 6.0 Hz, 2H), 6.77 (dd, ^3J = 8.5 Hz, ^4J = 2.0 Hz, 2H), 7.20 (d, ^3J = 8.5 Hz, 2H), 7.71 (d, ^4J = 2.0 Hz, 2H).

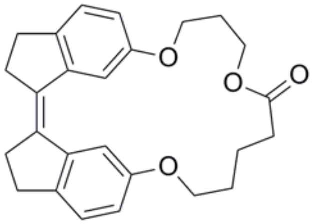

Compound S15: Yield: 73%. ^{1}H NMR (CDCl$_3$, 500 MHz): δ 2.13 (m, 4H), 2.60 (m, 2H), 2.83 (m, 4H), 2.93 (m, 4H), 3.94 (t, ^3J = 6.0 Hz, 4H), 4.34 (t, ^3J = 5.5 Hz, 2H), 6.78 (dd, ^3J = 8.5 Hz, ^4J = 2.5 Hz, 1H), 6.79 (dd, ^3J = 8.5 Hz, ^4J = 2.5 Hz, 1H), 7.19 (d, ^3J = 8.5 Hz, 2H), 7.55 (d, ^4J = 2.5 Hz, 1H), 7.57 (d, ^4J = 2.5 Hz, 1H).

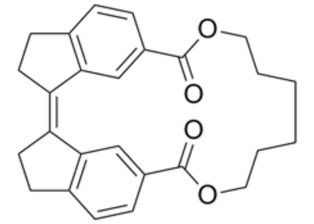

Compound S41: Yield: 65%. ^{1}H NMR (CDCl$_3$, 500 MHz): δ 1.51 (m, 4H), 1.80 (m, 4H), 2.86 (t, ^3J = 7.0 Hz, 4H), 3.04 (t, ^3J = 7.0 Hz, 4H), 4.35 (t, ^3J = 5.5 Hz, 4H), 7.39 (d, ^3J = 8.0 Hz, 2H), 7.95 (dd, ^3J = 8.0 Hz, ^4J = 1.5 Hz, 2H), 8.60 (d, ^4J = 1.5 Hz, 2H).

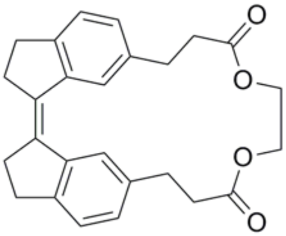

Compound S43: Yield: 76%. ^{1}H NMR (400 MHz, CDCl$_3$): δ 2.69 (m, 4H), 2.80 (m, 4H), 2.93 (t, ^3J = 4H),2.96 (m, 4H), 4.31 (s, 4H),7.01 (d, ^3J = 7.7 Hz, 2H), 7.23 (d, ^3J = 7.8 Hz, 2H), 7.96 (d, ^4J = 0.8 Hz, 2H).

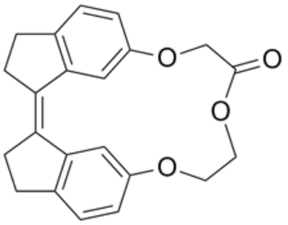

Compound S48: Yield: 52%. ^{1}H NMR (CDCl$_3$, 500 MHz): δ 2.81 (m, 4H), 2.92 (m, 4H), 4.35 (t, ^3J = 4.0 Hz, 2H), 4.56 (t, ^3J = 4.8 Hz, 2H), 4.67 (s, 2H), 6.77 (dd, ^3J = 8.5 Hz, ^4J =

2.5 Hz, 1H), 6.89 (dd, ^3J = 8.0 Hz, ^4J = 2.5 Hz, 1H), 7.18 (d, ^3J = 8.5 Hz, 1H), 7.22 (d, ^3J = 8.0 Hz, 1H), 7.45 (d, ^4J = 2.5 Hz, 1H), 7.53 (d, ^4J = 2.5 Hz, 1H).

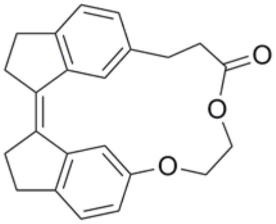

Compound S54: Yield 78%. ^{1}H NMR ($CDCl_3$, 400 MHz): δ 2.76-2.84 (br m, 6H), 2.89-2.96 (br m, 4H), 3.03 (br m, 2H), 4.40 (m, 2H), 4.28 (m, 2H), 6.80 (dd, ^3J = 8.2 Hz, ^4J = 2.4 Hz, 1H), 7.03 (dd, ^3J = 7.8 Hz, ^4J = 1.5 Hz, 1H), 7.18 (dd, ^3J = 8.1 Hz, ^4J = 0.4 Hz, 1H), 7.22 (dd, ^3J = 7.6 Hz, ^4J = 0.5 Hz, 1H), 7.61 (d, ^4J = 2.3 Hz, 1H), 7.82 (br s, 1H),

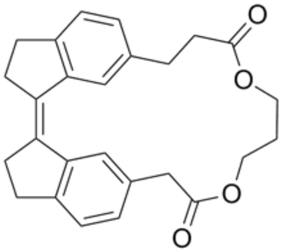

Compound S60: Yield: 60%. ^{1}H NMR ($CDCl_3$, 500MHz): δ 1.98 (quintet, ^3J = 5.5 Hz, 2H), 2.66 (t, ^3J = 8.0 Hz, 2H), 2.80 (t, ^3J = 7.0 Hz, 4H), 2.88 (t, ^3J = 8.0 Hz, 2H), 2.96(m, 4H), 3.60 (s, 2H), 4.17 (t, ^3J = 5.5 Hz, 2H), 4.35 (t, ^3J = 5.5 Hz, 2H), 7.01 (d, ^3J = 7.5 Hz, 1H), 7.12 (d, ^3J = 7.5 Hz, 1H), 7.20 (d, ^3J = 7.5 Hz, 1H), 7.28 (overlap with solvent peak, 1H), 7.95 (s, 2H).

General Procedure for the Reduction of the Macrocyclic Esters

To a stirred solution of ester **S10**, **S11**, **S12**, **S13**, **S14**, **S15**, **S41**, **S43**, **S48**, **S54**, or **S60** (~400 mg) in dry THF (~40 mL), $LiAlH_4$ (2 equiv.) was added under N_2. The resulting mixture was heated at reflux for 4 h. After cooling to RT, the reaction was quenched with water and the solid was removed by filtration. The filtrate was concentrated to a small volume, dissolved in Dichloromethane, washed with water, and dried over magnesium sulfate. The solvent was evaporated, and the product (**S17**, **S18**, **S19**, **S20**, **S22**, **S23**, **S16**, **S44**, **S49**, **S55**, or **S61**) was used without further purification.

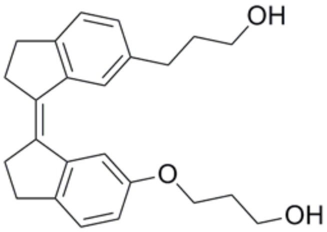

(*Z*)-6-(3-hydroxypropyl)-6′-(3-hydroxypropyloxy)biindanylidene, S17: Yield: 67%. ^{1}H NMR (CDCl$_3$, 400 MHz): δ 1.90 (m, 2H), 2.02 (quint, ^3J = 6.0 Hz, 2H), 2.66 (t, ^3J = 8.0 Hz, 2H), 2.81 (m, 4H), 2.94 (m, 4H), 3.69 (t, ^3J = 6.8 Hz, 2H), 3.85 (^3J = 5.6 Hz, 2H), 4.13 (t, ^3J = 6.0 Hz, 2H), 6.75 (dd, ^3J = 8.4 Hz, ^4J = 2.4 Hz, 1H), 7.00 (dd, ^3J = 8.0 Hz, ^4J = 1.2 Hz, 1H), 7.19 (d, ^3J = 8.4 Hz, 1H), 7.22 (d, ^3J = 8.0 Hz, 1H), 7.66 (d, ^4J = 2.4 Hz, 1H), 7.95 (s, 1H).

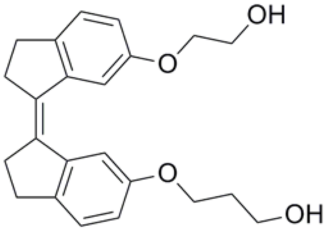

(*Z*)-6-(2-hydroxyethyloxy)-6′-(3-hydroxypropyloxy)biindanylidene, S18: Yield: 87%. ^{1}H NMR (CDCl$_3$, 400 MHz): δ 2.02 (quint, ^3J = 5.6 Hz, 2H), 2.81 (m, 4H), 2.92 (m, 4H), 3.89 (m, 4H), 4.01 (t, ^3J = 4.8 Hz, 2H), 4.12 (t, ^3J = 6.0 Hz, 2H), 6.74 (dd, ^3J = 8.0 Hz, ^4J = 2.4 Hz, 1H), 6.76(dd, ^3J = 8.4 Hz, ^4J = 2.4 Hz, 1H), 7.18 (d, ^3J = 8.4 Hz, 2H), 7.67 (two overlapping doublets, ^4J = 2.4 Hz, 2H).

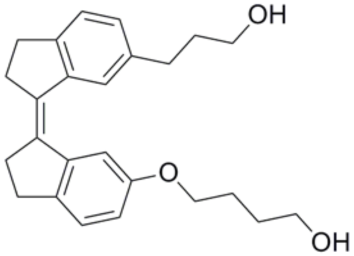

(*Z*)-6-(3-hydroxypropyl)-6′-(4-hydroxybutoxy)biindanylidene, S19: Yield: 87%. ^{1}H NMR (CDCl$_3$, 500 MHz): δ 1.75 (m, 2H), 1.88 (m, 4H), 2.67 (t, ^3J = 8.0 Hz, 2H), 2.81 (m, 2H), 2.94 (m, 4H), 3.70 (m, 4H), 3.99 (t, ^3J = 6.0 Hz, 2H), 6.75 (dd, ^3J = 8.5 Hz, ^4J = 2.5 Hz, 1H), 7.01 (dd, ^3J = 8.0 Hz, ^4J = 1.5 Hz, 1H), 7.19 (d, ^3J = 8.0 Hz, 1H), 7.22 (d, ^3J = 8.0 Hz, 1H), 7.65 (d, ^4J = 2.5 Hz, 1H), 7.96 (s, 1H).

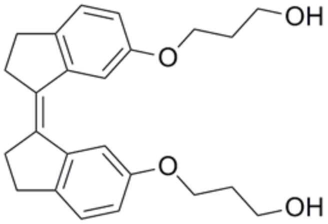

(*Z*)-6,6′-bis(3-hydroxypropyloxy)biindanylidene, S20: Product containing 20% *E* isomer was directly used without further isolation. Yield: 89% (*Z* + *E*). ^{1}H NMR of *Z*-**S20** (CDCl$_3$, 400 MHz): δ 1.99 (quint, ^3J = 6.0 Hz, 4H), 2.79 (t, ^3J = 6.8 Hz, 4H), 2.89 (m, 4H), 3.82 (t, ^3J = 5.6 Hz, 4H), 4.07 (t, ^3J = 5.6 Hz, 2H), 6.73 (dd, ^3J = 8.0 Hz, ^4J = 2.4 Hz, 2H), 7.16 (d, ^3J = 8.0 Hz, 2H), 7.63 (d, ^4J = 2.4 Hz, 2H).

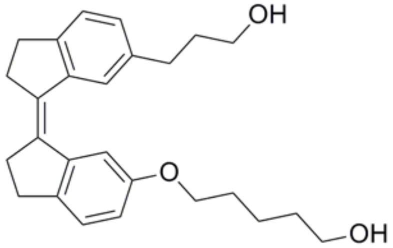

(*Z*)-6-(3-hydroxypropyl)-6′-(5-hydroxypentyloxy)biindanylidene, S22: Yield: 85%. ^{1}H NMR (CDCl$_3$, 400 MHz): δ 1.58 (m, 4H), 1.80 (m, 2H), 1.89 (m, 2H), 2.68 (t, ^3J = 7.2 Hz, 2H), 2.81 (m, 4H), 2.94 (m, 4H), 3.67 (m, 4H), 3.95 (t, ^3J = 6.4 Hz, 2H), 6.75 (dd, ^3J = 8.4 Hz, ^4J = 2.4 Hz, 1H), 7.01 (dd, ^3J = 7.6 Hz, ^4J = 1.6 Hz, 1H), 7.18 (d, ^3J = 8.4 Hz, 1H), 7.22 (d, ^3J = 7.6 Hz, 1H), 7.63 (d, ^4J = 2.4 Hz, 1H), 7.96 (s, 1H).

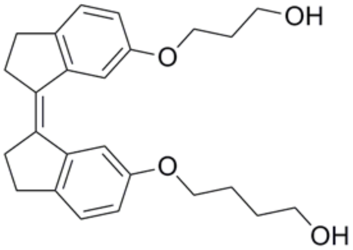

(*Z*)-6-(3-hydroxypropyloxy)-6′-(4-hydroxybutyloxy)biindanylidene, S23: Yield: 89%. ^{1}H NMR (CDCl$_3$, 500 MHz): δ 1.76 (m, 2H), 1.85 (m, 2H), 2.02 (quint, ^3J = 6.0 Hz, 2H), 2.81 (t, ^3J = 7.0 Hz, 4H), 2.92 (m, 4H), 3.70 (t, ^3J = 6.0 Hz, 2H), 3.84 (t, ^3J = 6.0 Hz, 2H), 3.97 (t, ^3J = 6.0 Hz, 2H), 4.09 (t, ^3J = 6.0 Hz, 2H), 6.75 (dd, ^3J = 8.0 Hz, ^4J = 2.5 Hz, 1H), 6.76 (dd, ^3J = 8.0 Hz, ^4J = 2.5 Hz, 1H), 7.18 (d, ^3J = 8.0 Hz, 2H), 7.65 (d, ^4J = 2.5 Hz, 1H), 7.66 (d, ^4J = 2.5 Hz, 1H).

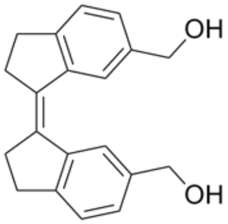

(*Z*)-6,6′-bis(3-hydroxymethyl)biindanylidene, S16: Yield: 86%. ^{1}H NMR (CDCl$_3$, 500 MHz): δ 2.24 (brs, 2H), 2.84 (t, ^{3}J = 7.0 Hz, 4H), 3.00 (t, ^{3}J = 7.0 Hz, 4H), 4.66 (s, 4H), 7.08 (dd, ^{3}J = 7.5 Hz, ^{4}J = 2.0 Hz, 2H), 7.26 (d, ^{3}J = 7.5 Hz, 2H), 8.24 (s, 2H).

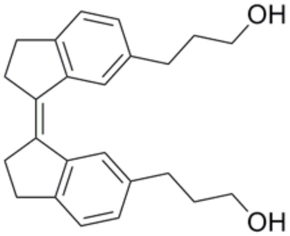

(*Z*)-6,6′-bis(3-hydroxypropyl)biindanylidene, S44: Yield: 86%. ^{1}H NMR (CDCl$_3$, 400 MHz): δ 1.93 (m, 4H), 2.66 (m, 4H), 2.81 (m, 4H), 2.96 (m, 4H), 3.71 (t, ^{3}J = 6.6 Hz, 4H), 7.01 (dd, ^{3}J = 7.7 Hz, ^{4}J = 1.4 Hz, 2 H), 7.22 (d, ^{3}J = 7.7 Hz, 2H), 7.97 (d, ^{3}J = 0.7 Hz, 2H).

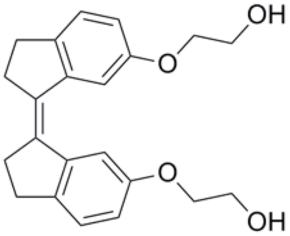

(*Z*)-6,6′-bis(2-hydroxyethyloxy)biindanylidene, S49: Yield: 89%. ^{1}H NMR (CDCl$_3$, 400 MHz): δ 2.72 (t, ^{3}J = 6.0 Hz, 2H), 2.81 (t, ^{3}J = 6.8 Hz, 4H), 2.93 (m, 4H), 3.93 (t, ^{3}J = 4.8 Hz, 4H), 4.05 (t, ^{3}J = 4.8 Hz, 4H), 6.76 (dd, ^{3}J = 8.0 Hz, ^{4}J = 2.4 Hz, 2H), 7.18 (d, ^{3}J = 8.0 Hz, 2H), 7.68 (d, ^{4}J = 2.4 Hz, 2H).

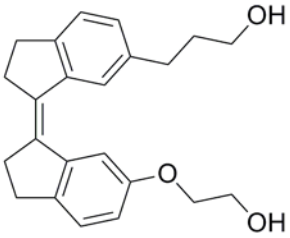

(*Z*)-6-(2-hydroxyethyloxy)-6′-(3-hydroxypropyl)biindanylidene, S55: Yield 72%. ^{1}H NMR (CDCl$_3$, 400 MHz): δ 1.93 (quint, ^{3}J = 6.9 Hz, 2H), 2.66 (br t, ^{3}J = 7.3 Hz, 2H), 2.80 (br m, 2H), 2.82 (br m, 2H), 2.94 (br t, ^{3}J = 7.6 Hz, 2H), 2.95 (br t, ^{3}J = 6.9 Hz, 2H), 3.72 (br t, ^{3}J =

6.7 Hz, 2H), 3.92 (br t, ^3J = 4.2 Hz, 2H), 4.04 (dd, ^3J = 5.0 Hz, ^4J = 4.2 Hz, 2H), 6.75 (dd, ^3J = 8.3 Hz, ^4J = 2.5 Hz, 1H), 7.00 (dd, ^3J = 7.7 Hz, ^4J = 1.5 Hz, 1H), 7.19 (d, ^3J = 8.4 Hz, 1H), 7.22 (d, ^3J = 8.1 Hz, 1H), 7.68 (d, ^4J = 2.4 Hz, 1H), 7.95 (br s, 1H).

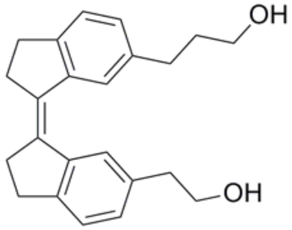

(*Z*)-6-(3-hydroxypropyl)-6′-(2-hydroxyethyl)biindanylidene, S61: Yield: 81%. ^{1}H NMR (CDCl$_3$, 500MHz): δ 1.94 (m, 2H), 2.66 (t, ^3J = 8.0 Hz, 2H), 2.82 (m, 6H), 2.96(m, 4H), 3.72 (t, ^3J = 6.5 Hz, 2H), 3.88 (t, ^3J = 7.0Hz, 2H), 7.02 (m, 2H), 7.21 (d, ^3J = 7.5 Hz, 1H), 7.24 (d, ^3J = 7.5 Hz, 1H), 7.98 (s, 1H), 8.01 (s, 1H).

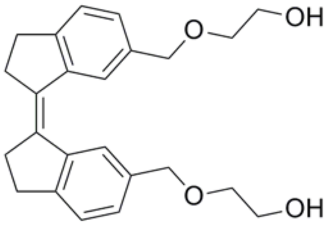

***Z*-6,6′-bis(2-hydroxyethyloxymethyl)biindanylidene, S21**: To a solution of **S16** (300 mg) in dry DMF was added NaH (4 equiv.), and the resulting mixture was stirred for 5 min. Then Br(CH$_2$)OTHP (4 equiv.) was added. The resulting mixture was stirred overnight. Water was added to quench the reaction and the product was extracted with dichloromethane. The combined organic phase was dried over magnesium sulfate, filtered, and concentrated under vacuum to afford a pale yellow oil, which was dissolved in 80 ml THF/1M HCl (3:1). The resulting solution was stirred at RT overnight and then poured into 50 mL water. The product was extracted with Dichloromethane. The combined organic phase was dried over magnesium sulfate, filtered, and concentrated under vacuum to give **S21** as a pale brown oil. The crude product was purified with preparative centrifugally-accelerated radial thin layer chromatography eluting with a gradient from ether/DCM (4:1) to ether to ether/methanol (10:1) to afford pure product as pale yellow oil. Yield: 71%. ^{1}H NMR (CDCl$_3$, 500 MHz): δ 2.83 (t, ^3J = 6.0 Hz, 4H), 2.99 (t, ^3J = 6.0 Hz, 4H), 3.60 (t, ^3J = 4.5 Hz, 4H), 3.73 (t, ^3J = 4.5 Hz, 4H), 4.52 (s, 4H), 7.08 (dd, ^3J = 7.5 Hz, ^4J = 1.0 Hz, 2H), 7.26 (d, ^3J = 7.5 Hz, 2H), 8.17 (s, 2H).

General Procedure for the Bromination of Stiff Stilbene Diols

To a stirred solution of ~300 mg diol **S17**, **S18**, **S19**, **S20**, **S21**, **S22**, **S23**, **S44**, **S49**, **S55**, or **S61** in 20 mL dichloromethane containing several drops of acetone, CBr_4 (4 equiv.) was added, and then PPh_3 (4 equiv.) was added carefully. The resulting mixture was stirred 10–15 min and then purified immediately with flash column chromatography on silica gel eluting with a gradient from hexanes to dichloromethane. The product-containing fractions were collected and the solvent was removed under reduced pressure. The product was further purified with preparative centrifugally-accelerated radial thin layer chromatography to afford the pure dibromo compound **S24**, **S25**, **S26**, **S27**, **S28**, **S29**, **S30**, **S45**, **S50**, **S56**, or **S62**.

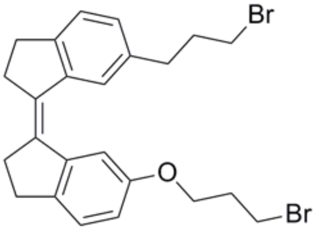

(*Z*)-6-(3-bromopropyl)-6′-(3-bromopropyloxy)biindanylidene, S24: Yield: 92%. ^{1}H NMR ($CDCl_3$, 500 MHz): δ 2.18 (m, 2H), 2.32 (quint, ^3J = 6.0 Hz, 2H), 2.77 (t, ^3J = 7.5 Hz, 2H), 2.84 (m, 4H), 2.97 (m, 4H), 3.43 (t, ^3J = 7.0 Hz, 2H), 3.63 (^3J = 6.5 Hz, 2H), 4.08 (t, ^3J = 6.0 Hz, 2H), 6.78 (dd, ^3J = 8.0 Hz, ^4J = 2.5 Hz, 1H), 7.04 (dd, ^3J = 7.5 Hz, ^4J = 2.0 Hz, 1H), 7.21 (d, ^3J = 8.0 Hz, 1H), 7.25 (d, ^3J = 7.5 Hz, 1H), 7.64 (d, ^4J = 2.5 Hz, 1H), 7.96 (s, 1H).

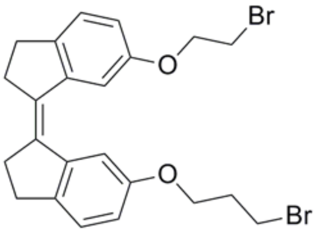

(*Z*)-6-(2-bromoethyloxy)-6′-(3-bromopropyloxy)biindanylidene, S25: Yield: 90%. ^{1}H NMR ($CDCl_3$, 500 MHz): δ 2.31 (quint, ^3J = 6.0 Hz, 2H), 2.83 (m, 4H), 2.94 (m, 4H), 3.62 (t, ^3J = 6.5 Hz, 2H), 3.64 (t, ^3J = 6.0 Hz, 2H), 4.08 (t, ^3J = 6.0 Hz, 2H), 4.27 (t, ^3J = 6.0 Hz, 2H), 6.78 (m, 2H), 7.21 (two doublet overlap, 2H), 7.63 (d, ^4J = 2.5 Hz, 1H), 7.65 (d, ^4J = 2.5 Hz, 1H).

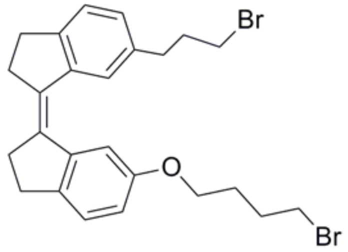

(*Z*)-6-(3-bromopropyl)-6′-(4-bromobutoxy)biindanylidene, S26: Yield: 78%. ^{1}H NMR (CDCl$_3$, 400 MHz): δ 1.93 (m, 2H), 1.99 (m, ^3J = 7.0 Hz, 2H), 2.06 (m, 2H), 2.17 (m, 2H), 2.74 (t, ^3J = 7.6 Hz, 2H), 2.81 (m, 2H), 2.94 (m, 4H), 3.42 (t, ^3J = 6.8 Hz, 2H), 3.48 (t, ^3J = 6.8 Hz, 2H), 3.95 (t, ^3J = 6.0 Hz, 2H), 6.75 (dd, ^3J = 8.4 Hz, ^4J = 2.4 Hz, 1H), 7.02 (d, ^3J = 7.6 Hz, 1H), 7.19 (d, ^3J = 8.4 Hz, 1H), 7.23 (d, ^3J = 7.6 Hz, 1H), 7.60 (d, ^4J = 2.4 Hz, 1H), 7.93 (s, 1H).

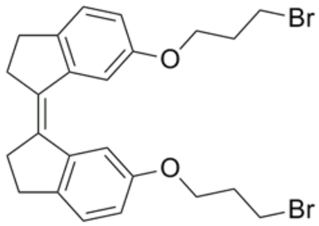

(*Z*)-6,6′-(3-bromopropyloxy)biindanylidene, S27: Product containing 9% *E* isomer was directly used without further purification. Yield (*Z* + *E*): 70%. ^{1}H NMR of *Z*-**S27** (CDCl$_3$, 500 MHz): δ 2.29 (quint, ^3J = 6.0 Hz, 4H), 2.82 (t, ^3J = 6.5 Hz, 4H), 2.93 (m, 4H), 3.60 (t, ^3J = 6.5 Hz, 4H), 4.06 (t, ^3J = 6.0 Hz, 2H), 6.76 (dd, ^3J = 8.5 Hz, ^4J = 2.5 Hz, 2H), 7.19 (d, ^3J = 8.5 Hz, 2H), 7.63 (d, ^4J = 2.5 Hz, 2H).

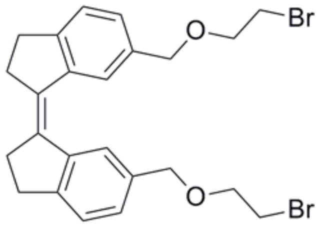

(*Z*)-6,6′-bis(2-bromoethyloxymethyl)biindanylidene, S28: Yield: 81%. ^{1}H NMR (CDCl$_3$, 500 MHz): δ 2.82 (t, ^3J = 7.0 Hz, 4H), 2.99 (t, ^3J = 7.0 Hz, 4H), 3.47 (t, ^3J = 6.5 Hz, 4H), 3.77 (t, ^3J = 6.5 Hz, 4H), 4.54 (s, 4H), 7.18 (d, ^3J = 7.5 Hz, 2H), 7.28 (d, ^3J = 7.5 Hz, 2H), 8.03 (s, 2H).

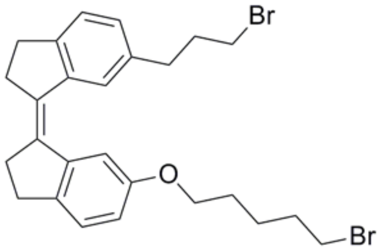

(*Z*)-6-(3-bromopropyl)-6′-(5-bromopentoxy)biindanylidene, S29: Yield: 95%. ^{1}H NMR ($CDCl_3$, 500 MHz): δ 1.61 (m, 2H), 1.80 (quint, ^3J = 7.0 Hz, 2H), 1.93 (quint, ^3J = 7.0 Hz, 2H), 2.16 (quint, ^3J = 7.0 Hz, 2H), 2.74 (t, ^3J = 7.5 Hz, 2H), 2.81 (m, 4H), 2.94 (m, 4H), 3.42 (m, 4H), 3.92 (t, ^3J = 6.0 Hz, 2H), 6.75 (dd, ^3J = 8.0 Hz, ^4J = 2.5 Hz, 1H), 7.02 (d, ^3J = 8.0 Hz, 1H), 7.18 (d, ^3J = 8.0 Hz, 1H), 7.23 (d, ^3J = 8.0 Hz, 1H), 7.60 (d, ^4J = 2.5 Hz, 1H), 7.94 (s, 1H).

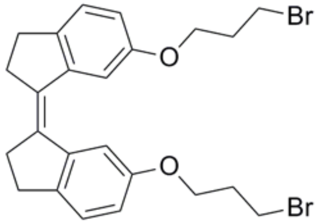

(*Z*)-6-(3-bromopropyloxy)-6′-(4-bromobutoxy)biindanylidene, S30: Yield: 72%. ^{1}H NMR ($CDCl_3$, 400 MHz): δ 1.89 (m, 2H), 2.02 (m, 2H), 2.26 (quint, ^3J = 6.0 Hz, 2H), 2.79 (t, ^3J = 6.4 Hz, 4H), 2.90 (m, 4H), 3.45 (t, ^3J = 6.8 Hz, 2H), 3.60 (t, ^3J = 6.4 Hz, 2H), 3.93 (t, ^3J = 6.0 Hz, 2H), 4.04 (t, ^3J = 6.0 Hz, 2H), 6.72 (dd, ^3J = 8.0 Hz, ^4J = 2.4 Hz, 1H), 6.73 (dd, ^3J = 8.0 Hz, ^4J = 2.4 Hz, 1H), 7.16 (d, ^3J = 8.0 Hz, 1H), 7.17 (d, ^3J = 8.0 Hz, 1H), 7.59 (d, ^4J = 2.4 Hz, 1H), 7.61 (d, ^4J = 2.4 Hz, 1H).

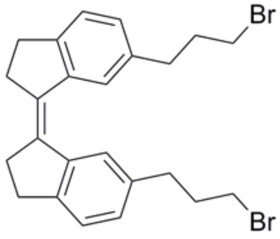

(*Z*)-6,6′-bis(3-bromopropyl)biindanylidene, S45: Yield: 52%. ^{1}H NMR ($CDCl_3$, 400 MHz): δ 2.18 (m, 4H), 2.75 (m, 4H), 2.82 (m, 4H), 2.97 (m, 4H), 3.43 (t, ^3J = 6.6 Hz, 4H), 7.03 (dd, ^3J = 7.7 Hz, ^4J = 1.4 Hz, 2H), 7.24 (d, ^3J = 7.7 Hz, 2H), 7.92 (d, ^4J = 0.7 Hz, 2H).

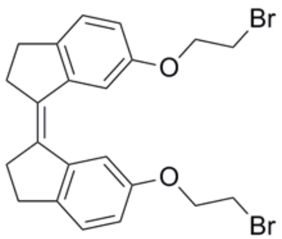

(*Z*)-6,6′-bis(2-bromoethyloxy)biindanylidene, S50: Yield: 66%.^{1}H NMR (CDCl$_3$, 500 MHz): δ 2.81 (t, ^{3}J = 7.0 Hz, 4H), 2.93 (t, ^{3}J = 7.0 Hz, 4H), 3.64 (t, ^{3}J = 6.0 Hz, 4H), 4.26 (t, ^{3}J = 6.0 Hz, 4H), 6.77 (dd, ^{3}J = 8.5 Hz, ^{4}J = 2.5 Hz, 2H), 7.20 (d, ^{3}J = 8.5 Hz, 2H), 7.63 (d, ^{4}J = 2.5 Hz, 2H).

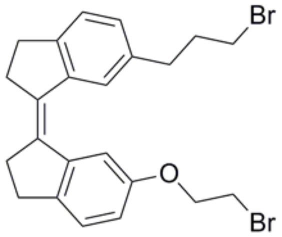

(*Z*)-6-(2-bromoethyloxy)-6′-(3-bromopropyl)biindanylidene, S56: Yield 31%. ^{1}H NMR (CDCl$_3$, 400 MHz): δ 2.18 (m, 2H), 2.75 (dd, ^{3}J = 7.7 Hz, ^{4}J = 7.2 Hz, 2H), 2.78-2.85 (br m, 4H), 2.91-2.98 (br m, 4H), 3.43 (t, ^{3}J = 6.6 Hz, 2H), 3.63 (t, ^{3}J = 6.3 Hz, 2H), 4.22 (t, ^{3}J = 6.3 Hz, 2H), 6.77 (dd, ^{3}J = 8.2 Hz, ^{4}J = 2.5 Hz, 1H), 7.03 (dd, ^{3}J = 7.6 Hz, ^{4}J = 1.5 Hz, 1H), 7.20 (d, ^{3}J = 8.2 Hz, 1H), 7.23 (d, ^{3}J = 7.7 Hz, 1H), 7.62 (d, ^{4}J = 2.4 Hz, 1H), 7.91 (br s, 1H).

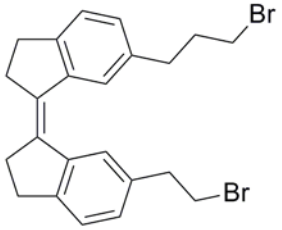

(*Z*)-6-(3-bromopropyl)-6′-(2-bromoethyl)biindanylidene, S62: Yield: 53%. ^{1}H NMR (CDCl$_3$, 500MHz): δ 2.17 (quint, ^{3}J = 7.0 Hz, 2H), 2.75 (t, ^{3}J = 7.0Hz, 2H), 2.81 (m, 4H), 2.96(m, 4H), 3.13 (t, ^{3}J = 7.5 Hz, 2H), 3.42 (t, ^{3}J = 7.0 Hz, 2H), 3.58 (t, ^{3}J = 7.5 Hz, 2H), 7.02 (m, 2H), 7.23 (d, ^{3}J = 7.5 Hz, 1H), 7.25 (overlap with solvent peak, 1H), 7.92 (s, 2H).

General Procedure for the Synthesis of Disulfides 1-11

To a solution of the dibromide **S24**, **S25**, **S26**, **S27**, **S28**, **S29**, **S30**, **S45**, **S50**, **S56**, or **S62** (~200 mg in 20 mL DMF), thiourea (4 equiv.) was added, and the resulting solution was stirred at 80 °C under N$_2$ overnight. After cooling to RT, 20 mL of degassed 1 M NaOH aqueous solution was added under N_2, and the resulting mixture was stirred at RT for 50 min, followed by acidification with degassed 1 M HCl to pH 3. The product was extracted with dichloromethane and dried with anhydrous magnesium sulfate. Filtration and evaporation of the solvent afforded dithiol **S31**, **S32**, **S33**, **S34**, **S35**, **S36**, **S37**, **S46**, **S51**, **S57**, or **S63**, which was immediately used for subsequent steps. To a solution of 1 mL triethylamine in 50 mL chloroform, a solution of iodine and a solution of the dithiol in chloroform were added via syringe pump at the same rate over ~3 h. The reaction mixture was then poured into water, 1 M HCl was added to acidify the mixture to pH 3, and a small amount of sodium thiosulfate was added to remove unreacted I_2. The organic phase was isolated and dried over magnesium sulfate, followed by filtration and evaporation of the solvent. The crude product was purified with preparative centrifugally-accelerated radial thin layer chromatography eluting with dichloromethane/hexanes (2:3) to afford the pure disulfide **7**, **6**, **3**, **5**, **4**, **2**, **1**, **8**, **9**, **10**, or **11**.

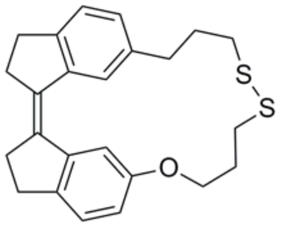

Compound 7: Yield: 25%. ^{1}H NMR (CDCl$_3$, 400 MHz): δ 2.13 (m, 4H), 2.63 (t, ^3J = 8.4 Hz, 2H), 2.81 (m, 6H), 2.94 (m, 4H), 3.00 (t, ^3J = 6.8 Hz, 2H), 4.10 (t, ^3J = 6.0 Hz, 2H), 6.73 (dd, ^3J = 8.4 Hz, ^4J = 2.4 Hz, 1H), 6.97 (dd, ^3J = 7.6 Hz, ^4J = 1.6 Hz, 1H), 7.18 (d, ^3J = 8.4 Hz, 1H), 7.21 (d, ^3J = 7.6 Hz, 1H), 7.73 (d, ^4J = 2.4 Hz, 1H), 7.96 (s, 1H). HRMS-EI (m/z) [M]$^+$ calc'd for $C_{24}H_{26}OS_2$ 394.1425, found 394.1424.

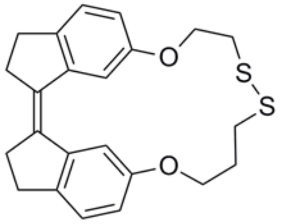

Compound 6: Yield: 23%. ^{1}H NMR (CDCl$_3$, 500 MHz): δ 2.13 (m, 2H), 2.83 (m, 4H), 2.93 (m, 4H), 2.96 (t, ^3J = 7.5 Hz, 2H), 3.12 (t, ^3J = 7.0 Hz, 2H), 4.15 (t, ^3J = 6.0 Hz, 2H), 4.25 (t, ^3J = 7.0 Hz, 2H), 6.72 (dd, ^3J = 8.0 Hz, ^4J = 2.5 Hz, 1H), 6.76 (dd, ^3J = 8.0 Hz, ^4J = 2.0 Hz, 1H), 7.19 (two doublet overlap, ^3J = 8.0 Hz, 2H), 7.70 (d, ^4J = 2.0 Hz, 1H), 7.75 (d, ^4J = 2.5 Hz, 1H). HRMS-EI (m/z) [M]$^+$ calc'd for $C_{23}H_{24}O_2S_2$ 396.1218, found 396.1221.

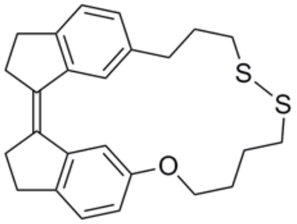

Compound 3: Yield: 26%. ^{1}H NMR (CDCl$_3$, 500 MHz): δ 1.90 (quint, ^3J = 6.5 Hz, 2H), 1.99 (m, 2H), 2.11 (m, 2H), 2.63 (t, ^3J = 8.0 Hz, 2H), 2.82 (m, 6H), 2.88 (t, ^3J = 8.0 Hz, 2H), 2.94 (m, 4H), 3.99 (t, ^3J = 5.5 Hz, 2H), 6.72 (dd, ^3J = 8.0 Hz, ^4J = 2.5 Hz, 1H), 6.99 (dd, ^3J = 7.5 Hz, ^4J = 1.5 Hz, 1H), 7.19 (d, ^3J = 8.0 Hz, 1H), 7.22 (d, ^3J = 7.5 Hz, 1H), 7.68 (d, ^4J = 2.5 Hz, 1H), 7.95 (s, 1H). HRMS-EI (m/z) [M]$^+$ calc'd for $C_{25}H_{28}OS_2$ 408.1582, found 408.1582.

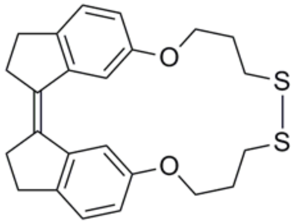

Compound 5: Yield: 29%. ^{1}H NMR (CDCl$_3$, 500 MHz): δ 2.19 (quint, ^3J = 6.0 Hz, 4H), 2.82 (t, ^3J = 7.0 Hz, 4H), 2.93 (two triplet overlap, ^3J = 7.0 Hz, 8H), 4.07 (t, ^3J = 5.5 Hz, 4H), 6.71 (dd, ^3J = 8.0 Hz, ^4J = 2.5 Hz, 2H), 7.18 (d, ^3J = 8.0 Hz, 2H), 7.80 (d, ^4J = 2.5 Hz, 2H). HRMS-EI (m/z) [M]$^+$ calc'd for $C_{24}H_{26}O_2S_2$ 410.13743, found 410.13715.

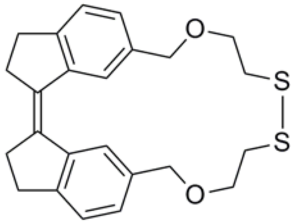

Compound 4: Yield: 34%. ^{1}H NMR (CDCl$_3$, 500 MHz): δ 2.82 (t, ^3J = 7.0 Hz, 4H), 2.96 (t, ^3J = 6.5 Hz, 4H), 2.98 (m, 4H), 3.81 (t, ^3J = 6.0 Hz, 4H), 4.47 (s, 4H), 7.13 (dd, ^3J = 7.5 Hz, ^4J = 1.5 Hz, 2H), 7.27 (d, ^3J = 7.5 Hz, 2H), 8.14 (s, 2H). HRMS-EI (m/z) [M]$^+$ calc'd for $C_{24}H_{26}O_2S_2$ 410.1374, found 410.1376.

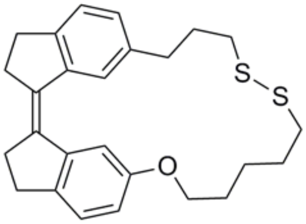

Compound 2: Yield: 24%. ^{1}H NMR (CDCl$_3$, 500 MHz): δ 1.71 (m, 2H), 1.82 (m, 4H), 2.11 (m, 2H), 2.69 (t, ^3J = 8.0 Hz, 2H), 2.77 (m, 4H), 2.82 (m, 4H), 2.94 (m, 4H), 3.97 (t, ^3J = 6.0 Hz, 2H), 6.74 (dd, ^3J = 8.5 Hz, ^4J = 2.5 Hz, 1H), 7.02 (dd, ^3J = 7.5 Hz, ^4J = 1.5 Hz, 1H), 7.18 (d, ^3J = 8.5 Hz, 1H), 7.23 (d, ^3J = 7.5 Hz, 1H), 7.69 (d, ^4J = 2.5 Hz, 1H), 8.00 (s, 1H). HRMS-EI (m/z) [M]$^+$ calc'd for $C_{26}H_{30}OS_2$ 422.1738, found 422.1741.

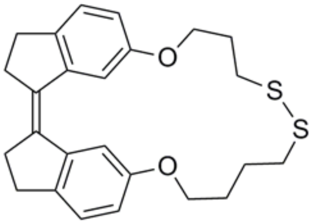

Compound 1: Yield: 25%. ^{1}H NMR (CDCl$_3$, 500 MHz): δ 1.96 (m, 4H), 2.14 (m, 2H), 2.80 (t, ^3J = 6.5 Hz, 2H), 2.82 (m, 4H), 2.93 (t, ^3J = 6.0 Hz, 4H), 2.98 (t, ^3J = 7.5 Hz, 2H), 4.00 (t, ^3J = 5.5 Hz, 2H), 4.07 (t, ^3J = 6.0 Hz, 2H), 6.72 (dd, ^3J = 8.0 Hz, ^4J = 2.5 Hz, 1H), 6.74 (dd, ^3J = 8.0 Hz, ^4J = 2.5 Hz, 1H), 7.18 (d, ^3J = 8.0 Hz, 1H), 7.19 (d, ^3J = 8.0 Hz, 1H), 7.68 (d, ^4J = 2.5 Hz, 1H), 7.72 (d, ^4J = 2.5 Hz, 1H). HRMS-EI (m/z) [M]$^+$ calc'd for $C_{25}H_{28}O_2S_2$ 424.1531, found 424.1530.

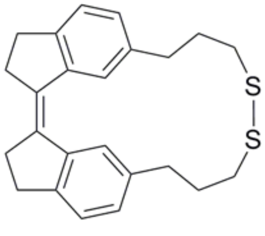

Compound 8: Yield: 26%. ^{1}H NMR (CDCl$_3$, 400 MHz): δ 2.08 (m, 4H), 2.69 (t, ^3J = 8.1 Hz, 4H), 2.82 (dd, ^3J = 7.4 Hz, ^3J = 6.6 Hz, 4H), 2.88 (t, ^3J = 7.3 Hz, 4H), 2.97 (m, 4H), 6.99 (dd, ^3J = 7.6 Hz, ^4J = 1.6 Hz, 2H), 7.23 (dd, ^3J = 7.6 Hz, ^4J = 0.5 Hz, 2H), 7.96 (d, ^4J = 1.0 Hz, 2H). HRMS-EI (m/z) [M]$^+$ calc'd for $C_{24}H_{26}S_2$ 378.1476, found 378.1473.

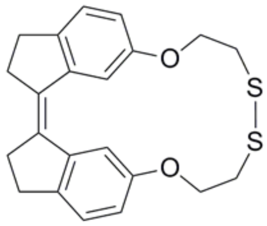

Compound 9: Yield: 29%. ^{1}H NMR ($CDCl_3$, 500 MHz): δ 2.84 (t, ^3J = 7.0 Hz, 4H), 2.94 (m, 4H), 3.09 (t, ^3J = 7.5 Hz, 4H), 4.28 (t, ^3J = 7.5 Hz, 4H), 6.78 (dd, ^3J = 8.0 Hz, ^4J = 2.5 Hz, 2H), 7.20 (d, ^3J = 8.0 Hz, 2H), 7.71 (d, ^4J = 2.5 Hz, 2H). HRMS-EI (m/z) $[M]^+$ calc'd for $C_{22}H_{22}O_2S_2$ 382.1061, found 382.1063.

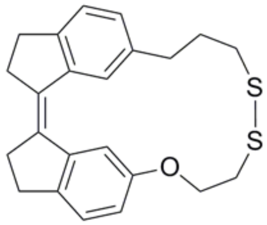

Compound 10: Yield: 37%. ^{1}H NMR ($CDCl_3$, 500 MHz): δ 2.07 (br quint, ^3J = 7.4 Hz, 2H), 2.76 (br t, ^3J = 7.1 Hz, 2H), 2.79-2.85 (br m, 4H), 2.90 (dd, ^3J = 7.7 Hz, ^4J = 7.4 Hz, 2H), 2.92-2.98 (br m, 4H), 3.09 (t, ^3J = 6.9 Hz, 2H), 4.19 (t, ^3J = = 6.9 Hz, 2H), 6.76 (dd, ^3J = 8.2 Hz, ^4J = 2.4 Hz, 1H), 6.99 (dd, ^3J = 7.7 Hz, ^4J = 1.4 Hz, 1H), 7.19 (d, ^3J = 8.2 Hz, 1H), 7.23 (d, ^3J = 7.7 Hz, 1H), 7.72 (d, ^4J = 2.4 Hz, 1H), 7.95 (br s, 1H). HRMS-EI (m/z) $[M]^+$ calc'd for $C_{23}H_{24}OS_2$ 380.1269, found 380.1268.

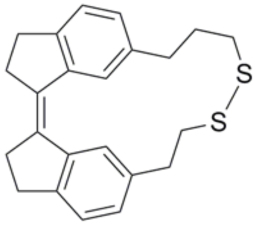

Compound 11: Yield: 25%. ^{1}H NMR ($CDCl_3$, 500MHz): δ 2.15 (m, 2H), 2.76 (t, ^3J = 8.0Hz, 2H), 2.82 (m, 4H), 2.90(m, 4H), 2.96 (m, 4H), 3.17 (t, ^3J = 8.0 Hz, 2H), 6.96 (dd, ^3J = 7.5 Hz, ^4J = 1.5 Hz, 1H), 7.01 (dd, ^3J = 7.5 Hz, ^4J = 1.5 Hz, 1H), 7.21 (d, ^3J = 7.5 Hz, 1H), 7.23 (d, ^3J = 7.5 Hz, 1H), 8.03 (s, 1H), 8.06 (1H). HRMS-EI (m/z) $[M]^+$ calc'd for $C_{23}H_{24}S_2$ 364.1319, found 364.1319.

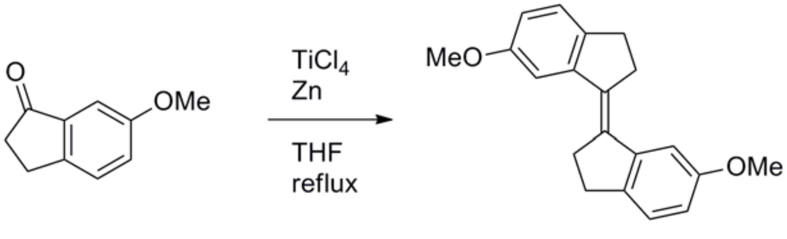

S64

(*E*)-6,6′-bismethoxybiindanylidene, S64: To a stirred suspension of zinc powder (8 equiv.) in dry THF (~30 mL), $TiCl_4$ (4 equiv.) was added over 10 minutes at 0 °C. The resulting slurry was heated at reflux for 1.5 h. A THF solution (~20 mL) of 6-methoxyindanone (~500 mg) was added over 5 min to the refluxing reaction mixture. The reflux was continued for 1 h. After cooling to RT, the reaction mixture was poured into a saturated aqueous solution of ammonium chloride, and the product was extracted with Dichloromethane. The combined organic solutions were dried over magnesium sulfate, and the solvent was evaporated. The product was purified with flash column chromatography using Dichloromethane/hexane (1:2) to afford the product as a pale yellow solid. Yield: 80% (*Z* + *E*). After recrystallizing twice from $CHCl_3$/hexane (1:1), pure *E* isomer was obtained as pale yellow solid. ^{1}H NMR ($CDCl_3$, 500 MHz): δ 3.05 (m, 4H), 3.19 (m, 4H), 3.86 (s, 6H), 6.79 (dd, ^3J = 8.5 Hz, ^4J = 2.5 Hz, 2H), 7.17 (d, ^4J = 2.5 Hz, 2H), 7.22 (d, ^3J = 8.5 Hz, 2H).

Table 4.1. Composition of photostationary states of disulfides **1**–**7** under irradiation at 375 ± 7 nm. Uncertainty is ±5% (mol)

Disulfide	Apparent fraction of *E* isomer at 340 nm
1	38%
2	62%
3	34%
4	19%
5	23%
6	4%
7	8%

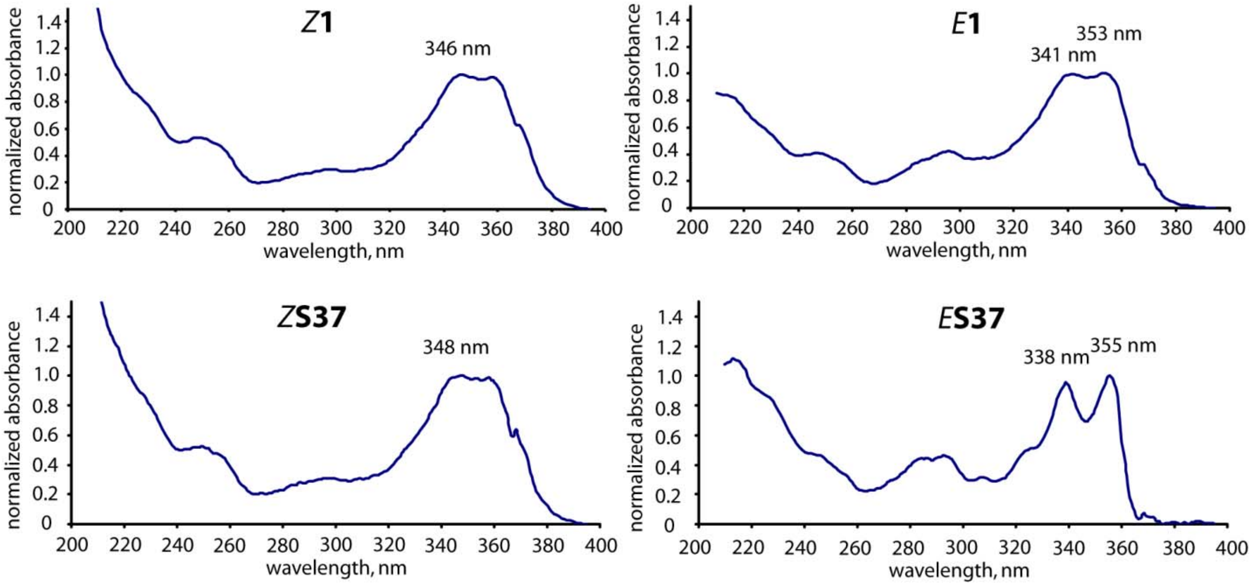

Fig. 4.7. UV spectra of the *Z* and *E* isomers of **1** and its corresponding dithiol **S37**.

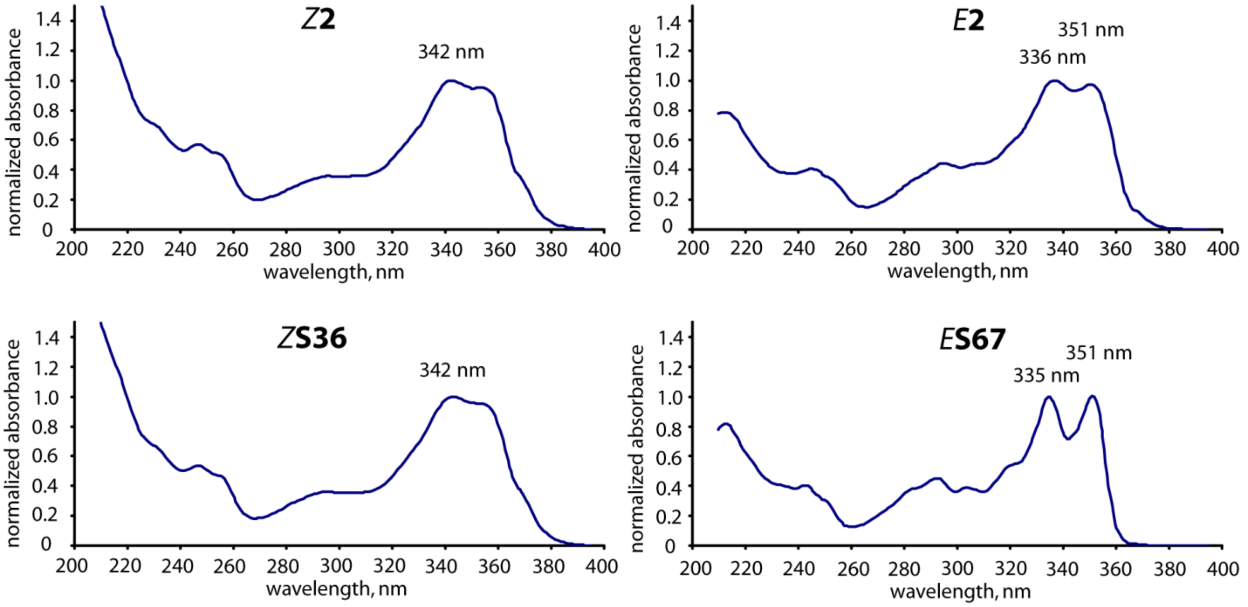

Fig. 4.8. UV spectra of the *Z* and *E* isomers of **2** and its corresponding dithiol **S67**.

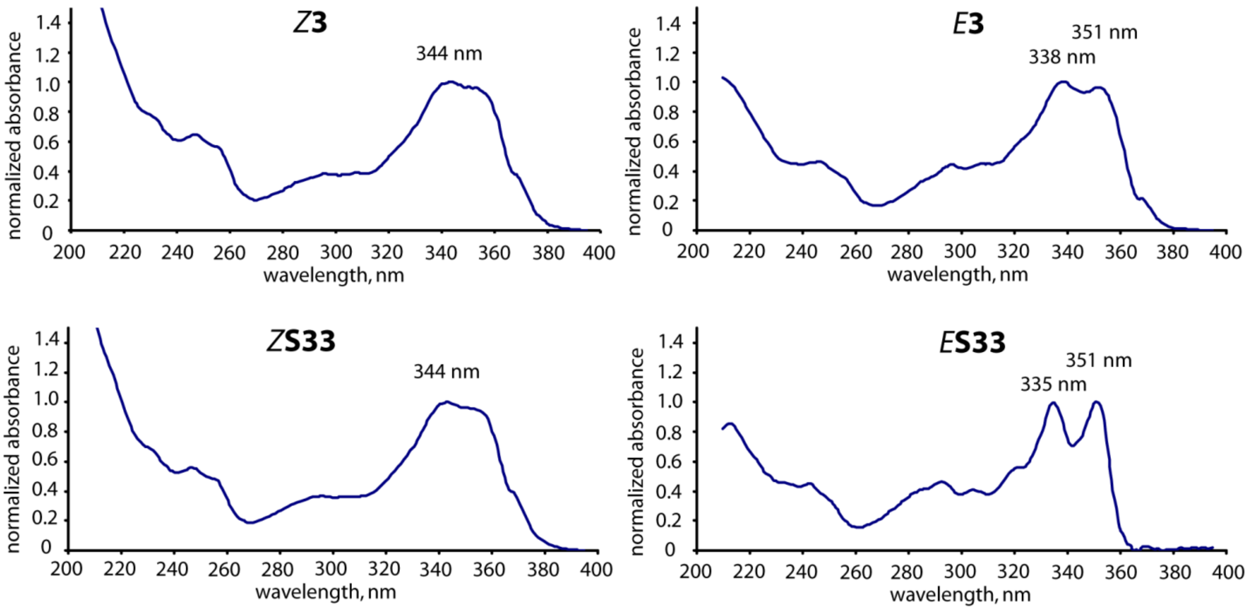

Fig. 4.9. UV spectra of the *Z* and *E* isomers of **3** and its corresponding dithiol **S33**.

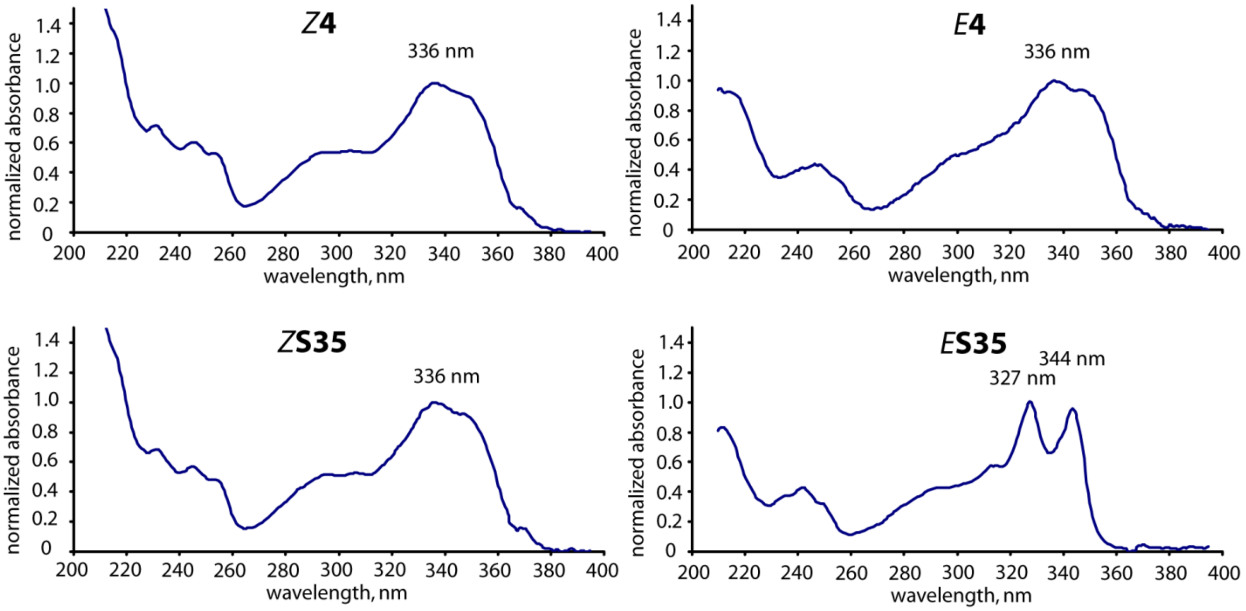

Fig. 4.10. UV spectra of the *Z* and *E* isomers of **4** and its corresponding dithiol **S35**.

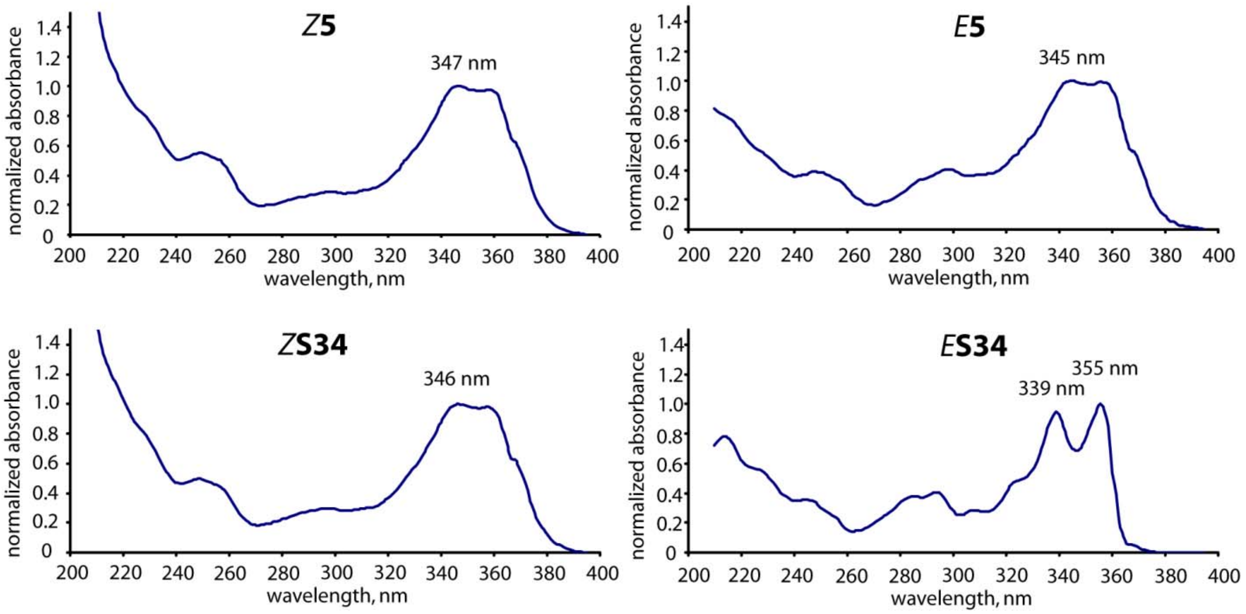

Fig. 4.11. UV spectra of the *Z* and *E* isomers of **5** and its corresponding dithiol **S34**.

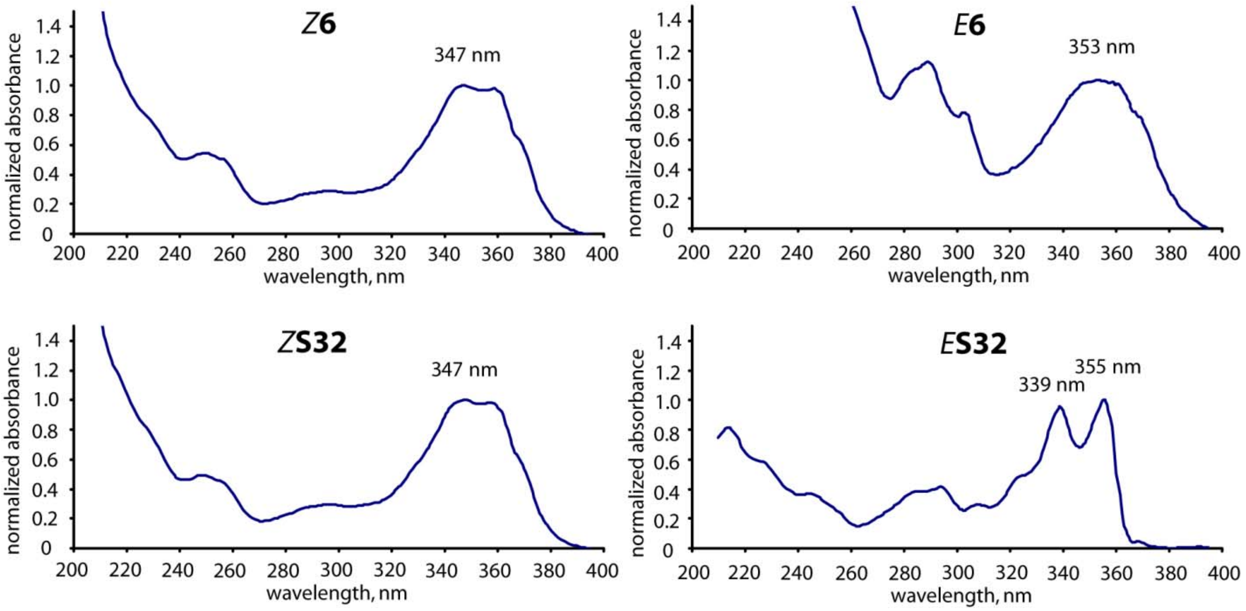

Fig. 4.12. UV spectra of the *Z* and *E* isomers of **6** and its corresponding dithiol **S32**.

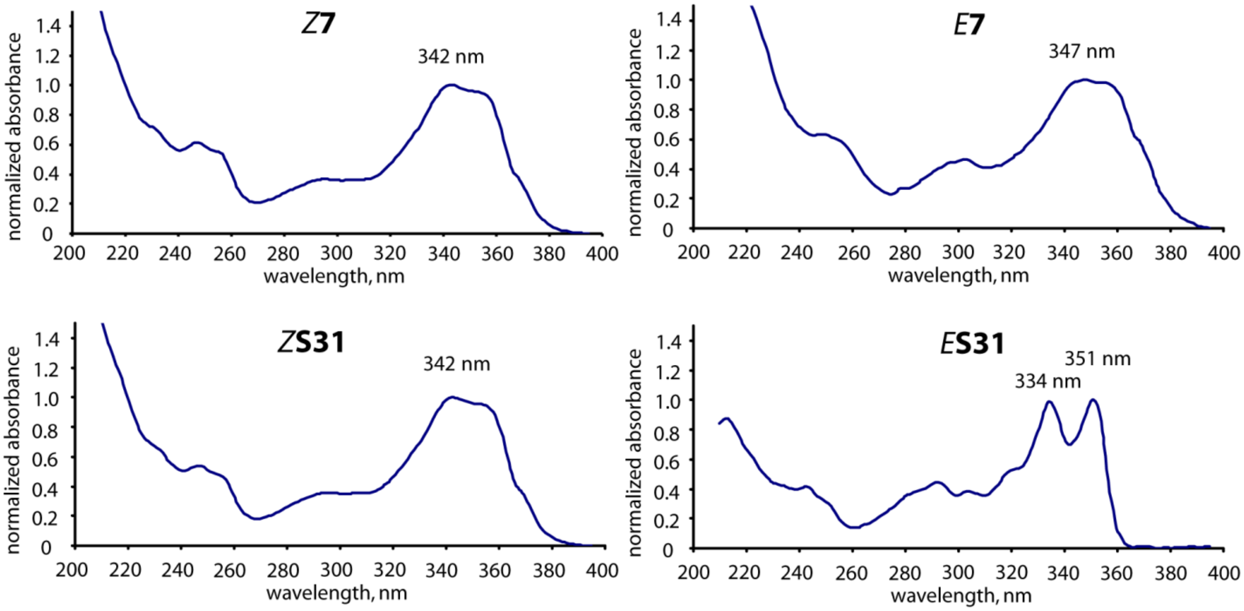

Fig. 4.13. UV spectra of the *Z* and *E* isomers of **7** and its corresponding dithiol **S31**.

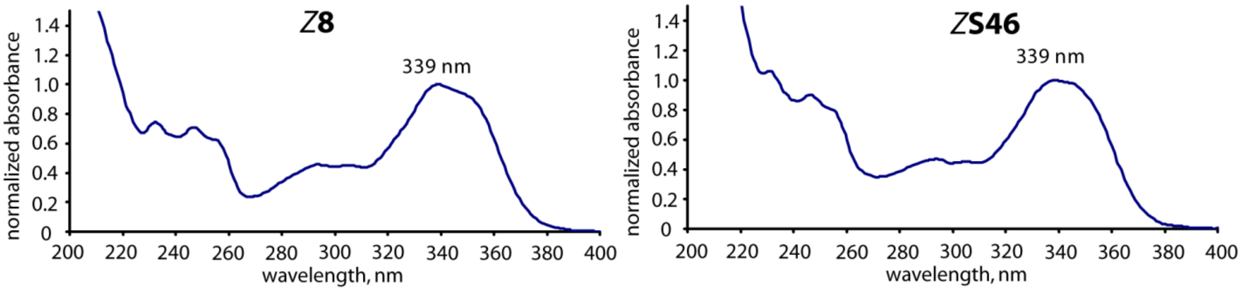

Fig. 4.14. UV spectra of *Z***8** and its corresponding dithiol Z**S46**.

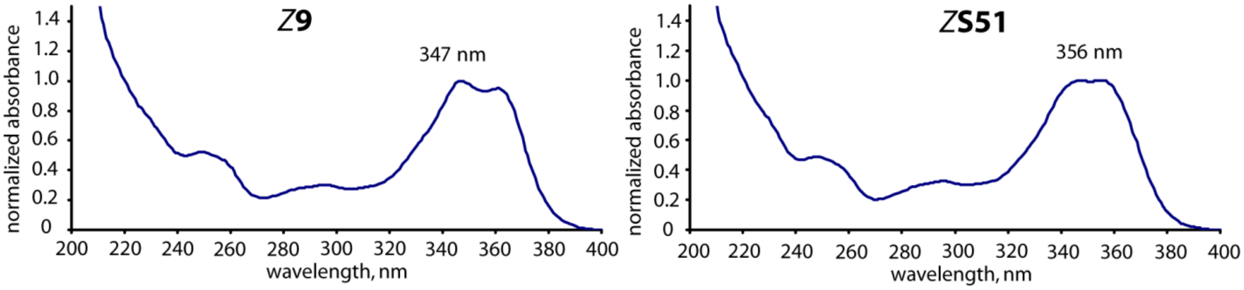

Fig. 4.15. UV spectra of *Z***9** and its corresponding dithiol Z**S51**.

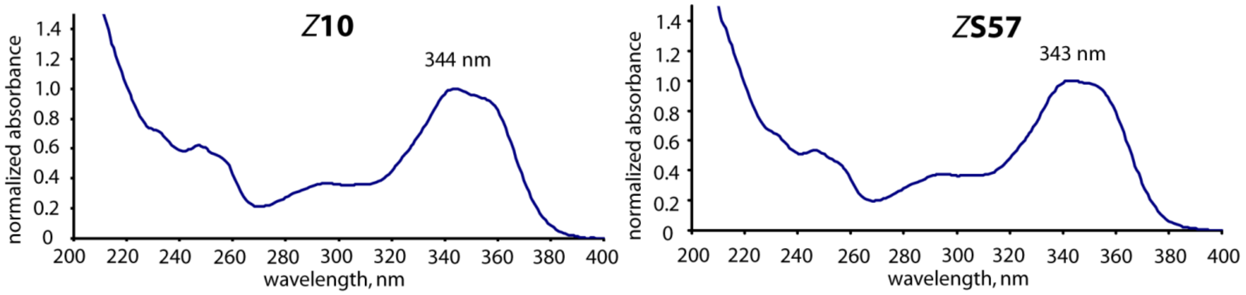

Fig. 4.16. UV spectra of *Z***10** and its corresponding dithiol Z**S57**.

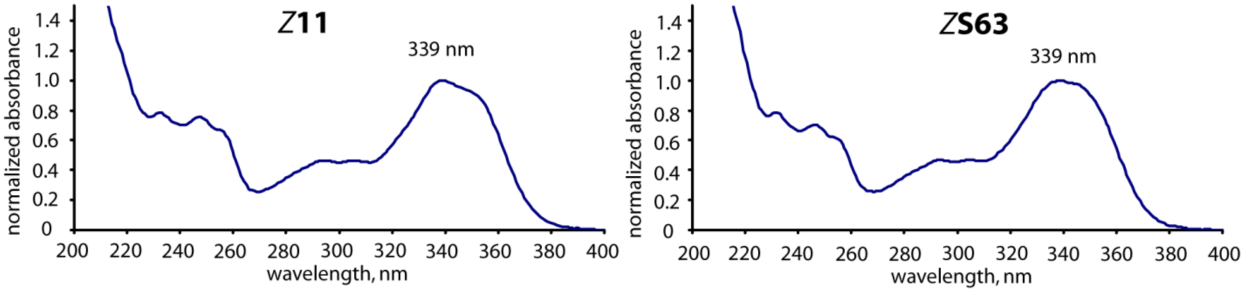

Fig. 4.17. UV spectra of *Z***11** and its corresponding dithiol Z**S63**.

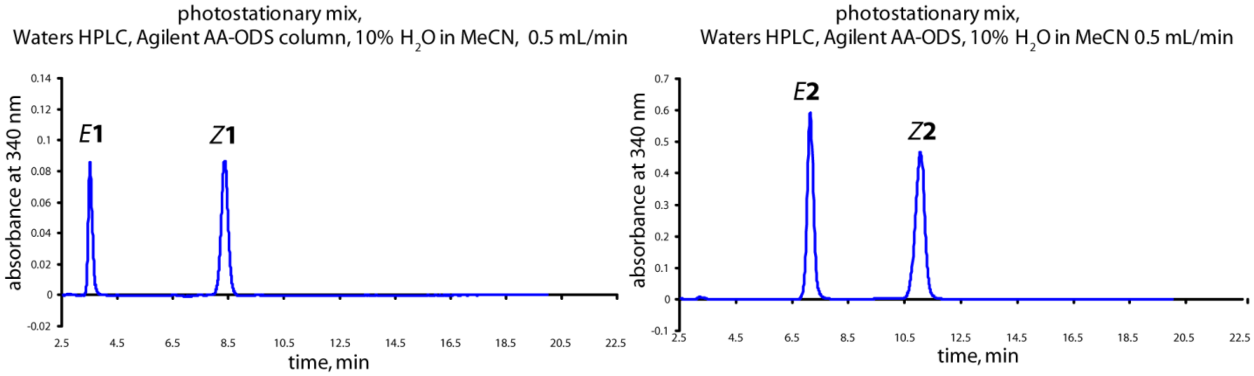

Fig. 4.18. Chromatograms of the photostationary mixtures of **1** and **2**.

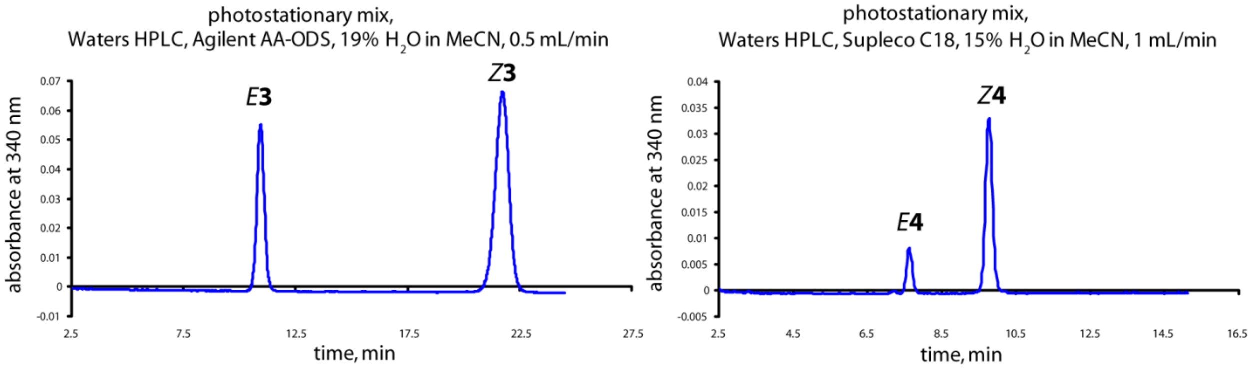

Fig. 4.19. Chromatograms of the photostationary mixtures of **3** and **4**.

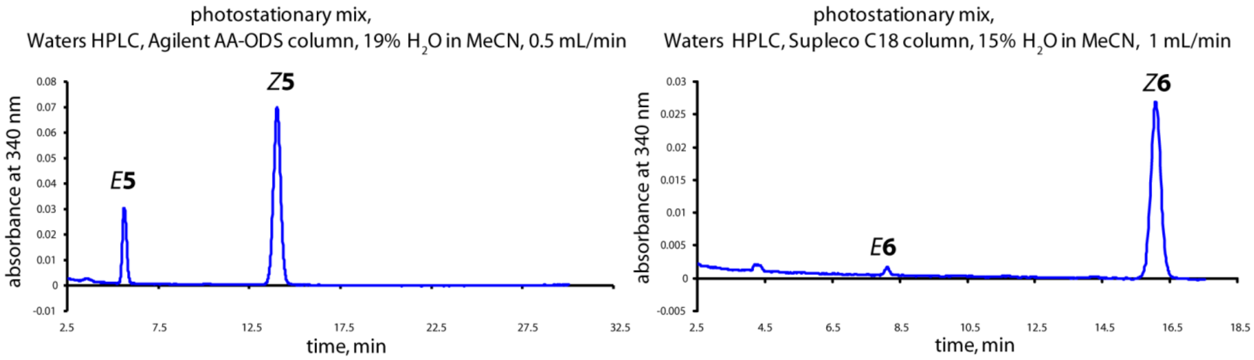

photostationary mix,
Waters HPLC, Agilent AA-ODS column, 19% H_2O in MeCN, 0.5 mL/min

photostationary mix,
Waters HPLC, Supleco C18 column, 15% H_2O in MeCN, 1 mL/min

Fig. 4.20. Chromatograms of the photostationary mixtures of **5** and **6**.

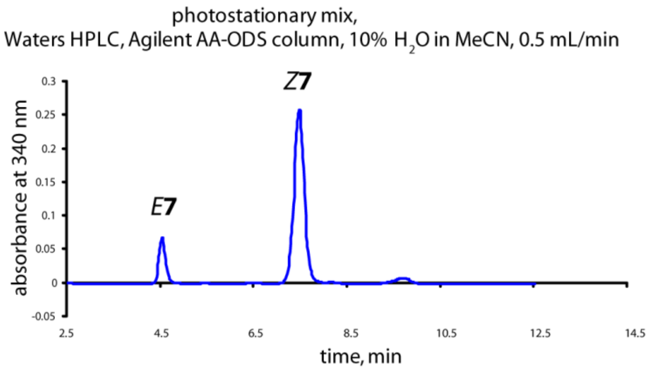

photostationary mix,
Waters HPLC, Agilent AA-ODS column, 10% H_2O in MeCN, 0.5 mL/min

Fig. 4.21. Chromatograms of the photostationary mixture of **7**.

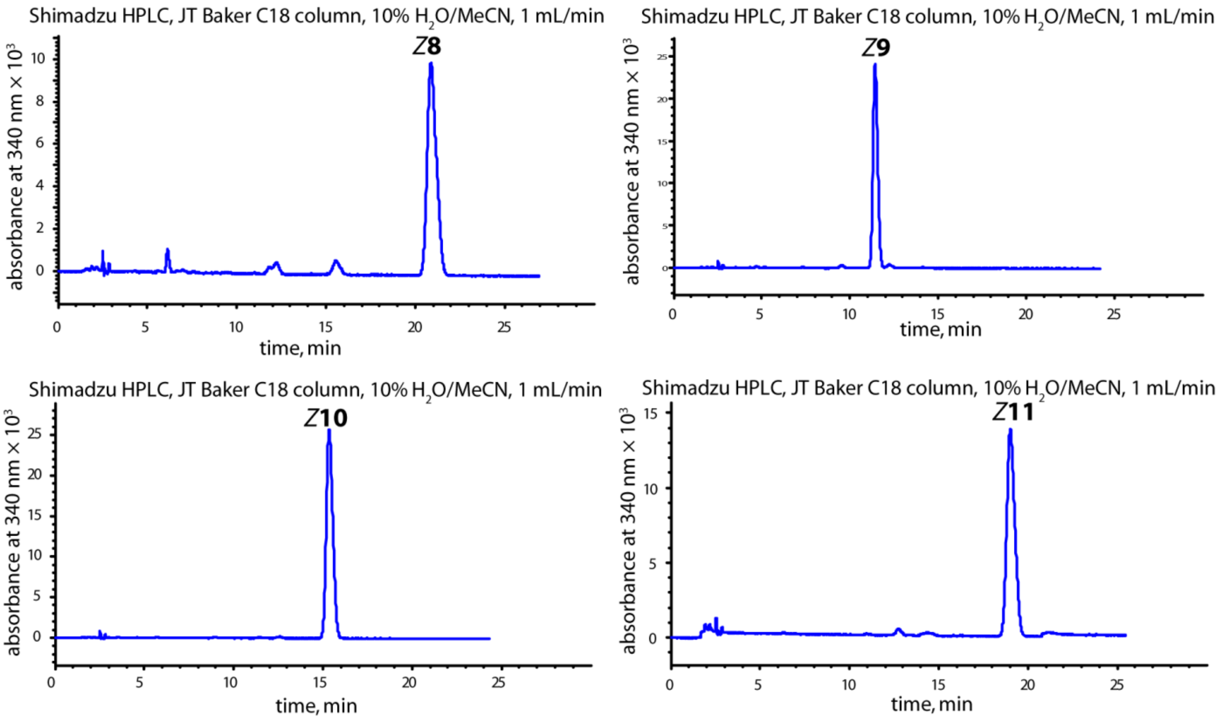

Shimadzu HPLC, JT Baker C18 column, 10% H_2O/MeCN, 1 mL/min

Shimadzu HPLC, JT Baker C18 column, 10% H_2O/MeCN, 1 mL/min

Shimadzu HPLC, JT Baker C18 column, 10% H_2O/MeCN, 1 mL/min

Shimadzu HPLC, JT Baker C18 column, 10% H_2O/MeCN, 1 mL/min

Fig. 4.22. Chromatograms of the *Z* isomers of **8**–**11**.

4.6.3 Kinetics

Methods

Photostationary mixtures of the two isomers for competition experiments (disulfides **1**–**7**) were prepared by irradiating a solution of each *Z* isomer in acetonitrile in a cuvette sealed under N_2 with 375 nm light until the UV-vis spectrum no longer changed. Irradiation of the *Z* isomers of **8**–**11** lead to homolysis of the S–S bond, so only the kinetics of thiol/disulfide exchange in the *Z* isomers of these disulfides was experimentally determined. Stock solutions of the disulfides were stored at -35 °C under N_2.

To prevent re-oxidation of the product dithiols by molecular oxygen, competition experiments were carried out in a glovebag under continuous N_2 purge. Solvents used were thoroughly sparged with N_2 before introduction into the glovebag. ^{1}H NMR spectroscopy confirmed that acetonitrile solutions of 1,4-butanedithiol were stable for weeks when prepared under these conditions and stored in vials sealed under N_2. Reactions were carried out in sealed vials, using a gas-tight syringe to withdraw samples for the composition analysis. These samples were transferred to clean vials and either analyzed immediately, or sealed under N_2 and stored at -35 °C. In the latter case, immediately before analysis vials were taken out of the freezer and a 100 μL aliquot was withdrawn with a gas-tight syringe through a septum without exposing the sample to air and immediately injected into the HPLC instrument.

The reaction vials were kept in a custom-made heating block with resistance heaters and thermocouple connected to an active-feedback temperature controller which enabled the temperature of the reaction mixtures to be maintained with the stability of ±0.1 °C. The reaction temperature was recorded every 6 s. To prevent photoisomerization between the *E* and *Z* dithiols by ambient light, amber-glass vials were used and all samples were kept away from light. No changes in *E*/*Z* ratio could be detected in control samples stored in this manner for weeks.

Stock solutions of the disulfides were diluted with a mixture of water and acetonitrile to give the total absorbance of ~0.3, corresponding to ~20 μM total concentration of disulfide, a total volume of 800 or 1200 μL and the water/acetonitrile ratio of 1:1.4 (molar). (We did not measure the molar absorptivities of disulfides **1**–**11**; however, molar absorptivities of many stiff stilbene derivates previously measured by us invariably were between ~14000 and ~20000 $M^{-1}cm^{-1}$ and we used these values to estimate the concentrations of disulfides. The kinetic analysis does not require the knowledge of absolute concentrations or extinction coefficients).

For non-competition experiments, an internal standard, **S64**, was added. **S64** was chosen because it has a readily identifiable UV spectrum, is sufficiently polar to elute before any disulfide or dithiol during reverse-phase HPLC analysis and is easily synthesized in high purity. The solution was allowed to equilibrate to a desired temperature in the heating block. A 30–50 μL aliquot of 1,4-butanedithiol in acetonitrile was added to the reaction mixture, the vial was shaken vigorously for ~2 s and returned immediately to the heating block. Samples of ~110 μL were withdrawn (see above) at regular intervals, collecting at least 6 samples in each kinetic run. In competition experiments, the reaction mixture was then heated to 60 °C to reduce the disulfides fully.

The chemical identity of the products in the kinetics runs was confirmed by comparison of the retention times of their components with authentic samples. Only disulfides and fully reduced dithiols were observed by HPLC. We also carried out the reaction of the *Z* isomers of the disulfides with 1,4-butanedithiol in CD_3CN–D_2O mixtures in sealed NMR tubes, following the reaction progress by ^1H NMR and confirmed the formation of dithiols and 1,2-dithiane. No other products were observed.

HPLC Analysis

We tested both reverse and normal phase HPLC to identify the best conditions for the analysis of the mixtures. The use of the normal-phase HPLC was precluded by extensive decomposition of the disulfides. In contrast, no decomposition was observed in reverse-phase HPLC; for example, using a gradient composition of H_2O–CH_3CN/CH_2Cl_2 as the mobile phase for analysis of the disulfides resulted in elution of all compounds with H_2O–CH_3CN and none were detected with CH_2Cl_2. The optical absorbance spectrum of the eluent was monitored at 250–450 nm.

Separation conditions were identified by separately analyzing a sample containing only a *Z* isomer, a sample containing both a *Z* disulfide and its dithiol (obtained by reduction with 1,4-butanedithiol), a sample of a photostationary mixture and a sample containing both *E* and *Z* isomers of the dithiol. The total absorbance of each fraction was obtained by integrating at 340 nm (close to $\lambda_{\max}$ for all of the components) over time. Separation conditions and retention times are listed below in Table 4.2. Retention times were generally reproducible to within ±0.1 min.

Table 4.2. HPLC separation conditions.

analyte	**HPLC system**	**column**	**mobile phase**	**retention time, min**	**UV absorption peaks, nm**
*Z***1**	a	a	10% H2O/MeCN, 0.50 mL/min	8.73	346, 250
*E***1**				3.68	353, 296
*Z***S37**				6.06	347
*E***S37**				4.67	356, 339, 294
*Z***2**	a	a	10% H2O/MeCN, 0.50 mL/min	11.06	342
*E***2**				7.15	336, 295, 245
*Z***S36**				7.73	342, 295
*E***S36**				6.50	351, 335, 292
*Z***3**	a	a	19% H2O/MeCN, 0.50 mL/min	21.63	342
*E***3**				10.93	339, 246
*Z***S33**				14.16	342, 296
*E***S33**				12.01	351, 335, 292
*Z***4**	a	b	15% H2O/MeCN, 1.00 mL/min	9.74	336
*E***4**				7.60	338
*Z***S35**				8.92	339
*E***S35**				7.06	344, 327
*Z***5**	a	a	19% H2O/MeCN, 0.50 mL/min	14.18	347
*E***5**				5.68	345, 298
*Z***S34**				10.83	346, 296
*E***S34**				8.24	356, 339, 294
*Z***6**	a	b	15% H2O/MeCN, 1.00 mL/min	16.02	347, 297
*E***6**				8.06	351, 290
*Z***S32**				11.77	346, 294
*E***S32**				8.93	356, 338
*Z***7**	a	a	15% H2O/MeCN, 0.50 mL/min	11.25	342, 295
*E***7**				6.45	346, 303
*Z***S31**				8.42	342, 295
*E***S31**				7.04	351, 334, 292
*Z***8**	b	c	10% H2O/MeCN, 1.00 mL/min	20.88	340
*Z***S46**				11.50	339
*Z***9**	a	b	15% H2O/MeCN, 1.00 mL/min	14.21	346, 295
*Z***S51**				9.66	346, 296

HPLC systems: a: Waters, b: Shimadzu; Columns: a: Agilent AA-ODS, b: Supleco C_{18}, c: J.T. Baker C_{18}

Table 4.2 (cont.)

*Z***10**	b	c	10% H2O/MeCN, 1.00 mL/min	14.67	344
*Z***S57**				8.77	344
*Z***11**	b	c	10% H2O/MeCN, 1.00 mL/min	19.01	339
*Z***S63**				9.84	339
S64	a	b	15% H2O/MeCN, 1.00 mL/min	4.87	356, 339, 294
	b	c	10% H2O/MeCN, 1.00 mL/min	6.67	356, 339, 293

Analysis of Kinetic Data

The kinetic experiments were carried out with at least 250-fold excess of 1,4-butanedithiol to achieve pseudo-first order kinetics.

The competition experiments (using photostationary mixtures) were analyzed according to eqs. (4.11) and (4.12) derived as follows: For a pair of pseudo-first order reactions

$$\mathrm{A} \xrightarrow{k_1} \mathrm{PA}$$

$$\mathrm{B} \xrightarrow{k_2} \mathrm{PB}$$

the rate laws are given by eqs. (1.3)–(4.4).

$$A = A_0 e^{-k_1 t} \tag{4.1}$$

$$PA = A_0(1 - e^{-k_1 t}) \tag{4.2}$$

$$B = B_0 e^{-k_2 t} \tag{4.3}$$

$$PB = B_0(1 - e^{-k_2 t}) \tag{4.4}$$

Then the ratios α and β can be defined as in eqs. (4.5) and (4.6), where IA is the integrated area of the HPLC peak for that compound for a reaction sample at time *t*, the rate laws may be expressed as eqs. (4.8) and (4.10). Rearranging then yields eqs. (4.11) and (4.12).

$$\alpha \equiv \frac{IA_{\mathrm{A}}}{IA_{\mathrm{B}}} = \frac{\varepsilon_{\mathrm{A}} A}{\varepsilon_{\mathrm{B}} B} \tag{4.5}$$

$$\beta \equiv \frac{IA_{\mathrm{PA}}}{IA_{\mathrm{PB}}} = \frac{\varepsilon_{\mathrm{PA}} PA}{\varepsilon_{\mathrm{PB}} PB} \tag{4.6}$$

$$\frac{IA_{\mathrm{A}}}{IA_{\mathrm{B}}} = \frac{\varepsilon_{\mathrm{A}}A}{\varepsilon_{\mathrm{B}}B} = \frac{\varepsilon_{\mathrm{A}}A_0 e^{-k_1 t}}{\varepsilon_{\mathrm{B}}B_0 e^{-k_2 t}} \tag{4.7}$$

$$\alpha = \alpha_0 e^{(k_2 - k_1)t} \tag{4.8}$$

$$\frac{IA_{\mathrm{PA}}}{IA_{\mathrm{PB}}} = \frac{\varepsilon_{\mathrm{PA}}PA}{\varepsilon_{\mathrm{PB}}PB} = \frac{\varepsilon_{\mathrm{PA}}A_0(1 - e^{-k_1 t})}{\varepsilon_{\mathrm{PB}}B_0(1 - e^{-k_2 t})} \tag{4.9}$$

$$\beta = \beta_\infty \frac{1 - e^{-k_1 t}}{1 - e^{-k_2 t}} \tag{4.10}$$

$$k_1 t = \ln\left(\frac{\frac{\alpha_0}{\alpha} - \frac{\beta_\infty}{\beta}}{1 - \frac{\beta_\infty}{\beta}}\right) \tag{4.11}$$

$$k_2 t = \ln\left(\frac{\alpha}{\alpha_0}\right) + k_1 t \tag{4.12}$$

The corresponding semi-logarithmic plots of eqs. (4.11) and (4.12) were linear, and the rate constants k_1 and k_2 were determined from the slopes of the least-squares regression fits to the data. This analysis does not require the knowledge of molar absorptivities and is insensitive to the variations in the injection volume from one run to another. Furthermore, combining eqs. (4.11) and (4.12) for competition experiments yields eq. (4.13), which allows the values of k_Z/k_E (i.e., k_2/k_1) to be determined without the knowledge of individual rate constants and hence with higher accuracy. Values for k_Z/k_E obtained with eq. (4.13) are shown in Table 4.3. Eyring plots derived from eq. (4.13) are shown in Fig. 4.25.

$$\frac{k_2}{k_1} = \frac{\ln\left(\frac{\alpha}{\alpha_0}\right)}{\ln\left(\frac{\frac{\alpha_0}{\alpha} - \frac{\beta_\infty}{\beta}}{1 - \frac{\beta_\infty}{\beta}}\right)} + 1 \tag{4.13}$$

Non-competition experiments are conveniently analysed using an internal standard. The rate law given by eq. (1.3) is equivalent to eq. (4.14), where IA_{std} is the integrated absorbance of the HPLC peak for the internal standard in a sample of the reaction mixture at time t, and $IA_{\mathrm{std,0}}$ is that at time 0. For each kinetic run the corresponding semi-logarithmic plot was linear, and the rate constant k was determined from the slope of the least-squares regression fit to the data.

$$kt = \ln\left(\frac{IA_{\mathrm{A},0} IA_{\mathrm{std}}}{IA_{\mathrm{std},0} IA_{\mathrm{A}}}\right) \tag{4.14}$$

The kinetics of thiol/disulfide exchange in **4** was measured using both competition and internal standard methods. The activation parameters obtained by the two methods were equal within experimental error. Apparent bimolecular rate constants for all of the macrocycles are tabulated in Table 4.3. The Eyring plots are shown in Fig. 4.23–Fig. 4.25, and the activation parameters are tabulated in Table 4.4.

The individual measurements for the linear least-squares regressions were weighted with the inverse of their variances. The standard errors of individual measurements were determined as square roots of the sums of squares of the deviations of individual measurements from the mean of identical measurements divided by the number of identical measurement minus 1. The errors of the regression coefficients were determined by the error propagation and include the uncertainty in both the rates and temperatures or compositions and reaction times.

Table 4.3. Apparent bimolecular rate constants for **1–11**.

	T, °C	σ	k_Z, M^{-1} s^{-1}	σ	k_E, M^{-1} s^{-1}	σ	k_E/k_Z, eq. (4.13)	σ
1	23.9	1.0	0.029	0.002	0.031	0.003	0.87	0.09
1	40.0	0.1	0.069	0.006	0.073	0.006	0.90	0.04
1	60.0	0.3	0.44	0.02	0.50	0.03	0.88	0.02
2	26.0	0.3	0.0036	0.0002	0.0016	0.0001	2.3	0.1
2	41.4	0.1	0.021	0.002	0.0094	0.0008	2.28	0.05
2	59.9	0.1	0.123	0.008	0.056	0.004	2.46	0.04
2	59.9	0.1	0.179	0.006	0.075	0.002	2.43	0.2
3	26.0	0.2	0.026	0.001	0.0121	0.0005	2.02	0.07
3	41.6	0.1	0.076	0.007	0.041	0.004	1.91	0.02
3	60.0	0.1	0.327	0.008	0.163	0.004	2.25	0.04
4	24.7	0.3	0.047	0.003	0.077	0.003	0.61	0.04
4	40.0	0.1	0.104	0.002	0.156	0.004	0.63	0.04
4	60.0	0.1	0.354	0.010	0.467	0.004	0.71	0.06
5	24.1	0.5	0.0035	0.0003	0.0068	0.0006	0.48	0.03
5	40.0	0.1	0.0122	0.0007	0.022	0.001	0.52	0.03
5	60.0	0.2	0.080	0.006	0.13	0.01	0.52	0.09
6	24.4	0.5	0.127	0.008	0.096	0.006	0.69	0.01

Table 4.3 (cont.)

6	40.0	0.1	0.614	0.005	0.49	0.01	0.71	0.02
6	59.9	0.2	2.1	0.2	1.6	0.1	0.67	0.02
7	25.3	0.2	0.037	0.001	0.026	0.001	1.49	0.04
7	40.5	0.1	0.24	0.02	0.185	0.009	1.36	0.04
7	50.2	0.1	0.36	0.03	0.26	0.02	1.40	0.02
8	24.2	0.2	0.00126	0.00009				
8	40.0	0.1	0.0086	0.0004				
8	59.7	0.3	0.017	0.002				
9	24.3	0.3	0.050	0.007				
9	40.0	0.1	0.12	0.01				
9	60.0	0.1	0.80	0.09				
10	25.0	0.1	0.028	0.002				
10	40.0	0.1	0.143	0.004				
10	60.0	0.1	1.01	0.04				
11	24.2	0.2	0.00135	0.00009				
11	40.0	0.1	0.0094	0.0004				
11	59.7	0.3	0.018	0.002				

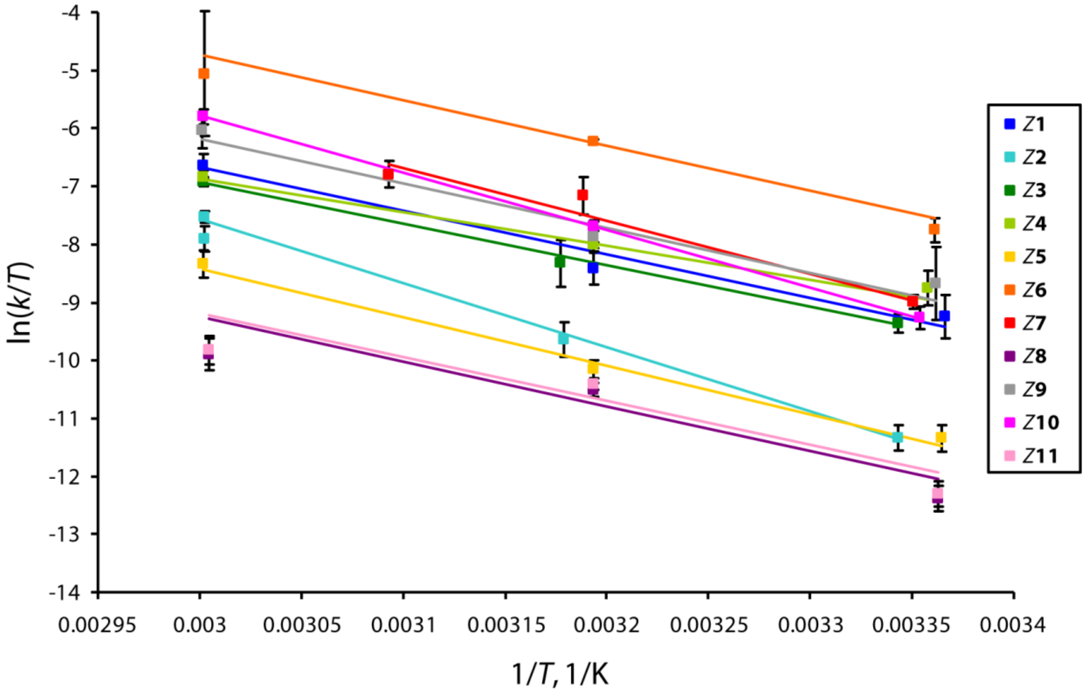

Fig. 4.23. Eyring plots for *Z* isomers of **1–11**; error bars define the 95% confidence intervals.

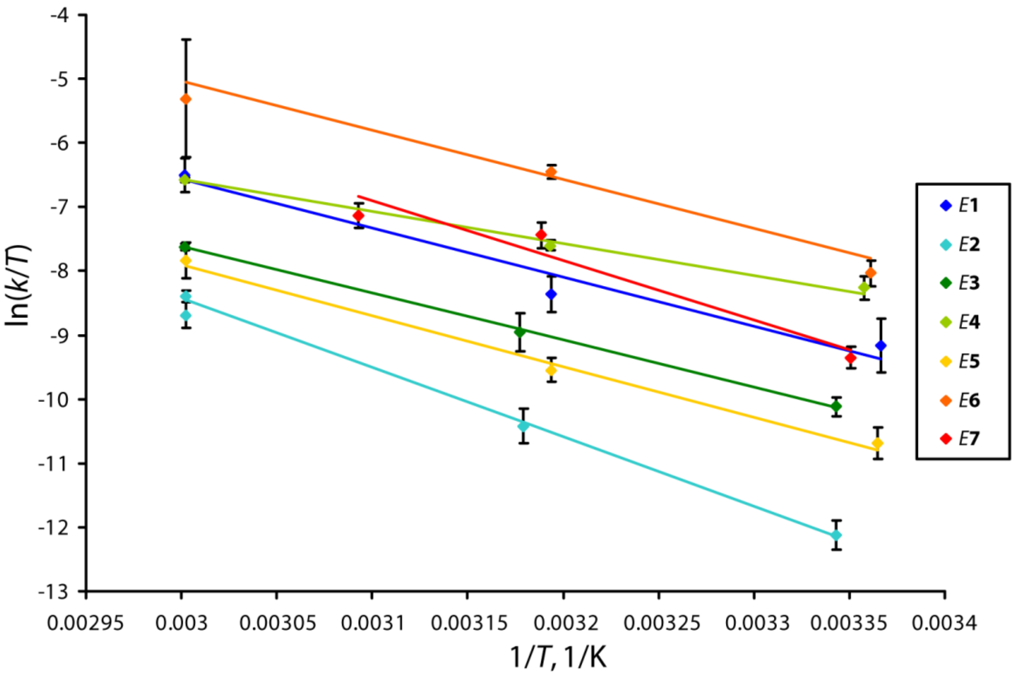

Fig. 4.24. Eyring plots for *E* isomers of **1**–**7**; error bars define the 95% confidence intervals.

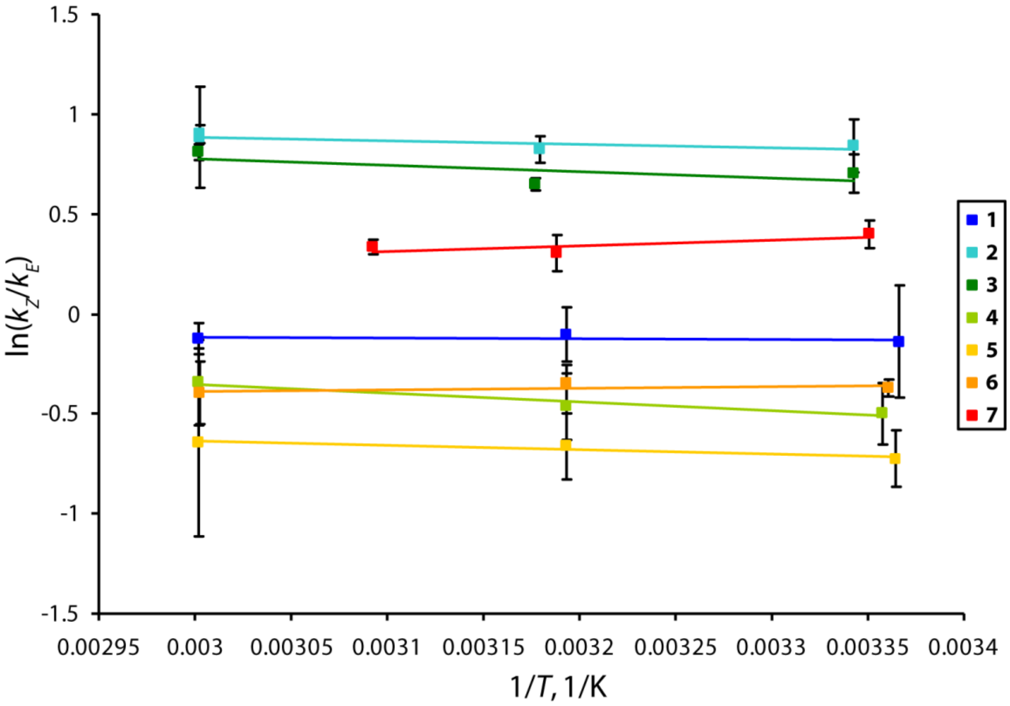

Fig. 4.25. Eyring plots for k_Z/k_E eq. (4.13) for **1**–**7**; error bars define the 95% confidence intervals.

Table 4.4. Apparent activation parameters of **1**–**11**, errors are standard deviations.

	Z isomers			*E* isomers			Differences			
							Eqs. (4.11) and (4.12), time-dependent values		Eq. (4.13), time-independent values	
	$\Delta H^{\ddagger}_{app}$, kcal/mol	$\Delta S^{\ddagger}_{app}$, e.u.	R^2	$\Delta H^{\ddagger}_{app}$, kcal/mol	$\Delta S^{\ddagger}_{app}$, e.u.	R^2	$\Delta\Delta H^{\ddagger}_{app}$, kcal/mol	$\Delta\Delta S^{\ddagger}_{app}$, e.u.	$\Delta\Delta H^{\ddagger}_{app}$, kcal/mol	$\Delta\Delta S^{\ddagger}_{app}$, e.u.
1	15.0 ± 0.5	-15.6 ± 1.6	0.96661	15.2 ± 0.6	-14.5 ± 1.9	0.96106	-0.3 ± 0.8	-1.0 ± 2.5	0.1 ± 0.2	0.0 ± 0.5
2	21.9 ± 0.4	3.5 ± 1.3	0.98855	21.6 ± 0.4	0.9 ± 1.3	0.99267	0.3 ± 0.6	2.5 ± 1.8	0.4 ± 0.2	2.8 ± 0.6
3	14.3 ± 0.3	-18.2 ± 1.0	0.99386	14.5 ± 0.3	-18.7 ± 0.9	0.99936	-0.3 ± 0.4	0.6 ± 1.3	0.6 ± 0.7	3.4 ± 2.3
4	11.6 ± 0.3	-26.1 ± 0.9	0.97756	10.0 ± 0.2	-30.2 ± 0.6	0.98939	1.6 ± 0.3	4.1 ± 1.1	0.9 ± 0.2	1.9 ± 0.8
5	16.7 ± 0.6	-14.0 ± 1.9	0.99152	15.8 ± 0.7	-15.7 ± 2.2	0.99278	0.9 ± 0.9	1.7 ± 2.9	0.4 ± 0.2	0.1 ± 0.5
6	15.5 ± 0.6	-10.2 ± 1.8	0.96158	15.2 ± 0.5	-11.5 ± 1.7	0.96740	0.2 ± 0.8	1.3 ± 2.5	-0.2 ± 0.2	-1.2 ± 0.7
7	18.1 ± 0.6	-4.5 ± 1.8	0.95124	18.4 ± 0.6	-4.0 ± 1.9	0.93807	-0.3 ± 0.8	-0.5 ± 2.7	-0.6 ± 0.5	-1.1 ± 1.5
8	15.3 ± 0.6	-19.8 ± 2.1	0.83449							
9	15.4 ± 1.0	-13.4 ± 3.2	0.96069							
10	19.6 ± 0.4	0.1 ± 1.3	1.00000							
11	14.9 ± 0.6	-20.6 ± 1.9	0.83158							

Solvent Composition Dependence of Disulfide Reduction Kinetics

The limited aqueous solubility of 1,4-butanedithiol required the use of acetonitrile as a co-solvent. To determine how sensitive the differences of the activation parameters, $\Delta\Delta H^{\ddagger}$ and $\Delta\Delta S^{\ddagger}$, were to the fraction of acetonitrile, we measured the kinetics of thiol/disulfide exchange for **2** in water/acetonitrile mixtures ranging in composition from 1:1.4 (mol) to ~3:1 (mol). At the lowest concentration of acetonitrile examined, the saturation concentration of 1,4-butanedithiol was ~5 mM. Lower concentrations of 1,4-butanedithiol were inconvenient because they required either a decrease in the excess relative to the disulfide, or a decrease in the concentration of the disulfide. The latter increase the error of the compositions by HPLC particularly at low or high conversions. Though the absolute rates of thiol/disulfide exchange varied with water composition of the reaction mixture, the observed values of $\Delta\Delta H^{\ddagger}$ and $\Delta\Delta S^{\ddagger}$ were found to not depend on water composition, as demonstrated with **2** (

Table 4.5).

Table 4.5. Apparent bimolecular rate constants of thiol/disulfide exchange with **2** in different solvent compositions.

		k, M^{-1} s^{-1} and the standard deviation, σ					
	H_2O:MeCN (mol)	1:1.4		1.6:1		2.9:1	
		k	σ	*k*	σ	*k*	σ
*Z***2**	RT	0.0036	0.0002	0.0035	0.0003	0.031	0.002
	40 °C	0.021	0.002	0.0184	0.0002	0.139	0.003
	60 °C	0.15	0.01	0.091	0.003	0.797	0.007
*E***2**	RT	0.0016	0.0001	0.0014	0.0001	0.0127	0.0007
	40 °C	0.0094	0.0008	0.00718	0.00009	0.055	0.001
	60 °C	0.066	0.004	0.0347	0.0009	0.327	0.003

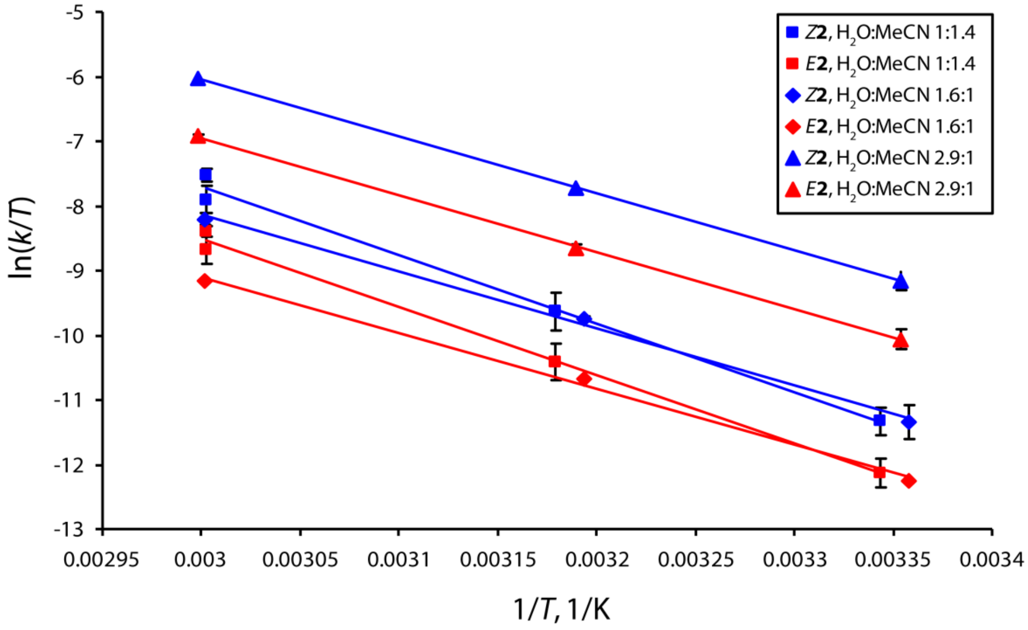

Fig. 4.26. Eyring plots of thiol/disulfide exchange with **2** in solvents of varying water content, error bars represent the 95% confidence interval.

Table 4.6. Activation parameters of thiol/disulfide exchange with **2** in solvents acetonitrile–water of varying composition

	*Z***2**				*E***2**				difference			
H_2O fraction	$\Delta H^‡$, kcal/mol	σ	$\Delta S^‡$, e.u.	σ	$\Delta H^‡$, kcal/mol	σ	$\Delta S^‡$, e.u.	σ	$\Delta\Delta H^‡$, kcal/mol	σ	$\Delta\Delta S^‡$, e.u.	σ
0.42	21.9	0.4	3.5	1.3	21.6	0.4	0.9	1.3	0.3	0.6	2.5	1.8
0.61	16.3	0.3	-14.6	1.1	16.0	0.3	-17.4	0.9	0.3	0.4	2.7	1.4
0.74	17.5	0.2	-6.8	0.6	17.8	0.2	-7.7	0.6	-0.3	0.3	0.9	0.8

4.7 References

1. Yang, Q.-Z.; Huang, Z.; Kucharski, T. J.; Khvostichenko, D.; Chen, J.; Boulatov, R., A Molecular Force Probe. *Nat. Nanotechnol.* **2009**, *4*, 302–306.
2. Bhasin, N.; Carl, P.; Harper, S.; Feng, G.; Lu, H.; Speicher, D. W.; Discher, D. E., Chemistry on a Single Protein, Vascular Cell Adhesion Molecule-1, during Forced Unfolding. *J. Biol. Chem.* **2004**, *279*, 45865–45874.
3. Vogel, V., Mechanotransduction Involving Multimodular Proteins: Converting Force into Biochemical Signals. *Annu. Rev. Biophys. Biomol. Struct.* **2006**, *35*, 459–488.
4. Ainavarapu, S. R. K.; Wiita, A. P.; Dougan, L.; Uggerud, E.; Fernandez, J. M., Single-Molecule Force Spectroscopy Measurements of Bond Elongation during a Bimolecular Reaction. *J. Am. Chem. Soc.* **2008**, *130*, 6479–6487.
5. Leffler, J. E.; Grunwald, E., *Rates and Equilibria of Organic Reactions*. Wiley: New York, 1963.
6. Kersey, F. R.; Yount, W. C.; Craig, S. L., Single-Molecule Force Spectroscopy of Bimolecular Reactions: System Homology in the Mechanical Activation of Ligand Substitution Reactions. *J. Am. Chem. Soc.* **2006**, *128*, 3886–3887.
7. Reimann, P., Brownian Motors: Noisy Transport Far from Equilibrium. *Phys. Rep.* **2002**, *361*, 57–265.
8. Huang, Z.; Yang, Q.-Z.; Khvostichenko, D.; Kucharski, T. J.; Chen, J.; Boulatov, R., Method to Derive Restoring Forces of Strained Molecues from Kinetic Measurements. *J. Am. Chem. Soc.* **2009**, *131*, 1407–1409.
9. Nakayama, J.; Ishii, A., Chemistry of Dithiiranes, 1,2-Dithietanes, and 1,2-Dithietes. *Adv. Heterocycl. Chem.* **2000**, *77*, 221–284.
10. Hayes, J. M.; Bachrach, S. M., Effect of Micro and Bulk Solvation on the Mechanism of Nucleophilic Substitution at Sulfur in Disulfides. *J. Phys. Chem. A* **2003**, *107*, 7952–7961.
11. Burns, J. A.; Whitesides, G. M., Predicting the Stability of Cyclic Disulfides by Molecular Modeling: Effective Concentrations in Thiol–Disulfide Interchange and the Design of Strongly Reducing Dithiols. *J. Am. Chem. Soc.* **1990**, *112*, 6296–6303.
12. Ruggles, E. L.; Deker, P. B.; Hondal, R. J., Synthesis, Redox Properties, and Conformational Analysis of Vicinal Disulfide Ring Mimics. *Tetrahedron* **2009**, *65*, 1257–1267.

13. Huang, Z.; Yang, Q.-Z.; Kucharski, T. J.; Khvostichenko, D.; Wakeman, S. M.; Boulatov, R., Macrocyclic Disulfides for Studies of Sensitized Photolysis of the S–S Bond. *Chem. Eur. J.* **2009**, *15*, 5212–5214.

14. Singh, R.; Whitesides, G. M., Thiol–Disulfide Interchange. In *Supplement S: The Chemistry of Sulphur-Containing Functional Groups*, Patai, S.; Rappoport, Z., Eds. Wiley: New York, 1993; pp 633–658.

15. Singh, R.; Whitesides, G. M., Degenerate Intermolecular Thiolate–Disulfide Interchange Involving Cyclic Five-Membered Disulfides Is Faster by ~10^3 Than That Involving Six- or Seven-Membered Disulfides. *J. Am. Chem. Soc.* **1990**, *112*, 6304–3609.

16. Tomasi, J.; Munnucci, B.; Cammi, R., Quantum Mechanical Contimuum Solvation Models. *Chem. Rev.* **2005**, *105*, 2999–3094.

17. Kucharski, T. J.; Huang, Z.; Yang, Q.-Z.; Tian, Y.; Rubin, N. C.; Concepcion, C. D.; Boulatov, R., Kinetics of Thiol/Disulfide Exchange Correlate Weakly with the Restoring Force in the Disulfide Moiety. *Angew. Chem. Int. Ed.* **2009**, *48*, 7040–7043.

18. Bach, R. D.; Dmitrenko, O.; Thorpe, C., Mechanism of Thiolate–Disulfide Interchange Reactions in Biochemistry. *J. Org. Chem.* **2008**, *73*, 12–21.

19. Hyeon, C.; Thirumalai, D., Measuring the Energy Landscape Roughness and the Transition State Location of Biomolecules Using Single Molecule Mechanical Unfolding Experiments. *J. Phys.: Condens. Matter* **2007**, 113101/1–27.

20. Regan, C. K.; Craig, S. L.; Brauman, J. I., Steric Effects and Solvent Effects in Ionic Reactions. *Science* **2002**, *295*, 2245–2257.

21. Shaik, S. S.; Schlegel, H. B.; Wolfe, S., *Theoretical Aspects of Physical Organic Chemistry: The S_N2 Mechanism*. Wiley: New York, 1992.

22. Lenhardt, J. M.; Craig, S. L., Mechanochemistry: Force probes in a Bottle. *Nat. Nanotechnol.* **2009**, *4*, 284–285.

23. Smith, C. E.; Williamson, W. R. N.; Cashin, C. H.; Kitchen, E. A., Potential Antiinflammatory Compounds. 3. Compounds Derived from Acenaphthene and Indan. *J. Med. Chem.* **1979**, *22*, 1464–1469.

24. Neudeck, H. K., Aromatic Spirane. XIV. Syntheses of 2,2'-Spirobi(σ-hydrindacene) and Its Precursors. *Monatsh. Chem.* **1987**, *118*, 627–657.

Chapter 5. The Inverted Region of Mechanochemical Kinetics: Inhibition of Bond Cleavage by Tensile Force

5.1 Introduction

The preceding chapters have discussed the ways in which mechanical forces at the macromolecular, supramolecular, or microscopic levels can affect chemical reactivity of reactive moieties at the molecular level. Here I re-emphasize the importance of such changes in reactivity for functional materials, as has also been emphasized in recent reviews.[1,2] However, if we are to truly take advantage of all that mechanochemicsty offers for the design of novel, mechanoresponsive matierals, not only must we gain an understanding of how and why mechanical force affects chemical reactivity and how chemical reactions can generate mechanical forces in materials, but we must also be conscious of other mechanochemical phenomena beyond the widely recognized mechanical acceleration of reactions and mechanochemical actuation. By articulating the fundamental relationships between force and reactivity, we can now not only better explain how environmental conditions (temperature, material strain, photon flux, chemical composition, etc.) or the act of operation itself will affect the kinetics and thermodynamics of operation, but we can also explore previously unrecognized possibilities for exploiting mechanochemical phenomena. This chapter discusses an example of mechanochemistry in which bond scission is inhibited by tensile force projected along the scissile bond, an effect that seems counterintuitive from a macroscopic point of view and requires an understanding of the physical relationship between mechanical force and chemical reactivity.

Other general relationships between molecular properties (e.g., electron donating/withdrawing abilities of functional groups, nucleophilicities, polarizabilities) or environmental conditions (e.g., solvent dielectric constants, pH, electric field strength) and the standard and activation energies of chemical reactions have advanced our understanding of chemical reactivity over the past century.[3-7] Examples include the Hammett, Brønsted, Taft, Grunwald–Winstein, Swain–Scott and Edwards and Ritchie relationships, the so-called Bema Hapothela,[8] Marcus theory,[9] and other extrathermodynamic relationships.[10] In some cases, these theories have revolutionized chemists' thinking. The best example may be that of Marcus theory: the widely applicable Hammond–Leffler postulate[10-12] indicates that the increasing the enthalpic difference between two states (i.e., making one more strained) in turn decreases the enthalpic barrier for thermal conversion from the metastable to the stable form. Marcus theory does so as well, but only to a point: it also predicts an inverted region in which $\Delta G^{\ddagger}$ increases as the driving force continues to increase (i.e., as ΔG^{o} becomes more exergenic). Analogously, in mechanochemical phenomena, increasing the restoring force along a molecular degree of freedom may decrease the thermal barrier for chemical conversion to a more stable form, as it has been noted to do in many cases (see Chapter 1 and refs. 1, 2 and 13), but it can also *inhibit* chemical reactivity, a concept that (to our knowledge) has not been recognized prior to our work.[13-16] Our model for mechanochemical kinetics predicts such an "inverted region" in phase space, in that $\Delta G^{\ddagger}$ increases with increasing restoring force along a local molecular degree of freedom, F_q, when that degree of freedom, q, must contract to reach the transition state configuration from the reactant configuration.

The inhibition of chemical reactions in strained molecules is certainly not a new concept. Some heavily studied examples include various strained ring systems, particularly the prismane/dewarbenzene/benzene system (Fig. 5.1).[4,17] Such highly strained prismanes and Dewar benzenes are kinetically stable, despite the large exergonicity of their isomerization to the less-strained (Kekulé) benzene. Their stability, however, usually is explained in somewhat qualitative means, based on arguments that their conformational rigidity prevents the adoption of conformations that would stabilize biradical transition states enough to make them thermally accessible or that the formation of the (closed-shell) transition state(s) would require the molecule to become even more highly strained. While accurate, such arguments for these and other similar compounds do not provide the framework for a quantitative relationship between molecular strain and reactivity that would be useful in describing the mechanochemical phenomena in extended systems, particularly those involving multi-scale dynamic processes in which the definition of strain energy is entirely impractical. Instead, the mechanochemical phenomena must be explained in terms of the only parameter which relates strain to reactivity: force. To do so, we developed the model for mechanochemical kinetics that has been discussed throughout this dissertation.

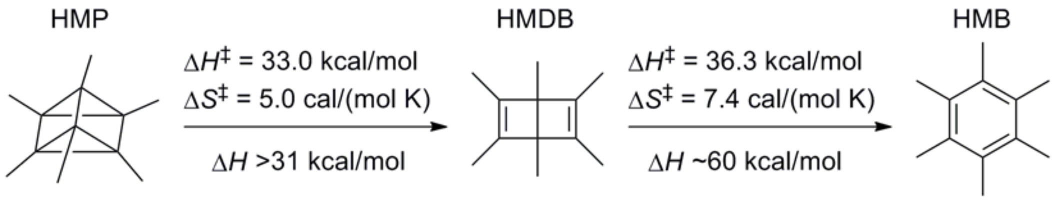

Fig. 5.1. The thermal isomerization of hexamethylprismane (HMP) to hexamethyl Dewar benzene (HMDB), and the thermal isomerization of HMDB to (Kekulé) hexamethyl benzene, showing the activation parameters[18] and enthalpies of reaction[4,17-19] for each step.

5.2 The Inverted Region of Mechanochemistry

Our model also predicts an inverted region of mechanochemical kinetics that is analogous to the qualitative explanations of inhibition by the accumulation of additional molecular strain in a molecule's transition state: though the driving force increases (i.e., the energy gradient along a local molecular degree of freedom becomes more negative), the activation free energy increases because that local molecular degree of freedom must contract against the restoring force (i.e., traveling up the energy gradient) to reach the transition state. Thus, rather than behaving as a rubber band, which breaks more rapidly when stretched, a better (though still inexact) analogy to macroscopic experience would be that of a Chinese finger trap: traveling directly towards the product geometry (freed fingers) increases the strain in the system (the grip on the fingers) other mechanisms, such as homolysis, for bond scission are achievable (the trap breaks; external aid in freeing the fingers would correspond to changing the potential energy surface in such a manner that the restoring force is negated).

Recall the discussion of the mechanochemistry of nucleophilic substitution reactions discussed in Chapter 1. As shown in Fig. 5.2, the separation of the two atoms bound that attach the electrophilic atom to the rest of the strained system defines the local molecular degree of freedom, q, which dictates the response of the reactive moiety to force along that degree of freedom, F_q. The scissile bond (red) may either be perpendicular to (Fig. 5.2A) or aligned with (Fig. 5.2B) q. Neglecting second-order effects, in the former case acceleration by tensile force along q is expected in all cases, because the formation of the transition state necessitates the elongation of q as the spectator atoms separate, thereby decreasing the energy of the system by traveling down the energetic gradient, F_q.

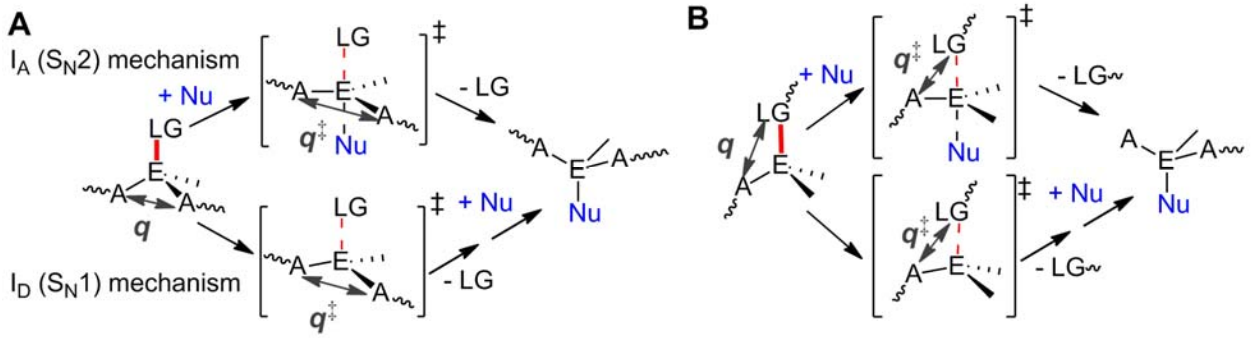

Fig. 5.2. An intuitive local coordinate *q* for analysis of force-dependent kinetics of single-barrier nucleophilic displacement in which the restoring force along *q*, F_q, is orthogonal to (**A**) or along (**B**) the scissile bond (red). A are the spectator atoms bound to E, Nu is the nucleophile, and wavy lines represent the rest of the strained (macro)molecule.

In the later case (Fig. 5.2B), again neglecting second-order effects, the change in *q* between the ground and transition states comprises contributions from the contraction of the A–E–LG angle and the elongation of the scissile E–LG bond. As discussed before, there are three possible outcomes, depending on whether one factor dominates the other or if their effects cancel. If scissile bond elongation dominates, *q* will elongate and acceleration by increasing force is expected; the hydrolysis of primary sulfonates exhibited this behavior (Chapter 3). If the effects of the two contributions cancel, *q* does not change and therefore magnitude (and direction) of the energy gradient F_q is irrelevant because the molecule does not travel along it; we found the reduction of alkyl disulfides by an alkyl thiol to exhibit this behavior (Chapter 4). If the effect of A–E–LG angle contraction is greater than that of scissile E–LG bond elongation, *q* will contract to reach the transition state, thereby increasing the energy of the transition state by $|F_q\Delta q|$, inhibiting the reaction.

When would such contraction of *q* and inhibition of nucleophilic substitution reactions be expected? The bond between the electrophilic atom E and the spectator atom A that partially defines *q* serves as a lever. If the "lever" is longer, the contraction of the A–E–LG angle has a greater effect on *q*. If E–LG bond elongation is similar for different reactions, that with a longer A–E bond will be (in the absence of calculations to find out the exact magnitudes of the contributions) more likely to result in a contractile *q*. Some bond lengths and (rough estimates of) partial bond lengths calculated from single-bond covalent radii and van der Waals radii are shown in Table 5.1. Based on these rough estimates, it appears that the scissile bonds elongate by roughly the same amount (0.8–0.9 Å) in the transition states for primary sulfonate hydrolysis (C–

O), thiol/disulfide exchange (S–S), and silyl ether solvolysis (Si–O). (Note, however, that this does not account for the transition state being either early or late and likely overestimates the elongation: scissile bond elongation in the transition state was calculated to be 0.65 and 0.42 Å for the hydrolysis of EtOMs and thiol/disulfide exchange between EtSSEt and EtS$^-$, respectively (Chapter 3). However, shorter bond elongations in the transition state only make the following argument stronger.) The spectator bond in sulfonate hydrolysis (C–C) was short, and scissile bond elongation was the dominant effect on q. The spectator bond in thiol/disulfide exchange (S–C) was longer, and the effect of scissile bond elongation on q was negated by that of C–S–S angle contraction. Increasing the length of the spectator bond further may then lead to A–E–LG angle contraction being the dominant effect, resulting in contraction of q in the transition state. Alternatively, the length of the scissile bond can be decreased, which may result in the same effect (i.e., the effect of the spectator bond is increased). Si–O bonds are similarly long to S–C bonds but are ~0.2 Å shorter than S–S bonds. Therefore, the nucleophilic substitution of a silyl ether by a nucleophilic oxygen atom is a case where contraction in q may occur.

Table 5.1. Some estimated single and partial bond lengths.

bond	calculated length,[a] Å	partial bond	estimated length,[b] Å	estimated elongation at TS, Å
C–C	1.54			
C–O	1.43	C--O in [O--C--O]‡	2.3	0.9
S–C	1.81			
S–S	2.08	S--S in [S--S--S]‡	2.8	0.8
Si–O	1.83	Si--O in [O--Si--O]‡	2.7	0.9

[a] Calculated from the single-bond covalent radii in ref. 20; [b] Calculated as $(l_{A–B} + r_{W,A} + r_{W,B})/2$, where $l_{A–B}$ is the calculated single bond length for A–B and $r_{W,A}$ and $r_{W,B}$ are the mean van der Waals radii for atoms A and B reported in ref. 21.

Keeping in mind the argument that it may be possible that q may contract in siloxane hydrolysis/alcoholysis leading to inhibition by increasing F_q, it is interesting to note the few theoretical and experimental studies on the force-dependent rupture of Si–O bonds. Some of the first experimental examinations of the force-induced rupture of single covalent bonds were carried out by Hermann Gaub: single macromolecules covalently bound to a surface were stretched by AFM until they ruptured, presumably by homolysis.[22] Carr-Parrinello molecular dynamics (CPMD) studies of the rupture of polydimethylsiloxane (PDMS) chains covalently bound to a silica surface[23] supported these and other experimental observations[24] of accelerated rupture with increasing force. Later CPMD studies revealed the nature of rupture events by nucleophilic solvent molecules[25] or fragements of adjacent ruptured chains,[26] suggesting some mechanisms for bulk material degradation.

In all of the above cases, stretching accelerated the rupture of the Si–O bonds, in contrast with the expectations of potential inhibition discussed further above. Why the disparity? Are the predictions above inaccurate and Si–O bond cleavage is accelerated, not inhibited, by increasing tensile force, or can Si–O bond cleavage be inhibited by force in some cases but other mechanisms are operative in the examples above? First, in all of the above examples, the stretching forces were >500 pN, in some cases even reaching the several nN of force required for covalent bond homolysis. Once forces are large enough to induce bond homolysis, rupture will almost certainly be accelerated by increasing force as the transformation becomes barrierless. In cases where the Si–O bond is not cleaved by homolysis, the evidence is less clear: Significant steric effects were noted to be present in the simulated solvolysis of stretched dimethylsiloxane oligomers. When stretched, conformational rearrangement of the oligomer allows for greater access of water molecules to the Si–O backbone, allowing for barrierless substitution to occur at high enough tensile forces; however, the methyl groups of hexamethyldisiloxane prevented it from approaching the backbone closely enough to induce chain scission under otherwise identical conditions.[25]

In an effort to clarify the issue and to further investigate the mechanochemical behavior of nucleophilic cleavage of Si–O bonds, we undertook a study of the methanolysis of the O–SiR_2–O reactive moiety by incorporating it into a series of stiff-stilbene-containing macrocycles in a manner similar to our previous studies.

5.3 Methods

We synthesized a series of 12 macrocycles by adding R_2SiCl_2 to the corresponding (*Z*)-stiff stilbenes with alcohol-terminated linkers of varying length. Strained *E* isomers were obtained as components of photostationary mixtures by irradiating dilute acetonitrile solutions of the macrocycles with 375 ± 7 nm light. The structures are defined in Fig. 5.3. To help distinguish steric effects from mechanochemical ones, some macrocycles contained $SiMe_2$ and some contained $SiPh_2$.

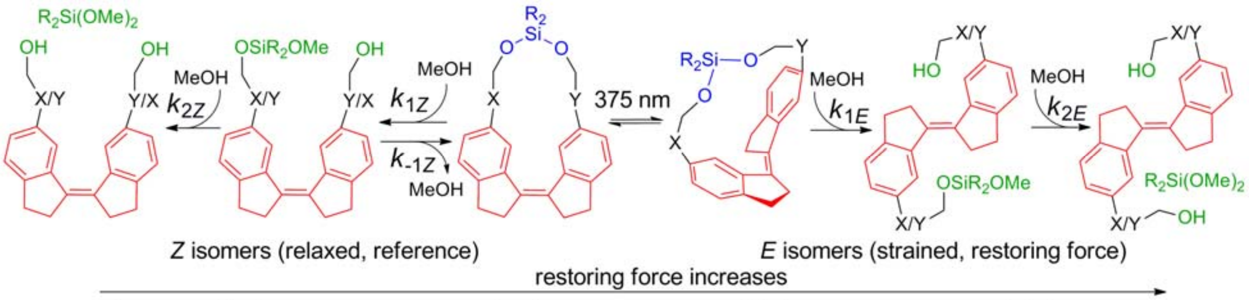

size:		R	X	Y
20 atoms	**1**	Ph	OCH_2	$O(CH_2)_4$
	2	Ph	$O(CH_2)_2$	$O(CH_2)_3$
19 atoms	**3**	Me	$(CH_2)_2$	$O(CH_2)_3$
	4	Me	$O(CH_2)_2$	$O(CH_2)_2$
	5	Ph	$O(CH_2)_2$	$O(CH_2)_2$
18 atoms	**6**	Ph	$(CH_2)_2$	$O(CH_2)_2$
	7	Me	$(CH_2)_2$	$O(CH_2)_2$
	8	Ph	OCH_2	$O(CH_2)_2$
	9	Me	OCH_2	$O(CH_2)_2$
17 atoms	**10**	Me	$(CH_2)_2$	$(CH_2)_2$
	11	Ph	$(CH_2)_2$	$(CH_2)_2$
	12	Ph	OCH_2	OCH_2

Fig. 5.3. The macrocycles used to study the force-dependent methanolysis kineics of Si–O bonds. Stiff stilbene is red, the reactive moiety is blue, and the methanolysis products are green. In the definition of X and Y, the leftmost atoms are bound to the stiff stilbene. Methanolysis takes place in two steps as the siloxane moiety is displaced first from one linker and then the other; the first step is reversible for the *Z* isomers.

Methanolysis of the reactive moiety takes place in two steps as it is displaced by solvent from first one linker and then the other. In the *Z* isomers, the first cleavage step is reversible because the displaced siloxane and alcohol-terminated linker are still in close proximity; methanol may be eliminated to reform the *Z* macrocycle. Subsequent elimination of $R_2Si(OMe)_2$ from the intermediate yields the (*Z*)-stiff stilbene diol. In the dilute solutions used (~20 μM combined concentration of the *E* and *Z* isomers) reformation of the intermediate is unlikely. In the *E* isomers, the initial Si–O bond cleavage by methanol is irreversible; following macrocyclic rupture, the distorted (*E*)-stiff stilbene relaxes to its planar, minimum-energy conformation, preventing the recombination of the alcohol-terminated linker and the intermediate siloxane. Subsequent conversion to the (*E*)-stiff stilbene diol is analogous to that in the *Z* isomers, but because this step has no bearing on the force-dependent kinetics of the initial cleavage step or the reference process in the *Z* isomers, it was not monitored, alleviating some requirements for the HPLC analysis.

To minimize the effect of sample variation on the ratios of measured rate constants for the initial cleavage steps of the *Z* and *E* isomers of **1**–**12**, competition experiments were carried out in which an initially photostationary mixture of *Z* and *E* isomers of a given macrocycle were allowed to react in methanol solution over a range of 25–60 °C. The HPLC chromatograms of samples of these reaction mixtures did not indicate the formation of any oligomers or mixed products, the reaction rates of *Z* isomers measured alone and in the presence of *E* isomers were indistinguishable within experimental error and final products were confirmed by comparison on HPLC retention times and UV spectra to authentic samples of the precursor diols. The phenyl-substituted macrocycles (**1**, **2**, **5**, **6**, **8**, **11** and **12**) reacted readily under neutral conditions. In contrast, the methanolysis of methyl-substituted macrocycles (**3**, **4**, **7**, **9** and **10**) required the addition of 450–500 µM sodium methoxide to the reaction to obtain reaction rates measured on convenient time scales (e.g., ≥7 samples collected over ~9 h). Though reasonable efforts were made to maintain control over the volumes of reaction mixtures combined, the lack of independent verification of the final methoxide concentration for individual samples (e.g., by titration) and small variations in methoxide concentration between samples prevented the determination of bimolecular rate constants for the methyl-substituted macrocycles. However, the pseudo-first order rate constants of the *E* and *Z* isomers in a given sample were affected identically, and thus their ratio was still accurate and comparable to other experiments, yielding differential activation parameters $\Delta\Delta H_{Z\text{–}E}^{\ddagger}$ and $\Delta\Delta S_{Z\text{–}E}^{\ddagger}$ from plots of $\ln(k_E/k_Z)$ vs. $1/T$. For the phenyl-substituted series, individual and differential activation parameters were obtained.

5.4 Results and Discussion

In all cases inhibition was observed: *E* isomers reacted with methanol/methoxide more slowly than *Z* isomers. Furthermore, a general trend of increasing inhibition (more negative values of $\Delta\Delta G_{Z\text{–}E}^{\ddagger}$) with decreasing macrocycle size (with the exception of **11** and **12**, see below). The differential activation free energies at 298 K are shown in Table 5.2; differential activation parameters are shown in Table 5.5; individual activation parameters for the methanolysis of the phenyl-substitued macrocycles are shown in Table 5.6.

Table 5.2. Force-dependent free energy barrier changes; derived from $\ln(k_E/k_Z)$ at 298 K.

macrocycle	$\Delta\Delta G_{Z\text{–}E}^{\ddagger}$ at 298K, kcal/mol
1	-2.0 ± 0.1
2	-0.65 ± 0.09
3	-1.7 ± 0.1
4	-1.7 ± 0.1
5	-1.8 ± 0.3
6	-1.7 ± 0.9
7	-1.6 ± 0.2

Table 5.2 (cont.)

8	-1.78 ± 0.09
9	-2.3 ± 0.2
10	-2.6 ± 0.1
11	-0.1 ± 0.5
12	-1.03 ± 0.08

The DFT calculations to support this experimental work are still in progress. However, for all of the macrocycles except **3** and **4**, the restoring force vectors for structural analogs in which the $OSiR_2O$ fragment is replaced with $OP(O)R'O$ have been calculated. Using these net force values (i.e., the net restoring force vector, $\langle F_{\mathrm{total}}\rangle_E - \langle F_{\mathrm{total}}\rangle_Z = F_{\mathrm{net}}$) as a proxy for those in **1**, **2** and **5**–**12** and using rough estimates of intermediate values for **3** and **4** based on similar structures one may make a (rough) semi-quantitative analysis of the effect of increasing force on siloxane methanolysis. The resulting plot of $\Delta\Delta G_{Z\text{–}E}^{\ddagger}$ vs. $|F_{\mathrm{net}}|$ is shown in Fig. 5.4, with the following caveats: 1) the forces are estimates based on structural analogs and may be inaccurate and 2) the magnitude of the restoring force vector is plotted, not a projection along q. With regard to the later caveat, however, the anisotropic nature of the stiff stilbene system can be expected to result in the magnitude of the projection along q being ~80% of that of the total force vector, resulting in a nearly uniform shift of the data to the left along the x-axis though maintaining the approximate ordering of the points.

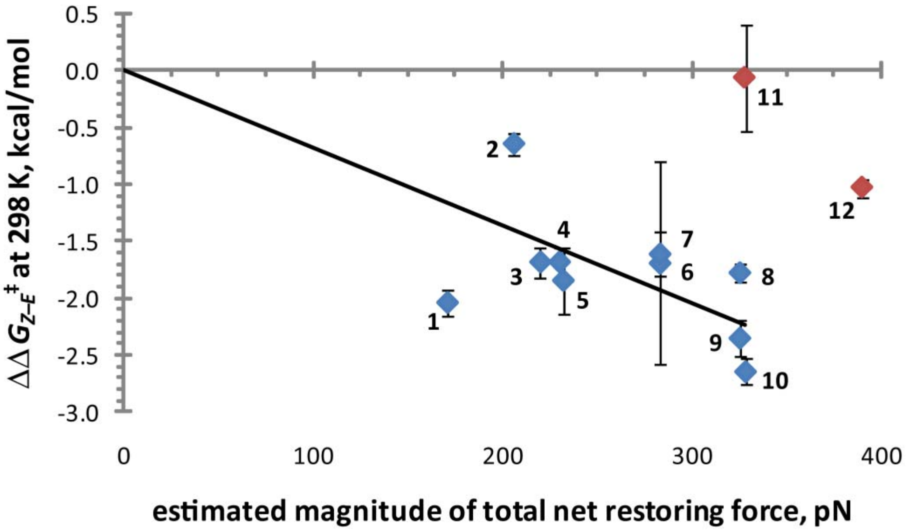

Fig. 5.4. Apparent force-dependent inhibition of silyl ether methanolysis. Force values are estimated from calculations on structural analogs containing phosphotriesters as the reactive moiety for all macrocycles, except **3** and **4**, which were estimated as an intermediate value between two of the closest structural analogs for each. The blue points appear to follow a trend where Δq = -0.47 Å, neglecting second-order effects; the red points appear to fall out of this trend which may either be due to inaccurate force estimates or a change in the mechanism at higher restoring forces.

The majority of the data in Fig. 5.4 appears to follow a linear trend corresponding to $\Delta\Delta G_{Z\text{–}E}^{\ddagger} \approx F_q\Delta q \approx F_{\text{net}}\Delta q$, where $\Delta q = q_{\text{gs}} - q_{\text{ts}}$. Similar to other S_N2 reactions we have studied (Chapter 3 and Chapter 4), second-order effects appear to be negligible. Note also that there is no apparent trend corresponding to the identity of the substituents on the Si atom—methyl (**3**, **4**, **7**, **9** and **10**) vs. phenyl (**1**, **2**, **5**, **6**, **8**, **11** and **12**)—indicating that steric effects are likely not the cause of the apparent inhibition. The slope of the line shown in Fig. 5.4 yields an apparent value of Δq = -0.47 Å, indicating a significant contraction of q in the methanolysis transition state. This contraction seems very large—it is larger in magnitude than the elongation of q exhibited by sulfonate hydrolysis. However, the fits of the kinetic model to the HPLC data were in general very good (see section 5.7.3 below), so while the magnitude of this metric may be somewhat inaccurate, Δq is still likely negative—the E isomers are observed to react more slowly than the Z isomers. Such an observation could be explained by a failure to account for the reversibility of initial macrocyclic cleavage in the Z isomers (which would lead to overestimation of the ratio k_E/k_Z), but this was accounted for in the kinetic model.

Macrocycles **11** and **12** (red points, Fig. 5.4) appear to fall out of the trend exhibited by the rest of the data (blue points). There are (at least) two possible explanations for this: 1) the force values used are not representative of the actual force values and 2) the restoring force is large enough in these macrocycles that a different reaction pathway is enabled, one in which q does not contract nearly as much. The former explanation is rather unlikely because for **11** and **12** to fall into the trend, they would need to have forces ~200 pN smaller, though the 17-atom macrocycles generally have the largest restoring forces. Thus, the second explanation is more likely, particularly in light of the CPMD calculations that indicate acceleration of solvolysis at tensile forces >500 pN.[25] However, in the absence of completed DFT calculations of our macrocycles, the explanation remains clouded, particularly in light of the caveats of the estimates discussed above.

5.5 Conclusions

Despite various experimental and theoretical studies on the cleavage of Si–O bonds that report acceleration with increasing tensile force >500 pN,[22-27] we observed inhibition of siloxane methanolysis in a series of strained macrocycles. There is no apparent trend corresponding to the identity of the substituents on the electrophilic Si atom, indicating that steric effects likely are not the cause of the observed inhibition, in contrast to the steric/conformational effects partially responsible for acceleration in some CPMD simulations.[25] A rough ordering of the differential activation free energies at 298 K using values from structural analogs yields a linear trend for 10 of the macrocycles corresponding to a contraction of q, presumably the $O_{spectator}\cdots O_{LG}$ internuclear separation, of 0.47 Å. The two phenyl-substituted macrocycles with the largest estimated restoring forces fall out of this trend and instead exhibit very little inhibition.

One explanation is that these two macrocycles are beginning to exhibit Si–O bond cleavage by a different mechanism than that which dominates in the low-force regime. If true, these results then do not contradict those which indicate acceleration at forces >500 pN and instead indicate both that the mechanochemical reponse of Si–O bonds is more complex than previously acknowledged and that an inverted region of mechanochemistry exists in the low-force regime. Such an inverted region of mechanochemistry in which increasing restoring force further inhibits chemical reactivity would be a novel tool to use in the design of fatigue-resistant materials and also would enable the conception of new material functions at the molecular level.

However, before such concepts can be exploited, the mechanochemistry of different reactive moieties that lack alternative (undesired) reaction pathways that are thermally accessible until much higher restoring forces (ideally up to a few nN, where covalent bonds are homolyzed) will need to be identified.

5.6 Acknowledgments

The contributions of the following individuals are gratefully acknowledged: Dr. Sergey Akbulatov and Dr. Binglin Wang synthesized the macrocycles. Ho Yee Hui assisted with the kinetics experiments. Dr. Yancong Tian continues to work on the computational modeling for these reactions. Funding for this project is similar to that listed elsewhere in the dissertation.

5.7 Supporting Experimental Information

5.7.1 Materials and General Methods

All solvents used were HPLC grade or better. Anhydrous tetrahydrofuran was collected from an MBraun Solvent Purification System. Water was obtained from a Milli-Q water purification system. Anhydrous acetonitrile was graciously provided by Christopher Letko and Bryan Barton in the Rauchfuss laboratory. Anhydrous dichloromethane and methanol were purchased from Aldrich and were stored in an inert-atmosphere (N_2) glovebox.

Irradiation was performed in vessels sealed under a N_2 atmosphere using high-intensity diode light sources from Opto Technology with light output at 375 ± 7 nm. Light intensity was controlled with a custom-made constant-current controller. UV-vis spectra were recorded on a Cary 50 UV-vis spectrophotometer.

High-resolution mass spectrometry was performed on a Micromass 70-VSE mass spectrometer (EI) at the University of Illinois Mass Spectrometry Center. HPLC was performed on a Shimadzu Prominence system with an LC-20AT solvent delivery unit, DGU-20A5 degasser, SPD-M20A photodiode array detector, CBM-20A system controller and Rheodyne 7725i manual injector or on a Waters system with a 600E multisolvent delivery system with He gas solvent sparging, 996 photodiode array detector, and Rheodyne 7725i manual injector. Three columns were used for the HPLC analysis, as specified in the separation conditions: J.T. Baker C_{18} column (25 cm × 4.6 mm, 5 μm particles), Supleco C_{18} column (15 cm × 4.6 mm, 5 μm particles) or Machery–Nagel C18 gravity column (25 cm × 4.6 mm, 3 μm particles). Least squares regressions for kinetic data obtained from photostationary mixtures were carried out with custom-written scripts in Matlab (7.9.0 R2009b).

The synthesis and NMR characterization of **1**–**12** will be reported elsewhere. The high-resolution mass spectrometry data confirming molecular formulas is shown in Table 5.3.

Table 5.3. High-resolution mass spectrometry (EI) confirmation of molecular formulas for **1**–**12**.

	formula	calc'd, g/mol	found, m/z	error, ppm
1	$C_{37}H_{38}O_4Si$	574.2539	574.25299	-1.7
2	$C_{37}H_{38}O_4Si$	574.2539	574.25311	-1.4
3	$C_{27}H_{34}O_3Si$	434.2277	434.2274	-0.7
4	$C_{26}H_{32}O_4Si$	436.207	436.20729	0.7
5	$C_{36}H_{36}O_4Si$	560.2383	560.23860	0.6
6	$C_{36}H_{36}O_3Si$	544.2434	544.24267	-1.3
7	$C_{26}H_{32}O_3Si$	420.2121	420.21214	0.2
8	$C_{35}H_{34}O_4Si$	546.2226	546.22309	0.8
9	$C_{25}H_{30}O_4Si$	422.1913	422.19146	0.3
10	$C_{26}H_{32}O_2Si$	404.2172	404.2166	-1.4
11	$C_{36}H_{36}O_2Si$	528.2485	528.24988	2.7
12	$C_{34}H_{32}O_4Si$	532.207	532.20756	1.1

5.7.2 Experimental Methods for Kinetics Measurements

Photostationary mixtures of the *E* and *Z* isomers were prepared by irradiating a solution with maximum absorbance ~1 of each *Z* isomer in acetonitrile in a cuvette sealed under N_2 with 375 nm light until the UV-vis spectrum no longer changed. Stock solutions of the photostationary mixtures and *Z* isomers were stored at -35 °C under N_2.

Reactions were carried out in sealed vials, using gas-tight syringes to withdraw samples for compositional analysis. Samples were either analyzed by HPLC immediately following withdrawal or were transferred to empty vials and stored at -35 °C until being analyzed by HPLC. The reaction vials were kept in a custom-made heating block with resistance heaters and thermocouple connected to an active-feedback temperature controller which enabled the temperature of the reaction mixtures to be maintained with the stability of ±0.1 °C. The reaction temperature was recorded every 6 s. To prevent photoisomerization between the *E* and *Z* dithiols by ambient light, amber-glass vials were used and all samples were kept away from light. No changes in *E*/*Z* ratio could be detected in control samples stored in this manner for weeks.

For the phenyl-substituted macrocycles, 100-μL aliquots of stock solutions of the photostationary mixtures were diluted with 655 μL of anhydrous methanol, and 35 μL of a solution of (*E*)-6,6′-dimethoxy stiff stilbene as an internal standard. The vials were shaken vigorously for 1–2 s and then were placed in the heating block for the duration of the experiment. Samples removed for compositional analysis were ~100 μL.

For the methyl-substituted macrocycles, 100-μL aliquots of stock solutions of the photostationary mixtures were placed in sealed vials and to minimize the opportunity for contamination with atmospheric moisture, which would lead to a mixture of hydroxide and methoxide under the basic reaction conditions, the vials were transferred to a glovebag with a continuous N_2 purge. The samples were then each diluted with 365 μL of anhydrous methanol, and 35 μL of a solution of (*E*)-6,6′-dimethoxy stiff stilbene as an internal standard. Then 300 μL of 1.26 mM sodium methoxide in methanol was added, the vials were sealed and shaken vigorously for 1–2 s and then were placed in the heating block (also inside the glovebag) for the duration of the experiment. Samples removed for compositional analysis were injected into vials sealed under N_2 and stored at -35 °C unless injected directly into the HPLC system for analysis.

The HPLC retention times and isocratic separation conditions for the components of the reaction mixtures are shown below in Table 5.4. Product diols whose retention times are not listed were not resolved into individual peaks and eluted with a time equal or shortly after the dead time. In two cases (**8** and **9**) both regioisomers of the intermediate (i.e., initial displacement of linker X and initial displacement of linker Y where X and Y are not identical) were resolved as two separate peaks; in all other cases only a single peak for the *Z* intermediate was observed, indicating either a high degree of regioselectivity in the initial cleavage step or, more likely, that the two intermediate regioisomers behaved similarly enough under the given separation conditions as to render them unresolvable. In only one case (**8**) were both regioisomers of the *E* intermediate resolved as two separate peaks. In other cases, the *E* intermediate isomers eluted with the *E* and/or *Z* product diols; resolution of the *E* intermediates required separation conditions that led to impractically long retention times (>80 min) for the slowest eluting compounds. However, because the rate of initial cleavage of the *E* isomers could be determined solely from the depletion of the *E* macrocycle, it was not necessary to resolve the *E* intermediates. To enable comparison of cases in which both regioisomers of the *Z* intermediates were resolved, the two peak areas were summed (as was physically the case for unresolved peaks) and then treated identically as other kinetic data, as described below.

Table 5.4. Retention times in min for reaction mixture components; n.r. = not resolved; A = Supelco C18 column, B = JT Baker C18 column, C = Machery–Nagel C18 gravity column

	Z macro	*Z* intermediate	*Z* diol	*E* macro	*E* intermediate	*E* diol	separation conditions
1	17.7	7.6	n.r.	8.5	n.r.	n.r.	A, 4% water in methanol, 1 mL/min
2	20.2	7.7	n.r.	7.5	n.r.	n.r.	A, 4% water in methanol, 1 mL/min
3	19.9	7.1	4.7	7.6	n.r.	n.r.	B, 6% water in methanol, 1 mL/min
4	65.4	22.3	9.6	19.4	n.r.	7.2	B, 18% water in methanol, 1 mL/min
5	17.6	7.1	3.1	7.9	n.r.	2.4	A, 4% water in methanol, 1 mL/min
6	23.6	8.7	3.4	26.0	n.r.	n.r.	A, 5% water in methanol, 1 mL/min
7	24.7	8.4	5.2	9.7	n.r.	4.4	B, 9% water in methanol, 1 mL/min
8	85.7	28.0, 30.1	6.2	36.2	22.9, 24.3	3.8	C, 11% water in methanol, 1 mL/min
9	67.0	24.9, 26.3	n.r.	28.7	n.r.	n.r.	C, 15% water in methanol, 0.8 mL/min
10	34.8	9.9	5.8	13.1	n.r.	4.7	B, 10% water in methanol, 1 mL/min
11	33.1	11.0	n.r.	18.7	n.r.	n.r.	C, 2% water in methanol, 0.8 mL/min
12	29.3	11.5	3.4	8.4	n.r.	2.4	A, 10% water in methanol, 1 mL/min

5.7.3 The Kinetic Model for the Methanolysis of Macrocycles

The (apparent) rate constants for methanolysis of the *E* macrocycles were determined from the slopes of linear semilogarithmic plots of $\ln(IA_{E\text{macro}}/IA_{\text{std}})$ vs. t, where $IA_{E\text{macro}}$ and IA_{std} are the integrated areas of the peaks for the *E* macrocycle and the internal standard in a given chromatogram and t is the time elapsed between initial reaction mixture combination and sample withdrawal.

The methanolysis of *Z* isomers was modeled as the transformation shown in Fig. 5.5, which gives the differential equations (1.2) and (5.2).

$$\mathrm{A} \underset{k_{-1}}{\overset{k_1}{\rightleftharpoons}} \mathrm{B} \xrightarrow{k_2} \mathrm{C}$$

Fig. 5.5. The kinetic scheme for the methanolysis of *Z* macrocycles

$$\frac{d[A]_t}{dt} = -k_1[A]_t + k_{-1}[B]_t \tag{5.1}$$

$$\frac{d[B]_t}{dt} = k_1[A]_t - (k_2 + k_{-1})[B]_t \tag{5.2}$$

Then integration yields eqs. (5.3) and (5.4), where u is defined by eq. (5.5), $A_0 = [A]_{t=0}$ and $B_0 = [B]_{t=0}$.

$$\begin{aligned}[A]_t = \frac{1}{u}\left(\cosh\frac{(k_1 + k_2 + k_{-1})t}{2} - \sinh\frac{(k_1 + k_2 + k_{-1})t}{2}\right)\bigg(A_0 u \cosh\frac{ut}{2} \\ + \big(2B_0 k_{-1} + A_0(-k_1 + k_2 + k_{-1})\big)\sinh\frac{ut}{2}\bigg)\end{aligned} \tag{5.3}$$

$$\begin{aligned}[B]_t = \frac{1}{u}\left(\cosh\frac{(k_1 + k_2 + k_{-1})t}{2} - \sinh\frac{(k_1 + k_2 + k_{-1})t}{2}\right)\bigg(B_0 u \cosh\frac{ut}{2} \\ + \big(2A_0 k_1 + B_0(k_1 - k_2 - k_{-1})\big)\sinh\frac{ut}{2}\bigg)\end{aligned} \tag{5.4}$$

$$u = \sqrt{-4k_1k_2 + (k_1 + k_2 + k_{-1})^2} \tag{5.5}$$

Recalling that $\sinh x = \frac{e^x - e^{-x}}{2}$ and $\cosh x = \frac{e^x + e^{-x}}{2}$, eqs. (5.3) and (5.4) may be simplified further to

$$[A]_t = \frac{1}{u}e^{-\frac{(k_1+k_2+k_{-1})t}{2}}\left(A_0 u \cosh\frac{ut}{2} + \big(2B_0k_{-1} - A_0(k_1 - k_2 - k_{-1})\big)\sinh\frac{ut}{2}\right) \tag{5.6}$$

$$[B]_t = \frac{1}{u}e^{-\frac{(k_1+k_2+k_{-1})t}{2}}\left(B_0 u \cosh\frac{ut}{2} + \big(2A_0k_1 + B_0(k_1 - k_2 - k_{-1})\big)\sinh\frac{ut}{2}\right) \tag{5.7}$$

Fitting of eqs. (5.6) and (5.7) to determine values of k_1, k_{-1} and k_2 for the methanolysis of *Z* isomers was carried out with a custom script in Matlab (v7.9.0, R2009b). The experimental integrated areas of *Z* macrocycle and *Z* intermediate peaks in the chromatograms normalized to the internal standard (i.e., $IA_{Z\text{macro}}/IA_{\text{std}}$ and $IA_{Z\text{int}}/IA_{\text{std}}$) were input for $[A]_t$ and $[B]_t$, respectively. Then the values of k_1, k_{-1} and k_2 were optimized by the Matlab function lsqnon, which sought to minimize the sums of absolute values of the residuals $[A]_{t,\text{expt}} - [A]_{t,\text{calc}}$ and $[B]_{t,\text{expt}} - [B]_{t,\text{calc}}$. Errors on the fitted rate constants were calculated using the methods in ref. 28 but reflect only the error due to fitting because 1) the responses of the HPLC systems were not calibrated against a standard and 2) the ratios of integrated areas also depend on the ratios of extinction coefficients of the macrocycles, intermediates, and internal standard, which were not practical to quantify. A typical fit is shown in Fig. 5.6.

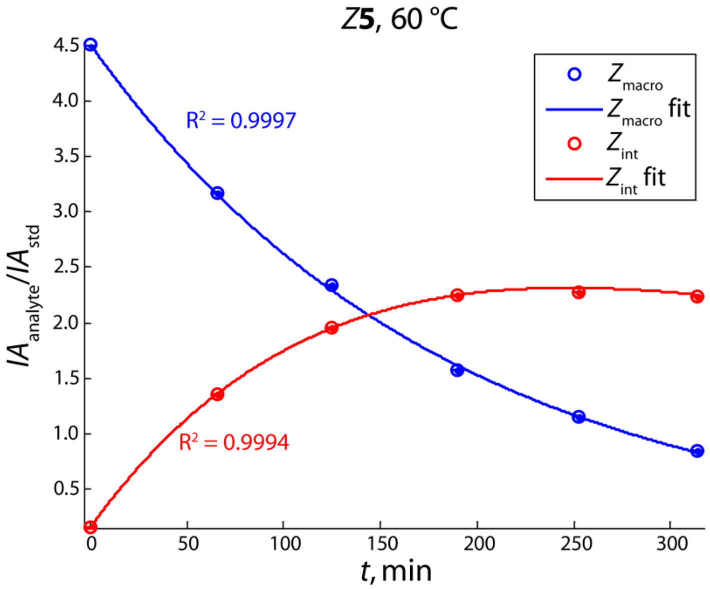

Fig. 5.6. A typical fit for the methanolysis of *Z***5**

Eyring plots of ratios of rate constants (i.e., k_E/k_Z for all macrocycles) and rate constants (phenyl-substituted macocycles) yielded the differential and individual activation parameters shown in Table 5.5 and Table 5.6. The rate constants for the reverse step in phenyl-substituted macrocycles did not yield good Eyring plots, likely due to the same reason the errors calculated for the fitted values of k_{-1} were larger than those for the corresponding values of k_1 and k_2.

Table 5.5. Differential activation parameters for methanolysis; derived from $\ln(k_E/k_Z)$ vs. $1/T$

macrocycle	$\Delta\Delta H_{Z\text{–}E}^{\ddagger}$, kcal/mol	$\Delta\Delta S_{Z\text{–}E}^{\ddagger}$, cal/(mol K)
1	-7.7 ± 0.3	-19 ± -1
2	-2.8 ± 0.9	-7 ± -3
3	0.9 ± 0.6	9 ± 2
4	0.9 ± 0.2	8.6 ± 0.7
5	-4.5 ± 0.7	-9 ± -2
6	-2 ± 3	-1 ± -9
7	1 ± 2	10 ± 5
8	-3.9 ± 0.2	-7.3 ± -0.7
9	-2 ± 2	0 ± 5
10	1 ± 3	12 ± 9
11	-6 ± 2	-20 ± -5

Table 5.5 (cont.)

12	5.8 ± 0.8	23 ± -3

Table 5.6. Activation parameters for the methanolysis of phenyl-substituted macrocycles and the correlation coefficients of the respective Eyring plots

	cleavage of *Z* macrocycle			*Z* intermediate to *Z* diol			cleavage of *E* macrocycle		
	$\Delta H^{\ddagger}$, kcal/mol	$\Delta S^{\ddagger}$, kcal/mol	R^2	$\Delta H^{\ddagger}$, kcal/mol	$\Delta S^{\ddagger}$, kcal/mol	R^2	$\Delta H^{\ddagger}$, kcal/mol	$\Delta S^{\ddagger}$, kcal/mol	R^2
1	12.1 ± 0.8	-41 ± 2	0.996	14 ± 3	-35 ± 8	0.969	19.8 ± 0.4	-22 ± 1	0.9995
2	11 ± 3	-44.2 ± 9.7	0.933	11 ± 2	-45 ± 7	0.960	14 ± 4	-40 ± 10	0.926
5	7.1 ± 0.5	-56 ± 2	0.995	11.1 ± 0.1	-45.5 ± 0.5	0.9998	11.6 ± 0.1	-47.1 ± 0.5	0.9998
6	11 ± 1	-45 ± 4	0.989	10 ± 4	-50 ± 10	0.892	13 ± 2	-45 ± 5	0.982
8	14 ± 2	-32 ± 5	0.977	19 ± 3	-21.5 ± 9.6	0.948	18 ± 2	-24 ± 5	0.982
11	10 ± 3	-50 ± 10	0.908	8 ± 7	-60 ± 20	0.561	16 ± 5	-30 ± 20	0.917
12	10 ± 2	-44 ± 6	0.969	9 ± 1	-48 ± 5	0.976	5 ± 1	-67 ± 3	0.949

5.8 References

1. Black, A. L.; Lenhardt, J. M.; Craig, S. L., From Molecular Mechanochemistry to Stress-Responsive Materials. *J. Mater. Chem.* **2011**, *21*, 1655–1663.
2. Caruso, M. M.; Davis, D. A.; Shen, Q.; Odom, S. A.; Sottos, N. R.; White, S. R.; Moore, J. S., Mechanically-Induced Chemical Changes in Polymeric Materials. *Chem. Rev.* **2009**, *109*, 5755–5798.
3. Anslyn, E. V.; Dougherty, D. A., *Modern Physical Organic Chemistry*. University Science Books: Sausalito, CA, 2006.
4. Smith, M. B.; March, J., *March's Advanced Organic Chemistry: Reactions, Mechanisms, and Structure*. 5th ed.; John Wiley & Sons, Inc.: New York, 2001.
5. Grunwald, E., Linear Free Energy Relationships: A Historical Perspective. *Chemtech* **1984**, *14*, 698–705.
6. Lowry, T. H.; Richardson, K. S., *Mechanism and Theory in Organic Chemistry*. 2nd ed.; Harper & Row Publishers: New York, 1981.
7. Chapman, N. B.; SHorter, J., *Advances in Linear Free Energy Relationships*. Plenum Press: New York, 1972.

8. Jencks, W. P., A Primer for the Bema Hapothle. An Empirical Approach to the Characterization of Changing Transition-State Structures. *Chem. Rev.* **1985**, *85*, 511–527.
9. Marcus, R. A.; Sutin, N., Electron Transfers in Chemistry and Biology. *BBA Bioenergetics* **1985**, *811*, 265–322.
10. Leffler, J. E.; Grunwald, E., *Rates and Equilibria of Organic Reactions*. John Wiley and Sons, Inc.: New York, 1963.
11. Hammond, G. S., A Correlation of Reaction Rates. *J. Am. Chem. Soc.* **1955**, *77*, 334–338.
12. Leffler, J. E., Parameters for the Description of Transition States. *Science* **1953**, *117*, 340–341.
13. Huang, Z.; Boulatov, R., Chemomechanics: Reaction Kinetics in Multiscale Phenomena. *Chem. Soc. Rev.* **2011**, *40*, 2359–2384.
14. Kucharski, T. J.; Yang, Q.-Z.; Tian, Y.; Boulatov, R., Strain-Dependent Acceleration of a Paradigmatic S_N2 Reaction Accurately Predicted by the Force Formalism. *J. Phys. Chem. Lett.* **2010**, *1*, 2820–2825.
15. Kucharski, T. J.; Boulatov, R., The Physical Chemistry of Mechanoresponsive Polymers. *J. Mater. Chem.* **2011**, *21*, 8237–8255.
16. Boulatov, R., Reaction Dynamics in the Formidable Gap. *Pure Appl. Chem.* **2011**, *83*, 25–41.
17. Woodward, R. B.; Hoffmann, R., The Conservation of Orbital Symmetry. *Angew. Chem. Int. Ed. Engl.* **1969**, *8*, 781–853.
18. Oth, J. F. M., The Kinetics and Thermochemistry of the Termal Rearrangement of Hexamethylbicyclo[2.2.0]hexa-2,5-diene (Hexamethyldewarbenzene) and of Hexamethyltetracyclo[2.2.0,$0^{2,6}$.$0^{3,5}$]hexane (Hexamethylprismane). *Recl. Trav. Chim. Pays-Bas* **1968**, *87*, 1185–1195.
19. Ferrar, L.; Mis, M.; Robello, D. R., Thermal isomerization of dewarbenzene derivatives. *Tetrahedron Lett.* **2008**, *49*, 4130–4133.
20. Cotton, F. A.; Wilkinson, G., *Advanced Inorganic Chemistry*. 3rd ed.; Interscience Publishers: New York, 1972.
21. Bondi, A., van der Waals Volumes and Radii. *J. Phys. Chem.* **1964**, *68*, 441–451.
22. Grandbois, M.; Beyer, M.; Rief, M.; Clausen-Schaumann, H.; Gaub, H. E., How Strong Is a Covalent Bond? *Science* **1999**, *283*, 1727–1730.

23. Lupton, E. M.; Achenbach, F.; Weis, J.; Bräuchle, C.; Frank, I., Molecular Origins of Adhesive Failure: Siloxane Elastomers Pulled from a Silica Surface. *Physical Review B* **2007**, *76*, 125420/1–9.
24. Schwaderer, P.; Funk, E.; Achenbach, F.; Weis, J.; Brauchle, C.; Michaelis, J., Single-Molecule Measurement of the Strength of a Siloxane Bond. *Langmuir* **2008**, *24*, 1343–1349.
25. Lupton, E. M.; Achenbach, F.; Weis, J.; Brauchle, C.; Frank, I., Modified Chemistry of Siloxanes under Tensile Stress: Interaction with Environment. *J. Phys. Chem. B* **2006**, *110*, 14557–14563.
26. Lupton, E. M.; Achenbach, F.; Weis, J.; Bräuchle, C.; Frank, I., Origins of Material Failure in Siloxane Elastomers from First Principles. *ChemPhysChem* **2009**, *10*, 119–123.
27. Schmidt, S. W.; Beyer, M. K.; Clausen-Schaumann, H., Dynamic Strength of the Silicon-Carbon Bond Observed over Three Decades of Force-Loading Rates. *J. Am. Chem. Soc.* **2008**, *130*, 3664–3668.
28. Gans, P., *Data Fitting in the Chemical Sciences By the Method of Least Squares*. John Wiley & Sons: New York, 1992.

Chapter 6. Inhibiting and Accelerating the Same Reaction by Varying the Direction of the Restoring Force: Implications for Enzymatic Catalysis

6.1 Introduction

Enzymes are responsible for some of the largest chemical rate enhancements known. Under physiological conditions, they rapidly carry out reactions that would otherwise take millennia, thereby enabling many of the biochemical reactions that underpin life on Earth. For example, the phosphatases (which convert phosphate monoesters to inorganic phosphate) involved in signal transduction and regulation have been noted to accelerate reactions by as much as ~10^{21}-fold.[1] Phosphate transfer reactions are ubiquitous in biological systems; adenosine triphosphate (ATP) is the cellular energy carrier for many organisms, and its hydrolysis provides the free energy for numerous endergonic processes, such as various biochemical syntheses and mechanochemical phenomena. The enzymatic hydrolysis of ATP by motor proteins drives intracellular transport (e.g., the cargo-moving motion of kinesin[2-5] and myosin[6,7]) and cellular motility (e.g., flagellar motion[8]). Indeed, the synthesis of ATP can be mechanically induced, as in the reversible operation of F_1-ATPase.[9] It is important to note, however, that the mechanochemical properties of the pyrophosphate solvolysis step itself is not in general directly a component of the mechanochemistry of these biological processes. Though these processes clearly involve the coupling of meso- and/or micro-scale motions to the motions of a small subset of the system's atoms (i.e., a localized chemical reaction), the solvolysis of ATP is not the reaction that leads to the conformational changes necessary for the "mechano" part of the mechanochemical process; instead, its role is the fuel that provides the energy to drive chemical part of the process. Yet, mechanochemistry is still relevant in the process of releasing the energy from ATP: the effect of force on its reaction kinetics may enlighten our understanding of the mechanism for this important enzymatic conversion.

Explanations for the rate enhancements afforded by enzymes have circulated for more than 60 years, and many still shape our thinking of enzymatic catalysis today. For example, Pauling proposed in 1946 that enzymes bind the transition state of the catalyzed reaction more strongly than the reactant state;[10] this argument often accompanies those of reactant destabilization leading to effective barrier lowering. A host of other explanations exist,[11,12] from those which involve the distortion of the enzyme (the induced fit mechanism), to those which involve the distortion of the substrate (the entatic state) and those which involve both (the rack mechanism). These different mechanisms apply to individual cases to differing degrees, but they all have a key feature in common: the coupling of degrees of freedom of a larger extended system (the enzyme) to those of a small subset of atoms in which the reaction occurs (the substrate). Indeed, in certain cases in which the enzyme adopts a strained configuration upon binding of the substrate, the acceleration of the substrate reaction has been attributed to partial relief of the enzyme's strain in the transition state.[10] Such is precisely the case for the mechanochemical systems discussed elsewhere in this dissertation: Acceleration of a reactive moiety's chemical conversion can be accelerated by partial strain relief in the non-reacting part of the system, such as the relaxation accompanying an increase in contour length of a stretched polymer chain or that accompanying the partial opening of a pseudo-(*E*)-stiff stilbene.

Given these similarities, can our understanding of mechanochemical kinetics inform our understanding of enzymatic catalysis? With mechanochemical phenomena and enzymatic reactions defined as described above, yes. Not only do both processes depend on the manner in which the degrees of freedom of the reactive moiety (e.g., internuclear distances, angles and dihedral angles) are coupled to those of the extended system, they also span multiple length scales, often making the explicit consideration of the extended system impractical. Enzymes function by modifying the substrate's potential energy surface, biasing it such that otherwise unfavorable reaction pathways become readily accessible. These changes are often described in terms of a change in hydrophilic/hydrophobic character or dielectric constant or the formation of favorable electronic interactions such as hydrogen bonds or other non-covalent interactions. In cases where the substrate (or enzyme) adopts a configuration other than that of its global minimum, the energetic consequences are often described in terms of induced (macro)molecular strain. However, the aim of all of these traditional descriptions is the same: to describe the manner in which the substrate's potential energy surface is modified in the presence of the enzyme (and vice versa). Though these descriptions certainly have allowed for great advances in enzymology and related fields, it is conceivable that a mechanochemical description may provide additional insights into these enhancements of chemical reactivity, at least for those involving changes in substrate and/or macromolecular strain.

At present, several tools have been employed in the effort towards understanding the subtle, yet energetically important structural changes that accompany substrate binding and the subsequent reaction. In addition to the ever-increasing power of computational modeling to determine structural information about the interaction between substrates and active sites in proteins, various experimental techniques have been used to extract structural information about proteins and their substrates, including x-ray crystallography and various spectroscopies suitable for determining small structural differences from experimental observables (e.g., vibrational spectroscopy[13]). For example, a crystal structure of an inorganic pyrophosphatase indicating that the substrate is distorted when bound in the active site has been suggested to provide mechanistic insight into its operation.[14] Even for simple reactions, however, gaining experimental structural information about the fleetingly present transition states is even more challenging and necessitates the use of femtosecond spectroscopies. Alternatively, a mechanochemical analysis of a substrate also provides experimental information about the structure of a transition state. By determining the force–rate relationships of a given reactive moiety by connecting it to a source of strain through different pairs of nuclei, the elongation or contraction of the pairs' separation can be quantified by varying the restoring force of the strained system. In this sense, such a mechanochemical analysis serves as a molecular ruler for experimentally determining ground-state–transition-state structural changes. Furthermore such an analysis may also speak to the relative importance of observed or proposed structural distortions to the enhancement of reactivity observed in enzymatic transformations by mapping out the energetic consequences of specific elongations and contractions in terms of the gradients of energy along those coordinates (i.e., force).

In this work, we used this approach by investigating the force–rate relationships for force projected along two different internuclear separations, one that incorporated the scissile P–O bond and one that was orthogonal to it. In principle, these results indicate the relative importance of different manners of stretching the pyrophosphate substrate with respect to kinetic barrier lowering upon binding in an enzyme's active site.

6.2 Methods

To investigate the questions above, we synthesized two series of macrocyclic pyrophosphates: one in which the scissile bond of the pyrophosphate moiety is contained within the macrocycle (endocyclic pyrophosphates, Fig. 6.1A) and one in which the scissile bond of the pyrophosphate moiety is not within the macrocycle (exocyclic pyrophosphates, Fig. 6.1B). We then measured the methanolysis kinetics in the *E* and *Z* isomers to determine the effect of the force present in the *E* isomers on the reaction kinetics. For the endocyclic pyrophosphates, we synthesized the dimethyl esters to reduce the steric bulk of the groups neighboring the electrophilic P atoms. In the exocyclic pyrophosphates, we followed the same reasoning, but additionally needed to ensure that nucleophlic substitution would preferentially occur at the P atom contained in the macrocycle, the one which would be affected by varying the amount of molecular strain in the pseudo-*E* macrocycle. To do so, we used the 2-oxo-1,3,2-dioxaphosphorinanyl fragment as the exocyclic portion of the pyrophosphate. This 6-membered heterocycle resists opening in the presence of nucleophiles (e.g., water, methanol and other phosphates)[15] and phenylated derivatives have been used as chiral auxiliaries in asymmetric synthesis.[16] Presumably while maintaining similar electronic characteristics to the other alkyl substituents in this study, this six-membered ring effectively blocked nucelophlic scission of the directly adjacent P–O bond, thereby becoming a better leaving group than electrophilic center. A full analysis of the stereochemistry of the pyrophosphates used in this study is discussed in sections 6.6.3 and 6.6.4.

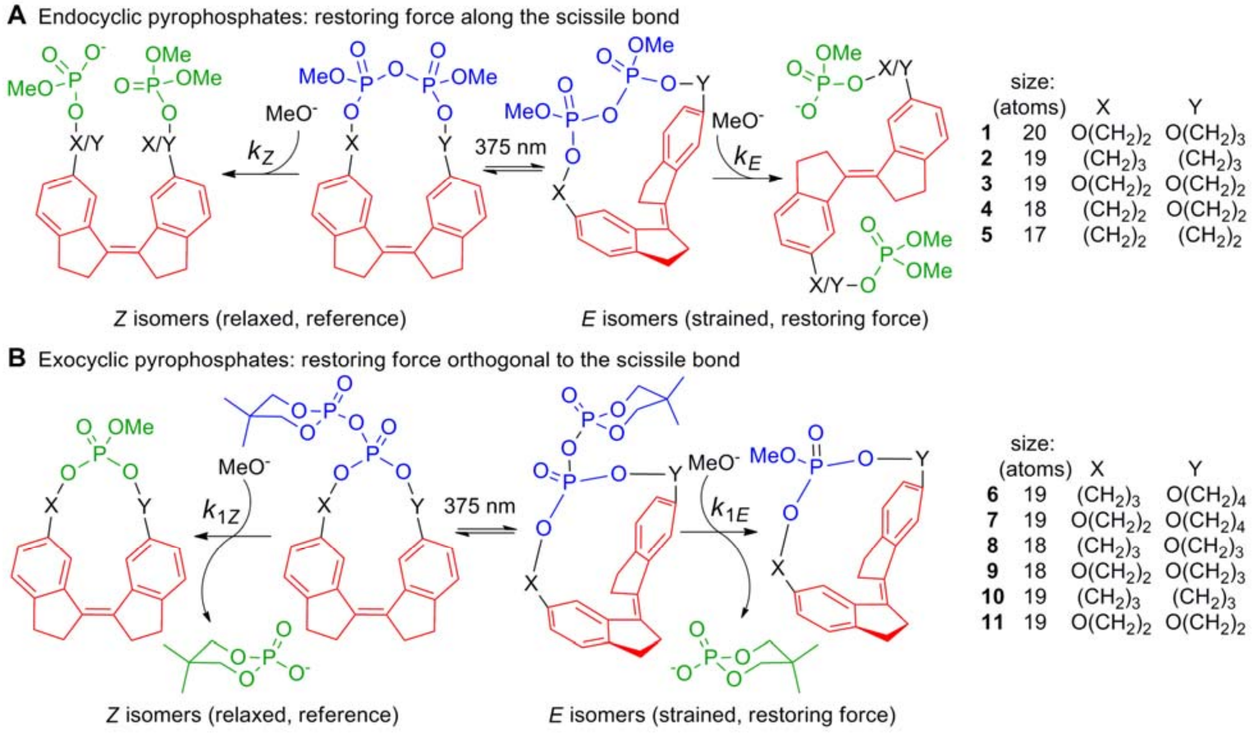

Fig. 6.1. Two series of macrocycles containing stiff stilbene (red) and pyrophosphates (blue) contained within (**A**) or pendant to (**B**) the macrocycle. Methanolysis under basic conditions selectively cleaves the pyrophosphate P–O bond, resulting in two monophosphates (green). The restoring force will have a major component along the scissile P–O bond in the endocyclic pyrophosphates (**A**) and will have a major component perpendicular to the scissile P–O bond in the exocyclic pyrophosphates (**B**).

To demonstrate the validity of our kinetic methods and to demonstrate the desired level of chemo- and regioselectivity of methanolysis for these substrates, we measured the reaction kinetics for a model compound, 5,5-dimethyl-2-oxo-1,3,2-dioxaphosphorinan-2-yl dibutylphosphate (**12** ,Fig. 6.2), both by NMR spectroscopy and with a variation on spectrophotometric method we have previously demonstrated (Chapter 3). For the exocyclic pyrophosphates, NMR spectroscopy (section 6.6.3) indicated >99% regioselectivity for nucelophilic substitution at the endocyclic P atom rather than the exocyclic P atom. Furthermore, the alkyl groups were not cleaved from the phosphoester (H–P coupling to the attached alkyl groups was retained), indicating that the reaction is also >99% chemoselective for the methanolysis of the pyrophosphate P–O bond (vs. the alkoxide P–O bonds), thereby providing for the conclusion that the consumption of methoxide in solution corresponds in a 1:1 ratio to the reaction of pyrophosphates in solution.

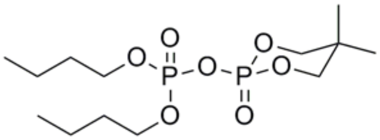

12

Fig. 6.2. The structure of the model compound used to validate our kinetic methods and the chemo- and regioselectivity of basic methanolysis.

The spectrophotometric method monitored the consumption of methoxide using phenol red in anhydrous methanol over a range of 10–60 °C. Phenol red was titrated in anhydrous methanol and found to have a ${}_{s}^{s}pK_a = 12.8$ (${}_{s}^{s}K_a = (1.5 \pm 0.2) \times 10^{-13}$ M; ${}_{s}^{s}pK_{ap}$ for MeOH is 16.77,[18] see section 3.8.2 for further discussion about pH and acidity in non-aqueous or aqueous–organic solvent mixtures). Phenol red was found to be stable under the desired reaction conditions at 60 °C; the small amount of drift over time was characterized by a zero-order rate constant more than five orders of magnitude slower than even the slowest pyrophosphate methanolysis reaction measured and was therefore ignored.

The spectrophotometric measurements of the rate of basic methanolysis of **12** yielded $\Delta H^{\ddagger} = 9.8 \pm 0.4$ kcal/mol and $\Delta S^{\ddagger} = -28 \pm 1$ cal/(mol K) (R^2 for the Eyring plot was 0.987 for 11 measurements). The rate constant determined by NMR at 19.6 °C was within 5% of that predicted by the data obtained with the spectrophotometric method. The experiments also indicated that the reaction was first order in both methoxide and pyrophosphate (second order overall). Furthermore, these activation parameters correspond well to those for the hydrolysis of tetraethyl pyrophosphate ($\Delta H^{\ddagger}$ = 9.6 ± 0.2 kcal/mol and $\Delta S^{\ddagger}$ = -14.6 ± 0.7 cal/(mol K)).[17] For the endocyclic pyrophosphates, we made the reasonable assumption that the chemoselectivity of the pyrophosphate P–O bond over the alkoxide P–O bonds also holds; the regioselectivity for nucleophilic attack is less of an issue because both sites for nucleophlic attack involve a P atom within the macrocycle. As we have done in other work, the compositional difference between the linkers X and Y was assumed to impart little or no regioselectivity.

We monitored the basic methanolysis of the pyrophosphate macrocycles over a range of 10 to 60 °C, allowing for the calculation of individual activation parameters. In doing so, we used the independently determined (HPLC and NMR spectroscopy) ratios of diastereomers to determine the weighting of the rate constants used in the fitting, allowing for the assignment of rate constants to diastereomeric groupings (e.g., A, B, C or D). For all of the exocyclic pyrophosphates, the *Z* isomer of each macrocycle comprises only a pair of enantiomers, so the activation parameters for both diastereomeric sets of *E* isomers were meaningfully compared to those of the *Z* isomer. For the endocyclic pyrophosphates, the relative stereochemistry (syn vs. anti) at the phosphorus atoms was only assignable in the cases of *E***2** and *E***3**, and the complete absolute stereochemistry was only assignable as *M*,*S*,*R*[a] and its enantiomer, *P*,*S*,*R*, for the diastereomers *E***2**C and *E***3**C. In all cases for the endocyclic pyrophosphates, there are two possible ways to compare the activation parameters of the *E* isomers to those of the *Z* isomers; only the comparisons of syn at P to syn at P and anti at P to anti at P are meaningful, but the stereochemistry at the P atoms in all of the *Z* isomers and most of the *E* isomers could not be assigned by NMR spectroscopy. Therefore, both comparisons are reported below. See section 6.6.4 for a discussion of the stereochemical analysis of the macrocycles.

In the cases where the relative stereochemistry of the *E* and *Z* isomers was certain, differential activation parameters were also determined; in other cases, both possible comparisons are reported (see details below).

6.3 Results and Discussion

The discussion of the mechanochemistry of S_N2 reactions discussed in previous chapters made evident the fact that it is possible that a reaction showing inhibition by force along the

---

[a] *M* and *P* refer to the axial chirality of the stiff stilbene, *S* and *R* refer to the stereochemistry at the P atoms.

scissile bond would still be accelerated by force perpendicular to the scissile bond. The two situations being studied here are depicted in Fig. 6.3. In the endocyclic pyrophosphates, the local molecular degree of freedom satisfying the conditions for the local approximation, *q*, predicted in previous chapters to dictate the force–rate relationship for S_N2 reactions contains the scissile P–O bond (Fig. 6.3A). In these pyrophosphates, the restoring force vector will have a major component parallel to the scissile bond, and *q* may either elongate, contract or remain unchanged, depending on the relative magnitudes of scissile bond elongation and $O–P–O_{LG}$ angle contraction. In the exocyclic pyrophosphates, *q* does not contain the scissile bond and is instead between two of the spectator O atoms. In these pyrophosphates, the restoring force vector will have a major component parallel to the scissile bond, and *q* will elongate in all cases.

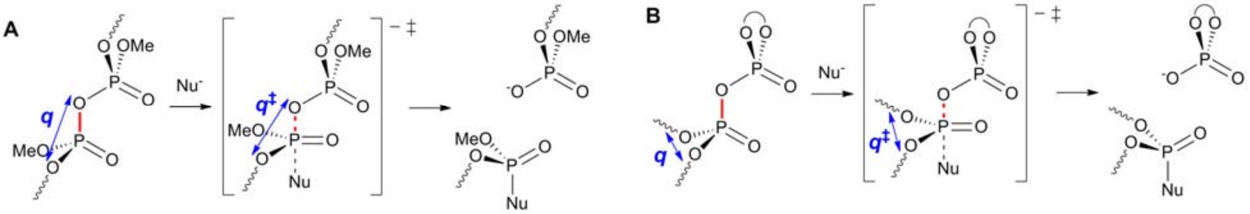

Fig. 6.3. Illustration of the relationship between the scissile bond (red) and the local molecular degree of freedom, *q* (blue), predicted in previous chapters to dictate the force–rate relationship for the nucleophlic displacement shown. Wavy bonds represent the rest of the strained system. The two relationships between *q* and the scissile bond present in the two series of macrocyclic pyrophosphates **1**–**11** are shown: *q* containing the scissile bond as in the endocyclic pyrophosphates (**A**) and *q* orthogonal to the scissile bond as in the exocyclic pyrophosphates (**B**).

Though the DFT calculations examining the methanolysis of these macrocycles and quantifying the restoring force vectors are still in progress, we may still draw conclusions based on our experience with such macrocyclic systems. In particular, we expect that the magnitude of the restoring force vector will be larger in smaller macrocycles, leading to a larger mechanochemical effect. The sizes of the macrocycles are listed in Fig. 6.1. The activation free-energy lowering determined by the ratio of average rate constants k_E/k_Z at 298 K are listed in Table 6.1; due to the presence of multiple diastereomers, each macrocycle yields at least two data points for the force–rate relationship (different diastereomers have different structures and therefore should exhibit slightly different restoring forces as well as different reactivities).

Table 6.1. Kinetic barrier lowering (values < 0 correspond to inhibition) as $\Delta\Delta G_{Z\text{-}E}^{\ddagger}$ determined from $\ln(k_E/k_Z)$ using the average rate constants at 298 K.

macrocycle	$\Delta\Delta G_{Z\text{-}E}^{\ddagger}$ at 298 K, kcal/mol; assignment 1 ; assignment 2	macrocycle	$\Delta\Delta G_{Z\text{-}E}^{\ddagger}$ at 298 K, kcal/mol
*E***2**A	-2.1 ; -1.2	*E***6**A	0.4
*E***2**B	-2.1 ; -1.2	*E***6**B	-0.6
*E***2**C	-0.2 ; -1.1	*E***7**A	0.5
*E***3**A	-1.7 ; -0.9	*E***7**B	-0.6
*E***3**B	-1.7 ; -0.9	*E***8**A	1.2
*E***3**C	0.0 ; -0.8	*E***8**B	0.0
*E***4**A	-1.1 ; -0.2	*E***9**A	2.2
*E***4**B	-2.0 ; -1.1	*E***9**B	1.1
*E***4**C	-1.3 ; -0.4	*E***10**	1.9
*E***4**D	-2.1 ; -1.2	*E***11**	1.9

In general, we can see that though we cannot experimentally identify the relative stereochemistry at the P atoms in the endocyclic pyrophosphates (i.e., syn vs. anti), both of the possible comparisons yield the same general conclusion: pyrophosphate methanolysis is inhibited by tensile force projected along the scissile bond (all barriers for *E* isomers are larger than those for the *Z* isomers). This observation suggests that pyrophosphate methanolysis is similar to silyl ether methanolysis in that *q* appears to decrease, leading to an increase in the energy of the system when it must contract against the restoring force to reach the geometry of the transition state. The magnitude of this trend, however, is difficult to discern not only because of the presence of two possibilities for the meaningful comparison of *E* to *Z* but also because *E* isomer kinetics was obtainable only for three endocyclic macrocycles, **2**–**4**, which though their diastereomers should exhibit different restoring forces, the likely span a smaller range than in the exocyclic pyrophosphates.

However, for the exocyclic pyrophosphates, we observe acceleration in the *E* isomers relative to their *Z* analogs, and there is a general trend of increasing acceleration with decreasing macrocycle size, up to ~25-fold acceleration in *E***11** (~40-fold for *E***9**A) at 298 K. Acceleration is expected in this case, because the separation of the spectator O atoms contained in the macrocycle must increase from the ground state to form the (pseudo)trigonal-bipyramidal configuration in the transition state, thereby allowing for partial relaxation of the pseudo-*E* stiff stilbene.

6.4 Conclusions

Though the DFT calculations for the methanolysis of these macrocycles are not yet complete, we can still observe general trends in the experimental data that agree with the predictions of our model for mechanochemical kinetics. Once the computational modeling and determination of the restoring force vectors is complete, we will be able to confirm the general trends that we observe (only in the case of *E***2**C and *E***3**C will calculations be unambiguously comparable to experimental measurements for the endocyclic pyrophosphates). The results for the endocyclic pyrophosphates indicate inhibition of the S_N2 solvolysis reaction by tensile force along the scissile bond. Based on our model, this implies that the local molecular degree of freedom, q, contracts in the transition state relative to the ground state, which in turn implies that the effect of scissile bond elongation is negated by that due to $O–P–O_{LG}$ angle contraction. The results of the exocyclic pyrophosphates indicate acceleration of the S_N2 solvolysis reaction by tensile force perpendicular to the scissile bond, as predicted by our model. Thus, we demonstrate that different orientations of force with respect to the reactive moiety can not only change the magnitude of the mechanochemical effect but also its sign.

The results of this work allow us to reach a few key conclusions regarding the enzymatic transformation of adenosine triphosphate to the diphosphate. Though the reactions are slightly different (aqueous solution instead of methanol, slightly different substrates), I argue that the differences are slight enough that they will not entirely invalidate the following conclusions: First, should mechanochemistry be responsible for the enzymatic rate enhancement (e.g., through the enzyme's enforcing a geometry on the substrate that stretches it), it likely would be stretched perpendicular to the scissile bond rather than along the scissile bond. This could be accomplished through the formation of non-covalent interactions that draw the anionic O atoms away from the pyrophosphate backbone, effectively biasing the geometry in a manner analogous to pulling. Second, the magnitude of the accelerations observed here (<50-fold) are far smaller than those observed in enzymatic phosphoryl transfer (up to 10^{21}-fold for the hydrolysis of phosphate monoesters), leading to two possible explanations: that the forces studied here are far smaller than those than those present in enzymatic systems or that the rate enhancement is due to a different cause. The former would require huge forces: 10^{21}-fold acceleration at 298 K corresponds to $\Delta\Delta G^{\ddagger} \approx 29$ kcal/mol; even if Δq for the hydrolysis of phosphate monoesters is as large as 0.5 Å, that much barrier lowering would necessitate nearly 4 nN of force, a value that is large enough to homolyze covalent bonds. Therefore, the latter is more likely the case, and though the restriction of substrate conformational space upon active site binding is real, explanations of enzymatic catalysis in terms of weakening bonds by induced stretching are likely misinterpreting the observed or proposed geometrical changes when the rate enhancements should be attributed to other effects. In light of the common misconception that tensile force will always increase reactivity, this is unsurprising, but the continued conceptual development of the field of mechanochemistry may in time remedy this, prompting re-investigations of old doctrine and the advancement of our understanding of the role of (macro)molecular strain in catalysis.

6.5 Acknowledgments

The contributions of the following individuals are gratefully acknowledged: Dr. Sergey Akbulatov synthesized macrocycles. Sizhu You, Xinxin Feng, David Kim, John Nash, and Nathan Johlas also carried out many of the UV-vis kinetics experiments. Nicholas C. Rubin assisted with and Matt Hermes and Dr. Yancong Tian continue to work on the computational modeling of these reactions. Funding for this project is similar to that listed elsewhere in the dissertation.

6.6 Supporting Experimental Information

6.6.1 Materials and General Methods

All solvents used were HPLC grade or better. Anhydrous tetrahydrofuran was collected from an MBraun Solvent Purification System. Water for HPLC was obtained from a Milli-Q water purification system. Anhydrous acetonitrile was graciously provided by Christopher Letko and Bryan Barton in the Rauchfuss laboratory. Anhydrous dichloromethane and methanol were purchased from Aldrich and were stored in an inert-atmosphere (N_2) glovebox.

Irradiation was performed in vessels sealed under a N_2 atmosphere using high-intensity diode light sources from Opto Technology with light output at 375 ± 7 nm. Light intensity was controlled with a custom-made constant-current controller. UV-vis spectra were recorded on a

Cary 50 UV-vis spectrophotometer. UV-vis kinetic data was processed and models were fitted to the resulting data with custom-written scripts in Matlab (7.9.0 R2009b).

High-resolution mass spectrometry was performed on a Micromass 70-VSE mass spectrometer (EI) at the University of Illinois Mass Spectrometry Center. NMR spectra were recorded on 400, 500, or 600 MHz Unity-INOVA Varian spectrometers at room temperature, and are reported as chemical shifts in ppm relative to tetramethylsilane . Spin multiplicities are reported as singlet (s), doublet (d), triplet (t), quartet (q) and quintet (quint) with coupling constants (*J*) given in Hz, or multiplet (m); br = broad; app = apparent.

HPLC was performed on a Shimadzu Prominence system with an LC-20AT solvent delivery unit, DGU-20A5 degasser, SPD-M20A photodiode array detector, CBM-20A system controller and Rheodyne 7725i manual injector or on a Waters system with a 600E multisolvent delivery system with He gas solvent sparging, 996 photodiode array detector, and Rheodyne 7725i manual injector. Three columns were used for the HPLC analysis, as specified in the separation conditions: J.T. Baker C_{18} column (25 cm × 4.6 mm, 5 µm particles), Supelco C_{18} column (15 cm × 4.6 mm, 5 µm particles) or Macherey–Nagel C18 gravity column (25 cm × 4.6 mm, 3 µm particles). Preparative-scale HPLC was performed using a Vydac C_{18} column (25 cm × 2 cm, 10 µm particles).

6.6.2 Characterization of Marocycles 1–11

The synthesis and NMR characterization of **1**–**11** (other than the stereochemical analysis below) will be reported elsewhere. The high-resolution mass spectrometry data confirming molecular formulas is shown in Table 6.2.

Table 6.2. High-resolution mass spectrometry (EI) confirmation of molecular formulas for **1**–**11**.

	formula	calc'd, g/mol	found, m/z	error, ppm
1	$C_{25}H_{30}O_9P_2$	536.13651	536.13665	0.3
2	$C_{26}H_{32}O_7P_2$	518.16233	518.16260	0.5
3	$C_{24}H_{28}O_9P_2$	522.12086	522.12089	0.1
4	$C_{24}H_{28}O_8P_2$	506.12594	506.12700	2.1
5	$C_{24}H_{28}O_7P_2$	490.13103	490.13135	0.7
6	$C_30H_{38}O_8P_2$	588.20419	588.20338	-1.4
7	$C_{29}H_{36}O_9P_2$	590.18346	590.1840	0.9
8	$C_{29}H_{36}O_8P_2$	574.18854	574.1886	0.1

Table 6.2 (cont.)

9	$C_{28}H_{34}O_9P_2$	576.16781	576.1680	0.3
10	$C_{29}H_{36}O_7P_2$	558.19363	558.19275	-1.6
11	$C_{27}H_{32}O_9P_2$	562.15216	562.15152	-1.1

The chromatograms for the purified *Z* isomers of the endocyclic pyrophosphates are shown in Fig. 6.4. The chromatograms for the photostationary states of the exocyclic pyrophosphates are shown in Fig. 6.5, indicating their clean photochemistry. Wavelengths of maximum light absorbance and the corresponding extinction coefficients for *Z***1**–*Z***11** are shown in Table 6.3.

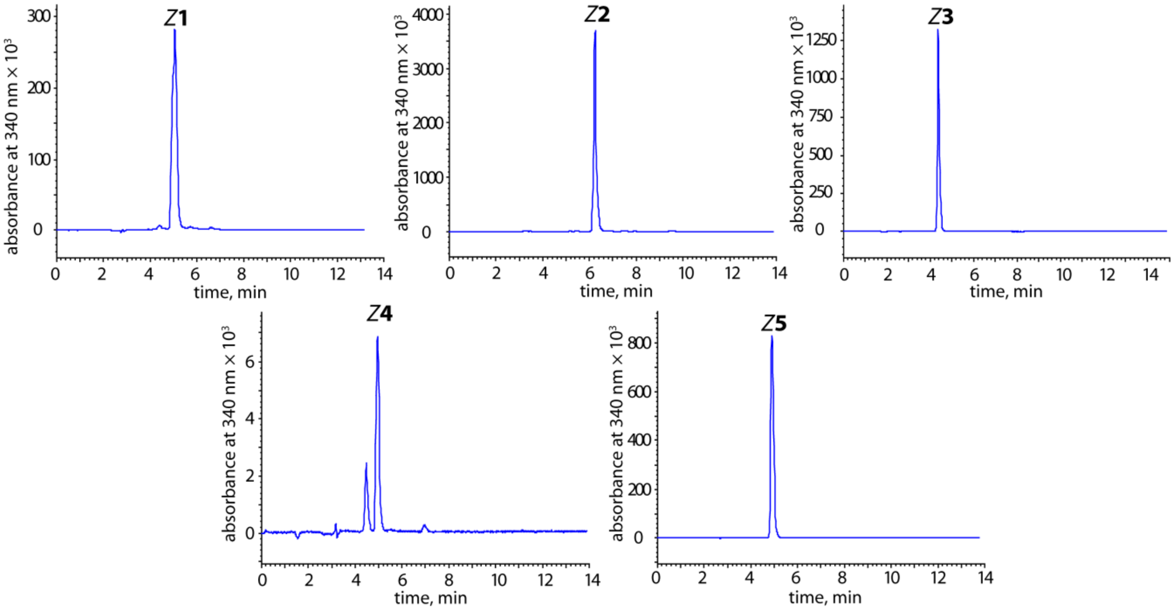

Fig. 6.4. Chromatograms of the *Z* isomers of the endocyclic pyrophosphates using the JT Baker C18 column with 10% water in acetonitrile at 1 mL/min.

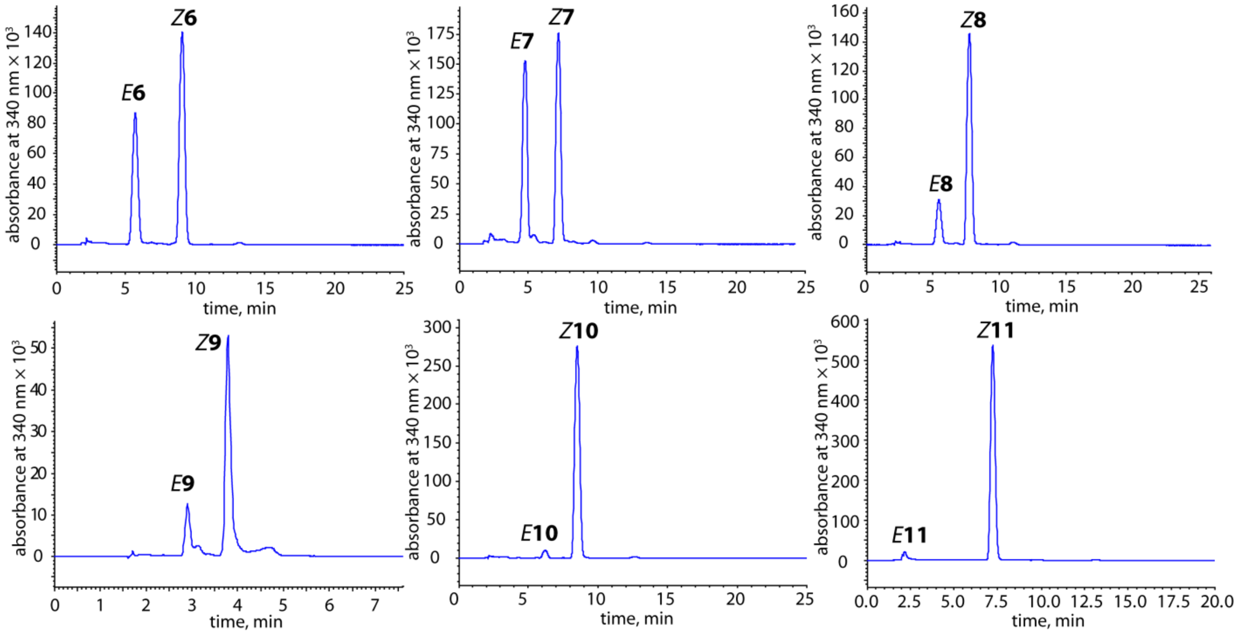

Fig. 6.5. Chromatorgrams of the photostationary mixtures of exocyclic pyrophosphates using the Macherey–Nagel C18 gravity column (**6**–**8**, **10**, **11**) or the Supelco C18 column (**9**) with 10% water in methanol at 1 mL/min.

Table 6.3. Wavelengths of maximum light absorbance and the corresponding extinction coefficients for *Z***1**–*Z***11**.

	λ_{max}, nm	$\varepsilon\,(\lambda_{max})$, $M^{-1}\ cm^{-1}$
1	346	13000
2	338	4000
3	346	20000
4	340	13000
5	337	11000
6	340	18000
7	344	14000
8	341	13000
9	346	15000
10	335	19000
11	346	14000

6.6.3 Stereochemical Analysis and Proof of Methanolysis Chemoselectivity by NMR Spectroscopy for the Exocyclic Pyrophosphate Model

The structure of the model compound for the exocyclic pyrophosphates (5,5-dimethyl-2-oxo-1,3,2-dioxaphosphorinan-2-yl dibutylphosphate) is shown in Fig. 6.6. In neutral CD_3OD, there is no detectable reaction after 3 d at room temperature. The fact that the $H_{e/f}$ and $H_{g/h}$ pairs are anisochronous indicates that ring flipping is either slow on the NMR time scale or (more likely) that the ring is fixed in one conformation, as the O–P(O)(OBu)$_2$ fragment is much larger than the oxo on P_b and thus prefers an equatorial position (Fig. 6.6). The assignment of H_g and H_h are straightforward, they are singlets. H_a is a triplet, H_b and H_c are multiplets, and H_d is a doublet of triplets, coupled to H_c (t, 6.7 Hz) and P_a (d, 7.4 Hz). H_e and H_f exhibit coupling constants that follow the Karplus relationship for $^3J_{\text{P-O-C-H}}$ in phosphates.[19,20] H_f shows geminal coupling to H_e (10.9 Hz) and is not coupled to P_b because it is at ~90° dihedral angle to P_b. H_e shows the geminal coupling (10.9 Hz) and is strongly coupled to P_b (d, 24.2 Hz) because it is at ~180° dihedral angle to P_b. P_a and P_b are coupled (18.8 Hz). P_a is coupled to H_d (quintet, 7.4 Hz), and P_b is coupled to H_e (triplet, 24.2 Hz).

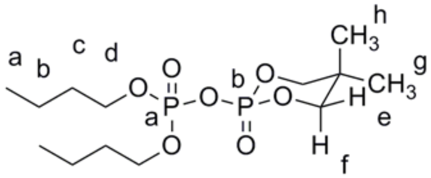

Fig. 6.6. Labels for the assignment of the ^{1}H and ^{31}P NMR spectra for the model compound for the exocyclic pyrophosphate series.

^{1}, s,, s, m, m = 24.2 Hz, d: $^2J_{\text{He-Hf}}$ = 10.9 Hz4$H_{\text{dHd-}}$ = 6.7 Hz), 4.345 (2H_f, d, $^2J_{\text{Hf-He}}$ = 10.9 Hz).

^{31}P{^{1}H} NMR (CD$_3$OD, 202 MHz): δ -12.139 (d, $^2J_{\text{Pa-Pb}}$ = 18.8 Hz), -18.785 (d, $^2J_{\text{Pb-Pa}}$ = 18.8 Hz).

^{31}P NMR (CD$_3$OD, 202 MHz): δ -19.785 (P_b, dt, d: $^2J_{\text{Pb-Pa}}$ = 18.8 Hz, t: $^3J_{\text{Pb-He}}$ = 24.2 Hz), -12.139 (P_a, dquint, d: $^2J_{\text{Pa-Pb}}$ = 18.8 Hz, quint: $^3J_{\text{Pa-Hd}}$ = 7.4 Hz).

The assignment of chemical shifts for the 2-oxo-1,3,2-dioxaphosphorinane fragment is supported by the previously reported[21] assignment of the spectrum of phenyl 2-oxo-1,3,2-dioxaphsphorinanate, shown in Fig. 6.7A (in CDCl$_3$, H_e: 3.95 ppm, $^3J_{\text{P-H}}$ = 22.5 Hz; H_f: 4.22 ppm, $^3J_{\text{P-H}}$ = 1.7 Hz; H_g: 0.84 ppm; H_h: 1.26 ppm). The assignments and magnitudes of coupling constants also agree well with parameters recently used to accurately reproduce experimental NMR spectra of a dimeric phenyl-substituted analog.[15]

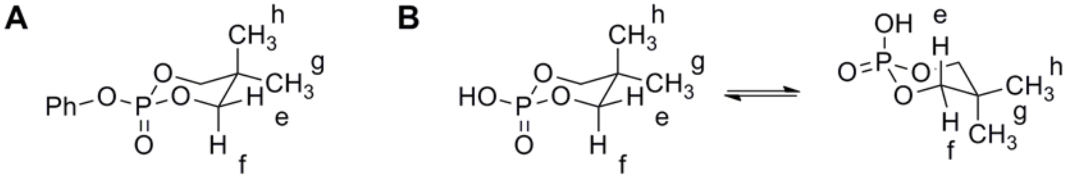

Fig. 6.7. 2-Oxo-1,3,2-dioxaphosphorinane systems whose ^{1}H NMR spectra have been previously reported.[21]

Following the addition of sodium methoxide-d_3 and waiting for full conversion, the resonances for H_g and H_h collapse into a single 6H singlet, and those for H_e and H_f collapse into a single doublet coupled to P_b (11.8 Hz), indicating that the ring flips rapidly on the NMR time scale, and identifying P_a and P_b (Fig. 6.8). P_a and P_b are no longer coupled, but P_a shows a multiplet when the decoupling to H is turned on, indicating that it is coupled to the deuterium nuclei in the OCD_3 group. H_a remains a triplet coupled to H_b (7.6 Hz), and H_b and H_c remain multiplets. H_d is coupled to P_a (6.9 Hz), further identifying P_a and P_b.

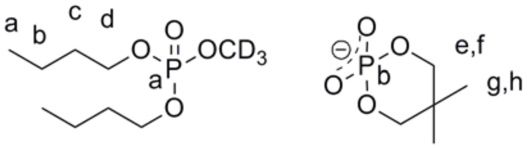

Fig. 6.8. Labels for the assignment of the ^{1}H and ^{31}P NMR spectra of the model compound for the exocyclic pyrophosphate series following methanolysis in methanol-d_4.

^{1}H NMR (CD_3OD, 500 MHz): δ 0.961 (6H_a, t, $^{3}J_{Ha\text{-}Hb}$ = 7.6 Hz), 1.003 (6$H_{g,h}$, s), 1.437 (4H_b, m), 1.671 (4H_c, m), 3.865 (4$H_{e,f}$, d, $^{3}J_{He,f\text{-}Pb}$ = 11.8 Hz), 4.057 (4H_d, dt, d: $^{3}J_{Hd\text{-}Pa}$ = 6.9 Hz, t: $^{3}J_{Hd\text{-}Hc}$ = 6.5 Hz)

^{31}P{^{1}H} NMR (CD_3OD, 202 MHz): δ -1.765 (P_b, s), 1.011 (P_a, m)

^{31}P NMR (CD_3OD, 202 MHz): δ -1.765 (P_b, quint, $^{3}J_{Pb\text{-}He,f}$ = 11.8), 1.011 (P_a, m).

The assignment of chemical shifts for 2-oxo-1,3,2-dioxaphosphorinate is supported by the previously reported[21] assignment of the spectrum of 2-oxo-1,3,2-dioxaphsphorinanic acid, shown in Fig. 6.7A (in acetone-d_6, $H_{e,f}$: 4.00 ppm, $^{3}J_{P\text{-}H}$ = 12.0 Hz; $H_{g,h}$: 1.06 ppm). There are no additional products observed, indicating a high degree (>99%) of regio- and chemoselectivity in the nucelophilic attack (i.e., substitution will occur at the P atom contained in the macrocycle, cleaving the pyrophosphate P–O bond and leaving the alkoxide P–O bonds intact).

6.6.4 Stereochemical Analysis and Quantification of Diastereomeric Ratios of Pyrophosphate Macrocycles

The substituents on the central double bond in stiff stilbene do not lie in a single plane, and thus the double bond exhibits either left- (*M*) or right-handed (*P*) axial chirality.[b] In *Z* isomers, the barrier for interconversion of (*M*)- and (*P*)-stiff stilbene is only a few kcal/mol and thus they rapidly equilibrate at room temperature; in this case the axial chirality of the stiff stilbene may be ignored, as the two forms are more accurately classified as conformers, rather than stereoisomers given that they cannot be distinguished at the temperatures of interest. In the *E* isomers, however, this does not occur, and the stiff stilbene is fixed in either the *M* or *P* configuration for the timescale of the reactions of interest. For both series, there are two types of macrocycles, those in which the linkers X and Y (Fig. 6.9) are identical and those in which they are not. For endocyclic pyrophosphates, the two methoxy (or oxo) groups on the P atoms may either be syn (*R*,*S* or *S*,*R*) or anti (*R*,*R* or *S*,*S*). In the *Z* isomers, only the two P atoms are stereogenic. Thus, when X = Y, two sets of diastereomers are expected: the syn configuration is a meso compound, and the anti isomers are a pair of enantiomers (*R*,*R*; *S*,*S*). For the *Z* isomers in which X ≠ Y, two sets of diastereomers are again expected: syn (*R*,*S*; *S*,*R*) and anti (*R*,*R*; *S*,*S*).

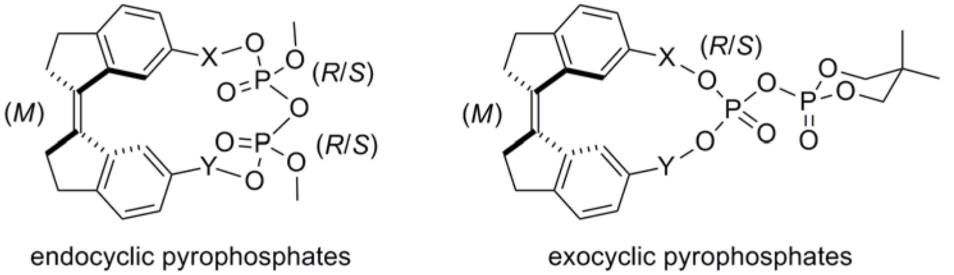

Fig. 6.9. General structures of the two series of macrocyclic pyrophosphates containing stiff stilbene to illustrate the stereochemical possibilities discussed in the text.

In the *E* isomers, the axial chirality of the stiff stilbene must be considered. For *E* isomers in which X = Y, there are three sets of diastereomers: one pair of syn enantiomers ((*M*,*S*,*R*; *P*,*R*,*S*); these are identical to (*M*,*R*,*S*; *P*,*S*,*R*)), and two pairs of anti enantiomers: (*M*,*R*,*R*; *P*,*S*,*S*) and (*M*,*S*,*S*; *P*,*R*,*R*). In the *E* isomers in which X ≠ Y, no pairs of enantiomers are identical and

---

[b] I use the helical chirality descriptors *M* and *P* instead of S_a and R_a in to describe the axial chirality in stiff stilbenes to make it easier to distinguish these symbols from the *R* and *S* stereochemical assignments at P atoms.

therefore all four sets of diastereomers exist: two pairs of syn enantiomers, (*M*,*S*,*R*; *P*,*R*,*S*) and (*M*,*R*,*S*; *P*,*S*,*R*), and two pairs of anti enantiomers (*M*,*R*,*R*; *P*,*S*,*S*) and (*M*,*S*,*S*; *P*,*R*,*R*).

The resonances from the methyl groups are readily identified in the ^{1}H NMR spectra of mixtures of diastereomers of the endocyclic pyrophosphates (the rest of the spectra are incredibly complicated with many signals from different diastereomers overlapping). Integration of these peaks allows for the quantification of the molar ratios of the diastereomers present. However, due to the complexity of ^{1}H NMR spectra of photostationary mixtures of endocyclic pyrophosphates, the combined molar fraction of all *E* isomers vs. all *Z* isomers was not measurable by NMR spectroscopy. Furthermore, the large number of diastereomers present in such mixtures (as many as six) necessitated their separation by HPLC to allow kinetics measurements to be made on smaller groupings of diastereomers, thereby reducing the number of fitted parameters in any given kinetics experiment.

Typically several dilute (maximum absorbance near 340 nm ~ 1, 1–2 μmol of macrocycle total) solutions of a given macrocycle were irradiated with 375 nm light until photostationary states were produced. The solvent was removed from these solutions; the residues were taken up in a minimal amount of acetonitrile or methanol, combined and then injected into HPLC for separation. The conditions for separation are listed in Table 6.4. The fractions indicated were collected, evaporated to dryness, and then analyzed by ^{1}H and ^{31}P NMR to determine the molar ratios of diastereomers. These mixtures were then used for kinetics experiments. In two cases (**2** and **4**) the individual diastereomers were separable by analytical-scale HPLC, providing more evidence that the expected numbers of diastereomers (Table 6.5, below) are present; these chromatograms are shown in Fig. 6.10. It was not possible to achieve such separation with the large-scale HPLC column. The small molar fraction of *E* isomers for **5** precluded its practical collection following separation.

Table 6.4. HPLC separation conditions for the isolation of *E* diastereomers of endocyclic pyrophosphates. Separation was carried out on a 25 cm × 2 cm Vydac C_{18} column with 10 μm particles.

	conditions	retention time, min
*Z***1** A,B	15% H2O in MeOH, 7 mL/min	25.1
*E***1** A,B		15.6
*E***1** C,D		17.2
*Z***2** A,B	40% H2O in MeCN, 5 mL/min	43.6

Table 6.4 (cont.)

*E***2** A,B,C	40% H2O in MeCN, 5 mL/min	39.5
*Z***3** A,B	50% H2O in MeCN, 5 mL/min	22.9
*E***3** A,B,C		21.0
*Z***4**, A,B	15% H2O in MeOH, 7 mL/min	21.8
*E***4** A,B		15.5
*E***4** C,D		17.1

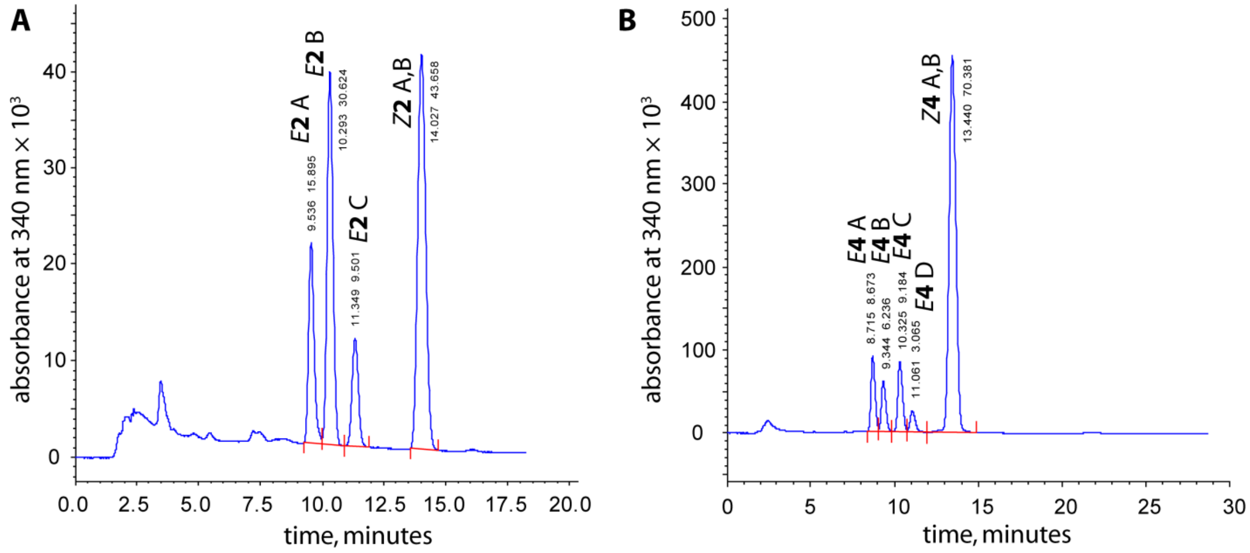

Fig. 6.10. Analytical-scale chromatograms confirming the presence of the expected number of diastereomers for *E* isomers of **2** and **4**. Separations used a 25 cm × 4.6 mm Macherey–Nagel C18 gravity column with 3 µm particles. Mobile phases were 5% water in methanol at 1 mL/min (**A**) and 10% water in methanol at 1 mL/min (**B**).

The stereochemical relationships between the methyl groups in the pyrophosphates for endocyclic pyrophosphates are listed in Table 6.5. Only in the case of *E* isomers of endocyclic pyrophosphates where X = Y can the syn and anti diastereomers be differentiated (syn has two Me resonances in a 1:1 ratio, and each diastereomeric pair of anti enantiomers has a single Me resonance, which will differ in magnitude unless the diastereomeric ratio (d.r.) is exactly 2:1:1. Though the absolute stereochemistry of all other stereoisomers is not assignable by NMR spectroscopy, the ratios are quantifiable.

Table 6.5. Stereoisomers of endocyclic pyrophosphate macrocycles and the relationships between the Me groups within them. Note that here, A, B, and C are labels that will be systematically changed, depending on the chemical shifts of the corresponding resonances; see below for details.

	Z isomers			*E* isomers		
	stereoisomers	stereochemical relationship of Me groups	fraction by NMR	stereoisomers	stereochemical relationship of Me groups	fraction by NMR
X = Y, syn	*meso*	enantiotopic by S_2, isochronous	χ_A	(*M*,*S*,*R*; *P*,*R*,*S*) = (*M*,*R*,*S*; *P*,*S*,*R*)	diastereotopic, anisochronous	χ_A, χ_A
X = Y, anti	*R*,*R*; *S*,*S*	homotopic by C_2, isochronous	χ_B	(*M*,*R*,*R*; *P*,*S*,*S*)	homotopic by C_2, isochronous	$2\chi_B$
				(*M*,*S*,*S*; *P*,*R*,*R*)	homotopic by C_2, isochronous	$2\chi_C$
X ≠ Y, syn	*S*,*R*; *R*,*S*	diastereotopic, anisochronous	χ_A, χ_A	(*M*,*S*,*R*; *P*,*R*,*S*)	diastereotopic, anisochronous	χ_A, χ_A
				(*M*,*R*,*S*; *P*,*S*,*R*)	diastereotopic, anisochronous	χ_B, χ_B
X ≠ Y, anti	*R*,*R*; *S*,*S*	diastereotopic, anisochronous	χ_B, χ_B	(*M*,*R*,*R*; *P*,*S*,*S*)	diastereotopic, anisochronous	χ_C, χ_C
				(*M*,*S*,*S*; *P*,*R*,*R*)	diastereotopic, anisochronous	χ_D, χ_D

Confirmation that the selected signals were the Me resonances from macrocycles (and not impurities) was provided by selective decoupling by irradiating the sample at a frequency equal to that of the corresponding ^{31}P resonance, which resulted in the collapse of the characteristic doublet with significant second-order character into a narrow singlet with a Lorentzian lineshape. An example is shown below for *E***3**. For a given *Z* or *E* macrocycle the diastereomers were arbitrarily labeled as A, B, C and D in order of ^{31}P resonant frequencies as (downfield) $\delta_A > \delta_B > \delta_C > \delta_D$ (upfield). Interestingly, for *Z* isomers, this corresponded to the reverse ordering of the chemical shifts of the corresponding methyl ^{1}H resonances: (upfield) $\delta_A < \delta_B$ (upfield), and in all cases, $\chi_A > \chi_B$. There was no clear correlation between ^{31}P and ^{1}H resonant frequencies for the *E* isomers. Note that diastereomer A for an *E* isomer is not necessarily produced from diastereomer A for the *Z* isomer, etc.

In *E***3**, X = Y, so three sets of diastereomers are expected with Me resonances are expected, as shown in Table 6.5. In the anti isomers, the ^{31}P nuclei are also homotopic (related by C_2), so these $^{31}P\{^1H\}$ resonances will be singlets. In the syn isomers, the ^{31}P nuclei are diastereotopic, and thus are anisochronous and may therefore couple, yielding two doublets; this is observed in the $^{31}P\{^1H\}$ NMR spectrum ($CDCl_3$, 243 MHz: δ -12.156 (diastereomer C, d, $^3J_{P\text{-}P}$ = 7.7 Hz), -12.006 (diastereomer C, d, $^3J_{P\text{-}P}$ = 7.7 Hz), -11.460 (diastereomer B, s), -10.453 (diastereomer A, s)). Irradiation at the frequencies corresponding to these resonances with narrow enough decoupler frequency modulation allows for selective decoupling, as shown in Fig. 6.11, thereby identifying which methyl ^1H resonances are coupled to which ^{31}P resonances. Following this identification, broadband ^{31}P decoupling is used to collapse all methyl signals to singlets (thereby increasing their S/N and separation from other signals in the more complex spectra), allowing for integration to yield the molar ratios of sets of diastereomers present. For the example shown in Fig. 6.11, broadband irradiation of the ^{31}P nuclei resulted in singlets in the ^1H NMR spectrum at 3.855, 3.526, 3.429 and 3.367 ppm in a ratio of 1:0.96:0:97:0.43. The resonances at 3.526 and 3.429 ppm are coupled to the ^{31}P nuclei that results in doublets in the $^{31}P\{^1H\}$ NMR spectrum and therefore belong to the syn diastereomers (i.e., diastereomer C, χ_C, χ_C). The resonances at 3.855 and 3.367 ppm therefore belong to the anti diastereomers (diastereomers B and A, respectively, $2\chi_B$, $2\chi_A$). The d.r. is then 1:2.3:4.5 A:B:C. The same procedure was followed for all *E* and *Z* isomers of the endocyclic macrocycles; the results are shown in Table 6.6.

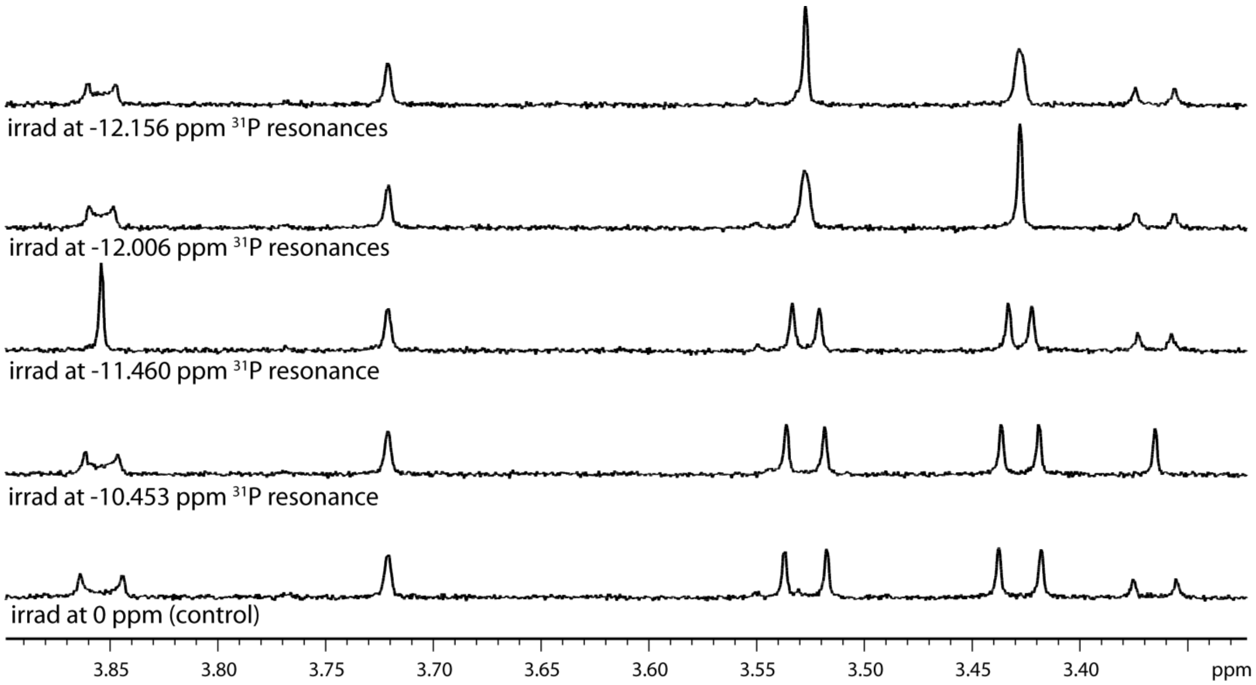

Fig. 6.11. Methoxy resonances in the 600 MHz ^{1}H NMR spectra of the mixture of *E***3** diastereomers with selective decoupling of ^{31}P resonances.

Table 6.6. Diastereomeric ratios (d.r.) of endocyclic pyrophosphates determined by NMR spectroscopy as prepared (*Z* isomers) or as the combined product of HPLC isolations carried out to isolate *E* macrocycles from photostationary mixtures. See below for isolation details. Note that diastereomer A for *E* is not necessarily produced from diastereomer A of the *Z* isomer. See footnotes for the assignment of stereochemistry where possible.

	d.r.	χ_A	χ_B	χ_C	χ_D
*Z***1** A,B	1.3 : 1	0.56	0.44		
*E***1** A,B	2.5 : 1	0.71	0.29		
*E***1** C,D	7.9 : 1			0.89	0.11
*Z***2** A,B	2.1 : 1	0.68	0.32		
*E***2** A,B,C	1.3 : 1 : 2.8	0.25[a]	0.20[a]	0.55[b]	
*Z***3** A,B	3.5 : 1	0.78	0.22		
*E***3** A,B,C	1 : 2.3 : 4.5	0.13[a]	0.30[a]	0.57[b]	
*Z***4**, A,B	2 : 1	0.66	0.34		
*E***4** A,B	1 : 1.6	0.39	0.61		
*E***4** C,D	1.5 : 1			0.61	0.39
*Z***5** A,B	1.4 : 1	0.59	0.41		

[a] Stereochemistry at the P atoms is anti: (*R*,*R*; *S*,*S*); pairing with axial chirality of (*E*)-stiff stilbene is uncertain; [b] Stereochemistry at the P atoms is syn and the linkers are identical, therefore, there is only a single pair of enantiomers: (*M*,*S*,*R*; *P*,*R*,*S*) ≡ (*M*,*R*,*S*; *P*,*S*,*R*).

The stereochemical analysis of the exocyclic pyrophosphates was much more straightforward. The presence of P–P coupling in the $^{31}P\{^{1}H\}$ NMR spectra indicate that the pyrophosphate is indeed intact (e.g., in *Z***10**, $^{31}P\{^{1}H\}$ NMR ($CDCl_3$, 202 MHz): δ -20.502 (d, $^{3}J_{P\text{-}P}$ = 19.7 Hz), -11.631 (d, $^{3}J_{P\text{-}P}$ = 19.7 Hz)). Broadband irradiation of the ^{31}P nuclei results in the collapse of the equatorial ^{1}H resonance in the 1,3,2-dioxaphosphorinane fragment, as shown in Fig. 6.12A for *Z***10** ($CDCl_3$, 500 MHz: ^{1}H: δ 3.974 (ddm, d: $^{2}J_{Heq\text{-}Hax}$ = 10.8 Hz, d: $^{3}J_{Heq\text{-}P}$ = 24.0 Hz), 4.340 (d, $^{2}J_{Hax\text{-}Heq}$ = 10.8 Hz)). The same is true of *Z***9** (Fig. 6.12B, $CDCl_3$, 500 MHz: ^{1}H: δ 3.983 (ddm, d: $^{2}J_{Hax\text{-}Heq}$ = 11.2 Hz, d: $^{3}J_{Heq\text{-}P}$ = 23.9 Hz), 4.341 (d, $^{2}J_{Hax\text{-}Heq}$ = 11.2 Hz)). The ^{1}H NMR spectra of other macrocycles are more complex, but are also consistent with their structures.

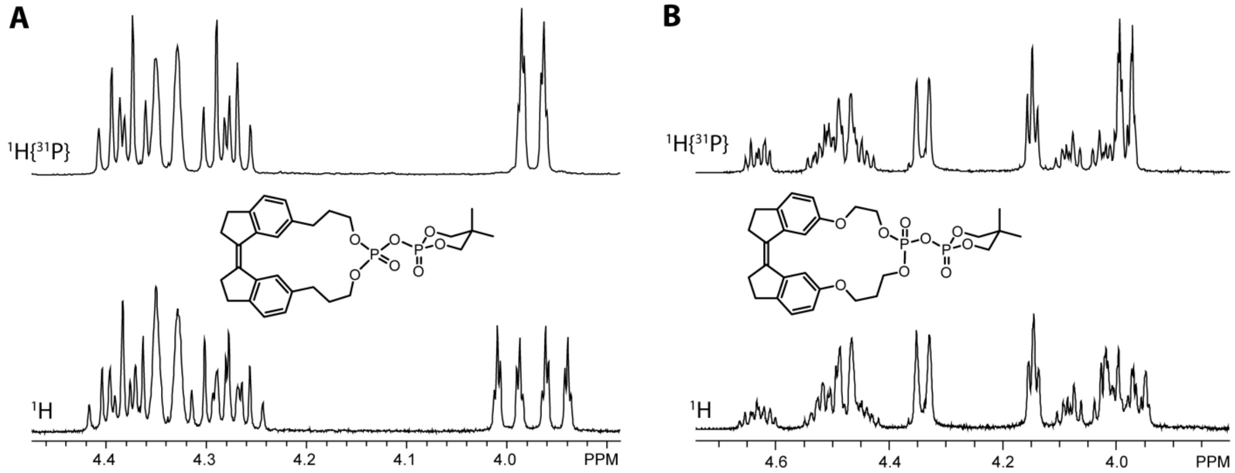

Fig. 6.12. Presence of the 1,3,2-dioxaphosphorinane fragment in *Z***10** (**A**) and *Z***9** (**B**) indicated by the ^{31}P–^{1}H coupling to the equatorial ^{1}H nuclei.

The compositions of linkers X and Y must be non-identical for the P atom in the macrocycle to be chiral. When X and Y are identical, the two *E* isomers formed (*M* and *P*) are enantiomers, and there is only a single *Z* isomer. When X and Y are non-identical, the two *Z* isomers (*R* or *S* at P) are enantiomers, and the *E* isomers comprise two diastereomeric sets of enantiomers: (*M*,*R*; *P*,*S*) and (*M*,*S*; *P*,*R*). Because the number of isomers is limited, it was feasible to determine the ratios of *E* and *Z* isomers and the ratios of *E* diastereomers by ^{1}H NMR spectroscopy in a single sample. Because it is often well-separated from other resonances, the endocyclic C_{aryl}–H ^{1}H resonances (i.e., those corresponding to the C–H closest to the other aromatic ring in the macrocycle) were used to determine the ratios of stereoisomers. For the *E* isomers with non-identical linkers X and Y, the diastereomer with the more downfield aromatic resonance of interest was arbitrarily assigned as diastereomer A; the other was diastereomer B. Degassed samples of the *Z* isomers in toluene-d_8 were irradiated with 375 nm light in a J. Young tube until their ^{1}H NMR spectra no longer changed after further irradiation. Then the selected signals in the spectra were integrated. The results are shown in Table 6.7.

Table 6.7. Diastereomeric ratios (d.r.) of photostationary mixtures of exocyclic pyrophosphates determined by ^{1}H NMR spectroscopy.

	d.r. (Z:E_A:E_B)	χ_E as $(\chi_{E\mathrm{A}} + \chi_{E\mathrm{B}})/(\chi_Z + \chi_{E\mathrm{A}} + \chi_{E\mathrm{B}})$	$\chi_{E\mathrm{A}}$ of *E* isomers as $\chi_{E\mathrm{A}}/(\chi_{E\mathrm{A}} + \chi_{E\mathrm{B}})$
6	3.4 : 1.1 : 1	0.38	0.52
7	3.6 : 1 : 1.4	0.40	0.42
8	14.4 : 2.2 : 1	0.18	0.69
9	17.5 : 1 : 1.4	0.12	0.42

The molar fractions of *E* isomers in **10** and **11** was <5%. However, because the linkers X and Y are identical for **10** and **11**, there is only a single *E* isomer, precluding the need to attempt to separate different diastereomers by HPLC. Thus, χ_E for photostationary mixtures of **10** and **11** was determined by HPLC to be 0.045 and 0.036, respectively.

6.6.5 Kinetic Methods

The kinetic methods employed for the basic methanolysis of pyrophosphates was essentially identical to that used in Chapter 3. Phenol red was titrated in anhydrous methanol and found to have a ${}_\mathrm{s}^\mathrm{s}\mathrm{p}K_\mathrm{a}$ of 12.8 (${}_\mathrm{s}^\mathrm{s}K_\mathrm{a} = (1.5 \pm 0.2) \times 10^{-13}$ M; ${}_\mathrm{s}^\mathrm{s}\mathrm{p}K_\mathrm{ap}$ for MeOH is 16.77[18]). The UV-vis spectra for one of these spectrophotometric titrations are shown in Fig. 6.13. The extinction coefficients for the protonated and anionic forms of the indicator were obtained from the initial and final spectra of these titrations, as described in Chapter 3.

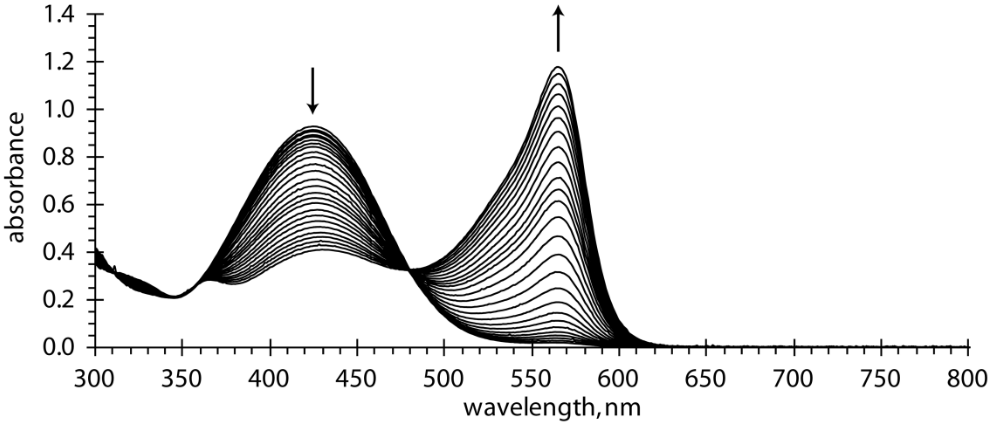

Fig. 6.13. The UV-vis spectra for one of the spectrophotometric titrations of phenol red with sodium methoxide in anhydrous methanol.

Processing of the UV-vis kinetic data yielded methoxide concentration vs. time. Having demonstrated that the reaction is >99% selective for methanolysis of the pyrophosphate P–O bond, we assumed that the depletion of methoxide corresponded to the reaction of an equal amount of pyrophosphate.

For the endocyclic pyrophosphates, the methanolysis kinetics are governed by the system of differential equations (5.2)–(6.4) ($[\mathrm{C}]_t = 0$ for mixtures of only two diastereomers; only in the cases of *E***2** and *E***3** were the methanolyses of three diastereomers measured simultaneously).

$$\frac{d[\mathrm{A}]_t}{dt} = -k_\mathrm{A}[\mathrm{A}]_t[\mathrm{OMe}]_t \tag{6.1}$$

$$\frac{d[\mathrm{B}]_t}{dt} = -k_\mathrm{B}[\mathrm{B}]_t[\mathrm{OMe}]_t \tag{6.2}$$

$$\frac{d[\mathrm{C}]_t}{dt} = -k_\mathrm{C}[\mathrm{C}]_t[\mathrm{OMe}]_t \tag{6.3}$$

$$\frac{d[\mathrm{OMe}]_t}{dt} = -[\mathrm{OMe}]_t(k_\mathrm{A}[\mathrm{A}]_t + k_\mathrm{B}[\mathrm{B}]_t + k_\mathrm{C}[\mathrm{C}]_t) \tag{6.4}$$

Provided the knowledge of the absolute methoxide and pyrophosphate concentrations, the second-order rate constants k_A, k_B and k_C could be fitted by carrying out a least-squares minimization of the residuals between the calculated and experimental curves for $[\mathrm{OMe}]_t$ vs. t. The calculated curve was found by numerically integrating eqs. (5.2)–(6.4) with the initial values $[\mathrm{OMe}]_0$, $[\mathrm{A}]_0$, $[\mathrm{B}]_0$ and $[\mathrm{C}]_0$, which were determined from the initial UV-vis spectrum in the data set. $[\mathrm{A}]_0$, $[\mathrm{B}]_0$ and $[\mathrm{C}]_0$ were determined using the total initial macrocycle concentration, [macro]$_0$, and the diatereomeric ratios measured by NMR spectroscopy. For *Z* isomers, [macro]$_0$ was determined from the deconvoluted spectra and the independently measured effective extinction coefficients for the as-synthesized mixture of diastereomers. Because it was not technically practical to measure the extinction coefficients for the different sets of diastereomers of *E* isomers, [macro]$_0$ was initially assigned a reasonable value and then also fitted as a parameter in the minimization process for *E* isomers.

For the exocyclic pyrophosphates, a procedure analogous to that used in Chapter 3 was used. The rate constants for the *Z* isomers were determined individually (eqs. (5.2) and (6.4) with $[B]_t = [C]_t = 0$). Then the methanolysis of photostationary mixtures were measured and the resulting data was analyzed with the process above using eqs. (5.2)–(6.4) with A assigned as the *Z* isomer and k_A fixed as the independently measured rate constant for the *Z* isomer. For each experiment, the initial concentration of all *E* isomers was determined by HPLC analysis of a small aliquot of the photostationary mixture used, and the initial concentrations of the diastereomers of *E* isomers determined were determined by the ratios determined by NMR spectroscopy. This yielded the rate constants for the two sets of *E* diastereomers as k_B and k_C. Because the P atom in the macrocycle in **10** and **11** is not a stereogenic center (the linkers X and Y are identical), $[C]_t = 0$ for those experiments.

In all cases, errors on the fitted parameters were calculated using the methods described in ref. 22. The activation parameters and their standard errors obtained from the linear Eyring plots are listed in Table 6.8–Table 6.10. The activation parameters for *E* isomers of **1** and **5** were not determined due to a lack of quality data. However, the activation parameters for the corresponding *Z* isomers are reported, both to lend credence to the values of other *Z* isomers and should further experiments be undertaken to remedy the lack of *E* isomer data. Yet, the latter is less likely; each diastereomer will have a slightly different restoring force, so the data set below already provides 10 data points for the endocyclic pyrophosphates and 10 data points for the exocyclic pyrophosphates for an analysis of acceleration/inhibition by force.

Table 6.8. Activation parameters for the basic methanolysis of individual stereoisomers of endocyclic pyrophosphates; n.d. = not determined.

macrocycle	$\Delta H^‡$, kcal/mol	$\Delta S^‡$, cal/(mol K)	absolute stereochemistry
*Z***1**A	17 ± 2	0 ± 6	n.d.
*Z***1**B	16 ± 1	-8 ± 5	n.d.

Table 6.8 (cont.)

*Z***2**A	16 ± 2	-3 ± 6	n.d.
*Z***2**B	10 ± 2	-26 ± 5	n.d.
*E***2**A	8 ± 1	-37 ± 4	{ (*M*,*R*,*R*; *P*,*S*,*S*) ; (*M*,*S*,*S*; *P*,*R*,*R*) }
*E***2**B	7.2 ± 0.6	-40 ± 2	
*E***2**C	4 ± 0.7	-47 ± 2	(*M*,*S*,*R*; *P*,*R*,*S*)
*Z***3**A	15.2 ± 0.7	-6 ± 2	n.d.
*Z***3**B	12.7 ± 0.6	-17 ± 2	n.d.
*E***3**A	21 ± 1	8 ± 4	{ (*M*,*R*,*R*; *P*,*S*,*S*) ; (*M*,*S*,*S*; *P*,*R*,*R*) }
*E***3**B	21 ± 1	8 ± 4	
*E***3**C	22.4 ± 0.3	16 ± 1	(*M*,*S*,*R*; *P*,*R*,*S*)
*Z***4**A	13 ± 2	-11 ± 5	n.d.
*Z***4**B	2.9 ± 0.3	-46.6 ± 0.9	n.d.
*E***4**A	15.6 ± 0.3	-4.5 ± 0.9	n.d.
*E***4**B	10 ± 2	-27 ± 6	n.d.
*E***4**C	23 ± 3	20 ± 9	n.d.
*E***4**D	17 ± 2	-1 ± 8	n.d.
*Z***5**A	16 ± 2	-3 ± 7	n.d.
*Z***5**B	15.1 ± 0.9	-9 ± 3	n.d.

Table 6.9. Activation parameters for the basic methanolysis of individual stereoisomers of exocyclic pyrophosphates.

macrocycle	$\Delta H^{‡}$, kcal/mol	$\Delta S^{‡}$, cal/(mol K)
*Z***6**	16 ± 2	-6 ± 5
*E***6**A	22 ± 2	16 ± 6
*E***6**B	17 ± 1	-4 ± 4
*Z*7	8 ± 1	-32 ± 4
*E*7A	11 ± 1	-21 ± 4
*E*7B	9 ± 1	-28 ± 4
*Z***8**	7.7 ± 0.6	-35 ± 2
*E***8**A	20 ± 1	12 ± 5
*E***8**B	20 ± 2	8 ± 6
*Z***9**	8 ± 1	-31 ± 4
*E***9**A	10.3 ± 0.4	-17 ± 1

Table 6.9 (cont.)

_E_**9**B	12 ± 0.7	-15 ± 2
_Z_**10**	10.8 ± 0.4	-22 ± 1
_E_**10**	15.6 ± 0.9	0 ± 3
_Z_**11**	5.48 ± 0.03	-39.55 ± 0.09
_E_**11**	12.7 ± 0.4	-9 ± 1

Table 6.10. Differential activation parameters for the basic methanolysis of individual stereoisomers of exocyclic pyrophosphates; determined from plots of $\ln(k_E/k_Z)$ vs. $1/T$.

macrocycle	$\Delta\Delta H_{\text{Z-E}}^{\ddagger}$, kcal/mol	$\Delta\Delta S_{\text{Z-E}}^{\ddagger}$, cal/(mol K)
_E_**6**A	-7 ± 2	-23 ± 6
_E_**6**B	-1 ± 1	-3 ± 3
_E_**7**A	-3 ± 1	-11 ± 4
_E_**7**B	-1 ± 1	-4 ± 4
_E_**8**A	-13 ± 2	-46 ± 5
_E_**8**B	-13 ± 1	-43 ± 5
_E_**9**A	-2.4 ± 0.4	-15 ± 1
_E_**9**B	-4 ± 0.7	-17 ± 2
_E_**10**	-4.8 ± 0.9	-22 ± 3
_E_**11**	-7.1 ± 0.5	-30 ± 2

6.7 References

1. Cleland, W. W.; Hengge, A. C., Enzymatic Mechanisms of Phosphate and Sulfate Transfer. *Chem. Rev.* **2006**, *106*, 3252–3278.
2. Mikhailenko, S. V.; Oguchi, Y.; Ishiwata, S. i., Insights into the Mechanisms of Myosin and Kinesin Molecular Motors from the Single-Molecule Unbinding Force Measurements. *J. R. Soc. Interface* **2010**, *7*, S295–S306.
3. Miller, K. E.; Heidemann, S. R., What Is Slow Axonal Transport? *Exp. Cell Res.* **2008**, *314*, 1981–1990.
4. Yardimci, H.; van Duffelen, M.; Mao, Y.; Rosenfeld, S. S.; Selvin, P. R., The Mitotic Kinesin CENP-E is a Processive Transport Motor. *Proc. Natl. Acad. Sci.* **2008**, *105*, 6016–6021.

5. Hua, W.; Chung, J.; Gelles, J., Distinguishing Inchworm and Hand-Over-Hand Processive Kinesin Movement by Neck Rotation Measurements. *Science* **2002**, *295*, 844–848.
6. Kodera, N.; Yamamoto, D.; Ishikawa, R.; Ando, T., Video Imaging of Walking Myosin V by High-Speed Atomic Force Microscopy. *Nature* **2010**, *468*, 72–76.
7. Yildiz, A.; Forkey, J. N.; McKinney, S. A.; Ha, T.; Goldman, Y. E.; Selvin, P. R., Myosin V Walks Hand-Over-Hand: Single Fluorophore Imaging with 1.5-nm Localization. *Science* **2003**, *300*, 2061–2065.
8. Allen, M. J.; Rudd, R. E.; McElfresh, M. W.; Balhorn, R., Time-Dependent Measure of a Nanoscale Force-Pulse Driven By the Axonemal Dynein Motors in Individual Live Sperm Cells. *Nanomed-Nanotechnol* **2010**, *6*, 510–515.
9. Watanabe, R.; Iino, R.; Noji, H., Phosphate Release in F_1-ATPase Catalytic Cycle Follows ADP Release. *Nat. Chem. Biol.* **2010**, *6*, 814–820.
10. Gao, J.; Byun, K. L.; Kluger, R., Catalysis by Enzyme Conformational Change. In *Top. Curr. Chem.*, Lee, J. K.; Tantillo, D. J., Eds. Springer-Verlag: New York, 2004; Vol. 238, pp 113–136.
11. Comba, P., Coordination Compounds in the Entatic State. *Coord. Chem. Rev.* **2000**, *200–202*, 217–245.
12. Jencks, W. P., *Catalysis in Chemistry and Enzymology*. Dover Publications, Inc.: New York, 1969.
13. Carey, P. R., Spectroscopic Characterization of Distortion in Enzyme Complexes. *Chem. Rev.* **2006**, *106*, 3043–3054.
14. Fabrichniy, I. P.; Lehtio, L.; Tammenkoski, M.; Zyryanov, A. B.; Oksanen, E.; Baykov, A. A.; Lahti, R.; Goldman, A., A Trimetal Site and Substrate Distortion in a Family II Inorganic Pyrophosphatase. *J. Biol. Chem.* **2007**, *282*, 1422–1431.
15. Cullis, P. M.; Fawcett, J.; Griffith, G. A.; Harger, M. J. P.; Lee, M., Mechanism and Stereochemistry of Diphosphate Formation from Dioxaphosphorinanes: A Critical Reassessment. *J. Am. Chem. Soc.* **2001**, *123*, 4147–4154.
16. Weener, J.-W.; Versleijen, J. P. G.; Meetsma, A.; ten Hoeve, W.; van Leusen, A. M., cis- and trans-2-(Isocyanomethyl)-5,5-dimethyl-2-oxo-4-phenyl-1,3,2-dioxaphosphorinane – Synthesis and Structure of the First Chiral Isocyanomethylphosphonate Synthons. *Eur. J. Org. Chem.* **1998**, *1998*, 1511–1516.

17. Bel'skii, V. E., Hydrolysis of Organic Pyrophosphates. II. Kinetics of Pyrophosphate and Tetraethyl Pyrophosphate Hydrolysis. *B. Acad. Sci. USSR Ch.* **1967**, 1236–1240.

18. Canals, I.; Portal, J. A.; Bosch, E.; Rosés, M., Retention of Ionizable Compounds on HPLC. 4. Mobile-Phase pH Measurement in Methanol/Water. *Anal. Chem.* **2000**, *72*, 1802–1809.

19. Bentrude, W. G.; Setzer, W. N., Stereospecificity in ^{31}P–Element Couplings: Proton–Phosphorus Couplings. In *Phosphorus-31 NMR Spectroscopy in Stereochemical Analysis*, Verkade, J. G.; Quin, L. D., Eds. VCH Publishers: Deerfield Beach, FL, 1987; Vol. 8.

20. Lee, C.-H.; Sarma, R. H., Aqueous Solution Conformation of Rigid Nucleosides and Nucleotides. *J. Am. Chem. Soc.* **1976**, *98*, 3541–3548.

21. Hall, L. D.; Malcolm, R. B., Studies of Organophosphorus Derivatives. Part I. Nuclear Magnetic Resonance Studies of the 2-Oxo-1,3,2-dioxaphosphorinane System. *Can. J. Chem.* **1972**, *50*, 2092–2101.

22. Gans, P., *Data Fitting in the Chemical Sciences By the Method of Least Squares*. John Wiley & Sons: New York, 1992.

Chapter 7. Changing Reaction Mechanisms with Force: Selective Pathway Suppression in Disulfide Reduction by Phosphines

Adapted from Kucharski, T. J.; Tian, Y.; Yang, Q.-Z.; Rubin, N. C.; Concepcion, C. D.; Boulatov, R., In preparation.

7.1 Introduction

The field of chemomechanics/mechanochemistry[1] has been receiving an increasing amount of attention as more investigators find creative ways to take advantage of the dramatic changes in chemical reactivity that can be induced by mechanical action. Greater than 10^{15}-fold accelerations have been observed for localized reactions in polymers subjected to micro- or macroscopic loads[2-4] or shear flows[5-10] or those at evolving interfaces.[11,12] Chemomechanical energy coupling forms the basis of the operation of motor proteins[13] and molecular photoactuating materials.[14-19] Single-molecule pulling experiments have been used to study diverse mechanochemical phenomena, including dissociations of covalent bonds,[20] ligands from metals,[21-23] and arrays of hydrogen bonds,[24-26] as well as nucleophilic displacements[27-31] and conformational transitions.[32] The phenomenology of mechanochemistry and its promise for enabling responsive materials has been recently reviewed,[4,33,34] but despite all of this experimental effort and the increasing use of quantum chemical modeling[35-37] and molecular dynamics simulations[3,5,8,38-42] to rationalize such mechanochemical phenomena, a general, predictive and physically sound model for multiscale dynamics has until recently been lacking (Chapter 1, refs. 43 and 44).

We have previously demonstrated that only force, not material strain or strain energy, relates strain and reactivity (Chapter 1, refs. 43 and 44). As in any other object, a strained molecule develops a restoring force, which as the gradient of strain energy is a size-invariant and directional quantifier of the changes in energy that alter the molecule's reactivity. Restoring force is thus a convenient and accurate predictor for mechanochemical phenomena, as it is readily determined from quantum chemical calculations or statistical, rheological, or empirical models for small molecules, polymers, flows, or flexible objects. In order to enable the truly rational design of actuating and stress-responsive materials, the force-dependent kinetics of reactive moieties must be understood at the molecular level. Our local approximation for chemomechanical kinetics does precisely that in its assertions that 1) the dynamics of the larger system are dictated by changes in an internal coordinate q of a much more tractable minimal reactant and 2) the restoring force of this q approximates that of the larger system (Chapter 1, refs. 43 and 44).

Here we examine chemomechanical kinetics on arguably the simplest corrugated energy landscape, that of pre-equilibrium systems ($\mathrm{R} \rightleftharpoons \mathrm{I} \rightarrow \mathrm{P}$), such as the rapid, reversible reactions in biomolecular systems[42,45,46] and enzymatic catalysis described by Michaelis–Menten kinetics,[47] which are ubiquitous in nature. I present a simple model for multibarrier mechanochemical kinetics that accurately predicts the effect of force on the observed kinetics in systems characterized by multiple barriers, using our current understanding of mechanochemistry as a starting point. In certain limiting cases, reverse steps can be completely suppressed by small forces due to large changes in the intermediate's stretching compliance, effectively changing the kinetic profile of the overall chemical transformation from R ⇌ I → P to R → I → P and leading to dramatic changes in the perceived kinetics of the formation of P. Ignoring the changes that cause such suppression can lead to dramatic overestimations of reaction rates and incorrect assignments of which kinetic barriers were lowered. We use such a limiting case to experimentally validate our model by predicting the observed $>10^4$-fold force-induced acceleration for disulfide reduction by phosphines even though the process of bond cleavage is accelerated by force by less than a factor of 5.

The rest of this article is organized as follows: First, I briefly review the points of the standard phenomenological model for mechanochemical kinetics relevant to this discussion, highlighting seemingly subtle, yet crucial, conceptual distinctions that are sometimes ignored. Second, I briefly derive our extended model, accounting for changes in substrate compliance during the chemical transformation. Third, I discuss the salient differences between the two models, using numeric simulations of kinetic crossover in two-barrier systems as illustrative examples. I then discuss the experimental validation of our model for multibarrier kinetics and conclude with a discussion of the model's implications.

7.2 The Standard Model

Because of its simplicity, the Eyring–Bell–Evans[48-51] (EBE) formalism is widely used and is often referred to as the standard (phenomenological) model[52-55] for mechanochemical kinetics. The underlying concept of the EBE formalism was first described by Eyring 70 years ago.[48] Nearly 40 years later, Bell posited a phenomenological model[49] describing the forced unbinding of adhesive contacts (bonds), using a modified Eyring rate expression, and this model was further developed by Evans and Ritchie.[50,51] Essentially, the EBE formalism can be viewed as accounting for the effects of tilting a potential energy surface (PES) with a constant potential so that the PES is modified by $-F \cdot x$, i.e., the projection of force F along the reaction coordinate

x.[51,54] Thus, the decrease of the kinetic barrier due to force is described as $\Delta\Delta G^{\ddagger}(F) = F\Delta x$ (i.e., $\Delta G^{\ddagger}(F) = \Delta G^{\ddagger} - \Delta\Delta G^{\ddagger}(F)$), where Δx (sometimes elsewhere written $x^{\ddagger}$ or x_{β}) is the difference in the reaction coordinate between the ground and transition states. The EBE equation can also be derived[54,56,57] within Kramers' formalism for diffusive escape from a potential well,[58,59] but then the inclusion of second-order (Hammond) effects[60] is problematic.[61] However, the EBE formalism has been experimentally validated, both in single molecule studies[54] using various microscopic force probes[62] and more recently by our work[63] using molecular force probes.[64,65]

Several researchers have used the EBE formalism or its variants (e.g., the so-called cusp model[57,61]) to extract information about (bio)macromolecules' PESs; such single-molecule force (SMF) experiments provide a context for comparison of the EBE formalism to the model described in this work and are briefly summarized here to present the need for a physically unambiguous model and to clarify the analysis of the simulations discussed below. Two major types of SMF experiments have been used: dynamic force loading experiements[51,54] in which time is related to the instantaneous applied force and so-called force-clamp experiments[66] in which a constant force is applied to the (bio)macromolecule. In dynamic SMF experiments, histograms of the force leading to rupture at different force-loading rates are collected, and then the most probable rupture force, F^*, from each histogram is plotted against the logarithm of the force-loading rate at which it was collected. The slope of such a plot is related to the characteristic thermal force scale for the dominant barrier, which is in turn related to the value of Δx for that barrier. Extrapolation to $F^* = 0$ yields a force-loading rate related to Δx and an apparent strain-free rupture rate. Analogously, in force-clamp SMF experiments, at each value of applied force, F, an overlay of rupture events vs. time is fitted to obtain a rate constant for rupture, and the logarithm of these rate constants is plotted against the applied force at which they were determined. The slope of such a plot is related to Δx for the dominant barrier, and extrapolation to $F = 0$ yields an apparent strain-free rupture rate for that barrier. Despite these successes, it is important to note that there is no reason that the apparent strain-free rupture rates obtained from extrapolation to $F^* = 0$ or $F = 0$ equal the true strain-free rupture rates, particularly when there are multiple barriers on the PES.[51] To our knowledge, such agreement has been demonstrated through careful experiments in only one study.[22] Further details of SMF experiments and micromanipulation techniques have been reviewed elsewhere.[43,62,67]

Treatments of data obtained from SMF experiments within the EBE formalism involve the (tacit) assumption that the variable conjugate to F is a good approximation to the reaction coordinate.[54,55,57] However, this approximation is questionable,[55] particularly when the orientation of the reactive moiety, and hence the physical structure determining the reaction coordinate, relative to the force vector is unknown. Within the EBE formalism, Δx is often discussed as the generalized distance to the transition state (or well-to-barrier distance),[51,54,56,57] which may or may not correlate well with any internuclear distance in the reactive moiety.[61] Though it may be tempting to interpret the value of Δx obtained from SMF experiments as the elongation of the scissile bond between the ground and transition states,[29-31] doing so assumes both that the length of the scissile bond is a good approximation of the reaction coordinate and that its alignment with the restoring force vector is known, either of which is only rarely true. Therefore, within the EBE formalism it is difficult, if not impossible, to ascribe an unambiguous atomistic meaning to Δx in the absence of quantum chemical modeling or other *a priori* knowledge.[27]

The EBE formalism has been criticized in an increasing number of cases for its failure to reproduce transition state locations and rates obtained from more sophisticated microscopic models,[56] overestimating strain-free rupture rates in those cases by more than an order of magnitude.[55] It has also been noted that the EBE formalism fails when the transition state is significantly compliant,[54] which makes the linear modification of activation energy, $\Delta\Delta G^{\ddagger}(F) = -F\Delta x$, an extreme approximation. A model incorporating changes in substrate compliance was proposed in biophysics,[68,69] but other reports asserted that, at least in the cases studied up to that point, the quadratic term in F was negligible.[70,71] Thus, that model appears to have been largely ignored despite reexaminations of the effect of macromolecular compliance on the position[54,72] or force-sensitivity of the transition state,[73] and other suggested extensions of the standard model involving quadratic terms in F to improve agreement with experimental data.[53] In the following sections I discuss the physical basis for our model and demonstrate its ability to make accurate predictions where the EBE formalism cannot.

7.3 Extension of the Local Approximation to Multibarrier Energy Surfaces

Chemomechanical phenomena in stretched polymers or other macromolecular systems can be understood as a result of the relief of strain energy due to (partial) relaxation not only of the strained macromolecule but also of the potential that constrains it. In many cases, the stretching behavior of the macromolecule (e.g., a polymer "overstretched" to a length greater than its strain-free contour length) and that of the constraining potential (e.g., an oscillating atomic force microscope (AFM) cantilever) can be described as that of harmonic potentials. Though long polymer chains exhibit anharmonic stretching behavior, they can generally be approximated as harmonic under the conditions of interest. For example, in a chain of polyethylene (PE) long enough to exhibit mechanochemical scission of its bonds by ultrasonication, length changes on the order of those involved in covalent bond rearrangements change the stretching compliance λ by <1%. Thus, the macromolecule and the object(s) that constrain its end-to-end length can be described as a pair of springs, one compressed and one elongated, where the distance between the endpoints of both the constraining object and the substrate can be assigned as the mechanical coordinate, τ (Fig. 7.1).

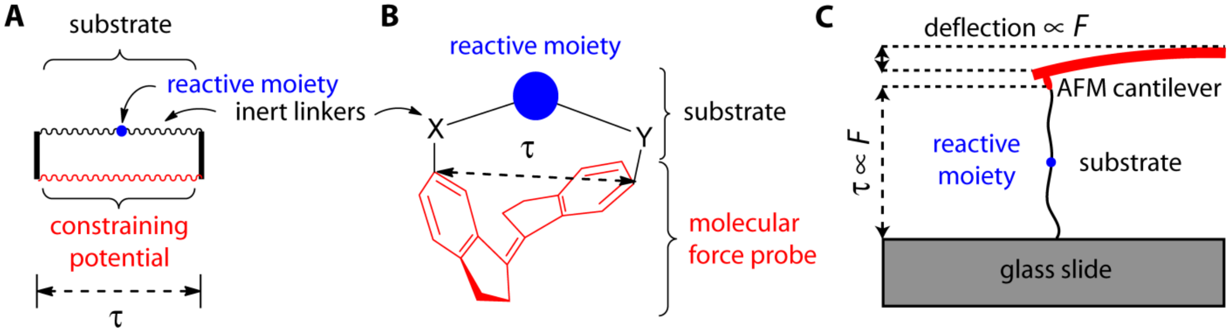

Fig. 7.1. Three examples of force probes: a generic scheme (**A**), a molecular force probe based on stiff-stilbene (**B**) and a force probe using an AFM (**C**).

Even when molecules are far from thermodynamic equilibrium, they are still in mechanical equilibrium with their environment;[74] at stationary points on their PESs, molecules are necessarily in internal mechanical equilibrium. The condition of internal mechanical equilibrium specifies that the restoring force along the mechanical coordinate, F_τ, which the substrate and the constraining potential exert on each other are equal in magnitude and opposite in sign. The mechanochemical system is then fully determined by knowledge of the strain-free value of the substrate's mechanical coordinate, τ^{o}, the stretching compliances of the mechanical coordinate in the substrate, λ_{τ}, that of the constraining potential, λ_{c}, and the restoring force, F_{τ}.

Given that changes in the global conformational structure of a macromolecule occur on much longer time scales (μs–ms) than localized covalent bond rearrangements (ps), it is natural to describe these with separate degrees of freedom, the mechanical coordinate τ and the chemical coordinate ζ, as shown in Fig. 7.2. The mechanical coordinate is best defined by considering the conditions of the mechanochemical system in question. In stretched polymer chains, the end-to-end distance R_z is a convenient mechanical coordinate because it is affected by both the molecule's enthalpic and entropic stretching properties (see below and section 7.8.3 for examples). However, because $\langle R_z \rangle \rightarrow 0$ in ensembles of *unconstrained* polymer chains, the contour length L can sometimes be a better assignment of τ, though its change reflects only enthalpic stretching properties. The chemical coordinate ζ is a generalized degree of freedom that describes the pattern of chemical bonding at the reactive moiety. Because of the differences in timescale, rather than following the curvilinear minimum-energy paths between minima and saddle points as in small molecules, localized chemical transformations in macromolecules occur along ζ at a fixed value of τ (white arrows, Fig. 7.2). Because a localized reaction within the macromolecule, e.g. R → I, may occur when $\tau \neq \tau_{R}^{o}$ due to thermal fluctuations in τ (wavy black lines, Fig. 7.2), the free energy of the highest point along the reaction path, $G(\tau,\zeta_{TS1})$ (Fig. 7.2A), may be different from that of the strain-free transition state, $G(\tau_{TS1}^{o},\zeta_{TS1})$.

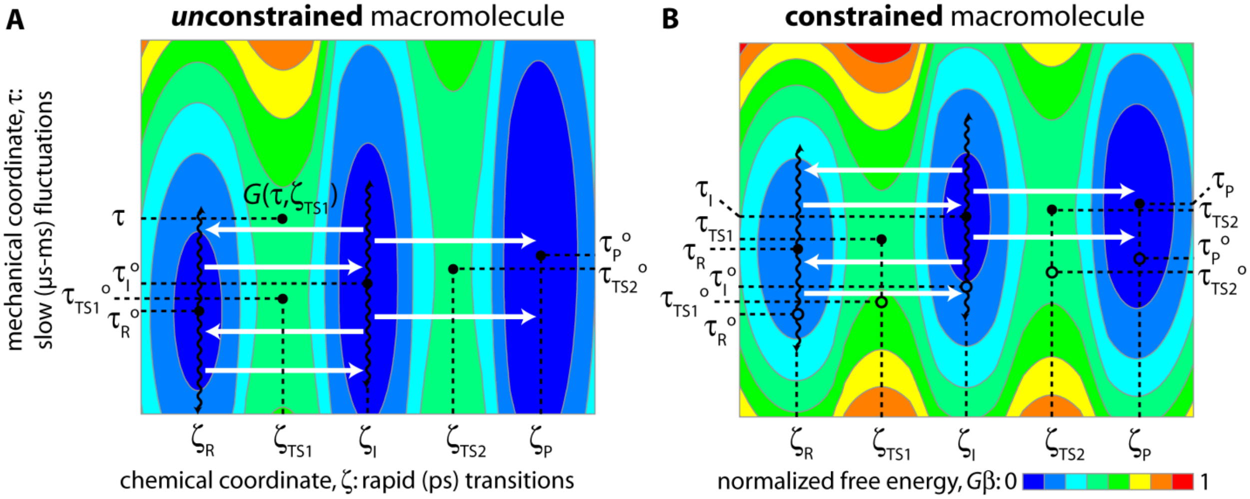

Fig. 7.2. Reduced-dimensionality PESs ($G(\tau,\zeta)$) for the chemical transformation R ⇌ I → P in (**A**) an unconstrained macromolecule and (**B**) a macromolecule in the presence of a constraining potential that stretches it. The PESs are

plotted in terms of the global conformational structure described by the mechanical coordinate, τ, and the chemical coordinate, ζ, which describes the pattern of chemical bonding at the reactive moiety. The axes and energy scales are identical for **A** and **B**. Slow (μs–ms) thermal fluctuations in τ are indicated by the black wavy lines, while rapid (ps) chemical transformations (changes in ζ) are indicated by the white arrows. In **B**, open circles denote the positions of the minima in the absence of the constraining potential (closed circles in **A**).

Neither the presence of the macromolecule (Fig. 7.2A) nor the constraining potential (Fig. 7.2B) inherently changes the PES for the reaction. The constraining potential only affects the PES by shifting the equilibrium positions of τ (filled dots, Fig. 7.2B) away from the strain-free values τ^{o} (filled dots in Fig. 7.2A, open dots in Fig. 7.2B) and by changing the free energy of reaction for the system, increasing the exergonicity as strain is relieved. In the example shown in Fig. 7.2, τ is the contour length of the polymer chain normalized to its strain-free value in the reactant, i.e. $\tau = L/L_{\mathrm{R}}^{o}$, and the reactive moiety is more compliant in I, TS2 and P than in R and TS1, as evidenced by their flatter potentials along τ. Thus, the stationary points I, TS2 and P are shifted further along τ by the constraining potential, making $\Delta\tau_{\mathrm{I,TS1}} > \Delta\tau_{\mathrm{I,TS1}}^{o}$. Note also that the constraining potential effectively narrows the distribution of thermally accessible values of τ at each stationary point, as we have noted elsewhere.[43]

For a mechanochemical system (e.g., Fig. 7.1) in any chemical state n, mechanical equilibrium, both internal and with any constraint, specifies a potential for fluctuations in τ symmetric about the equilibrium value τ_n. When the strain-free values of τ for the substrate and the constraining potential (τ_n^{o} and τ_{c}^{o}) differ, the ensemble-average restoring force along τ, $\langle F_{\tau n}\rangle$, is nonzero, and the system is inherently strained. (A detailed derivation and a list of all mathematical symbols used can be found in Table 7.3.) If the mechanochemical system is in thermal equilibrium with its surroundings, it obeys a Boltzmann distribution over τ, and the probability density function for the reactant R is given by eq. (1.1), where the compliances of τ in the substrate and the constraining potential are $\lambda_{\tau\mathrm{R}}$ and λ_{c}, respectively, $\lambda_{\mathrm{R}} = \lambda_{\tau\mathrm{R}} + \lambda_{\mathrm{c}}$, and β is inverse thermal energy. Defining the standard state as the *unconstrained macromolecule* yields (7.2) as its probability density function for fluctuations in τ.

$$\rho_{\mathrm{R}}(\tau, \langle F_{\tau\mathrm{R}}\rangle) = \sqrt{\frac{\beta\lambda_{\mathrm{R}}}{2\pi\lambda_{\mathrm{c}}\lambda_{\tau\mathrm{R}}}}\, e^{-\beta\frac{\lambda_{\mathrm{R}}(\langle F_{\tau\mathrm{R}}\rangle\lambda_{\tau\mathrm{R}}-\tau+\tau_{\mathrm{R}}^{o})^2}{2\lambda_{\mathrm{c}}\lambda_{\tau\mathrm{R}}}} \tag{7.1}$$

$$\rho_{\mathrm{R}}^{\mathrm{o}}(\tau) = \sqrt{\frac{\beta}{2\pi\lambda_{\tau\mathrm{R}}}}\, e^{-\beta\frac{(\tau-\tau_{\mathrm{R}}^{\mathrm{o}})^2}{2\lambda_{\tau\mathrm{R}}}} \tag{7.2}$$

The ensemble-average rate constants for the elementary reaction R → I in a macromolecule stretched to an average restoring force $\langle F_{\tau\mathrm{R}}\rangle$ in the reactant, $k_{\mathrm{R,I}}(\langle F_{\tau\mathrm{R}}\rangle)$, and that in the unconstrained macromolecule, $k_{\mathrm{R,I}}{}^{\mathrm{o}}$, are given by eqs. (7.3) and (7.4), respectively, where $k_{\mathrm{R,I}}(\tau)$ is the rate constant of the chemical transformation $\mathrm{R} \rightarrow [\mathrm{TS1}]^{\ddagger} \rightarrow \mathrm{I}$ for the macromolecule with mechanical coordinate τ. The canonical transition-state theory expression[75] for $k_{\mathrm{R,I}}(\tau)$ is given by eq. (7.5), where ζ_{R} and ζ_{TS1} are the values of the chemical coordinate for the ground state reactant and the transition state connecting the reactant and the intermediate, respectively.

$$k_{\mathrm{R,I}}(\langle F_{\tau\mathrm{R}}\rangle) \propto \int_{-\infty}^{\infty} \rho_{\mathrm{R}}(\tau, \langle F_{\tau\mathrm{R}}\rangle) k_{\mathrm{R,I}}(\tau) d\tau \tag{7.3}$$

$$k_{\mathrm{R,I}}^{\mathrm{o}} \propto \int_{-\infty}^{\infty} \rho_{\mathrm{R}}^{\mathrm{o}}(\tau) k_{\mathrm{R,I}}(\tau) d\tau \tag{7.4}$$

$$k_{\mathrm{R,I}}(\tau) \propto e^{-(G(\tau,\zeta_{\mathrm{TS1}}) - G(\tau,\zeta_{\mathrm{R}}))\beta} \tag{7.5}$$

Assuming that ζ is much stiffer than τ, $G(\tau,\zeta)$ can be expanded as Taylor series using the strain energy about the strain-free ground and transition states in the standard state (see section 7.8.1). Combining eqs. (1.1)–(7.5) then yields the ratio of the ensemble-average rate constant for the chemical transformation $\mathrm{R} \rightarrow [\mathrm{TS1}]^{\ddagger} \rightarrow \mathrm{I}$ in a macromolecule constrained to an average restoring force $\langle F_{\tau\mathrm{R}}\rangle$ to that in the unconstrained macromolecule. If $\lambda_{\tau\mathrm{TS1}} > 0$, this expression reduces to eq. (7.6), where the quantity $\Delta\Delta G_{\mathrm{R,I}}{}^{\ddagger}(\langle F_{\tau\mathrm{R}}\rangle)$ is the *force-dependent barrier lowering*, i.e., $\Delta G_{\mathrm{R,I}}{}^{\ddagger}(\langle F_{\tau\mathrm{R}}\rangle) = \Delta G_{\mathrm{R,I}}{}^{\ddagger\mathrm{o}} - \Delta\Delta G_{\mathrm{R,I}}{}^{\ddagger}(\langle F_{\tau\mathrm{R}}\rangle)$. This is our general formulation of chemomechanical kinetics for $\mathrm{R} \rightarrow [\mathrm{TS1}]^{\ddagger} \rightarrow \mathrm{I}$ with all terms shown explicitly. Following similar reasoning but writing expressions only in terms of λ, τ, and the control parameter $\langle F_{\tau\mathrm{R}}\rangle$, the analogous expressions for the reverse process $\mathrm{I} \rightarrow [\mathrm{TS1}]^{\ddagger} \rightarrow \mathrm{R}$ and the subsequent forward process $\mathrm{I} \rightarrow [\mathrm{TS2}]^{\ddagger} \rightarrow \mathrm{P}$ can be written, as shown in eqs. (7.7) and (7.8).

$$\begin{aligned}\beta^{-1} \ln \frac{k_{\mathrm{R,I}}(\langle F_{\tau\mathrm{R}}\rangle)}{k_{\mathrm{R,I}}^{\mathrm{o}}} &= \frac{\lambda_{\mathrm{R}}}{\lambda_{\mathrm{TS1}}}\left(\frac{\langle F_{\tau\mathrm{R}}\rangle^2}{2}\Delta\lambda_{\mathrm{R,TS1}} + \langle F_{\tau\mathrm{R}}\rangle \Delta\tau_{\mathrm{R,TS1}}^{\mathrm{o}} + \frac{{\Delta\tau_{\mathrm{R,TS1}}^{\mathrm{o}}}^2}{2\lambda_{\mathrm{R}}}\right) + \frac{1}{2\beta}\ln\frac{\lambda_{\mathrm{R}}}{\lambda_{\mathrm{TS1}}} \\ &\equiv \Delta\Delta G_{\mathrm{R,I}}^{\ddagger}(\langle F_{\tau\mathrm{R}}\rangle)\end{aligned} \tag{7.6}$$

$$\begin{aligned}\beta^{-1}\ln\frac{k_{\mathrm{I,R}}(\langle F_{\tau\mathrm{R}}\rangle)}{k^{\mathrm{o}}_{\mathrm{I,R}}}&\\ &=\frac{\lambda_{\mathrm{R}}}{\lambda_{\mathrm{I}}\lambda_{\mathrm{TS1}}}\left(\frac{\langle F_{\tau\mathrm{R}}\rangle^2}{2}\Delta\lambda_{\mathrm{I,TS1}}\lambda_{\mathrm{R}}+\langle F_{\tau\mathrm{R}}\rangle\left(\Delta\tau^{\mathrm{o}}_{\mathrm{R,TS1}}\lambda_{\mathrm{I}}-\Delta\tau^{\mathrm{o}}_{\mathrm{R,I}}\lambda_{\mathrm{TS1}}\right)\right)+\frac{{\Delta\tau^{\mathrm{o}}_{\mathrm{R,I}}}^2}{2\lambda_{\mathrm{I}}}\\ &-\frac{{\Delta\tau^{\mathrm{o}}_{\mathrm{R,TS1}}}^2}{2\lambda_{\mathrm{TS1}}}+\frac{1}{2\beta}\ln\frac{\lambda_{\mathrm{I}}}{\lambda_{\mathrm{TS1}}}\equiv\Delta\Delta G^{\ddagger}_{\mathrm{I,R}}(\langle F_{\tau\mathrm{R}}\rangle)\end{aligned}\tag{7.7}$$

$$\begin{aligned}\beta^{-1}\ln\frac{k_{\mathrm{I,P}}(\langle F_{\tau\mathrm{R}}\rangle)}{k^{\mathrm{o}}_{\mathrm{I,P}}}&\\ &=\frac{\lambda_{\mathrm{R}}}{\lambda_{\mathrm{I}}\lambda_{\mathrm{TS2}}}\left(\frac{\langle F_{\tau\mathrm{R}}\rangle^2}{2}\Delta\lambda_{\mathrm{I,TS2}}\lambda_{\mathrm{R}}+\langle F_{\tau\mathrm{R}}\rangle\left(\Delta\tau^{\mathrm{o}}_{\mathrm{R,TS2}}\lambda_{\mathrm{I}}-\Delta\tau^{\mathrm{o}}_{\mathrm{R,I}}\lambda_{\mathrm{TS2}}\right)\right)+\frac{{\Delta\tau^{\mathrm{o}}_{\mathrm{R,I}}}^2}{2\lambda_{\mathrm{I}}}\\ &-\frac{{\Delta\tau^{\mathrm{o}}_{\mathrm{R,TS2}}}^2}{2\lambda_{\mathrm{TS2}}}+\frac{1}{2\beta}\ln\frac{\lambda_{\mathrm{I}}}{\lambda_{\mathrm{TS2}}}\equiv\Delta\Delta G^{\ddagger}_{\mathrm{I,P}}(\langle F_{\tau\mathrm{R}}\rangle)\end{aligned}\tag{7.8}$$

Elsewhere (Chapter 1, refs. 43 and 44) we have also derived the expression for the force-dependent barrier lowering, though only for the process analogous to R → $[\mathrm{TS1}]^{\ddagger}$ → I. In some cases (Chapter 1, ref. 44) the formula was derived with the *constrained but strain-free* macromolecule as the standard state (i.e., $k_{\mathrm{R,I}}{}^{\mathrm{o}} \rightarrow k_{\mathrm{R,I}}(\langle F_{\tau\mathrm{R}}\rangle = 0)$), while in other cases[43] the formula was derived with the *unconstrained* macromolecule as the standard state, as I have done here. In the former case, terms in $(\Delta\tau^{\mathrm{o}})^2$ and $(2\beta)^{-1}\ln(\lambda_n/\lambda_m)$ do not appear because of the presence of the constraining potential in the standard state's distribution function. In the latter case, the logarithmic term was omitted for the reasons discussed below.

Compliances are more convenient to use than force constants because they may be readily determined from high-level quantum mechanical frequency calculations for small molecules by inverting the Hessian, and, unlike force constants, compliances obtained thus so are independent of the choice of coordinate system or any redundancies therein.[76-80] Representative compliances for molecular or microscopic objects often present in mechanochemical systems are shown in Table 7.1, which demonstrate that even for shorter, stiffer polymer chains stretched to an average restoring force large enough to cause covalent bond rupture (2 nN),[20] compliances are several orders of magnitude larger than those of covalent bonds. Because enthalpic compliances of objects in series are additive, the contribution of the compliance of a specific bond buried inside a polymer chain may be quite small, e.g., a few ppm for a C≡C bond in the middle of an ~50 nm PE chain stretched to an average restoring force of 100 pN.

Table 7.1. Representative stretching compliances of molecular and microscopic constructs.

bond or distance	λ, Å nN^{-1}	flexible object	$\langle F_{Rz}\rangle$, pN	R_z,[a] nm	λ_{total}, Å nN^{-1}	$\lambda_{\mathrm{enthalpic}}$, Å nN^{-1}
O–H in water[b]	0.0119	PE chain, L_o = 1 μm[c]	100	869	14100	352
typical C–C[b]	0.025		500	991	904	367
typical C=C[b]	0.011		2000	1070	479	446
typical C≡C[b]	0.005	PE chain, L_o = 25 nm[c]	100	21.7	400	8.80
C–O in EtOMs[d,e]	>0.0239		500	24.8	23	9.19
S–S in Et$_2$S$_2$[d,f]	>0.0209		2000	26.8	12	11.1
Me···Me in *trans*-Me$_2$cb[c,g]	0.192	AFM cantilever[h]			20–3000	

[a] R_z is end-to-end separation. [b] ref. 78. [c] See section 7.8.3 for details. [d] The "relaxed force constant," whose inverse is the compliance constant λ, is always smaller than the harmonic vibrational force constant,[77,79,80] which therefore provides a lower limit for the compliance constant. [e] Calculated from data in ref. 81. [f] Calculated from data in refs. 82-84. [g] cb is cyclobutene. [h] Values for those typically used in SMF experiments.[19,67]

For localized reactions involving the rearrangement of covalent bonds, $\Delta\tau^{\mathrm{o}}$ is generally less than a few Å. The large stretching compliances of long, flexible polymers therefore makes the contributions of the $(\Delta\tau^{\mathrm{o}})^2$ terms in eqs. (7.6)–(7.8) negligible compared to the terms in $\langle F_{\tau i}\rangle$. Provided that at least some covalent bond remains intact to prevent rupture of the macromolecule, changes in the compliance of a reactive moiety are likely to have little impact on the sums of compliances (i.e., $\lambda_n = \lambda_{\mathrm{c}} + \lambda_{\tau n}$), particularly if the compliance of the constraining potential, λ_{c}, is on the order of a typical AFM cantilever (Table 7.1). Therefore, the ratios of these sums in many cases can be approximated as unity, simplifying eqs. (7.6)–(7.8). The values of $\Delta\lambda$ reflect only the changes in the reactive moiety, as the effect of the constraining potential is cancelled by the difference and compliance changes in the non-reacting portions of the macromolecule are negligible for small changes in size.

The real utility of this model lies in the relationship of its parameters to those of the minimal reactant, which can be determined with chemical accuracy from high-level quantum mechanical calculations because of its small size. Our previously proposed local approximation (Chapter 1, refs. 43 and 44) to the mechanochemical kinetics of R → I is readily applied to the formulas for the reverse and subsequent forward steps. Doing so, eqs. (7.6)–(7.8) are rewritten as eqs. (7.9)–(7.11), entirely in terms of parameters of the minimal reactant: the *strain-free* change in a local molecular degree of freedom, $\Delta q_{m,n}^{\mathrm{o}}$, the change in the compliance of q, $\Delta\lambda_{qm,qn}$, and the average restoring force along q in the initial chemical state of the mechanochemical system, $\langle F_{q\mathrm{R}}\rangle$.

$$\beta^{-1}\ln\frac{k_{\mathrm{R,I}}\big(\langle F_{q\mathrm{R}}\rangle\big)}{k^{\mathrm{o}}_{\mathrm{R,I}}}=\frac{\langle F_{q\mathrm{R}}\rangle^2}{2}\Delta\lambda_{q\mathrm{R},q\mathrm{TS1}}+\langle F_{q\mathrm{R}}\rangle\Delta q^{\mathrm{o}}_{\mathrm{R,TS1}} \tag{7.9}$$

$$\beta^{-1}\ln\frac{k_{\mathrm{I,R}}\big(\langle F_{q\mathrm{R}}\rangle\big)}{k^{\mathrm{o}}_{\mathrm{I,R}}}=\frac{\langle F_{q\mathrm{R}}\rangle^2}{2}\Delta\lambda_{q\mathrm{I},q\mathrm{TS1}}+\langle F_{q\mathrm{R}}\rangle\Delta q^{\mathrm{o}}_{\mathrm{I,TS1}} \tag{7.10}$$

$$\beta^{-1}\ln\frac{k_{\mathrm{I,P}}\big(\langle F_{q\mathrm{R}}\rangle\big)}{k^{\mathrm{o}}_{\mathrm{I,P}}}=\frac{\langle F_{q\mathrm{R}}\rangle^2}{2}\Delta\lambda_{q\mathrm{I},q\mathrm{TS2}}+\langle F_{q\mathrm{R}}\rangle\Delta q^{\mathrm{o}}_{\mathrm{I,TS2}} \tag{7.11}$$

If, however, the substrate (macromolecule) is cleaved during one of the chemical transformations, eqs. (7.9)–(7.11) change significantly. If there is no longer a bond to connect the two fragments of the molecule, they will be drawn apart until all of the strain energy in the system is relieved. Interpreting the compliances as infinite or some arbitrary large value only reduces eqs. (7.6)–(7.8) to infinite or arbitrary values. Instead, consider that if the macromolecule is cleaved by the process R → I, the force-dependent free energy of the reaction is increased by the amount of inherent strain energy relieved (see section 7.8.2). Therefore, the *force-dependent barrier lowering* ($\Delta G_{\mathrm{I,R}}{}^{\ddagger}(\langle F_{\tau\mathrm{R}}\rangle)=\Delta G_{\mathrm{I,R}}{}^{\ddagger\mathrm{o}}-\Delta\Delta G_{\mathrm{I,R}}{}^{\ddagger}(\langle F_{\tau\mathrm{R}}\rangle)$) can be calculated effectively as the energetic consequence of re-straining the system to bring the fragments back together to reach the transition state, yielding eq. (7.12). Application of the same approximations as above then yields eq. (7.13), where the contributions from the constraining potential and the substrate beyond just the reactive moiety need still be considered in the last term. If the substrate does not reconnect beyond the intermediate, further barriers are force-independent.

$$\begin{aligned}\Delta\Delta G^{\ddagger}_{\mathrm{I,R}}(\langle F_{\tau\mathrm{R}}\rangle)&=\Delta\Delta G^{\ddagger}_{\mathrm{R,I}}(\langle F_{\tau\mathrm{R}}\rangle)-\frac{\lambda_{\mathrm{R}}\langle F_{\tau\mathrm{R}}\rangle^2}{2}\\&=\frac{\lambda_{\mathrm{R}}}{\lambda_{\mathrm{TS1}}}\left(\frac{\langle F_{\tau\mathrm{R}}\rangle^2}{2}\Delta\lambda_{\mathrm{R,TS1}}+\langle F_{\tau\mathrm{R}}\rangle\Delta\tau^{\mathrm{o}}_{\mathrm{R,TS1}}+\frac{{\Delta\tau^{\mathrm{o}}_{\mathrm{R,TS1}}}^2}{2\lambda_{\mathrm{R}}}\right)+\frac{1}{2\beta}\ln\frac{\lambda_{\mathrm{R}}}{\lambda_{\mathrm{TS1}}}-\frac{\lambda_{\mathrm{R}}\langle F_{\tau\mathrm{R}}\rangle^2}{2}\end{aligned} \tag{7.12}$$

$$\Delta\Delta G^{\ddagger}_{\mathrm{I,R}}\big(\langle F_{q\mathrm{R}}\rangle\big)=\frac{\langle F_{q\mathrm{R}}\rangle^2}{2}\Delta\lambda_{q\mathrm{R},q\mathrm{TS1}}+\langle F_{q\mathrm{R}}\rangle\Delta q^{\mathrm{o}}_{\mathrm{R,TS1}}-\frac{\lambda_{\mathrm{R}}\langle F_{\tau\mathrm{R}}\rangle^2}{2} \tag{7.13}$$

7.4 Comparison of the Two Models for Multibarrier Kinetics

The differences between the two models are more than semantics. As I will show below, under certain circumstances the model presented here and the EBE formalism yield qualitatively different predictions. However, it is important to first distinguish between the meanings of the

EBE formalism's Δx and what we have defined as $\Delta \tau$ and Δq. If Δx were not an empirical value and were instead treated as a vector in $3N - 6$ dimensions encompassing all changes in molecular structure along the reaction coordinate, it could possibly serve as a predictive tool. However, such a parameter would still have very limited utility, because it is overly detailed to the point of being impractical for chemists accustomed to describing the course of a reaction with a few selected internuclear distances of interest. Instead, a useful model should yield accurate predictions with less-than-complete information about the system.

Though Δx can certainly be fitted to experimental plots of log(k) vs. F, because it need not equal any internuclear distance change, it is difficult to see how it can be predictive for chemists and materials scientists interested in tailoring a particular molecule's response to force. As I show below, even in cases where such fits may misleadingly appear reasonable, Δx can still be devoid of any useful molecular information. Instead, we claim that in anisotropically strained systems, our local approximation of chemomechanical kinetics (Chapter 1, refs. 43 and 44) applies and thus an appropriately chosen q allows for coarse-graining of the majority of the degrees of freedom into force, thereby yielding easy access to accurate predictions "by shielding us from irrelevant details,"[85] with the caveat that higher-order terms should not be neglected out of hand.

When the magnitude of compliance changes in the reactive moiety are indeed small, second-order effects are minimized, and the formalism reduces to a formulation analogous to the empirical EBE ansatz. This is likely one reason for the successes of the EBE formalism in interpreting various mechanochemical phenomena. An application where the EBE formalism has been used is the experimental determination of various features of corrugated potential energy surfaces of biomacromolecules. However, the predictions of the two models diverge rapidly when second-order effects are present or when the conditions for the simplifications discussed above are not met. Furthermore, even in the absence of second-order effects, the possibilities for force-dependent changes of multibarrier energy surfaces that determine the observed kinetics are far richer and more complex than previously acknowledged in the literature.

The effect of force on multibarrier kinetics has been examined by SMF experiments on a number of biomacromolecular systems. Cases in which equilibria have been shifted have been identified,[45,46] as well as cases exhibiting kinetic crossover, i.e. which of the barriers is rate-determining changes as increasing force is applied.[28,86] Such crossover is repeatedly attributed to the suppression of “outer” barriers (those further along the reaction coordinate) resulting in “inner” barriers becoming rate-limiting.[28,51,86] While this claim is true in some cases, it is not true in general because it incorrectly presupposes that the “inner” barrier must at some point be rate limiting if a change in the kinetic behavior is observed. The second example below illustrates a case where this is not so.

In the two-barrier system $R \rightleftharpoons I \rightarrow P$, there are four (GS,TS) pairs: (R,TS1), (R,TS2), (I,TS1) and (I,TS2); three of these define energy differences that dictate reaction kinetics in the forward direction. There are six permutations of these three pairs for the rate-limiting difference being first one and then another, defining the six possible types of kinetic crossover. Listed as the rate-limiting differences at low force and then at high force, they are: Type 1: $\Delta G_{\mathrm{R,TS2}}$ then $\Delta G_{\mathrm{R,TS1}}$; Type 2: $\Delta G_{\mathrm{R,TS2}}$ then $\Delta G_{\mathrm{I,TS2}}$; Type 3: $\Delta G_{\mathrm{I,TS2}}$ then $\Delta G_{\mathrm{R,TS1}}$; and Types 4, 5 and 6 are the reverse of Types 3, 2 and 1, respectively. At the crossover between the low- and high-force regimes, the energy differences that dominate each regime are equal to each other, thereby determining what energy differences can be extracted from the equality describing the crossover, using the force at which it occurs, $\langle F_{q\mathrm{R}} \rangle_{\mathrm{crossover}}$, and the characteristics of the plots of $\ln(k_{\mathrm{obsP}})$ vs. $\langle F_{q\mathrm{R}} \rangle$ before and after crossover, where k_{obsP} is the observed rate constant for the formation of the product P.

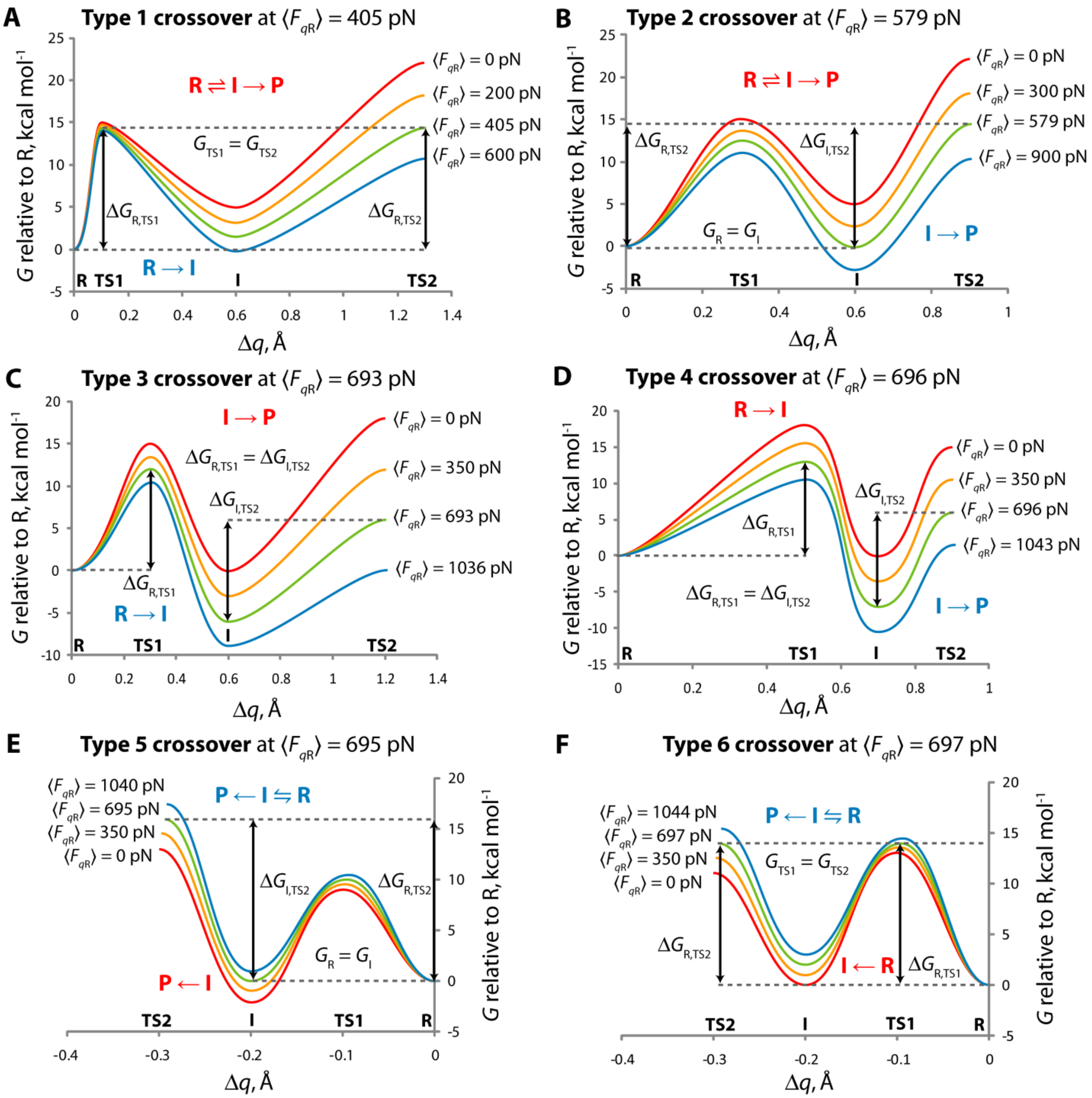

Fig. 7.3. Simplified reaction energy diagrams illustrating the six possible types of kinetic crossover in the two-barrier system R ⇌ I → P. In each example, the curves are shown as a progression of the strain-free PES ($\langle F_{q\mathrm{R}} \rangle = 0$, red), the PES at low $\langle F_{q\mathrm{R}} \rangle$ (orange), the PES at crossover (green), and the PES that high $\langle F_{q\mathrm{R}} \rangle$ (blue). The positions of R, TS1, I and TS2 are labeled along the Δq for convenience, and the energy differences that define each crossover type are indicated by the black arrows. The observed rate-limiting step before and after crossover is indicated for each type in red and blue, e.g. R ⇌ I → P before (red) and R → I after (blue) for Type 1 (**A**). Though the curves are stylized, the positions of the stationary points on the curves are quantitatively correct; see section 7.8.5 for detailed parameters and simulated kinetic data from each example. Note that because Δq is negative (contraction) in **E** and **F**, the reaction energy increases with increasing $\langle F_{q\mathrm{R}} \rangle$. In all cases shown here, second-order effects are minimal but still are evident from the slight shifts in stationary points along q ($\Delta\lambda$ are not all exactly 0).

In Type 1 crossover (Fig. 7.3A), the system initially exhibits pre-equilibrium kinetics. As $\langle F_{q\text{R}}\rangle$ increases, $\Delta G_{\text{R,TS2}}$ decreases until it is equal to $\Delta G_{\text{R,TS1}}$, after which point the kinetics are limited only by the first barrier ($\Delta G_{\text{R,TS1}}$). This is the type of crossover described in the literature.[51,86] By fitting the model parameters to plots of $\ln(k_{\text{obsP}})$ vs. $\langle F_{q\text{R}}\rangle$ in the regimes before and after crossover, the equality (7.14) may be solved to determine the *difference in strain-free transition state energies*, $G_{\text{TS2}}{}^{\text{o}} - G_{\text{TS1}}{}^{\text{o}}$. In the absence of second-order effects, the two regimes are linear, and eq. (7.14) simplifies to eq. (7.15).

$$\Delta G^{\text{o}}_{\text{R,TS2}} - \Delta\Delta G_{\text{R,TS2}}\big(\langle F_{q\text{R}}\rangle\big) = \Delta G^{\text{o}}_{\text{R,TS1}} - \Delta\Delta G_{\text{R,TS1}}\big(\langle F_{q\text{R}}\rangle\big) \tag{7.14}$$

$$\Delta G^{\text{o}}_{\text{R,TS2}} - \langle F_{q\text{R}}\rangle \Delta q^{\text{o}}_{\text{R,TS2}} = \Delta G^{\text{o}}_{\text{R,TS1}} - \langle F_{q\text{R}}\rangle \Delta q^{\text{o}}_{\text{R,TS1}} \tag{7.15}$$

The system again initially exhibits pre-equilibrium kinetics in Type 2 crossover (Fig. 7.3B), but upon increasing $\langle F_{q\text{R}}\rangle$ the rate-limiting barrier changes to the second barrier, $\Delta G_{\text{I,TS2}}$. In this case, the equality describing the crossover point instead yields information to determine the *difference in strain-free energy minima*, $G_{\text{R}}{}^{\text{o}} - G_{\text{I}}{}^{\text{o}}$. In a system exhibiting only Type 2 crossover, at no point are the kinetics determined by any difference including the inner transition state, TS1. In Type 3 crossover (Fig. 7.3C), the rate-limiting barrier changes from the second barrier, $\Delta G_{\text{I,TS2}}$, to the first barrier, $\Delta G_{\text{R,TS1}}$. In this case, because none of the components of these two differences are the same in both, the equality describing the crossover point only provides data about the *difference in strain-free barrier heights*, $\Delta G_{\text{I,TS2}}{}^{\text{o}} - \Delta G_{\text{R,TS1}}{}^{\text{o}}$. The ancillary inequalities describing the conditions for each type of crossover are listed in section 7.8.4.

Because Types 4, 5 and 6 involve the reverses of the changes in rate-limiting barriers involved in Types 3, 2 and 1, respectively, the equalities that describe their crossover points, and thus the information about differences on the strain-free energy surfaces, are identical to their respective counterparts just described. Types 5 and 6, however, are slightly more restrictive in that crossover from non-pre-equilibrium to pre-equilibrium kinetics necessitates that at least one of the changes in q be negative, i.e., contraction against the restoring force $\langle \text{F}_{\text{qR}}\rangle > 0$. For example, Type 5 crossover is the reverse of Type 2 crossover, so initially $G_{\text{I}} < G_{\text{R}} < G_{\text{TS1}}$ and $G_{\text{I}} < G_{\text{TS2}}$, but after crossover $G_{\text{R}} < G_{\text{I}} < G_{\text{TS1}} < G_{\text{TS2}}$. In the absence of second-order effects, the pair of inequalities $G_{\text{R}}(\langle F_{q\text{R}}\rangle) < G_{\text{I}}(\langle F_{q\text{R}}\rangle)$ and $G_{\text{I}}{}^{\text{o}} < G_{\text{R}}{}^{\text{o}}$ may only be simultaneously true if $\Delta q_{\text{R,I}}{}^{\text{o}} < 0$. Similarly, Type 6 crossover implies that $\Delta q_{\text{TS1,TS2}}{}^{\text{o}} < 0$. Though other differences in q may still be positive, the examples shown in Fig. 7.3E and F have monotonically decreasing values of

q to make the diagrams simpler to visualize. Note that when q is contracting against the restoring force, energies increase with increasing $\langle F_{q\mathrm{R}} \rangle$.

The difficulty inherent in extracting such information from semi-logarithmic plots of force-dependent kinetics is two-fold: First, even when second-order effects are entirely absent and Δx can be replaced with Δq, the meaning of the energy difference obtained from the crossover equality is still unknown. Without supplemental knowledge about which type of crossover is observed in any given set of data, the energy difference calculated could have any of the six possible meanings (three differences, two orders for each). Given that $\Delta q < 0$ can possibly occur in any of the six types and that the differences between the different types arise from only subtle distinctions between the underlying parameters, it is difficult to see how identification of the crossover type can be made from a plot of force-dependent kinetic data alone. Second, use of the EBE formalism assumes that the $\ln(k_{\mathrm{obsP}})$ vs. $\langle F_{\mathrm{R}} \rangle$ data is suitably described by the linear expression $\langle F_{\mathrm{R}} \rangle \Delta x$. Traditionally, shifts in the positions of the stationary points on the PES (Hammond effects[60]) are folded into the EBE parameter Δx because the model lacks any other mechanism for incorporating such changes. However, changes in the proportionality of the force-dependent barrier lowering (i.e., Δx or Δq) are conceptually different from second-order effects. Changes in the proportionality constant reflect crossover, as described above, *not* changes in the positions of stationary points as the PES is perturbed by force. Thus, using only Δx (or Δq or $\Delta \tau$) to describe second-order effects is inaccurate in more ways than simply approximating a quadratic function with a linear one; it is a misappropriation of changes due to one effect to another. Even when a linear fit may appear reasonable, the fitted value no longer correlates with any distance change in the strain-free reactant, as shown in the example below.

If the changes in the compliance of the reactive moiety along q are only a few times larger, the differences between the EBE formalism and our model become significant. Fig. 7.4 shows how the force-dependent reaction energy diagram for a system changes if the intermediate and second transition state are significantly (~10-fold) more compliant than the reactant and first transition state. Clearly, second-order effects are substantial, as the equilibrium positions of q_{I} and q_{TS2} shift by more than 1 Å as $\langle F_{q\mathrm{R}} \rangle$ increases to 600 pN.

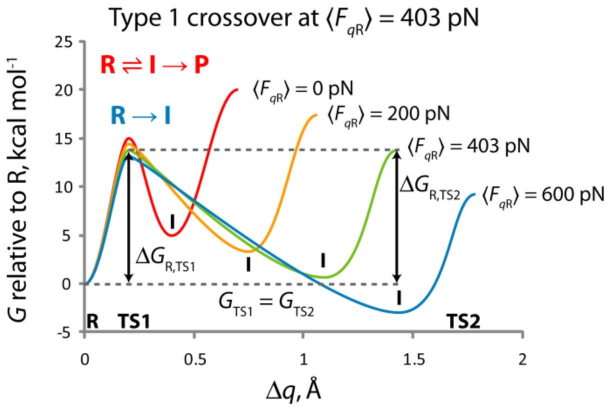

Fig. 7.4. An example of Type 1 crossover in a system that exhibits significant second-order effects because I and TS2 are significantly more compliant than R and TS1. The coloring and labeling are identical to that in Fig. 7.3.

The semi-logarithmic plot for the kinetics simulated for the force-dependent energy surface depicted in Fig. 7.4 is shown in Fig. 7.5. In the absence of second-order effects, the data points before and after the crossover point would be linear. Near the crossover point the differences between the barriers can be small, which means that neither barrier is strictly rate-limiting. If this difference remains small for a significantly large area near the crossover point, deviations from the force-dependence of the rest of the low- and high-force regimes can be seen near the crossover point. This is evident in the simulated data in Fig. 7.5; close inspection reveals that the data points between 350 and 550 pN deviate both from the quadratic function that would describe the low-force regime and the approximately linear function that would describe the high-force regime. Because of this and the fact that the low-force regime is fitted with a linear function, crossover (the intersection of the lines) appears to occur at 453 pN, a full 50 pN above the value of 403 pN calculated with eq. (7.14). Furthermore, though the linear fit to the low-force regime may at first seem somewhat reasonable, its slope indicates a value of $\Delta x = 1.00$ Å, which is a 43% overestimation of the value $\Delta q = 0.70$ Å used to generate the data. If a quadratic function is fitted to the data with $0 < \langle F_{q\mathrm{R}} \rangle < 350$ pN, a value of $\Delta q = 0.74$ Å (5% error) for this regime is obtained instead. Given the limited number of experimental data points in many such force-dependent kinetic studies, it is likely difficult to distinguish such small deviations from linearity from experimental scatter. However, though the deviations may be small, this example illustrates how the conclusions drawn from the data can be affected dramatically.

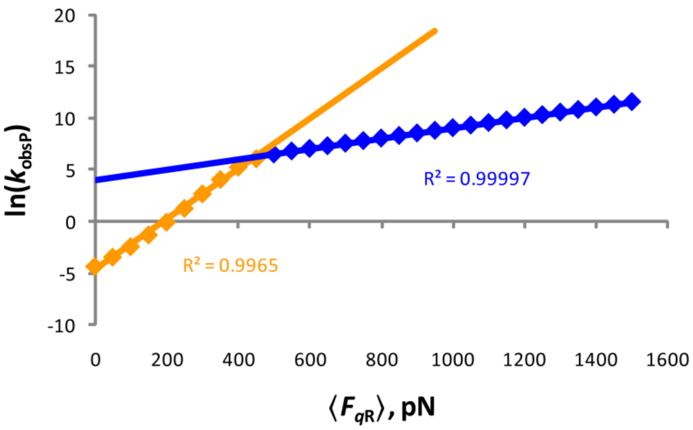

Fig. 7.5. The semi-logarithmic plot of ln(k_{obsP}) vs. $\langle F_{q\mathrm{R}} \rangle$ for the simulated kinetics on the force-dependent PES shown in Fig. 7.4. The lines are least squares linear fits to the simulated data points before (orange) and after (blue) crossover. See section 7.8.5 for simulation details. Note that though the linear fit in the low-force (orange) regime may appear at first glance to be reasonable (R^2 of 0.997), upon closer inspection the systematic deviations from the fit indicate that a quadratic function would yield a better fit to the data with $0 < \langle F_{q\mathrm{R}} \rangle < 350$ pN.

In addition to the arguably subtle, yet important, differences between our model and the EBE formalism outlined above, under some circumstances the two models offer qualitatively different predictions. For example, if the reactant and intermediate are isoenergetic but the two transition states are not, the EBE formalism predicts that there will never be any crossover for $\langle F_{q\mathrm{R}} \rangle > 0$ if $\Delta q_{\mathrm{R,TS1}} \geq \Delta q_{\mathrm{I,TS2}}$. However, if second-order effects exist, for which the EBE formalism cannot account, crossover will occur, following which the kinetics would be dictated by a different set of barriers.

Though the magnitude of second-order effects may in many cases be negligible, in many cases commonly examined with SMF techniques, such effects are likely present at significant levels, though they are sometimes ignored. For example, the unmasking of "hidden length" by cleaving a bond clasping closed a side loop of a (bio)polymer, allowing the loop to expand as part of the load-bearing main chain, is seen in many cases. Following cleavage of the bond that had masked the side loop, not only does q increase by an amount on the order of the contour length of the previously hidden loop, but the compliance of this internuclear distance increases significantly. As shown in Table 7.1, even for hidden loops similar in length to those used in SMF experiments (L_{o} = 25 nm), the increase in compliance from a typical covalent bond is at least as large as that causing the second-order effects exhibited in Fig. 7.4 and Fig. 7.5. Indeed, simulated data for the unmasking of "hidden length" by allowing a 5-nm side-chain loop to open in upon R → I indicates that kinetic crossover occurs at extremely low forces, as shown in Fig. 7.6. Once the side chain is included in the contour length of the (bio)polymer and stretched, the energetic cost for its reformation becomes quite high. The effects are even more substantial with the inclusion of longer side-chain loops.

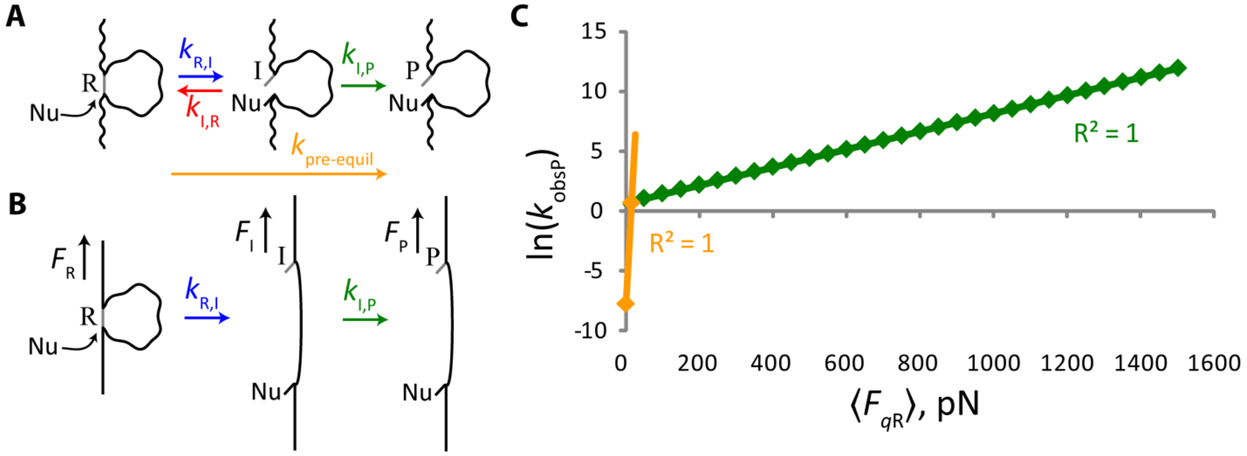

Fig. 7.6. Cartoon illustration of a polymer containing a side-chain loop that is unmasked and included in the polymer contour length in the step R → I in the overall nucleophile-assisted transformation R ⇌ I → P in the absence of a restoring force (**A**) or in the presence of a restoring force (**B**). The individual steps R → I, I → R and I → P are colored blue, red and green, respectively, and the apparent rate constant for R → P in the pre-equilibrium system is indicated in orange. **C**: Semi-logarithmic plot of the simulated "observed" force-dependent rate constant for conversion of R to P in which a 5-nm side-chain loop is unmasked and included in the polymer contour length when R → I. The color of the points corresponds to the rate-determining rate constant in parts **A** and **B**. Type 2 kinetic crossover occurs at ~15 pN. In this simulation, both second-order effects and the extremely low crossover force come *only* from the inclusion of the flexible side-chain loop in the contour length of the polymer; if not for the unmasking of the side-chain loop, this system would instead exhibit Type 1 kinetic crossover at 405 pN; see section 7.8.5 for simulation details.

The energetic consequences of such dramatic changes in distance and compliance, which are seen to an even greater degree when the substrate is cleaved entirely (see section 7.8.5 for an example), rapidly change the observed kinetics of the mechanochemical system by effectively suppressing chemical transformations in the reverse direction (i.e., those involving distance changes antiparallel to direction of molecular restoring force). Within the context described above, such changes effectively shift the kinetic crossover point to very small but nonzero values of $\langle F_{q\mathrm{R}} \rangle$. This can be advantageous if suppression of reverse reactions is desired to allow for selective probing of separate force-dependent barriers on the reaction PES, but it must be kept in mind when mapping trends and conclusions back to the strain-free system. Indeed, failing to account for this leads to inaccurate conclusions. For example, in the situation shown in Fig. 7.6 the post-crossover data provides consistent predictions within that force regime (i.e., above the crossover point), but a failure to recognize the existence of kinetic crossover at extremely low forces leads to inaccurate predictions if the post-crossover data is extrapolated to $\langle F_{q\mathrm{R}} \rangle = 0$.

In the next section, we experimentally examine the force-dependent kinetics of disulfide reduction by phosphines in a series of increasingly strained macrocycles, a pre-equilibrium system exhibiting kinetic crossover at extremely low force values.

7.5 Experimental Validation

The reduction of disulfides by phosphines in aqueous environments (Fig. 7.7A) is a system which may exhibit Type 1 crossover involving substrate scission. In the absence of strain, it is a pre-equilibrium system ($\mathrm{R} \rightleftharpoons \mathrm{I} \rightarrow \mathrm{P}$); in the presence of strain, the reformation of the disulfide bond is suppressed by the relief of the mechanochemical system's strain energy once the disulfide bond is cleaved. As discussed above, reformation of the bond necessitates the reformation of the (macro)molecular strain, which can be considerable even at low forces. The well-established mechanism for disulfide reduction by phosphines[87-90] indicates that with decreasing pH, the zwitterionic intermediate is increasingly protonated, thereby suppressing the reformation of the disulfide bond at low pH, similar to the acidic suppression of thiol/disulfide exchange.[91] This pH-dependence allows for "artificial" suppression (i.e., without using force) of the reverse of the first step, allowing for the experimental determination of rate constants, rather than their ratios to those of the reverse process (i.e., equilibrium constants). We used this ability to validate the interpretation of force-dependent acceleration of pre-equilibrium systems discussed above by measuring the kinetics of disulfide reduction by phosphines in both strained and unstrained isomers of a series of macrocycles at varying pH in order to determine the relative magnitudes of the simultaneous effects of forward barrier lowering and reverse reaction suppression to the overall observed acceleration by force.

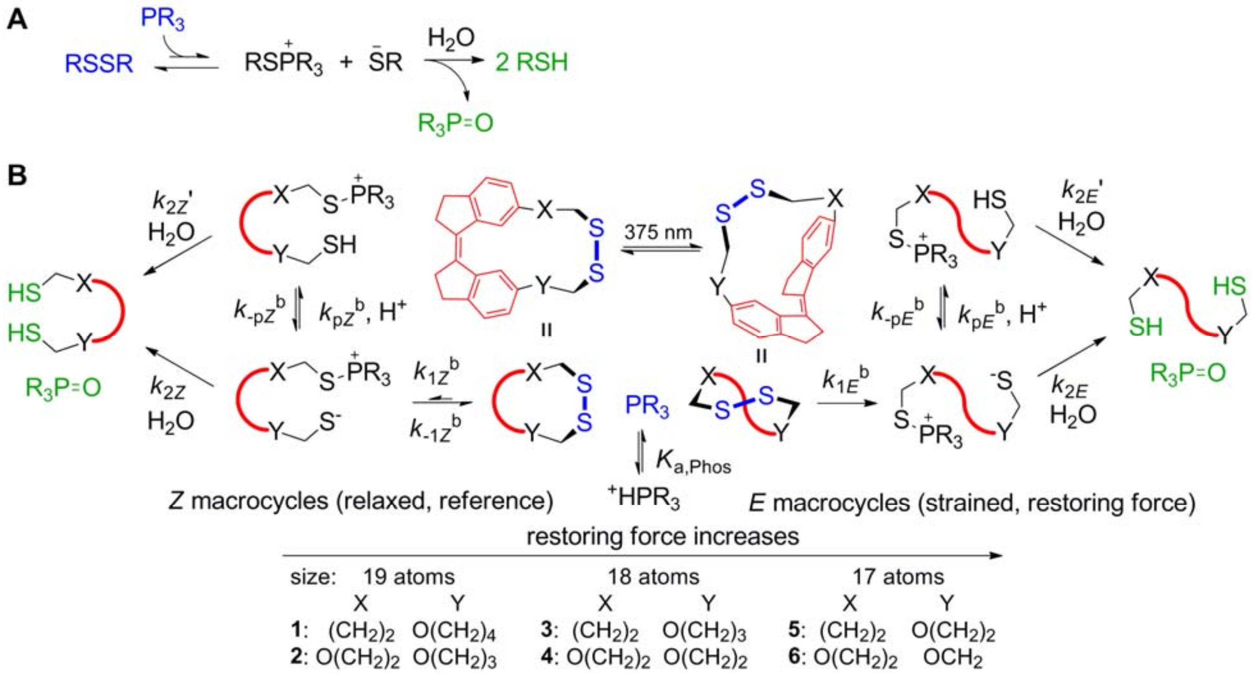

Fig. 7.7. **A:** The general chemical transformation for disulfide reduction by phosphines in aqueous environments. **B**: The kinetic scheme for the reduction of disulfides in a series of six macrocycles containing stiff stilbene (red). The inert linkers X and Y are short enough to prevent the photochemically generated *E* isomers from relaxing to their planar conformations. In the list of compositions of X and Y, the leftmost atoms are connected to the stiff stilbene.

We synthesized a series of strain-free macrocycles containing (*Z*)-stiff stilbene (red, Fig. 7.7B). The strained *E* isomers of **1**–**6** were obtained as components of photostationary mixtures with clean photochemistry by irradiating acetonitrile solutions of the *Z* isomers with 375 nm light in cuvettes sealed under N_2. Consistent with observations in the literature,[89] at neutral pH we did not observe any overall reduction of the strain-free disulfides by PPh_3 in solutions of water/acetonitrile (37:13 mol/mol) by HPLC. Even in the presence of the more strongly reducing phosphine PBu_3, the ^{1}H and ^{31}P NMR spectra of *Z***5** in anhydrous CD_3CN show no detectable conversion to intermediate over 3 days at RT, implying that the reaction is either incredibly slow or that the equilibrium is very unfavorable. However, in the photostationary mixture of **2**, the *E* isomer reacts rapidly with PBu_3 (full conversion in <20 min) under identical conditions while the *Z* isomer in the same sample does not. The $^{31}P\{^1H\}$ NMR spectrum following the addition of PBu_3 shows a new peak at 209.80 ppm, supporting the identification of the *E* isomer as the zwitterionic phosphonium thiolate intermediate. Because conversion to the intermediate is irreversible in the *E* isomers, this experiment further indicates that the apparent lack of reactivity in the *Z* isomers is due to a highly unfavorable equilibrium rather than an incredibly high kinetic barrier.

Kinetics experiments were carried out with excess phosphine (250-fold excess PPh_3 or 10–220-fold excess PPh_2Me) in water/acetonitrile (37:13 mol/mol). The chemical identities of the products in the kinetics samples were confirmed by comparison of the retention times and UV spectra with those of authentic samples under identical separation conditions. Only disulfides and fully reduced dithiols were observed by HPLC. In all cases, pseudo-first order kinetics were observed, as evidenced by good fits to semi-logarithmic plots of $\ln(R/R_0)$ vs. t and linear increases in observed rates with increases in phosphine concentration. For *Z* isomers, the application of the steady state approximation is justified by both the observation of overall pseudo-first order kinetics and the NMR studies discussed above which indicate that the intermediate is both highly reactive and is present in small quantities. See section 7.8.10 for a detailed derivation of the pH-dependent kinetic model.

Under neutral conditions, only the reduction of the *E* isomers by PPh_2Me proceeded quickly enough below 338 K to allow for kinetic measurements over a range of temperatures to obtain the activation parameters directly. In other cases, pH-dependent kinetics were measured at 338 K in with increasing amounts of TfOH to further suppress the reverse reaction of initial cleavage by protonation of the zwitterionic intermediate. We fitted our kinetic model to the entire set of pH-dependent kinetic data to determine the ratio of bimolecular rate constants (indicated by the superscript ^{b}) for cleavage in the *E* and *Z* isomers (i.e., k_{1E}^{b}/k_{1Z}^{b}, which is equivalent to the ratio of pseudo-first order rate constants in a competition experiment, k_{1E}/k_{1Z}) and other ratios of rate constants for the *Z* isomers as well as a single value for the pK_a in water/acetonitrile (37:13 mol/mol) for the phosphine used (see section 7.8.10 for details of the fitting).

The values obtained for k_{1E}^{b}/k_{1Z}^{b} are listed in Table 7.2. Under neutral conditions (in water–acetonitrile 37:13 mol/mol, ${}_{s}^{s}pH = 7.74$,[92] see section 3.8.2 for details about acidity in aqueous–organic solvent mixtures), the presence of any amount of restoring force immediately increases the observed rate of product formation by ~4 orders of magnitude, as evidenced by the ratios of rate constants for the observed consumption of disulfide, $k_{E\text{obs}}/k_{Z\text{obs}}$. However, this acceleration is clearly due to Type 1 crossover at a very low restoring force because the rates for the initial cleavage, which are indicative of the decrease of $\Delta G_{\text{R,TS1}}$ with increasing restoring force, increase by less than a factor of 5. This disparity illustrates the importance of being aware that stationary points on the strain-free PES, and thus their energy differences which determine kinetics, can be affected differently by force.

Table 7.2. The ratios of rate constants for initial disulfide cleavage and observed conversion to dithiol under neutral conditions at 338 K.

		PPh_3		PPh_2Me	
macrocycle	$\langle F_q \rangle$, pN[a]	k_{1E}^{b}/k_{1Z}^{b}	$k_{E\mathrm{obs}}/k_{Z\mathrm{obs}}$ neutral	k_{1E}^{b}/k_{1Z}^{b}	$k_{E\mathrm{obs}}/k_{Z\mathrm{obs}}$ neutral
1	100	1.5 ± 0.3	3.5×10^3	1.3 ± 0.6	4.5×10^3
2	150	1.6 ± 1.2	2.7×10^4	2.2 ± 0.3	1.7×10^4
3	180	2.3 ± 0.2	7.4×10^3	2.4 ± 0.1	6.1×10^3
4	225	2.4 ± 0.5	4.1×10^4	2.1 ± 0.4	1.7×10^4
5	280	3.4 ± 0.2	2.8×10^4	2.5 ± 0.2	1.3×10^4
6	270	2.9 ± 0.2	2.8×10^4	3.4 ± 0.2	3.4×10^4

[a] Force values from Chapter 4 are used here; see text for a discussion.

The values for $\langle F_q \rangle$ shown in Table 7.2 are the net restoring forces from Chapter 4; the DFT calculations (and thus the determination of the restoring force vectors and compliances) for this series of reactions is still pending. However, these values should be reasonably accurate; if using the methods in Chapter 2, Chapter 3 or Chapter 4 to determine the net restoring force vector, only the transition-state structure would be different from those in Chapter 4. Plotting the values of $\ln(k_E/k_Z)$ vs. $\langle F_q \rangle$ yields linear trends (minimal second-order effects), as shown in Fig. 7.8 and Fig. 7.9. Linear fits to $\ln(k_{1E}^{b}/k_{1Z}^{b})$ vs. $\langle F_q \rangle$ yield $\Delta q_{\mathrm{R,TS1}} = (0.21 \pm 0.03)$ Å for PPh_3 and $\Delta q_{\mathrm{R,TS1}} = (0.17 \pm 0.06)$ Å for PPh_2Me, which supports the conclusion of the Hammond–Leffler postulate[93-95] that disulfide reduction with a stronger nucleophile (PPh_2Me) will proceed through an earlier transition state.

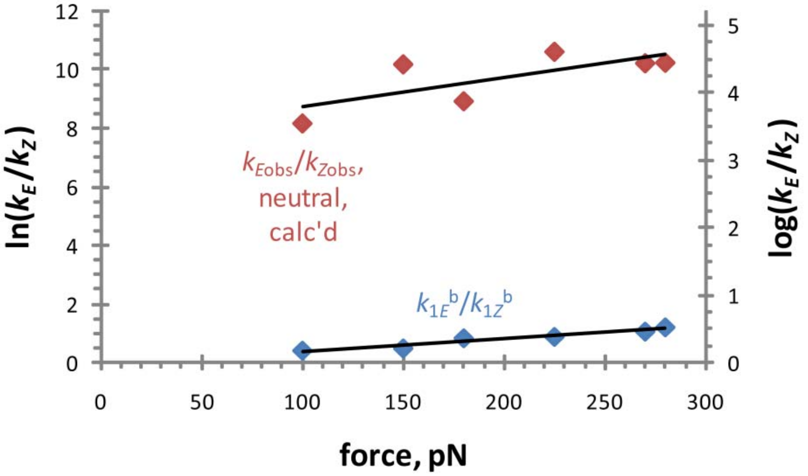

Fig. 7.8. Force-dependent acceleration of disulfide reduction by PPh_3 in water/acetonitrile (37:13 mol/mol) at 338 K; the error bars for $\ln(k_{1E}{}^{b}/k_{1Z}{}^{b})$ are smaller than the symbols; for errors on $\ln(k_{E\mathrm{obs}}/k_{Z\mathrm{obs}})$, see Table 7.16.

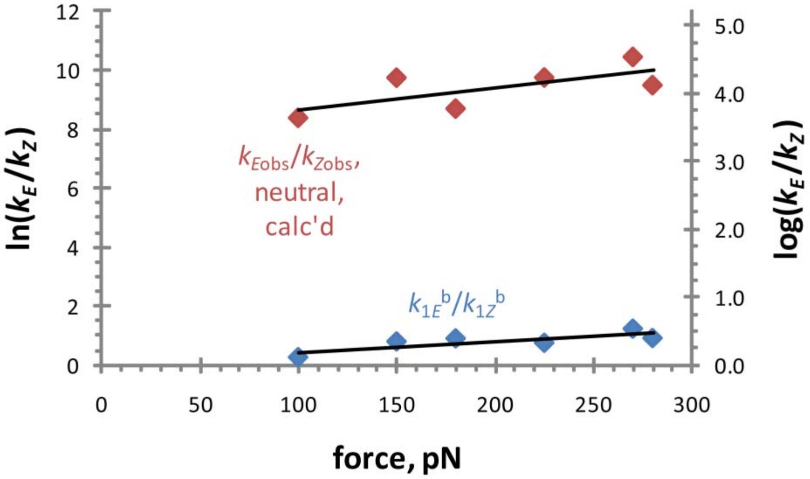

Fig. 7.9. Force-dependent acceleration of disulfide reduction by PPh_2Me in water/acetonitrile (37:13 mol/mol) at 338 K; the error bars for $\ln(k_{1E}{}^{b}/k_{1Z}{}^{b})$ are smaller than the symbols; for errors on $\ln(k_{E\mathrm{obs}}/k_{Z\mathrm{obs}})$, see Table 7.17.

The linear trends for the semi-logarithmic plots of the ratios of observed[c] force-dependent rate constants for the depletion of disulfide ($\ln(k_{E\mathrm{obs}}/k_{Z\mathrm{obs}})$ vs. $\langle F_q \rangle$) under neutral conditions yield different conclusions. The plots of $\ln(k_{E\mathrm{obs}}/k_{Z\mathrm{obs}})$ vs. $\langle F_q \rangle$ yield $\Delta\Delta G^{\ddagger}(\langle F_q \rangle = 0) \approx 5$ kcal/mol, whereas the plots of $\ln(k_{1E}{}^{b}/k_{1Z}{}^{b})$ vs. $\langle F_q \rangle$ yield $|\Delta\Delta G^{\ddagger}(\langle F_q \rangle = 0)| < 0.1$ kcal/mol. Because these are semi-logarithmic plots of "reduced" rate constants (i.e., they are a ratio of the

---

[c] I use "observed" here in that it is the rate constant derived from the depletion of disulfide when accounting for the overall process; however, these values were extrapolated based on the fitted parameters in Table 7.16 and Table 7.17.

strained to the strain-free case), the trends should pass through the origin (i.e., $k_{\text{strained}}/k_{\text{reference}}$ should be unity in the absence of force). The fact that the plots of $\ln(k_{E\text{obs}}/k_{Z\text{obs}})$ vs. $\langle F_q \rangle$ do not do so indicates that the mechanism for the strained case is not the same as that in the reference case. Here we already know this to be the case because we recognize that the *E* macrocycles relax fully following S–S bond cleavage, preventing the intermediate products from recombining by separating them in space, thereby suppressing the reverse reaction entirely. Thus, in this case $k_{E\text{obs}}/k_{Z\text{obs}}$ references $\mathrm{R} \rightarrow \mathrm{I}$ to $\mathrm{R} \rightleftharpoons \mathrm{I} \rightarrow \mathrm{P}$.

Such semi-logarithmic plots of "reduced" rate constants enable this kind of analysis of the suitability of the reference case. However, semi-logarithmic plots of only the force-dependent rate constants (e.g., $\ln(k_{\text{strained}})$ vs. $\langle F_q \rangle$) do not pass through the origin in general, and thus do not inherently indicate the suitability of the strain-free reference case. Given independent knowledge of the kinetics of the strain-free reference case, a comparison of $k_{\text{strained}}(F = 0)$ to $k_{\text{reference}}$ can be made; in the absence of such independent knowledge, however, conclusions about the kinetics of the strain-free reference case drawn from extrapolations to zero force (as is done in SMF experiments seeking to understand the strain-free dynamics of reactions in biomacromolecules) are speculative at best and may fail to identify a mechanistic mismatch similar to the one discussed above.

Not only can such a mechanistic mismatch be impossible to detect without independent knowledge of the strain-free reference case, but the conclusions drawn from the force regime where the force-dependent kinetics were measured may also be incorrect. The plots of $\ln(k_{E\text{obs}}/k_{Z\text{obs}})$ vs. $\langle F_q \rangle$ in Fig. 7.8 and Fig. 7.9 yield $\Delta q = 0.47$ Å and 0.35 Å for the reactions with PPh_3 and PPh_2Me, respectively. These values are more than twice those derived from the semi-logarithmic plots of the bimolecular rate constants for initial disulfide cleavage. Because of the mechanistic mismatch (referencing $\mathrm{R} \rightarrow \mathrm{I}$ to $\mathrm{R} \rightleftharpoons \mathrm{I} \rightarrow \mathrm{P}$), their physical meaning is not immediately clear, and when making such a comparison, the results appear to be susceptible to error. However, calculations for our work remain to be completed and compared to experiment to validate these claims.

7.6 Conclusions

The EBE formalism can be immensely successful when applied correctly to the many cases in which second-order effects are minimal, but it fails to yield accurate predictions in certain cases. Above, I demonstrated an example in which a reasonably good-looking linear fit (as the EBE formalism requires) to a semi-logarithmic plot of force-dependent rate constants exhibiting second-order effects that would be difficult to distinguish from experimental noise results in conclusions devoid of any physical meaning. Such second-order effects can be accurately accounted for within our model, which includes the contributions of molecular compliances' variation between the different critical points on the PES. Such compliance variations are most extreme in cases in which an initially hidden side-chain loop is incorporated into the substrate's contour length or when the substrate is cleaved entirely. In these cases, kinetic crossover not only occurs, but does so at extremely low restoring forces.

Though recognized to exist in general, the descriptions of force-dependent kinetic crossover in the literature suggest a general lack of understanding as to the different forms in which it may appear. Here, I have presented a detailed description of the six possible types of kinetic crossover for the simplest corrugated energy surface, that of $R \rightleftharpoons I \rightarrow P$. Based on the type of kinetic crossover, certain logical conclusions can be made regarding the relative ordering of the energies of minima and saddle points on the strain-free PES. Importantly, I noted that the application of tensile force does not in general lower outer barriers to reveal inner barriers and that the final two types of crossover necessitate contraction of the relevant molecular degree(s) of freedom. The existence of six types of kinetic crossover is based only on first-order effects and thus is predicted (though previously unrecognized) by the EBE formalism. The presence of significant second-order terms does not create new forms of kinetic crossover (or rule any out); instead, it enables kinetic crossover to occur in situations in which the EBE formalism predicts that it will not (e.g., when changes in compliances are significant but those in q are not, even in the absence of substrate rupture).

Here, we experimentally examined a system characterized by the transformation $R \rightleftharpoons I \rightarrow P$: the reduction of alkyl disulfides by phosphines in the presence of water. By measuring the pH-dependent kinetics, we were able to determine the ratios of bimolecular rate constants for the initial disulfide cleavage step, demonstrating that though the overall process is accelerated by ~4 orders of magnitude by small restoring forces (<100 pN), the initial cleavage step is only accelerated by less than a factor of 5. I explained this disparity by isothermal selective pathway suppression analogous to the effect of lowering the pH of the reaction medium. In this case, both increasing molecular restoring force and increasing the concentration of protons in solution both lower the potential energy of the intermediate and later states. Consequently, this relative stabilization changes the PES such that its kinetic profile changes such that the rate determining steps change from R ⇌ I → P to R → I, leading to Type 1 kinetic crossover. Because the alkyl disulfide substrate is cleaved in the R → I step, kinetic crossover occurs at extremely low restoring forces.

Though further validation of the conceptual framework presented here will come with the completion of the corresponding DFT calculations for these reactions, the above interpretation of the experimental results and the conclusions reached above together suggest that similar situations with a mismatch between the strained and strain-free reference kinetic profiles exist elsewhere when the kinetics of observed processes are considered. In such cases, the failure to recognize and account for the existence of kinetic crossover can lead to inaccurate conclusions and physically ambiguous comparisons. However, given the conceptual framework presented here, a better understanding of the richly complex possibilities for diverse mechanochemical phenomena involving muti-step reaction sequences is within reach, and thus so are the possibilities for chemists and materials scientists to exploit such effects in the conception of new mechanochemical systems.

7.7 Acknowledgments

The work was supported by the National Science Foundation (NSF) CAREER Award (CHE-0748281), the US Air Force Office of the Scientific Research Young Investigator Award (FA9550-08-1-0072), the American Chemical Society Petroleum Research Fund (48454-AC3 and 43354-G3), and the University of Illinois. T.K. thanks the Office of Naval Research and the NSF for predoctoral fellowships. The HPCMP of the DoD and NSF NCSA provided grants of computational time.

7.8 Supporting Information

Table 7.3. Table of mathematical symbols used.

symbol	**meaning**
sub- and superscripts and general notations	
n, m	variables indicating the state of the system being referred to; $n = \{i, j, k\}$ and $m = \{i, j, k\}$
i, j, k	subscripts corresponding to specific states of the system in question; they need not be different, e.g., for R → $[\mathrm{TS1}]^{\ddagger}$ → I, $i = j =$ R, $k =$ TS1 for $\Delta\Delta G^{\ddagger}_{\mathrm{R,I}}(\langle F_{\tau\mathrm{R}}\rangle)$ or $i = j =$ R, $k =$ I for $\Delta\Delta G_{\mathrm{R,I}}(\langle F_{\tau\mathrm{R}}\rangle)$
R, I, P, TS1 and TS2	indicate the reactant, intermediate, product, transition state between the reactant and intermediate and the transition state between the intermediate and the product, respectively: $\mathrm{R} \rightleftharpoons \mathrm{I} \rightarrow \mathrm{P}$
$^{\mathrm{o}}$	sub- or superscript indicating to the strain-free state
$_{\mathrm{c}}$	subscript indicating that the preceding variable is that of the constraining potential/object
‡	superscript indicating a structure or an energy difference between a transition state and a ground state, e.g., $\Delta\Delta G^{\ddagger}_{\mathrm{R,I}}(\langle F_{\tau\mathrm{R}}\rangle) = \Delta\Delta G_{\mathrm{R,TS1}}(\langle F_{\tau\mathrm{R}}\rangle)$
$^{\mathrm{b}}$	superscript indicating a bimolecular rate constant, rather than a pseudo-first order one
$\langle\ \rangle$	indicates the ensemble-average of the quantity inside the angled braces
$\lvert\ \rvert$	absolute value of the quantity inside the vertical lines
variables for the model for force-dependent kinetics	
β	inverse thermal energy per mole or per molecule, depending on context
χ	molar fraction of the state indicated in the subscript
Δ	difference of the quantity to the right between the two states indicated in the quantity's subscripts or between the strained and strain-free reference
L	the contour length of a polymer chain
λ	stretching compliance of the degree of freedom indicated in the subscript
F	restoring force of the degree of freedom indicated in the subscript
G	Gibbs free energy
$\Delta H^{\ddagger}$	enthalpy of activation for the process specified in the subscript
k	rate constant for a process
q	molecular degree of freedom (e.g., an internuclear distance, bond angle or dihedral angle) that satisfies the requirements of the local approximation
R_z	the end-to-end distance for a polymer chain

Table 7.3 (cont.)

ρ	probability density as a function of F and/or τ
$\Delta S^{\ddagger}$	entropy of activation for the process specified in the subscript
T	absolute temperature
τ	the mechanical coordinate, e.g. the end-to-end distance of a polymer chain
ζ	the chemical coordinate; a numerical representation of the pattern of bonding in the reactive moiety that indicates the extent of a reaction
E_{strain}	strain energy of the system of the type specified in the subscript (e.g., inherent strain, additional strain, etc.)
variables for the pH-dependent kinetic model	
H	molar concentration of H^+ in the reaction mixture
$K_{\text{a,phos}}$	acid dissociation constant of the protonated phosphine
$Phos$	molar concentration of free phosphine in the reaction mixture
$PhosH$	molar concentration of protonated phosphine in the reaction mixture
T_{phos}	total concentration of phosphine in the reaction mixture, assuming that the amount of reactant, intermediate, and product are negligibly small in comparison: $T_{\text{phos}} = Phos + PhosH$
T_{H}	total concentration of acid added to the reaction mixture: $T_{\text{H}} = H + PhosH + IntH$

7.8.1 Detailed Derivation and Extension of the Mechanochemical Model to Multiple Barriers

Note that the subscripts used in this derivation are the more generalized ones; see Table 7.3 above for definitions of i, j and l. The substrate and the constraining potential (Fig. 7.10) are in mechanical equilibrium,[74] which means that the forces along the mechanical coordinate τ, F_{τ}, that they exert on each other are equal in magnitude and opposite in sign as indicated by eq. (7.16), where subscripts i and c refer to the substrate in chemical state i and the constraining potential, respectively, $\lambda_{\tau i}$ and λ_{c} are their stretching compliances and τ_i^{o} and $\tau_{\text{c}}^{\text{o}}$ are their strain-free values of the mechanical coordinate. Rearranging yields eqs. (7.17) and (7.18), where $\lambda_i = \lambda_{\tau i} + \lambda_{\text{c}}$. Knowledge of τ_i^{o}, $\lambda_{\tau i}$, λ_{c} and $\tau_{\text{c}}^{\text{o}}$ is sufficient information to determine $F_{\tau i}$ and τ_i; alternatively, $\tau_{\text{c}}^{\text{o}}$ can be determined if $F_{\tau i}$ and the other characteristics are known. Because it is more easily determined experimentally, we will use F_{ti} as the control parameter.

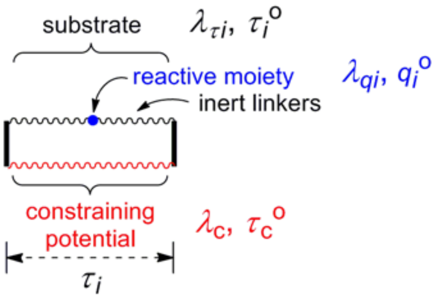

Fig. 7.10. The general model for a substrate coupled to a constraining potential.

$$F_{\tau i} = \frac{\tau - \tau_i^{\mathrm{o}}}{\lambda_{\tau i}} = \frac{\tau_{\mathrm{c}}^{\mathrm{o}} - \tau}{\lambda_{\mathrm{c}}} \tag{7.16}$$

$$\tau = F_{\tau i}\lambda_{\tau i} + \tau_i^{\mathrm{o}} = \tau_{\mathrm{c}}^{\mathrm{o}} - F_{\tau i}\lambda_{\mathrm{c}} \tag{7.17}$$

$$\tau_{\mathrm{c}}^{\mathrm{o}} = F_{\tau i}\lambda_i + \tau_i^{\mathrm{o}} \tag{7.18}$$

$F_{\tau i}$ is minimized at the equilibrium value $\tau = \tau_i$, and because $F_{\tau i}(\tau)$ is symmetric about $\tau = \tau_i$, $F_{\tau i} = \langle F_{\tau i}\rangle$ (eq. (7.19)), where $\langle F_{\tau i}\rangle$ is the ensemble-average restoring force if there are thermal fluctuations in τ. $\langle F_{\tau i}\rangle = 0$ if and only if $\tau_i^{\mathrm{o}} = \tau_{\mathrm{c}}^{\mathrm{o}}$, which implies and is implied by $\tau_i = \tau_i^{\mathrm{o}}$. If $\tau_i^{\mathrm{o}} \neq \tau_{\mathrm{c}}^{\mathrm{o}}$, then $\tau_i \neq \tau_i^{\mathrm{o}}$ and $\langle F_{\tau i}\rangle \neq 0$.

$$F_{\tau i} = \frac{\tau_i - \tau_i^{\mathrm{o}}}{\lambda_{\tau i}} = \frac{\tau_{\mathrm{c}}^{\mathrm{o}} - \tau_i}{\lambda_{\mathrm{c}}} = \langle F_{\tau i}\rangle \tag{7.19}$$

When $\langle F_{\tau i}\rangle \neq 0$, the system of two springs has an inherent amount of strain energy, which is given by eq. (7.20) and is based on the individual springs' compliances and strain-free values of the mechanical coordinate. If the system is extended to any other value of τ, its total strain energy is given by eq. (7.21), with the additional strain energy given by the difference, eq. (7.22). At $\tau = \tau_i$, $E_{\text{total strain},i} = E_{\text{inherent strain},i}$ and $E_{\text{additional strain},i} = 0$.

$$E_{\text{inhernent strain},i} = \frac{(\tau_{\mathrm{c}}^{\mathrm{o}} - \tau_i)^2}{2\lambda_{\mathrm{c}}} + \frac{(\tau_i - \tau_i^{\mathrm{o}})^2}{2\lambda_{\tau i}} = \frac{\lambda_i(\tau_i - \tau_i^{\mathrm{o}})^2}{2{\lambda_{\tau i}}^2} = \frac{\lambda_i\langle F_{\tau i}\rangle^2}{2} \tag{7.20}$$

$$\begin{aligned} E_{\text{total strain, }i}(\tau) &= \frac{(\tau - \tau_{\mathrm{c}}^{\mathrm{o}})^2}{2\lambda_{\mathrm{c}}} + \frac{(\tau - \tau_i^{\mathrm{o}})^2}{2\lambda_{\tau i}} = \frac{\lambda_i(\lambda_{\tau i}(\tau - \tau_i)^2 + \lambda_{\mathrm{c}}(\tau_i - \tau_i^{\mathrm{o}})^2)}{2\lambda_{\mathrm{c}}{\lambda_{\tau i}}^2} \\ &= \frac{\lambda_i(\langle F_{\tau i}\rangle^2\lambda_{\mathrm{c}}\lambda_{\tau i} + (\langle F_{\tau i}\rangle\lambda_{\tau i} - \tau + \tau_i^{\mathrm{o}})^2)}{2\lambda_{\mathrm{c}}\lambda_{\tau i}} \end{aligned} \tag{7.21}$$

$$\begin{aligned} E_{\text{additional strain},i}(\tau) &= \frac{(\tau - \tau_i)^2}{2\lambda_{\mathrm{c}}} + \frac{(\tau - \tau_i)^2}{2\lambda_{\tau i}} = \frac{\lambda_i(\tau - \tau_i)^2}{2\lambda_{\mathrm{c}}\lambda_{\tau i}} = E_{\text{total strain, }i}(\tau) - E_{\text{inherent strain},i} \\ &= \frac{\lambda_i(\langle F_{\tau i}\rangle\lambda_{\tau i} - \tau + \tau_i^{\mathrm{o}})^2}{2\lambda_{\mathrm{c}}\lambda_{\tau i}} \end{aligned} \tag{7.22}$$

If the reference state is defined as the *unconstrained* macromolecule, there is no inherent strain energy in τ, and the total strain energy for a given value of τ in the unconstrained macromolecule in chemical states i and tsij, $E_{\text{total strain},i}{}^{\text{o}}(\tau)$ and $E_{\text{total strain,ts}ij}{}^{\text{o}}(\tau)$, are given by eqs. (7.23) and (7.24).

$$E^{\text{o}}_{\text{total strain},i}(\tau) = \frac{(\tau - \tau_i^{\text{o}})^2}{2\lambda_{\tau i}} \tag{7.23}$$

$$E^{\text{o}}_{\text{total strain,ts}ij}(\tau) = \frac{\left(\tau - \tau_{\text{ts}ij}^{\text{o}}\right)^2}{2\lambda_{\tau\text{ts}ij}} \tag{7.24}$$

Based on the reasonable assumption that the system obeys a Boltzmann distribution over the mechanical coordinate τ (vertical axis, Fig. 7.2), the probability density function for thermal fluctuations in τ for the constrained macromolecule in chemical state i (ζ_i, Fig. 7.2), $\rho_i(\tau,\langle F_{\tau i}\rangle)$, is given by eq. (7.25). (This distribution function uses the additional strain energy of the constrained system given by eq. (7.22). Properly normalized, this distribution is identical to that given by the more complicated formula obtained using the total strain energy given by eq. (7.21), as these equations differ only by a constant term, the inherent strain energy, eq. (7.20).) The distribution function for thermal fluctuations in τ in the unconstrained macromolecule, $\rho_i{}^{\text{o}}(\tau)$, is given by eq. (7.26). The ensemble-average rate constant of an elementary reaction $i \rightarrow j$ in the macromolecule stretched to the average restoring force $\langle F_{\tau i}\rangle$ in chemical state i, $k_{i,j}(\langle F_{\tau i}\rangle)$, and that in the unconstrained macromolecule, $k_{i,j}{}^{\text{o}}$, are given by eqs. (7.27) and (7.28), respectively, where $k_{i,j}(\tau)$ is the rate constant of the chemical transformation $i \rightarrow [\text{ts}ij]^{\ddagger} \rightarrow j$ for the macromolecule with mechanical coordinate τ. The canonical transition-state theory expression[75] for $k_{i,j}(\tau)$ is given by eq. (7.29), where ζ_i and $\zeta_{\text{ts}ij}$ are the values of the chemical coordinate for the ground state (chemical state i) and the transition state between the chemical states i and j (tsij), respectively.

$$\rho_i(\tau,\langle F_{\tau i}\rangle) = \sqrt{\frac{\beta\lambda_i}{2\pi\lambda_{\text{c}}\lambda_{\tau i}}}\, e^{-\beta\frac{\lambda_i\left(\langle F_{\tau i}\rangle\lambda_{\tau i} - \tau + \tau_i^{\text{o}}\right)^2}{2\lambda_{\text{c}}\lambda_{\tau i}}} \tag{7.25}$$

$$\rho_i^{\text{o}}(\tau) = \sqrt{\frac{\beta}{2\pi\lambda_{\tau i}}}\, e^{-\beta\frac{\left(\tau - \tau_i^{\text{o}}\right)^2}{2\lambda_{\tau i}}} \tag{7.26}$$

$$k_{i,j}(\langle F_{\tau i}\rangle) \propto \int_{-\infty}^{\infty} \rho_i(\tau,\langle F_{\tau i}\rangle) k_{i,j}(\tau) d\tau \tag{7.27}$$

$$k_{i,j}^{\mathrm{o}} \propto \int_{-\infty}^{\infty} \rho_i^{\mathrm{o}}(\tau) k_{i,j}(\tau) d\tau \tag{7.28}$$

$$k_{i,j}(\tau) \propto e^{-\left(G(\tau,\zeta_{\mathrm{ts}ij}) - G(\tau,\zeta_i)\right)\beta} \tag{7.29}$$

Determination of the value of $k_{i,j}(\langle F_{\tau i}\rangle)$ and $k_{i,j}{}^{\mathrm{o}}$ requires the knowledge of $k_{i,j}(\tau)$, and hence of $G(\tau,\zeta)$, at least at the chemical states ζ_i and $\zeta_{\mathrm{ts}ij}$. One approach to determining the values of $G(\tau,\zeta)$ is to make the reasonable assumption that ζ is much stiffer than τ and that $G(\tau,\zeta)$ can be expanded as a Taylor series around the strain-free ground and transition states that; the constraining potential does not inherently change the potential energy surface along τ but instead merely shifts the position and width of the distribution of accessible values of τ. Thus, the effect of the constraining potential is captured in the probability density function $\rho_i(\tau,\langle F_{\tau i}\rangle)$. Using the expression for the strain energy from variation in τ, eq. (7.22), to determine the partial derivatives $\partial^n G/\partial\tau^n$ yields eqs. (7.30) and (7.31).

$$\begin{aligned} G(\tau,\zeta_i) &= G(\tau_i^{\mathrm{o}},\zeta_i) + \left.\frac{\partial G(\tau,\zeta_i)}{\partial\tau}\right|_{\tau=\tau_i^{\mathrm{o}}} (\tau-\tau_i^{\mathrm{o}}) + \left.\frac{\partial^2 G(\tau,\zeta_i)}{\partial\tau^2}\right|_{\tau=\tau_i^{\mathrm{o}}} \frac{(\tau-\tau_i^{\mathrm{o}})^2}{2} + \cdots \\ &= G(\tau_i^{\mathrm{o}},\zeta_i) + \left.\frac{\partial E_{\text{total strain},i}^{\mathrm{o}}(\tau)}{\partial\tau}\right|_{\tau=\tau_i^{\mathrm{o}}} (\tau-\tau_i^{\mathrm{o}}) + \left.\frac{\partial^2 E_{\text{total strain},i}^{\mathrm{o}}(\tau)}{\partial\tau^2}\right|_{\tau=\tau_i^{\mathrm{o}}} \frac{(\tau-\tau_i^{\mathrm{o}})^2}{2} + \cdots \\ &\approx G(\tau_i^{\mathrm{o}},\zeta_i) + \frac{(\tau-\tau_i^{\mathrm{o}})^2}{2\lambda_{\tau i}} \end{aligned} \tag{7.30}$$

$$\begin{aligned} G(\tau,\zeta_{\mathrm{ts}ij}) &= G(\tau_{\mathrm{ts}ij}^{\mathrm{o}},\zeta_{\mathrm{ts}ij}) + \left.\frac{\partial G(\tau,\zeta_{\mathrm{ts}ij})}{\partial\tau}\right|_{\tau=\tau_{\mathrm{ts}ij}^{\mathrm{o}}} (\tau-\tau_{\mathrm{ts}ij}^{\mathrm{o}}) + \left.\frac{\partial^2 G(\tau,\zeta_{\mathrm{ts}ij})}{\partial\tau^2}\right|_{\tau=\tau_{\mathrm{ts}ij}^{\mathrm{o}}} \frac{(\tau-\tau_{\mathrm{ts}ij}^{\mathrm{o}})^2}{2} + \cdots \\ &= G(\tau_{\mathrm{ts}ij}^{\mathrm{o}},\zeta_i) + \left.\frac{\partial E_{\text{total strain,ts}ij}^{\mathrm{o}}(\tau)}{\partial\tau}\right|_{\tau=\tau_{\mathrm{ts}ij}^{\mathrm{o}}} (\tau-\tau_{\mathrm{ts}ij}^{\mathrm{o}}) \\ &\quad + \left.\frac{\partial^2 E_{\text{total strain,ts}ij}^{\mathrm{o}}(\tau)}{\partial\tau^2}\right|_{\tau=\tau_{\mathrm{ts}ij}^{\mathrm{o}}} \frac{(\tau-\tau_{\mathrm{ts}ij}^{\mathrm{o}})^2}{2} + \cdots \approx G(\tau_{\mathrm{ts}ij}^{\mathrm{o}},\zeta_{\mathrm{ts}ij}) + \frac{(\tau-\tau_{\mathrm{ts}ij}^{\mathrm{o}})^2}{2\lambda_{\tau\mathrm{ts}ij}} \end{aligned} \tag{7.31}$$

Substituting the expanded expressions for $G(\tau,\zeta)$ into eq. (7.29) and integrating the right side of eq. (7.28) yields eq. (7.32), confirming that considering fluctuations in τ in the macromolecule in the absence of a constraining potential does not inherently change the reaction's activation free energy.

$$k_{i,j}^{\mathrm{o}} \propto \sqrt{\frac{\lambda_{\tau\mathrm{ts}ij}}{\lambda_{\tau i}}}\, e^{-\beta\left(G(\tau_{\mathrm{ts}ij}^{\mathrm{o}},\zeta_{\mathrm{ts}ij}) - G(\tau_i^{\mathrm{o}},\zeta_i)\right)} = \sqrt{\frac{\lambda_{\tau\mathrm{ts}ij}}{\lambda_{\tau i}}}\, e^{-\beta\Delta G_{i,j}^{\ddagger\mathrm{o}}} \tag{7.32}$$

Combining eqs. (7.25)–(7.31) yields eq. (7.33) for the ratio of the ensemble-average rate constant for the chemical transformation $i \rightarrow [\mathrm{ts}ij]^{\ddagger} \rightarrow j$ in a macromolecule stretched to an average restoring force $\langle F_{\tau i}\rangle$, $k_{i,j}(\langle F_{\tau i}\rangle)$, to that in the unconstrained macromolecule, $k_{i,j}^{\mathrm{o}}$, where $\Delta G_{i,j}^{\ddagger\mathrm{o}} = G(\tau_{\mathrm{ts}ij}^{\mathrm{o}},\zeta_{\mathrm{ts}ij}) - G(\tau_i^{\mathrm{o}},\zeta_i)$. If $\lambda_{\tau\mathrm{ts}ij} > 0$, then eq. (7.33) reduces to eq. (7.34), which is the general formulation of chemomechanical kinetics we have discussed elsewhere (Chapter 1, refs. 43 and 44), where $\Delta\tau_{i,\mathrm{ts}ij}^{\mathrm{o}} = \tau_{\mathrm{ts}ij}^{\mathrm{o}} - \tau_i^{\mathrm{o}}$ and $\Delta\lambda_{i,\mathrm{ts}ij} = \lambda_{\tau\mathrm{ts}ij} - \lambda_{\tau i}$. (For an explanation of the differences between these equations and those we have presented elsewhere, see below.) Note that the quantity $\Delta\Delta G_{i,j}^{\ddagger}(\langle F_{\tau i}\rangle)$ is the force-dependent *barrier lowering*, i.e., $\Delta G_{i,j}^{\ddagger}(\langle F_{\tau i}\rangle) = \Delta G_{i,j}^{\ddagger\mathrm{o}} - \Delta\Delta G_{i,j}^{\ddagger}(\langle F_{\tau i}\rangle)$.

$$\frac{k_{i,j}(\langle F_{\tau i}\rangle)}{k_{i,j}^{\mathrm{o}}} = \frac{\sqrt{\frac{\beta\lambda_i}{2\pi\lambda_{\mathrm{c}}\lambda_{\tau i}}}\, e^{-\beta\left(\Delta G_{i,j}^{\ddagger\mathrm{o}}\right)} \int_{-\infty}^{\infty} e^{-\frac{\beta}{2}\left(\frac{\lambda_i\left(\langle F_{\tau i}\rangle\lambda_{\tau i}+\tau_i^{\mathrm{o}}-\tau\right)^2}{\lambda_{\mathrm{c}}\lambda_{\tau i}}+\frac{\left(\tau-\tau_{\mathrm{ts}ij}^{\mathrm{o}}\right)^2}{\lambda_{\tau\mathrm{ts}ij}}-\frac{\left(\tau-\tau_i^{\mathrm{o}}\right)^2}{\lambda_{\tau i}}\right)} d\tau}{\sqrt{\frac{\beta}{2\pi\lambda_{\tau i}}}\, e^{-\beta\left(\Delta G_{i,j}^{\ddagger\mathrm{o}}\right)} \int_{-\infty}^{\infty} e^{-\frac{\beta}{2}\left(\frac{\left(\tau-\tau_i^{\mathrm{o}}\right)^2}{\lambda_{\tau i}}+\frac{\left(\tau-\tau_{\mathrm{ts}ij}^{\mathrm{o}}\right)^2}{\lambda_{\tau\mathrm{ts}ij}}-\frac{\left(\tau-\tau_i^{\mathrm{o}}\right)^2}{\lambda_{\tau i}}\right)} d\tau} \tag{7.33}$$

$$\beta^{-1}\ln\frac{k_{i,j}(\langle F_{\tau i}\rangle)}{k_{i,j}^{\mathrm{o}}} = \frac{\lambda_i}{\lambda_{\mathrm{ts}ij}}\left(\frac{\langle F_{\tau i}\rangle^2}{2}\Delta\lambda_{i,\mathrm{ts}ij} + \langle F_{\tau i}\rangle\Delta\tau_{i,\mathrm{ts}ij}^{\mathrm{o}} + \frac{{\Delta\tau_{i,\mathrm{ts}ij}^{\mathrm{o}}}^2}{2\lambda_i}\right) + \frac{1}{2\beta}\ln\frac{\lambda_i}{\lambda_{\mathrm{ts}ij}} \equiv \Delta\Delta G_{i,j}^{\ddagger}(\langle F_{\tau i}\rangle) \tag{7.34}$$

For the reverse chemical transformation, $j \rightarrow [\mathrm{ts}ij]^{\ddagger} \rightarrow i$, the same methods apply. If the characteristics of the constraining potential are constant, then eq. (7.18) can be used to relate the ensemble-average restoring force in the two states, as shown in eq. (7.35). Then the strain energy of the constrained system in chemical state j can be expressed in terms of the control parameter $\langle F_{\tau i}\rangle$, as shown in eq. (7.36)–(7.38).

$$\langle F_{\tau j}\rangle = \frac{\langle F_{\tau i}\rangle\lambda_i + \tau_i^{\mathrm{o}} - \tau_j^{\mathrm{o}}}{\lambda_j} \tag{7.35}$$

$$E_{\text{inherent strain},j} = \frac{\lambda_j\left(\tau_j - \tau_j^{\mathrm{o}}\right)^2}{2{\lambda_{\tau j}}^2} = \frac{\left(\langle F_{\tau i}\rangle\lambda_i + \tau_i^{\mathrm{o}} - \tau_j^{\mathrm{o}}\right)^2}{2\lambda_j} \tag{7.36}$$

$$\begin{aligned} E_{\text{total strain},\,j}(\tau) &= \frac{\left(\tau-\tau_j^{\mathrm{o}}\right)^2}{2\lambda_{\mathrm{c}}} + \frac{\left(\tau-\tau_j^{\mathrm{o}}\right)^2}{2\lambda_{\tau j}} = \frac{\lambda_j\left(\lambda_{\tau j}\left(\tau-\tau_j\right)^2 + \lambda_{\mathrm{c}}\left(\tau_j-\tau_j^{\mathrm{o}}\right)^2\right)}{2\lambda_{\mathrm{c}}{\lambda_{\tau j}}^2} \\ &= \frac{\lambda_j}{2\lambda_{\mathrm{c}}\lambda_{\tau j}}\left(\frac{\lambda_{\mathrm{c}}\lambda_{\tau j}\left(\langle F_{\tau i}\rangle\lambda_i + \tau_i^{\mathrm{o}} - \tau_j^{\mathrm{o}}\right)^2}{{\lambda_j}^2} + \left(\frac{\lambda_{\tau j}\left(\langle F_{\tau i}\rangle\lambda_i + \tau_i^{\mathrm{o}} - \tau_j^{\mathrm{o}}\right)}{\lambda_j} + \tau_j^{\mathrm{o}} - \tau\right)^2\right) \end{aligned} \tag{7.37}$$

$$E_{\text{additional strain},j}(\tau) = \frac{\lambda_j\left(\tau-\tau_j\right)^2}{2\lambda_{\mathrm{c}}\lambda_{\tau j}} = \frac{\lambda_j}{2\lambda_{\mathrm{c}}\lambda_{\tau j}}\left(\frac{\lambda_{\tau j}\left(\langle F_{\tau i}\rangle\lambda_i + \tau_i^{\mathrm{o}} - \tau_j^{\mathrm{o}}\right)}{\lambda_j} + \tau_j^{\mathrm{o}} - \tau\right)^2 \tag{7.38}$$

The strain energy of the unconstrained macromolecule in chemical state j is given by eq. (7.39), and $G(t,\zeta_j)$ can be expanded similarly (eq. (7.40)).

$$E^{0}_{\text{total strain},j}(\tau) = \frac{\left(\tau - \tau_j^0\right)^2}{2\lambda_{\tau j}} \tag{7.39}$$

$$\begin{aligned} G\left(\tau, \zeta_j\right) &= G\left(\tau_j^0, \zeta_j\right) + \left.\frac{\partial G\left(\tau,\zeta_j\right)}{\partial \tau}\right|_{\tau=\tau_j^0}\left(\tau - \tau_j^0\right) + \left.\frac{\partial^2 G\left(\tau,\zeta_j\right)}{\partial \tau^2}\right|_{\tau=\tau_j^0}\frac{\left(\tau-\tau_j^0\right)^2}{2} + \cdots \\ &= G\left(\tau_j^0, \zeta_j\right) + \left.\frac{\partial E^0_{\text{total strain},j}(\tau)}{\partial \tau}\right|_{\tau=\tau_j^0}\left(\tau - \tau_j^0\right) + \left.\frac{\partial^2 E^0_{\text{total strain},j}(\tau)}{\partial \tau^2}\right|_{\tau=\tau_j^0}\frac{\left(\tau-\tau_j^0\right)^2}{2} + \cdots \\ &\approx G\left(\tau_j^0, \zeta_j\right) + \frac{\left(\tau-\tau_j^0\right)^2}{2\lambda_{\tau j}} \end{aligned} \tag{7.40}$$

Similarly, the distribution function for thermal fluctuations in τ in the constrained system in chemical state j is given by eq. (7.41), and that for the unconstrained macromolecule in chemical state j is given by eq. (7.42). The ensemble-average rate constants for the transformation $j \rightarrow i$ in the macromolecule constrained to an average restoring force $\langle F_{\tau i}\rangle$ in chemical state i, $k_{j,i}(\langle F_{\tau i}\rangle)$, and the same transformation in the unconstrained macromolecule, $k_{j,i}^{\mathrm{o}}$, are given by eqs. (7.43) and (7.44), respectively, where the canonical transition-state theory expression for $k_{i,j}(\tau)$ is given by eq. (7.45).

$$\rho_j(\tau, \langle F_{\tau i}\rangle) = \sqrt{\frac{\beta\lambda_j}{2\pi\lambda_{\mathrm{c}}\lambda_{\tau j}}}\, e^{-\beta\frac{\lambda_j}{2\lambda_{\mathrm{c}}\lambda_{\tau j}}\left(\frac{\lambda_{\tau j}\left(\langle F_{\tau i}\rangle\lambda_i + \tau_i^0 - \tau_j^0\right)}{\lambda_j} + \tau_j^0 - \tau\right)^2} \tag{7.41}$$

$$\rho_j^0(\tau) = \sqrt{\frac{\beta}{2\pi\lambda_{\tau j}}}\, e^{-\beta\frac{\left(\tau-\tau_j^0\right)^2}{2\lambda_{\tau j}}} \tag{7.42}$$

$$k_{j,i}(\langle F_{\tau i}\rangle) \propto \int_{-\infty}^{\infty} \rho_j(\tau, \langle F_{\tau i}\rangle) k_{j,i}(\tau)\, d\tau \tag{7.43}$$

$$k_{j,i}^0 \propto \int_{-\infty}^{\infty} \rho_j^0(\tau) k_{j,i}(\tau)\, d\tau \tag{7.44}$$

$$k_{j,i}(\tau) \propto e^{-\left(G\left(\tau,\zeta_{\mathrm{ts}ij}\right) - G\left(\tau,\zeta_j\right)\right)\beta} \tag{7.45}$$

Combining eqs. (7.31) and (7.41)–(7.45) yields the ratio of rate constants for the transformation $j \rightarrow i$ in a macromolecule constrained to an average restoring force $\langle F_{\tau i}\rangle$ in chemical state i to that in the unconstrained macromolecule, eq. (7.46). If $\lambda_{\tau \mathrm{ts}ij} > 0$, eq. (7.46) reduces to eq. (7.47). As before, the quantity $\Delta\Delta G_{j,i}^{\ddagger}(\langle F_{\tau i}\rangle)$ is the force-dependent *barrier lowering*, i.e., $\Delta G_{j,i}^{\ddagger}(\langle F_{\tau i}\rangle) = \Delta G_{j,i}^{\ddagger\mathrm{o}} - \Delta\Delta G_{j,i}^{\ddagger}(\langle F_{\tau i}\rangle)$.

$$\frac{k_{j,i}(\langle F_{\tau i}\rangle)}{k^{\mathrm{o}}_{j,i}} = \frac{\sqrt{\frac{\beta\lambda_j}{2\pi\lambda_{\mathrm{c}}\lambda_{\tau j}}}\, e^{-\beta\left(\Delta G^{\ddagger\mathrm{o}}_{j,i}\right)} \int_{-\infty}^{\infty} e^{-\frac{\beta}{2}\left(\frac{\lambda_j}{\lambda_{\mathrm{c}}\lambda_{\tau j}}\left(\frac{\lambda_{\tau j}\left(\langle F_{\tau i}\rangle\lambda_i+\tau^{\mathrm{o}}_i-\tau^{\mathrm{o}}_j\right)}{\lambda_j}+\tau^{\mathrm{o}}_j-\tau\right)^2+\frac{\left(\tau-\tau^{\mathrm{o}}_{\mathrm{ts}ij}\right)^2}{\lambda_{\tau\mathrm{ts}ij}}-\frac{\left(\tau-\tau^{\mathrm{o}}_j\right)^2}{\lambda_{\tau j}}\right)} d\tau}{\sqrt{\frac{\beta}{2\pi\lambda_{\tau j}}}\, e^{-\beta\left(\Delta G^{\ddagger\mathrm{o}}_{j,i}\right)} \int_{-\infty}^{\infty} e^{-\frac{\beta}{2}\left(\frac{\left(\tau-\tau^{\mathrm{o}}_j\right)^2}{\lambda_{\tau j}}+\frac{\left(\tau-\tau^{\mathrm{o}}_{\mathrm{ts}ij}\right)^2}{\lambda_{\tau\mathrm{ts}ij}}-\frac{\left(\tau-\tau^{\mathrm{o}}_j\right)^2}{\lambda_{\tau j}}\right)} d\tau} \tag{7.46}$$

$$\begin{aligned}\beta^{-1}\ln\frac{k_{j,i}(\langle F_{\tau i}\rangle)}{k^{\mathrm{o}}_{j,i}} \\ &= \frac{\lambda_i}{\lambda_j\lambda_{\mathrm{ts}ij}}\left(\frac{\langle F_{\tau i}\rangle^2}{2}\Delta\lambda_{j,\mathrm{ts}ij}\lambda_i+\langle F_{\tau i}\rangle\left(\Delta\tau^{\mathrm{o}}_{i,\mathrm{ts}ij}\lambda_j-\Delta\tau^{\mathrm{o}}_{i,j}\lambda_{\mathrm{ts}ij}\right)\right)+\frac{\Delta\tau^{\mathrm{o}\ 2}_{i,j}}{2\lambda_j}-\frac{\Delta\tau^{\mathrm{o}\ 2}_{i,\mathrm{ts}ij}}{2\lambda_{\mathrm{ts}ij}} \\ &\quad+\frac{1}{2\beta}\ln\frac{\lambda_j}{\lambda_{\mathrm{ts}ij}} \equiv \Delta\Delta G^{\ddagger}_{j,i}(\langle F_{\tau i}\rangle)\end{aligned} \tag{7.47}$$

The equations for strain energy in the unconstrained macromolecule in chemical state ts*ij*, eq. (7.24), and thus the corresponding Taylor expansion for $G(\tau,\zeta_{\mathrm{ts}ij})$, eq. (7.26), are equivalent for chemical state ts*jl*. Thus the ratio of the ensemble-average rate constant for the transformation $j \rightarrow [\mathrm{ts}jl]^{\ddagger} \rightarrow l$ in a macromolecule constrained to the average restoring force $\langle F_{\tau i}\rangle$ in chemical state *i* to that in the unconstrained macromolecule is analogous to eq. (7.46) and reduces to eq. (7.48).

$$\begin{aligned}\beta^{-1}\ln\frac{k_{j,l}(\langle F_{\tau i}\rangle)}{k^{\mathrm{o}}_{j,l}} \\ &= \frac{\lambda_i}{\lambda_j\lambda_{\mathrm{ts}jl}}\left(\frac{\langle F_{\tau i}\rangle^2}{2}\Delta\lambda_{j,\mathrm{ts}jl}\lambda_i+\langle F_{\tau i}\rangle\left(\Delta\tau^{\mathrm{o}}_{i,\mathrm{ts}jl}\lambda_j-\Delta\tau^{\mathrm{o}}_{i,j}\lambda_{\mathrm{ts}jl}\right)\right)+\frac{\Delta\tau^{\mathrm{o}\ 2}_{i,j}}{2\lambda_j}-\frac{\Delta\tau^{\mathrm{o}\ 2}_{i,\mathrm{ts}jl}}{2\lambda_{\mathrm{ts}jl}} \\ &\quad+\frac{1}{2\beta}\ln\frac{\lambda_j}{\lambda_{\mathrm{ts}jl}} \equiv \Delta\Delta G^{\ddagger}_{j,l}(\langle F_{\tau i}\rangle)\end{aligned} \tag{7.48}$$

Further Simplification for Reactions in Long Flexible Polymers

For reactions in constrained long flexible polymers, eqs. (7.34), (7.47) and (7.48) may be reduced to eqs. (7.49)–(7.51) for the reasons discussed in section 7.3. In brief, in polymers, λ_n is $> \Delta\tau_{n,\mathrm{ts}nm}{}^{\mathrm{o}} / (0.1\ \langle F_{\tau i}\rangle)$ if $\Delta\tau_{n,\mathrm{ts}nm}{}^{\mathrm{o}} <$ ~5 Å, which makes the $(\Delta\tau^{\mathrm{o}})^2$ terms < 5% of the $\langle F_{\tau i}\rangle$ terms.

$$\beta^{-1}\ln\frac{k_{i,j}(\langle F_{\tau i}\rangle)}{k^{\mathrm{o}}_{i,j}} = \frac{\lambda_i}{\lambda_{\mathrm{ts}ij}}\left(\frac{\langle F_{\tau i}\rangle^2}{2}\Delta\lambda_{i,\mathrm{ts}ij}+\langle F_{\tau i}\rangle\Delta\tau^{\mathrm{o}}_{i,\mathrm{ts}ij}\right) \tag{7.49}$$

$$\beta^{-1}\ln\frac{k_{j,i}(\langle F_{\tau i}\rangle)}{k^{\mathrm{o}}_{j,i}} = \frac{\lambda_i}{\lambda_j\lambda_{\mathrm{ts}ij}}\left(\frac{\langle F_{\tau i}\rangle^2}{2}\Delta\lambda_{j,\mathrm{ts}ij}\lambda_i+\langle F_{\tau i}\rangle\left(\Delta\tau^{\mathrm{o}}_{i,\mathrm{ts}ij}\lambda_j-\Delta\tau^{\mathrm{o}}_{i,j}\lambda_{\mathrm{ts}ij}\right)\right) \tag{7.50}$$

$$\beta^{-1}\ln\frac{k_{j,l}(\langle F_{\tau i}\rangle)}{k_{j,l}^{\mathrm{o}}}=\frac{\lambda_i}{\lambda_j\lambda_{\mathrm{ts}jl}}\left(\frac{\langle F_{\tau i}\rangle^2}{2}\Delta\lambda_{j,\mathrm{ts}jl}\lambda_i+\langle F_{\tau i}\rangle\left(\Delta\tau_{i,\mathrm{ts}jl}^{\mathrm{o}}\lambda_j-\Delta\tau_{i,j}^{\mathrm{o}}\lambda_{\mathrm{ts}jl}\right)\right) \tag{7.51}$$

Then they may be further simplified to eqs. (7.52)–(7.54).

$$\beta^{-1}\ln\frac{k_{i,j}(\langle F_{\tau i}\rangle)}{k_{i,j}^{\mathrm{o}}}=\frac{\langle F_{\tau i}\rangle^2}{2}\Delta\lambda_{i,\mathrm{ts}ij}+\langle F_{\tau i}\rangle\Delta\tau_{i,\mathrm{ts}ij}^{\mathrm{o}} \tag{7.52}$$

$$\beta^{-1}\ln\frac{k_{j,i}(\langle F_{\tau i}\rangle)}{k_{j,i}^{\mathrm{o}}}=\frac{\langle F_{\tau i}\rangle^2}{2}\Delta\lambda_{j,\mathrm{ts}ij}+\langle F_{\tau i}\rangle\Delta\tau_{j,\mathrm{ts}ij}^{\mathrm{o}} \tag{7.53}$$

$$\beta^{-1}\ln\frac{k_{j,l}(\langle F_{\tau i}\rangle)}{k_{j,l}^{\mathrm{o}}}=\frac{\langle F_{\tau i}\rangle^2}{2}\Delta\lambda_{j,\mathrm{ts}jl}+\langle F_{\tau i}\rangle\Delta\tau_{j,\mathrm{ts}jl}^{\mathrm{o}} \tag{7.54}$$

7.8.2 Equations for Substrate Scission in the Intermediate

If the substrate (macromolecule) is cleaved in chemical state *j*, then all of the inherent strain energy in chemical state i, eq. (7.20), is relieved. Then, the force-dependent free energy of reaction becomes eq. (7.55), which then yields eqs. (7.56) and (7.57) as the force-dependent free energy of activation and the force-dependent barrier lowering, respectively, for *j* → *i*.

$$\Delta G_{i,j}(\langle F_{\tau i}\rangle)=\Delta G_{i,j}^{\mathrm{o}}-\frac{\lambda_i\langle F_{\tau i}\rangle^2}{2} \tag{7.55}$$

$$\Delta G_{j,i}^{\ddagger}(\langle F_{\tau i}\rangle)=\Delta G_{i,j}^{\ddagger}(\langle F_{\tau i}\rangle)-\Delta G_{i,j}(\langle F_{\tau i}\rangle)=\Delta G_{i,j}^{\ddagger\mathrm{o}}-\Delta\Delta G_{i,j}^{\ddagger}(\langle F_{\tau i}\rangle)-\Delta G_{i,j}^{\mathrm{o}}-\frac{\lambda_i\langle F_{\tau i}\rangle^2}{2} \tag{7.56}$$

$$\begin{aligned}\Delta\Delta G_{j,i}^{\ddagger}(\langle F_{\tau i}\rangle)&=\Delta\Delta G_{i,j}^{\ddagger}(\langle F_{\tau i}\rangle)-\frac{\lambda_i\langle F_{\tau i}\rangle^2}{2}\\&=\frac{\lambda_i}{\lambda_{\mathrm{ts}ij}}\left(\frac{\langle F_{\tau i}\rangle^2}{2}\Delta\lambda_{i,\mathrm{ts}ij}+\langle F_{\tau i}\rangle\Delta\tau_{i,\mathrm{ts}ij}^{\mathrm{o}}+\frac{{\Delta\tau_{i,\mathrm{ts}ij}^{\mathrm{o}}}^2}{2\lambda_i}\right)+\frac{1}{2\beta}\ln\frac{\lambda_i}{\lambda_{\mathrm{ts}ij}}-\frac{\lambda_i\langle F_{\tau i}\rangle^2}{2}\end{aligned} \tag{7.57}$$

The transformation *j* → *l* is then unaffected by force, provided that the substrate (macromolecule) does not reform. For the same reasons as before, eq. (7.57) simplifies to eq. (7.58); application of the local approximation can only simplify eq. (7.58) further to eq. (7.59), where the contributions from the constraining potential and the substrate (macromolecule) are still present in the last term.

$$\Delta\Delta G_{j,i}^{\ddagger}(\langle F_{\tau i}\rangle)=\frac{\langle F_{\tau i}\rangle^2}{2}\Delta\lambda_{i,\mathrm{ts}ij}+\langle F_{\tau i}\rangle\Delta\tau_{i,\mathrm{ts}ij}^{\mathrm{o}}-\frac{\lambda_i\langle F_{\tau i}\rangle^2}{2} \tag{7.58}$$

$$\Delta\Delta G_{j,i}^{\ddagger}\left(\langle F_{qi}\rangle\right)=\frac{\langle F_{qi}\rangle^2}{2}\Delta\lambda_{qi,q\mathrm{ts}ij}+\langle F_{qi}\rangle\Delta q_{i,\mathrm{ts}ij}^{\mathrm{o}}-\frac{\lambda_i\langle F_{\tau i}\rangle^2}{2} \tag{7.59}$$

7.8.3 Anharmonicity and the Compliance of Stretched Single Chains of Polyethylene

Force-extension curves for single polymer chains that give excellent agreement with experimental data can be calculated by reported methods.[96] Normalized extension–force curves (R_z/L_o vs. F_{Rz}, where R_z is the end-to-end separation and L_o is the strain-free contour length) obtained in this manner agree quite well with those obtained from the rotational isomeric state model; compare Fig. 7.11 to the analogous plots for n-$C_{40}H_{82}$, n-$C_{100}H_{202}$, and n-$C_{300}H_{602}$ in Fig. 10C of ref. 43.

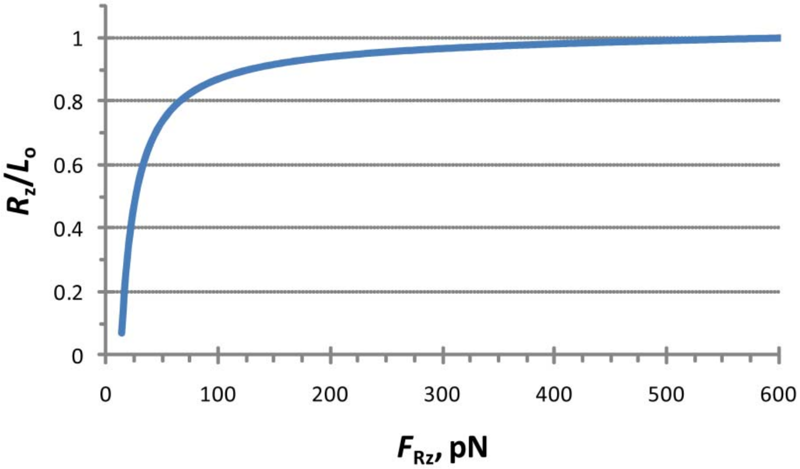

Fig. 7.11. Normalized extension–force curve for polyethylene calculated by the methods in ref. 96.

The stretching compliance of single molecules is then readily obtained by differentiation. The results of calculations for two molecules of polyethylene with different strain-free contour lengths, L_o, are shown in Fig. 7.12. Note that the absolute value of the end-to-end stretching compliance $\lambda_{Rz}(R_z/L_o)$ depends on the value of L_o while the end-to-end restoring force $F_{Rz}(R_z/L_o)$ does not. Solutions of short polymer chains do not exhibit chain fragmentation during ultrasonication; polymer chains must be above a minimum length before they are affected by shear flows from ultrasonic cavitation.[4] The two example calculations shown here for $L_o = 25$ nm and $L_o = 1$ μm are below and above the minimum length required for mechanochemical activation by ultrasonication.[6] Though the stretching behavior of polymer chains is obviously anharmonic (λ varies with L and thus also with R_z), the behavior is accurately approximated as being harmonic over short distance changes. For example, for a single chain of polyethylene with

$L_o = 1$ μm stretched to $R_z/L_o = 0.96$, an elongation of L by 3.5 Å (e.g., due to a chemical transformation of a reactive moiety buried in the chain) changes the value of λ by <1%.

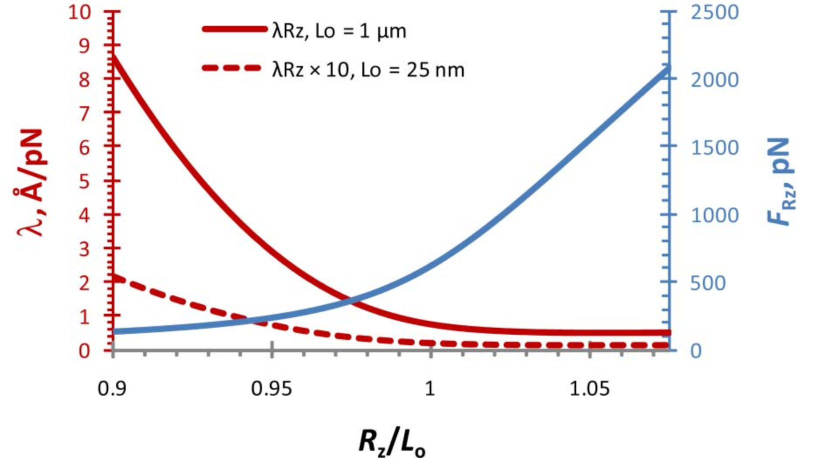

Fig. 7.12. The end-to-end stretching compliance, λ_{Rz}, of a single molecule of polyethylene with strain-free contour lengths $L_o = 1$ μm (red line), 10 times that of a single polyethylene molecule with $L_o = 25$ nm (red dashes), and the end-to-end restoring force (F, blue) as functions of the end-to-end length R_z normalized to the strain-free contour length L_o.

The compliances of the end-to-end distance, λ_{Rz}, discussed consist of entropic and enthalpic contributions. For long, flexible polymer chains, at low R_z, F_{Rz} is low and is mostly due to the energetic penalty of the decrease in entropy associated with stretching.[43,97] As R_z increases, the contribution of enthalpic stretching to the overall compliance increases. Plotting Fig. 7.12 over the entire stretching regime reveals the relative magnitude of the enthalpic and entropic contributions to the compliance (Fig. 7.13).

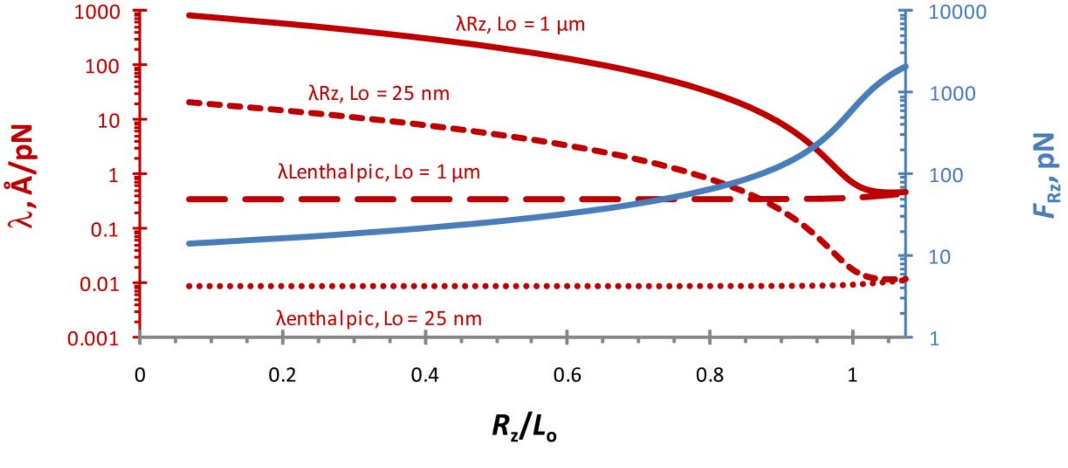

Fig. 7.13. The full range of data calculated for the stretching of a single chain of polyethylene. See also Fig. 7.12.

The data indicates that a polymer chain must be overstretched ($R_z/L_o > 1$) before the enthalpic contributions of elongating the contour length L to the overall compliance dominate, as shown in Fig. 7.14.

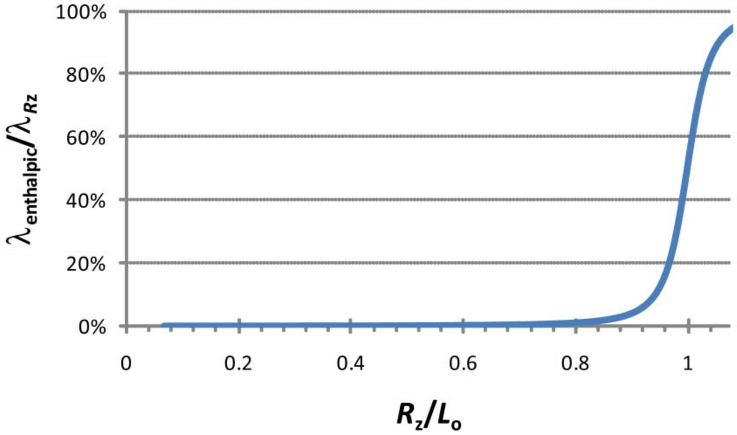

Fig. 7.14. The relative contribution of the enthalpic compliance of the contour length L to the overall compliance of the end-to-end distance R_z.

7.8.4 Conditions for Crossover

For a two-barrier system $R \rightleftharpoons I \rightarrow P$, in all cases $G_I < G_{TS1}$, $G_I < G_{TS2}$, and $G_R < G_{TS1}$ by definitions of the critical points on the PES (minima and saddle points). When $\Delta G_{R,TS2}$ is rate-limiting, the system exhibits pre-equilibrium kinetics; $\Delta G_{R,TS2} > \Delta G_{R,TS1}$ which means that $G_{TS2} > G_{TS1}$, $\Delta G_{R,TS2} > \Delta G_{I,TS2}$ which means that $G_I > G_R$ and therefore $G_R < G_I < G_{TS1} < G_{TS2}$. When $\Delta G_{R,TS1}$ is rate-limiting, $\Delta G_{R,TS1} > \Delta G_{R,TS2}$ which means that $G_{TS1} > G_{TS2}$ and $\Delta G_{R,TS1} > \Delta G_{I,TS2}$. When $\Delta G_{I,TS2}$ is rate-limiting, $\Delta G_{I,TS2} > \Delta G_{R,TS2}$ which means that $G_R > G_I$ and $\Delta G_{I,TS2} > \Delta G_{R,TS1}$.

There are six types of crossover; based on the type of crossover and the orderings of energies or energy differences in the preceding paragraph, certain conclusions can be made in each case:

1. Type 1 kinetic crossover: before crossover the kinetics are determined by the difference between R and TS2, and then after crossover the kinetics are determined by the difference between R and TS1. The system initially exhibits pre-equilibrium kinetics, and $G_R < G_I < G_{TS1} < G_{TS2}$. Crossover occurs when $G_{TS1} = G_{TS2}$, at and then $G_I > G_R$ changes to $\Delta G_{R,TS1} > \Delta G_{I,TS2}$.

2. Type 2 kinetic crossover: before crossover the kinetics are determined by the difference between R and TS2, and then after crossover the kinetics are determined by the difference between I and TS2. The system initially exhibits pre-equilibrium kinetics, and $G_{\mathrm{R}} < G_{\mathrm{I}} < G_{\mathrm{TS1}} < G_{\mathrm{TS2}}$. Crossover occurs when $G_{\mathrm{R}} = G_{\mathrm{I}}$, and then $G_{\mathrm{TS2}} > G_{\mathrm{TS1}}$ changes to $\Delta G_{\mathrm{I,TS2}} > \Delta G_{\mathrm{R,TS1}}$.
3. Type 3 kinetic crossover: before crossover the kinetics are determined by the difference between I and TS2, and then after crossover the kinetics are determined by the difference between R and TS1. Crossover occurs when $\Delta G_{\mathrm{R,TS1}} = \Delta G_{\mathrm{I,TS2}}$, and then $G_{\mathrm{R}} > G_{\mathrm{I}}$ changes to $G_{\mathrm{TS1}} > G_{\mathrm{TS2}}$. No additional conclusions can be made.
4. Type 4 kinetic crossover: before crossover the kinetics are determined by the difference between R and TS1, and then after crossover the kinetics are determined by the difference between I and TS2. This is the reverse of Type 3 kinetic crossover. Thus, crossover occurs when $\Delta G_{\mathrm{R,TS1}} = \Delta G_{\mathrm{I,TS2}}$, and then $G_{\mathrm{TS1}} > G_{\mathrm{TS2}}$ changes to $G_{\mathrm{R}} > G_{\mathrm{I}}$.
5. Type 5 kinetic crossover: before crossover the kinetics are determined by the difference between I and TS2, and then after crossover the kinetics are determined by the difference between R and TS2. This is the reverse of Type 2 kinetic crossover. Thus, crossover occurs when $G_{\mathrm{R}} = G_{\mathrm{I}}$, where $\Delta G_{\mathrm{I,TS2}} > \Delta G_{\mathrm{R,TS1}}$ changes to $G_{\mathrm{TS2}} > G_{\mathrm{TS1}}$, and the system begins to exhibit pre-equilibrium kinetics with $G_{\mathrm{R}} < G_{\mathrm{I}} < G_{\mathrm{TS1}} < G_{\mathrm{TS2}}$. Initially $G_{\mathrm{I}} < G_{\mathrm{R}} < G_{\mathrm{TS1}}$ and $G_{\mathrm{I}} < G_{\mathrm{TS2}}$, and after crossover $G_{\mathrm{R}} < G_{\mathrm{I}} < G_{\mathrm{TS1}} < G_{\mathrm{TS2}}$. If $G_{\mathrm{I}}^{\mathrm{o}} < G_{\mathrm{R}}^{\mathrm{o}}$ but $G_{\mathrm{R}} < G_{\mathrm{I}}$ after crossover, then $G_{\mathrm{R}} - G_{\mathrm{I}} < 0$. Then $G_{\mathrm{R}}^{\mathrm{o}} - F_{q\mathrm{R}}\, q_{\mathrm{R}}^{\mathrm{o}} - G_{\mathrm{I}}^{\mathrm{o}} + F_{q\mathrm{R}}\, q_{\mathrm{I}}^{\mathrm{o}} < 0$ and $F_{q\mathrm{R}}(q_{\mathrm{I}}^{\mathrm{o}} - q_{\mathrm{R}}^{\mathrm{o}}) < 0$. Thus, for $F_{q\mathrm{R}} > 0$, $q_{\mathrm{I}}^{\mathrm{o}} - q_{\mathrm{R}}^{\mathrm{o}} < 0$, indicating that the local molecular degree of freedom q must contract from R to I. So long as $q_{\mathrm{I}}^{\mathrm{o}} - q_{\mathrm{R}}^{\mathrm{o}} < 0$ (net contraction of q from R to I), $q_{\mathrm{TS2}}^{\mathrm{o}} - q_{\mathrm{R}}^{\mathrm{o}} > 0$ (net elongation of q from R to TS2) is allowed.
6. Type 6 kinetic crossover: before crossover the kinetics are determined by the difference between R and TS1, and then after crossover the kinetics are determined by the difference between R and TS2. This is the reverse of Type 1 kinetic crossover. Thus, crossover occurs when $G_{\mathrm{TS1}} = G_{\mathrm{TS2}}$, and $\Delta G_{\mathrm{R,TS1}} > \Delta G_{\mathrm{I,TS2}}$ changes to $G_{\mathrm{I}} > G_{\mathrm{R}}$. The system then begins to exhibit pre-equilibrium kinetics with $G_{\mathrm{R}} < G_{\mathrm{I}} < G_{\mathrm{TS1}} < G_{\mathrm{TS2}}$. Initially $G_{\mathrm{I}} < G_{\mathrm{TS2}} < G_{\mathrm{TS1}}$ and $G_{\mathrm{R}} < G_{\mathrm{TS1}}$, and after crossover $G_{\mathrm{R}} < G_{\mathrm{I}} < G_{\mathrm{TS1}} < G_{\mathrm{TS2}}$. If $G_{\mathrm{TS2}}^{\mathrm{o}} < G_{\mathrm{TS1}}^{\mathrm{o}}$ but $G_{\mathrm{TS1}} < G_{\mathrm{TS2}}$ after crossover, then $G_{\mathrm{TS1}} - G_{\mathrm{TS2}} < 0$. Then $G_{\mathrm{TS1}}^{\mathrm{o}} - F_{q\mathrm{R}}$

$q_{\mathrm{TS1}}^{\mathrm{o}} - G_{\mathrm{TS2}}^{\mathrm{o}} + F_{q\mathrm{R}}\, q_{\mathrm{TS2}}^{\mathrm{o}} < 0$ and $F_{q\mathrm{R}}(q_{\mathrm{TS2}}^{\mathrm{o}} - q_{\mathrm{TS1}}^{\mathrm{o}}) < 0$. Thus, for $F_{q\mathrm{R}} > 0$, $q_{\mathrm{TS2}}^{\mathrm{o}} - q_{\mathrm{TS1}}^{\mathrm{o}} < 0$, indicating that the local molecular degree of freedom q must contract from TS1 to TS2.

7.8.5 Details of Numerical Simulations of Pre-equilibrium Systems

Given a set of parameters, the force-dependent energy differences $\Delta G_{\mathrm{R,TS1}}(\langle F_{q\mathrm{R}}\rangle)$ (R → I, $\Delta G_{\mathrm{R,I}}^{\ddagger}(\langle F_{q\mathrm{R}}\rangle)$), $\Delta G_{\mathrm{R,TS2}}(\langle F_{q\mathrm{R}}\rangle)$ (effective barrier for pre-equilibrium kinetics, R → P), $\Delta G_{\mathrm{I,TS2}}(\langle F_{q\mathrm{R}}\rangle)$ (I → P, $\Delta G_{\mathrm{I,P}}^{\ddagger}(\langle F_{q\mathrm{R}}\rangle)$) and $\Delta G_{\mathrm{I,TS1}}(\langle F_{q\mathrm{R}}\rangle)$ (I → R, $\Delta G_{\mathrm{I,R}}^{\ddagger}(\langle F_{q\mathrm{R}}\rangle)$) were calculated using both the EBE formalism and our model (specifically, eqs. (7.9)–(7.11) and (7.13)) in increments of 10 pN, yielding the ΔG vs. $\langle F_{q\mathrm{R}}\rangle$ plots below. At every 50 pN starting at 0 pN, the energy differences calculated with our model were used to simulate the conversion of R to P by numerically propagating in time the full system of differential equations governing the system $\mathrm{R} \rightleftharpoons \mathrm{I} \rightarrow \mathrm{P}$. Step sizes for t ranged from 1 ps to 1 μs, depending on the stability of the individual solutions. The relative concentrations vs. t thus obtained were then analyzed by plotting $\ln(\chi_{\mathrm{P}})$ vs. t; the slopes of these linear plots yielded the "observed" rate constant for conversion of R to P for that value of $\langle F_{q\mathrm{R}}\rangle$. This value was then compared against that predicted by TST using the aforementioned energy differences to determine which GS/TS pair determines the observed kinetics; these comparisons are shown in the "error in k_{obsP} comparisons" vs. $\langle F_{q\mathrm{R}}\rangle$ plots below. Plotting $\ln(k_{\mathrm{obsP}})$ vs. $\langle F_{q\mathrm{R}}\rangle$ yields plots comparable to those commonly used in the analysis of SMF experiments to indicate kinetic crossover. Several examples are shown below.

Example 1: Type 1 crossover from effective $\Delta G_{\mathrm{R,TS2}}(\langle F_{q\mathrm{R}}\rangle)$ to $\Delta G_{\mathrm{R,TS1}}(\langle F_{q\mathrm{R}}\rangle)$

The parameters used are shown in Table 7.4. This system exhibits Type 1 kinetic crossover: as $\langle F_{q\mathrm{R}}\rangle$ increases, the largest barrier in the forward direction changes from $\Delta G_{\mathrm{R,TS2}}(\langle F_{q\mathrm{R}}\rangle)$ (orange, Fig. 7.15) to $\Delta G_{\mathrm{R,TS1}}(\langle F_{q\mathrm{R}}\rangle)$ (blue) at 405 pN. In this case, second-order effects are minimal, and the EBE formalism and our model yield nearly identical predictions. The semi-logarithmic plot of $\ln(k_{\mathrm{obsP}})$ vs. $\langle F_{q\mathrm{R}}\rangle$ indicates kinetic crossover at 415 pN (intersection of orange and blue lines), with Δq = 1.25 Å (1.30 Å based on parameters) before crossover and Δq = 0.11 Å (0.10 Å based on parameters) after crossover.

Table 7.4. Parameters for the simulation of Type 1 kinetic crossover.

	q^{o}, Å	λ_q, Å/pN	ΔG relative to R at $\langle F_{q\mathrm{R}}\rangle = 0$, kcal/mol
R	1.50	1.92E-04	0
TS1	1.60	1.98E-04	15
I	2.10	1.92E-04	5
TS2	2.80	2.00E-04	22

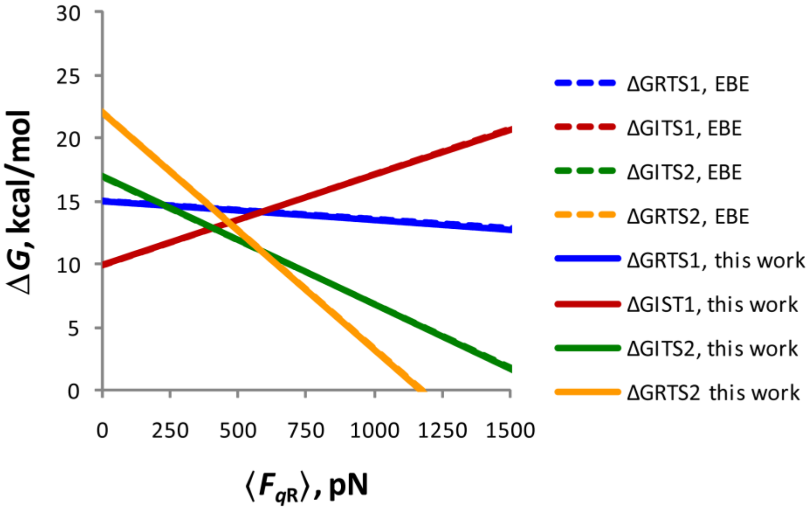

Fig. 7.15. Calculated force-dependent energy differences for the simulation of Type 1 kinetic crossover; parameters are in Table 7.4. Crossover occurs at 405 pN when the largest barrier in the forward direction changes from $\Delta G_{\mathrm{R,TS2}}(\langle F_{q\mathrm{R}}\rangle)$ (orange) to $\Delta G_{\mathrm{R,TS1}}(\langle F_{q\mathrm{R}}\rangle)$ (blue).

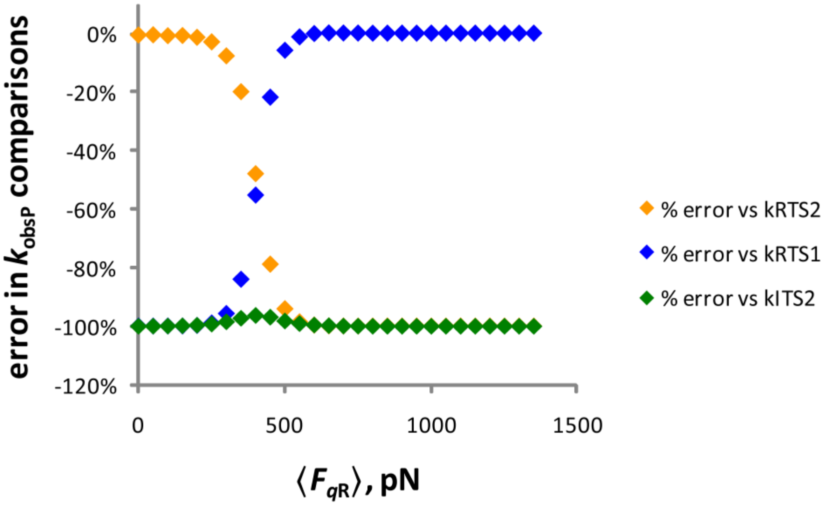

Fig. 7.16. Comparison of the simulated "observed" force-dependent rate constant for conversion of R to P to rate constants dictated by the indicated GS/TS pairs; parameters for the simulation are in Table 7.4.

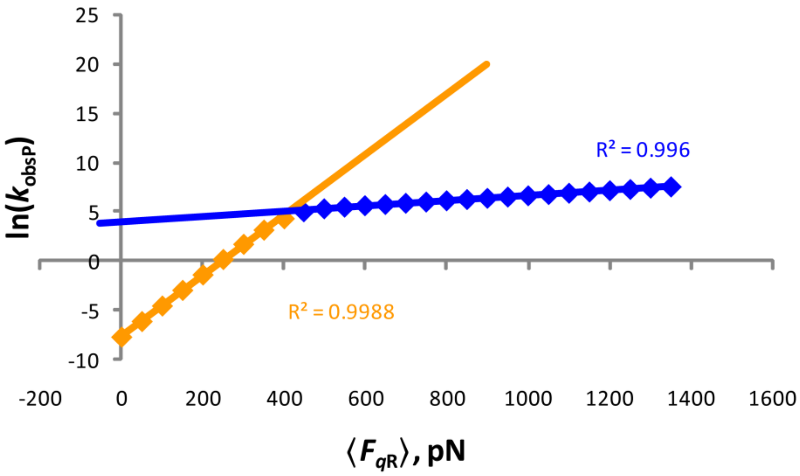

Fig. 7.17. Semi-logarithmic plot of the simulated "observed" force-dependent rate constant for conversion of R to P exhibiting Type 1 kinetic crossover at 415 pN; parameters for the simulation are in Table 7.4.

Example 2: Type 2 crossover from effective $\Delta G_{R,TS2}(\langle F_{qR} \rangle)$ to $\Delta G_{I,TS2}(\langle F_{qR} \rangle)$

The parameters used are shown in Table 7.5. This system exhibits Type 2 kinetic crossover: as $\langle F_{qR} \rangle$ increases, the largest barrier in the forward direction changes from $\Delta G_{R,TS2}(\langle F_{qR} \rangle)$ (orange, Fig. 7.18) to $\Delta G_{I,TS2}(\langle F_{qR} \rangle)$ (green) at 579 pN. In this case, second-order effects are minimal, and the EBE formalism and our model yield nearly identical predictions. The semi-logarithmic plot of $\ln(k_{obsP})$ vs. $\langle F_{qR} \rangle$ indicates kinetic crossover at 620 pN (intersection of orange and green lines), with Δq = 0.84 Å (0.90 Å based on parameters) before crossover and Δq = 0.31 Å (0.30 Å based on parameters) after crossover.

Table 7.5. Parameters for the simulation of Type 2 kinetic crossover.

	q^o, Å	λ_q, Å/pN	ΔG relative to R at $\langle F_{qR} \rangle = 0$, kcal/mol
R	1.50	1.92E-04	0
TS1	1.80	1.98E-04	15
I	2.10	1.92E-04	5
TS2	2.40	2.00E-04	22

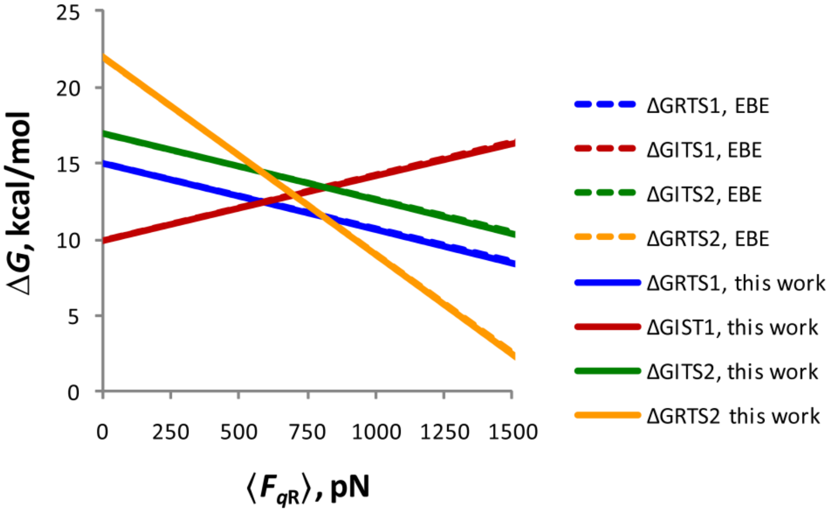

Fig. 7.18. Calculated force-dependent energy differences for the simulation of Type 2 kinetic crossover; parameters are in Table 7.5. Crossover occurs at 579 pN when the largest barrier in the forward direction changes from $\Delta G_{\mathrm{R,TS2}}(\langle F_{q\mathrm{R}}\rangle)$ (orange) to $\Delta G_{\mathrm{I,TS2}}(\langle F_{q\mathrm{R}}\rangle)$ (green).

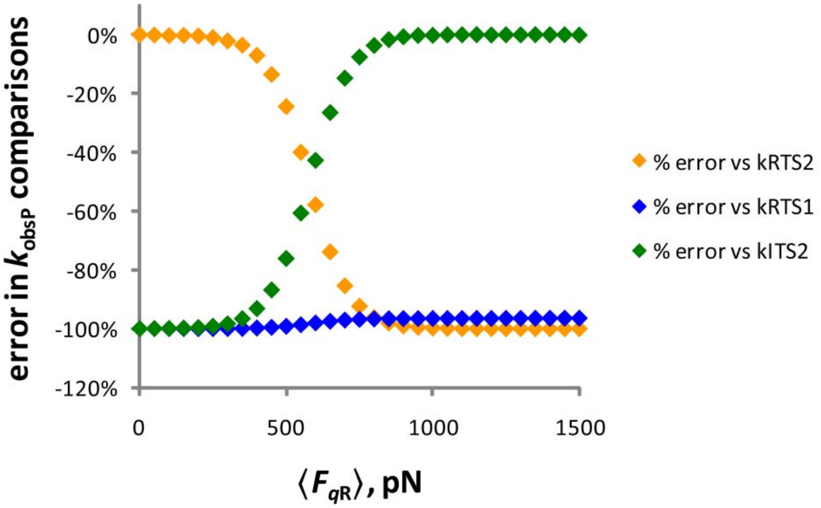

Fig. 7.19. Comparison of the simulated “observed” force-dependent rate constant for conversion of R to P to rate constants dictated by the indicated GS/TS pairs; parameters for the simulation are in Table 7.5.

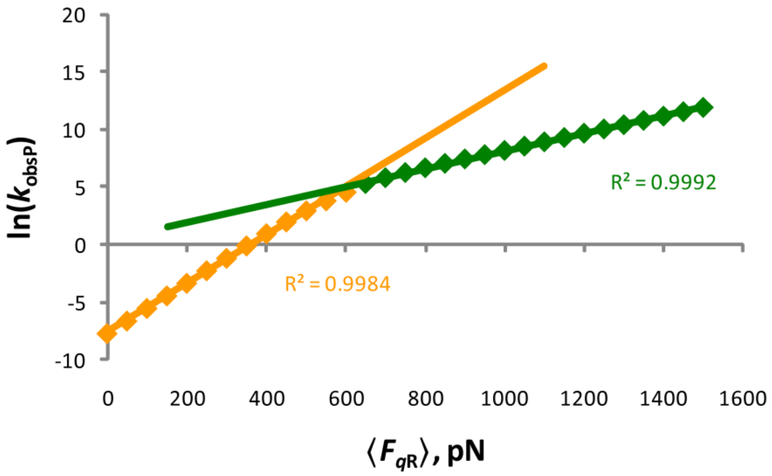

Fig. 7.20. Semi-logarithmic plot of the simulated "observed" force-dependent rate constant for conversion of R to P exhibiting Type 2 kinetic crossover at 620 pN; parameters for the simulation are in Table 7.5.

Example 3: Type 2 crossover from effective $\Delta G_{R,TS2}(\langle F_{qR}\rangle)$ to $\Delta G_{I,TS2}(\langle F_{qR}\rangle)$, then Type 3 crossover from $\Delta G_{I,TS2}(\langle F_{qR}\rangle)$ to $\Delta G_{R,TS1}(\langle F_{qR}\rangle)$

The parameters used are shown in Table 7.6. This system exhibits Type 2 kinetic crossover followed by Type 3 crossover: as $\langle F_{qR}\rangle$ increases, the largest barrier in the forward direction changes from $\Delta G_{R,TS2}(\langle F_{qR}\rangle)$ (orange, Fig. 7.21) to $\Delta G_{I,TS2}(\langle F_{qR}\rangle)$ (green) at 347 pN and then to $\Delta G_{R,TS1}(\langle F_{qR}\rangle)$ at 694 pN. In this case, second-order effects are minimal, and the EBE formalism and our model yield nearly identical predictions. The semi-logarithmic plot of ln(k_{obsP}) vs. $\langle F_{qR}\rangle$ indicates kinetic crossover at 333 pN (intersection of orange and green lines) and 682 pN (intersection of green and blue lines) with Δq = 1.25 Å (1.30 Å based on parameters) before the first crossover, Δq = 0.79 Å (0.70 Å based on parameters) after the first crossover, and Δq = 0.11 Å (0.10 Å based on parameters) after the second crossover.

Table 7.6. Parameters for the simulation of Type 2 and then Type 3 kinetic crossover.

	q^o, Å	λ_q, Å/pN	ΔG relative to R at $\langle F_{qR}\rangle = 0$, kcal/mol
R	1.50	1.92E-04	0
TS1	1.60	1.98E-04	11
I	2.10	1.92E-04	3
TS2	2.80	2.00E-04	20

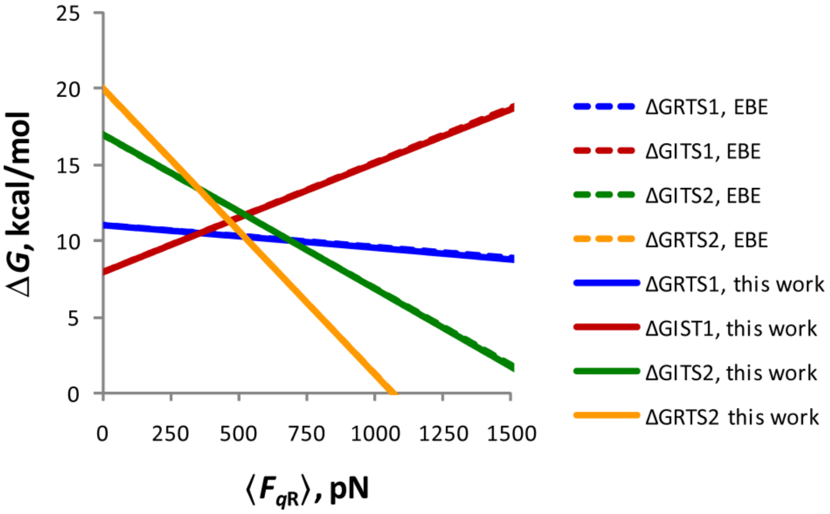

Fig. 7.21. Calculated force-dependent energy differences for the simulation of Type 2 and then Type 3 kinetic crossover; parameters are in Table 7.6. Crossover occurs at 347 pN when the largest barrier in the forward direction changes from $\Delta G_{\mathrm{R,TS2}}(\langle F_{q\mathrm{R}}\rangle)$ (orange) to $\Delta G_{\mathrm{I,TS2}}(\langle F_{q\mathrm{R}}\rangle)$ (green) and then at 694 pN when the largest barrier in the forward direction changes from $\Delta G_{\mathrm{I,TS2}}(\langle F_{q\mathrm{R}}\rangle)$ (green) to $\Delta G_{\mathrm{R,TS1}}(\langle F_{q\mathrm{R}}\rangle)$ (blue).

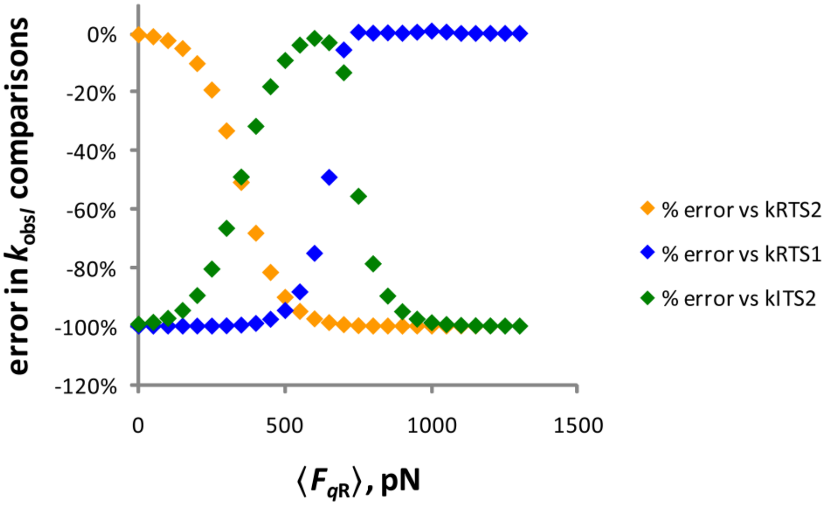

Fig. 7.22. Comparison of the simulated "observed" force-dependent rate constant for conversion of R to P to rate constants dictated by the indicated GS/TS pairs; parameters for the simulation are in Table 7.6.

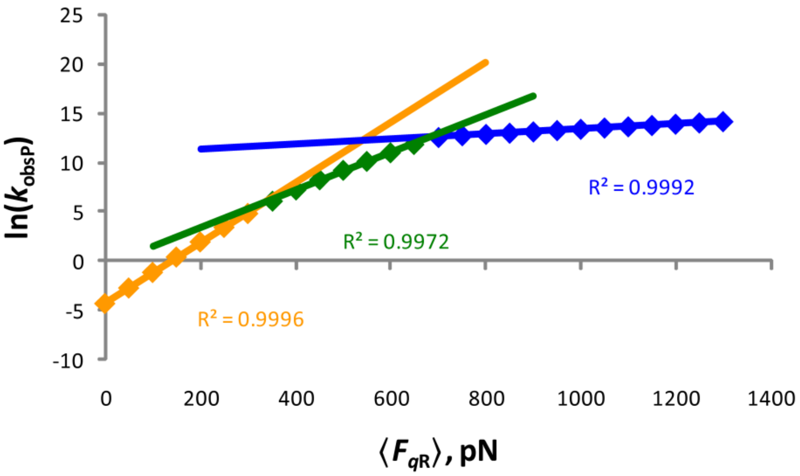

Fig. 7.23. Semi-logarithmic plot of the simulated "observed" force-dependent rate constant for conversion of R to P exhibiting Type 2 kinetic crossover at 333 pN and then Type 3 kinetic crossover at 682 pN; parameters for the simulation are in Table 7.6.

Example 4: Type 1 crossover from effective $\Delta G_{R,TS2}(\langle F_{qR} \rangle)$ to $\Delta G_{R,TS1}(\langle F_{qR} \rangle)$ with significant changes in substrate compliance

The parameters used are shown in Table 7.7. This system exhibits Type 1 kinetic crossover: as $\langle F_{qR} \rangle$ increases, the largest barrier in the forward direction changes from $\Delta G_{R,TS2}(\langle F_{qR} \rangle)$ (orange, Fig. 7.24) to $\Delta G_{R,TS1}(\langle F_{qR} \rangle)$ (blue). While our model predicts that this crossover will occur at 403 pN, the EBE formalism predicts that it will occur only at 695 pN (~73% difference) because it fails to account for second-order effects. Note the curvature of our model's prediction for $\Delta G_{R,TS2}(\langle F_{qR} \rangle)$ (solid orange line, Fig. 7.24); the prediction for $\Delta G_{I,TS1}(\langle F_{qR} \rangle)$ (solid red line) exhibits the same effect. The semi-logarithmic plot of $\ln(k_{obsP})$ vs. $\langle F_{qR} \rangle$ is shown in Fig. 7.5 above; the linear fits indicates kinetic crossover at 453 pN (intersection of orange and blue lines), with Δq = 1.00 Å (0.70 Å based on parameters) before crossover and Δq = 0.21 Å (0.20 Å based on parameters, 43% overestimation) after crossover.

Table 7.7. Parameters for the simulation of Type 1 kinetic crossover with significant changes in substrate compliance.

	q^o, Å	λ_q, Å/pN	ΔG relative to R at $\langle F_{qR} \rangle = 0$, kcal/mol
R	1.50	1.92E-04	0
TS1	1.70	1.98E-04	15
I	1.90	1.92E-03	5
TS2	2.20	2.00E-03	20

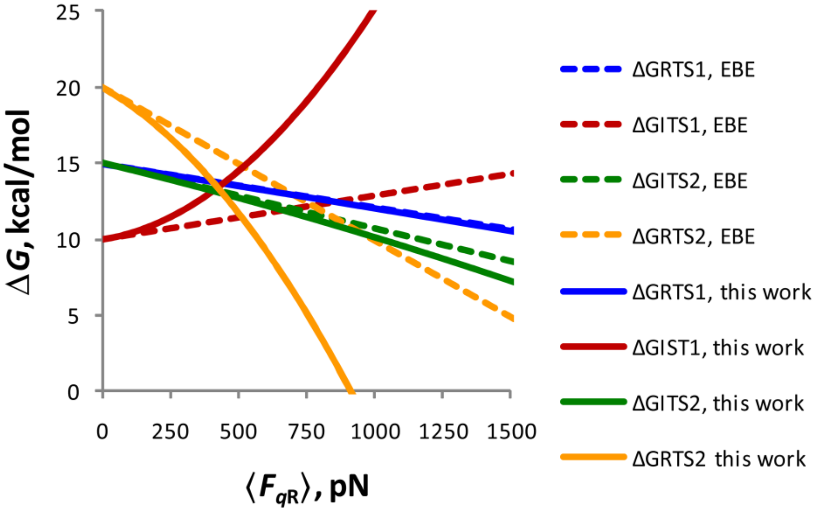

Fig. 7.24. Calculated force-dependent energy differences for the simulation of Type 1 kinetic crossover; parameters are in Table 7.7. Crossover occurs at 403 pN (our model) when the largest barrier in the forward direction changes from $\Delta G_{R,TS2}(\langle F_{qR} \rangle)$ (orange) to $\Delta G_{R,TS1}(\langle F_{qR} \rangle)$ (blue).

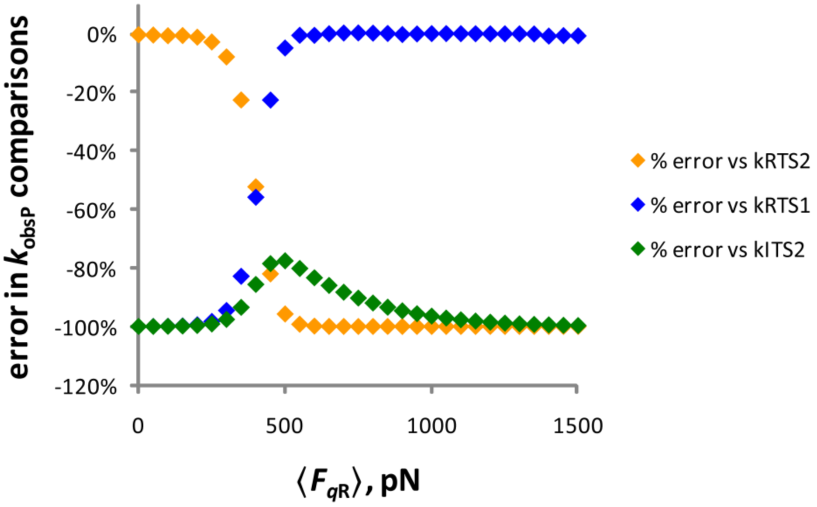

Fig. 7.25. Comparison of the simulated "observed" force-dependent rate constant for conversion of R to P to rate constants dictated by the indicated GS/TS pairs; parameters for the simulation are in Table 7.7.

Example 5: Type 2 crossover from effective $\Delta G_{\mathrm{R,TS2}}(\langle F_{q\mathrm{R}}\rangle)$ to $\Delta G_{\mathrm{I,TS2}}(\langle F_{q\mathrm{R}}\rangle)$ with the unmasking of a 5-nm side-chain loop

The parameters used are shown in Table 7.8. The values of $L(\langle F_{q\mathrm{R}}\rangle)$ and $\lambda(\langle F_{q\mathrm{R}}\rangle)$ were calculated as described in section 7.8.3 above. This system exhibits Type 2 kinetic crossover: as $\langle F_{q\mathrm{R}}\rangle$ increases, the largest barrier in the forward direction changes from $\Delta G_{\mathrm{R,TS2}}(\langle F_{q\mathrm{R}}\rangle)$ (orange, Fig. 7.26) to $\Delta G_{\mathrm{I,TS2}}(\langle F_{q\mathrm{R}}\rangle)$ (green) at $\langle F_{q\mathrm{R}}\rangle < 20$ pN. Clearly, there are significant second-order effects. The semi-logarithmic plot of $\ln(k_{\mathrm{obsP}})$ vs. $\langle F_{q\mathrm{R}}\rangle$ is shown above in Fig. 7.6 and indicates kinetic crossover at ~15 pN (intersection of orange and green lines), with Δq = 23.2 Å (0.90 Å based on parameters ignoring the 5-nm side-chain loop) before crossover and Δq = 0.31 Å (0.30 Å based on parameters) after crossover. Note that if not for the side-chain loop, this system would be identical to that in Example 1 above and would instead exhibit Type 1 crossover at 415 pN (405 pN based on parameters).

Table 7.8. Parameters for the simulation of Type 2 kinetic crossover with the inclusion of a side-chain loop when R → I.

	q^{o}, Å	λ_q, Å/pN	ΔG relative to R at $\langle F_{q\mathrm{R}}\rangle = 0$, kcal/mol
R	1.5	1.92E-04	0
TS1	1.8	1.98E-04	15
I	$2.1 + L(\langle F_{q\mathrm{R}}\rangle)$	$1.92\mathrm{E}{-}04 + \lambda(\langle F_{q\mathrm{R}}\rangle)$	5
TS2	$2.4 + L(\langle F_{q\mathrm{R}}\rangle)$	$2.00\mathrm{E}{-}04 + \lambda(\langle F_{q\mathrm{R}}\rangle)$	22

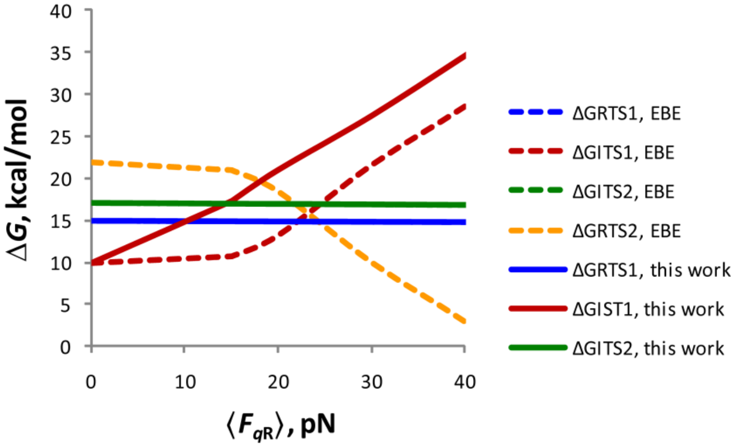

Fig. 7.26. Calculated force-dependent energy differences for the simulation of Type 2 kinetic crossover due to the unmasking of a 5-nm side-chain loop in the polymer; parameters are in Table 7.8. Crossover occurs when the largest

barrier in the forward direction changes from $\Delta G_{R,TS2}(\langle F_{qR}\rangle)$ (orange) to $\Delta G_{I,TS2}(\langle F_{qR}\rangle)$ (green); our model predicts this at $\langle F_{qR}\rangle < 20$ pN.

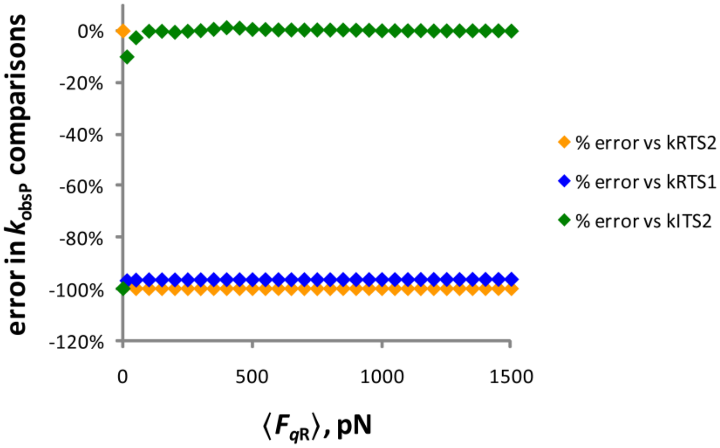

Fig. 7.27. Comparison of the simulated "observed" force-dependent rate constant for conversion of R to P to rate constants dictated by the indicated GS/TS pairs; parameters for the simulation are in Table 7.8.

Example 6: Type 2 crossover from effective $\Delta G_{R,TS2}(\langle F_{qR}\rangle)$ to $\Delta G_{I,TS2}(\langle F_{qR}\rangle)$ with complete substrate rupture

The parameters used are shown in Table 7.9. This system exhibits Type 2 kinetic crossover: as $\langle F_{qR}\rangle$ increases, the largest barrier in the forward direction changes from $\Delta G_{R,TS2}(\langle F_{qR}\rangle)$ (orange, Fig. 7.28) to $\Delta G_{I,TS2}(\langle F_{qR}\rangle)$ (green). Our model predicts this crossover occurs as soon as $\langle F_{qR}\rangle$ becomes non-zero; ignoring the change in compliance and using only the changes in q^o (i.e., the EBE formalism) suggests that crossover will occur at 579 pN. The semi-logarithmic plot of $\ln(k_{obsP})$ vs. $\langle F_{qR}\rangle$ for the simulated data is shown in Fig. 7.30. Following rupture of the substrate, the constraining potential relaxes fully; subsequent steps are force-independent, and reformation of the reactant requires the re-straining of the entire system (which is why it is necessary in this simulation to know the compliance of the constraint).

Table 7.9. Parameters for the simulation of Type 2 kinetic crossover with substrate rupture when R → I.

	q^o, Å	λ_q, Å/pN	ΔG relative to R at $\langle F_{qR}\rangle = 0$, kcal/mol
R	1.5	1.92E-04	0
TS1	1.8	1.98E-04	15
I	2.1	∞	5
TS2	2.4	∞	22
constraint		2.00E+01	

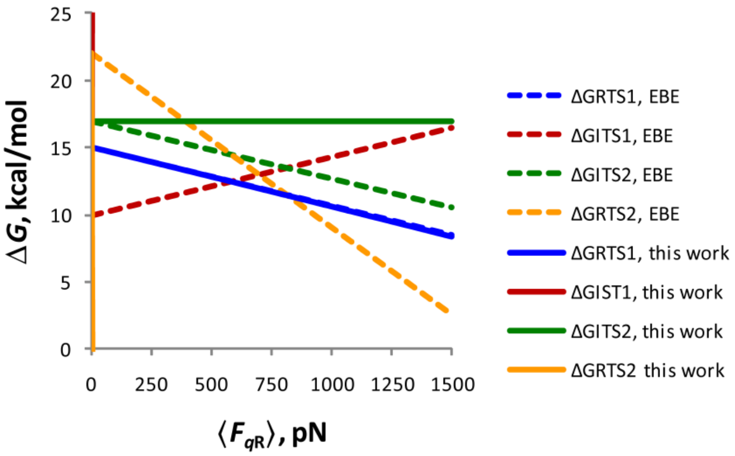

Fig. 7.28. Calculated force-dependent energy differences for the simulation of Type 2 kinetic crossover due to complete substrate rupture when R → I; parameters are in Table 7.9. Crossover occurs when the largest barrier in the forward direction changes from $\Delta G_{\mathrm{R,TS2}}(\langle F_{q\mathrm{R}}\rangle)$ (orange) to $\Delta G_{\mathrm{I,TS2}}(\langle F_{q\mathrm{R}}\rangle)$ (green); our model predicts this at and $\langle F_{q\mathrm{R}}\rangle > 0$.

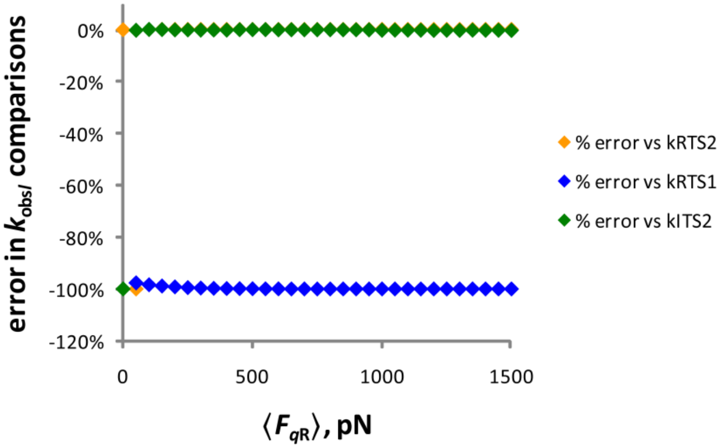

Fig. 7.29. Comparison of the simulated "observed" force-dependent rate constant for conversion of R to P to rate constants dictated by the indicated GS/TS pairs; parameters for the simulation are in Table 7.9.

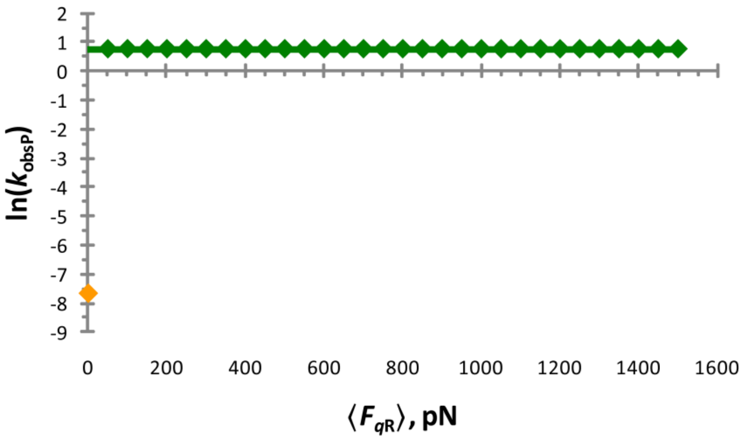

Fig. 7.30. Semi-logarithmic plot of the simulated “observed” force-dependent rate constant for conversion of R to P exhibiting Type 2 kinetic crossover at $\langle F_{q\mathrm{R}} \rangle > 0$; parameters for the simulation are in Table 7.9.

7.8.6 Materials and Instruments Used

Commercial reagents of the highest available purity from Aldrich or Fisher were used without further purification unless stated otherwise. Water was obtained from a Milli-Q water purification system. Analytical and preparative thin layer chromatography (TLC) was performed on silica gel 60 from Fisher and Aldrich. The concentrations of aqueous trifluoromethanesulfonic acid (TfOH) solutions were determined by titration with commercial standards. Tri-*n*-butylphosphine was a gift from Scott Daly in the Girolami lab.

Irradiation was performed in vessels sealed under N_2 using high-intensity diode light sources from Opto Technology with light output at 375 ± 7 nm. Light intensity was controlled with a custom-made constant-current controller. UV-vis absorption spectra were recorded on a Cary 50 UV-vis spectrophotometer. The diode light source was oriented 90° from the spectrophotometer beam path so that UV-vis absorbance spectra could be measured during irradiation to monitor reaction progress.

Analytical-scale HPLC was performed on a Shimadzu Prominence LC system with LC-20AT solvent delivery unit, DGU-20A5 degasser, SPD-M20A photodiode array detector, CBM-20A system controller, and Rheodyne 7725i manual injector, with either a J. T. Baker C_{18} column (25 cm × 4.6 mm, 5 µm particles), Supelco C_{18} column (15 cm × 4.6 mm, 5 µm particles), or Agilent Hypersil AA-ODS (C_{18}) column (20 cm × 2.1 mm, 5 µm particles).

High-resolution mass spectrometry (HRMS) was performed on a Micromass 70-VSE mass spectrometer (EI) or a Waters Q-Tof Ultima mass spectrometer (ESI) at the University of

Illinois Mass Spectrometry Center. NMR spectra of macrocycles **1**–**6** and synthetic intermediates were recorded on 400 or 500 MHz Unity-INOVA Varian spectrometers at room temperature (~20 °C). Chemical shifts are reported in ppm downfield from that of tetramethylsilane and are referenced to the residual ^{1}H resonances of the deuterated solvents. ^{31}P{^{1}H} resonances are reported in ppm downfield from 85% H_3PO_4, but were not externally referenced. Spin multiplicities are reported as singlet (s), doublet (d), triplet (t), quartet (q) and quintet (quint) with coupling constants (*J*) given in Hz or multiplet (m); br = broad; app = apparent.

Models were fitted to the kinetic data using custom-written scripts in Matlab (7.10.0 R2010a).

The synthesis and characterization of **1**–**6** is described in Chapter 4.

7.8.7 NMR Studies of Initial Disulfide Cleavage

In the absence of water, the zwitterionic intermediate of the reaction of disulfides with phosphines cannot continue on to phosphine oxide and dithiol. Because of this, the initial cleavage of macrocyclic disulfides can be examined conveniently by NMR spectroscopy. Tri-*n*-butylphsophine was used because it is a stronger nucleophile than triphenylphosphine or methyldiphenylphosphine (and thus it is more convenient to observe the cleavage process, which is significantly slower with triphenylphosphine and methyldiphenylphosphine), and its ^{1}H resonances do not obscure either the aromatic or alkyl resonances of macrocyclic disulfides. 1,3,5-Trioxane was used as a convenient internal standard for determining the concentrations of macrocycles and phosphine by preparing solutions of known concentration of trioxane in acetonitrile-d_3. Following the addition of phosphine or macrocycle, comparison of integrated areas (with sufficiently long relaxation delay times) of analyte to trioxane in the ^{1}H NMR spectra allowed for the determination of concentrations of analyte (phosphine or macrocycle) solutions. Reaction mixtures were the prepared by combining the appropriate amounts of each solution to achieve the desired molar ratio or phosphine to macrocycle.

The following chemical shifts were determined from spectra of the individual compounds: PBu_3: ^{1}H NMR (CD_3CN, 400 MHz): δ 0.897 (m, 9H), 1.362 (m, 18H); ^{31}P{^{1}H} NMR (CD_3CN, 162 MHz): δ -31.151. 1,3,5-trioxane: ^{1}H NMR (CD_3CN, 400 MHz): δ 5.108 (s, 6H).

As shown by the ^{1}H NMR spectra below, *Z***5** does not appear to react with PBu_3 in CD_3CN to any appreciable extent at RT over 3 d, implying that the reaction is either very slow or that the equilibrium is very unfavorable.

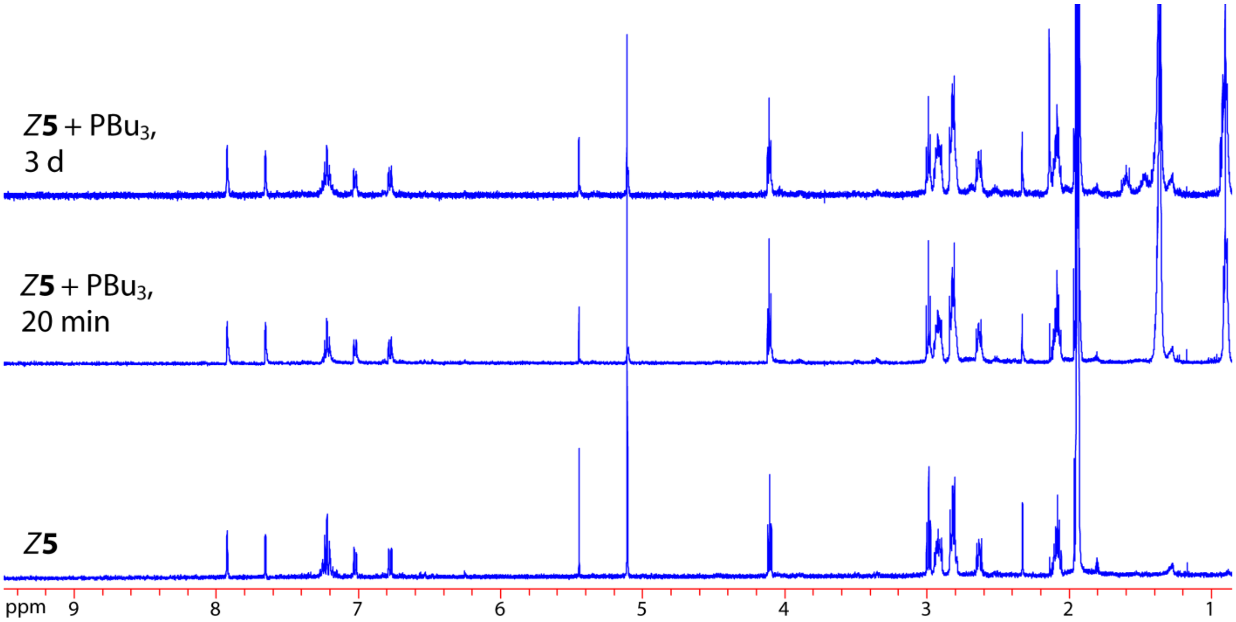

Fig. 7.31. ^{1}H NMR spectra of *Z***5** + PBu_3 in CD_3CN at RT

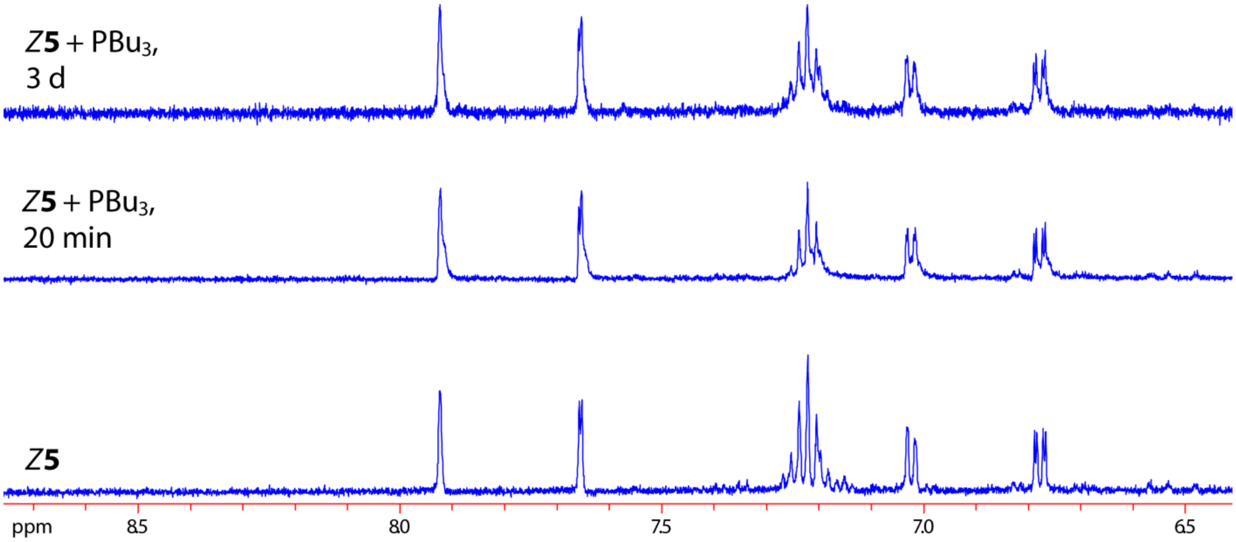

Fig. 7.32. Aromatic region of ^{1}H NMR spectra of *Z***5** + PBu_3 in CD_3CN at RT

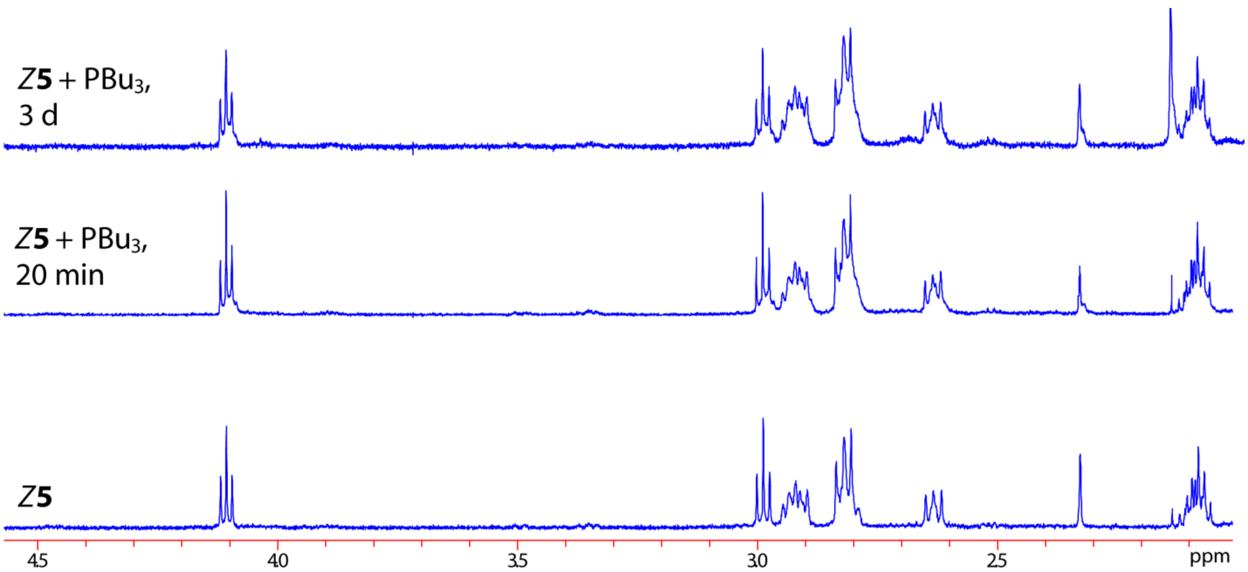

Fig. 7.33. Alkyl region of ^{1}H NMR spectra of *Z***5** + PBu$_3$ in CD$_3$CN at RT

The observation that *E***2** reacts rapidly with PBu$_3$ (apparent full conversion in < 20 min) under the same conditions, while *Z***2** does not, suggests an unfavorable equilibrium rather than an inherently slow process. The ^{31}P{^{1}H} NMR spectrum following the addition of PBu$_3$ shows a new (though broad and weak) signal at 209.80 ppm. The inference of an unfavorable equilibrium for the *Z* isomer is corroborated by the reported mechanism for disulfide reduction by phosphines in mixed aqueous-organic phases[87-89] and the pH-dependent kinetics measured by HPLC. The chemical identity of reaction products in the presence of water is discussed below.

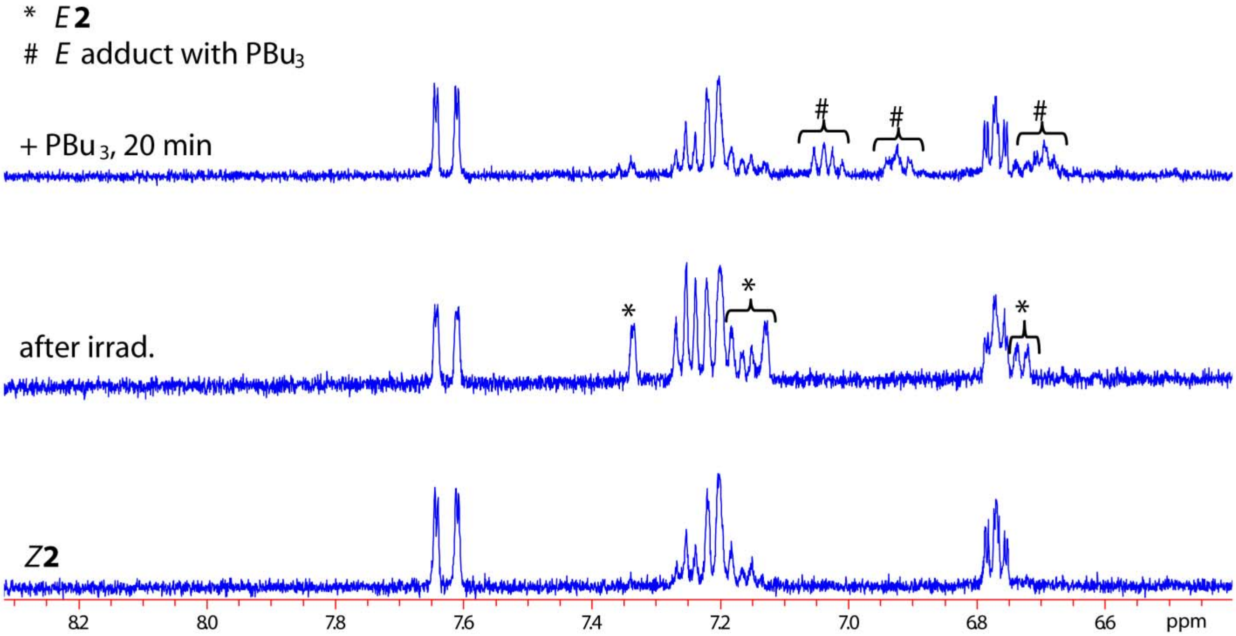

Fig. 7.34. Aromatic region of ^{1}H NMR spectra of a photostationary mixture of **2** + PBu$_3$

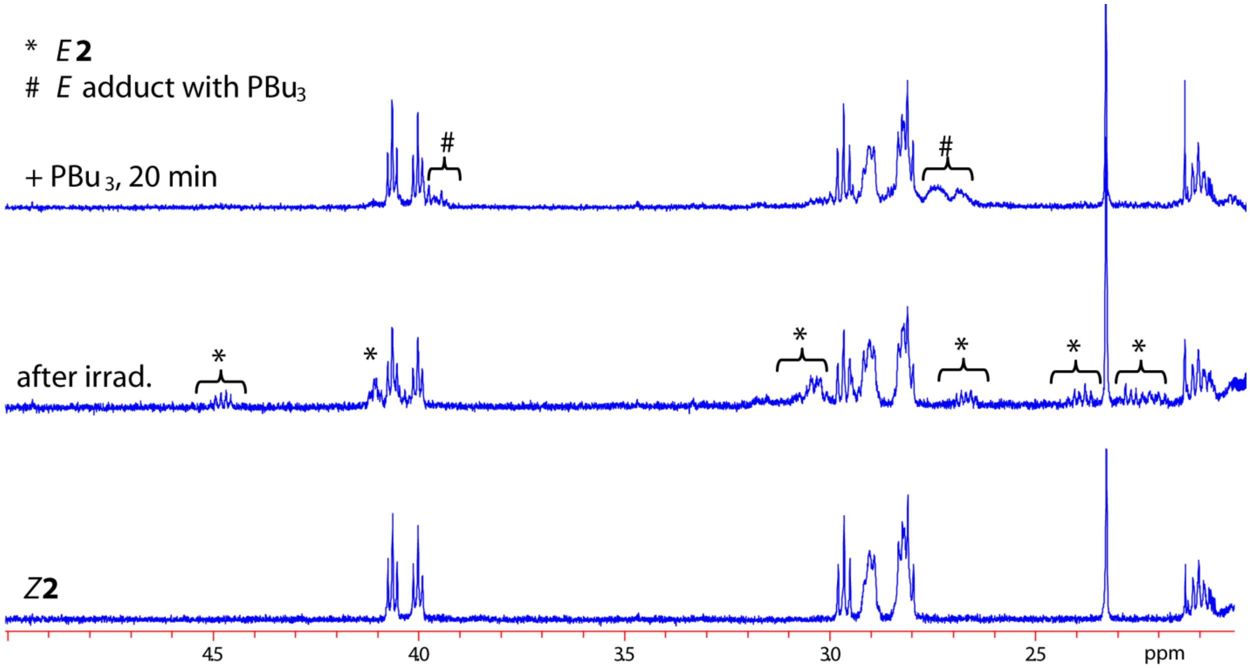

Fig. 7.35. Alkyl region of ^{1}H NMR spectra of the photostationary mixture of **2** + PBu$_3$

7.8.8 Kinetic Measurements

Experimental Methods

Photostationary mixtures of the *E* and *Z* isomers of disulfides **1**–**6** were prepared by irradiating a dilute solution of each *Z* isomer in acetonitrile in a cuvette sealed under N_2 with 375 nm light until the UV-vis absorption spectrum of the sample no longer changed over time. Stock solutions of the disulfides were stored at –35 °C under N_2. For the apparent composition of photostationary mixtures determined from HPLC chromatograms at 340 nm, see above.

We found that the reduction kinetics of **1**–**6** could be conveniently measured by analyzing the changing compositions of mixtures of different macrocycles. There was no measureable effect on the kinetics of any individual macrocycle from the presence of other macrocycles in the same reaction mixture. Based on the composition of the mixtures whose constituents could be conveniently separated (see below), one of two internal standards was used: *E***S34** or *Z***S10**. These two compounds were chosen because of their availability in high purity, their chemical inertness towards all other components in the reaction mixtures, and their retention times on reverse-phase HPLC.

The chemical identities of the products in the kinetics samples were confirmed by comparison of the retention times and UV spectra with those of authentic samples under identical separation conditions. Only disulfides and fully reduced dithiols were observed by HPLC. Our interpretation of the overall mechanism is further corroborated by the NMR studies described above and reports in the literature.[87-89] To prevent re-oxidation of the product dithiols by atmospheric oxygen, kinetics experiments were carried out in a glovebag under continuous N_2 purge. HPLC-grade acetonitrile and water used to prepare reaction mixtures were thoroughly sparged with N_2 before introduction into the glovebag. ^1H NMR spectroscopy confirmed that acetontrile solutions of PBu_3, PPh_3, and PPh_3Me were stable for weeks when prepared under these conditions and stored in vials sealed under N_2. Reactions were carried out in sealed vials, using a gas-tight syringe to withdraw samples for composition analysis by HPLC. These samples were transferred to clean vials and either analyzed immediately or sealed under N_2 and stored at –35 °C until analysis. For analysis, an ~100-µL aliquot was withdrawn from the sample vial with a gas-tight syringe through the septum without exposing the sample to air, and the sample was immediately injected into the HPLC system.

Reaction vials were held in a custom-made heating block with resistance heaters and a thermocouple connected to an active-feedback temperature controller which enabled the temperature of the reaction mixtures to be maintained with a stability of ±0.1 °C. The reaction temperature was recorded every 6 s. To prevent photoisomerization between *E* and *Z* isomers by ambient light, amber glass vials were used and all samples were kept away from light. No changes in *E*/*Z* ratios could be detected in samples stored for weeks under these conditions.

Reaction mixtures were prepared by diluting combinations of stock solutions of the disulfides or their photostationary mixtures (for compositions of mixtures, see below) with acetonitrile, water, trifluoromethanesulfonic acid (TfOH) in water, and phosphine in acetonitrile to give a total absorbance of ~0.3, corresponding to ~20 μM total concentration of disulfide, a total volume of 800 or 1200 μL, the desired concentrations of phosphine and TfOH, and a water/acetonitrile ratio of 37:13 (molar). Reaction mixtures were allowed to equilibrate to the temperature of the heating block before the addition of the phosphine solution. After the addition of the phosphine solution to the reaction mixture, the reaction vial was shaken vigorously for ~2 s and returned to the thermostated heating block. Samples were then collected at regular intervals, as described above. Stock solutions of phosphines used were sufficiently concentrated so that the volume of the addition required was minimal (~10–20 μL out of the total 800–1200 μL), minimizing cooling of the reaction mixture upon addition.

We did not measure the molar absorptivities of disulfides **1**–**6**. However, molar absorptivities of many similar stiff stilbene derivates previously measured in our lab were between ~14000 and ~15000 M^{-1} cm^{-1}. We used these values to estimate the concentrations of disulfides in solutions of **1**–**6**. The kinetic analysis does not require the knowledge of absolute concentrations or extinction coefficients provided that an order-of-magnitude estimate of macrocycle concentrations are known to assure pseudo-first order conditions given the concentration of phosphine used in a given experiment.

7.8.9 Compositional Analysis of Kinetics Samples by HPLC

The components of reaction mixtures were identified by matching retention times and UV spectra of authentic components (*Z* isomers) or photostationary mixtures (*Z*+*E* isomers to identify *E* isomers once *Z* isomers are known) under identical separation conditions. In all cases the peaks of interest were well separated from other peaks in the chromatogram. In cases where product peaks slightly overlapped (e.g., **5** photostationary state in water/methanol), the identities were still confirmed by the chromatograms of authentic samples. The kinetic analysis does not require the integrated areas of product peaks, so overlap of these peaks does not affect the quality of the kinetic data. In some cases not all of the product dithiols are listed (e.g., _Z_**S30** and _Z_**S31** are not listed in mixture E using water/acetonitrile) because these products did not form to any appreciable extent under the reaction conditions for which these separation conditions were used as evidenced both by the absence of those peaks and by the lack of decrease in the integrated area of the corresponding macrocyclic disulfide relative to that of the internal standard.

Table 7.10. Retention times of reaction mixture components using water/acetonitrile mobile phases

mixture A	_Z_**5**, _Z_**3**, _Z_**4**	
Shimadzu HPLC, JT Baker C$_{18}$ column, 10% H$_2$O in MeCN, 1 mL/min		
retention time, min	compound	UV absorption maxima, nm
4.52	**S34**	356, 339, 294
9.60	_Z_**S31**	348, 248
10.80	_Z_**S28**	344, 294, 247
12.18	_Z_**S30**	344, 245
14.80	_Z_**4**	247, 249
17.13	_Z_**5**	343, 295, 247
22.25	_Z_**3**	343, 247
mixture B	_Z_**6**, _Z_**1**, _Z_**2**	
Waters HPLC, Supelco C$_{18}$ column, 15% H$_2$O in MeCN, 1 mL/min		
retention time, min	compound	UV absorption maxima, nm
6.38	**S34**	356, 339, 294
11.81	_Z_**S29**	347, 297
16.09	_Z_**6**	347, 297
17.62	_Z_**S33**	347, 296
24.84	_Z_**S32**	342, 295
27.84	_Z_**2**	346
37.41	_Z_**1**	342
mixture D	**1** photostationary state, **2** photostationary state	
Shimadzu HPLC, Supelco C$_{18}$ column, 10% H$_2$O in MeCN, 1 mL/min		
retention time, min	compound	UV absorption maxima, nm
4.52	**S34**	356, 339, 294
6.02	_E_**2**	352, 344, 296
7.56	_E_**S33**	355, 349, 292
9.95	_Z_**S33**	348, 248
11.34	_E_**S23**	351, 335, 292
12.69	_E_**1**	350, 338, 296

Table 7.10 (cont.)

13.54	_Z_**S32**	344, 245
15.46	_Z_**2**	347, 249
20.25	_Z_**1**	343, 246
mixture E	**3** photostationary state, **4** photostationary state	
Waters HPLC, Agilent AA-ODS column, 19% H_2O in MeCN, 0.5 mL/min		
retention time, min	compound	UV absorption maxima, nm
4.44	**S34**	356, 339, 294
5.79	_E_**4**	346, 300
8.34	_E_**S31**	356, 339, 294
11.57	_E_**3**	338, 297
12.79	_E_**S30**	351, 335, 292
14.20	_Z_**4**	347, 297
22.98	_Z_**3**	342
mixture F	**5** photostationary state, **6** photostationary state	
Waters HPLC, Supelco C_{18} column, 15% H_2O in MeCN, 1 mL/min		
retention time, min	compound	UV absorption maxima, nm
6.39	**S34**	356, 339, 294
8.28	_E_**6**	354, 289
9.21	_E_**S29**	356, 339, 294
13.07	_E_**5**	348, 303
14.56	_E_**S28**	351, 355
16.12	_Z_**6**	347, 297
24.75	_Z_**5**	342, 295

Table 7.11. Retention times of reaction mixture components using water/methanol mobile phases

mixture A	_Z_**5**, _Z_**3**, _Z_**4**	
Shimadzu HPLC, JT Baker C_{18} column, 7% H_2O in MeOH, 1 mL/min		
retention time, min	compound	UV absorption maxima, nm
13.36	**S34**	353, 339
15.02	_Z_**S28**	342, 295
19.60	_Z_**S30**	342, 245
23.44	_Z_**4**	346, 248
28.57	_Z_**5**	342, 247
35.89	_Z_**3**	342, 246
mixture B	_Z_**6**, _Z_**1**, _Z_**2**	
Waters HPLC, Supelco C_{18} column, 5% H_2O in MeOH, 1 mL/min		
retention time, min	compound	UV absorption maxima, nm
6.10	**S34**	353, 337
7.46	_Z_**S29**	245, 296

Table 7.11 (cont.)

9.91	_Z_**S33**	346
11.42	_Z_**6**	346, 296
13.91	_Z_**S32**	341, 295
16.18	_Z_**2**	345
21.13	_Z_**1**	339
mixture D	**1** photostationary state, **2** photostationary state	
Waters HPLC, Supelco C$_{18}$ column, 5% H$_2$O in MeOH, 1 mL/min		
retention time, min	compound	UV absorption maxima, nm
4.99	_Z_**S10**	341, 295
6.00	_E_**2**	351, 295
11.45	_E_**1**	336, 295
15.97	_Z_**2**	345, 250
20.83	_Z_**1**	340
mixture E	**3** photostationary state, **4** photostationary state	
Shimadzu HPLC, JT Baker C$_{18}$ column, 2% H$_2$O in MeOH, 1 mL/min		
retention time, min	compound	UV absorption maxima, nm
5.63	_E_**4**	354, 345
8.22	_E_**3**	350, 338, 297
8.96	**S34**	353, 337
12.77	_Z_**4**	355, 346
17.65	_Z_**3**	342, 246
5 photostationary state		
Waters HPLC, Supelco C$_{18}$ column, 5% H$_2$O in MeOH, 1 mL/min		
retention time, min	compound	UV absorption maxima, nm
6.086	**S34**	353, 338, 292
7.498	_E_**5**	346, 302
9.75	_E_**S28**, _Z_**S28**	348, 292
15.02	_Z_**5**	341, 295
6 photostationary state		
Waters HPLC, Supelco C$_{18}$ column, 5% H$_2$O in MeOH, 1 mL/min		
retention time, min	compound	UV absorption maxima, nm
5.50	_E_**6**	354, 289
6.22	**S34**	353, 338, 292
7.08	_E_**S29**	354, 338, 294
7.37	_Z_**S29**	353
11.64	_Z_**6**	346, 296

7.8.10 Kinetic Model for pH-Dependent Disulfide Reduction by Phosphines

In the overall reduction of disulfides by phosphines to produce dithiols and phosphine oxides, one equivalent of phosphine and one equivalent of water are consumed; though free H^+ can protonate the intermediate, it is regenerated in the overall chemical transformation, and thus only the initial concentration need be known. Kinetics experiments were carried out with excess phosphine (250-fold excess for PPh_3, 10–220-fold excess for PPh_2Me) and excess water (74 mol% of the solvent); in all cases, pseudo-first order kinetics were observed, as evidenced by good fits to semi-logarithmic plots of $\ln(R/R_0)$ vs. t and linear increases in observed rates with increases in phosphine concentration. For *Z* isomers, the application of the steady state approximation is justified by both the observation of overall pseudo-first order kinetics and the NMR studies discussed above which indicate that the intermediate is both highly reactive and is present in small quantities. In the following derivation of the rate laws, the square brackets indicating molar concentrations of species have been omitted for clarity.

The reaction scheme for the reduction of *Z* macrocyclic disulfides by phosphines is shown in Fig. 7.36.

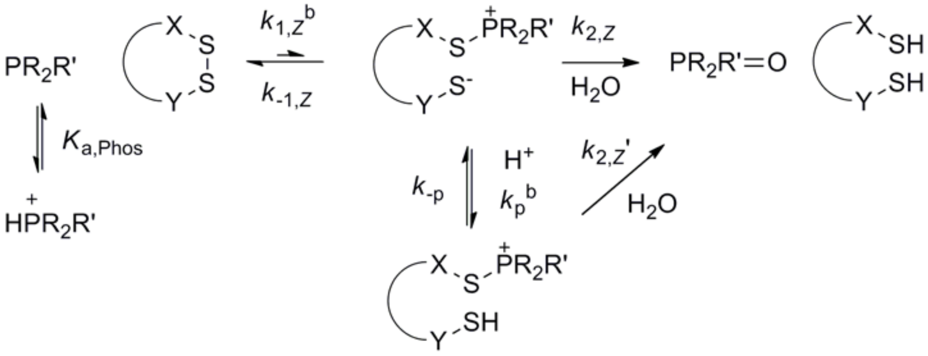

Fig. 7.36. Reaction scheme for the reduction of *Z* macrocyclic disulfides by phosphines

The pseudo-first order rate constants k_1 and k_p are given by eqs. (7.60) and (7.61), where the superscripts ^{b} indicate bimolecular rate constants, *Phos* is the concentration of free phosphine, and *H* is the concentration of H^+ in solution.

$$k_1 = k_1^{\mathrm{b}} Phos \tag{7.60}$$

$$k_{\mathrm{p}} = k_{\mathrm{p}}^{\mathrm{b}} H \tag{7.61}$$

The system is described by the system differential equations (7.62)–(7.65), where *R*, *Int*, *IntH*, and *Prod* are the molar concentrations of reactant, intermediate, protonated intermediate and product, respectively.

$$\frac{dR}{dt} = -k_1 R + k_{-1} Int \tag{7.62}$$

$$\frac{dInt}{dt} = k_1 R + k_{-\mathrm{p}} IntH - \left(k_{-1} + k_{\mathrm{p}} + k_2\right) Int \tag{7.63}$$

$$\frac{dIntH}{dt} = k_{\mathrm{p}} Int - \left(k_{-\mathrm{p}} + k_2{}'\right) IntH \tag{7.64}$$

$$\frac{dProd}{dt} = k_2 Int + k_2{}' IntH \tag{7.65}$$

Assuming a steady state ($dInt/dt = dIntH/dt = 0$) and rearranging yields eq. (7.66). Thus, the reaction should exhibit apparent first-order behavior (as is observed), and k_{obs} can be obtained from plots of $\ln(R/R_0)$ vs. t. Note that in the limit of low pH, the reverse reaction is suppressed (eq. (7.67)) so that k_{obs} is only k_1, and in the limit of high pH the reaction exhibits the behavior of a two-step sequence with a reversible first step (eq. (7.68)).

$$\frac{dR}{dt} = k_1 \left(\frac{k_{-1}\left(k_{-\mathrm{p}} + k_2{}'\right)}{\left(k_{-1} + k_{\mathrm{p}} + k_2\right)\left(k_{-\mathrm{p}} + k_2{}'\right) - k_{-\mathrm{p}} k_{\mathrm{p}}} - 1 \right) R = -k_{\mathrm{obs}} R \tag{7.66}$$

$$\lim_{H \to \infty} k_{\mathrm{obs}} = k_1 \tag{7.67}$$

$$\lim_{H \to 0} k_{\mathrm{obs}} = \frac{k_1 k_2}{k_{-1} + k_2} \tag{7.68}$$

For the E isomers, the first step should be irreversible, because all of the strain is relieved in the intermediate (i.e., once the disulfide is cleaved, the stiff stilbene relaxes to the fully E configuration, moving the phosphonium and thiolate moieties away from each other, preventing intramolecular recombination). The kinetic scheme is shown in Fig. 7.37, and $k_{\mathrm{obs}} = k_1$.

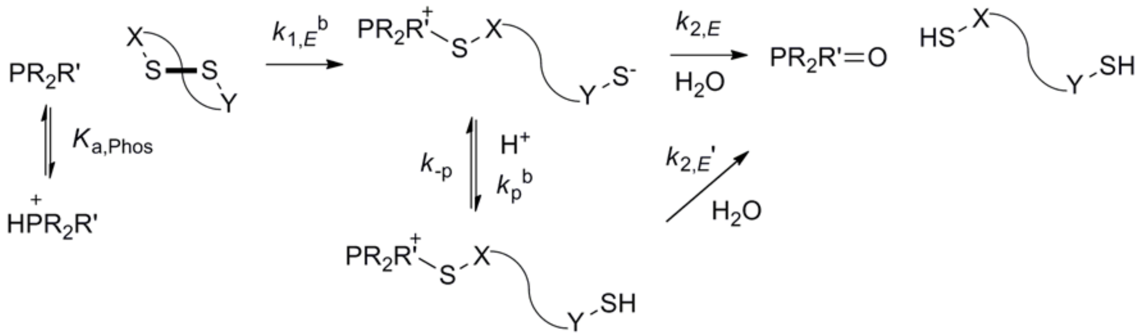

Fig. 7.37. Reaction scheme for the reduction of E macrocyclic disulfides by phosphines

The ratio of observed rates is given by eq. (7.69), which simplifies (without any assumptions) to eq. (7.70) where the constant K' is given by eq. (7.71), rate constants without E or Z specified are for Z, $^{\mathrm{b}}$ indicates a bimolecular rate constant, and other rate constants are first order. H is the molar concentration of H^+ in solution.

$$\frac{k_{E\mathrm{obs}}}{k_{Z\mathrm{obs}}} = \frac{k_{1E}}{k_{1Z}\left(1 - \dfrac{k_{-1}\left(k_{-\mathrm{p}} + k_2{}'\right)}{\left(k_{-1} + k_{\mathrm{p}} + k_2\right)\left(k_{-\mathrm{p}} + k_2{}'\right) - k_{-\mathrm{p}}k_{\mathrm{p}}}\right)} \tag{7.69}$$

$$\frac{k_{E\mathrm{obs}}}{k_{Z\mathrm{obs}}} = \frac{k_{1E}^{\mathrm{b}}}{k_{1Z}^{\mathrm{b}}}\left(1 + \frac{k_{-1}}{k_2}\left(1 - \frac{H}{K' + H}\right)\right) \tag{7.70}$$

$$K' = \frac{k_2\left(k_{-\mathrm{p}} + k_2{}'\right)}{k_{\mathrm{p}}^{\mathrm{b}}k_2{}'} \tag{7.71}$$

Defining T_{H} as the total concentration of acid initially added to the reaction mixture (eq. (7.72)) and T_{phos} as the total concentration of phosphine initially added to the reaction mixture (eq. (7.73)), H is determined from the equilibration of H^+ with free phosphine (eq. (7.74)), and the concentration of free phosphine, $Phos$, is given by eq. (7.75).

$$T_{\mathrm{H}} = H + T_{\mathrm{phosH}} + IntH \approx H + T_{\mathrm{phosH}} = H + T_{\mathrm{phos}} - \frac{T_{\mathrm{phos}}K_{\mathrm{a,phos}}}{K_{\mathrm{a,phos}} + H} \tag{7.72}$$

$$T_{\mathrm{phos}} = Phos + PhosH + Int + IntH + Prod \approx Phos + PhosH \tag{7.73}$$

$$H = \frac{1}{2}\left(T_{\mathrm{H}} - K_{\mathrm{a,phos}} - T_{\mathrm{phos}} + \sqrt{4K_{\mathrm{a,phos}}T_{\mathrm{H}} + \left(K_{\mathrm{a,phos}} - T_{\mathrm{H}} + T_{\mathrm{phos}}\right)^2}\right) \tag{7.74}$$

$$Phos = \frac{T_{\mathrm{phos}}K_{\mathrm{a,phos}}}{K_{\mathrm{a,phos}} + H} \tag{7.75}$$

Note that given a set of reasonable parameter values(T_{phos} = 5 mM, $k_{E1}{}^{\mathrm{b}}/k_{Z1}{}^{\mathrm{b}} = 1.5$, $k_{-1}/k_2 = 5 \times 10^6$, $K' = 5 \times 10^{-9}$, $\mathrm{p}K_{\mathrm{a,phos}} = 3$), the expression for $k_{E\mathrm{obs}}/k_{Z\mathrm{obs}}$ (red, Fig. 7.38) exhibits the expected titration-like behavior.

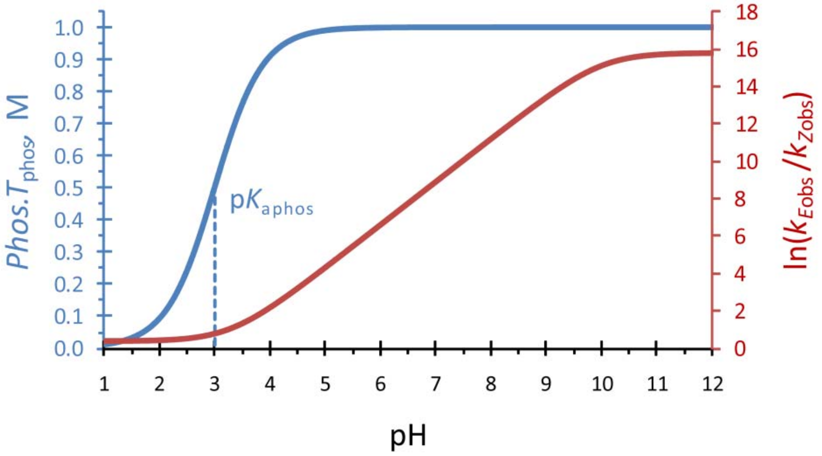

Fig. 7.38. Example calculation of the effect of changes in pH on ln($k_{E\mathrm{obs}}/k_{Z\mathrm{obs}}$)

Eq. (7.70) was simultaneously fitted to all of the rate constants obtained as k_{obs} from plots of ln(R/R_0) vs. t) with a given phosphine, determining values of k_{1E}^{b}/k_{1Z}^{b}, k_{-1}/k_2 and K' for each macrocycle and a single value for pK_{aphos} for the phosphine in water/acetonitrile 37:13 (molar). Fitting was carried out in Matlab using custom-written scritps to optimize the parameters through a least-squares regression, in each case employing the methods described by Gans[98] to calculate the variance-covariance matrix for the fitted parameters from the Jacobian returned by the lsqnonlin function in Matlab. In all cases, the optimization found (local) minima (presumably other minima could be found with non-physically meaningful values of the parameters). There were too few data points to apply a meaningful χ^2 goodness-of-fit test on the residuals; instead the correlation coefficients (R^2) for the fits of individual macrocycles are reported. Errors on the originally measured values were propagated through the calculations by solving the total differential for each fitted parameter in the kinetic model. Errors reported for the fitted parameters are a sum of the errors propagated and the error introduced by the regression itself.

7.8.11 Observed Rate Constants and Fitted Parameters

Reduction of *E***1**–*E***6** by PPh_2Me proceeded quickly enough under neutral conditions that it was possible to determine the observed rate constants for their reduction at multiple temperatures (Table 7.12). Because the first step in the reduction of *E* macrocyclic disulfides is irreversible, these observed rate constants characterize the energy required to traverse the first barrier in the forward direction. Thus, the Eyring plots and derived activation parameters for these data are shown below (Fig. 7.39, in most cases the error bars are smaller than the symbols; Table 7.13). The reduction of *E* macrocyclic disulfides by PPh_3 under neutral conditions was too slow at temperatures lower than 338 K to allow for convenient determination of the rate constants. This observation is in agreement with reports in the literature.[89]

Table 7.12. Observed rate constants for the reduction of *E***1**–*E***6** by PPh_2Me under neutral conditions

macrocycle	T, °C	T_{phos}, M	k_{obs}, s^{-1}	s
1	60	0.0002	3.0E-04	3E-05
	40	0.0002	1.37E-04	1E-06
	25	0.0002	6.27E-05	8E-07
2	60	0.0002	8.2E-04	8E-05
	40	0.0002	3.6E-04	1E-05

Table 7.12 (cont.)

	25	0.0002	1.53E-04	2E-06
3	60	0.0002	5.5E-04	4E-05
	40	0.0002	1.80E-04	5E-06
	25	0.0002	8.22E-05	8E-07
4	60	0.0002	1.30E-03	8E-05
	40	0.0002	4.4E-04	4E-05
	25	0.0002	2.20E-04	7E-06
5	60	0.0002	8E-04	3E-04
	40	0.0002	2.3E-04	4E-05
	10	0.0005	1.17E-04	3E-06
6	60	0.0002	3E-03	2E-03
	40	0.0002	1.1E-03	2E-04
	10	0.0005	4.8E-04	1E-05

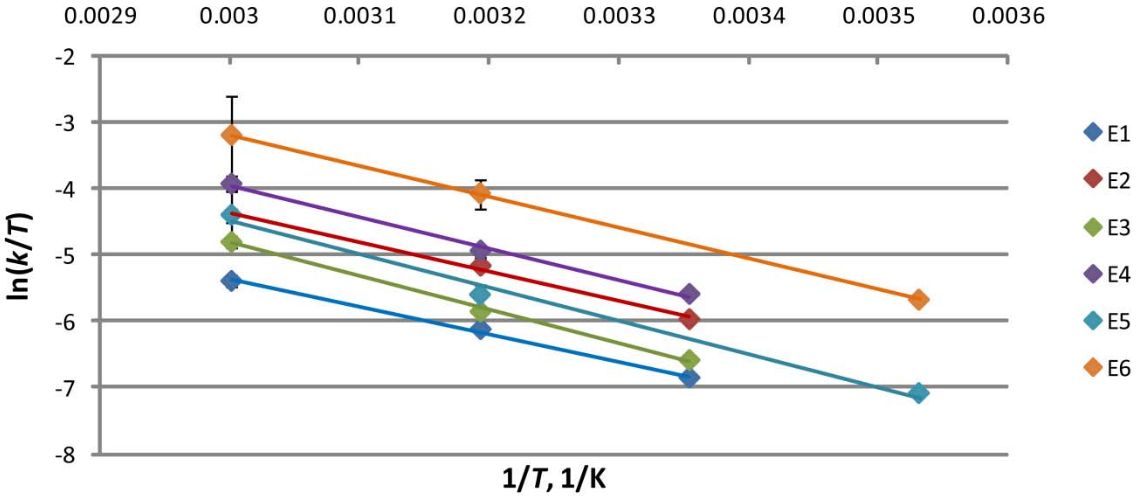

Fig. 7.39. Eyring plots for the reduction of *E***1**–*E***6** by PPh_2Me under neutral conditions

Table 7.13. Activation parameters for initial disulfide cleavage in *E***1**–*E***6** by PPh_2Me under neutral conditions

macrocycle	$\Delta H^{\ddagger}$, kcal/mol	$\Delta S^{\ddagger}$, e.u
*E***1**	8.2 ± 0.4	-33 ± 1
*E***2**	8.8 ± 0.6	-29 ± 2
*E***3**	10.1 ± 0.5	-26 ± 2
*E***4**	9.4 ± 0.7	-27 ± 2
*E***5**	10 ± 1	-26 ± 3
*E***6**	9.3 ± 0.1	-25.6 ± 0.3

For *Z***1**–*Z***6**, the reduction by either PPh_3 or PPh_2Me under neutral conditions did not occur to any measurable extent (see NMR experiments and discussion in section 7.8.7 above). The average observed rate constants in the presence of varied amounts of TfOH (T_H) and phosphine (T_{phos}) for the reduction of both isomers of disulfides **1**–**6** by PPh_3 and PPh_2Me are shown in Fig. 7.40, Fig. 7.41, Table 7.16 and Table 7.17. Because the bimolecular rate constants for reduction of the *E* isomers can be determined solely from the values of k_{Eobs} and *Phos* (i.e., k_{Eobs} at a single combination of T_H and T_{phos} provides sufficient information for the fitting method used), the reduction of the *E* isomers was not carried out at multiple combinations of T_H and T_{phos} in all cases. The fitted values of $pK_{a,phos}$ in this solvent mixture for PPh_3 and PPh_2Me were indistinguishable within the uncertainties of the fits ($pK_{a,phos} \approx 3.4$).

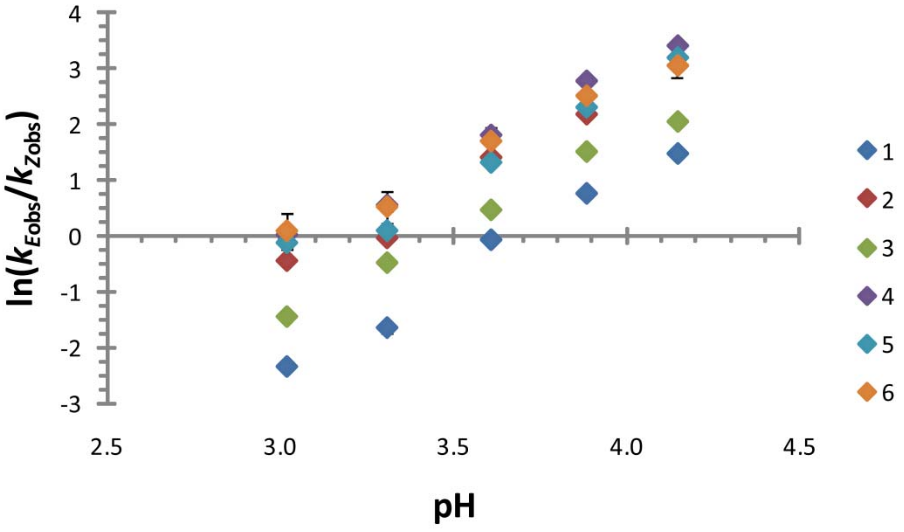

Fig. 7.40. pH-dependent acceleration of the reduction of **1**–**6** by PPh_3 at 338 K

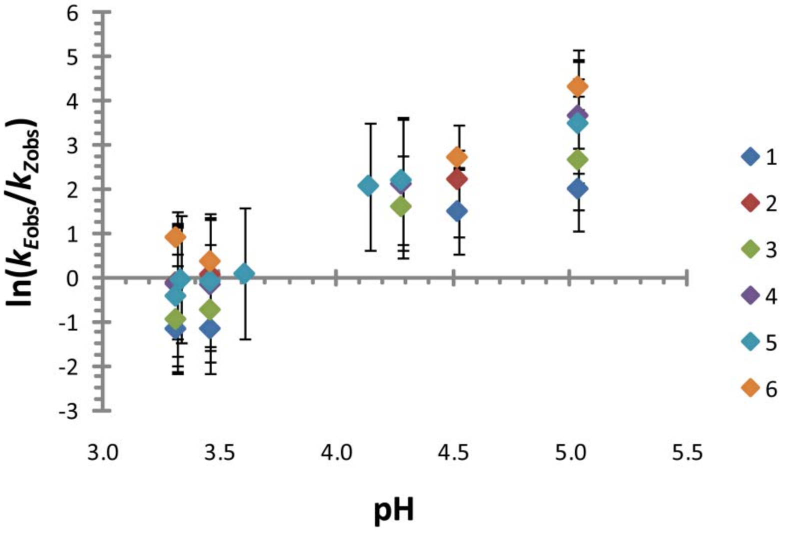

Fig. 7.41. pH-dependent acceleration of the reduction of **1**–**6** by PPh_2Me at 338 K

Table 7.14. Observed pH-dependent rate constants and standard errors *s* for the reduction of **1**–**6** by PPh_3 at 338 K

	***Z* isomers**				***E* isomers**			
macrocycle	T_H, M	T_{phos}, M	average k_{obs}, s^{-1}	*s*	T_H, M	T_{phos}, M	average k_{obs}, s^{-1}	*s*
1	3.15×10^{-4}	5.00×10^{-3}	1.43×10^{-4}	1×10^{-7}	0	5.00×10^{-3}	7.27×10^{-4}	4.06×10^{-6}
	5.60×10^{-4}	5.00×10^{-3}	2.59×10^{-4}	4×10^{-7}				
	1.00×10^{-3}	5.00×10^{-3}	4.87×10^{-4}	3×10^{-6}				
	1.80×10^{-3}	5.00×10^{-3}	1.7×10^{-3}	2×10^{-4}				
	3.00×10^{-3}	5.00×10^{-3}	2.2×10^{-3}	1×10^{-4}				
2	3.15×10^{-4}	5.00×10^{-3}	9.53×10^{-5}	1×10^{-7}	0	5.00×10^{-3}	2.36×10^{-3}	3.07×10^{-5}
	5.60×10^{-4}	5.00×10^{-3}	2.03×10^{-4}	1×10^{-7}				
	1.00×10^{-3}	5.00×10^{-3}	3.62×10^{-4}	1×10^{-6}				
	1.80×10^{-3}	5.00×10^{-3}	1.12×10^{-3}	2×10^{-5}				
	3.00×10^{-3}	5.00×10^{-3}	1.11×10^{-3}	2×10^{-5}				
3	3.15×10^{-4}	5.00×10^{-3}	1.23×10^{-4}	3×10^{-8}	0	5.00×10^{-3}	1.12×10^{-3}	2.49×10^{-5}
	5.60×10^{-4}	5.00×10^{-3}	1.87×10^{-4}	2×10^{-7}				
	1.00×10^{-3}	5.00×10^{-3}	4.36×10^{-4}	2×10^{-6}				
	1.80×10^{-3}	5.00×10^{-3}	8.1×10^{-4}	2×10^{-5}				
	3.00×10^{-3}	5.00×10^{-3}	1.40×10^{-3}	3×10^{-5}				
4	3.15×10^{-4}	5.00×10^{-3}	1.18×10^{-4}	2×10^{-8}	0	5.00×10^{-3}	4.18×10^{-3}	5.01×10^{-5}
	5.60×10^{-4}	5.00×10^{-3}	1.97×10^{-4}	1×10^{-7}				

Table 7.14 (cont.)

	1.00×10^{-3}	5.00×10^{-3}	4.24×10^{-4}	2×10^{-6}				
	1.80×10^{-3}	5.00×10^{-3}	1.1×10^{-3}	1×10^{-4}				
	3.00×10^{-3}	5.00×10^{-3}	1.20×10^{-3}	6×10^{-5}				
5	3.15×10^{-4}	5.00×10^{-3}	9.65×10^{-5}	6×10^{-7}	0	5.00×10^{-3}	2.68×10^{-3}	7.34×10^{-5}
	5.60×10^{-4}	5.00×10^{-3}	2.08×10^{-4}	2×10^{-7}	1.00×10^{-4}	5.00×10^{-3}	2.88×10^{-3}	7.26×10^{-5}
	1.00×10^{-3}	5.00×10^{-3}	4.60×10^{-4}	2×10^{-6}	3.15×10^{-4}	5.00×10^{-3}	2.51×10^{-3}	3.92×10^{-5}
	1.80×10^{-3}	5.00×10^{-3}	1.13×10^{-3}	8×10^{-6}	5.60×10^{-4}	5.00×10^{-3}	2.78×10^{-3}	1.79×10^{-5}
	3.00×10^{-3}	5.00×10^{-3}	9.23×10^{-4}	6×10^{-6}	1.00×10^{-3}	5.00×10^{-3}	2.08×10^{-3}	3.63×10^{-5}
6	3.15×10^{-4}	5.00×10^{-3}	2.35×10^{-4}	1×10^{-6}	0	5.00×10^{-3}	6.9×10^{-3}	1.70×10^{-4}
	5.60×10^{-4}	5.00×10^{-3}	3.60×10^{-4}	3×10^{-6}	1.00×10^{-4}	5.00×10^{-3}	6.5×10^{-3}	3.90×10^{-4}
	1.00×10^{-3}	5.00×10^{-3}	6.68×10^{-4}	4×10^{-6}	3.15×10^{-4}	5.00×10^{-3}	3.33×10^{-3}	4.09×10^{-5}
	1.80×10^{-3}	5.00×10^{-3}	1.58×10^{-3}	4×10^{-5}	3.15×10^{-4}	5.00×10^{-3}	4.9×10^{-3}	3.19×10^{-4}
	3.00×10^{-3}	5.00×10^{-3}	1.60×10^{-3}	6×10^{-5}	5.60×10^{-4}	5.00×10^{-3}	3.8×10^{-3}	2.60×10^{-4}
					5.60×10^{-4}	5.00×10^{-3}	4.9×10^{-3}	3.16×10^{-4}
					1.00×10^{-3}	5.00×10^{-3}	4.4×10^{-3}	5.03×10^{-4}
					3.00×10^{-3}	5.00×10^{-3}	4.7×10^{-3}	3.40×10^{-4}

Table 7.15. Observed pH-dependent rate constants and standard errors *s* for the reduction of **1**–**6** by PPh_2Me at 338 K

macrocycle	***Z* isomers**				***E* isomers**			
	T_H, M	T_{phos}, M	average k_{obs}, s^{-1}	*s*	T_H, M	T_{phos}, M	average k_{obs}, s^{-1}	*s*
1	1.00×10^{-4}	4.50×10^{-3}	1.13×10^{-3}	4×10^{-6}	0	2.00×10^{-4}	3.8×10^{-4}	4×10^{-4}
	3.15×10^{-4}	4.50×10^{-3}	1.79×10^{-3}	2×10^{-5}				
	5.60×10^{-4}	5.00×10^{-4}	1.7×10^{-3}	4×10^{-4}				
	1.00×10^{-3}	1.00×10^{-3}	2.9×10^{-3}	4×10^{-4}				
2	1.00×10^{-4}	4.50×10^{-3}	6.02×10^{-4}	2×10^{-6}	0	2.00×10^{-4}	1.0×10^{-3}	1×10^{-3}
	3.15×10^{-4}	4.50×10^{-3}	2.41×10^{-3}	4×10^{-5}				
	5.60×10^{-4}	5.00×10^{-4}	1.4×10^{-3}	2×10^{-4}				
	1.00×10^{-3}	1.00×10^{-3}	2.8×10^{-3}	2×10^{-4}				
3	1.00×10^{-4}	4.50×10^{-3}	1.04×10^{-3}	8×10^{-6}	0	2.00×10^{-4}	6.8×10^{-4}	8×10^{-4}
	3.15×10^{-4}	2.50×10^{-3}	1.53×10^{-3}	8×10^{-5}				
	5.60×10^{-4}	5.00×10^{-4}	2.0×10^{-3}	3×10^{-4}				

Table 7.15 (cont.)

	1.00×10^{-3}	1.00×10^{-3}	4×10^{-3}	2×10^{-3}				
4	1.00×10^{-4}	4.50×10^{-3}	9.15×10^{-4}	7×10^{-6}	0	2.00×10^{-4}	1.6×10^{-3}	2×10^{-3}
	3.15×10^{-4}	2.50×10^{-3}	2.2×10^{-3}	2×10^{-4}				
	5.60×10^{-4}	5.00×10^{-4}	2.6×10^{-3}	4×10^{-4}				
	1.00×10^{-3}	1.00×10^{-3}	4×10^{-3}	3×10^{-3}				
5	1.00×10^{-4}	4.50×10^{-3}	1.07×10^{-3}	9×10^{-6}	0	2.00×10^{-4}	9.3×10^{-4}	2×10^{-3}
	1.00×10^{-4}	2.00×10^{-4}	1.7×10^{-4}	1×10^{-5}	0	2.00×10^{-4}	1.3×10^{-3}	3×10^{-4}
	3.15×10^{-4}	2.50×10^{-3}	1.9×10^{-3}	1×10^{-4}	1.00×10^{-4}	2.00×10^{-4}	1.2×10^{-3}	1×10^{-4}
	3.15×10^{-4}	2.00×10^{-4}	9×10^{-4}	3×10^{-4}	3.15×10^{-4}	2.00×10^{-4}	1.3×10^{-3}	6×10^{-4}
	5.60×10^{-4}	5.00×10^{-4}	2×10^{-3}	1×10^{-3}	5.60×10^{-4}	2.00×10^{-4}	1.1×10^{-3}	2×10^{-4}
	5.60×10^{-4}	2.00×10^{-4}	8×10^{-4}	1×10^{-4}				
	1.00×10^{-3}	1.00×10^{-3}	6×10^{-3}	4×10^{-3}				
6	1.00×10^{-4}	4.50×10^{-3}	1.03×10^{-3}	4×10^{-6}	0	2.00×10^{-4}	3.4×10^{-3}	7×10^{-4}
	3.15×10^{-4}	4.50×10^{-3}	4.8×10^{-3}	1×10^{-4}				
	5.60×10^{-4}	5.00×10^{-4}	3×10^{-3}	1×10^{-3}				
	1.00×10^{-3}	1.00×10^{-3}	3.4×10^{-3}	9×10^{-4}				

Table 7.16. Fitted parameters for disulfide reduction by PPh_3 at 338 K

macrocycle	k_{1E}^{b}/k_{1Z}^{b}	k_{-1}/k_2	K'
1	1.5 ± 0.3	$(21 \pm 48) \times 10^{5}$	$(0.2 \pm 0.9) \times 10^{-10}$
2	1.6 ± 1.2	$(15 \pm 12) \times 10^{5}$	$(2 \pm 1.2) \times 10^{-10}$
3	2.3 ± 0.2	$(23 \pm 28) \times 10^{5}$	$(0.3 \pm 0.5) \times 10^{-10}$
4	2.4 ± 0.5	$(20 \pm 11) \times 10^{5}$	$(1.6 \pm 0.6) \times 10^{-10}$
5	3.4 ± 0.2	$(21 \pm 10) \times 10^{5}$	$(0.7 \pm 0.4) \times 10^{-10}$
6	2.9 ± 0.2	$(16 \pm 9) \times 10^{5}$	$(1.1 \pm 0.6) \times 10^{-10}$

Table 7.17. Fitted parameters for disulfide reduction by PPh_2Me at 338 K

macrocycle	k_{1E}^{b}/k_{1Z}^{b}	k_{-1}/k_2	K'
1	1.3 ± 0.6	$(7 \pm 10) \times 10^{5}$	$(0.8 \pm 2.4) \times 10^{-10}$
2	2.2 ± 0.3	$(11 \pm 7) \times 10^{5}$	$(1.3 \pm 0.9) \times 10^{-10}$
3	2.4 ± 0.1	$(9 \pm 8) \times 10^{5}$	$(0.5 \pm 1) \times 10^{-10}$
4	2.1 ± 0.4	$(14 \pm 9) \times 10^{5}$	$(1.1 \pm 0.8) \times 10^{-10}$
5	2.5 ± 0.2	$(7 \pm 4) \times 10^{5}$	$(1.5 \pm 1.4) \times 10^{-10}$
6	3.4 ± 0.2	$(16 \pm 6) \times 10^{5}$	$(1.2 \pm 0.4) \times 10^{-10}$

7.9 References

1. Kucharski, T. J.; Boulatov, R., The Physical Chemistry of Mechanoresponsive Polymers. *J. Mater. Chem.* **2011**, *21*, 8237–8255.
2. Lee, C. K.; Davis, D. A.; White, S. R.; Moore, J. S.; Sottos, N. R.; Braun, P. V., Force-Induced Redistribution of a Chemical Equilibrium. *J. Am. Chem. Soc.* **2010**, *132*, 16107–16111.
3. Davis, D. A.; Hamilton, A.; Yang, J.; Cremar, L. D.; Van Gough, D.; Potisek, S. L.; Ong, M. T.; Braun, P. V.; Martinez, T. J.; White, S. R.; Moore, J. S.; Sottos, N. R., Force-Induced Activation of Covalent Bonds in Mechanoresponsive Polymeric Materials. *Nature* **2009**, *459*, 68–72.
4. Caruso, M. M.; Davis, D. A.; Shen, Q.; Odom, S. A.; Sottos, N. R.; White, S. R.; Moore, J. S., Mechanically-Induced Chemical Changes in Polymeric Materials. *Chem. Rev.* **2009**, *109*, 5755–5798.
5. Lenhardt, J. M.; Ong, M. T.; Choe, R.; Evenhuis, C. R.; Martinez, T. J.; Craig, S. L., Trapping a Diradical Transition State by Mechanochemical Polymer Extension. *Science* **2010**, *329*, 1057–1060.
6. Lenhardt, J. M.; Black, A. L.; Craig, S. L., gem-Dichlorocyclopropanes as Abundant and Efficient Mechanophores in Polybutadiene Copolymers under Mechanical Stress. *J. Am. Chem. Soc.* **2009**, *131*, 10818–10819.
7. Wiggins, K. M.; Hudnall, T. W.; Shen, Q.; Kryger, M. J.; Moore, J. S.; Bielawski, C. W., Mechanical Reconfiguration of Stereoisomers. *J. Am. Chem. Soc.* **2010**, *132*, 3256–3257.

8. Kryger, M. J.; Ong, M. T.; Odom, S. A.; Sottos, N. R.; White, S. R.; Martinez, T. J.; Moore, J. S., Masked Cyanoacrylates Unveiled by Mechanical Force. *J. Am. Chem. Soc.* **2010**, *132*, 4558–4559.
9. Piermattei, A.; Karthikeyan, S.; Sijbesma, R. P., Activating Catalysts with Mechanical Force. *Nat Chem* **2009**, *1*, 133–137.
10. Karthikeyan, S.; Potisek, S. L.; Piermattei, A.; Sijbesma, R. P., Highly Efficient Mechanochemical Scission of Silver-Carbene Coordination Polymers. *J. Am. Chem. Soc.* **2008**, *130*, 14968–14969.
11. Park, I.; Shirvanyants, D.; Nese, A.; Matyjaszewski, K.; Rubinstein, M.; Sheiko, S. S., Spontaneous and Specific Activation of Chemical Bonds in Macromolecular Fluids. *J. Am. Chem. Soc.* **2010**, *132*, 12487–12491.
12. Sheiko, S. S.; Sun, F. C.; Randall, A.; Shirvanyants, D.; Rubinstein, M.; Lee, H.-i.; Matyjaszewski, K., Adsorption-induced scission of carbon-carbon bonds. *Nature* **2006**, *440*, 191–194.
13. Schliwa, M., *Molecular Motors*. Wiley-VCH: New York, 2003.
14. Hosono, N.; Kajitani, T.; Fukushima, T.; Ito, K.; Sasaki, S.; Takata, M.; Aida, T., Large-Area Three-Dimensional Molecular Ordering of a Polymer Brush by One-Step Processing. *Science* **2010**, *330*, 808–811.
15. Corbett, D.; Warner, M., Changing Liquid Crystal Elastomer Ordering with Light - A Route to Opto-Mechanically Responsive Materials. *Liq. Cryst.* **2009**, *36*, 1263–1280.
16. Koerner, H.; White, T. J.; Tabiryan, N. V.; Bunning, T. J.; Vaia, R. A., Photogenerating Work from Polymers. *Materials Today* **2008**, *11*, 34–42.
17. Ikeda, T.; Mamiya, J. i.; Yu, Y., Photomechanics of Liquid-Crystalline Elastomers and Other Polymers. *Angew. Chem. Int. Ed.* **2007**, *46*, 506–528.
18. Holland, N. B.; Hugel, T.; Neuert, G.; Cattani-Scholz, A.; Renner, C.; Oesterhelt, D.; Moroder, L.; Seitz, M.; Gaub, H. E., Single Molecule Force Spectroscopy of Azobenzene Polymers: Switching Elasticity of Single Photochromic Macromolecules. *Macromolecules* **2003**, *36*, 2015–2023.
19. Hugel, T.; Holland, N. B.; Cattani, A.; Moroder, L.; Seitz, M.; Gaub, H. E., Single-Molecule Optomechanical Cycle. *Science* **2002**, *296*, 1103–1106.

20. Grandbois, M.; Beyer, M.; Rief, M.; Clausen-Schaumann, H.; Gaub, H. E., How Strong Is a Covalent Bond? *Science* **1999**, *283*, 1727–1730.
21. Kersey, F. R.; Loveless, D. M.; Craig, S. L., A Hybrid Polymer Gel with Controlled Rates of Cross-Link Rupture and Self-Repair. *J. R. Soc. Interface* **2007**, *4*, 373–380.
22. Kersey, F. R.; Yount, W. C.; Craig, S. L., Single-Molecule Force Spectroscopy of Bimolecular Reactions: System Homology in the Mechanical Activation of Ligand Substitution Reactions. *J. Am. Chem. Soc.* **2006**, *128*, 3886–3887.
23. Kudera, M.; Eschbaumer, C.; Gaub, H. E.; Schubert, U. S., Analysis of Metallo-Supramolecular Systems Using Single-Molecule Force Spectroscopy. *Adv. Funct. Mater.* **2003**, *13*, 615–620.
24. Shan, Z.; Holger, S.; Vancso, G. J., Stretching and Rupturing Individual Supramolecular Polymer Chains by AFM. *Angew. Chem. Int. Ed.* **2005**, *44*, 956–959.
25. Zou, S.; Schonherr, H.; Vancso, G. J., Force Spectroscopy of Quadruple H-Bonded Dimers by AFM: Dynamic Bond Rupture and Molecular Time–Temperature Superposition. *J. Am. Chem. Soc.* **2005**, *127*, 11230–11231.
26. Embrechts, A.; Schönherr, H.; Vancso, G. J., Rupture Force of Single Supramolecular Bonds in Associative Polymers by AFM at Fixed Loading Rates. *J. Phys. Chem. B* **2008**, *112*, 7359–7362.
27. Liang, J.; Fernández, J. M., Mechanochemistry: One Bond at a Time. *ACS Nano* **2009**, *3*, 1628–1645.
28. Garcia-Manyes, S.; Liang, J.; Szoszkiewicz, R.; Kuo, T.-L.; Fernández, J. M., Force-Activated Reactivity Switch in a Bimolecular Chemical Reaction. *Nature Chemistry* **2009**, *1*, 236–242.
29. Koti Ainavarapu, S. R.; Wiita, A. P.; Dougan, L.; Uggerud, E.; Fernandez, J. M., Single-Molecule Force Spectroscopy Measurements of Bond Elongation during a Bimolecular Reaction. *J. Am. Chem. Soc.* **2008**, *130*, 6479–6487.
30. Wiita, A. P.; Perez-Jimenez, R.; Walther, K. A.; Grater, F.; Berne, B. J.; Holmgren, A.; Sanchez-Ruiz, J. M.; Fernandez, J. M., Probing the Chemistry of Thioredoxin Catalysis with Force. *Nature* **2007**, *450*, 124–127.

31. Wiita, A. P.; Ainavarapu, S. R. K.; Huang, H. H.; Fernandez, J. M., Force-Dependent Chemical Kinetics of Disulfide Bond Reduction Observed with Single-Molecule Techniques. *Proc. Natl. Acad. Sci. U.S.A.* **2006**, *103*, 7222–7227.
32. Rief, M.; Oesterhelt, F.; Heymann, B.; Gaub, H. E., Single Molecule Force Spectroscopy on Polysaccharides by Atomic Force Microscopy. *Science* **1997**, *275*, 1295–1297.
33. Black, A. L.; Lenhardt, J. M.; Craig, S. L., From Molecular Mechanochemistry to Stress-Responsive Materials. *J. Mater. Chem.* **2011**, *21*, 1655–1663.
34. Beyer, M. K.; Clausen-Schaumann, H., Mechanochemistry: The Mechanical Activation of Covalent Bonds. *Chem. Rev.* **2005**, *105*, 2921–2948.
35. Ribas-Arino, J.; Shiga, M.; Marx, D., Mechanochemical Transduction of Externally Applied Forces to Mechanophores. *J. Am. Chem. Soc.* **2010**, *132*, 10609–10614.
36. Ribas-Arino, J.; Shiga, M.; Marx, D., Unravelling the Mechanism of Force-Induced Ring-Opening of Benzocyclobutenes. *Chem. Eur. J.* **2009**, *15*, 13331–13335.
37. Ribas-Arino, J.; Shiga, M.; Marx, D., Understanding Covalent Mechanochemistry. *Angew. Chem. Int. Ed.* **2009**, *48*, 4190–4193.
38. Turanský, R.; Konôpka, M.; Doltsinis, N. L.; Štich, I.; Marx, D., Switching of Functionalized Azobenzene Suspended between Gold Tips by Mechanochemical, Photochemical, and Opto-Mechanical Means. *Phys. Chem. Chem. Phys.* **2010**, *12*, 13922–13932.
39. Hofbauer, F.; Frank, I., Disulfide Bond Cleavage: A Redox Reaction Without Electron Transfer. *Chem. Eur. J.* **2010**, *16*, 5097–5101.
40. Ong, M. T.; Leiding, J.; Tao, H.; Virshup, A. M.; MartiÌ□nez, T. J., First Principles Dynamics and Minimum Energy Pathways for Mechanochemical Ring Opening of Cyclobutene. *J. Am. Chem. Soc.* **2009**, *131*, 6377–6379.
41. Guzmán, D. L.; Roland, J. T.; Keer, H.; Kong, Y. P.; Ritz, T.; Yee, A.; Guan, Z., Using steered molecular dynamics simulations and single-molecule force spectroscopy to guide the rational design of biomimetic modular polymeric materials. *Polymer* **2008**, *49*, 3892-3901.
42. Sotomayor, M.; Schulten, K., Single-Molecule Experiments in Vitro and in Silico. *Science* **2007**, *316*, 1144–1148.

43. Huang, Z.; Boulatov, R., Chemomechanics: Chemical Kinetics for Multiscale Phenomena. *Chem. Soc. Rev.* **2011**, *40*, 2359–2384.

44. Boulatov, R., Reaction Dynamics in the Formidable Gap. *Pure Appl. Chem.* **2011**, *83*, 25–41.

45. Kim, J.; Zhang, C.-Z.; Zhang, X.; Springer, T. A., A Mechanically Stabilized Receptor-Ligand Flex-Bond Important in the Vasculature. *Nature* **2010**, *466*, 992–995.

46. Barsegov, V.; Thirumalai, D., Dynamics of Unbinding of Cell Adhesion Molecules: Transition From Catch to Slip Bonds. *Proc. Natl. Acad. Sci. U.S.A.* **2005**, *102*, 1835–1839.

47. Garcia-Viloca, M.; Gao, J.; Karplus, M.; Truhlar, D. G., How Enzymes Work: Analysis by Modern Rate Theory and Computer Simulations. *Science* **2004**, *303*, 186–195.

48. Kauzmann, W.; Eyring, H., The Viscous Flow of Large Molecules. *J. Am. Chem. Soc.* **1940**, *62*, 3113–3125.

49. Bell, G. I., Models for the Specific Adhesion of Cells to Cells. *Science* **1978**, *200*, 618–627.

50. Evans, E.; Ritchie, K., Dynamic Strength of Molecular Adhesion Bonds. *Biophys. J.* **1997**, *72*, 1541–1555.

51. Evans, E., Probing the Relation Between Force—Lifetime—and Chemistry in Single Molecular Bonds. *Annu. Rev. Biophys. Biomol. Struct.* **2001**, *30*, 105–128.

52. Hummer, G.; Szabo, A., Free Energy Surfaces from Single-Molecule Force Spectroscopy. *Acc. Chem. Res.* **2005**, *38*, 504–513.

53. Raible, M.; Evstigneev, M.; Bartels, F. W.; Eckel, R.; Nguyen-Duong, M.; Merkel, R.; Ros, R.; Anselmetti, D.; Reimann, P., Theoretical Analysis of Single-Molecule Force Spectroscopy Experiments: Heterogeneity of Chemical Bonds. *Biophys. J.* **2006**, *90*, 3851–3864.

54. Hyeon, C.; Thirumalai, D., Measuring the Energy Landscape Roughness and the Transition State Location of Biomolecules Using Single Molecule Mechanical Unfolding Experiments. *J. Phys.: Condens. Matter* **2007**, *19*, 113101/1–27.

55. Dudko, O. K.; Hummer, G.; Szabo, A., Intrinsic Rates and Activation Free Energies from Single-Molecule Pulling Experiments. *Phys. Rev. Lett.* **2006**, *96*, 108101/1–4.

56. Dudko, O. K.; Hummer, G.; Szabo, A., Theory, Analysis, and Interpretation of Single-Molecule Force Spectroscopy Experiments. *Proc. Natl. Acad. Sci. U.S.A.* **2008**, *105*, 15755–15760.

57. Hummer, G.; Szabo, A., Kinetics from Nonequilibrium Single-Molecule Pulling Experiments. *Biophys. J.* **2003**, *85*, 5–15.

58. Kramers, H. A., Brownian Motion in a Field of Force and the Diffusion Model of Chemical Reactions. *Physica* **1940**, *7*, 284–304.

59. Hänggi, P.; Talkner, P.; Borkovec, M., Reaction-Rate Theory: Fifty Years after Kramers. *Rev. Mod. Phys.* **1990**, *62*, 251–341.

60. Jencks, W. P., A Primer for the Bema Hapothle. An Empirical Approach to the Characterization of Changing Transition-State Structures. *Chem. Rev.* **1985**, *85*, 511–527.

61. Wu, D.; Lenhardt, J. M.; Black, A. L.; Akhremitchev, B. B.; Craig, S. L., Molecular Stress Relief through a Force-Induced Irreversible Extension in Polymer Contour Length. *J. Am. Chem. Soc.* **2010**, *132*, 15936–15938.

62. Neuman, K. C.; Nagy, A., Single-Molecule Force Spectroscopy: Optical Tweezers, Magnetic Tweezers and Atomic Force Microscopy. *Nat. Methods* **2008**, *5*, 491–505.

63. Kucharski, T. J.; Yang, Q.-Z.; Tian, Y.; Boulatov, R., Strain-Dependent Acceleration of a Paradigmatic S_N2 Reaction Accurately Predicted by the Force Formalism. *J. Phys. Chem. Lett.* **2010**, *1*, 2820–2825.

64. Yang, Q.-Z.; Huang, Z.; Kucharski, T. J.; Khvostichenko, D.; Chen, J.; Boulatov, R., A Molecular Force Probe. *Nat. Nanotechnol.* **2009**, *4*, 302–306.

65. Huang, Z.; Boulatov, R., Chemomechanics with Molecular Force Probes. *Pure Appl. Chem.* **2010**, *82*, 931–951.

66. Schlierf, M.; Li, H.; Fernandez, J. M., The Unfolding Kinetics of Ubiquitin Captured with Single-Molecule Force-Clamp Techniques. *Proc. Natl. Acad. Sci. U.S.A.* **2004**, *101*, 7299–7304.

67. Hugel, T.; Seitz, M., The Study of Molecular Interactions by AFM Force Spectroscopy. *Macromol. Rapid Commun.* **2001**, *22*, 989–1016.

68. Sachs, F.; Lecar, H., Stochastic Models for Mechanical Transduction. *Biophys. J.* **1991**, *59*, 1143–1145.

69. Lecar, H.; Morris, C. E., Biophysics of Mechanotransduction. In *Mechanoreception by the Vascular Wall*, Rubanyi, G. M., Ed. Futura Publishing Co.: Mount Kisco, NY, 1993; pp 1–11.
70. Corey, D. P.; Howard, J., Models for Ion Channel Gating with Compliant States. *Biophys. J.* **1994**, *66*, 1254–1257.
71. Howard, J., *Mechanics of Motor Proteins and the Cytoskeleton*. Sinauer Associates, Inc.: Sunderland, Massachusetts, 2001.
72. Hyeon, C.; Thirumalai, D., Forced-Unfolding and Force-Quench Refolding of RNA Hairpins. *Biophys. J.* **2006**, *90*, 3410–3427.
73. Neuert, G.; Hugel, T.; Netz, R. R.; Gaub, H. E., Elasticity of Poly(azobenzene-peptides). *Macromolecules* **2005**, *39*, 789–797.
74. Astumian, R. D., The Unreasonable Effectiveness of Equilibrium Theory for Interpreting Nonequilibrium Experiments. *Am. J. Phys.* **2006**, *74*, 683–688.
75. Berry, R. S.; Rice, S. A.; Ross, J., *Physical and Chemical Kinetics*. 2nd ed.; Oxford University Press: New York, 2001.
76. Brandhorst, K.; Grunenberg, J., Efficient Computation of Compliance Matrices in Redundant Internal Coordinates from Cartesian Hessians for Nonstationary Points. *J. Chem. Phys.* **2010**, *132*, 184101/1–7.
77. Brandhorst, K.; Grunenberg, J., How Strong Is It? The Interpretation of Force and Compliance Constants as Bond Strength Descriptors. *Chem. Soc. Rev.* **2008**, *37*, 1558–1567.
78. Brandhorst, K.; Grunenberg, J., Characterizing Chemical Bond Strengths Using Generalized Compliance Constants. *ChemPhysChem* **2007**, *8*, 1151–1156.
79. Baker, J., A Critical Assessment of the Use of Compliance Constants as Bond Strength Descriptors for Weak Interatomic Interactions. *J. Chem. Phys.* **2006**, *125*, 014103/1–6.
80. Jones, L. H.; Swanson, B. I., Interpretation of Potential Constants: Application to Study of Bonding Forces in Metal Cyanide Complexes and Metal Carbonyls. *Acc. Chem. Res.* **1976**, *9*, 128–134.
81. Tuttolomondo, M. E.; Navarro, A.; Peña, T.; Varetti, E. L.; Altabef, A. B., Theoretical Structure and Vibrational Analysis of Ethyl Methanesulfonate, $CH_3SO_2OCH_2CH_3$. *J. Phys. Chem. A* **2005**, *109*, 7946–7956.

82. Kato, M.; Tsuchiya, H.; Taniguchi, Y., Raman Study of Pressure and Temperature Effects on the Conformational Equilibrium of Diethyl Disulfide in Solutions. *Bull. Chem. Soc. Jpn.* **2005**, *78*, 1411–1416.
83. Van Wart, H. E.; Cardinaux, F.; Scheraga, H. A., Low Frequency Raman Spectra of Dimethyl, Methyl Ethyl, and Diethyl Disulfides, and Rotational Isomerism about Their Carbon–Sulfur Bonds. *J. Phys. Chem.* **1976**, *80*, 625–630.
84. Sugeta, H., Normal Vibrations and Molecular Conformations of Dialkyl Disulfides. *Spectrochim. Acta, Part A* **1975**, *31*, 1729–1737.
85. Wilczek, F., Whence the Force of F = ma? I: Culture Shock. *Physics Today* **2004**, *57*, 11–12.
86. Evans, E.; Leung, A.; Hammer, D.; Simon, S., Chemically Distinct Transition States Govern Rapid Dissociation of Single L-Selectin Bonds Under Force. *Proc. Natl. Acad. Sci. U.S.A.* **2001**, *98*, 3784–3789.
87. Overman, L. E.; Matzinger, D.; O'Connor, E. M.; Overman, J. D., Nucleophilic Cleavage of the Sulfur–Sulfur Bond by Phosphorus Nucleophiles. Kinetic Study of the Reduction of Aryl Disulfides with Triphenylphosphine and Water. *J. Am. Chem. Soc.* **1974**, *96*, 6081–6089.
88. Overman, L. E.; Petty, S. T., Nucleophilic Cleavage of the Sulfur–Sulfur Bond by Phosphorus Nucleophiles. III. Kinetic Study of the Reduction of a Series of Ethyl Aryl Disulfides with Triphenylphosphine and Water. *J. Org. Chem.* **1975**, *40*, 2779–2782.
89. Overman, L. E.; O'Connor, E. M., Nucleophilic Cleavage of the Sulfur–Sulfur Bond by Phosphorus Nucleophiles. IV. Kinetic Study of the Reduction of Alkyl Disulfides with Triphenylphosphine and Water. *J. Am. Chem. Soc.* **1976**, *98*, 771–775.
90. Dmitrenko, O.; Thorpe, C.; Bach, R. D., Mechanism of S_N2 Disulfide Bond Cleavage by Phosphorus Nucleophiles. Implications for Biochemical Disulfide Reducing Agents. *J. Org. Chem.* **2007**, *72*, 8298–8307.
91. Singh, R.; Whitesides, G. M., Thiol–Disulfide Interchange. In *Supplement S: The Chemistry of Sulphur-Containing Functional Groups*, Patai, S.; Rappoport, Z., Eds. John Wiley & Sons: New York, 1993; pp 633–658.

92. Espinosa, S.; Bosch, E.; Rosés, M., Retention of Ionizable Compounds on HPLC. 5. pH Scales and the Retention of Acids and Bases with Acetonitrile–Water Mobile Phases. *Anal. Chem.* **2000**, *72*, 5193–5200.
93. Hammond, G. S., A Correlation of Reaction Rates. *J. Am. Chem. Soc.* **1955**, *77*, 334–338.
94. Leffler, J. E., Parameters for the Description of Transition States. *Science* **1953**, *117*, 340–341.
95. Leffler, J. E.; Grunwald, E., *Rates and Equilibria of Organic Reactions*. John Wiley and Sons, Inc.: New York, 1963.
96. Hugel, T.; Rief, M.; Seitz, M.; Gaub, H. E.; Netz, R. R., Highly Stretched Single Polymers: Atomic-Force-Microscope Experiments Versus *Ab-Initio* Theory. *Phys. Rev. Lett.* **2005**, *94*, 048301.
97. Rubinstein, M.; Colby, R. H., *Polymer Physics*. Oxford University Press: New York, 2003.
98. Gans, P., *Data Fitting in the Chemical Sciences by the Method of Least Squares*. John Wiley & Sons: New York, 1992.

Chapter 8. Fundamentals of Molecular Photoactuation

Adapted from Kucharski, T. J.; Boulatov, R., Fundamentals of Molecular Photoactuation. In *Optical Nano and Micro Actuator Technology*, Knopf, G. K.; Otani, Y., Eds. CRC Press: **2011**, accepted (*invited book chapter*). Reproduced with permission. © CRC Press, 2011.

8.1 Introduction

Photoactuating materials convert photon energy into directional translation at meso- to macroscales by reversibly changing their shape or volume when irradiated with light. Because they can be powered wirelessly and controlled remotely and are insensitive to magnetic noise and potentially compatible with rapid (>100 Hz) work cycles, particularly when compared to materials that require diffusive mass transport, photoactuating materials are of growing interest in chemistry, materials science, engineering and soft matter physics. Here we define photophysical actuation as due to heating, pyroelectric and piezoelectric effects[1] resulting from photon absorption, radiation forces,[2] or their combination. This chapter is devoted to photochemical actuation, in which aspect ratio(s) of an irradiated material change due to photoisomerization of its constituent molecular components (e.g., photoactive monomers or dopants), and we will use the terms *photoactuation* and *photochemical actuation* interchangeably. Photochemical actuating materials are ensembles of molecular chromophores which exist in at least two isomers of significantly different molecular shape (Fig. 8.1). Dimensional change at the macroscale is a cumulative effect of a large number of often independent molecular-scale structural rearrangements each induced by the absorption of a photon. Photochemical actuation provides perhaps the most direct link between chemical reactivity at the molecular level and useful properties of the bulk material. Consequently, the classical chemical concepts, including molecular design and reaction dynamics, may be particularly impactful in the development of new photoactuating materials and understanding the behavior of the existing ones at the molecular level.

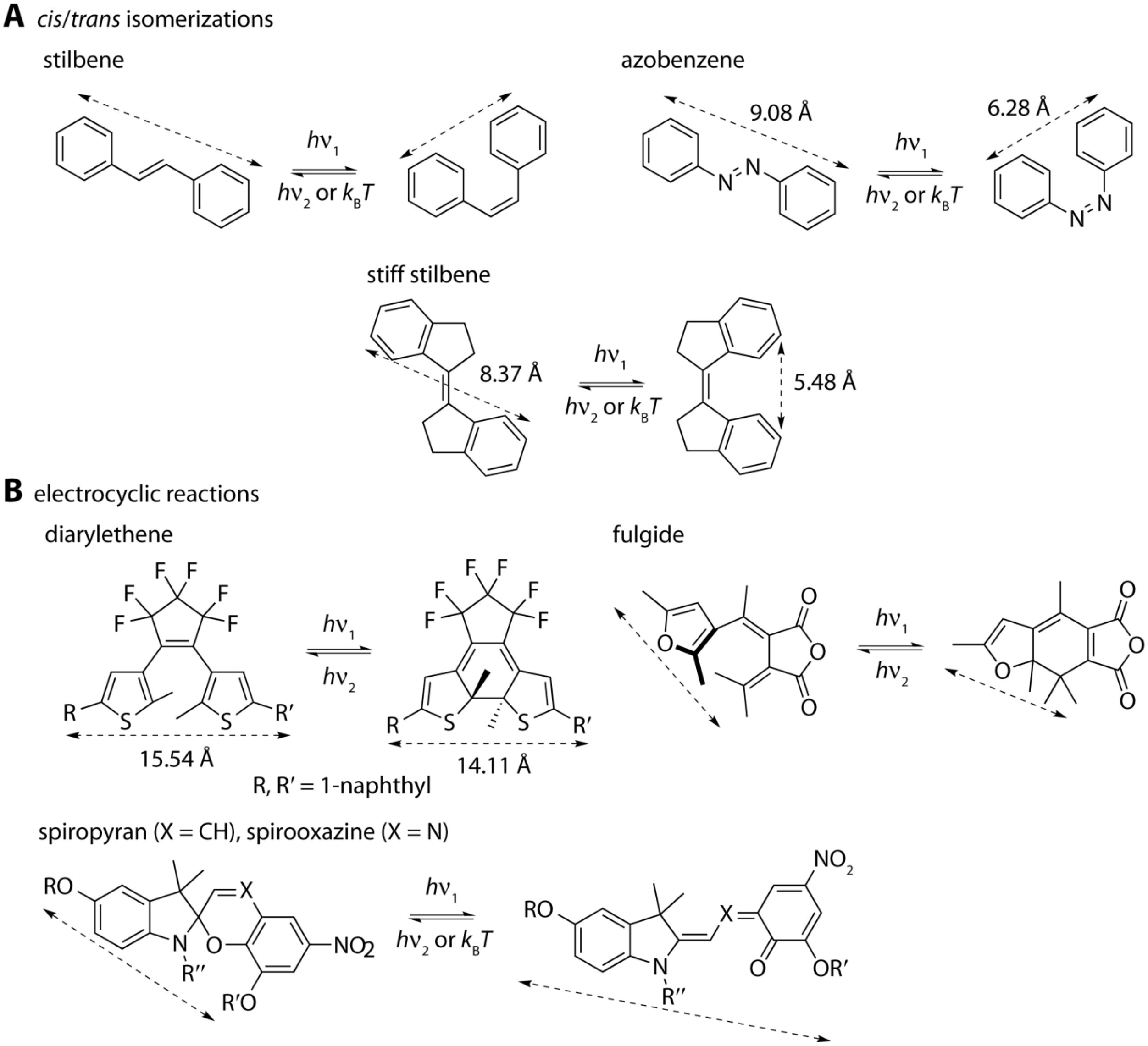

Fig. 8.1. Representative molecules of different classes of photochromic systems suitable for photoactuation, categorized as (**A**) *cis*/*trans* isomerizations or (**B**) electrocyclic reactions. Selected interatomic distances that change between the two forms and could serve as points of attachment for extended strctures are indicated by the dashed arrows. Distances for azobenzene and stiff stilbene were calculated at the B3LYP/6-31G(d) level of density functional theory in the gas phase; distances for the diarylethene shown were determined crystalographically.[3] h, k_B and T are Plank's constant, Boltzmann's constant and absolute temperature, respectively.

Photoactuation has been demonstrated in molecular crystals, liquid-crystalline films and polymers. Amorphous photoactuating polymers typically contain ≤10% of photoisomerizable groups, often in crosslinks, and can change their dimensions by a few percent upon irradiation.[4] This dimensional change is called photo-induced strain (photostrains), although unconstrained samples are strain-free before and after irradiation. Larger photostrains appear accessible in molecular crystals[5] and cocrystals[3] of photoisomerizable diarylethenes (Fig. 8.1B), which undergo single-crystal–single-crystal transitions when irradiated with either UV or visible light, resulting in reversible macroscopic shape changes. Liquid crystal (LC) films doped with photoisomerizable dyes[6] and liquid crystal elastomers (LCEs) with photoisomerizable mesogens[4,7-9] have been shown to move micro- and macroscopic objects when irradiated with light. Several aspects of photoactuating materials, including their syntheses and proof-of-concept demonstrations of potential applications have been previously reviewed[4,10-15] and are not repeated here.

The design of photoactuating materials presents several conceptual and technical challenges. The key operating parameters of such materials—strain, stress, energy conversion efficiency, power output and operating frequency—cannot be adjusted independently, and their coupling is complex and little understood. Particularly little studied is the effect of bulk stresses on the kinetics and thermodynamics of the molecular processes, both productive (e.g., photoisomerization) and parasitic (e.g., side-reactions and thermal relaxations of strained molecules without changes in bulk aspect ratios). In this chapter, we will briefly describe a chemist's view of the operation of photoactuating materials and the challenges in optimizing their performance, focusing on how molecular thermal and photochemical processes dictate the fundamental limits of a material's operating capabilities.

The remainder of the chapter is organized as follows: First, the molecular basis for photochemical actuation will be examined. Second, general design criteria for photoactuating materials will be discussed, followed by an examination of the outstanding questions that remain, in both cases noting the existing molecular approaches for understanding these issues. Then we will briefly introduce the principles of the chemomechanical formalism and will subsequently discuss the force-dependent kinetics of photoactuating monomers within this conceptual framework. Finally, we will examine how the kinetics and thermodynamics of actuating reactions impose the fundamental limits on the achievable performance characteristics of photoactuating polymers and will conclude with our speculations regarding future prospects for advancing the field.

8.2 The Molecular Basis for Photochemical Actuation

8.2.1 Effecting Changes in Molecular Shape

In photochemical actuation, irradiation-induced changes in aspect ratio(s) of bulk material is the end result of a photochemical process, isomerization of a chromophore upon photon absorption. Chromophores that exist as several isomers are typically photochromic, i.e., the isomers have different absorption spectra. Photochromism has long been studied, and because many physical properties of photochromic isomers are different, such molecules are used in a variety of applications.[16-18] The most important properties of photochromes for photoactuating applications are differences in (1) molecular dimensions and (2) absorption spectra of the two isomers, and (3) high quantum efficiency of photoisomerization with minimal side-reactions. Of the numerous photochromic molecules known, those that have been considered for photoactuating applications include (Fig. 8.1) stilbenes,[19] azobenzenes,[11,14] stiff stilbenes,[20] diarylethenes,[21,22] fulgides[23,24] and spiropyrans/spirooxazines.[25] All these chromophores have at least one internuclear distance that differs significantly in the two isomers.

Upon photon absorption a molecule is excited to a new electronic state. In a photochrome the stable nuclear configuration of the ground electronic state differs significantly from that of the excited states. Consequently, upon excitation, the molecule undergoes rapid structural rearrangement that brings it to a conical intersection (seam) connecting the ground and excited energy surfaces, followed by further evolution of the structure to an energy minimum of the ground state.[26,27] The whole process is extremely rapid, occurring on the ps time scale.[17] Even in sterically congested systems, ps-timescale C=C photoisomerizations enable directed rotation at MHz frequencies.[28]

Azobenzene is the most popular photochrome for use in photoactuating materials and the mechanism of its photoisomerization has been studied extensively. In the gas phase[29,30] light absorption in the singlet ground state (S_0) of the *E* isomer can excite the molecule to either the first excited singlet state ($S_0 \rightarrow S_1$, n–π^* transition, ~450 nm light) or the second excited singlet state ($S_0 \rightarrow S_2$, π–π^* transition, ~320 nm light). The S_1 state generated directly from the S_0 state has a lifetime of 2.6 ps, during which the molecule rotates around the N–C bond (Fig. 8.2A). The S_2 state rapidly relaxes to the S_1 state, which then isomerizes by a concerted-inversion mechanism with a lifetime of only 500 fs. In condensed phases the steric restrictions of the environment[30,31] may result in a mixed rotation–inversion mechanism of $E \rightarrow Z$ photoisomerization (Fig. 8.2B).

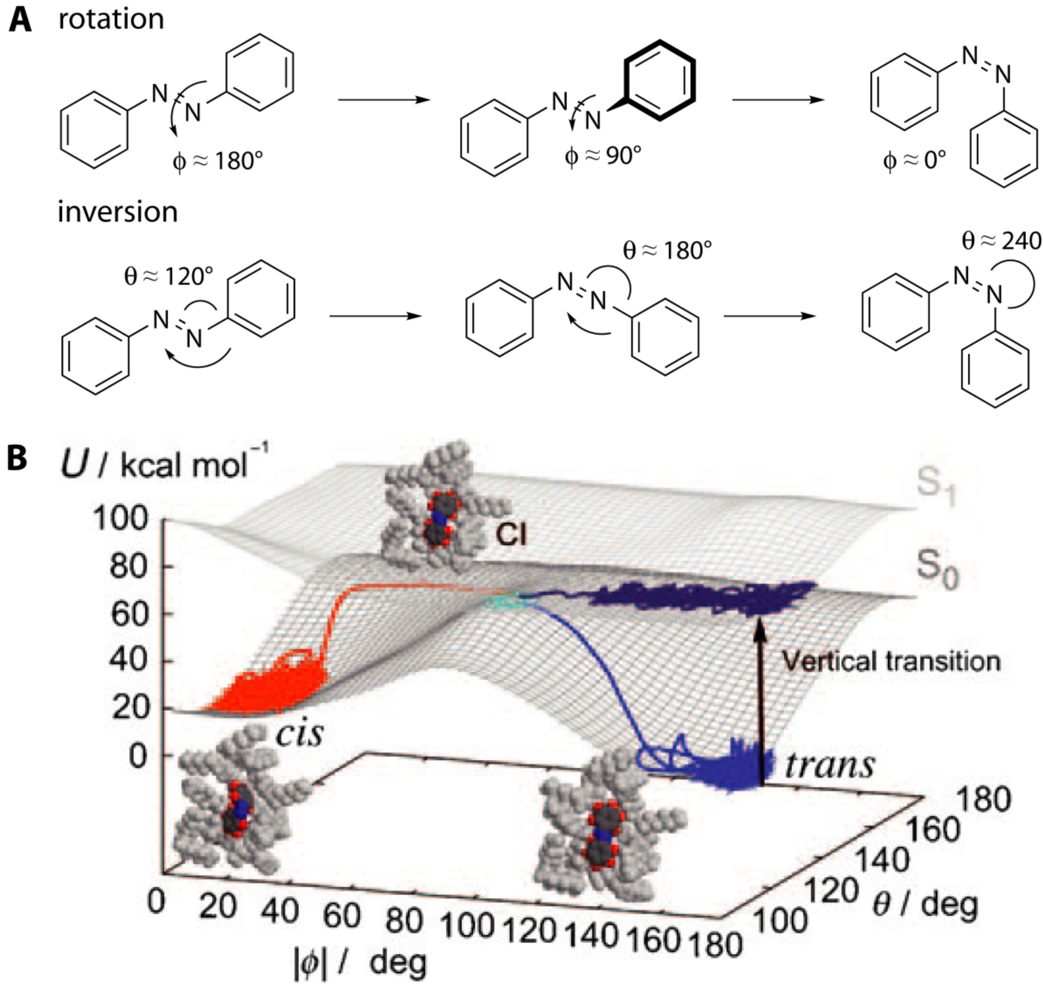

Fig. 8.2. **A**: $E \rightarrow Z$ isomerization by rotation and inversion in azobenzene, showing the changes in the C–N=N–C dihedral angle (ϕ) and the C–N=N angle (θ). **B**: Molecular dynamics simulation in *n*-hexane (light gray molecules) of $S_0 \rightarrow S_1$ photoisomerzation of *trans*-azobenzene to *cis*-azobenzene (dark gray, blue, and red molecule), proceding through the conical intersection (CI) connecting the first excited singlet (S_1) and ground state singlet (S_0) potential energy surfaces; U is internal energy. Reproduced from ref. 30.

Typically, isomerization of C=C or N=N bonds (Fig. 8.1A) results in larger structural differences than electrocyclic ring opening/closing (Fig. 8.1B). The shorter Z isomers of photochromic molecules containing a photoisomerizable C=C or N=N bond are less thermodynamically stable than the longer E isomers, with free energy differences of up to ~11 kcal/mol for azobenzenes. Constraining an internuclear distance that is different in the two isomers perturbs the relative stability of the two isomers up to the point of making the Z isomer the global energy minimum.[32,33] Large structural differences between the two isomers have also been used to photochemically generate highly strained molecules not easily accessible by conventional synthetic routes.[20]

8.2.2 Transmitting Molecular Shape Changes to Larger Length Scales

Photoisomerization of a chromophore connected to the polymer matrix at two atoms whose separation differs significantly in the two isomers (Fig. 8.1) transiently creates a strained isomer because molecular isomerization is too fast for the rest of the polymer matrix to adjust to the new local structure (red arrows, Fig. 8.3). This local strain slowly dissipates by rearrangement of polymer chains. Irradiation-induced changes in the aspect ratio(s) of amorphous photoactuating polymers reflect primarily the total difference in molecular dimensions of individual chromophores projected onto a specific macroscopic axis. Consequently, the relative magnitude of accessible photostrain is limited to the relative elongation (contraction) of a monomer upon isomerization times the fraction of the material made up of the monomers. The net change is usually modest[4] and often occurs on the ms time scale[13] because the macromolecular rearrangement can be inhibited by chain entanglement.

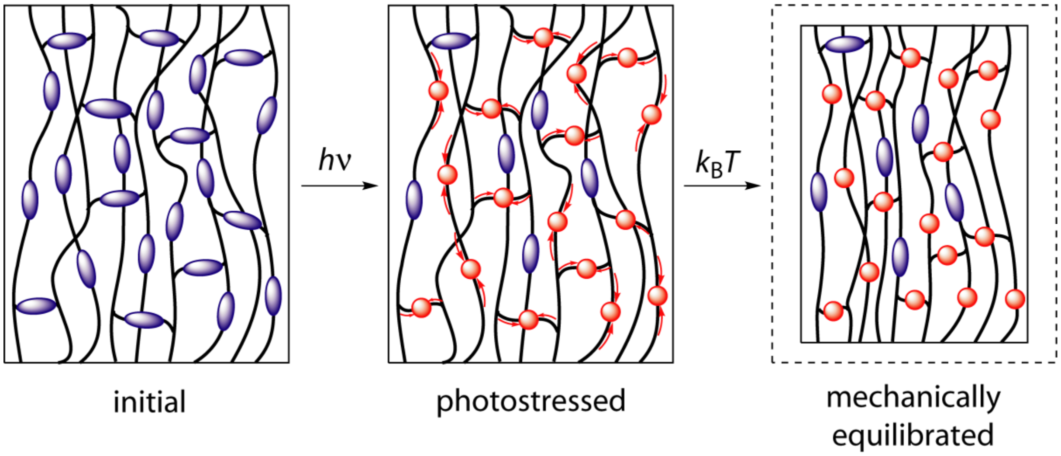

Fig. 8.3. The molecular mechanism for photoactuation in a nanoscopic region of a bulk polymer sample. In the initial state, photoisomerizable comonomers are in their elongated state (blue ovals, e.g. (*E*)-azobenzene). Irradiation leads to photoisomerization of the photoactive units to their shorter state (red circles, e.g. (*Z*)-azobenzene), which creates local strains in their vicinity (red arrows). Relaxation of these strains requires relatively slow, thermally-activated, rearrangement of macromolecular chains, which results in contraction of the bulk material.

In highly-ordered materials with long-range interactions, such as liquid-crystal elastomers or single crystals, photoisomerization can induce a phase change resulting from the disruption of long-range order,[34] rapidly generating photostrains that may exceed 100%.

Photoinduced single-crystal–single-crystal transitions, which yield macroscopic dimensional changes, have been observed in single crystals of diarylethenes.[5,13] Optically thick (the irradiation is completely absorbed within a fraction of the material) single crystal cantilevers exhibit macroscopic bending due to photoisomerization of the constituent molecules only near the transiently irradiated surface (Fig. 8.4). Expansion of only those unit cells that are within the penetration depth of incident irradiation creates internal stresses in the crystal that are relieved by its reversible deformation. Large-scale photoactuation in such systems can be very rapid, with <5 μs response times for 8 ns pulses, even at 4.7 K.[3] Such rapid responses are possible because each individual unit cell expands or contracts independently of other cells (Fig. 8.4, compared to the rearrangement of individual macromolecules in polymer films, Fig. 8.3). In the example shown in Fig. 8.4, *in situ* X-ray diffraction studies revealed that photoactuation was accompanied by the elongation of the crystal axis *orthogonal* to the molecular axis of the chromophore that undergoes the largest dimensional change upon isomerization.[3] The contraction along the *a* axis (i.e., parallel to the diarylethene axis indicated in Fig. 8.1), did not cause the macroscopic response. This example shows that designing photoactuating molecular crystals is a problem of both crystal engineering (the relationship between crystal packing and molecular shape) and molecular design (the difference in molecular shapes of the two isomers).

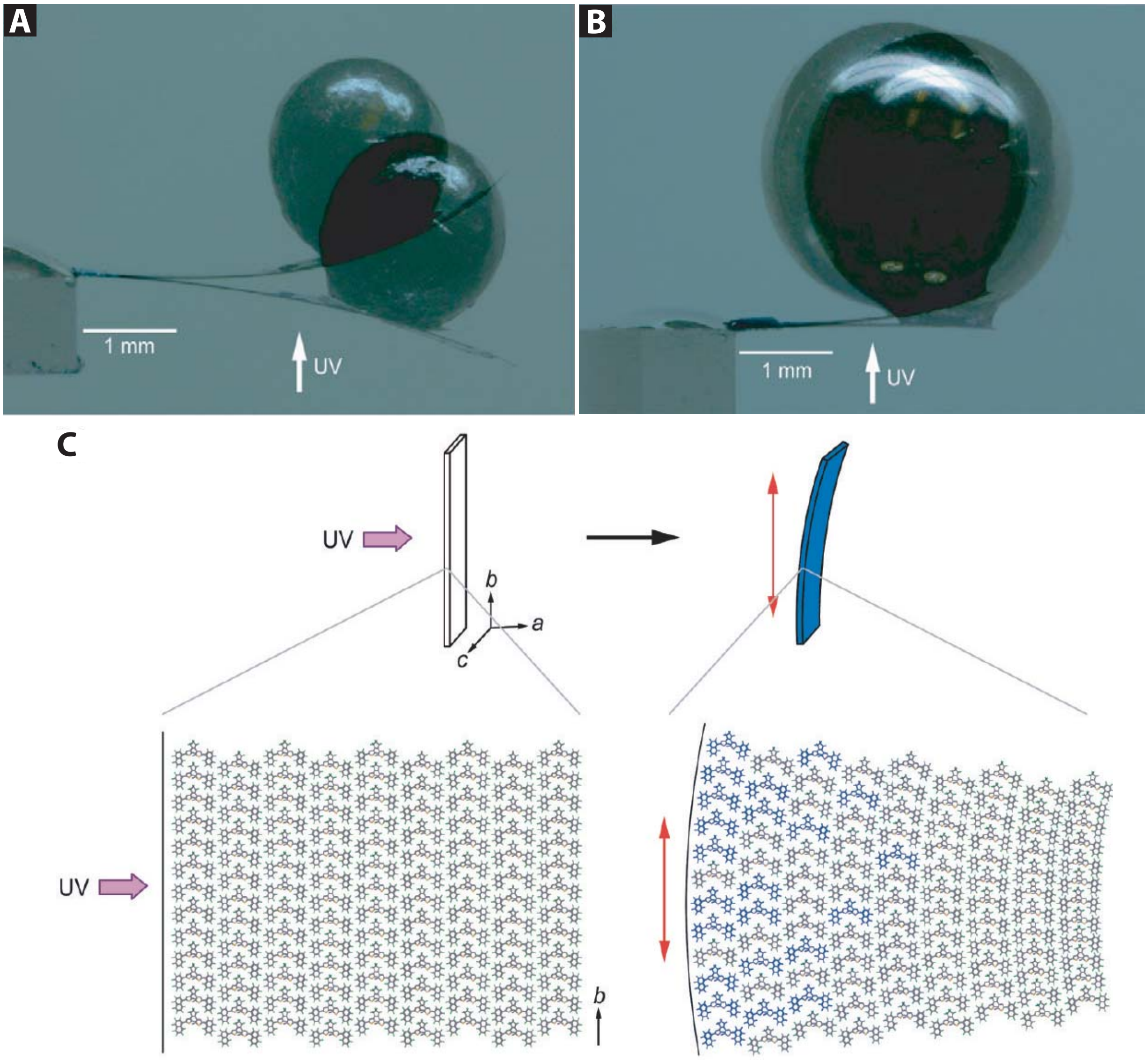

Fig. 8.4. Superimposed photographs before and after irradiation with UV light (direction indicated) of a molecular crystal cantilever holding (**A**) a 2-mm lead ball, 46.77 mg (0.17 mg cantilever) or (**B**) a 3-mm steel ball, 110.45 mg (0.18 mg cantilever); (**C**) the proposed mechanism of photoacutation; the blue molecules are the ring-*closed* form of the diarylethene following photoisomerization, which have a unit cell that is *longer* along the *b* axis. Modified from ref. 3.

Photoisomerization has also been used to control long-range order of liquid crystal films, both monomeric and polymeric.[6] Alignment in LC films can be directed either by photoactive mesogens dispersed throughout the film or by a layer of photoactive molecules on the contacting surface. With such photoactive "command surfaces," the geometric effects of photoisomerization can be amplified as much as ~10^4-fold due to the strong dependence of the long-range order of a liquid crystal on the properties of the contacting surface.[34] In films that exhibit textured surfaces, such as cholesteric liquid crystals with helix axes aligned parallel to the surface, photoisomerization of dopants can modify the texture of the surface, which can yield directional microscopic translation. In one example, photoisomerization of the central C=C bond in the dopant and its subsequent thermal rearrangement inverted the handedness of molecule's helicity (Fig. 8.5A). The cholesteric liquid crystal film containing ~1% by weight of this dopant responded to irradiation by bulk reordering, causing a rotation of the surface texture and with it the rotation of a µm-sized glass rod resting on the surface (Fig. 8.5C, ref. 6).

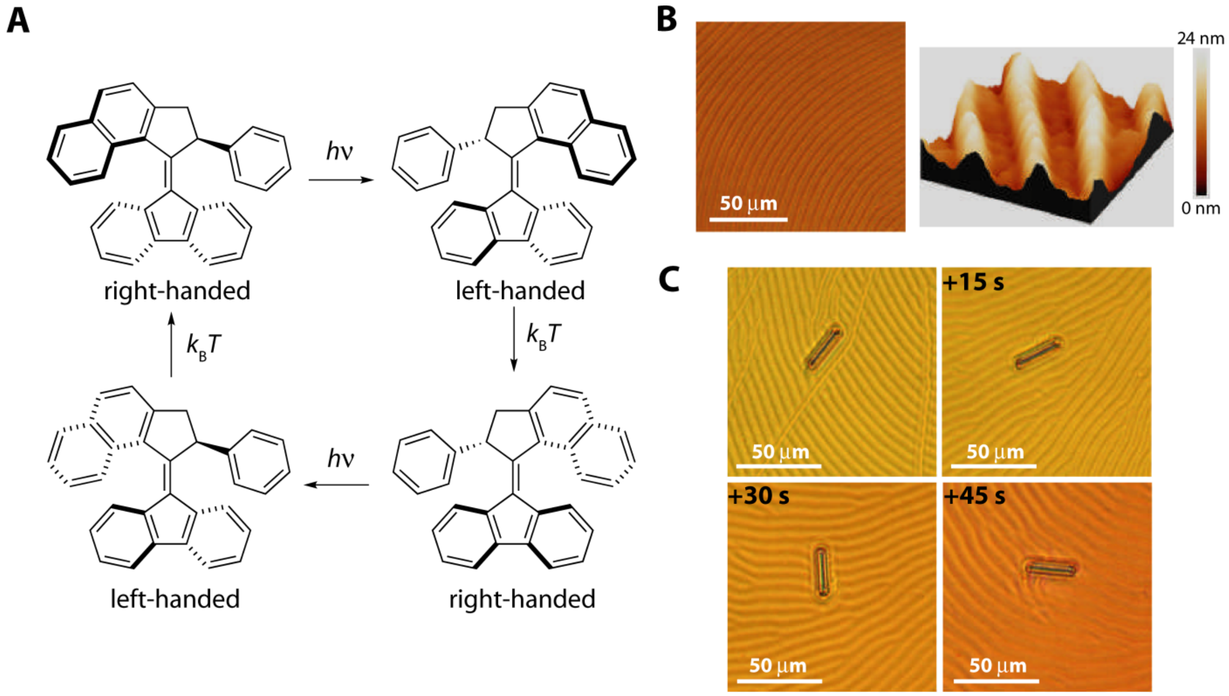

Fig. 8.5. Photoactuation in LC films. **A**: The molecular shape changes induced by alternating steps of photoisomerization ($h\nu$) and thermal rearrangement (k_BT). The handedness of the molecular helix is indicated for each conformation. **B**: The surface relief of a cholesteric LC film containing 1% by weight of the molecule in **A**. **C**: A series of images taken at 15 s intervals showing the rotation of a glass rod as the surface texture of the LC film rotates under UV irradiation. The glass rod is rotated by 28°, 141°, and 226° relative to the first frame. Modified from ref. 6.

Liquid crystal elastomers (LCEs) are free-standing materials composed of crosslinked polymer chains that incorporate mesogens in the polymer backbones, side chains, and/or the crosslinks. These materials have attracted increasing interest for photochemical actuation because the phase transition triggered by photoisomerization of mesogens can greatly amplify the difference in the molecular structure of the two isomers.[4,7-9] The mechanism for photoacutation in LCEs based on a phototriggered nematic-isotropic transition is illustrated in Fig. 8.6. Nematic mesogens (e.g., (*E*)-azobenzene, Fig. 8.1) are rod-shaped molecules that induce long-range ordering by aligning their long axes (nematic directors) to maximize π-π interactions in aromatic systems and allow internal flow. Polymers containing a few mol percent of nematic mesogens can form long-range structures in which the polymer backbones are aligned preferentially along a single axis (nematic director, typically the long molecular axis of the mesogen, Fig. 8.6A). Regions of the material in which molecules have the same orientation of their nematic directors compose domains, and bulk LCEs may be mono- or polydomain. Upon irradiation, the photoisomerization of a critical fraction of the mesogens to the non-mesogenic (bent) geometry diminishes the enthalpic gain of optimal π-π stacking below the entropic cost of maintaining a long-range order and triggers a nematic → isotropic phase change. In the isotropic phase, the polymer molecule adopts a spherical shape distribution. This shape change corresponds to a contraction along the direction of the (now eliminated) nematic director and an expansion perpendicular to that direction. If the material is constrained to the initial shape by an external load, photoisomerization creates stress, whose relaxation can drive translation of the load (mechanical work). If the non-mesogenic isomer is thermodynamically metastable, its thermal isomerization of the mesogenic form restores the long-range nematic order. Alternatively, the mesogens can be regenerated by photoisomerization, completing an actuation cycle.

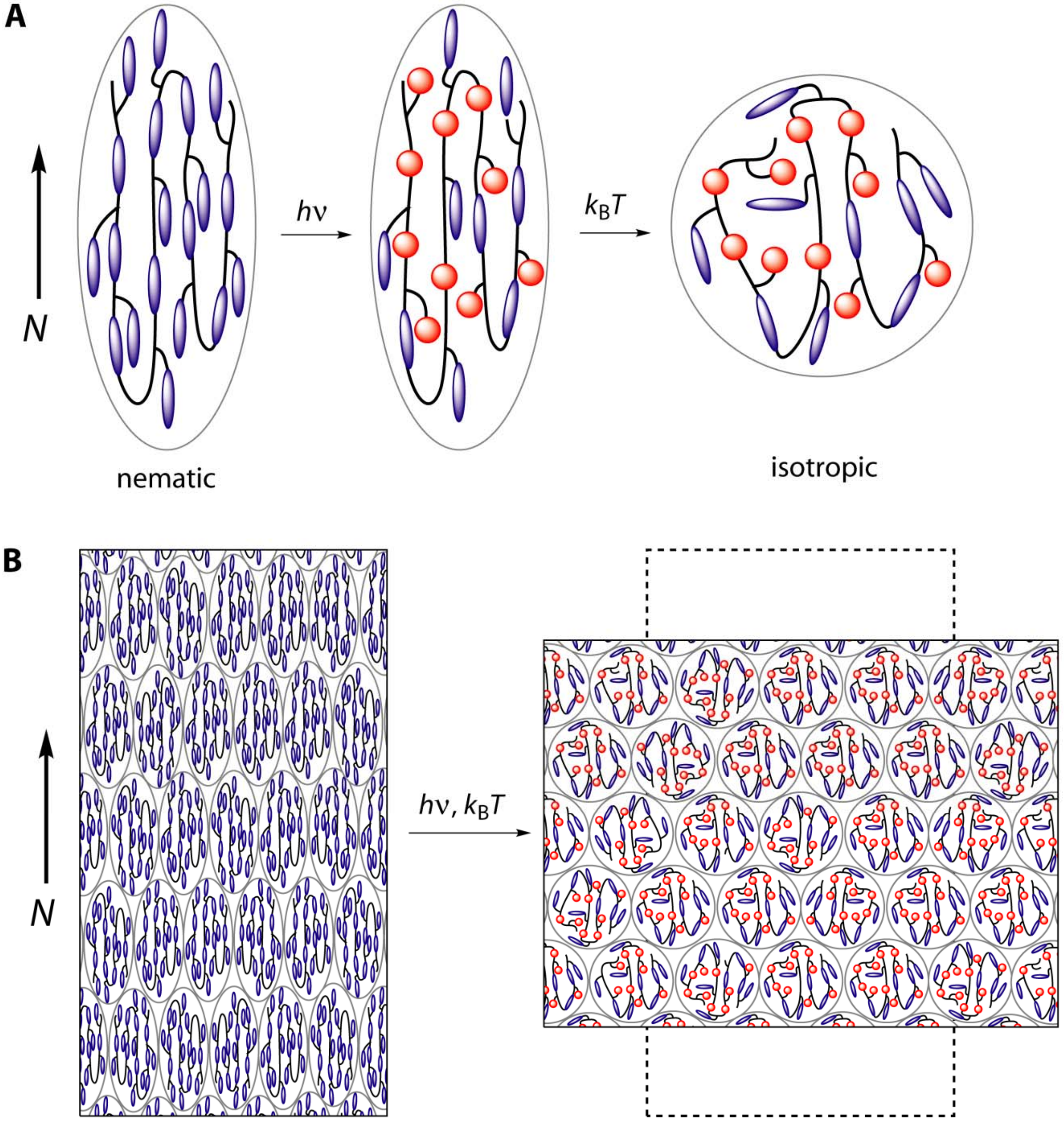

Fig. 8.6. The molecular mechanism for photoactuation in LCEs. **A**: The shape distributions of polymer chains in the nematic (with director *N*) and isotropic states with photoisomerizable mesogens in the backbone and in side chains, shown in their rod-like (blue, e.g. (*E*)-azobenzene) and bent (red, e.g. (*Z*)-azobenzene). Irradiation leads to photoisomerization, which disrupts the nematic ordering of the mesogens, leading to thermal rearrangement of the polymer chain to an isotropic state. **B**: The isothermal nematic → isotropic phase change induced by photoisomerization leads to contractile strain parallel to the nematic director of a region of an LCE and expansion perpendicular to it (assuming sample volume is conserved). Crosslinks between polymer chains are omitted for clarity.

Single-domain optically thick LCE cantilevers bend when irradiated on one face because only a thin layer of the film undergoes nematic-isotropic phase transition, similar to the molecular crystal cantilevers described above. The response can be rapid, indicating a more facile macromolecular rearrangement in the LCEs compared to amorphous photoactuating polymers. In one example, a monodomain LCE cantilever containing azobenzene-based mesogens could be made to oscillate by >110° at 270 Hz[35,36] in the absence of an external load. For comparison, a hummingbird beats its wings at 20–80 Hz.[36] Applications of such LCE cantilevers as actuators in autonomous micro areal devices have been suggested. However, it remains to be established whether such oscillations can support loads as the wings of a hummingbird do.

Amorphous and liquid crystal elastomers, molecular crystals and monomeric LC films generate large-scale actuation by transmitting the effects of molecular shape changes to large length scales. LC films and LCEs also magnify the molecular-level shape changes to achieve strains >100%[7,34] even in response to subtle variations in the molecular geometry or orientation.[37] Macroscopic changes in shape result from elastic mechanical equilibration of local strains created by photoisomerization of individual chromophores. Maximum internal stresses that can be sustained are determined by the elastic moduli of the material, which range from <1 MPa for liquid-crystal photoelastomers[38] to >11 GPa for molecular crystals and glassy liquid-crystal networks[3] (LCNs). Consequently, the maximum stresses that a photoactuating material can operate against vary from <2 kPa for LCEs to >2 MPa for LCNs.

8.3 General Design Criteria for Photoactuating Systems

Designing a photoactuating material for specific applications may require the optimization of several coupled characteristics, such as maximum strain, stall stress, energy conversion efficiency, power output and operating frequency. The relative importance of these parameters is application specific. For example, applications in a high-volume pump require large strains but modest cycle frequencies and stall stresses can be acceptable. Alternatively, high-pressure pumps require shape changes against large stresses. Photoactuators intended to rapidly move rigid levers (e.g., microaerial vehicles) would require the generation of large stresses and high cycle frequencies, and those that served as cantilevers themselves may also require large strains. In this section, we will examine how the thermodynamics and kinetics of the photochemical reaction limits the achievable combination of these performance characteristics with the goal of defining molecular-design criteria in terms of the engineering properties of the resultant material.

8.3.1 The Importance of Anisotropy for Photoactuation

Isotropic photoactuation has been demonstrated in some materials, e.g. the reversible expansion and contraction of solvent-swollen polymer gels by changing the hydrophobicity/hydrophilicity of dyes via their photoisomerization.[39,40] Because of the coupling between macroscopic response and molecular-level changes in ordered materials (e.g., LC systems), anisotropy at the micro- or nanoscale usually results in anisotropic responses at the macroscale. However, not only is anisotropic photoactuation desirable for applications such as flapping cantilevers[35] or bending films that swim,[41] for the vast majority of photoacutating materials not dependent on mass transport, anisotropy in either the material or the irradiation conditions is essential for bulk photoactuation itself, regardless of the specific application intended.

The necessity for anisotropy is best explained with the example of photoacutating nematic LCEs.[7-9] Nematic mesogens (Fig. 8.1) are anisotropic molecules, which typically have distinct molar absorptivities along their molecular axes.[42] Consequently, polarized light can be used to photoisomerize a subset of mesogens with appropriate alignment relative to the materials axes. In polydomain LCEs, the orientation of the nematic director of individual domains (typically μm-size) is random. When such a material is irradiated with unpolarized light (a uniform distribution of electric field vectors), photoactive mesogens in all of the domains absorb light, resulting in contraction of each domain along one axis and expansion along the other two. Because the domains have random orientation, the polydomain sample does not change its aspect ratio upon irradiation.[7] In other words, the microscopic anisotropy (i.e, within each domain) is defeated by macroscopic isotropy (i.e., bulk material and unpolarized light). However, if plane-polarized light is used, only domains comprised of locally-aligned mesogens with an optical axis parallel with the incident light absorb light and change dimensions. Hence, bulk photoactuation is achieved with a macroscopically isotropic material.

It was established early in the development of photoactuating LCEs that the actuation induced by irradiation of monodomain samples was the same as that obtained by heating the samples above their nematic–isotropic phase transition temperatures.[7-9] The photochemical and photothermal actuation mechanisms were differentiated by irradiating polydomain samples with polarized light.[43] If actuation were due to irradiative heating, no bulk actuation would be observed (as is indeed the case for thermally induced nematic → isotropic transitions) because heat generated by optical absorption in the properly aligned domains would rapidly diffuse to nearby domains, leading to stresses in conflicting directions. Because actuation was observed, only a subset of domains changed dimensions upon irradiation, suggesting primarily photochemical, rather than photothermal, actuation.[7,43] Thermal effects may be important in photochemical actuation using intense light sources.[44]

Photoactuation can also be achieved with unpolarized light and monodomain LCEs[45] or molecular crystals[3], which are macroscopically anisotropic. The enabling breakthrough in preparing monodomain LCEs was the development of a two-step crosslinking process[46] in which a lightly crosslinked polydomain LC polymer sample is stretched until all domains are aligned with their directors along the strain axis, which causes the sample to become transparent. The stretched polymer then undergoes further crosslinking due to the presence of slowly-reacting moieties in the polydomain sample, preserving the long-range ordering once the applied stress is removed. This method was used to prepare the first example of photoactuating polymers capable of significant (20%) photostrains.[45] Monodomain LCEs can also be prepared by crosslinking LC polymers aligned by boundary conditions, e.g., by photocrosslinking in a thin cell coated with polyimide layers which have been physically aligned by rubbing.[47] This method is the only one that yields highly-crosslinked (glassy) LC polymers, but it has also been applied to the preparation of photoactuating LCEs.[35-37]

The photoactuating properties of the material are also affected by the location of the photoactive mesogens: one study indicated that LCEs containing azobenzene in crosslinkers were more effective photoactuators than LCEs with azobenzene in side chains.[48]

8.3.2 Photophysical Considerations for Photoactuating Materials

As mentioned above, different material responses are observed for optically thick and optically thin samples. Optical thickness refers to the amount of light absorbed as it passes though the material in the sense that optically thick samples absorb more light than optically thin ones. The optical thickness is determined not only by the physical thickness of the material but also by the concentration of photoactive constituents present and the intensity of the irradiation source. In optically thin samples, photoactuation is manifested as contractile stresses and strains, because the light transmitted through the material is sufficient to achieve the same degree of actuation throughout. Optically thick samples exhibit bending/curling when irradiated because of the non-uniform distribution of photostresses along the depth of the sample; this bending can be reversed either by thermal relaxation or by irradiating the opposite side of the material to symmetrize the distribution of photostresses with respect to the midplane of the sample.[3,35]

If bending/curling is inhibited by macroscopic constraints (e.g. a strain gauge), larger net contractile stresses are obtained for samples with lower concentrations of photoisomerizable molecules.[48] In LCEs, once a domain has undergone its isothermal nematic → isotropic phase change, photoisomerization of more mesogens by the absorption of additional light does not increase the photostress generated. It may, however, increase the penetration depth of the incident irradiation, with more material experiencing internal stresses. The maximally efficient use of light energy in terms of photostress generation would therefore occur in materials that have the minimum concentration of photoactive mesogens needed to induce nematic → isotropic phase changes when irradiated. This concentration, however, may also depend on the imposed load: for a more highly strained LCE sample, a larger fraction of its mesogens need to be eliminated by photoisomerization to induce the isothermal nematic → isotropic phase transition.[9,34] The effect of concentration of covalently bound photoactive mesogens on the performance characteristics of the material has been relatively little studied.

Experimentally observed bending/curling of optically thick samples of photoelastomers can be modeled by the distribution of photostresses.[49] The effect of light polarization on the photoactuation of polydomain LCEs has also been modeled.[49-51] In addition to the nonlinear responses with respect to light intensity in those studies, nonlinear penetration of the light (i.e., deviations of from Beer's law) in optically thick samples irradiated with intense beams has also been considered.[44,52]

8.3.3 Stress, Strain, and Energy Conversion Efficiency

Stress and strain in a material are related by its modulus of elasticity. Soft materials exhibit large strains at small stresses, and stiff materials require large stresses to achieve small strains. The amount of energy required to deform a material is given by the area under its stress–

strain curve $\sigma(\varepsilon)$, where σ is stress and ε is strain. Integrating $\sigma(\varepsilon)$ from $\varepsilon=0$ to the yield strain defines the material's modulus of resilience and thus its capacity to absorb mechanical energy without undergoing irreversible (plastic) deformation. During an actuating cycle, the elastic modulus of the material may change by as much as 500% for skeletal muscle and polypyrrole electromechanical actuators.[53]

The simplest photoactuating work cycle is shown in Fig. 8.7, using the example of a photoactuating LCE. (The related single-molecule cycle is presented in the following section.) Starting with an unstrained polydomain nematic LCE containing mostly the *E* isomers of photoactive mesogens, the material is axially loaded in the dark to stress $\sigma_{\max}$. At stresses below $\sigma_{\min}$ the material undergoes a strain-induced polydomain–monodomain transition[7,9] (path I, Fig. 8.7). Above $\sigma_{\min}$ the (now monodomain) sample behaves elastically (path II). Irradiation the material with light of frequency ν_1 to cause $E \rightarrow Z$ photoisomerization of the photoactive mesogens while maintaining constant stress results in its axial contraction (path III) due to a decrease in the nematic order. This contraction performs work on the external load. Slowly relaxing the external load down to $\sigma_{\min}$ allows further contraction of the material (path IV) and generates more useful work. Irradiation of the isotropic phase at stress $\sigma_{\min}$ with light of frequency ν_2 to cause $Z \rightarrow E$ photoisomerization of the photoactive mesogens returns them to their rod-like state and induces an isothermal isotropic → nematic phase change, during which the sample elongates (path V).

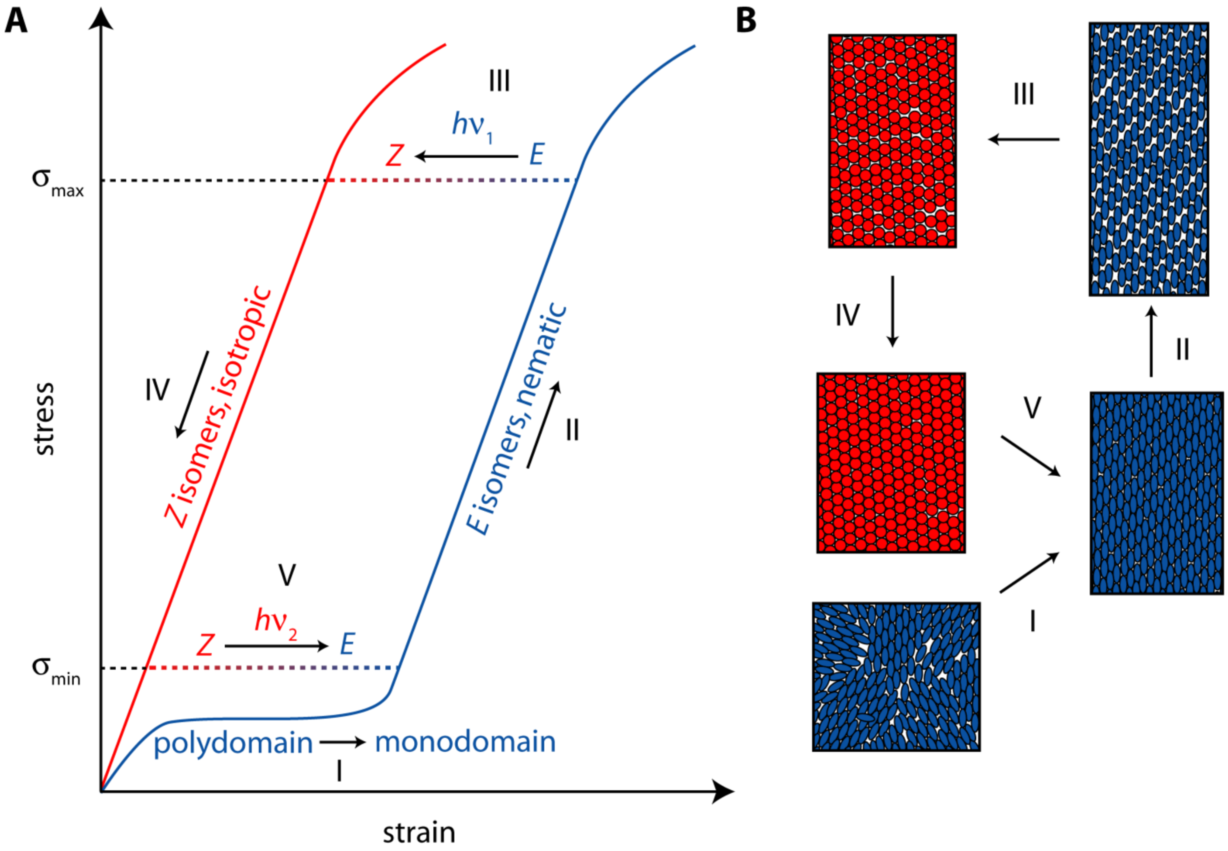

Fig. 8.7. A model work cycle for a photoactuating polydomain LCE; the *E* isomers of the photoactive mesogens are rod-like, and the *Z* isomers are bent. **A**: The work cycle depicted on a stress–strain plot. The descriptions of the steps (I–V) in the work cycle are described in the main text. **B**: Illustrations of the material's microstructural changes in steps I–V, depicting the shape distributions of polymer chains in the nematic (blue ovals) and isotropic (red circles) states.

The reversible work w_{rev} done by the material in one cycle is given by the area inside the curves II → III → IV → V if each step is performed infinitely slowly, i.e., w_{rev} is the thermodynamic limit of conversion of light to mechanical work by the material. The corresponding maximum external energy conversion efficiency is, therefore,

$$\eta_{\max} = \frac{w_{\text{rev}}}{h\nu_1\Phi_1 + h\nu_2\Phi_2} \tag{8.1}$$

where h is Plank's constant and Φ_1 and Φ_2 are the total absorbed photon fluxes during the first and second irradiation steps, respectively. The maximum work achievable depends on the elastic moduli of the nematic and isotropic phases. The elastic moduli of LCEs have been shown to depend on the degree of molecular alignment and the crosslinking density[38] and are somewhat tunable through molecular design. The maximum energy conversion efficiency additionally depends on the number of photons that must be absorbed by the material to induce the phase transition and the frequencies of light used, which depends on the quantum yields and absorption spectra of the chromophore and is also amenable to molecular design. For example, the effect of substituents on the wavelengths of *E*/*Z* photoisomerization of C=C and N=N bonds in stilbenes, azobenzenes and more recently isoindigos has been studied extensively computationally[54-56] and experimentally.[57-61]

8.3.4 Outstanding Questions in Molecular Photoactuator Design

The general rules for the design of photoactuating materials and monomeric chromophores remain to be formulated, but several trends have emerged. For example, available photostresses could be increased by working with highly cross-linked polymers with high elastic moduli,[62] or microstructurally ordered glassy LC polymers[38,63] in which the nematic director twists by 90° through the sample, similar to the helical director ordering in cholesteric LC phases. Improving the long-range order of LCEs is thought to increase accessible photostrains. Potential strategies for maximizing work capacity and energy conversion efficiencies of photoactuating materials are less clear. From the molecular-design perspective, this goal requires optimizing work-generating molecular parameters, by maximizing quantum yields for photoisomerization, the difference in the extinction coefficients of the two isomers and isomerization wavelength, while minimizing dissipative processes, including photochemical and thermal side reactions and unproductive relaxation of the metastable isomer, particularly at high bulk stresses. Other parameters, including the concentration of the chromophores, their localization in the polymer matrix and molecular compliances of non-chromophoric parts of the material may also be critical for achieving acceptable energy conversion efficiencies and work densities.

It may be more efficient to understand the chemistry of photoactuation in individual macromolecules before moving to the less tractable bulk materials. The advances in micromanipulation techniques in the past few decades have allowed individual macromolecules to be stretched controllably.[64] Photochemical actuation by individual chains of oligoazobenzene was demonstrated in 2002.[65,66] An azobenzene-containing oligomer (Fig. 8.8A) was bound at its termini to a glass slide and an Au-coated AFM tip allowing it to be stretched by separating the force probes while recording the force required to maintain the probe separation (Fig. 8.8B). The oligomer was stretched to 80 pN and irradiated at 420 nm to increase the fraction of its azobenzenes in the *E* form. The oligomer was then stretched to 200 pN (path I, Fig. 8.8C) and subsequently irradiated with 365 nm light (path II) to photoisomerize azobenzene monomers to the shorter *Z* form. The stretching force was gradually reduced to 85 pN (path III) allowing the oligomer to contract. Irradiation with 420 nm light increases the fraction of *E* isomers, completing the optomechanical cycle (path IV).

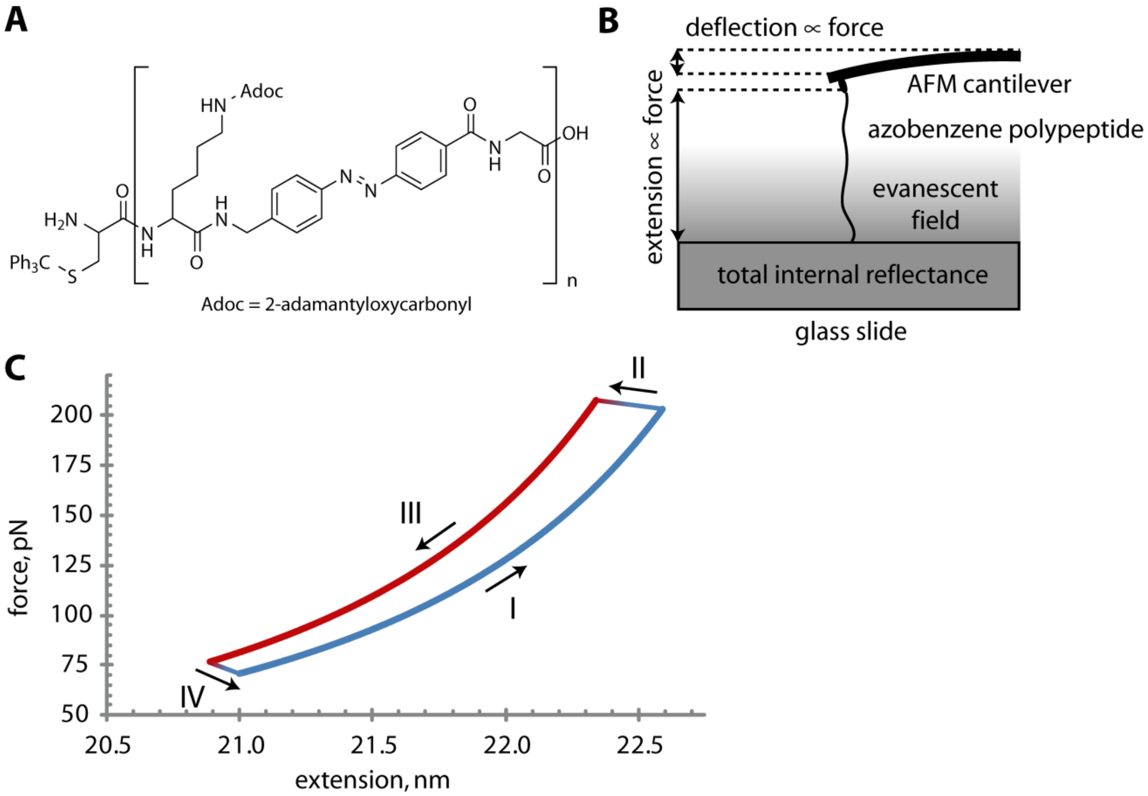

Fig. 8.8. The experimental demonstration of a single molecule optomechanical work cycle. **A**: The chemical structure of the azobenzene-containing oligomer used; $n \approx 47$. **B**: The experimental setup for stretching a single oligomer between the glass slide and atomic force microscope (AFM) cantilever with photoisomerization of the N=N bonds being induced by the evanescent field due to total internal reflection of the excitation irradiation in the glass slide. **C**: Wormlike chain fits (paths I and III) to an experimentally demonstrated optomechanical cycle[65] plotted in terms of molecular restoring force vs. extension. The molecule predominantly contains *E*-azobenzene units in the blue trace and *Z*-azobenzene units in the red trace. Paths I–IV are described in the main text.

This and similar experiments can be understood quantitatively within a general single-chain work cycle (Fig. 8.9), comprised of loading (stretching the polymer by applying an increasing tensile force to its termini), irradiation, unloading, and recovery (steps I–IV, respectively). The single-chain cycle is comparable to that for a bulk material (Fig. 8.7) except that stress (volumetric energy density) is replaced with force (linear energy density), because a macromolecule is effectively 2-dimensional. The relationship between the average applied tensile force and the average separation of the polymer's termini divided by the number of chromophores in the polymer is described by eq. (8.2) where s_0 and λ are the contour length and stretching compliance per chromophore of the all-*E* strain-free polymer, Δs and $\Delta\lambda$ are the differences in these variables between the all-*E* and all-*Z* forms, χ_E is the molar fraction of the *E* isomers of the chromophores in the polymer, *b* is the Kuhn length derived from a modified isomeric state model for the all-*E* polymer,[67] α is an empirical parameter that accounts for the loss of entropy per chromophore upon photoisomerization and β is inverse thermal energy (i.e., $\beta = (k_B T)^{-1}$).

$$s(F) = \left(s_0 + \chi_E \Delta s + F(\lambda + \chi_E \Delta\lambda)\right)\left(\coth\left(F\left(b + \chi_E(\Delta s + \alpha)\right)\beta\right) - \frac{1}{F\left(b + \chi_E(\Delta s + \alpha)\right)\beta}\right) \tag{8.2}$$

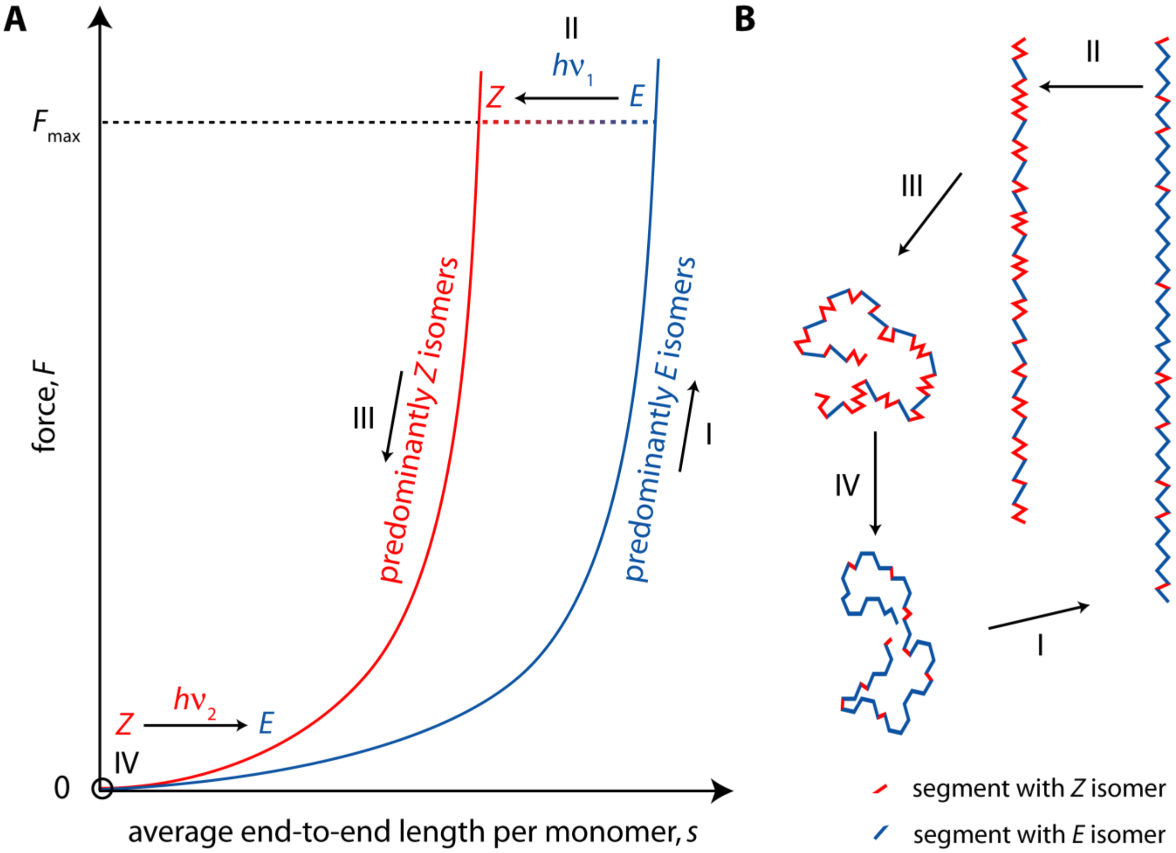

Fig. 8.9. A model work cycle for a single molecule of a photoactuating polymer. **A**: The work cycle depicted on a force–extension plot. The descriptions of the steps (I–IV) in the work cycle are described in the main text. **B**: Illustrations of the polymer shape changes in steps I–IV, indicating the *E* (blue) and *Z* (red) isomers in each state.

Similarly to the macroscopic cycle, the reversible work per monomer per cycle is given by the area bound by the two solid force-extension curves and the broken line describing isotensional photochemical contraction. This cycle can be performed reversibly only at 0 K because at higher temperatures thermal relaxation of the metastable *Z* isomer to the *E* analog would collapse the two force-extension curves.

The structural and kinetic parameters of eq. (8.2) (s, Δs, λ, $\Delta\lambda$ and χ_E) all depend on the force experienced by the macromolecule. For example, thermal $Z \rightarrow E$ isomerization would be accelerated in an overstretched polymer relative to the strain-free analog and the quantum yields of generating the more strained *Z* isomer will be suppressed. Such effects maybe neglected for polymers operating against stresses <1 MPa, as is typical for demonstrations of photoactuation by LCEs, but must be taken into account in designing polymers for operation against larger stresses. There is evidence of such effects in the experiment described in Fig. 8.9,[65] where maximum contraction of the stretched oligoazobenzene corresponded to conversion of only ~28% (mol) of azobenzene monomers into the *Z* isomer, compared to ~55% in the absence of strain. Part of the difference may be attributed to the non-uniform irradiation of the macromolecule in these experiments. This comparison and other demonstrations of the effects of macroscopic stresses on thermal and photochemical kinetics[68] highlight the need for a general kinetic model incorporating stress as a kinetic variable.

8.4 Multiscale Reaction Dynamics

The (typical) acceleration of chemical reactions in bulk strained materials is often called mechanochemistry. The effects can be quite dramatic, with up to 10^{15}-fold accelerations in reaction rates reported. Mechanochemical phenomenology, its biological and technological significance and the experimental and computational methods of study have been reviewed previously.[67,69-71] Until our work, the quantitative predictions of kinetic and/or thermodynamic stabilities of reactive sites in stretched polymers have been prevented by the failure of traditional chemical and physical models to bridge the "formidable gap" of the length scale spanning ~50 nm and ~1 nm, where coupling between large-scale strains and chemical reactions is important (Fig. 8.10, refs. 69 and 72). Chemomechanics is a conceptual framework to allow such predictions.

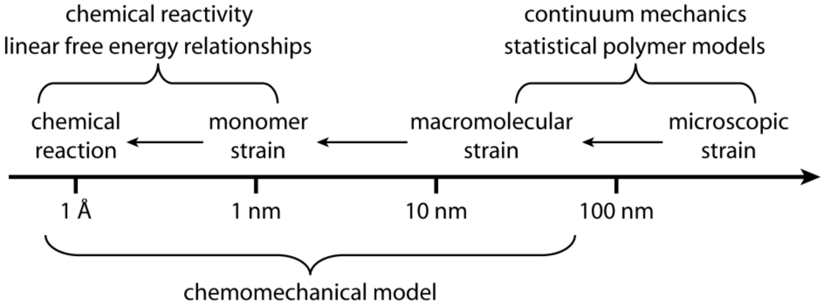

Fig. 8.10. The hierarchy of length scales involved in multiscale phenomena and the regimes of the established models that describe phenomena at various length scales (top). Since the length scales of continuum mechanics and chemical kinetics do not overlap, a new model integrating the two formalisms is required to arrive at quantitative descriptions of mechanochemical phenomena. Reproduced from ref. 69.

8.4.1 Basic Principles of the Chemomechanical Formalism

Qualitatively, mechanochemistry can be viewed as the effect of molecular strain on chemical reactivity, a topic that chemists have studied for the past 100 years. However, mechanochemical phenomena are not amenable to a quantitative description within the formalism of linear free energy relationships (LFERs) that underlie the kinetic models of molecular strain. The reason is that materials and molecular strain are different concepts. Materials strain is rigorously defined and quantitative,[73] but molecular strain is qualitative.[69] The quantitative discussion of strain-induced chemistry relies on the concept of strain energy, which is defined formally as the difference in the enthalpy of formation of a strained molecule and its hypothetical strain-free analog. Within the formalism of the LFERs, strain energy allows semi-quantitative estimates of strain-induced differences in activation barriers of reactions without any information about the transition state. This is possible in conventional chemical reactions because the kinetically-relevant changes in strain energy are confined to small and well-defined volumes of space (strained reactant and product) and are fairly easy to estimate. In contrast, in reactions in bulk anisotropically strained environments, strain energies of the initial and final states are difficult, if not impossible, to define, and the strain-energy change that contributes to the reaction barrier is only a tiny fraction of the total strain energy.

A quantitative relationship between large-scale strain and localized reaction kinetics requires an intensive quantifier of strain, such as force.[67,69,72] Force is the gradient of strain energy along a constrained degree of freedom. A macroscopically constrained degree of freedom, such as an axis of anistropic material, is often called the mechanical coordinate. The simplest example is a reaction within an inert polymer that is stretched, with the mechanical coordinate being the separation of the polymer termini, τ (Fig. 8.11A). Either τ, or its conjugate variable, mechanical force, F_τ, is the control parameter. The two parameters for isolated macromolecules are related by several models (e.g., Fig. 8.11B).

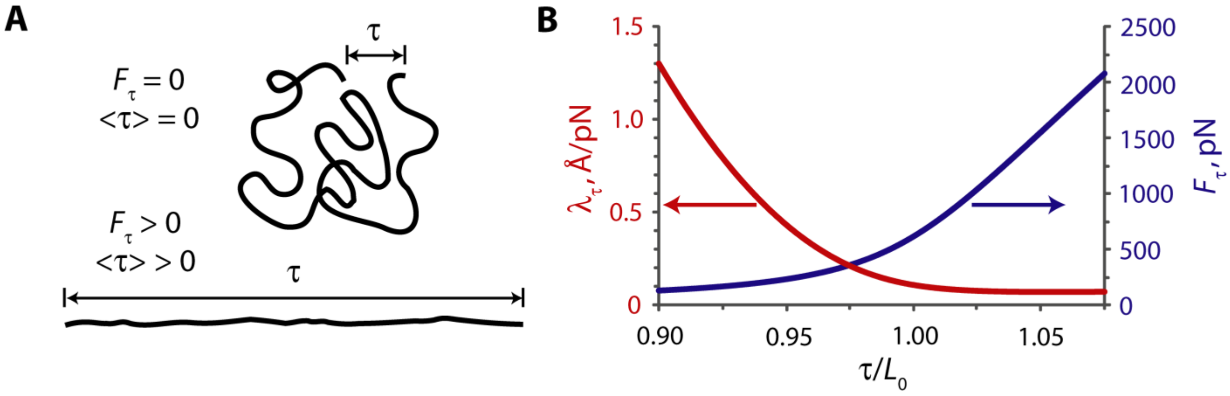

Fig. 8.11. **A**: Depiction of the mechanical coordinate τ in single polymer chains; ⟨ ⟩ denotes ensemble average values. **B**: The compliance (λ_τ, red) and restoring force (F_τ, blue) of a single molecule of polyethylene as a function

of its strain τ/L_o; the contour length, L_o, is 150 nm. Note considerable restoring force at the polymer end-to-end distances below its contour length, reflecting the considerable reduction of macromolecular entropy as the polymer termini are constrained.[74,75] Calculated with data and methods in ref. 76. Modified from ref. 69.

If the mechanical coordinate remains in thermal equilibrium with its environment during an elementary localized reaction, the corresponding rate constant of a long flexible polymer stretched to average restoring force F_τ, $k(F_\tau)$, relative to the same reaction in the strain-free reactant, k_o, is given by eq. (8.3), where λ is the total stretching compliance of mechanical coordinate τ in the ground state, τ_{ts} and $\Delta\lambda$ are the differences in the strain-free end-to-end separation and in the compliances of τ between the ground and transition states. The famous Eyring–Bell–Evans ansatz[77-80] postulating exponential dependence of the reaction rate with restoring force is a limiting case of eq. (8.3).

$$\beta^{-1}\ln\frac{k(F_\tau)}{k_o} = \frac{\lambda}{\lambda+\Delta\lambda}\left(F_\tau\tau_{ts} + \frac{F_\tau^2}{2}\Delta\lambda\right) \tag{8.3}$$

Macroscopic stretching compliances, λ, of many polymers have been measured by single-molecule force spectroscopy. However, τ_{ts} and $\Delta\lambda$, which characterize strain-free macromolecular *transition states*, are not available for reactions of interest to materials chemists. To allow practical applications of eq. (8.3), e.g., for predicting the changes in the kinetic or thermodynamic stability of a reactive site as the polymer containing it is stretched, we formulated and computationally validated the local approximation of chemomechanics. In its simplest formulation, which applies to reactions in stretched polymers, the local approximation postulates the existence of a molecular coordinate of the reactive site, q, such that

1. the strain-free difference in the mechanical coordinate of the macromolecular reactant between its ground and transition states approximately equals the difference in coordinate q between the strain-free ground and transition states of the minimal reactant, i.e., $\tau_{ts} \approx \Delta q$, and
2. the mechanical force (i.e., the restoring force of the mechanical coordinate), equals the molecular restoring force of the local coordinate q (i.e., $F_\tau \approx F_q$).

With these assumptions, eq. (8.3) can be re-written in terms of readily available structural and kinetic parameters of the minimal reactant, Δq and $\Delta\lambda_q$, i.e., the strain-free difference in the dimensions and compliance of a local molecular coordinate between the ground and transition states of the reaction[67,69,72] (eq. (8.4)). Unlike the more familiar molecular force constants, molecular compliances are independent of the coordinate system, so that in the absence of electronic effects, the compliance of a localized degree of freedom in a large molecule (e.g., polymer) is the same as the compliance of the same degree of freedom in isolated site.[81,82]

$$\beta^{-1}\ln\frac{k(F_\tau)}{k_o} \approx \beta^{-1}\ln\frac{k(F_q)}{k_o} = \frac{\lambda}{\lambda+\Delta\lambda_q}\left(F_q\Delta q + \frac{F_q^2}{2}\Delta\lambda_q\right) \tag{8.4}$$

8.4.2 Force-Dependent Kinetics of Photoactuating Monomers and Mesogens

The local approximation cannot be validated experimentally by studying reactions in stretched polymers because the existing methods lack the resolution and reaction scope to yield the neccessary data. Therefore we developed an alternative to traditional micromanipulation techniques to measure reaction rates as a function of the restoring force of a molecular degree of freedom: molecular force probes.[20,67,69,72] The method relies on synthesizing a series of increasingly strained macrocycles in which a reactive site of interest is incorporated in a 5–10 atom-long inert strap constraining the *E* isomer of stiff stilbene (red, Fig. 8.12A). Quantum-chemical computations confirmed that in this molecular architecture the reactive site experiences approximately the same pattern of strain as it does in a stretched polymer. The magnitude of the restoring force of different molecular degrees of freedom of the reactive site is controlled by the length and conformational flexibility of the strap (X + reactive moiety + Y, Fig. 8.12B) so that a series of ~10–12 macrocycles of 15–20 endocyclic atoms can reproduce the range of the restoring forces accessible in a typical single-molecule force experiment (<100 pN to >650 pN) with small (<50 pN) increments between individual macrocycles. We have used molecular force probes to validate the chemomechanical formalism for force-dependent kinetics of broad reaction classes, including electrocyclic ring opening[83,84] and nucleophilic displacement.[85,86]

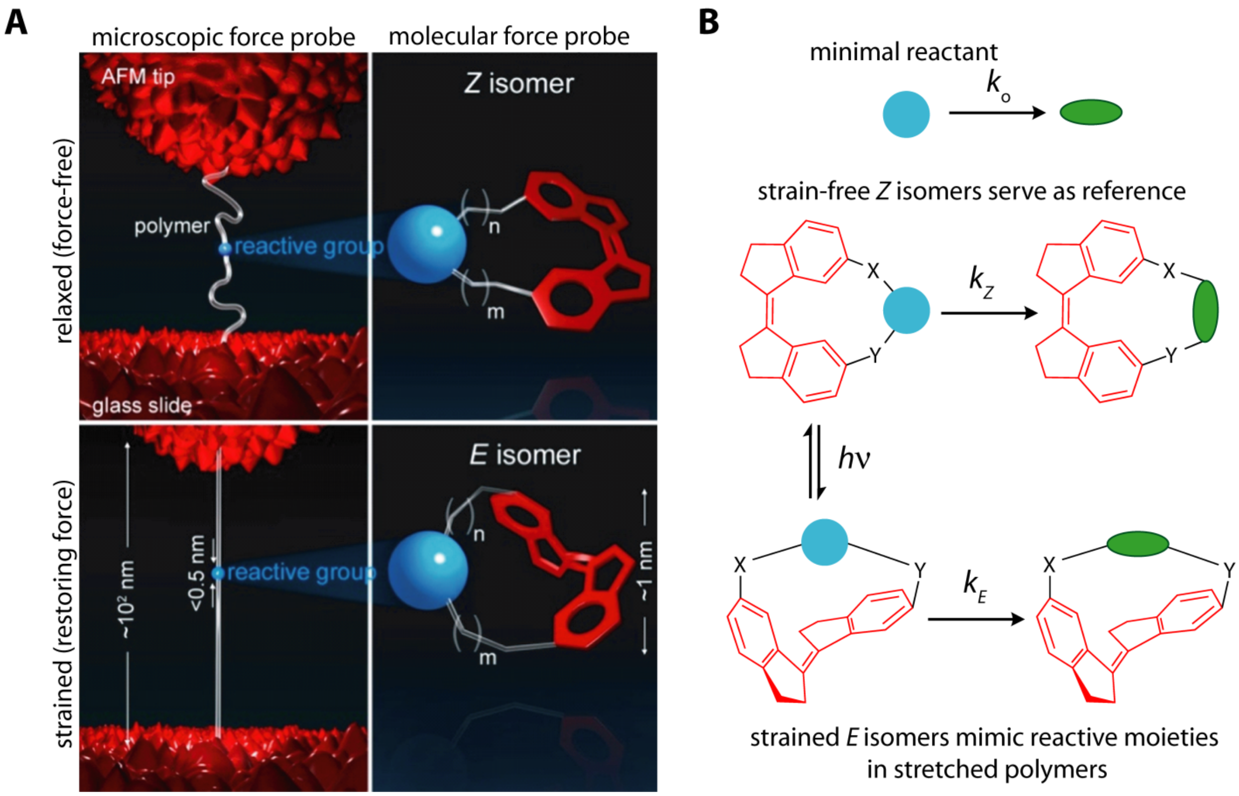

Fig. 8.12. **A**: A comparison of methods for measuring force-dependent kinetics of localized reactions. On the left, conventional single-molecule force spectroscopy requires the incorporation of the reactive moiety (blue sphere) into a long flexible polymer, attaching the polymer to a pair of microscopic force probes (here, the tip of the atomic force microscope cantilever and a glass slide on a piezoelectric stage) and stretching it by separating the probes. The size of the reactive moiety is typically less than the surface roughness of the probes or the magnitude of their thermal fluctuations, which significantly limits the accuracy of the measurements and the scope of reactions amenable to such studies. The right panels show a molecular force probe containing the same reactive moiety. Reproduced from ref. 83. **B**: The general method for measuring force-dependent kinetics with molecular force probes. The strained *E* isomers are obtained by photoisomerization of strain-free *Z* analogs, which are synthesized using conventional chemistry. Modified from ref. 85.

The same approach is useful in measuring the effect of axial strain on the kinetics of thermal and photochemical $Z \rightarrow E$ isomerization of stiff stilbene or another chromophore. This approach showed that both barriers for thermal and quantum yields of photochemical isomerization of C=C bonds decrease with force. Consequently, the composition of the photostationary state is particularly sensitive to applied force, varying by >1000-fold over 600 pN in case of stiff stilbene.

The sensitivity of different chromophores to imposed constraints is determined by the difference in the dimension of the constrained degree of freedom between the two isomers. This trend suggests that coupling chromophores to the polymeric network through rigid moieties such as fused aromatic rings or acetylene units would increase the maximum dimensional change upon irradiation of the material at the expense of decreasing both the quantum yields of generating the strained (typically *Z*) isomer and its thermal stability against relaxation to the less-strained (typically *E*) analog. The latter may limit the work density, the energy conversion efficiency and the maximum stress that can be practically generated by the material.

The stresses at which these effects would become significant can be estimated as follows. Neutron diffraction data suggests that in well-aligned polymeric materials, individual chains can be approximated as filling cylinders with a radius of 2 nm.[87] Assuming a hexagonal close packing of polymer molecules (area fraction of 0.9069), a tensile stress of 44 MPa (comparable to the stresses generated by photoacutating molecular crystals[3]) corresponds to an average tensile force of $F_\tau \approx 610$ pN per macromolecule. Using eq. (8.4) and neglecting the second-order effects ($\Delta\lambda = 0$) the contraction of the constrained molecular degree of freedom between the ground and transition states of $\Delta q \approx 2.85$ Å (e.g., that for thermal isomerization of stiff stilbene connected through its C6,C6′ positions or for azobenzene connected at the *para* positions), could correspond to a strain-induced decrease of the barrier for thermal relaxation of the *Z* isomer to its less strained *E* analog of $F_q\Delta q \approx 1735$ pN Å = 25 kcal/mol at room temperature. The value is more than half of that for strain-free $Z \rightarrow E$ isomerisation of stiff stilbene (38 kcal/mol) and is greater than that of azobenzene (23 kcal/mol)! Clearly, operation at high stresses would require correspondingly large barriers to thermal isomerization to avoid (nearly) barrierless thermal relaxation kinetics. Several strategies exist to increase the activation energies of isomerization by substitution, but such increases are typically coupled to (undesirable) increases in the energy of photoisomerization (Fig. 8.13). The correlation between the activation energy for thermal $Z \rightarrow E$ isomerization and the energy of the absorption band for the π system that leads to photoisomerization is striking, particularly because this data is for three different classes of compounds (alkenes, stilbenes, and azobenzenes) measured in a variety of media.

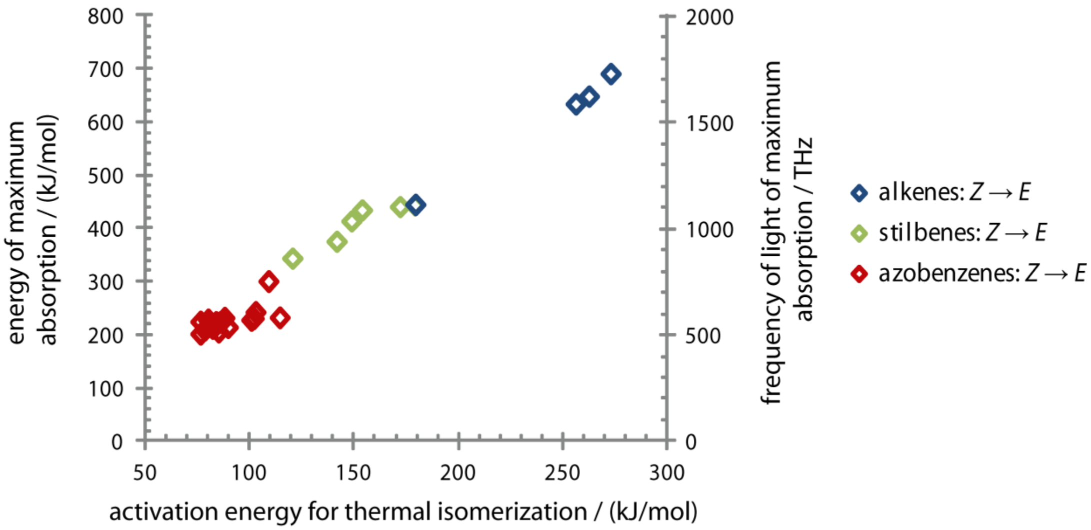

Fig. 8.13. The apparent relationship between the activation energy for thermal $Z \rightarrow E$ isomerization and the energy of the maximum absorption band leading to photoisomerization of the *Z* isomer. Absorption energies for the *Z* isomers of azobenzenes was estimated as the absorbance energy in the *E* isomer + the absorbance energy of (*Z*)-azobenzene – the absorbance energy of (*E*)-azobenzene. Alkene data from refs. 88-93, stilbene data from refs. 58 and 61, and azobenzene data from ref. 60.

Alternatively, in LCEs in which the photoisomerizable mesogens are in non-load-bearing fragments (i.e., side chains, rather than crosslinks or the main chain), F_q is probably determined solely by interaction with the environment and presently is difficult to estimate. Rather than relying on the translation of F_q into macroscopic stresses, photoactuating LC systems operate by photochemically inducing an isothermal phase change. If F_q for non-load-bearing photoisomerizable mesogens is significantly lower than that for their load-bearing analogs, their thermal relaxation kinetics may be far less perturbed by the macromolecular stresses present. However, increasing macroscopic stresses may instead reduce the effectiveness of such photoisomerizations, but this can be counteracted by increasing the concentration of such mesogens in the material, as mentioned above. Thus, if both isomers of a photoactive mesogen are sufficiently thermally stable in the absence of force, an LCE with such mesogens in side chains may be able to maintain high photostresses and photostrains for long periods of time. This may be one reason for the success of photoactuating LCE materials.

8.5 Conclusions

In this chapter we have reviewed the physical chemistry of photoactuation in polymers, molecular crystals, liquid crystals and liquid crystal elastomers. The two key events in photochemical actuation are isomerization following photon absorption, which results in structural changes at the molecular level, and the transmission of these changes to larger length scales. Bringing the full potential of chemistry to bear to yield new photoactuating materials requires a general, physically sound and quantitative model to describe dynamic coupling between the molecular and mesoscopic scales. By allowing useful estimates of the kinetics and thermodynamics of productive and parasitic reactions in materials under external loads, such a model would help guide the design of new chromophores and polymer architectures capable of achieving practically useful energy conversion efficiencies and work densities.

Chemomechanics is one such model, and within the local approximation it provides the only available approach to estimate the fundamental limits of photomechanical energy conversion using molecular isomerization. Bulk strains can significantly perturb the kinetics of actuating reactions, suppressing quantum efficiencies of generating and accelerating undesirable relaxation of metastable strained isomers.

8.6 References

1. Mizutani, Y.; Otani, Y.; Umeda, N., Optically Controlled Bimorph Cantilever of Poly(vinylidene difluoride). *Appl. Phys. Express* **2008**, *1*, 041601/1–3.
2. Juodkazis, S.; Mukai, N.; Wakaki, R.; Yamaguchi, A.; Matsuo, S.; Misawa, H., Reversible Phase Transitions in Polymer Gels Induced by Radiation Forces. *Nature* **2000**, *408*, 178–181.
3. Morimoto, M.; Irie, M., A Diarylethene Cocrystal that Converts Light into Mechanical Work. *J. Am. Chem. Soc.* **2010**, *132*, 14172–14178.
4. Ikeda, T.; Mamiya, J. i.; Yu, Y., Photomechanics of Liquid-Crystalline Elastomers and Other Polymers. *Angew. Chem. Int. Ed.* **2007**, *46*, 506–528.
5. Kobatake, S.; Takami, S.; Muto, H.; Ishikawa, T.; Irie, M., Rapid and Reversible Shape Changes of Molecular Crystals on Photoirradiation. *Nature* **2007**, *446*, 778–781.
6. Eelkema, R.; Pollard, M. M.; Vicario, J.; Katsonis, N.; Ramon, B. S.; Bastiaansen, C. W. M.; Broer, D. J.; Feringa, B. L., Nanomotor Rotates Microscale Objects. *Nature* **2006**, *440*, 163.
7. Corbett, D.; Warner, M., Changing Liquid Crystal Elastomer Ordering with Light - A Route to Opto-Mechanically Responsive Materials. *Liq. Cryst.* **2009**, *36*, 1263–1280.

8. Warner, M.; Terentjev, E., Thermal and Photo-Actuation in Nematic Elastomers. *Macromol. Symp.* **2003**, *200*, 81–92.
9. Warner, M.; Terentjev, E. M., *Liquid Crystal Elastomers*. Oxford University Press: New York, 2003.
10. Russew, M.-M.; Hecht, S., Photoswitches: From Molecules to Materials. *Adv. Mater.* **2010**, *22*, 3348–3360.
11. Yu, Y.; Ikeda, T., Photodeformable Materials and Photomechanical Effects Based on Azobenzene-Containing Polymers and Liquid Crystals. In *Smart Light-Responsive Materials*, Zhao, Y.; Ikeda, T., Eds. John Wiley & Sons, Inc.: Hoboken, NJ, 2008; pp 95–144.
12. Koerner, H.; White, T. J.; Tabiryan, N. V.; Bunning, T. J.; Vaia, R. A., Photogenerating Work from Polymers. *Mater. Today* **2008**, *11*, 34–42.
13. Irie, M., Photochromism and Molecular Mechanical Devices. *Bull. Chem. Soc. Jpn.* **2008**, *81*, 917–926.
14. Barrett, C. J.; Mamiya, J.-i.; Yager, K. G.; Ikeda, T., Photo-Mechanical Effects in Azobenzene-Containing Soft Materials. *Soft Matter* **2007**, *3*, 1249–1261.
15. Jiang, H. Y.; Kelch, S.; Lendlein, A., Polymers Move in Response to Light. *Adv. Mater.* **2006**, *18*, 1471–1475.
16. Kobatake, S.; Irie, M., Photochromism. *Annu. Rep. Prog. Chem., Sect. C, Phys. Chem.* **2003**, *99*, 277–313.
17. Tamai, N.; Miyasaka, H., Ultrafast Dynamics of Photochromic Systems. *Chem. Rev.* **2000**, *100*, 1875–1890.
18. Bouas-Laurent, H.; Dürr, H., Organic Photochromism. *Pure Appl. Chem.* **2001**, *73*, 639–665.
19. Waldeck, D. H., Photoisomerization Dynamics of Stilbenes. *Chem. Rev.* **1991**, *91*, 415–436.
20. Huang, Z.; Boulatov, R., Chemomechanics with Molecular Force Probes. *Pure Appl. Chem.* **2010**, *82*, 931–951.
21. Morimoto, M.; Irie, M., Photochromism of Diarylethene Single Crystals: Crystal Structures and Photochromic Performance. *Chem. Comm.* **2005**, 3895–3905.
22. Irie, M., Diarylethenes for Memories and Switches. *Chem. Rev.* **2000**, *100*, 1685–1716.

23. Yokoyama, Y., Molecular Switches with Photochromic Fulgides. In *Molecular Switches*, Wiley-VCH Verlag GmbH: 2001; pp 107–121.
24. Yokoyama, Y., Fulgides for Memories and Switches. *Chem. Rev.* **2000**, *100*, 1717–1740.
25. Minkin, V. I., Photo-, Thermo-, Solvato-, and Electrochromic Spiroheterocyclic Compounds. *Chem. Rev.* **2004**, *104*, 2751–2776.
26. Levine, B. G.; Martínez, T. J., Isomerization through Conical Intersections. *Annu. Rev. Phys. Chem.* **2007**, *58*, 613–634.
27. Domcke, W.; Yarkony, D. R.; Köppel, H., *Conical Intersections: Electronic Structure, Dynamics and Spectroscopy*. World Scientific: New Jersey, 2004; Vol. 15.
28. Klok, M.; Boyle, N.; Pryce, M. T.; Meetsma, A.; Browne, W. R.; Feringa, B. L., MHz Unidirectional Rotation of Molecular Rotary Motors. *J. Am. Chem. Soc.* **2008**, *130*, 10484–10485.
29. Bandara, H. M. D.; Friss, T. R.; Enriquez, M. M.; Isley, W.; Incarvito, C.; Frank, H. A.; Gascon, J.; Burdette, S. C., Proof for the Concerted Inversion Mechanism in the *trans→cis* Isomerization of Azobenzene Using Hydrogen Bonding to Induce Isomer Locking. *J. Org. Chem.* **2010**, *75*, 4817–4827.
30. Tiberio, G.; Muccioli, L.; Berardi, R.; Zannoni, C., How Does the *trans–cis* Photoisomerization of Azobenzene Take Place in Organic Solvents? *ChemPhysChem* **2010**, *11*, 1018–1028.
31. Creatini, L.; Cusati, T.; Granucci, G.; Persico, M., Photodynamics of Azobenzene in a Hindering Environment. *Chem. Phys.* **2008**, *347*, 492–502.
32. Norikane, Y.; Katoh, R.; Tamaoki, N., Unconventional Thermodynamically Stable *cis* Isomer and *trans* to *cis* Thermal Isomerization in Reversibly Photoresponsive [0.0](3,3′)-Azobenzenophane. *Chem. Comm.* **2008**, 1898–1900.
33. Funke, U.; Grützmacher, H.-F., Dithia-diaza[n.2]paracyclophane-enes. *Tetrahedron* **1987**, *43*, 3787–3795.
34. Ichimura, K., Photoalignment of Liquid-Crystal Systems. *Chem. Rev.* **2000**, *100*, 1847–1874.
35. Serak, S.; Tabiryan, N.; Vergara, R.; White, T. J.; Vaia, R. A.; Bunning, T. J., Liquid Crystalline Polymer Cantilever Oscillators Fueled by Light. *Soft Matter* **2010**, *6*, 779–783.

36. White, T. J.; Tabiryan, N. V.; Serak, S. V.; Hrozhyk, U. A.; Tondiglia, V. P.; Koerner, H.; Vaia, R. A.; Bunning, T. J., A High Frequency Photodriven Polymer Oscillator. *Soft Matter* **2008**, *4*, 1796–1798.

37. White, T. J.; Serak, S. V.; Tabiryan, N. V.; Vaia, R. A.; Bunning, T. J., Polarization-Controlled, Photodriven Bending in Monodomain Liquid Crystal Elastomer Cantilevers. *J. Mater. Chem.* **2009**, *19*, 1080–1085.

38. Harris, K. D.; Cuypers, R.; Scheibe, P.; Oosten, C. L. v.; Bastiaansen, C. W. M.; Lub, J.; Broer, D. J., Large Amplitude Light-Induced Motion in High Elastic Modulus Polymer Actuators. *J. Mater. Chem.* **2005**, *15*, 5043–5048.

39. van der Veen, G.; Prins, W., Photomechanical Energy Conversion in a Polymer Membrane. *Nature Phys. Sci.* **1971**, *230*, 70–72.

40. van der Veen, G.; Hoguet, R.; Prins, W., Photoregulation of Polymer Conformation by Photochromic Moieties–II. Cationic and Neutral Moieties on an Anionic Polymer. *Photochem. Photobiol.* **1974**, *19*, 197–204.

41. Camacho-Lopez, M.; Finkelmann, H.; Palffy-Muhoray, P.; Shelley, M., Fast Liquid-Crystal Elastomer Swims into the Dark. *Nat. Mater.* **2004**, *3*, 307–310.

42. Harris, D. C.; Bertolucci, M. D., *Symmetry and Spectroscopy: An Introduction to Vibrational and Electronic Spectroscopy*. Dover Publications, Inc.: New York, 1989.

43. Harvey, C. L. M.; Terentjev, E. M., Role of Polarization and Alignment in Photoactuation of Nematic Elastomers. *Eur. Phys. J. E* **2007**, *23*, 185–189.

44. Corbett, D.; Warner, M., Bleaching and Stimulated Recovery of Dyes and of Photocantilevers. *Phys. Rev. E* **2008**, *77*, 051710/1–11.

45. Finkelmann, H.; Nishikawa, E.; Pereira, G. G.; Warner, M., A New Opto-Mechanical Effect in Solids. *Phys. Rev. Lett.* **2001**, *87*, 015501/1–4.

46. Küpfer, J.; Finkelmann, H., Nematic Liquid Single Crystal Elastomers. *Makromol. Chem., Rapid Commun.* **1991**, *12*, 717–726.

47. Li, C.; Lo, C. W.; Zhu, D.; Li, C.; Liu, Y.; Jiang, H., Synthesis of a Photoresponsive Liquid-Crystalline Polymer Containing Azobenzene. *Macromol. Rapid Commun.* **2009**, *30*, 1928–1935.

48. Kondo, M.; Sugimoto, M.; Yamada, M.; Naka, Y.; Mamiya, J.-i.; Kinoshita, M.; Shishido, A.; Yu, Y.; Ikeda, T., Effect of Concentration of Photoactive Chromophores on

Photomechanical Properties of Crosslinked Azobenzene Liquid-Crystalline Polymers. *J. Mater. Chem.* **2010**, *20*, 117–122.

49. Dunn, M. L., Photomechanics of Mono- and Polydomain Liquid Crystal Elastomer Films. *J. Appl. Phys.* **2007**, *102*, 013506/1–7.
50. Corbett, D.; Warner, M., Polarization Dependence of Optically Driven Polydomain Elastomer Mechanics. *Phys. Rev. E* **2008**, *78*, 061701/1–13.
51. Corbett, D.; Warner, M., Nonlinear Photoresponse of Disordered Elastomers. *Phys. Rev. Lett.* **2006**, *96*, 237802/1–4.
52. Corbett, D.; van Oosten, C. L.; Warner, M., Nonlinear Dynamics of Optical Absorption of Intense Beams. *Phys. Rev. A* **2008**, *78*, 013823/1–4.
53. Spinks, G. M.; Truong, V.-T., Work-per-Cycle Analysis for Electromechanical Actuators. *Sensor. Actuat. A: Phys.* **2005**, *119*, 455–461.
54. Jacquemin, D.; Perpete, E. A.; Scuseria, G. E.; Ciofini, I.; Adamo, C., TD-DFT Performance for the Visible Absorption Spectra of Organic Dyes: Conventional versus Long-Range Hybrids. *J. Chem. Theory Comput.* **2007**, *4*, 123–135.
55. Perpète, E. A.; Preat, J.; André, J.-M.; Jacquemin, D., An ab Initio Study of the Absorption Spectra of Indirubin, Isoindigo, and Related Derivatives. *J. Phys. Chem. A* **2006**, *110*, 5629–5635.
56. Blevins, A. A.; Blanchard, G. J., Effect of Positional Substitution on the Optical Response of Symmetrically Disubstituted Azobenzene Derivatives. *J. Phys. Chem. B* **2004**, *108*, 4962–4968.
57. Lunák, S., Jr.; Horáková, P.; Lycka, A., Absorption and Fluorescence of Arylmethylidenoxindoles and Isoindigo. *Dyes Pigments* **2010**, *85*, 171–176.
58. Görner, H.; Kuhn, H. J., *Cis–Trans* Photoisomerization of Stilbenes and Stilbene-like Molecules. In *Advances in Photochemistry*, Neckers, D. C.; Volman, D. H.; Bünau, G. v., Eds. John Wiley & Sons, Inc.: 1995; Vol. 19, pp 1–117.
59. Forber, C. L.; Kelusky, E. C.; Bunce, N. J.; Zerner, M. C., Electronic spectra of *cis*- and *trans*-azobenzenes: consequences of ortho substitution. *J. Am. Chem. Soc.* **1985**, *107*, 5884–5890.

60. Nishimura, N.; Sueyoshi, T.; Yamanaka, H.; Imai, E.; Yamamoto, S.; Hasegawa, S., Thermal *Cis*-to-*Trans* Isomerization of Substituted Azobenzenes II. Substituent and Solvent Effects. *Bull. Chem. Soc. Jpn.* **1976**, *49*, 1381–1387.
61. Ross, D. L.; Blanc, J., Photochromism by *cis–trans* Isomerization. In *Photochromism*, Brown, G. H., Ed. 1971; pp 471–556.
62. Spillmann, C. M.; Naciri, J.; Chen, M.-S.; Srinivasan, A.; Ratna, B. R., Tuning the Physical Properties of a Nematic Liquid Crystal Elastomer Actuator. *Liq. Cryst.* **2006**, *33*, 373–380.
63. van Oosten, C.; Harris, K.; Bastiaansen, C.; Broer, D., Glassy Photomechanical Liquid-Crystal Network Actuators for Microscale Devices. *Eur. Phys. J. E* **2007**, *23*, 329–336.
64. Neuman, K. C.; Nagy, A., Single-Molecule Force Spectroscopy: Optical Tweezers, Magnetic Tweezers and Atomic Force Microscopy. *Nat. Methods* **2008**, *5*, 491–505.
65. Hugel, T.; Holland, N. B.; Cattani, A.; Moroder, L.; Seitz, M.; Gaub, H. E., Single-Molecule Optomechanical Cycle. *Science* **2002**, *296*, 1103–1106.
66. Holland, N. B.; Hugel, T.; Neuert, G.; Cattani-Scholz, A.; Renner, C.; Oesterhelt, D.; Moroder, L.; Seitz, M.; Gaub, H. E., Single Molecule Force Spectroscopy of Azobenzene Polymers: Switching Elasticity of Single Photochromic Macromolecules. *Macromolecules* **2003**, *36*, 2015–2023.
67. Huang, Z.; Boulatov, R., Chemomechanics: Reaction Kinetics in Multiscale Phenomena. *Chem. Soc. Rev.* **2011**, *40*, 2359–2384.
68. Lee, C. K.; Davis, D. A.; White, S. R.; Moore, J. S.; Sottos, N. R.; Braun, P. V., Force-Induced Redistribution of a Chemical Equilibrium. *J. Am. Chem. Soc.* **2010**, *132*, 16107–16111.
69. Kucharski, T. J.; Boulatov, R., The Physical Chemistry of Mechanoresponsive Polymers. *J. Mater. Chem.* **2011**, *21*, 8237–8255.
70. Black, A. L.; Lenhardt, J. M.; Craig, S. L., From Molecular Mechanochemistry to Stress-Responsive Materials. *J. Mater. Chem.* **2011**, *21*, 1655–1663.
71. Caruso, M. M.; Davis, D. A.; Shen, Q.; Odom, S. A.; Sottos, N. R.; White, S. R.; Moore, J. S., Mechanically-Induced Chemical Changes in Polymeric Materials. *Chem. Rev.* **2009**, *109*, 5755–5798.
72. Boulatov, R., Reaction Dynamics in the Formidable Gap. *Pure Appl. Chem.* **2011**, *83*, 25–41.

73. Tauchert, T. R., *Energy Principles in Structural Mechanics*. McGraw-Hill: New York, 1974.

74. Rubinstein, M.; Colby, R. H., *Polymer Physics*. Oxford University Press: New York, 2003.

75. Flory, P. J., *Statistical Mechanics of Chain Molecues*. Interscience Publishers: New York, 1969.

76. Hugel, T.; Rief, M.; Seitz, M.; Gaub, H. E.; Netz, R. R., Highly Stretched Single Polymers: Atomic-Force-Microscope Experiments Versus *Ab-Initio* Theory. *Phys. Rev. Lett.* **2005**, *94*, 048301/1–4.

77. Kauzmann, W.; Eyring, H., The Viscous Flow of Large Molecules. *J. Am. Chem. Soc.* **1940**, *62*, 3113–3125.

78. Bell, G. I., Models for the Specific Adhesion of Cells to Cells. *Science* **1978**, *200*, 618–627.

79. Evans, E.; Ritchie, K., Dynamic Strength of Molecular Adhesion Bonds. *Biophys. J.* **1997**, *72*, 1541–1555.

80. Evans, E., Probing the Relation Between Force—Lifetime—and Chemistry in Single Molecular Bonds. *Annu. Rev. Biophys. Biomol. Struct.* **2001**, *30*, 105–128.

81. Baker, J., A Critical Assessment of the Use of Compliance Constants as Bond Strength Descriptors for Weak Interatomic Interactions. *J. Chem. Phys.* **2006**, *125*, 014103/1–6.

82. Jones, L. H.; Swanson, B. I., Interpretation of Potential Constants: Application to Study of Bonding Forces in Metal Cyanide Complexes and Metal Carbonyls. *Acc. Chem. Res.* **1976**, *9*, 128–134.

83. Yang, Q.-Z.; Huang, Z.; Kucharski, T. J.; Khvostichenko, D.; Chen, J.; Boulatov, R., A Molecular Force Probe. *Nat. Nanotechnol.* **2009**, *4*, 302–306.

84. Huang, Z.; Yang, Q.-Z.; Khvostichenko, D.; Kucharski, T. J.; Chen, J.; Boulatov, R., Method to Derive Restoring Forces of Strained Molecules from Kinetic Measurements. *J. Am. Chem. Soc.* **2009**, *131*, 1407–1409.

85. Kucharski, T. J.; Yang, Q.-Z.; Tian, Y.; Boulatov, R., Strain-Dependent Acceleration of a Paradigmatic S_N2 Reaction Accurately Predicted by the Force Formalism. *J. Phys. Chem. Lett.* **2010**, *1*, 2820–2825.

86. Kucharski, T. J.; Huang, Z.; Yang, Q.-Z.; Tian, Y.; Rubin, N. C.; Concepcion, C. D.; Boulatov, R., Kinetics of Thiol/Disulfide Exchange Correlate Weakly with the Restoring Force in the Disulfide Moiety. *Angew. Chem. Int. Ed.* **2009**, *48*, 7040–7043.
87. Li, M. H.; Brûlet, A.; Davidson, P.; Keller, P.; Cotton, J. P., Observation of Hairpin Defects in a Nematic Main-Chain Polyester. *Phys. Rev. Lett.* **1993**, *70*, 2297–2300.
88. Bouman, T. D.; Hansen, A. E., Electronic Spectra of Mono-olefins. RPA Calculations on Ethylene, Propene, and *cis*- and *trans*-2-Butene. *Chem. Phys. Lett.* **1985**, *117*, 461–467.
89. Huh, D. S.; Um, J. Y.; Yun, S. J.; Choo, K. Y.; Jung, K.-H., Gas Phase Thermal cis-trans Isomerization Reaction of 1-Bromopropene. *Bull. Korean Chem. Soc.* **1990**, *11*, 391–395.
90. Walker, I. C.; Abuain, T. M.; Palmer, M. H.; Beveridge, A. J., The Electronic States of Propene Studied by Electron Impact Spectroscopy and ab initio Configuration Interaction Calculations. *Chem. Phys.* **1986**, *109*, 269–275.
91. Gary, J. T.; Pickett, L. W., The Far Ultraviolet Absorption Spectra of the Isomeric Butenes. *J. Chem. Phys.* **1954**, *22*, 599–602.
92. Molina, V.; Merchán, M.; Roos, B. O., A Theoretical Study of the Electronic Spectrum of cis-Stilbene. *Spectrochim. Acta A–M.* **1999**, *55*, 433–446.
93. Kistiakowsky, G. B.; Smith, W. R., Kinetics of Thermal Cis-Trans Isomerization. III. *J. Am. Chem. Soc.* **1934**, *56*, 638–642.

Chapter 9. Chemical Solutions for the Closed-Cycle Storage of Solar Energy

Adapted from Kucharski, T. J.; Tian, Y.; Akbulatov, S.; Boulatov, R., Chemical Solutions for the Closed-Cycle Storage of Solar Energy. *Energ. Environ. Sci.* **2011**, submitted. (*invited review*)

9.1 Abstract

The purpose of this review is to analyze an underexplored strategy of storing solar energy based on the photochemical generation of high-energy metastable compounds whose subsequent thermal isomerizations release large amounts of heat, making them suitable for use as solar thermal fuels. Such compounds may be stored at room temperature for days or months, regenerated using sunlight, and may be cycled many times without significant degradation. After highlighting some of the general challenges of solar energy conversion and storage, we discuss how recent advances in understanding the effect of molecular strain on the thermal and photochemical reactivity of small molecules offers new opportunities for a systematic approach to the molecular design of solar thermal fuels, defining the molecular properties which determine the fundamental limits of such a material's performance characteristics. (148 references)

9.2 Introduction

Meeting the ever-increasing global demand for energy in a sustainable manner is arguably the greatest scientific challenge of our time. Answering this challenge requires considerable innovations in technology, which in turn require advances in the underlying basic science, particularly in capture, conversion, and storage of solar energy. Considerable effort has been devoted to the development of photocatalytic splitting of H_2O to H_2 and O_2, of conversion of CO_2 and H_2O to CH_3OH and O_2 and similar endergonic transformations. This research receives widespread attention in the chemical and materials science literature. Here we will review and analyze another, so far relatively unexplored, strategy of storing solar energy based on photochemical generation of high-energy metastable compounds, whose subsequent thermal isomerization can release large amounts of heat. The sequence of photoisomerization followed by exothermic thermal isomerization can be repeated many times and represents a closed cycle of storing solar energy as high-energy chemical bonds. It offers unique attributes that make such a cycle a useful candidate for a mix of solutions for capture, storage and utilization of solar energy.

Below we first highlight some of the general challenges of solar energy conversion and storage, and then present and analyze the potential and emerging chemical solutions. Particularly, we will discuss the molecular design of chromophores whose photochemical products can be safely stored for days or even months at room temperature but can also be triggered to revert back to the stable isomer releasing large amounts of heat. This strategy garnered considerable attention several decades ago but the fundamental problems, largely related to molecular design, proved to be insurmountable at that time to yield a practical solution. We argue that recent advances in understanding the effect of molecular strain on the thermal and photochemical reactivity of small molecules offer an opportunity to approach the problem of designing closed-cycle solar fuels systematically. We also define the photophysical and chemical properties of a photochromic material needed to yield a practical solar thermal cell and speculate that a photochromic pair of isomers with the combination of such properties likely exists. Because the purpose of this review is to highlight a strategy of solar-energy storage that may have been overlooked by most chemists, the references in the text are necessarily selective rather than exhaustive.

9.3 Powered by the Sun

The most recent projections indicate that the annual global energy demand will increase from ~520 EJ (~17 TW annually-averaged consumption rate) in 2007 to ~780 EJ (~25 TW) in 2035.[1] In the United States the transportation sector, powered primarily by liquid fuels, is projected to continue to be the largest consumer of energy, growing from ~29 EJ (29% of total domestic energy consumption) in 2009 to ~33 EJ (28%) in 2035.[2] In Europe and Asia, energy use in transportation will increase from ~27 EJ (19%) and ~24 EJ (14%) in 2007 to ~28 EJ (18%) and ~51 EJ (15%) in 2035, respectively.[1] The energy consumed by households excluding transportation accounted for 14% of the global energy demand in 2007 and is projected to grow by 1.1% annually to 2035.[1] The majority of the growth in global energy demand will come from developing countries.[3] The economically, politically and societally acceptable solutions to meet this increase in energy demand are determined largely by three factors:

1. the nearly doubling of the worldwide number of energy users by mid-century,
2. the present (and presumably continuing) lack of large-scale (legacy) energy infrastructure in the areas that are expected to experience the largest increase of energy users[4] and
3. the effects of greenhouse gas (GHG) emissions on climate and the concomitant need to reduce CO_2 emissions by at least 50% (or more) by 2050 compared to the 2000 levels to avoid potentially catastrophic climate changes.[5,6]

The last consideration suggests that the proportion of renewable and non-CO_2-emitting (e.g., wind, hydropower and nuclear) sources of energy should represent at least 38% of the energy makeup by 2035.[3] In the OECD countries, new energy generating and distributing technologies compatible with the large energy grid systems would benefit from economies of scale, while those technologies that are incompatible with the legacy systems (e.g., transmission of electricity as DC current) may be hindered. In the less affluent countries, the lack of investment funds rather than the institutional inertia of the legacy infrastructures may be a particular strong barrier to adoption of new forms of energy storage and conversion.[7]

The competing and diverse demands for energy will likely be met by an array of carbon-neutral technologies each optimized for its own technological niche. Sunlight is by far the most abundant carbon-neutral energy source available on Earth, delivering 430 EJ of energy *each hour* (~120 PW), more than the *annual* global energy consumption in 2001 (410 EJ, average rate of 13 TW).[8] Though humanity has always relied on solar energy stored by natural photosynthesis as biomass and fossil fuels to satisfy its energy needs, photosynthesis alone will not be sufficient to continue doing so. The increasing atmospheric levels of CO_2 since the beginning of the industrial revolution indicate that we consume photosynthetically stored sunlight faster than the biosphere captures it as C–H and C–C bonds.

Photosynthesis-bypassing strategies of converting sunlight into forms of energy suitable for storage, distribution and terminal use include photovoltaic (conversion to electrostatic gradients, Fig. 9.1A),[9] photothermal (conversion to thermal gradients suitable to drive heat engines, Fig. 9.1B and C),[10]), and photocatalytic (conversion to electrochemical gradients, e.g., synthesis of CH_4 or CH_3OH from CO_2 and H_2O, of H_2 from H_2O or of Li from Li_2O_2 or Li_2CO_3). Of the three methods, photocatalysis in theory provides a means of storing solar energy with the highest energy density and longest lifetime, which is particularly important for mobile applications (e.g., transportation) and point-of-use power generation off established distribution grids (e.g., in developing countries or locations in developed countries where grid distribution has been interrupted).

Fig. 9.1. Existing technologies to convert sunlight into electricity on large scales include the use of arrays of photovoltaic cells (**A**) to do so directly and the use of parabolic troughs (**B**, Courtesy of DOE/NREL) or fields of sun-tracking reflectors (**C**) to concentrate sunlight on pipes containing heat-transfer fluids to drive steam turbines.

This review focuses on a strategy for converting solar energy into chemical potentials suitable for use in solar thermal batteries, i.e., on the design of molecules to allow the closed-cycle storage of solar energy (Fig. 9.2A). A solar thermal battery exchanges only energy with its environment but not matter, absorbing photons during charging and releasing only heat during discharge. In contrast, conventional fuels (either produced photocatalytically or extracted from geologic deposits) must be burned to extract their free energy, consuming O_2 and producing CO_2 and/or H_2O (Fig. 9.2B). A major objective in developing solar thermal batteries is to exceed what is thought to be a fundamental limit on energy and power density of conventional redox batteries, while improving the number of charge/discharge cycles, energy conversion efficiency, shelf-life of the charged state and/or usability and recyclability. If suitable molecules can be designed and synthesized, the corresponding batteries would provide means for the portable, non-CO_2-emitting storage of solar energy particularly suited for mobile and off-grid applications.

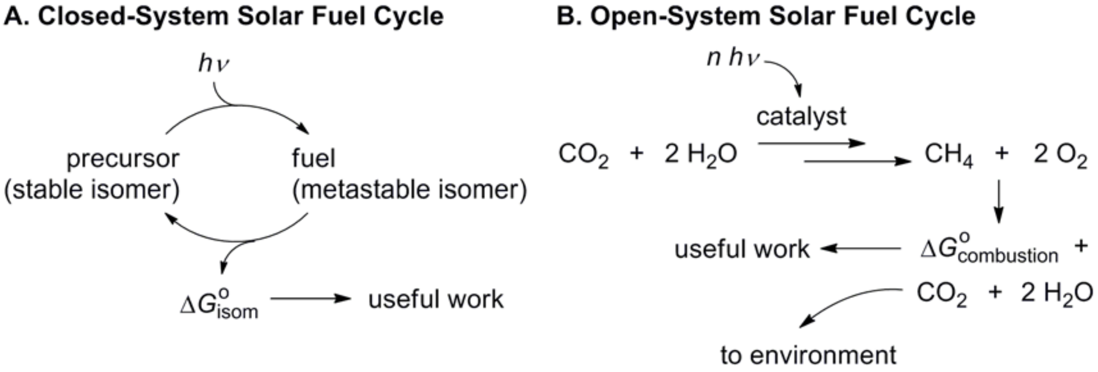

Fig. 9.2. General energy storage/release cycles for closed-system (**A**) and open-system (**B**) solar fuels. **A**: The precursor (stable iosmer) for a closed-system solar fuel uses the energy of an absorbed photon to drive its endergonic, unimolecular photoisomerization into the fuel form (metastable isomer). Upon heating or exposure to a catalyst, the fuel thermally isomerizes back to the precursor form without exchanging any material with the environment, releasing the stored energy $\Delta G_{\text{isom}}^{\text{o}}$ which can be used to do work. **B**: A catalyst absorbs the energy of

multiple photons to drive the multi-step endergonic conversion of the fuel precursor (here, CO_2 and H_2O) into fuel (CH_4). Though the necessary oxidant for combustion (O_2) is also produced, it is generally instead pulled from the environment (air) during the combustion process, and the combustion products are generally released into the environment. The free energy released during combustion represents the maximum amount of work that the system may perform.

The idea of closed-system solar thermal energy storage is old and much effort has been devoted to developing practical systems based on the norbornadiene/quadricyclane isomeric pair. In our opinion, the absence of a practical solar thermal battery is a failure of molecular design rather than evidence of the fundamental problem with the concept of storing energy as metastable molecules obtained by photoisomerization. Unlike the challenges in optimizing existing types of energy storage systems (e.g., redox batteries), which are more physical and engineering than chemical, and those of generating conventional fuels using solar energy, which are finding appropriate heterogeneous catalysts, the challenges in the development of portable solar thermal batteries are fundamentally chemical, particularly those of molecular design and exploiting the relationship between molecular strain and reactivity. Consequently, we speculate that it is an area of sustainable energy generation which can benefit particularly from the attention of synthetic, physical, materials and theoretical chemists.

9.4 Storage Is Essential

Utilization of any intermittent primary energy source, such as solar or wind, requires robust and efficient solutions for energy storage.[11,12] Despite its enormous flux, solar radiation is locally an intermittent energy source with the local insolation and demand curves out of phase.[11] Both closed-system and open-system schemes for solar energy storage are being considered.

Open-system solar energy storage typically consists of (1) hydrocarbons or their oxygenated derivatives synthesized from H_2O and CO_2 photocatalytically, (2) H_2 from photochemical, photoelectrochemical of photothermal[13] splitting of water or (3) alkali or alkaline-earth metals by electrolysis using photovoltaics, which can then be used in recycable metal-air "batteries." Energy densities of such fuels exceed those of other storage technologies by at least an order of magnitude, making them particularly well-suited for transportation, where demand is necessarily distributed and intermittent and the energy densities are paramount. Most solar fuels that release energy when oxidized (burned) are open-cycle, because the oxidation products (e.g., CO_2 for all carbon-based fuels) are released permanently in the environment (see below).

In closed-system storage, only energy (but not matter) is exchanged between the environment and the energy-storing system. Examples of closed-system solar-energy storage schemes are pumped water or compressed air (mechanical storage) and rechargeable batteries or supercapacitors (electrochemical or electrostatic), with the energy coming typically from photovoltaics or photothermal energy concentrators. The primary drawback of most existing closed-system energy storage technologies, both mechanical and electrochemical,[12] is their modest mass and/or volume energy densities (0.001–0.5 MJ/kg). Technologies with the highest specific energy density, such as overheated steam (up to 3 MJ/kg) or lithium ion batteries (up to 1 MJ/kg), either lack portability, are too costly for many applications and/or are not suitable for energy storage for longer than a week.[11,14] It seems unlikely that energy densities of most such technologies can be increased much further because of the fundamental limitations imposed by the physical properties of materials.[11]

Whereas the design of electrochemical batteries have attracted considerable attention, a complementary solution, solar thermal batteries based on the reversible photoisomerization of stable chromophores into highly strained isomers without changes in their chemical composition, have been comparatively little explored. In solar thermal batteries, the stored energy is released as heat when the strained isomer reverts to its stable analog in response to an external trigger. The development of chemistry for such solar thermal batteries presents unique challenges for chemists' ability to control chemical reactivity through molecular design. We suggest that these challenges can only be met by critically reexamining the conventional ideas about the relationship between molecular strain and reactivity.

9.5 Open-System Fuels

Conventional chemical fuels, such as gasoline or methane are stable in the absence of O_2 or another oxidant and release energy only upon oxidation (burning), with changes in the chemical composition. Because such fuels have been used extensively throughout human history, their chemistry is well studied. Efficient technologies and infrastructure exist to interconvert between various open-system chemical fuels on industrial scales (e.g., cracking, reforming, (de)hydrogenation, Fisher–Tropsch conversion) and to maximize the fraction of the free energy of their combustion that is converted to useful work, for example in driving a vehicle or a gas turbine. Liquid hydrocarbons and their partially oxygenated derivatives (e.g., methanol) possess unique advantages as fuels. They have high mass and volumetric energy densities (e.g., derived from standard enthalpies of combustion:[15] 22.7 MJ/kg or 17.9 MJ/L for CH_3OH and 47.9 MJ/kg or 33.7 MJ/L for n-C_8H_{18}, the primary component of gasoline) and useful power densities (50–500 W/kg).[11] Hence they require only simple precautions for safe handling and storage and can be transported fairly cheaply. They are relatively non-toxic (for an 85 kg human, LD_{50} values for methanol and gasoline correspond ingesting ~0.7 L and ~1.6 L, respectively, compared to only 1.4 g of strychnine or 2 mg of ricin). The primary challenge of using such fuels to store solar energy is the development of efficient photocatalysts to convert CO_2 and H_2O to hydrocarbons or their derivatives. In other words, we know what chemicals make good open-system solar fuels and we know how to extract free energy out of them using an abundant and free oxidant (air), but we do not know how to synthesize them effectively using solar energy.[16]

The major drawback of carbon-based solar fuels is the release of CO_2 upon combustion. Practical and economical non-biological conversion of CO_2 to fuels likely requires a feedstock with concentrations of CO_2 far higher than in ambient air. Consequently, CO_2 released by the combustion of solar fuels in a vehicle or at other distributed points of use cannot be practically recaptured. Such capture and sequestration is easier to accomplish if solar fuels are burned at large stationary consumers of energy (e.g., power plants),[17] but it is not clear how the use of solar fuels in such circumstances would be advantageous compared to direct photovoltaic or photothermal energy conversion, other than the improved capabilities for energy storage mentioned above. Therefore it seems that carbon-based solar fuels can decrease the CO_2 burden of human technology at best by two-fold, by converting the output of a fossil-fuel burning centralized power plant with high-concentrations CO_2 to liquid hydrocarbons using solar energy. Once this solar fuel is consumed (in a mobile application), the CO_2 is again released in the environment.

The combustion of H_2 produces only H_2O, making H_2 potentially a carbon-neutral method of storing solar energy. Because of this and its very high specific energy density (142 MJ/kg) the use of hydrogen as an energy carrier has attracted huge amount of attention.[13,18-23] In 2004, 50 million metric tons of H_2 was produced worldwide, mostly from steam reforming of hydrocarbons, eq. (9.1), and the water-gas shift reaction, eq. (9.2). In nature H_2 is produced by hydrogenases.[24-26] The photochemical, photoelectrochemical and photothermal splitting of water on various semiconductors, catalyst-functionalized electrodes, or with molecular photocatalysts,[18,20,27] is intensely investigated as a method of carbon-neutral generation of H_2.

$$CH_4 + H_2O \rightarrow CO + 3\ H_2 \tag{9.1}$$

$$CO + H_2O \rightarrow CO_2 + H_2 \tag{9.2}$$

Under ambient conditions H_2 is a gas with an impractically low volumetric energy density of 0.013 MJ/L (i.e., <0.01% that of gasoline). Its storage is a major challenge.[28] Photosynthetic organisms store and distribute hydrogen generated in water splitting as reducing equivalents of large complex molecules, such as NADPH and NADH for short-term storage, or carbohydrates for long-term storage.[29] One example of the technological use of small molecules as hydrogen carriers is the catalytic cycling between CO_2 and H_2 and formic acid (Fig. 9.3A).[28,30] The reversible hydrogenation/dehydrogenation of organic compounds has also been considered as a method for storing and transporting hydrogen equivalents for use in automotive applications (Fig. 9.3B).[31,32] Other methods of high-density hydrogen storage are hydrides[33-35] (e.g., Fig. 9.3C) and physisorption[36,37] or chemisorption[38] in high-surface-area materials. All H_2 storage methods require significant further development before they become practical.[39]

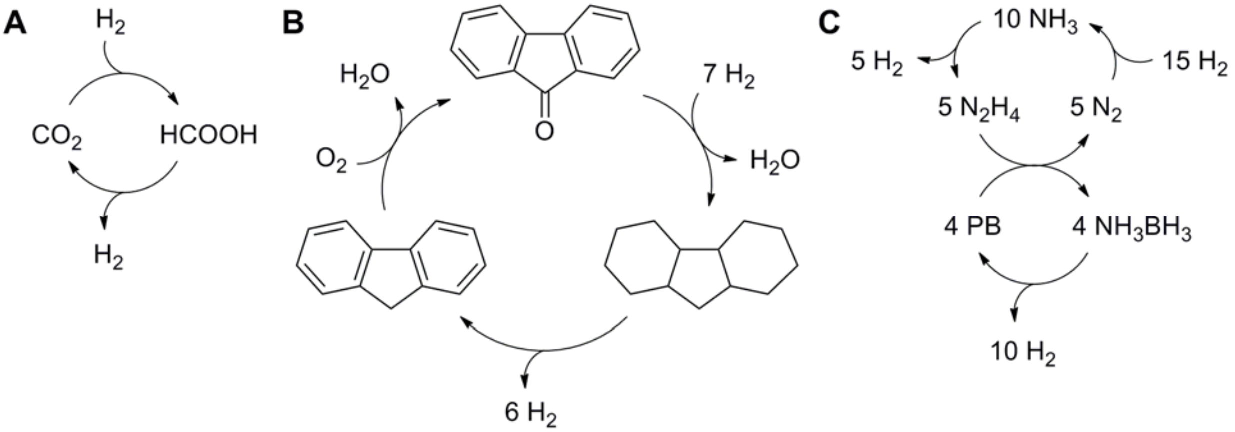

Fig. 9.3. Examples of operation cycles for molecular H_2 carriers: **A**: the cycling of CO_2 to carry H_2 as formic acid;[30] **B**: a H_2 storage and release cycle developed at Air Products and Chemicals, Inc. using a catalytic hydrogenation, dehydrogenation and oxidation cycle of π-conjugated organics (here, fluorene);[31,32] and **C**: the release of H_2 from ammonia borane and the regeneration of ammonia borane from the product polyborazylene (PB) using hydrazine in liquid ammonia.[35]

In summary, liquid open-system solar fuels are convenient to distribute and use due to their high energy densities, but it is unclear how to synthesize them efficiently and whether they can be carbon-neutral forms of energy storage. Combustion of H_2 releases no CO_2, and H_2 may be generated by photochemical, photoelectrochemical or photothermal[13,40] water splitting with reasonable efficiency. However, the impractically low volumetric energy density of H_2 under ambient conditions raises questions of whether it offers significant advantages over competing forms of solar energy storage, such advanced batteries, for mobile applications or direct photovoltaics for stationary ones.

9.6 Solar Thermal Batteries

As stated earlier in the review, we have a pretty good idea of what chemicals make good open-system fuels because we have used such chemicals for centuries. In solar thermal batteries, the exergonic reaction results in the rearrangement of chemical bonds without changes in the chemical composition of the molecule (i.e., the energy storing/releasing cycle involves isomerization). Beyond the obvious requirements that the metastable isomer be strained and the stable isomer absorb photons of useful wavelengths, no systematic knowledge yet exists to guide the design of closed-system fuels. The fundamental limit of the energy density of such fuels is not immediately clear, and neither is the achievable efficiency of photochemical energy conversion nor the relationships between the photoisomerization wavelength, the fraction of the photon energy stored in the metastable isomer and the half-life of this isomer. Thus, though the desired performance characteristics of a practical closed-system chemical fuel were articulated a long time ago,[41-46] the geometric and electronic parameters of molecular chromophores required to realize these characteristics remain unknown.

The advantages of closed-system solar energy storage strategies over open-system complements are

1. the elimination of oxidation products whose release may be detrimental to the environment,
2. the potentially simple recycling of spent fuel at the point of use (e.g., a properly designed closed-system solar fuel may be regenerated simply by exposing the stable isomer to sunlight) and
3. a greater tolerance to the cost of molecules used as fuel, which increases the flexibility in selecting the structural and electronic molecular parameters to yield fuel best suited for the intended application.

These advantages make solar thermal batteries potentially useful in mobile applications, for applications in areas lacking large legacy energy grids, including both developing countries and the remote areas of the developed countries, or areas where access to the existing grids has been temporarily interrupted, e.g., as a result of a natural disaster, war, terrorist attack or industrial accident. Scaled up, closed-system solar fuels offer a carbon-neutral means of storing large amounts of heat for long periods without significant heat dissipation due to thermal gradients.

A closed-system energy storage scheme can never match a conventional fuel in terms of mass and/or volume energy density, because energy-releasing (exergonic) reactions of conventional fuels draw O_2 from the environment, whose mass and volume is usually not included in calculations of energy density. For specific applications, the unique advantages of closed-system energy storage systems can outweigh their intrinsically lower energy densities, and the smaller the gap between the energy densities of the open- and closed- systems, the wider use rechargeable batteries will find. The maximum practically attainable energy density of a chemical battery is determined by the relationship between the activation and standard free energies of the exergonic reaction. Very broadly, across identical mechanistic classes of chemical reactions, reactions accelerate as they become more favorable (i.e., the so-called free energy relationship between the standard free energy of a reaction, ΔG°, and its free energy of activation, $\Delta G^\ddagger$, as established by the Leffler postulate[47]). For several mechanistic classes, Marcus theory adequately describes the quantitative relationship between ΔG° and $\Delta G^\ddagger$. The theory predicts an inverted region, in which $\Delta G^\ddagger$ increases as ΔG° decreases (becomes more exergonic).[48] This inverted region is thought to enable the initial charge-separation step of photosynthesis. Several energy donor/acceptor pairs have been rationally designed to access the inverted region, but such a region has not been observed for any other reaction type, and no battery exists that exploits the inverted region to increase its energy density without sacrificing its self-discharge rate.

The fundamental limit of the specific energy density of a redox battery can be estimated as follows: the highest energy-density cathode (reductant) is metallic Li (14 MJ/kg); presently the highest energy-density anode (oxidant) is probably Si (up to 10 MJ/kg).[49] A hypothetical mixture of metallic Li and Si in 4:1 molar ratio can release ~13 MJ/kg upon complete conversion to Li_4Si. In order for such a mixture to generate electromotive force (electrical current against opposing electrostatic potential), the cathode and anode need to be separated by an electrolyte.

The ratio of the masses of the electrolyte and the electrodes is determined by the desired self-discharge rate, impedance, electrode kinetics, etc. Existing redox batteries have energy densities below 1 MJ/kg and it has been argued[11] that further improvements in their energy density are unlikely.

The highest energy-density molecule known to date is probably nitrocubane, whose calculated standard free energy of formation is 717 kJ/mol.[50] Based on this number, its standard (i.e., pure solid at 298 K and 1 atm) calculated specific energy density for decomposition to N_2, H_2O and CO is ~31 MJ/kg or ~46 MJ/L. The standard energy densities of commercial monopropellants and explosives do not exceed half of this value, e.g., <12 MJ/kg for CH_3NO_2,[15] 9.4 MJ/kg for octogen (octahydro-1,3,5,7-tetranitro-1,3,5,7-tetrazocine, HMX),[51] 9.5 MJ/kg for RDX (cyclotrimethylenetrinitramine)[51] and 7.3 MJ/kg for the $C(NO_2)_4 + 3\ N_2H_4$ mixture (all values are for decomposition to CO, CO_2, H_2O and N_2).[15,52] Even conventional fuels fall in the same range when the mass of consumed O_2 is included, e.g., <11 MJ/kg for *n*-octane and ~16 MJ/kg for the discontinued high-energy aviation fuel based on boranes. Importantly, at least 35% of the standard free energy of these reactions is entropic, i.e., due to the generation of gases (CO_2, CO, N_2, steam). A reaction that is accompanied by large entropic changes (i.e., by large changes in molar volume) is unsuitable for use in a battery whose volume should remain constant throughout the charge/recharge cycle. Hence, it seems very unlikely that a material exists that is suitable for use in a battery with a specific energy density exceeding 10 MJ/kg.

We estimate that the maximum energy density of a solar thermal battery, based on *single-photon chemistry*, is limited by the shortest-wavelength solar radiation reaching the Earth's surface to ~1.5 MJ/kg, based on the following arguments.

At the Earth's surface, the intensity of light below ~340 nm is probably too low to be of practical interest in energy capture (Fig. 9.4). In the absence of multiphoton absorption (which requires very high fluxes[53]), the 340 nm cut-off is equivalent to a maximum amount of energy that can be deposited per chromophore of 3.50 eV. To reach a specific energy density of 10 MJ/kg in a material containing only the first- (H) and second-row elements (Li through F), the effective molecular weight of the chromophore should be <34 g/mol, i.e., the material should be able to absorb at least one 340 nm photon per 3 C atoms.

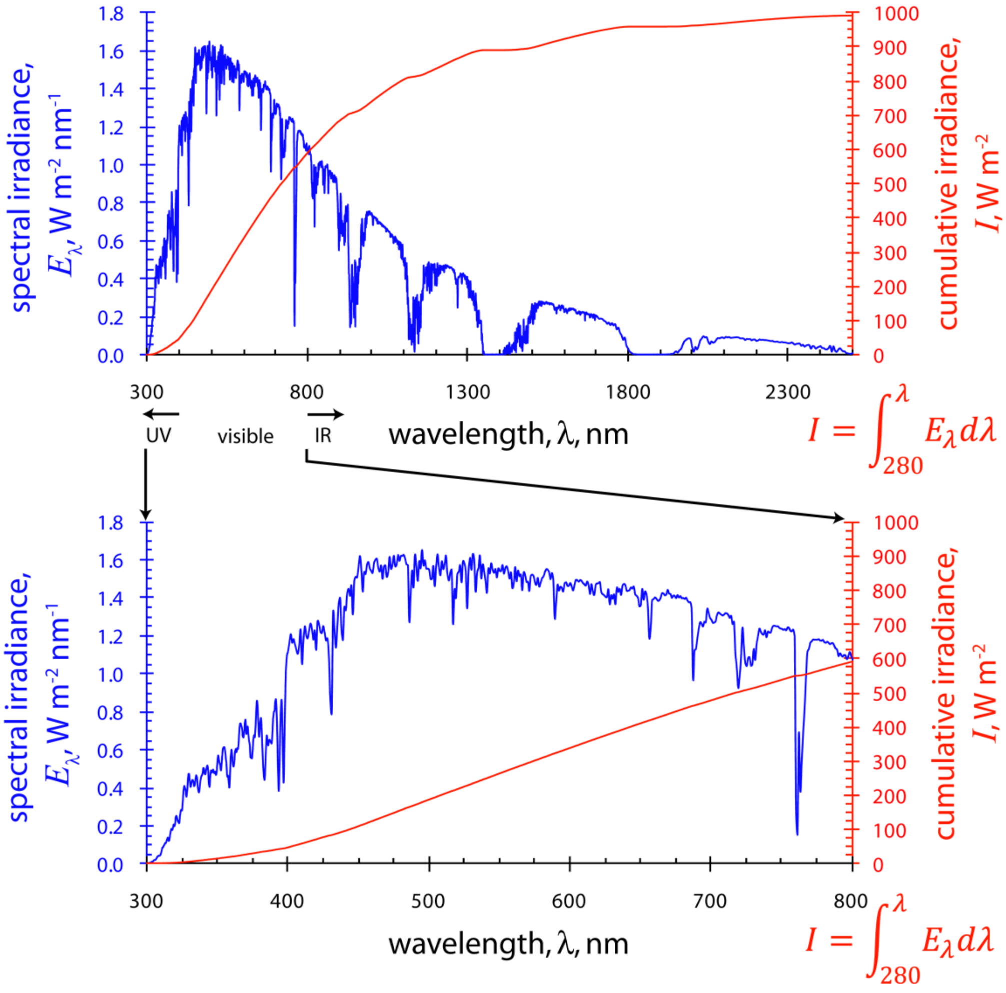

Fig. 9.4. Solar irradiance on an equator-facing surface with a 37° tilt for air mass 1.5. Data from ref. 54.

This is physically impossible. A particle-in-a-box calculation suggests that a HOMO–LUMO gap of 3.5 eV requires a linear π system of a minimum of three conjugated C=C bonds (i.e., a hexatriene, molecular weight 80 g/mol). In practice, the smallest chromophore with significant absorbance at ~340 nm we are aware of is $NCCH{=}CH{-}CH{=}CHN(CH_3)_2$.[55,56] Hence, the fundamental limit of the energy density of a chemical solar thermal battery is determined by the energy of available photons.

The standard free energy of isomerization of the stable isomer to its metastable analog, $\Delta G_{\text{isom}}°$, is the maximum energy that can be stored for any period of time per mole of chromophore (Fig. 9.5). $\Delta G_{\text{isom}}°$ must satisfy eq. (9.3), where $\Delta G_{\text{isom}}^{\ddagger}$ is the activation free energy of isomerization of the stable to metastable isomer, $\Delta G_{\text{rev}}^{\ddagger}$ is the free energy of activation for thermal reversion of the metastable isomer to the stable isomer, $\tau_{1/2}$ is the time (in seconds) during which half of the stored energy is dissipated spontaneously, T is the storage temperature and k_B, R and h are the Boltzmann, gas and Planck constants, respectively. Assuming a self-discharge rate at room temperature of 1% per week ($\tau_{1/2} = 4\ 10^7$ s) and $\Delta G_{\mathrm{isom}}{}^{\ddagger}/N_A = 3$ eV gives the maximum specific energy density of 1.7 MJ/kg for a fuel with a molecular weight of 100 g/mol. This density can be practically achieved only if the metastable photoisomer is transparent at the photoisomerization wavelength. Otherwise, irradiation of a discharged battery (i.e., of the stable isomer) can only yield a mixture of the two isomers whose ratio is determined by the ratio of the products of their molar absorbances at the irradiation wavelength and the photoisomerization quantum yields.

$$\Delta G^{\mathrm{o}}_{\mathrm{isom}} = \Delta G^{\ddagger}_{\mathrm{isom}} + RT\ln\frac{h\ln 2}{\tau_{1/2}\,k_B T} = \Delta G^{\ddagger}_{\mathrm{isom}} - \Delta G^{\ddagger}_{\mathrm{rev}} \tag{9.3}$$

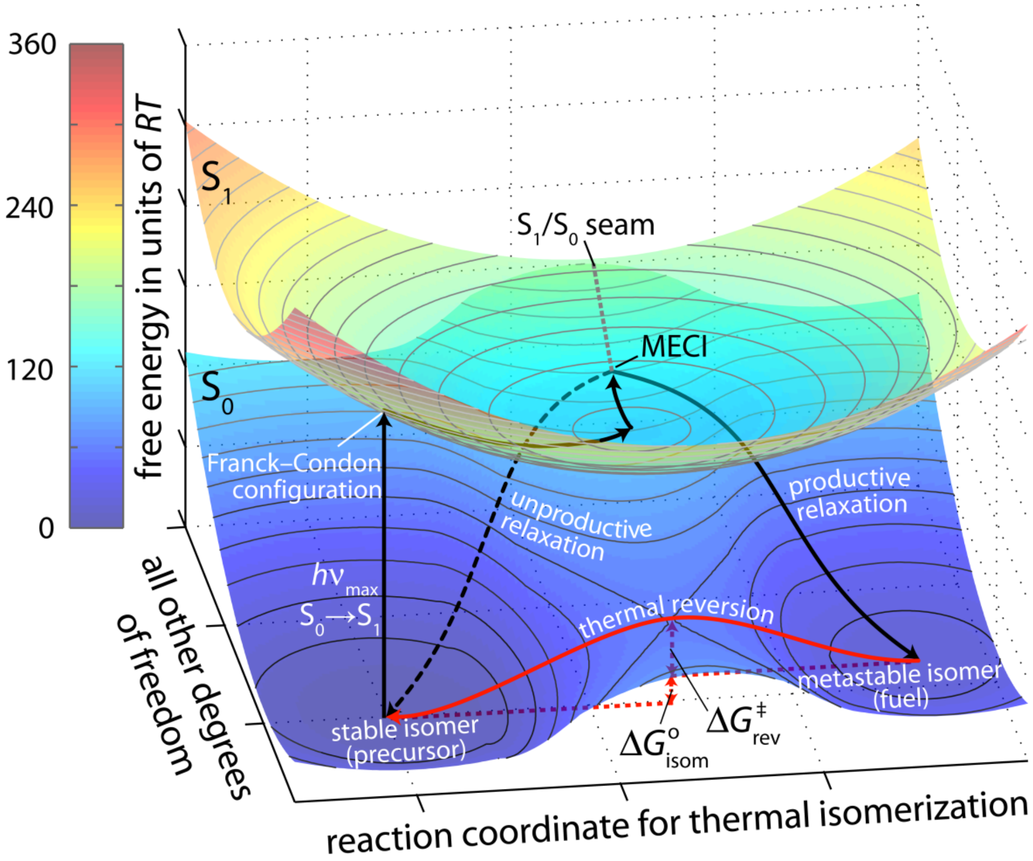

Fig. 9.5. Reduced-dimensionality energy surfaces for the singlet ground (S_0) and first excited (S_1) states of a hypothetical closed-system fuel. The photochemical conversion of the precursor to the fuel is indicated by the solid black arrows: The molecule absorbs a photon of energy $h\nu$ and is excited to its S_1 surface, it relaxes from the Franck–Condon configuration toward the S_1 minimum and then it reaches (ps timescale) the minimum energy conical intersection (MECI) between the two surfaces. On the S_0 surface, the molecule may then unproductively

relax (dashed black arrow) to the stable isomer (precursor) or relax productively (solid black arrow) to the metastable isomer (fuel). Thermal reversion (solid red arrow) over the barrier of $\Delta G_{\mathrm{rev}}^{\ddagger}$ then releases the stored energy, $\Delta G_{\mathrm{isom}}°$.

Entropies of many isomerization reactions are modest, allowing free energies to be replaced by enthalpies. Experimental evidence suggests the existence of a broad correlation between the enthalpy of activation of thermal isomerization and the frequency of photoisomerization (Fig. 9.6, Table 9.1). The correlation is particularly strong for isomerizations of C=C bond, is weaker in case of N=N bonds (Fig. 9.6B) and is nearly non-existent for electrocyclic reactions (Fig. 9.6C). The trend may reflect the increasing diversity of reaction pathways for the three sets of reactions (see below).

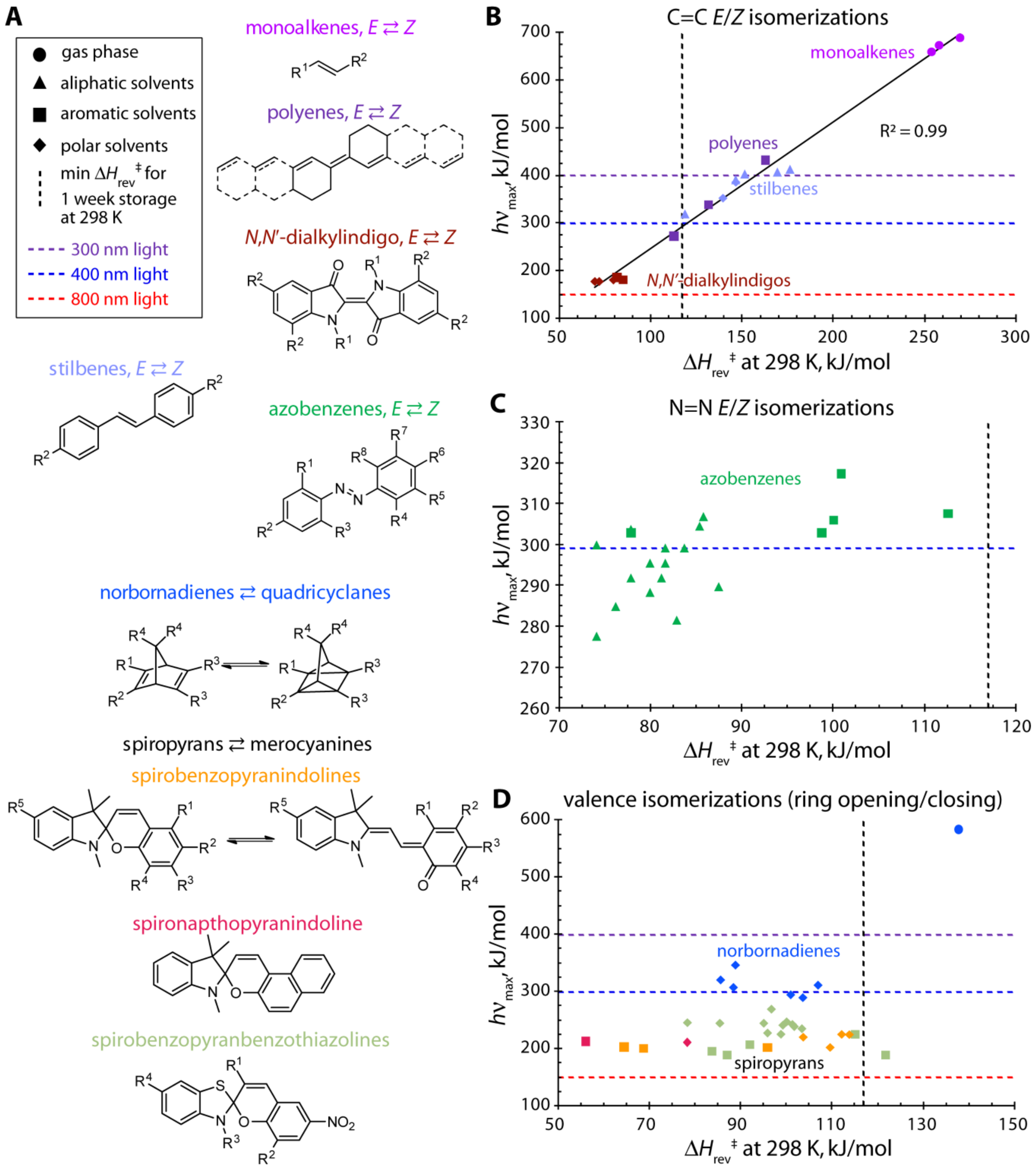

Fig. 9.6. Illustration of the general correlation or lack thereof between the energy of the most strongly absorbed light leading to photoisomerization to the less metastable isomer ($h\nu_{max}$) and the activation enthalpy for thermal reversion ($\Delta H_{rev}^{\ddagger}$) for several classes of photochromic molecules: *E*/*Z* isomerization of monoalkenes,[57-61] polyenes,[62] stilbenes,[63,64] *N*,*N*′-dialkylindigos[65] and azobenzenes,[66] and the valence isomerization of norbornadienes/quadricyclanes[67-69] and spiropyrans/merocyanines.[70] Points are color-coded to their structure classes, the shapes of the data points indicate the solvent in which the measurements were made and the dashed lines correspond to the energies of 300, 400 and 800 nm light and the minimum activation enthalpy required for long term storage at 298 K (neglecting the entropy of activation, $\Delta G^{\ddagger} = \Delta H^{\ddagger} = 117$ kJ/mol). For *N*,*N*′-dialkylindigos and

norbornadienes/quadricyclanes, $\Delta G_{\mathrm{rev}}^{\ddagger}$ at 298 K and 293 K, respectively, is shown instead of $\Delta H_{\mathrm{rev}}^{\ddagger}$. For azobenzenes, $h\nu_{\max}$ for the stronger ($\varepsilon \approx 2\text{–}4 \times 10^4$ M^{-1} cm^{-1}), symmetry-allowed $S_0 \rightarrow S_2$ (π–π*) transition is plotted; for unsubstituted azobenzene, $h\nu_{\max}$ for the weaker ($\varepsilon \approx 500$ M^{-1} cm^{-1}), symmetry-forbidden $S_0 \rightarrow S_1$ (n–π*) transition is ~100 kJ/mol smaller.[71,72] The data plotted is tabulated in Table 9.1.

Table 9.1. Data, substituent identities, and references for the data shown in Fig. 9.6.

solvent	$\Delta H_{\mathrm{rev}}^{\ddagger}$, kJ/mol[a]	$h\nu_{\max}$, kJ/mol								
spirobenzopyranindolines[b]			R^1	R^2	R^3	R^4	R^5			
ethanol	112	225	Cl	NO_2	Cl	H	H			
ethanol	114	225	H	NO_2	H	H	H			
ethanol	104	220	H	NO_2	H	H	Cl			
ethanol	110	202	Br	OMe	H	NO_2	Cl			
toluene	64	203	H	NO_2	H	OMe	H			
toluene	96	201	Cl	NO_2	Cl	H	H			
toluene	69	200	H	NO_2	H	H	H			
spironapthopyranindoline[b]										
EtOH	78	211								
toluene	56	212								
spirobenzopyranbenzothiazolines[b]			R^1	R^2	R^3	R^4				
ethanol	97	269	^{i}Pr	OMe	Me	H				
ethanol	100	247	Me	OMe	Me	CO_2H				
ethanol	78	245	Me	OMe	Me	OH				
ethanol	85	244	Me	OMe	Me	OMe				
ethanol	95	244	Me	OMe	Me	H				
ethanol	101	242	Et	OMe	Me	H				
ethanol	99	241	Me	OMe	Et	H				
ethanol	102	238	Me	OMe	Me	Cl				
ethanol	103	235	Me	OMe	Me	SMe				
ethanol	96	227	$4\text{-}ClC_6H_4$	OMe	Me	H				
ethanol	99	225	Ph	OMe	Me	H				
toluene	115	225	Me	OMe	Me	Br				
toluene	92	206	Me	H	Me	H				
toluene	84	195	Ph	OMe	Et	H				
toluene	122	189	Me	OMe	Me	H				
toluene	87	188	Et	OMe	Me	H				

Table 9.1 (cont.)

norbornadienes			R^1	R^2	R^3	R^4				
gas phase[c]	138	584	H	H	H	H				
PMMA solid film[d]	89[e]	346	4-MeOC$_6$H$_4$	4-MeOC$_6$H$_4$	CF$_3$	Me				
PMMA solid film[d]	88[e]	307	4-Me$_2$NC$_6$H$_4$	4-Me$_2$NC$_6$H$_4$	CF$_3$	Me				
PMMA solid film[d]	86[e]	320	4-Me$_2$NC$_6$H$_4$	4-MeOC$_6$H$_4$	CF$_3$	Me				
PMMA solid film[d]	107[e]	311	4-Me$_2$NC$_6$H$_4$	2-thiophenyl	CF$_3$	Me				
PMMA solid film[d]	101[e]	294	4-Me$_2$NC$_6$H$_4$	2-benzofuryl	CF$_3$	Me				
PMMA solid film[d]	104[e]	289	2-benzofuryl	2-benzofuryl	CF$_3$	Me				
azobenzenes[f]			R^1	R^2	R^3	R^4	R^5	R^6	R^7	R^8
cyclohexane	86	307	H	NMe$_2$	H	H	H	H	H	H
cyclohexane	82	299	H	NMe$_2$	H	H	H	Me	H	H
cyclohexane	81	292	H	NMe$_2$	H	H	H	Cl	H	H
cyclohexane	76	285	H	NMe$_2$	H	H	NO$_2$	H	H	H
cyclohexane	78	304	H	NMe$_2$	H	Me	H	H	H	H
cyclohexane	82	295	Me	NMe$_2$	H	H	H	H	H	H
cyclohexane	85	304	H	NMe$_2$	H	Me	H	Me	H	H
cyclohexane	87	290	H	NMe$_2$	H	Me	H	Cl	H	H
cyclohexane	80	295	Me	NMe$_2$	H	H	H	Me	H	H
cyclohexane	80	288	Me	NMe$_2$	H	H	H	Cl	H	H
cyclohexane	83	281	Me	NMe$_2$	H	Me	H	H	NO$_2$	H
cyclohexane	84	299	Me	NMe$_2$	H	Me	H	H	H	H
cyclohexane	74	300	Me	NMe$_2$	H	Me	H	Me	H	H
cyclohexane	78	292	H	NMe$_2$	H	H	H	NMe$_2$	H	H
cyclohexane	74	278	H	NEt$_2$	H	H	H	NEt$_2$	H	H
toluene	101	317	Me	NMe$_2$	H	Me	H	H	H	Me
toluene	113	308	H	NMe$_2$	H	Me	H	H	H	Me
toluene	100	306	Me	NMe$_2$	Me	H	H	H	H	H
toluene	99	303	Me	NMe$_2$	Me	H	H	Me	H	H
toluene	78	303	Me	NMe$_2$	Me	Me	H	H	H	H
monoalkenes			R^1	R^2						
gas phase[g]	269	689	H	H						
gas phase[h]	254	659	Me	H						
gas phase[i]	258	673	Me	Me						
stilbenes[j]			R^1	R^2						
methylcyclohexane–isopropanol	140	352	NO$_2$	H						

Table 9.1 (cont.)

methylcyclohexane–isopropanol	140	352	NO_2	H						
methylcyclohexane–isopropanol	147	386	OMe	H						
methylcyclohexane–decalin	119	320	NO_2	OMe						
cyclohexane	147	391	OMe	H						
cyclohexane	152	403	H	H						
heptanes	170	407	H	H						
isohexane	177	412	H	H						
polyenes[k]										
benzene; hexanes	163	432								
benzene; hexanes	132	338								
benzene; hexanes	113	272								
N,*N′*-dialkylindigos[l]			R^1	R^2						
benzene	81	186	Me	H						
chloroform	80	183	Me	H						
CCl4	76	187	Me	H						
ethanol–water	72	178	Me	H						
ethanol–water, pH 3	69	178	Me	H						
N,N-dimethylformamide	79	181	Me	Br						
benzene	85	180	Me	Br						

[a] calculated at 298 K from $\Delta H_{\mathrm{rev}}^{\ddagger} = E_{\mathrm{a}} - RT$. [b] ref. 70. [c] refs. 67,68. [d] ref. 69. [e] $\Delta G_{\mathrm{rev}}^{\ddagger}$ at 293 K. [f] ref. 66. [g] refs. 60,73,74. [h] refs. 58,75. [i] refs. 59,76-78. [j] refs. 63,64. [k] ref. 62. [l] ref. 65, $\Delta G_{\mathrm{rev}}^{\ddagger}$ at 298 K.

How important solar thermal batteries may ultimately be among the various solar-energy storage strategies may depend on understanding the fundamental relationship between the photoisomerization wavelength and the barrier of reversion to the stable isomer. This question remains to be answered.

9.7 Developments to Date

The potential for storing solar energy by reversible photoisomerizations was recognized in 1909[42] when the photodimerization of anthracene (Fig. 9.7A) was proposed for this purpose. Since the early 1970s, developments of the closed-system chemical storage of solar energy have been based on concerted (electrocyclic) conversion between double C=C and single C–C bonds (Fig. 9.7B and C)[46,79] and *E*/*Z* isomerizations of double N=N[44,80] (Fig. 9.7D) and C=C[81] bonds (Fig. 9.7E). More recently, certain organometallic photochromic compounds (Fig. 9.7F) have attracted attention. Inorganic photoreactions were considered in the 1960s but do not appear to be actively pursued any longer. So far the primary focus has been on maximizing the efficiency of energy conversion. As argued above, energy density rather than energy conversion efficiency may be of greater importance in determining the role of chemical solar thermal energy storage schemes.

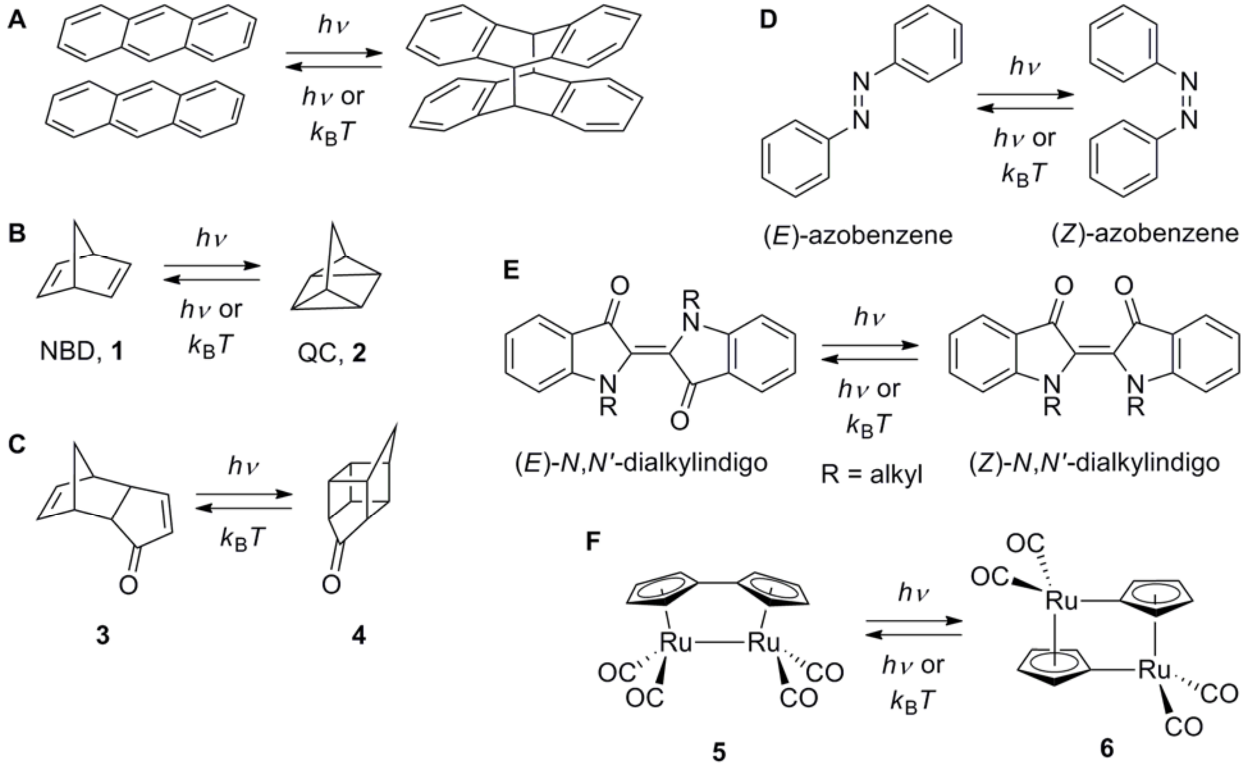

Fig. 9.7. Photoisomer classes previously studied as potential photothermal solar fuels: (**A**) anthracene and its dimer, (**B**) norbornadiene/quadricyclane (NBD/QC), (**C**) the tricyclic/bishomocubane pair **3**/**4**, (**D**) azobenzenes, (**E**) *N*,*N′*-dialkylindigos and (**F**) organometallics such as (fulvalene)tetracarbonyl-diruthenium. In all cases, the metastable isomer is on the right.

The most extensively studied chemical reaction for the closed-system storage of solar energy is the photoisomerization of norbornadiene (NBD, **1**) to quadricyclane (QC, **2**), or their derivatives.[46,79] Thermal reversion of QC to NBD has a standard enthalpy (-$\Delta H_{\mathrm{isom}}^{\mathrm{o}}$) of -89 kJ/mol,[82] corresponding to a specific energy density of neat QC of ~1 MJ/kg, and an activation energy of 140 kJ/mol[68] (corresponding to $\tau_{1/2}$ of 14 h at 140 °C[83]).

The S_1 state of NBD is optically dark and may not be accessed by direct photon absorption.[84] Weak absorption of NBD at ~236 and ~213 nm, corresponds to population of several valence and Rydberg states. QC appears within 500 fs after photon absorption by NDB and is thought to be formed through an S_1/S_0 conical intersection following rapid relaxation of the excited NBD from the initially generated higher-energy states. However, no computational studies of the mechanism have yet been reported.

Sensitized photoisomerization of NBD to QC is more efficient than the direct conversion and is thought to involve adiabatic NBD/QC isomerization on the T_1 surface prior to relaxation of either isomer to the ground electronic state.[79] Because NBD is transparent at wavelengths above 300 nm and has a singlet–triplet (S_0–T_1) gap of 257 kJ/mol (equivalent to the energy of ~475 nm photons), useful triplet photosensitizers have to satisfy rather demanding conditions. Sensitizers with triplet–single gaps above ~280 kJ/mol (such as aceto- or benzophenone) add to NBD in side reactions or participate in charge transfer, forming NBD cation radicals, which are prone to decomposition. Certain Cu complexes[85] appear to be the longest-wavelength sensitizers (~405 nm) capable of promoting photoisomerization of NBD, albeit with quantum yields on the order of 10^{-2}.

Considerable effort has been devoted to increasing the absorption wavelength of NBD (which also decreases the singlet-triplet gap) by incorporating the NBD core in a conjugated system or decorating it with donor/acceptor (electron-withdrawing/electron-donating) substituents.[46] Increasing the absorption wavelength is accompanied by a decrease of the activation energy of QC → NBD thermal reversion and of the quantum yield of the photoisomerization but also increases the photostability of NBD. For example, substituted NBD **7** was reported to photoisomerize to the QC isomer **8** upon irradiation at 510 nm with the QC isomer having lifetime of ~9000 h at room temperature.[69,86] The cycle could be repeated at least 10^3 times.

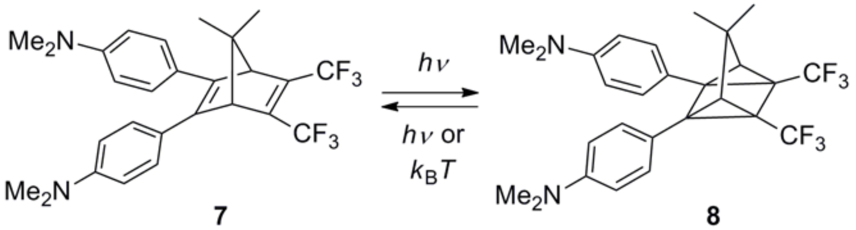

Fig. 9.8. A donor–acceptor substituted norbornadiene that has a long-wavelength absorption edge at 510 nm.

Thermal reversion of QC to NBD is forbidden by orbital symmetry, which explains its high activation barrier despite large exergonicity. It is catalyzed by many transition metal complexes and surfaces,[87] which probably allow the reaction to proceed through a formally triplet transition state. Heating donor–acceptor QCs, which have lower free energies of activation than unsubstituted QC, to 65–180 °C has also been used to initiate energy-releasing reversion of QC to NBD. Covalent attachment of the NBD chromophore and suitable sensitizers to inert polymers yielded energy-storage materials capable of storing between 44 and ~90 kJ of solar energy per mole of the NBD chromophore, albeit at the expense of low energy and power densities and energy conversion efficiencies relative to neat NBD.

Other intramolecular electrocyclizations, such as the photochemical formation of bishomocubanes (Fig. 9.7C) and similar cage compounds, have been examined for solar energy storage. The photoisomerization **3** → **4** has moderate quantum yields (0.35–0.40) in various solvents, but requires short wavelengths (330–380 nm).[41] Similarly to QC, the reversion of **4** to **3** can be catalyzed by transition metal complexes, but though its catalyst-free thermal reversion is even slower than that of QC (**4** is inert up to nearly 300 °C), the amount of solar energy stored is less ($\Delta H_{\mathrm{isom}}^{\mathrm{o}}$ = 67 kJ/mol).[41] High thermal stability is advantageous for long-term storage, but may complicate triggering energy release. The Rh catalysts suitable for thermal **4** → **3** isomerization do not catalyze analogous **10** → **9** reaction (Fig. 9.9A) even at elevated temperatures.[41] Likewise, **12** could not be thermally converted to **11** without significant decomposition at the required high temperatures.[88]

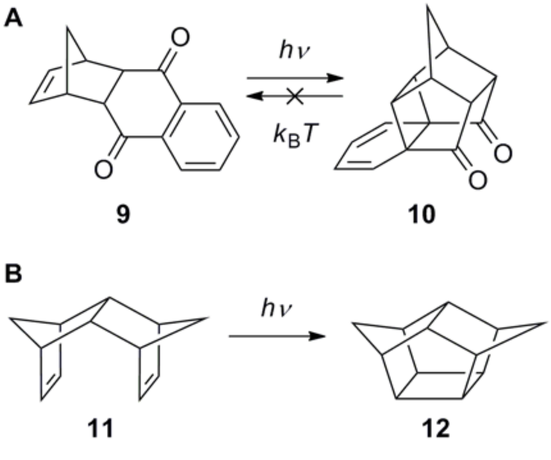

Fig. 9.9. Examples of photocyclizations with high quantum yields for forming cage compounds.

Hexamethylprismane (HMP, **13**)/hexamethyl Dewar benzene (HMDB, **14**)/hexamethylbenzene (HMB, **15**, Fig. 9.10)[89] make up another extensively studied system potentially suitable for solar energy storage. The formation of HMDB and MHP from HMB is endothermic by ~250 kJ/mol[90] and >380 kJ/mol,[91-93] respectively (corresponding to mass energy densities of 1.5 and 2.3 MJ/kg for neat HMDB and HMP, respectively). Both HMP and HMDB are generated upon irradiation of dilute solutions of HMB at ~204 nm,[89,93] with oxidizing sensitizers being particularly effective in promoting the isomerization, presumably by a radical cation chain mechanism.[94]

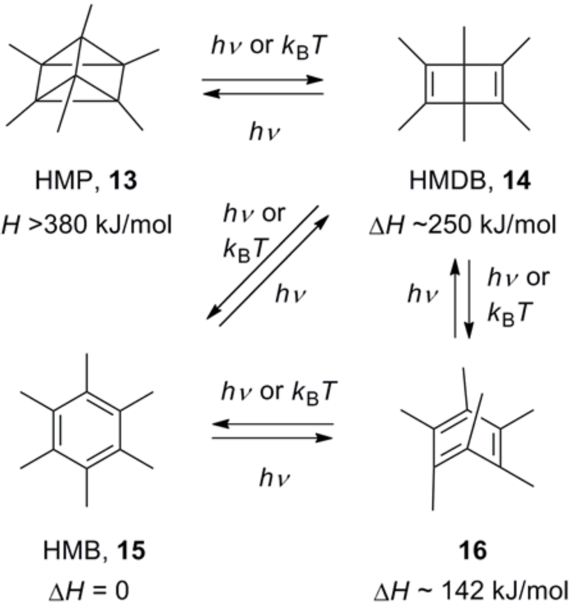

Fig. 9.10. The structures of hexamethylprismane (HMP, **13**) and its Dewar (**14**), Kekulé (**15**) and Möbius (**16**) benzene analogs. Energy differences: **13**, refs. 91-93; **14**, refs. 91 and 90; **16**, ref. 95.

In the absence of sensitizers, the isomerization is thought to proceed through a high-energy S_1/S_0 conical intersection, which cannot be accessed from the Franck-Condon region on the S_1 surface of HMB. However, the mechanism and energetics of photogeneration of Dewar benzene and prismane appear to have been relatively little-studied computationally.

The mechanism of thermal isomerization of HMP and HMDB to HMB remains a matter of controversy. Prismanes appear to convert to benzenes through the intermediacy of the Dewar benzene. The conversions of HMP to HMDB and HMDB to HMB are first order, with $\Delta H_{\mathrm{rev}}^{\ddagger}$ = 138 kJ/mol and $\Delta S_{\mathrm{rev}}^{\ddagger}$ = 21 J/(mol K) and $\Delta H_{\mathrm{rev}}^{\ddagger}$ = 152 kJ/mol and $\Delta S_{\mathrm{rev}}^{\ddagger}$ = 31 J/(mol K), respectively[91] (slightly different activation parameters were also reported[96,97]); thermal isomerization of unsubstitued Dewar benzene proceeds with $\Delta H_{\mathrm{rev}}{}^{\ddagger}$ = 105 kJ/mol and $\Delta S_{\mathrm{rev}}{}^{\ddagger}$ = 3 J/(mol K).[98] The Woodward–Hoffman rules of electrocyclic reactions suggest that the orbital symmetry-allowed concerted (conrotatory) dissociation of the central C–C bond in HMDB should produce one of the newly formed C=C bonds close to the trans configuration (so-called Möbius benzene, **16**, Fig. 9.10), which was thought to be "impossibly strained".[99] The alternative requires a biradical transition state. Recent reaction path computations on unsubstituted Dewar benzene at the CASSCF(10,10)/6-311G** level of theory found a concerted conrotatory (closed-shell) transition state that leads directly to benzene without the intermediacy of the Möbius isomer. The disrotatory (diradical) transition state leading to the Möbius isomer is 28 kJ/mol higher; the Möbius isomer must pass through another diradical transition state to convert to benzene.[100] In certain substituted Dewar benzenes, the Möbius benzene derivatives appear as shallow intermediates connecting different transition states on the path to benzene.[95] The kinetic stability of highly strained prismanes and Dewar benzenes can be ascribed to their conformational rigidity, which prevents biradical transition states from adopting geometries in which the relief of molecular strain would compensate for the uncoupling of an electron pair.

The isomerizations of QC to NBD, HMP to HMB and HMDB to HMB described above are fairly unique in their combination of high standard enthalpies (between -89 and -350 kJ/mol), which would potentially allow high energy densities, and high free energies of activation to give useful thermal stabilities of the metastable isomers. However, the integration of these metastable hydrocarbons into practical solar-energy storing schemes is complicated by the need for UV light and/or sensitizers for their generation, their complex photoisomerization mechanisms, their difficult synthesis and the limited opportunities for tuning their absorption, standard enthalpies of reactions and reactivities through substitution. Other limitations of these reactions have been discussed elsewhere.[43]

Adopting systems based on the photoisomerization of C=C or N=N bonds for solar-energy storage present its own set of challenges. Donor–acceptor azobenzenes are produced industrially for use as dyes because they absorb visible light (e.g., $\lambda_{\max}$ = 425 nm for 2,2′-dimethyl-4-(*N*,*N*-dimethylamino)-5′-nitroazobenzene).[66,72,101] However, azobenzenes suffer from:

4. low exothermicities of thermal isomerization of (*Z*)-azobenzenes to their *E* analogs[80] (<50 kJ/mol, corresponding to the energy densities <0.2 MJ/kg for pure Z azobenzenes)
5. low free energies of activation of *Z* → *E* isomerization (between 91 and 110 kJ/mol in solution corresponding to half-lives of <250 h at room temperature)[80] and
6. difficulties in preparing samples containing pure *Z* isomers (photostationary states of azobenzenes typically contain <75% of the metastable *Z* isomer due to modest ratio of the extinction coefficients of the two isomers at >400 nm).

No substitution pattern is known that significantly increases the activation barrier for *Z* → *E* isomerization above that of unsubstituted azobenzene.[102] The mechanisms of *E*/*Z* photo- and thermal isomerization remains controversial. Isomerization may occur by rotation about the N=N bond, by inversion of one of the N atoms or a combination of the two (concerted inversion,[71,103,104] Fig. 9.11). For thermal isomerization, the free volume of activation ($V^{‡} = -RT(\partial \ln k/\partial P)_T$) decreases from rotation to inversion and pressure-dependent thermal *Z* → *E* isomerization rates could help differentiate the mechanisms. The *Z* → *E* isomerization rates typically increase with pressure (i.e., $V^{‡} < 0$).[105-108] In contrast, *E* → *Z* isomerization is suppressed in closely packed films[109-111] and can in some cases cause bulk film deformation.[112]

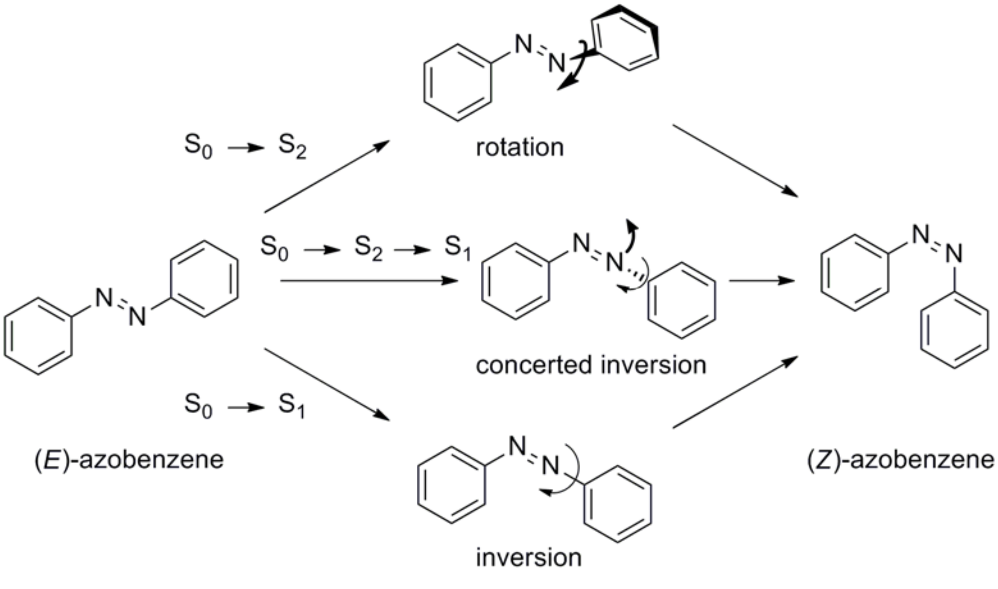

Fig. 9.11: The different mechanisms for photoisomerization of azobenzenes.

The molecular mechanism of *E* → *Z* photoisomerization is further complicated by the existence of two photochemically active optical absorbance bands: the weaker symmetry-forbidden n–π* ($S_0 \rightarrow S_1$) transition and the stronger, symmetry-allowed π–π* ($S_0 \rightarrow S_2$) transition. The relative importance of various mechanisms may be quite sensitive to subsitution and solvent.

Indigos (Fig. 9.7E and various derivatives carrying arene substituents) are industrially important dyes and have been considered for the chemical storage of solar energy. Many indigos have very low quantum yields of *E*/*Z* photoisomerization, presumably due to intramolecular hydrogen bonding[113] (Fig. 9.12) which creates significant barriers for the necessary nuclear rearrangement of the singly excited isomer (S_1 surface) from the Franck–Condon region to the S_1/S_0 conical intersection(s) (Fig. 9.5). Such hydrogen bonding is eliminated by alkylation of N, and *N*,*N′*-dialkylated indigos photoisomerize upon irradiation at >500 nm.[81] Strong absorption at such long wavelengths has been attributed to significant distortions of the central C=C bond in *N*,*N*-dimethylindigo due to steric repulsion of the *α*-C substituents.[114] Although indigos are amenable to tuning their properties by substitution, they suffer from similar deficiencies as azobenzenes:[44,115] low standard and activation free energies of *Z* → *E* isomerization (<34 kJ/mol and <100 kJ/mol, respectively).[81]

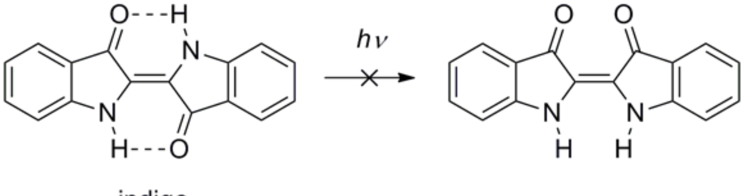

indigo

Fig. 9.12: Intramolecular hydrogen bonding in indigo prevents its photoisomerization.

Finally, the potential of a series of organometallic photochromic complexes to form the basis of a solar thermal battery was recently evaluated,[116] extending previous experimental work.[117,118] Irradiation of dilute solutions of $FvRu_2(CO)_4$ (**5**, Fig. 9.7F) in THF at or above 350 nm produces a photostationary mixture containing 80 mol% of the strained *anti* isomer **6**. Thermal reversion to **5** is two steps with overall standard and activation energies of 83 ± 6 kJ/mol and 125 ± 8 kJ/mol, respectively,[116] corresponding to a maximum specific energy density of ~0.2 MJ/kg and a self-discharge rate of ~5% per year (at room temperature). The complex could be cycled at least 10 times without evidence of degradation.[117] However, a Ru complex is unlikely to be attractive for practical applications both because of its cost and its large molecular weight (442 g/mol), which decreases the specific energy density. Computations suggest that the

Fe and Os analogs of **5** lack the favorable energy profile of the Ru system.[116] However, this example suggests that organometallic complexes should be considered along with the conventional organic photochromic molecules as potential constituents of solar thermal batteries.

9.8 Whitherward?

Despite the large amount of work devoted to photochromic compounds, including those for solar thermal energy storage, the potential of this strategy relative to alternatives (e.g., electrochemical batteries) remains unclear. We ascribe the situation to the apparent lack of any systematic effort to design chromophores expressly to meet the minimum necessary and desired performance characteristics of a practical solar thermal fuel cell. So far any such effort has relied on the few basic photochromic pairs with large differences in the enthalpies of formation of the two isomers, supplemented by attempts to adjust the absorption properties of the stable isomer by substitution. Such a strategy is rather limiting: few known photochromic pairs show a large enough difference in the formation enthalpies of the two isomers, with the current examples being limited to [2+2] photocycloadditions of strained cyclic dienes or related hydrocarbons. Little is known about how to design new photochromic pairs de novo, often because of the complex and poorly understood photoisomerization mechanisms of the existing examples.

The alternative approach is (1) to identify a photochromic pair with suitable photophysical and spectrokinetic properties but potentially small difference in the formation enthalpies of the two isomers and (2) to adjust the structure of one of the isomers to maximize the standard free energy of thermal isomerization through molecular design. A starting point for such an approach is the expression of the performance characteristics of a solar thermal battery in terms of the molecular properties of its photochromic material. Below we attempt to do so and speculate about which questions may need to be answered first in any quest for a practical chemical solution to solar thermal energy storage.

The important performance parameters of a thermal battery include energy and power densities, energy conversion efficiency, self-discharge rate and cost per MJ of energy in addition to ease of use (both regeneration and discharge) and the probability and severity of catastrophic failure. Molecular properties of the isomeric pair (i.e., its chemical composition, thermodynamics, kinetics and photophysics; see Fig. 9.2) place fundamental upper limits on some of these parameters.

Table 9.2. Performance characteristics of a closed-system solar fuel system and the molecular parameters that determine their fundamental limits.

Metric	Determinant Molecular Parameters
specific energy density	molecular weight, standard energy of isomerization, molar absorptivities and the quantum yields of photoisomerization of the two isomers at the photoisomerization-inducing wavelength(s)
specific power density	activation energy of thermal reversion at operating temperature, standard energy of isomerization, molecular weight, molar fraction of the metastable isomer
energy conversion efficiency	quantum yields, molar absorptivities of the two isomers at the photoisomerization-inducing wavelength(s), standard energy of isomerization
cost per MJ	cost of initial synthesis vs. material lifetime determined by the thermal and photochemical degradation kinetics
self-discharge rate	activation energy of thermal reversion, storage temperature
runaway (catastrophic) discharge	activation energy of thermal reversion, ambient temperature, specific energy density, material density, heat capacity

9.8.1 Energy Density

The effect of molecular properties on the maximum specific energy density of a photochromic material was discussed earlier in the review. Limited solar flux at wavelengths below ~340 nm at the Earth's surface places the upper limit on the energy that can be deposited into a chromophore at ~3.5 eV. In theory this amount can be increased if absorption of one photon creates a sufficiently long-lived metastable intermediate that converts into an even higher-energy isomer upon absorption of another photon. One such case is the photodimerization of 2-cyanonaphthalene (**17**, Fig. 9.13A) to form the (presumably highly strained) cubane derivatives **18**–**20**.[119] The dimerization is a two-photon process proceeding through the intermediacy of a [4 + 4] adduct (**22**),[120,121] though the standard enthalpy of isomerization for these compounds was not reported. In contrast to the photodimerization of anthracenes,[122] many naphthalenes do not photodimerize in solution without supramolecular complex formation or even in the solid state,[119,121] At present very few compounds are known to manifest stepwise photoisomerizations, and the standard enthalpy of isomerization between the least and most strained isomers may be only a small fraction of the energy of the two absorbed photons.[123] Nonetheless, we are not aware of any physical laws that fundamentally prevent such a multi-photon, multi-step photoisomerization mechanism from being exploited for solar energy storage.

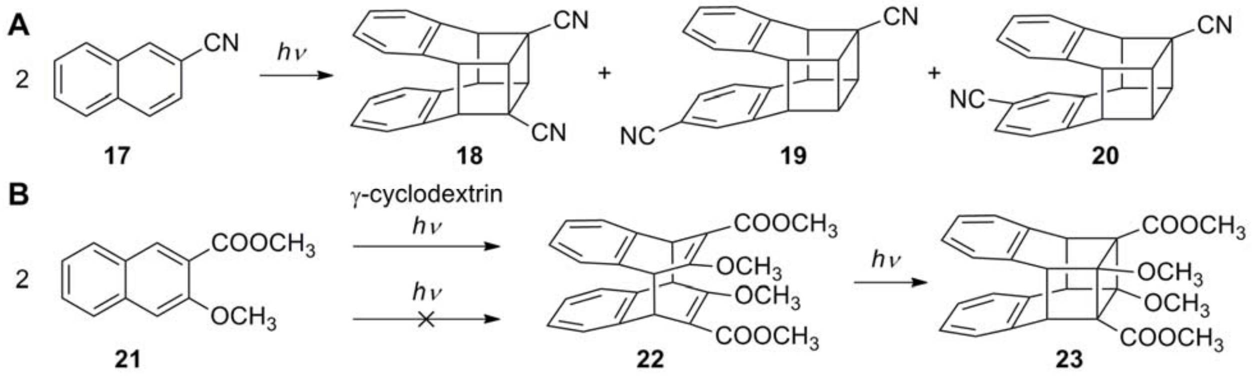

Fig. 9.13. **A**: The photodimerization of 2-cyanonaphthalene with $\lambda_{\mathrm{irrad}} > 280$ nm results in a mixture of *anti*-head-to-head (**18**) and *anti*- and *syn*-head-to-tail (**19** and **20**) regioisomers of cubane derivatives, presumably by a two-step process involving a [4 + 4] intermediate.[119] **B**: The first step of the photodimerization of methyl 3-methoxy-2-naphthoate with $\lambda_{\mathrm{irrad}} > 280$ nm requires the presence of a supramolecular template, γ-cyclodextrin, making the formation of the [4 + 4] intermediate **22** enantioselective; further irradiation (with or without γ-cyclodextrin present) subsequently affords a [2 + 2] photocycloaddition, yielding the cubane derivative **23**.[120,121]

Another strategy of maximizing the energy density of a solar thermal battery is to increase the fraction of the absorbed photon energy that is stored in the metastable isomer (Fig. 9.5). In many existing photochromic compounds for which kinetic data for thermal relaxation is available, the photon energy required to convert the stable isomer to its metastable analog is 2–3 times greater than the activation barrier separating the stable from the metastable isomer, $\Delta G_{\mathrm{isom}}^{\ddagger}$. Because the standard free energy of isomerization of the metastable to the stable isomer, $\Delta G_{\mathrm{isom}}^{\mathrm{o}}$, which is the energy stored per mole of chromophore, must be less than the activation barrier, $\Delta G_{\mathrm{isom}}^{\ddagger}$ ($\Delta G_{\mathrm{isom}}^{\ddagger} = \Delta G_{\mathrm{isom}}^{\mathrm{o}} + \Delta G_{\mathrm{rev}}^{\ddagger}$), most photochromic compounds can store < 30% of absorbed photon energy.

In the simplest case, the rest of the photon energy can be separated into the energy gaps (1) on the S_1 surface between the Franck–Condon configuration and the minimum–energy conical intersection (MECI) leading to the metastable conformer, E_1, and (2) on the S_0 surface, between the MECI and the transition state of thermal isomerization, E_0. In theory the fraction of the photon energy that could be stored in the metastable isomer can be increased by bringing the geometry of the S_0 transition state closer to that of the MECI and/or the MECI geometry closer to the Franck–Condon geometry, i.e., by redistributing the photon energy from E_0 and E_1 to $\Delta G_{\mathrm{isom}}^{\mathrm{o}}$.

Calculated values of E_1 (and its fraction of the vertical excitation energy in parentheses) vary from <42 kJ/mol (0.15) in azobenzene[124] to ~60–85 kJ/mol (0.17–0.25) in conjugated olefins, such as stilbene or rhodopsin **24**,[56,125] to ~40 kJ/mol (0.3) in benzadithiophene, **26** (the S_1 state is dark and the excitation to the S_2 state is required for photoisomerization)[126]) and >330 kJ/mol (>0.5) in hypothetical tetrahydro-cyclopenta[a]pentalene, **28**.[127] The largest fraction of the absorbed photon energy is dissipated in the excited states in valence photoisomerization reactions, reactions in which the S_1 state of the stable isomer is dark or photoisomerizations in which the MECI does not lead to the desired product (e.g., the formation of the Dewar benzene). We are not aware of any studies that have systematically explored how substituents of a chromophore affect the energy of the MECI relative to that of the excitation energy. Qualitatively, lowering E_1 and hence the energy gradient along the reaction path on the S_1 surface may also lower the quantum yield of the productive photoisomerization process by increasing the residence time of the electronically excited chromophore in the vicinity of the Franck–Condon configuration. This increase could promote relaxation of the excited chromophore to the stable instead of metastable isomer by several mechanisms, as illustrated by temperature- and viscosity-dependent quantum yield of E/Z photoisomerization of stilbene.[128]

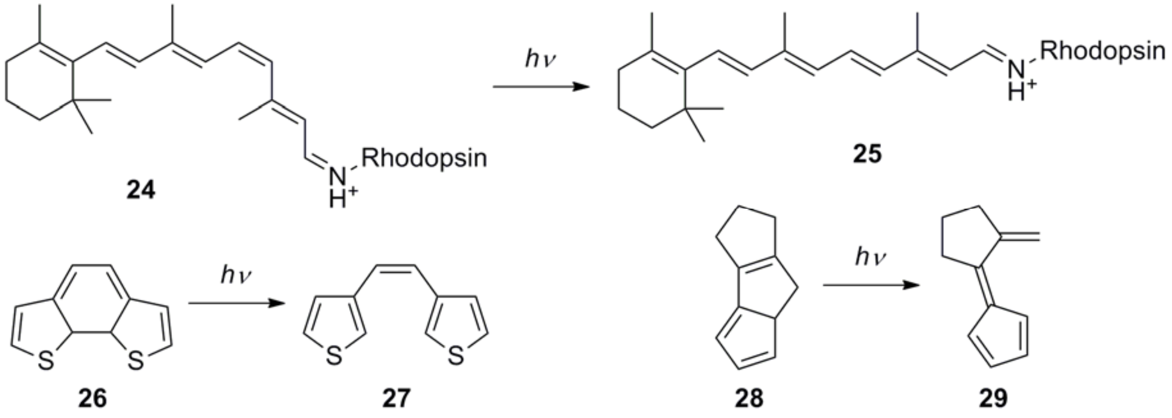

Fig. 9.14. Structures for which values of E_1 have been calculated; structures not shown are defined elsewhere in the text. In **24** and **25**, "Rhodopsin" represents the rest of the protein.

Calculated values of the energy difference between the MECI and the transition state of thermal isomerization vary from ~42 kJ/mol (0.2) in the rhodopsin/bathorhodopsin pair[125,129] to ~105 kJ/mol in olefins and azobenzenes to >167 kJl/mol in valence isomerization reactions. The T_1–S_0 energy gap probably vanishes at the geometries of biradical transition states, which are common in thermal isomerization of olefins, and increasing the corresponding activation energies at constant photoisomerization wavelength would have to be accompanied by a decrease in the T_1–S_1 gap as well.

The maximum energy density of a photochromic material is determined both by the standard free energy of metastable-to-stable conversion reaction and the fraction of the metastable isomer at the photostationary state, χ_m. Ideally, the photostationary state is composed of only the metastable isomer ($\chi_m = 1$), which is only possible if at the photoisomerization wavelength the metastable isomer is either

7. transparent, i.e., $\varepsilon_s(\lambda)/\varepsilon_m(\lambda) \rightarrow \infty$, where ε_s and ε_m are the molar absorptivity of stable or metastable isomers, respectively or
8. photochemically inactive, i.e., quantum yields of all its photochemical processes are zero.

The former is preferable because it corresponds to the maximum achievable photochemical energy conversion efficiency for a given excitation wavelength and activation energy of thermal relaxation. Reliable wavelength-dependent molar absorptivities of both isomers are available for only a few photochromic compounds. In most cases, the metastable conformer absorbs at longer wavelengths than the stable one (positive photochromism[130]) and consequently $\varepsilon_s(\lambda)/\varepsilon_m(\lambda) = 0$ for wavelengths above a certain threshold. However, because most molecules are relatively less transparent to shorter rather than longer wavelengths, the $\varepsilon_s(\lambda)/\varepsilon_m(\lambda)$ ratio rarely exceeds 10 (Table 9.3). The notable exceptions are photocyclizations that lower the degree of conjugation. For example, the anthracene photodimer is transparent above ~290 nm, whereas anthracene absorbs strongly ($\varepsilon > 100$ M^{-1} cm^{-1}) up to ~380 nm. Larger acenes manifest even greater differences: acenaphthylenes and naphthacenes absorb up to at least 450–500 nm, whereas their dimers are transparent above ~350 nm. Azaacenes (e.g., acridizinium) and phanes manifest similar trends (Fig. 9.16).

Table 9.3. Representative structures in which the stable isomer absorbs more strongly than the metastable isomer at a the indicated wavelength; structures are shown in Fig. 9.15.

compound	solvent	stable isomer	metastable isomer	wavelength, nm	$\varepsilon_s/\varepsilon_m$
stiff stilbene, **30**, **31**[a]	benzene	*E*	*Z*	330	3.3
azobenzene[b]	ethanol	*E*	*Z*	316	8.9
				229	6.1

Table 9.3 (cont.)

4-(*N*,*N*′-dimethylamino)azobenzene[b]	benzene	*E*	*Z*	413	3.7
dihydroindolizine **32, 33**[c]	CH_2Cl_2	ring-closed	ring-open	415	1.4
dihydroindolizine **34, 35**[c]	CH_2Cl_2	ring-closed	ring-open	385	1.5
pyrazoline **36, 37**[c]	CH_2Cl_2	ring-closed	ring-open	460	2.1
dihydropyrazolo-pyridine **38**, **39**[c]	CH_2Cl_2	ring-closed	ring-open	~400	~1.2
spiropyran **40**, **41**[d]	ethanol	ring-closed	ring-open	240	3.1
fulgide **42**, **43**[e]	hexane	ring-closed	ring-open	304	4.4

[a] ref. 128. [b] ref. 131. [c] ref. 132. [d] ref. 133. [e] ref. 134

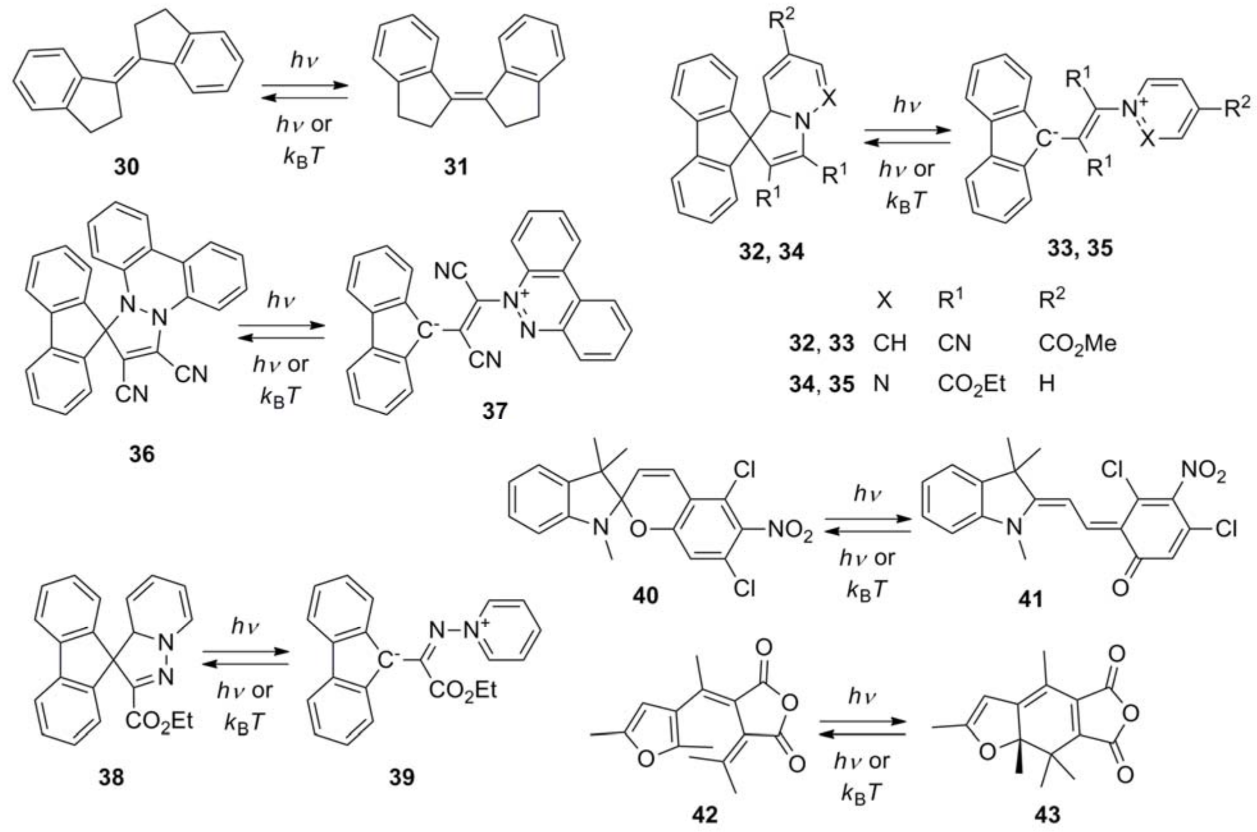

Fig. 9.15. Structures of the photochromic compounds described in Table 9.3. The metastable isomers are on the right.

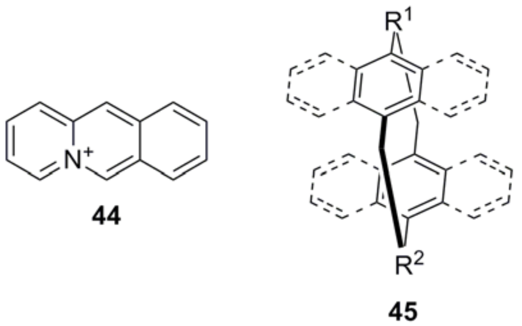

Fig. 9.16. The parent structures of the N-heterocycle acridizinium (**44**) and a cyclophane (**45**).

The dihydroazulene/vinylheptafulvene pair (Fig. 9.17) is an example of so-called "one-way" photochromism, i.e., dihydroazulene converts to vinylheptafulvene upon irradiation (with quantum yields of up to 1 for certain derivatives), whereas the reverse reaction can only be performed thermally. One-way photoisomerization of a stilbene dendrimer in H_2O was also reported.[135] In such "one-way" photochromism, significant absorption of incident light by the metastable isomer, even if it is not accompanied by photoisomerization, can result in photoheating of the battery, which may require active cooling during charging.

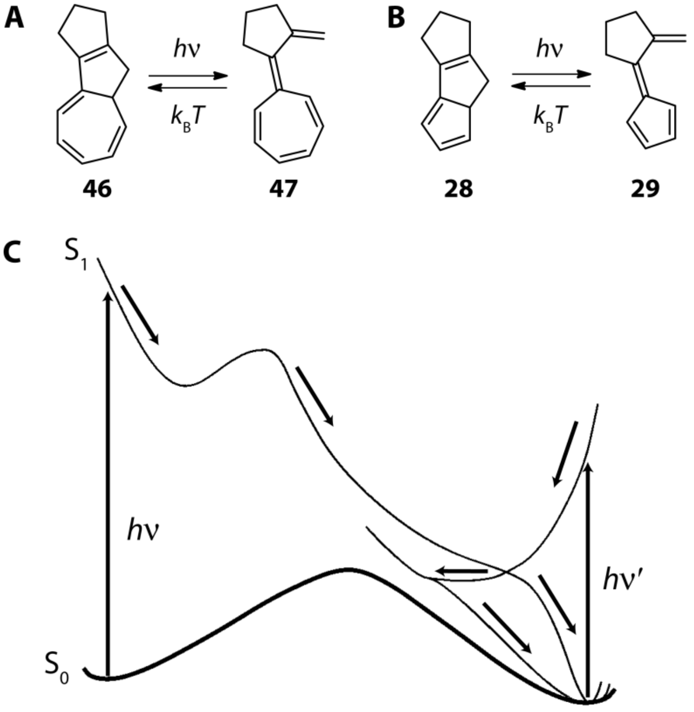

Fig. 9.17. (**A**) The structures of dihydroazulene (**46**) and vinylheptafulvene (**47**), (**B**) the compounds used to model them (**28** and **29**) and (**C**) the model compounds' energy surfaces that dictate their interconversion. Modified from ref 127.

The mechanism of "one-way" photochromism has been studied computationally and is thought to result from the minimum-energy conical intersection lying below the transition state of thermal isomerization (on the electronic ground state energy surface) and/or having geometry close to one of the isomers (Fig. 9.17).

Quantum yields of photoisomerization are generally different for wavelengths corresponding to the reactant excitation to different excited states. Such wavelength-dependent quantum yields may result in the irradiation wavelength yielding a photostationary state of the maximum energy density being different from the irradiation wavelength corresponding to the highest conversion efficiency of solar energy. For example, the quantum yields of photoisomerization of (*E*)-azobenzene to the metastable *Z* isomer are ~0.2 at λ < 320 nm (corresponding to $S_0 \rightarrow S_2$ excitation) and ~0.35 at λ > 400 nm (corresponding to $S_0 \rightarrow S_1$ excitation). The maximum $\varepsilon_E(\lambda)/\varepsilon_Z(\lambda)$ ratio of ~8 is observed at ~320 nm; at λ > 400 nm, the ratio is <4. Yet irradiation at >400 nm may be preferable, because it decreases photoheating and irreversible photobleaching due to side reactions.

9.8.2 Power Density

Under isothermal discharge, the average power density delivered by a fully charged cell as it discharges, *PD*, is related to its energy density, *ED*, by eq. (9.4), where $\Delta H_{\text{rev}}^{\ddagger}$ and $\Delta S_{\text{rev}}^{\ddagger}$ are the standard enthalpy and entropy of activation of thermal isomerization of the metastable isomer, *T* is the temperature, and k_B, *h* and *R* are the Boltzmann, Plank and gas constants, respectively. Many isomerization reactions have $\Delta S^{\ddagger} \sim 0$. At 100 °C, a fully charged solar thermal battery would deliver up to 0.5 kW/kg of power when fully charged ($\chi = 1$). Its average specific power density over 50% discharge at the same temperature is 2ln2 ~ 1.4 times lower (~0.3 kW/kg). These values correspond to isothermal discharge, i.e., mixing (passive or active) is assumed to be efficient enough to dissipate any thermal (and hence concentration) gradients within the cell throughout its discharge fast (relative to the total discharge time). If the temperature of the cell changes during discharge, power densities can be both lower and higher than the isothermal values cited above, because local heat fluxes depend approximately exponentially on local temperature (see below). The isothermal power densities are representative numbers and compare well to the maximum power density of Li ion batteries (0.1–1 kW/kg).[11]

$$\langle PD \rangle_{1\to\chi} = -\frac{\chi ED}{\ln(1-\chi)} \frac{k_\mathrm{B} T}{h} e^{-\frac{\Delta H_\mathrm{rev}^\ddagger}{RT} + \frac{\Delta S_\mathrm{rev}^\ddagger}{R}} \tag{9.4}$$

9.8.3 Explosion Hazard

We are not aware of any published analysis of the potential of a catastrophic failure of a solar thermal battery. A charged battery of any kind is thermodynamically metastable and may spontaneously discharge if the energy-releasing chemical reaction is accelerated in some way (e.g., by adventitious catalyst). As discussed earlier, the only strategy to increase the specific energy density of a solar thermal cell above 1.5 MJ/kg is either to use light of shorter wavelengths than those reaching the Earth's surface or to rely on multi-photon isomerization reactions. Neither option seems plausible at present. At 1.5 MJ/kg, the specific energy density of a solar thermal cell would be far less than that of conventional explosives (e.g., from standard enthalpies of combustion, TNT at ~15 MJ/kg,[15,136] octogen at 9.4 MJ/kg[51] and hexanitrobenzene at 7.4 MJ/kg[136]) but comparable to that of NH_4NO_3 (~0.9 MJ/kg)[136-138] and N_2H_4 (~1.6 MJ/kg),[52,138] both of which are used as monopropellants. The fundamental difference between monopropellants (and chemical explosives) and photochromic molecules for potential solar-thermal cell use is the enthalpic vs. entropic contributions to their exergonicity. Monopropellants and chemical explosives are designed to decompose into gaseous products, i.e., their exergonicity has a substantial entropic component. In contrast, an isomerization reaction suitable for reversible solar energy storage should have a minimal entropic component.

The only mode of catastrophic failure of a solar heat battery that seems plausible to us is spontaneous heating due to a runaway reaction, i.e., a situation when the rate at which the reaction generates heat exceeds the rate at which this heat is dissipated to the environment. Because the rate of a thermal reaction increases exponentially with temperature, sufficiently high local heating may conceivably set up a propagating, self-accelerating reaction front. If the average cell temperature becomes sufficiently high, the cell may lose structural integrity, the photochromic material may degrade irreversibly and/or damage to property or living organisms may result.

We envision two limiting mechanisms which can set off a runaway reaction: (1) the cell is placed in an environment whose ambient temperature exceeds the thermal stability limit of the cell or (2) the ambient temperature is below this threshold value, but the reaction is initiated in a small volume of the cell, for example by an adventitious catalyst.

The dynamics of cooling of a sphere in air is described adequately by a heat equation even for very large Grashof numbers.[139] To get a semi-quantitative idea of the low limit of the thermal stability of a solar thermal cell, we modeled the time-dependent temperature of a spherical cell of radius r_o (Fig. 9.18) initially at uniform temperature T_o placed in ambient environment of temperature T_{ext} by solving simultaneously a generalized 1-dimensional heat equation (eq. (9.5)), where the first term describes heating due to the reaction, and a differential unimolecular rate law with mass transport (eq. (9.6)). In eqs. (9.5)–(9.9), $T(t, r)$ is the temperature of an infinitely thin shell r meters from the center of the cell at t seconds after the initiation event; $\chi(t, r)$ is the molar fraction of the metastable isomer at t and r ($0 \le \chi \le 1$), $\Delta H_{rev}^{\ddagger}$ is the activation enthalpy of the exergonic reaction (we assume $\Delta S_{rev}^{\ddagger} \sim 0$, see discussion above), R is the gas constant, α is the thermal diffusivity of the photochromic material ($-r_o \le r \le r_o$) or of the surrounding medium ($r < -r_o$, $r > r_o$) and D is the effective diffusion coefficient of the photochromic material. Function $a(r)$ is defined by eq. (9.7), where ED is the volumetric energy density of the fully charged battery, ρ and C_v are the density and constant-volume heat capacity of the photochromic material, respectively, and k_B and h are the Boltzmann and Plank constants, respectively. Because the only source of heat is the reaction occurring within the cell, $a = 0$ outside of the cell.

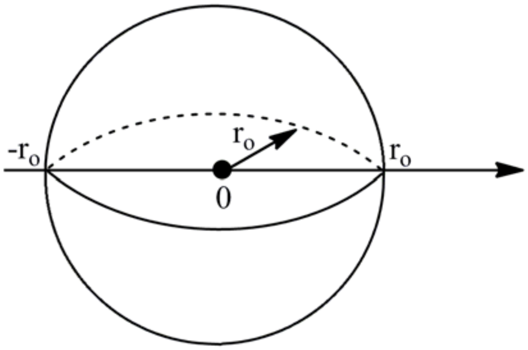

Fig. 9.18. The schematic of the solar thermal cell modeled.

$$\frac{\partial T}{\partial t} = \chi a T e^{-\frac{\Delta H_{rev}^{\ddagger}}{RT}} - \alpha \frac{\partial^2 T}{\partial r^2} \tag{9.5}$$

$$\frac{\partial \chi}{\partial t} = -\chi \frac{k_{\mathrm{B}} T}{h} e^{-\frac{\Delta H_{\mathrm{rev}}^{\ddagger}}{RT}} - D \frac{\partial^2 \chi}{\partial r^2} \tag{9.6}$$

$$a(-r_{\mathrm{o}} \leq r \leq r_{\mathrm{o}}) = ED \frac{k_{\mathrm{B}}}{hC_V \rho}, \ \ a(r \notin [-r_{\mathrm{o}}, r_{\mathrm{o}}]) = 0 \tag{9.7}$$

$$T(0, -r_{\mathrm{o}} \leq r \leq r_{\mathrm{o}}) = T_{\mathrm{o}}, \qquad T(0, r \notin [-r_{\mathrm{o}}, r_{\mathrm{o}}]) = T(\infty, r) = T(t, r \notin [-r_{\mathrm{c}}, r_{\mathrm{c}}]) = T_{\mathrm{ext}} \tag{9.8}$$

$$\chi(0, -r_{\mathrm{o}} \leq r \leq r_{\mathrm{o}}) = 1, \qquad \chi(t, r \notin [-r_{\mathrm{o}}, r_{\mathrm{o}}]) = \chi(\infty, r) = 0 \tag{9.9}$$

The boundary conditions, eqs. (9.8)–(9.9), have the following physical meaning:

9. Before the exergonic reaction is initiated, no temperature gradients exist inside or outside of the cell, although a temperature gradient may exist across the cell/environment boundary; the environment is assumed to be infinitely large so as to absorb all heat generated by the cell without changing the temperature at the ultimate thermal equilibrium ($t = \infty$), but its finite thermal conductivity allows transient heating of the environment in the vicinity of the cell above T_{ext}.
10. The final state of the cell is the absence of thermal gradients across the system and of chemical gradients across the cell (i.e. complete conversion of the metastable isomer to the stable isomer).

We modeled heat exchange between the cell and the ambient air as convection within $r_{\mathrm{c}} - r_{\mathrm{o}}$ meters from the surface of the cell, where r_{c} corresponds to the Rayleigh number, Ra = 10. The environment beyond this range was assumed to remain at the ambient temperature. The value of r_{c} was found self-consistently by eq. (9.10), where α, μ, ρ and γ are coefficients of thermal diffusivity, dynamic viscosity, density and thermal expansion of air under standard conditions, g is gravitational acceleration, $T(t - dt, r_{\mathrm{c}})$ is the temperature at the preceding temporal step of a simulation and | | signify absolute value. In our simulations, typical r_{c} values during catastrophic heating were on the order of 1 cm.

$$r_{\mathrm{c}}(t) = \left(\mathrm{Ra} \times \frac{\alpha\mu}{\rho g \gamma |T_{\mathrm{ext}} - T(t - dt, r_{\mathrm{c}})|}\right)^{1/3} \tag{9.10}$$

The results of this modeling are shown in Fig. 9.19, where the maximum sustained (over at least 1 s) surface temperatures of cells of different diameters are plotted against the ambient temperature. The threshold ambient temperature above which the cell is not stable is fairly insensitive to details of modeling of the heat exchange between the cell and the environment but the maximum sustained temperature is. We present the range of temperatures observed in simulations with somewhat different values of r_c (extrapolated and properly scaled from the data in refs. 139 and 140). As expected, the smaller the cell, the higher ambient temperatures are required to set off catastrophic discharge, because larger surface-to-volume ratios of smaller cells facilitate passive cooling. Spherical cells <0.4 L in volume (r_o <10 cm) appear to be stable against catastrophic discharge at any practical storage temperature. The highest ambient temperature at which cell is stable decreases from >85 °C for the 0.4 L cell (r_o = 10 cm) to ~45 °C for the largest cell we modeled (~42 L, r_o = 100 cm). Running-average (100 s interval) surface temperatures of the 0.4 L and 42 L cells as a function of time since the cell was exposed to high external temperature (color coded on the graph) are illustrated in Fig. 9.20.

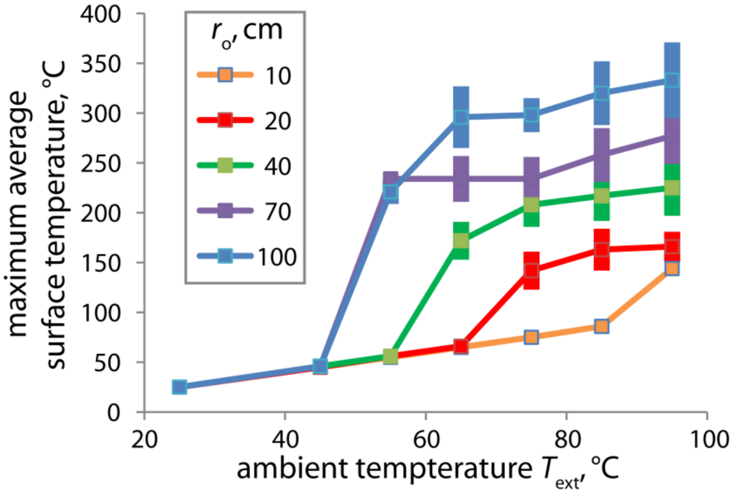

Fig. 9.19. The maximum surface temperatures sustained for at least 1 s of solar thermal cells of varying radii (r_o, cm) as a function of the ambient temperature, T_{ext}. A range of temperatures reflects different simulation parameters as described in the text.

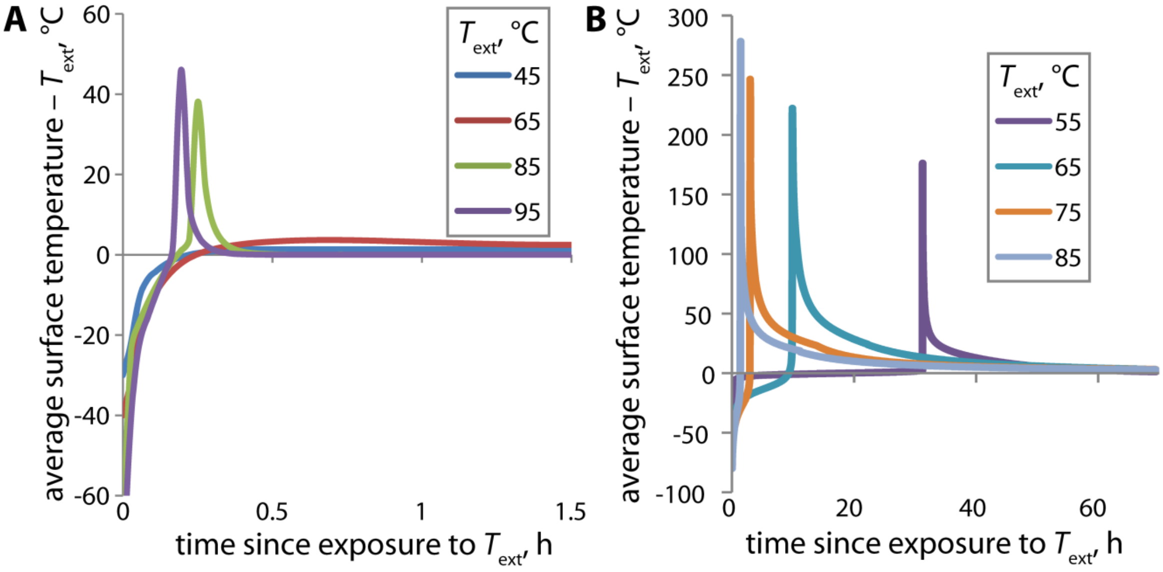

Fig. 9.20. Deviation of the surface temperature (running average over 100 s) of 0.4-L (**A**) and 42-L (**B**) thermal cells from the ambient temperature as a function of time since exposure of the cell to the ambient temperature.

Surface temperatures above 100 °C can result in injuries or damage to property but may not cause significant damage to the cell itself. Higher temperatures, however, which we estimate can remain above 200 °C for >100 s within larger cells (Fig. 9.20B) may result in decomposition of the photochromic material and the release of the material into the environment. Yet we tend to view these results as the "worst case" scenario because (1) a sphere has the lowest surface-to-volume ratio of any shape and hence is least amenable to passive cooling, (2) our simulations neglected convective mixing within the cell and probably underestimated the efficiency of convective cooling in air, and (3) the simulations are for a metastable isomer with the maximum attainable energy density using 1-photon chemistry and natural sunlight. We conclude that relatively small batteries (<100 mL) in different shapes would probably not be susceptible to catastrophic discharge and hence would be as practical as conventional redox batteries.

9.8.4 Stability, Life Cycles and Cost per MJ

Solar thermal cells are only practical if they can operate over many charge/discharge cycles. The photochromic material can degrade during either cycle, typically as a result of unimolecular side reactions of the electronically excited states during charging (so called photobleaching, e.g., the formation of dihydrophenanthrene from (*Z*)-stilbene followed by its oxidation to phenanthrene), in reactions with sensitizers if any are used (e.g., the photoaddition of ketones to NBD) or with ambient O_2 or H_2O or the material of the cell. Some of the most stable known photochromic pairs can undergo >10^4 cycles without degradation; examples include methyl-substituted dithienylperfluorocyclopentene **48**[141] bacteriorhodopsin,[142] anthracene[122] and certain azobenzenes and isoindigos. When both O_2 and H_2O are excluded, stiff stilbene appears to be quite resistant to photobleaching. Often photobleaching is more likely when shorter photoisomerization wavelengths and triplet sensitizers are used. For example, photoisomerization of NBD to QC (Fig. 9.7) is accompanied by the formation of toluene, among other byproducts. Toluene is a sensitizer for the reverse photoisomerization (QC→NBD) and its accumulation in the battery may significantly degrade the energy density and energy conversion efficiencies.

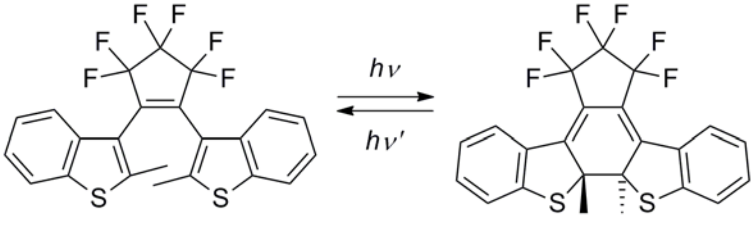

48 **49**

Fig. 9.21. The photocyclization and ring opening of a methyl-substituted dithienylperfluorocyclopentene, which exhibits thermally irreversible photochromism capable of cycling >10^4 times without significant degradation. In the dark, there is no interconversion between **48** and **49** at 80 °C for months.[141]

If both isomers absorb at the photoisomerization wavelength(s), the stability of the photochromic material will be lowered if significant concentration gradients are allowed to develop along the optical path during charging (photoisomerization). Under such conditions molecules closer to the entrance surface of incident radiation will undergo many more excitation events than molecules farther away. Such repeated excitation can be minimized by limiting the optical path so that <15% of incident irradiation is absorbed during a single passage through the cell or, at the expense of lower energy conversion efficiency, by forced convection.

The cost of photochromic material is probably not a significant determinant of the potential utility of solar thermal cells. A battery material with a specific power density of 1 MJ/kg and price of \$50/kg (i.e., an approximate wholesale price of azobenzene derivatives) would deliver power at \$0.15 per MJ at 1000 charge/discharge cycles if the overall system efficiency is 30%, assuming no maintenance costs. This compares to the mid-2011 retail price of gasoline of \$0.03 per MJ in the US[143] (and up to \$0.1 per MJ worldwide[1]), photovoltaics of

\$0.06–0.12 per MJ (without subsidy, assuming 75000 operating hours),[144] lead-acid batteries at \$0.07 per MJ at 750 cycles; Li-ion batteries of \$0.15 per MJ at 1000 cycles (including retail electricity at \$0.04 per MJ);[145] NiCd batteries at \$0.2 per MJ at 2000 cycles; NiMH at \$0.4 per MJ at 750 cycles; alkaline batteries at \$53 per MJ and disposable Zn batteries at \$75 per MJ.

9.8.5 Technological Niches for Closed-System Solar Thermal Batteries

We speculate that the first applications of solar thermal batteries would be to counterbalance diurnal temperature variations or to provide heat for personal needs, such as water heating, cooking or cleaning. Such uses could be of value both in stationary applications regardless of accessibility to a grid (e.g., from suburban houses to remote installations) and in mobile or rapid-deployment settings (e.g., military and humanitarian aid operations). Unlike conventional fuel supplies, which are depleted, solar thermal batteries would be rechargable. They may be preferable to photovoltaics by eliminating a second energy conversion step (i.e., solar to heat vs. solar to electrostatic potential to heat). A 1.5 MJ/kg solar thermal batter cycled only 100 times would deliver more energy per unit mass than hydrogen or 3 times more than gasoline (even neglecting the mass of oxygen required for their combustion). Though the single-cycle specific energy density obviously puts a limit on how much material would be needed for a given energy demand, practical amounts (a few kg) of such thermal batteries can meet the medium- to long-term energy needs of an individual. In situations where minimizing the mass of delivered material is crucial (e.g., the deployment of isolated military units or the delivery of aid materials to disaster areas), solar thermal batteries can readily meet the demands for basic necessities, as shown in the following examples.

In cooler climates, heating a living space can consume a considerable amount of energy especially at night or during cloudy periods when solar radiation is not available. For a cubic, 1 m^3 living space equipped with R19 insulation (thermal conductivity of 3.35 m^2 K W^{-1}), maintaining a 20 °C difference (e.g., 0 °C outside, 20 °C inside) requires ~36 W of power, or ~1 MJ of heat over 8 hours. A 2 kg solar battery of 0.5 MJ/kg energy density may suffice and it can be fit to <1% of the living space. The battery could then be recharged by placing it in the sun during the day. Even during cloudy periods, the units could be incrementally recharged by intermittent sunlight, and because a continuous week's worth of such heating would be provided by only 21 of these units, an individual's heating needs could still readily be met between infrequent sunny periods during which all the units could be recharged.

Cooking heat is required even when dwelling space heating is not. With suitable thermal insulation, a 1 MJ/kg solar thermal battery could be used to heat ~3 times its mass of water from 25 °C to its boiling point, or it could sustain an elevated temperature in a smaller amount of water for a longer period of time. Such a system could be used to cook, to disinfect drinking water, or to disinfect items placed in the boiling water. A single battery (or several smaller batteries which may be more safely stored) capable of delivering 1 MJ of energy (e.g., 1 L of 1 MJ/kg with density ~1 kg/L) could be used to heat 3 L of water from at 25 °C to 100 °C. If contained in a 4 L cylinder with an inner diameter of 16 cm and a internal height of 20 cm sheathed in ~2.5 cm of extruded polystyrene (R5 insulation, 0.88 m^2 K W^{-1}), the 75 °C difference between the interior and exterior could be maintained for more than 1 h. In places where electricity is unavailable or fuel delivery is impractical, such a rechargeable source of heat for cooking and water disinfection would be quite beneficial.

9.9 Conclusions

A single solution to the ever-increasing global energy demand is highly unlikely. Solar fuels make up an attractive solution that combines high energy densities and the ability to meet distributed demands in diverse applications. The development of the two types of solar fuels involves different sets of challenges. Conventional fuels (e.g., CH_4, CH_3OH, etc, which are open-cycle) synthesized from CO_2 and H_2O with solar energy input can be used in existing devices. The central scientific questions for their development are those of catalysis and how to couple endergonic reactions to photons. To be carbon-neutral, the use of such fuels must be coupled to their generation in a cycle that is effectively closed on the macroscopic level. To do so requires either isolating the combustion products at the point of generation or recapturing them from the environment once they are released. Either task is challenging to carry out efficiently.

A chemical solution for storing solar energy can also be closed at the molecular level, producing solar thermal batteries based on reversible isomerization of photochromic molecules. Despite a substantial amount of work over the past 40 years, practical photochromic molecules suitable for use in solar thermal batteries remain to be identified. In this review we analyzed briefly the pairs of isomers that have been considered in the past for solar energy storage, articulated a relationship between the molecular properties of the isomeric pair and the performance characteristics of the battery, which remains to be understood in detail, and proposed an alternative approach to developing the chemistry of solar thermal batteries. The traditional approach relies on designing a pair of isomers one of which is significantly strained followed by attempts to tune the photophysical properties of the strain-free (stable) isomer to make the pair suitable for solar energy storage.

We suggest the alternative approach of starting with a photochromic pair with suitable photophysical properties and modifying the chromophore to make one of the isomers strained. An example of such an approach is a macrocycle containing a stiff stilbene chromophore with phenyl rings bridged by an inert linker whose length is sufficient to accommodate strain-free *Z* isomer but is too short for the longer *E* isomer of stiff stilbene (Fig. 9.22).

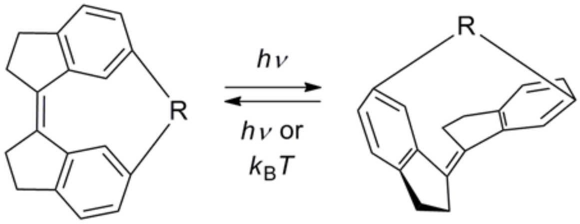

Fig. 9.22. When the phenyl rings of stiff stilbene are bridged by an inert linker, R, 11 atoms long or fewer, the *Z* isomer is the stable isomer, and the *E* isomer is highly strained.[146-148]

This approach requires a fundamental understanding of how to use molecular geometry to satisfy seemingly contradictory requirements, such as decreasing the high standard free energy of reaction while simultaneously increasing its activation energy (which is the inverse of the widely applicable linear free energy relationships) without decreasing the quantum yield of generation of the strained isomer or the photoisomerization wavelength (typically, photoisomerization wavelength and activation energy of thermal reversion correlate, Fig. 9.6).

Despite the molecular-design challenges posed by developing closed-system solar fuels, they offer unique advantages over other solutions for storing solar energy (e.g., combustible fuels, redox batteries, etc.), including carbon-neutral operation, potential ease of use and recycling, capacity for the long-term storage of energy, and suitability for mobile applications. Although energy densities of solar thermal batteries based on one-photon photochemistry cannot exceed a fraction of the energy densities of conventional fuels, their cumulative energy densities (energy stored and released over their operational lifetime) significantly exceeds that of a conventional fuel, thus relaxing constraints on which molecular structures would be economically feasible. Given these attributes, closed-system solar fuels can, with sufficient R&D investment and based on the fundamental understanding of the relationship between chemical reactivity and molecular strain, provide a strategy for capturing, storing and releasing solar energy.

9.10 References

1. *International Energy Outlook 2010*; U.S. Energy Information Administration: 2010.
2. *Annual Energy Outlook 2011*; U.S. Energy Information Administration: 2011.
3. *World Energy Outlook 2010*; International Energy Agency: Paris, France, 2010.
4. Nocera, D. G., Personalized Energy: The Home as a Solar Power Station and Solar Gas Station. *ChemSusChem* **2009**, *2*, 387–390.
5. Climate Change 2007: Mitigation of Climate Change. In *Fourth Assessment Report of the Intergovernmental Panel on Climate Change*, Metz, B.; Davidson, O. R.; Bosch, P. R.; Dave, R.; Meyer, L. A., Eds. Cambridge University Press: New York, 2007.
6. *Energy Technology Perspectives 2010*; International Energy Agency: Paris, France, 2010.
7. Davis, S. J.; Caldeira, K.; Matthews, H. D., Future CO_2 Emissions and Climate Change from Existing Energy Infrastructure. *Science* **2010**, *329*, 1330–1333.
8. Lewis, N. S.; Nocera, D. G., Powering the Planet: Chemical Challenges in Solar Energy Utilization. *Proc. Natl. Acad. Sci. U.S.A.* **2006**, *103*, 15729–15735.
9. Nozik, A. J.; Miller, J., Introduction to Solar Photon Conversion. *Chem. Rev.* **2010**, *110*, 6443–6445.
10. Schnatbaum, L., Solar Thermal Power Plants. *Eur. Phys. J. Special Topics* **2009**, *176*, 127–140.
11. Cook, T. R.; Dogutan, D. K.; Reece, S. Y.; Surendranath, Y.; Teets, T. S.; Nocera, D. G., Solar Energy Supply and Storage for the Legacy and Nonlegacy Worlds. *Chem. Rev.* **2010**, *110*, 6474–6502.
12. Lewis, N. S., Toward Cost-Effective Solar Energy Use. *Science* **2007**, *315*, 798–801.
13. Kodama, T.; Gokon, N., Thermochemical Cycles for High-Temperature Solar Hydrogen Production. *Chem. Rev.* **2007**, *107*, 4048–4077.
14. Nocera, D. G., Chemistry of Personalized Solar Energy. *Inorg. Chem.* **2009**, *48*, 10001–10017.

15. Cox, J. D.; Pilcher, G., *Thermochemistry of Organic and Organometallic Compounds*. Academic Press: New York, 1970; p 636.
16. Doherty, M. D.; Grills, D. C.; Muckerman, J. T.; Polyansky, D. E.; Fujita, E., Toward More Efficient Photochemical CO_2 Reduction: Use of $scCO_2$ or Photogenerated Hydrides. *Coord. Chem. Rev.* **2010**, *254*, 2472–2482.
17. Technical Summary. In *IPCC Special Report: Carbon Dioxide Capture and Storage*, Metz, B.; Davidson, O.; Coninck, H. d.; Loos, M.; Meyer, L., Eds. Cambridge University Press: New York, 2005.
18. Chen, Z.; Jaramillo, T. F.; Deutsch, T. G.; Kleiman-Shwarsctein, A.; Forman, A. J.; Gaillard, N.; Garland, R.; Takanabe, K.; Heske, C.; Sunkara, M.; McFarland, E. W.; Domen, K.; Miller, E. L.; Turner, J. A.; Dinh, H. N., Accelerating Materials Development for Photoelectrochemical Hydrogen Production: Standards for Methods, Definitions, and Reporting Protocols. *J. Mater. Res.* **2010**, *25*, 3–16.
19. Lubitz, W.; Tumas, W., Hydrogen: An Overview. *Chem. Rev.* **2007**, *107*, 3900–3903.
20. Esswein, A. J.; Nocera, D. G., Hydrogen Production by Molecular Photocatalysis. *Chem. Rev.* **2007**, *107*, 4022–4047.
21. Navarro, R. M.; Peña, M. A.; Fierro, J. L. G., Hydrogen Production Reactions from Carbon Feedstocks: Fossil Fuels and Biomass. *Chem. Rev.* **2007**, *107*, 3952–3991.
22. Barreto, L.; Makihira, A.; Riahi, K., The Hydrogen Economy in the 21st Century: A Sustainable Development Scenario. *Int. J. Hydrogen Energy* **2003**, *28*, 267–284.
23. Bak, T.; Nowotny, J.; Rekas, M.; Sorrell, C. C., Photo-Electrochemical Hydrogen Generation from Water Using Solar Energy. Materials-Related Aspects. *Int. J. Hydrogen Energy* **2002**, *27*, 991–1022.
24. Gloaguen, F.; Rauchfuss, T. B., Small Molecule Mimics of Hydrogenases: Hydrides and Redox. *Chem. Soc. Rev.* **2009**, *38*, 100–108.
25. Vignais, P. M.; Billoud, B., Occurrence, Classification, and Biological Function of Hydrogenases: An Overview. *Chem. Rev.* **2007**, *107*, 4206–4272.
26. Cammack, R.; Frey, M.; Robson, R., *Hydrogen as a Fuel: Learning from Nature*. Taylor and Francis: New York, 2001.
27. Walter, M. G.; Warren, E. L.; McKone, J. R.; Boettcher, S. W.; Mi, Q.; Santori, E. A.; Lewis, N. S., Solar Water Splitting Cells. *Chem. Rev.* **2010**, *110*, 6446–6473.

28. Schüth, F., Challenges in Hydrogen Storage. *Eur. Phys. J. Special Topics* **2009**, *176*, 155–166.
29. Barber, J., Photosynthetic Energy Conversion: Natural and Artificial. *Chem. Soc. Rev.* **2009**, *38*, 185–196.
30. Loges, B.; Boddien, A.; Gärtner, F.; Junge, H.; Beller, M., Catalytic Generation of Hydrogen from Formic Acid and Its Derivatives: Useful Hydrogen Storage Materials. *Top. Catal.* **2010**, *53*, 902–914.
31. Pez, G. P.; Scott, A. R.; Cooper, A. C.; Cheng, H.; Wilhelm, F. C.; Abdourazak, A. H. Hydrogen Storage by Reversible Hydrogenation of pi-Conjugated Substrates. US 7351395 (B1), 2008.
32. Pez, G. P.; Cooper, A. C.; Scott, A. R. Autothermal Hydrogen Storage and Delivery Systems. WO 2009005872 (A2), 2009.
33. Hamilton, C. W.; Baker, R. T.; Staubitz, A.; Manners, I., B-N Compounds for Chemical Hydrogen Storage. *Chem. Soc. Rev.* **2009**, *38*, 279–293.
34. Graetz, J., New Approaches to Hydrogen Storage. *Chem. Soc. Rev.* **2009**, *38*, 73–82.
35. Sutton, A. D.; Burrell, A. K.; Dixon, D. A.; Garner, E. B.; Gordon, J. C.; Nakagawa, T.; Ott, K. C.; Robinson, J. P.; Vasiliu, M., Regeneration of Ammonia Borane Spent Fuel by Direct Reaction with Hydrazine and Liquid Ammonia. *Science* **2011**, *331*, 1426–1429.
36. Collins, D. J.; Zhou, H.-C., Hydrogen Storage in Metal-Organic Frameworks. *J. Mater. Chem.* **2007**, *17*, 3154–3160.
37. Ströbel, R.; Garche, J.; Moseley, P. T.; Jörissen, L.; Wolf, G., Hydrogen Storage by Carbon Materials. *J. Power Sources* **2006**, *159*, 781–801.
38. Wang, L.; Yang, R. T., New Sorbents for Hydrogen Storage by Hydrogen Spillover—A Review. *Energ. Environ. Sci.* **2008**, *1*, 268–279.
39. Yang, J.; Sudik, A.; Wolverton, C.; Siegel, D. J., High Capacity Hydrogen Storage Materials: Attributes for Automotive Applications and Techniques for Materials Discovery. *Chem. Soc. Rev.* **2010**, *39*, 656–675.
40. Chueh, W. C.; Falter, C.; Abbott, M.; Scipio, D.; Furler, P.; Haile, S. M.; Steinfeld, A., High-Flux Solar-Driven Thermochemical Dissociation of CO_2 and H_2O Using Nonstoichiometric Ceria. *Science* **2010**, *330*, 1797–1801.

41. Jones, G., II; Ramachandran, B. R., Catalytic Activity in the Reversion of an Energy Storing Valence Photoisomerization. *J. Org. Chem.* **1976**, *41*, 798–801.
42. Jones, G., II; Chiang, S.-H.; Xuan, P. T., Energy Storage in Organic Photoisomers. *J. Photochem.* **1979**, *10*, 1–18.
43. Scharf, H.-D.; Fleischhauer, J.; Leismann, H.; Ressler, I.; Schleker, W.-g.; Weitz, R., Criteria for the Efficiency, Stability, and Capacity of Abiotic Photochemical Solar Energy Storage Systems. *Angew. Chem. Int. Ed. Engl.* **1979**, *18*, 652–662.
44. Olmsted, J., III; Lawrence, J.; Yee, G. G., Photochemical Storage Potential of Azobenzenes. *Sol. Energy* **1983**, *30*, 271–274.
45. Yoshida, Z.-i., New Molecular Energy Storage Systems. *J. Photochem.* **1985**, *29*, 27–40.
46. Bren, V. A.; Dubonosov, A. D.; Minkin, V. I.; Chernoivanov, V. A., Norbornadiene–Quadricyclane—An Effective Molecular System for the Storage of Solar Energy. *Russ. Chem. Rev.* **1991**, *60*, 451–469.
47. Leffler, J. E.; Grunwald, E., *Rates and Equilibria of Organic Reactions*. Dover Publications, Inc.: New York, 1989.
48. Marcus, R. A.; Sutin, N., Electron Transfers in Chemistry and Biology. *BBA Bioenergetics* **1985**, *811*, 265–322.
49. Ruffo, R.; Hong, S. S.; Chan, C. K.; Huggins, R. A.; Cui, Y., Impedance Analysis of Silicon Nanowire Lithium Ion Battery Anodes. *J. Phys. Chem. C* **2009**, *113*, 11390–11398.
50. Ju, X.-H.; Wang, Z.-Y., Theoretical Study on Thermodynamic and Detonation Properties of Polynitrocubanes. *Propellants, Explosives, Pyrotechnics* **2009**, *34*, 106–109.
51. Handrick, G. R. *Report of the Study of Pure Explosive Compounds. Part IV. Calculation of Heat of Combustion of Organic Compounds from Structural Features and Calculation of Power of High Explosives*; C-58247; Office of the Chief of Ordinance, Naval Ordinance Laboratory: Cambridge, MA, 1956; pp 467–573.
52. Chase, M. W., *NIST-JANAF Thermochemical Tables*. 4th ed.; American Chemical Society: Washington, DC, 1998; Vol. 9, p 1951.
53. He, G. S.; Tan, L.-S.; Zheng, Q.; Prasad, P. N., Multiphoton Absorbing Materials: Molecular Designs, Characterizations, and Applications. *Chem. Rev.* **2008**, *108*, 1245–1330.

54. *Standard Tables for Reference Solar Spectral Irradiances: Direct Normal and Hemispherical on 37° Tilted Surface*; G173–03; ASTM International: West Conshohocken, PN, 2008; pp 1–21.

55. Becher, J.; Finsen, L.; Winckelmann, I.; Rao Koganty, R.; Buchardt, O., Derivatives and Reactions of Glutaconaldehyde-XII : Photochemical and Thermal Preparation of 5-Amino-2,4-pentadienenitriles. *Tetrahedron* **1981**, *37*, 789–793.

56. Klán, P.; Wirz, J., *Photochemistry of Organic Compounds: From Concepts to Practice*. John Wiley & Sons, Ltd: 2009.

57. Bouman, T. D.; Hansen, A. E., Electronic Spectra of Mono-olefins. RPA Calculations on Ethylene, Propene, and cis- and trans-2-Butene. *Chem. Phys. Lett.* **1985**, *117*, 461–467.

58. Walker, I. C.; Abuain, T. M.; Palmer, M. H.; Beveridge, A. J., The Electronic States of Propene Studied by Electron Impact Spectroscopy and ab initio Configuration Interaction Calculations. *Chem. Phys.* **1986**, *109*, 269–275.

59. Gary, J. T.; Pickett, L. W., The Far Ultraviolet Absorption Spectra of the Isomeric Butenes. *J. Chem. Phys.* **1954**, *22*, 599–602.

60. Douglas, J. E.; Rabinovitch, B. S.; Looney, F. S., Kinetics of the Thermal Cis–Trans Isomerization of Dideuteroethylene. *J. Chem. Phys.* **1955**, *23*, 315–323.

61. Huh, D. S.; Um, J. Y.; Yun, S. J.; Choo, K. Y.; Jung, K.-H., Gas Phase Thermal cis-trans Isomerization Reaction of 1-Bromopropene. *Bull. Korean Chem. Soc.* **1990**, *11*, 391–395.

62. Doering, W. v. E.; Kitagawa, T., Thermal Cis–Trans Rearrangement of Semirigid Polyenes as a Model for the Anticarcinogen *β*-Carotene: An a*ll-trans*-Pentaene and an *all-trans*-Heptaene. *J. Am. Chem. Soc.* **1991**, *113*, 4288–4297.

63. Görner, H.; Kuhn, H. J., *Cis–Trans* Photoisomerization of Stilbenes and Stilbene-like Molecules. In *Advances in Photochemistry*, Neckers, D. C.; Volman, D. H.; Bünau, G. v., Eds. John Wiley & Sons, Inc.: 1995; Vol. 19, pp 1–117.

64. Ross, D. L.; Blanc, J., Photochromism by *cis-trans* Isomerization. In *Photochromism*, Brown, G. H., Ed. Wiley-Interscience: New York, 1971; Vol. 3, pp 471–556.

65. Giuliano, C.; Hess, L.; Margerum, J., *cis–trans* Isomerization and Pulsed Laser Studies of Substituted Indigo Dyes. *J. Am. Chem. Soc.* **1968**, *90*, 587–594.

66. Nishimura, N.; Sueyoshi, T.; Yamanaka, H.; Imai, E.; Yamamoto, S.; Hasegawa, S., Thermal *Cis*-to-*Trans* Isomerization of Substituted Azobenzenes II. Substituent and Solvent Effects. *Bull. Chem. Soc. Jpn.* **1976**, *49*, 1381–1387.
67. Dilling, W. L., Intramolecular Photochemical Cycloaddition of Nonconjugated Olefins. *Chem. Rev.* **1966**, *66*, 373-393.
68. Frey, H. M., The Thermal Isomerisation of Quadricyclene (Quadricyclo-[2,2,1,02,6,03,5]heptane). Part I. The Gas-Phase Reaction. *J. Chem. Soc.* **1964**, 365–367.
69. Nagai, T.; Fujii, K.; Takahashi, I.; Shimada, M., Trifluoromethyl-Substituted Donor–Acceptor Norbornadiene, Useful Solar Energy Material. *Bull. Chem. Soc. Jpn.* **2001**, *74*, 1673–1678.
70. Bertelson, R. C., Photochromic Processes Involving Heterolytic Cleavage. In *Photochromism*, Brown, G. H., Ed. Wiley-Interscience: New York, 1971; Vol. 3, pp 45–431.
71. Bandara, H. M. D.; Friss, T. R.; Enriquez, M. M.; Isley, W.; Incarvito, C.; Frank, H. A.; Gascon, J.; Burdette, S. C., Proof for the Concerted Inversion Mechanism in the *trans→cis* Isomerization of Azobenzene Using Hydrogen Bonding To Induce Isomer Locking. *J. Org. Chem.* **2010**, *75*, 4817–4827.
72. Dürr, H.; Bouas-Laurent, H., *Photochromism: Molecules and Systems*. Elsevier: New York, 2003.
73. Johnsonb, K. E.; Johnston, D. B.; Lipsky, S., The Electron Impact Spectra of Some Mono-olefinic Hydrocarbons. *J. Chem. Phys.* **1979**, *70*, 3844–3858.
74. McDiarmid, R., A Reinvestigation of the Absorption Spectrum of Ethylene in the Vacuum Ultraviolet. *J. Phys. Chem.* **1980**, *84*, 64–70.
75. Flowers, M. C.; Jonathan, N., Kinetics of the Thermal and Nitric Oxide-Catalyzed Geometrical Isomerization of cis- and trans-Propylene-1-d_1. *J. Chem. Phys.* **1969**, *50*, 2805–2812.
76. Rabinovitch, B. S.; Michel, K. W., The Thermal Unimolecular cis-trans Isomerization of cis-Butene-2. *J. Am. Chem. Soc.* **1959**, *81*, 5065–5071.
77. Cundall, R. B.; Palmer, T. F., Thermal Isomerization of Butene-2. Part 1. *Transactions of the Faraday Society* **1961**, *57*, 1936–1941.

78. Jeffers, P. M.; Shaub, W., Shock Tube cis-trans Isomerization Studies. *J. Am. Chem. Soc.* **1969**, *91*, 7706–7709.
79. Dubonosov, A. D.; Bren, V. A.; Chernoivanov, V. A., Norbornadiene–Quadricyclane as an Abiotic System for the Storage of Solar Energy. *Russ. Chem. Rev.* **2002**, *71*, 917–927.
80. Taoda, H.; Hayakawa, K.; Kawase, K.; Yamakita, H., Photochemical Conversion and Storage of Solar Energy by Azobenzene. *J. Chem. Eng. Jpn.* **1987**, *20*, 265–270.
81. Pouliquen, J.; Wintgens, V.; Toscano, V.; Jaafar, B. B.; Tripathi, S.; Kossanyi, J.; Valat, P., Photoisomerization of *N*,*N′*-Disubstituted Indigos. A Search for Energy Storage. *Can. J. Chem.* **1984**, *62*, 2478–2486.
82. An, X.-w.; Xie, Y.-d., Enthalpy of Isomerization of Quadricyclane to Norbornadiene. *Thermochim. Acta* **1993**, *220*, 17–25.
83. Hammond, G. S.; Turro, N. J.; Fischer, A., Photosensitized Cycloaddition Reactions. *J. Am. Chem. Soc.* **1961**, *83*, 4674–4675.
84. Fu; Pushpa, K. K.; Schmid, W. E.; Trushin, S. A., Ultrafast [2 + 2]-Cycloaddition in Norbornadiene. *Photochemical & Photobiological Sciences* **2002**, *1*, 60–66.
85. Zou, J.-J.; Liu, Y.; Pan, L.; Wang, L.; Zhang, X., Photocatalytic Isomerization of Norbornadiene to Quadricyclane over Metal (V, Fe and Cr)-Incorporated Ti-MCM-41. *Appl. Catal. B: Environmental* **2010**, *95*, 439–445.
86. Nagai, T.; Takahashi, I.; Shimada, M., Trifluoromethyl-Substituted Norbornadiene, Useful Solar Energy Material. *Chem. Lett.* **1999**, *28*, 897–898.
87. Bishop, K. C., Transition Metal Catalyzed Rearrangements of Small Ring Organic Molecules. *Chem. Rev.* **1976**, *76*, 461–486.
88. Jones, G., II; Becker, W. G.; Chiang, S. H., Variations in Mechanism for Photoinduced Valence Isomerization of an Electron-Donor Nonconjugated Diene. *J. Am. Chem. Soc.* **1983**, *105*, 1269–1276.
89. Schäfer, W.; Hellmann, H., Hexamethyl(Dewar Benzene) (Hexamethylbicyclo[2.2.0]hexa-2,5-diene). *Angew. Chem. Int. Ed. Engl.* **1967**, *6*, 518–525.
90. Ferrar, L.; Mis, M.; Robello, D. R., Thermal isomerization of dewarbenzene derivatives. *Tetrahedron Lett.* **2008**, *49*, 4130–4133.
91. Oth, J. F. M., The Kinetics and Thermochemistry of the Termal Rearrangement of Hexamethylbicyclo[2.2.0]hexa-2,5-diene (Hexamethyldewarbenzene) and of

Hexamethyltetracyclo[2.2.0,$0^{2,6}$.$0^{3,5}$]hexane (Hexamethylprismane). *Recueil des Travaux Chimiques des Pays-Bas* **1968**, *87*, 1185–1195.

92. Woodward, R. B.; Hoffmann, R., The Conservation of Orbital Symmetry. *Angew. Chem. Int. Ed. Engl.* **1969**, *8*, 781–853.
93. Smith, M. B.; March, J., *March's Advanced Organic Chemistry: Reactions, Mechanisms, and Structure*. 5th ed.; John Wiley & Sons, Inc.: New York, 2001.
94. Norton, J. E.; Olson, L. P.; Houk, K. N., Theoretical Studies of Quantum Amplified Isomerizations for Imaging Systems Involving Hexamethyl Dewar Benzene and Related Systems. *J. Am. Chem. Soc.* **2006**, *128*, 7835–7845.
95. Dračínský, M.; Castaño, O.; Kotora, M.; Bouř, P., Rearrangement of Dewar Benzene Derivatives Studied by DFT. *J. Org. Chem.* **2010**, *75*, 576–581.
96. Hogeveen, H.; Volger, H. C., Catalytic Effects in the Valence Isomerizations of Hexamethyltetracyclo[2,2,0,02,6,03,5]hexane. *Chemical Communications (London)* **1967**, 1133–1134.
97. Adam, W.; Chang, J. C., The Kinetics and Thermochemistry of Valence Isomerization by Differential Scanning Calorimetry: The Case of Hexamethylprismane and Hexamethyldewarbenzene. *Int. J. Chem. Kinet.* **1969**, *1*, 487–492.
98. Lechkten, P.; Breslow, R.; Schmidt, A. H.; Turro, N. J., Thermal Rearrangement of Dewar Benzenes to Benzene Triplet States. Examples of Spin Forbidden Nonadiabatic Pericyclic Reactions. *J. Am. Chem. Soc.* **1973**, *95*, 3025–3027.
99. Van Tamelen, E. E., Valence Bond Isomers of Aromatic Systems. *Acc. Chem. Res.* **1972**, *5*, 186–192.
100. Havenith, R. W. A.; Jenneskens, L. W.; van Lenthe, J. H., Disrotatory versus Conrotatory Electrocyclic Ring Opening of Dewar Benzene: The Conrotatory Pathway is Preferred and Does Not Involve *trans*-Benzene. *J. Mol. Struc.—THEOCHEM* **1999**, *492*, 217–224.
101. Zollinger, H., *Color Chemistry: Syntheses, Properties, and Applications of Organic Dyes and Pigments*. 2nd ed.; VCH Publishers: New York, 1991.
102. Tsuji, T.; Ohkita, M.; Kawai, H., Preparation and Kinetic Stabilization of Highly Strained Paracyclophanes. *Bull. Chem. Soc. Jpn.* **2002**, *75*, 415–433.
103. Diau, E. W.-G., A New Trans-to-Cis Photoisomerization Mechanism of Azobenzene on the S1(n,π*) Surface. *J. Phys. Chem. A* **2004**, *108*, 950–956.

104. Tiberio, G.; Muccioli, L.; Berardi, R.; Zannoni, C., How Does the *trans–cis* Photoisomerization of Azobenzene Take Place in Organic Solvents? *ChemPhysChem* **2010**, *11*, 1018–1028.

105. Asano, T.; Okada, T.; Shinkai, S.; Shigematsu, K.; Kusano, Y.; Manabe, O., Temperature and pressure dependences of thermal *cis*-to-*trans* isomerization of azobenzenes which evidence an inversion mechanism. *J. Am. Chem. Soc.* **1981**, *103*, 5161–5165.

106. Asano, T., Pressure Effects on the Thermal *cis→trans* Isomerization of 4-Dimethylamino-4'-nitroazobenzene. Evidence For a Change of Mechanism with Solvent. *J. Am. Chem. Soc.* **1980**, *102*, 1205–1206.

107. Asano, T.; Okada, T., Further Kinetic Evidence for the Competitive Rotational and Inversional *Z-E* Isomerization of Substituted Azobenzenes. *J. Org. Chem.* **1986**, *51*, 4454–4458.

108. Nishimura, N.; Tanaka, T.; Asano, M.; Sueishi, Y., A Volumetric Study on the Thermal *cis*-to-*trans* Isomerization of 4-(Dimethylamino)-4′-nitroazobenzene and 4,4′-Bis(dialkylamino)azobenzenes: Evidence of an Inversion Mechanism. *J. Chem. Soc., Perkin Trans. 2* **1986**, 1839–1845.

109. Weener, J. W.; Meijer, E. W., Photoresponsive Dendritic Monolayers. *Adv. Mater.* **2000**, *12*, 741–746.

110. Yabe, A.; Kawabata, Y.; Niino, H.; Tanaka, M.; Ouchi, A.; Takahashi, H.; Tamura, S.; Tagaki, W.; Nakahara, H.; Fukuda, K., cis–trans Isomerization of the Azobenzenes Included as Guests in Langmuir–Blodgett Films of Amphiphilic β-Cyclodextrin. *Chem. Lett.* **1988**, *17*, 1–4.

111. Nishiyama, K.; Fujihira, M., cis–trans Reversible Photoisomerization of an Amphiphilic Azobenzene Derivative in Its Pure LB Film Prepared as Polyion Complexes with Polyallylamine. *Chem. Lett.* **1988**, *17*, 1257–1260.

112. Matsumoto, M.; Miyazaki, D.; Tanaka, M.; Azumi, R.; Manda, E.; Kondo, Y.; Yoshino, N.; Tachibana, H., Reversible Light-Induced Morphological Change in Langmuir–Blodgett Films. *J. Am. Chem. Soc.* **1998**, *120*, 1479–1484.

113. Ikegami, M.; Arai, T., Photoisomerization and Fluorescence Properties of Hemiindigo Compounds Having Intramolecular Hydrogen Bonding. *Bull. Chem. Soc. Jpn.* **2003**, *76*, 1783–1792.

114. Miehe, G.; Süsse, P.; Kupcik, V.; Egert, E.; Nieger, M.; Kunz, G.; Gerke, R.; Knieriem, B.; Niemeyer, M.; Lüttke, W., Light Absorption as well as Crystal and Molecular Structure of N,N'-Dimethylindigo : An Example of the Use of Synchrotron Radiation. *Angew. Chem. Int. Ed. Engl.* **1991**, *30*, 964–967.

115. Adamson, A. W.; Vogler, A.; Kunkely, H.; Wachter, R., Photocalorimetry. Enthalpies of Photolysis of *trans*-Azobenzene, Ferrioxalate and Cobaltioxalate Ions, Chromium Hexacarbonyl, and Dirhenium Decarbonyl. *J. Am. Chem. Soc.* **1978**, *100*, 1298–1300.

116. Kanai, Y.; Srinivasan, V.; Meier, S. K.; Vollhardt, K. P. C.; Grossman, J. C., Mechanism of Thermal Reversal of the (Fulvalene)tetracarbonyldiruthenium Photoisomerization: Toward Molecular Solar–Thermal Energy Storage. *Angew. Chem. Int. Ed.* **2010**, *49*, 8926–8929.

117. Boese, R.; Cammack, J. K.; Matzger, A. J.; Pflug, K.; Tolman, W. B.; Vollhardt, K. P. C.; Weidman, T. W., Photochemistry of (Fulvalene)tetracarbonyldiruthenium and Its Derivatives: Efficient Light Energy Storage Devices. *J. Am. Chem. Soc.* **1997**, *119*, 6757–6773.

118. Vollhardt, K. P. C.; Weidman, T. W., Synthesis, Structure, and Photochemistry of Tetracarbonyl(fulvalene)diruthenium. Thermally Reversible Photoisomerization Involving Carbon–Carbon Bond Activation at a Dimetal Center. *J. Am. Chem. Soc.* **1983**, *105*, 1676–1677.

119. Liao, G.-H.; Luo, L.; Xu, H.-X.; Wu, X.-L.; Lei, L.; Tung, C.-H.; Wu, L.-Z., Formation of Cubane-like Photodimers from 2-Naphthalenecarbonitrile. *J. Org. Chem.* **2008**, *73*, 7345–7348.

120. Luo, L.; Cheng, S.-F.; Chen, B.; Tung, C.-H.; Wu, L.-Z., Stepwise Photochemical-Chiral Delivery in γ-Cyclodextrin-Directed Enantioselective Photocyclodimerization of Methyl 3-Methoxyl-2-Naphthoate in Aqueous Solution. *Langmuir* **2010**, *26*, 782–785.

121. Luo, L.; Liao, G.-H.; Wu, X.-L.; Lei, L.; Tung, C.-H.; Wu, L.-Z., γ-Cyclodextrin-Directed Enantioselective Photocyclodimerization of Methyl 3-Methoxyl-2-naphthoate. *J. Org. Chem.* **2009**, *74*, 3506–3515.

122. Bouas-Laurent, H.; Castellan, A.; Desvergne, J.-P.; Lapouyade, R., Photodimerization of Anthracenes in Fluid Solutions: (Part 2) Mechanistic Aspects of the Photocycloaddition and of the Photochemical and Thermal Cleavage. *Chem. Soc. Rev.* **2001**, *30*, 248–263.

123. Uchida, M.; Irie, M., Two-Photon Photochromism of a Naphthopyran Derivative. *J. Am. Chem. Soc.* **1993**, *115*, 6442–6443.

124. Ishikawa, T.; Noro, T.; Shoda, T., Theoretical Study on the Photoisomerization of Azobenzene. *J. Chem. Phys.* **2001**, *115*, 7503–7512.

125. Strambi, A.; Coto, P. B.; Frutos, L. M.; Ferré, N.; Olivucci, M., Relationship between the Excited State Relaxation Paths of Rhodopsin and Isorhodopsin. *J. Am. Chem. Soc.* **2008**, *130*, 3382–3388.

126. Asano, Y.; Murakami, A.; Kobayashi, T.; Goldberg, A.; Guillaumont, D.; Yabushita, S.; Irie, M.; Nakamura, S., Theoretical Study on the Photochromic Cycloreversion Reactions of Dithienylethenes; on the Role of the Conical Intersections. *J. Am. Chem. Soc.* **2004**, *126*, 12112–12120.

127. Boggio-Pasqua, M.; Bearpark, M. J.; Hunt, P. A.; Robb, M. A., Dihydroazulene/Vinylheptafulvene Photochromism: A Model for One-Way Photochemistry via a Conical Intersection. *J. Am. Chem. Soc.* **2002**, *124*, 1456–1470.

128. Saltiel, J.; Sun, Y.-P., Cis-Trans Isomerizations of C=C Double Bonds. In *Photochromism: Molecules and Systems*, Dürr, H.; Bouas-Laurent, H., Eds. Elsevier: New York, 2003; pp 64–162.

129. Schick, G. A.; Cooper, T. M.; Holloway, R. A.; Murray, L. P.; Birge, R. R., Energy Storage in the Primary Photochemical Events of Rhodopsin and Isorhodopsin. *Biochemistry* **1987**, *26*, 2556–2562.

130. Bouas-Laurent, H.; Dürr, H., Organic Photochromism. *Pure Appl. Chem.* **2001**, *73*, 639–665.

131. Rau, H., Azo Compounds. In *Photochromism: Molecules and Systems*, Dürr, H.; Bouas-Laurent, H., Eds. Elsevier: New York, 2003; pp 165–192.

132. Dürr, H., 4n+2 Systems Based on 1,5-Electrocyclization. In *Photochromism: Molecules and Systems*, Dürr, H.; Bouas-Laurent, H., Eds. Elsevier: New York, 2003; pp 210–269.

133. Guglielmetti, R., 4n+2 Systems: Spiropyrans. In *Photochromism: Molecules and Systems*, Dürr, H.; Bouas-Laurent, H., Eds. Elsevier: New York, 2003; pp 314–466.

134. Whittal, J., 4n+2 Systems: Fulgides. In *Photochromism: Molecules and Systems*, Dürr, H.; Bouas-Laurent, H., Eds. Elsevier: New York, 2003; pp 467–492.

135. Hayakawa, J.; Momotake, A.; Arai, T., Water-Soluble Stilbene Dendrimers. *Chem. Comm.* **2003**, 94–95.

136. Pepekin, V., Tendencies in the Development of Studies of High Explosives. *Russ. J. Phys. Chem. B* **2010**, *4*, 954–962.

137. Sinditskii, V. P.; Egorshev, V. Y.; Levshenkov, A. I.; Serushkin, V. V., Ammonium Nitrate: Combustion Mechanism and the Role of Additives. *Propellants, Explosives, Pyrotechnics* **2005**, *30*, 269–280.

138. Earnshaw, A.; Greenwood, N., *Chemistry of the Elements*. 2nd ed.; Butterworth–Heinemann: New York, 1997.

139. Kreith, F., *The CRC Handbook of Thermal Engineering*. CRC Press: Boca Raton, FL, 2000.

140. Jia, H.; Gogos, G., Laminar Natural Convection Heat Transfer from Isothermal Spheres. *Int. J. Heat Mass Transfer* **1996**, *39*, 1603–1615.

141. Irie, M.; Uchida, K., Synthesis and Properties of Photochromic Diarylethenes with Heterocyclic Aryl Groups. *Bull. Chem. Soc. Jpn.* **1998**, *71*, 985–996.

142. Hampp, N.; Bräuchle, C., Bacteriorhodopsin and Its Functional Variants: Potential Applications in Modern Optics. In *Photochromism: Molecules and Systems*, Dürr, H.; Bouas-Laurent, H., Eds. Elsevier: New York, 2003; pp 954–975.

143. U. S. Energy Information Administration Gasoline and Diesel Fuel Update. http://tonto.eia.doe.gov/oog/info/gdu/gasdiesel.asp

144. California Public Utilities Commission http://www.cpuc.ca.gov/puc/

145. Daniel, C., Materials and Processing for Lithium-Ion Batteries. *JOM* **2008**, *60*, 43–48.

146. Kucharski, T. J.; Boulatov, R., The Physical Chemistry of Mechanoresponsive Polymers. *J. Mater. Chem.* **2011**, *21*, 8237–8255.

147. Huang, Z.; Boulatov, R., Chemomechanics: Reaction Kinetics in Multiscale Phenomena. *Chem. Soc. Rev.* **2011**, *40*, 2359–2384.

148. Yang, Q.-Z.; Huang, Z.; Kucharski, T. J.; Khvostichenko, D.; Chen, J.; Boulatov, R., A Molecular Force Probe. *Nat. Nanotechnol.* **2009**, *4*, 302–306.

Timothy J. Kucharski

908 N Broadway Avenue, #523
Urbana, IL 61801
217-898-7556 tkuchar2@illinois.edu

Education

Ph.D., Chemistry, University of Illinois at Urbana–Champaign, anticipated May/June 2011
  Advisor: Prof. Roman Boulatov
  Dissertation Title: *A Quantitative and Predictive Model for Mechanochemical Kinetics and Its Experimental Validation*

B.S., *summa cum laude*, Chemistry, The University of Alabama, May 2006
  4.00/4.00 GPA
  Advisor: Prof. Silas C. Blackstock
  Honors Thesis Title: *Quinone Radical Anion Hydrogen Bonding and Donor-Acceptor Synthons for Crystal Engineering*

Research Positions

Postdoctoral Associate
  Massachusetts Institute of Technology, July 2011–
  Advisors: Prof. Daniel G. Nocera (Chemistry) and
  Prof. Jeffrey C. Grossman (Materials Science and Engineering)
  Synthesizing and characterizing novel materials for solar thermal fuels

NSF and NDSEG Fellow
  University of Illinois at Urbana–Champaign, July 2006–June 2011
  Advisor: Prof. Roman Boulatov
  Studying the effects of force on chemical reactivity and co-developing its conceptual framework

Undergraduate Researcher
  The University of Alabama, Spring 2004–Spring 2006, excluding Summer 2005
  Advisor: Prof. Silas C. Blackstock
  Studied electron donor-acceptor complexes of small organics and their co-crystallization

Research Internships in Science and Engineering
  Justus-Liebig Universität Gießen, Germany, Summer 2005
  Advisor: Prof. Peter R. Schreiner
  Synthesized conjugated enynes for the preparation of carbon-rich materials

Publications (8 total, 3 journal covers)

Ph.D.

Kucharski, T. J.; Boulatov, R., The Physical Chemistry of Mechanoresponsive Polymers. *J. Mater. Chem.* **2011**, *21*, 8237–8255. (invited review) **Journal cover**.

Kucharski, T. J.; Boulatov, R., Fundamentals of Molecular Photoactuation. In *Optical Nano and Micro Actuator Technology*, Knopf, G. K.; Otani, Y., Eds. CRC Press: **2011**, accepted. (invited book chapter)

Kucharski, T. J.; Yang, Q.-Z.; Tian, Y.; Boulatov, R., Strain-Dependent Acceleration of a Paradigmatic S_N2 Reaction Accurately Predicted by the Force Formalism. *J. Phys. Chem. Lett.* **2010**, *1*, 2820–2825.

Kucharski, T. J.; Huang, Z.; Yang, Q.-Z.; Tian, Y.; Rubin, N. C.; Concepcion, C. D; Boulatov, R., Kinetics of Thiol/Disulfide Exchange Correlates Weakly with the Restoring Force in the Disulfide Moiety. *Angew. Chem. Int. Ed.* **2009**, *48*, 7040–7043. **VIP article**; **Journal cover**; **Highlights**: *Chem. Eng. News* August 24, 2009, p 10; *Science Daily* June 28, 2009; *Inside Illinois* July 16, 2009, p 8.

Huang, Z.; Yang, Q.-Z..; **Kucharski, T. J.**; Khvostichenko, D.; Wakeman, S. M.; Boulatov, R., Macrocyclic disulfides for studies of sensitized photolysis of the S–S bond. *Chem. Eur. J.* **2009**, *15*, 5212–5214.

Yang, Q.-Z.*; Huang, Z.*; **Kucharski, T. J.***; Khvostichenko, D.*; Chen, J.; Boulatov, R., A Molecular Force Probe. *Nat. Nanotechnol.* **2009**, *4*, 302–306. (*equal contribution) **Journal cover**; **Editorial**: *Nat. Nanotechnol.* **2009**, *4*, 271; **Commentary**: *Nat. Nanotechnol.* **2009**, *4*, 284-285. **Highlights**: *Nature* **2009**, *458*, 552; MarketWatch.com, March 29, 2009; *Chemistry World*, March 31, 2009.

Huang, Z.; Yang, Q.-Z.; Khvostichenko, D.; **Kucharski, T. J.**; Chen, J.; Boulatov, R., Method to Derive Restoring Forces of Strained Molecules from Kinetic Measurements. *J. Am. Chem. Soc.* **2009**, *131* (4), 1407–1409.

Undergraduate

Kucharski, T. J.; Oxsher, J. R.; Blackstock, S. C., Pyrazine-*N*,*N'*-dioxide/Tetracyanoethylene Electron Donor–Acceptor Bonding and the Effect of Donor Steric Demand and Symmetry on the Cocrystal Assembly. *Tetrahedron Lett.* **2006**, *47* (27), 4569–4572.

Teaching and Mentoring Experience

Graduate Research Fellow, Boulatov research group

University of Illinois, Summer 2007–Summer 2010

Trained 2–5 undergraduates per semester in synthetic and analytical techniques relevant to the research

Instructed the students in the use of data recording and processing software

Provided further explanation of chemical concepts the students encounter in research and coursework

Illustrated principles of experimental design with multi-method kinetics experiments

Teaching Assistant, Advanced Inorganic Chemistry Laboratory

University of Illinois, Spring 2007

Demonstrated and taught procedures for air- and moisture-sensitive synthetic techniques

Instructed students (two sections of ~10) in safely handling toxic or pyrophoric chemicals and cryogens

Assessed written lab reports and provided feedback on technical writing skills

Prepared equipment and supplies for upcoming experiments

Teaching Assistant, Introductory Chemistry

University of Illinois, Fall 2006

Instructed two sections of 20–25 students in materials not covered in lecture

Instructed the students in the corresponding laboratory sections

Graded tests, quizzes, and lab reports

Held office hours

Research Presentations as Actual Presenter

Ph.D.

Kucharski, T. J.; Yang, Q.-Z.; Akbulatov, S.; Huang, Z.; Boulatov, R., Predicting the Observed Effect of Force on S_N2 Cleavage Kinetics of C–O, Si–O, and P–O Bonds. Oral presentation at the 240th ACS National Meeting, Boston, MA, August 22–26, 2010.

Boulatov, R.; **Kucharski, T. J.**, Molecular Force Probes for Studying Reaction Kinetics Under Force. Oral presentation at the 240th ACS National Meeting, Boston, MA, Augsust 22–26, 2010.

Kucharski, T. J.; Yang, Q.-Z.; Tian, Y.; Rubin, N. C.; Boulatov, R., Changing Reaction Mechanisms with Force. Poster presentation at the 240th ACS National Meeting, Boston, MA, August 22–26, 2010.

Kucharski, T. J.; Huang, Z.; Yang, Q.-Z.; Akbulatov, S.; Boulatov, R., Experimental Validation of a Chemomechanical Model: Bridging the μm–nm Gap. Poster presentation at the 240th ACS National Meeting, Boston, MA, August 22–26, 2010.

Research Presentations as Actual Presenter, Continued

Boulatov, R.; **Kucharski, T. J.**; Akbulatov, S., Using Force as a Molecular Ruler: Insights into Substitutions at Phosphorus. Poster presentation at the 240th ACS National Meeting, Boston, MA, August 22–26, 2010.

Kucharski, T. J.; Akbulatov, S.; Tian, Y.; Yang, Q.-Z.; Boulatov, R., A Predictive Model for Force-Dependent S_N2 Reaction Kinetics. Poster presentation at the Inorganic Chemistry Gordon Research Conference and Graduate Research Seminar, University of New England, Biddeford, ME, June 19–25, 2010.

Kucharski, T. J.; Huang, Z.; Yang, Q.-Z.; Khvostichenko, D.; Tian, Y.; Wang, B.; Li, C.; Rubin, N. C.; Concepcion, C. D.; Boulatov, R., Testing the Intuitive: Does Pulling Always Accelerate Bond Scission? Poster presentation at the Inorganic Chemistry Gordon Research Conference and Graduate Research Seminar, University of New England, Biddeford, ME, June 20–26, 2009.

Undergraduate

Kucharski, T. J.; McGee, B. J.; Blackstock, S. C., Neutral and Ionic Cocrystals: Determining the Nature of the Cation. Poster presentation at the 231st ACS National Meeting, Atlanta, GA, March 2006.

Kucharski, T. J.; McGee, B. J.; Blackstock, S. C., Proposal of a Unique Inner-Sphere Electron Transfer Cocrystallization Process. Poster presentation at the 56th Southeast Regional Meeting of the American Chemical Society, Durham, NC, November 2004.

Research Grants Awarded as Primary Investigator

TeraGrid Startup Allocation (renewal): The Inverted Region of Chemomechanics (TG-CHE080018), 2011

TeraGrid Startup Allocation: Validation of the Standard Chemomechanical Model for the Simplest Case of Corrugated Energy Landscapes (TG-CHE080018), 2010

TeraGrid Startup Allocation (renewal): The Effects of Tensile Force and Nucleophile Donation Ability on Transition State Structures for Disulfide Cleavage (TG-CHE080021N), 2009

TeraGrid Startup Allocation: Method Benchmarking and Preliminary Modeling of Disulfide Scission Reaction Kinetics Towards a Chemomechanical Model (TG-CHE080021N), 2008

Honors Conferred

Ph.D.

- Member of the US delegation to the 59th Meeting of Nobel Laureates in Lindau, Germany, 2009
- National Defense Science and Engineering Graduate (NDSEG) Fellowship, Sept 2007–Aug 2010

Honors Conferred, Continued

- National Science Foundation Graduate Research Fellowship (NSF GRF), Jun–Sept 2007, Sept 2010–June 2011
- Roger Adams Fellowship (University of Illinois, Department of Chemistry), 2006

Undergraduate

- Distinguished Undergraduate Scholar (highest scholastic average in the class of 2006)
- Phi Beta Kappa, 2006
- American Institute of Chemists Award, 2006
- Randal Undergraduate Research Award, 2006
- Outstanding Chemistry Student Award, 2005
- Analytical Chemistry Award, 2004
- Presidential Scholarship, 2002

Activities and Affiliations

- Solution checking and reworking for Wilson, R. *Solutions to Exercises*, Pearson Prentice Hall, Boston, 2012 (see credit in Introduction), to accompany Brown, T. E.; Lemay, H. E. H.; Bursten, B. E.; Murphy, C. and Woodward, P. *Chemistry: The Central Science*, 12th edn., Prentice Hall, Boston, 2011.
- Co-chair for the 2010 Inorganic Chemistry Gordon Conference Graduate Research Seminar
- Inorganic/Materials Chemistry Student-Selected Seminar Committee, 2007–2011
- Member of the American Chemical Society, 2006–present